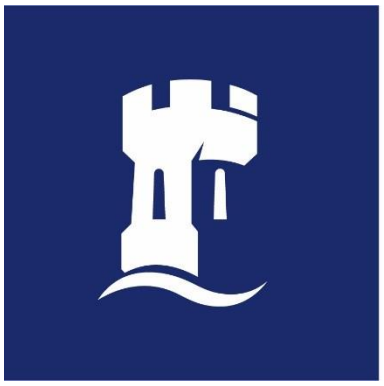


University of Nottingham

UK | CHINA | MALAYSIA

Fabrication and Investigation of Carbon Materials for Carbon Dioxide Capture and Hydrogen Storage Prepared via Templating or Activation Routes

Norah Balahmar

Thesis Submitted to The University of Nottingham for the Degree of Doctor of Philosophy

July 2018



وَمَا تَوْفِيقِي إِلَّا بِاللَّهِ عَلَيْهِ تَوَكَّلْتُ وَإِلَيْهِ أُنِيبُ

وَقُل رَّبِّ أَدْخِلْنِي مُدْخَلَ صِدْقٍ

وَأَخْرِجْنِي مُخْرَجَ صِدْق

وَاجْعَل لِّي مِن لَّدُنكَ سُلْطَانًا نَّصِيرًا

Research Aims and Objectives

The aims of my thesis are dedicated to the following aspects:

- Firstly, to design, fabricate and customize synthesis conditions to produce carbon-based solid adsorbent materials (that are either zeolite templated carbons ZTCs or activated carbons ACs) for enhanced gas storage (hydrogen and carbon dioxide).

- Secondly, to examine the chemical and physical properties (i.e. surface area, pore volume, and pore structure) of the generated carbons and their properties for CO_2 and H_2 uptake.

- Finally, to relate the fundamental properties of the synthesised materials to the mechanism of their preparation, and to examine and explore the effect of the carbon precursor, synthesis temperature, amount of activating agent (KOH) and/or post-synthesis modifications on their performance for CO_2 and H_2 uptake at low and high pressures and various temperatures.

Abstract

This thesis details the preparation, fabrication and characterization of nanostructured carbonaceous materials with tuneable porosity for gas storage (CO_2 and H_2) applications. Two types of carbon-based materials were investigated, namely zeolite templated carbons (ZTCs) and activated carbons (ACs). The ZTCs were prepared using zeolite 13X and zeolite Y as hard templates and furfural alcohol, ethylene, and acetonitrile as carbon precursors. The effects of zeolite compaction before use as hard templates were investigated through the compression of powder forms of zeolites at 370 MPa (equivalent to 5 tonnes) or 740 MPa (equivalent to 10 tonnes) prior to their use as templates. A combination of liquid impregnation (LI) with furfural alcohol and chemical vapour deposition (CVD) with ethylene, or acetonitrile was used to deposit the carbon precursor.

Activated carbons (ACs) were prepared using KOH as activating agent from various carbon precursors namely, (i) Eucalyptus wood sawdust (as a cheap, green, renewable and abundantly available raw material), (ii) Lignin-derived carbonaceous matter, (iii) Polythiophene as a sulphur-rich polymer, and (iv) Polypyrrole as a Nitrogen-rich polymer. The activated carbons were prepared *via* two different routes; (1) activation *via* thermal treatment of a powder mixture of starting materials and activating agent (KOH) or (2) compactivation (or mechanochemical activation) wherein the mixture of the starting material and KOH is compacted at 5 tonnes (equivalent to 370 MPa) or 10 tonnes (equivalent to 740 MPa) into a pellets/disks prior to activation. The compactivation route was found to be more efficient as it reduces/ removes interparticles voids and space between solid-solid and thus enhances chemical interaction between the precursor and KOH, and also improves both the porosity and the bulk density of the resulting activated carbon.

Thesis Structure

This thesis has seven chapters

Chapter 1

Introduction: Presents the motivation, challenges, foundation and background (by way of describing nanostructured materials and their fundamental proprieties and their applications).

Chapter 2

Methods and Characterization Techniques: Describes the synthesis tools/equipment used for material fabrication, production, characterization and assessment of potential applications.

Chapter 3

Templating of Carbon in Zeolites under Pressure: Synthesis of Pelletized Zeolite Templated Carbons with Improved Porosity and Packing Density for Superior Gas (CO_2 and H_2) Uptake Properties: This chapter explores the use of compacted zeolite Y and zeolite 13X as hard templates for the preparation of pelletized zeolite templated carbons (ZTCs).

Chapter 4

Polythiophene-Derived Activated Carbons: This chapter presents S-doped activated carbons from a sulphur-rich polymer (polythiophene).

Chapter 5

Generalized Mechanochemical Synthesis of Biomass - Derived Sustainable Carbons for High Performance CO_2 Storage: In this chapter, novel mechanochemical activation generates biomass-derived carbons with unprecedented CO_2 storage capacity due to higher porosity than analogous conventionally activated carbons but similar pore size.

Chapter 6

Biomass to Porous Carbon in One Step: Directly Activated Biomass for High Performance CO_2 Storage: This chapter explores the direct conversion of biomass to activated carbons in one step using biomass source namely, sawdust, to activated carbons *via* a direct activation process that negates the need for hydrothermal carbonization or pyrolysis. This is a departure from established practice that requires biomass sources to be first enriched to carbonaceous matter *via* hydrothermal carbonization or pyrolysis prior to activation.

Chapter 7

Premixed Precursors for Mediating the Porosity of Activated Carbons for Gas Storage (CO_2 and H_2) Applications: In this chapter, high to very high surface area activated carbons were successfully prepared from premixed precursors containing polypyrrole and sawdust or sawdust-derived hydrochar.

Chapter 8

Conclusions and Further Work: In this chapter, a brief overall conclusion, summaries, and suggestions on further work are presented.

List of Publications

1) Generalized Mechanochemical Synthesis of Biomass-Derived Sustainable Carbons for High Performance CO_2 Storage.

   Norah Balahmar, Andrew C. Mitchell, Robert Mokaya, *Adv. Energy Mater.,* **2015,** *5*, 1500867.

2) Templating of Carbon in Zeolites under Pressure: Synthesis of Pelletized Zeolite Templated Carbons with Improved Porosity and Packing Density for Superior Gas (CO_2 and H_2) Uptake Properties.

   Norah Balahmar, Alexander M. Lowbridge and Robert Mokaya*, J. Mater. Chem. A*, **2016**, 4, 14254–14266.

3) High Yield and High Packing Density Porous Carbon for Unprecedented CO_2 Capture from the First Attempt at Activation of Air-Carbonized Biomass.

   Ephraim Haffner-Staton, **Norah Balahmar**, Robert Mokaya, *J. Mater. Chem. A*, **2016**, 4, 13324-13335.

4) Highly Porous Renewable Carbons for Enhanced Storage of Energy-Related Gases (H_2 and CO_2) at High Pressures.

   Marta Sevilla, Wantana Sangchoom, **Norah Balahmar**, Antonio B. Fuertes, and R. Mokaya, *ACS Sustainable Chem. Eng.,* **2016,** 4, 4710-4716.

5) Biomass to Porous Carbon in One Step: Directly Activated Biomass for High Performance CO_2 Storage.

Norah Balahmar, Abdul S. Al-Jumialy and Robert Mokaya, *J. Mater. Chem. A*, 5, **2017**, 12330.

6) Oxygen-rich Microporous Carbons with Exceptional Hydrogen Storage Capacity.

Troy Scott Blankenship, **Norah Balahmar** and Robert Mokaya, *Nat. Commun.*, 8, **2017**, 12.

Poster and Presentation Sessions

Posters Presentations

1) Norah Balahmar and Robert Mokaya, Physical Chemistry Postgraduate Symposium, **13th July 2016**, University of Nottingham.

2) Norah Balahmar and Robert Mokaya, Synthesis, Modifications and Characterization of Activated and Compactivated Carbons for Gas Storage, the 6th Postgraduate Symposium on Nanoscience and Nanotechnology, **13th December 2016**, University of Birmingham.

3) Norah Balahmar and Robert Mokaya, Conference A Sustainable Future through New Materials for Energy by Energy Technologies Research Institute (ETRI), **10th Jan 2017**, Synthesis and Characterization of Polythiophene-Derived Activated and Compactivated Carbons for Gas Storage Applications, University of Nottingham.

Attendance

1) Engineering Distinguished Lecture in Collaboration with the Energy Research Accelerator by Prof Sir David King HonFEI 'COP21 and the Post-Paris Energy Transition, Organized by Faculty of Engineering Events Team, **2nd February 2017**, University of Nottingham.

2) Research Workshop Series–Hydrogen and Fuel Cells, Organized by Energy Technologies Research Institute (ETRI), **22nd March 2017**, University of Nottingham.

3) Navigating A Changing Energy Landscape by Dr Craig Edgar, Organized by Energy Technologies Research Institute (ETRI), **7th September 2017**, The University of Nottingham.

4) The 2nd One Day Meeting on the High-Pressure XPS of Energy Materials (HP-XPS-EM2), Organized by Energy Technologies Research Institute (ETRI), **20th September 2017**, University of Nottingham.

5) How Can We Ensure buildings are "Net Zero" Carbon by 2050, Organized by Energy Technologies Research Institute (ETRI), **30th October 2017**, The University of Nottingham.

6) Hydrogen Vehicles Discovery Day, Organized by Energy Technologies Research Institute (ETRI), **26th March 2018**, University of Nottingham.

7) Hydrogen for Energy Storage and Clean Fuel Production, Organized by Energy Technologies Research Institute (ETRI), **10th May 2018**, University of Nottingham.

Dedication

This work is dedicated to

My Greatest Sister Dr. Reham Balahmar

I do not have enough words other than to dedicate this thesis with love to you

Acknowledgments

Firstly, I reverently thank Almighty Allah (SW) for giving me the inspiration, determination, health and strength to complete my study, for seeing me through this research and for bringing these wonderful and kind people, whether named or not across my PhD.

Most importantly, I would like to begin by sincerely thanking my greatest supervisor Professor Robert Mokaya for the opportunity to complete my PhD. I have been amazingly fortunate to have an advisor who gave me continuous encouragement, excellent guidance and advice with endless kindness, precious support with unlimited patience, motivation and immense knowledge, keen of providing me an excellent atmosphere for doing research beside his belief in me helped me in all the time of research and writing of my thesis. I hope that one day I would become as great an advisor to my students as Professor Robert Mokaya has been to me, his office door was always open for me when I ever had a problem or a question about my research.

I am also thankful to my co-advisor, Professor Alexander Blake for carefully reading and give valuable feedbacks in my yearly reports.

I would like to thank other individuals, of notable significance, all the members of chemistry stores; Mr. Eric Delea, Mr. Jim Fyfe for all their efforts, invaluable assistance, and for their endless kind. I have to give a special mention for the support given by laboratory technicians who maintained all the machines in my lab efficiently; Neil Barnes, Mark Guyler, and Tom Clayton, I warmly appreciate the generosity and the extra help and technical assistance. I owe my gratitude to all those people members of chemistry workshop. I would like to profoundly thank the IT services.

I am deeply grateful to Tracey Hassall-Jones for helping me with Microsoft word. I also register my gratitude to all the staff of student support office of chemistry department especially, Wendy Kirkup, for her kindness and assistance.

Appreciation also goes to the Nanoscale and Microscale Research Centre NMRC practically to Professor. Andrei Khlobystov director of NMRC, Dr Elisabeth Steer for her endless assistance with SEM training, Dr Michael Fay and Dr Rhys Lodge for TEM analysis, Dr Emily Smith for XPS analysis, Dr Rance Graham for Raman analysis. I am also indebted to Tong Liu for her assistance with CHN analysis, William Lewis for PXRD training.

I am also grateful to all the former and the current colleagues in laboratory A30 for their various forms of support and friendship.

I would like to say very special thanks with respect to my dearest friend especially, Yas, and huge thanks for Dr. Eric Masika, Prof. Khadijah, Nada & Najla, Ejike, Eman, for keep checking on me during my PhD. My macaws which I skype them every day made my life fulfilled with happiness and joy.

None of this work would have been possible without the love, tremendous support and patience. I would like to express my heart-felt gratitude to my family: my parents for spiritually support they provided me throughout my PhD and my life in general and for being instrumental and great role models. They were always encouraging me with their best wishes and prayers, i cannot put into words what their support has meant to me over the years. I wish you two will be the happiest and most blessed parents in the world.

Very special and huge thanks with love to my sister Dr. Reham and my brother Obaid my lion, for being great and constant source of love, strength, and support for me through each step of the journey. Reham, I can't thank

you enough for your kind support, encouragement, advices, editing assistance, concern, helping me stay sane through these years cheering me up and stood by me through the good and bad times, your sacrificed to ensure that i am happy.

Very special thanks to my supervisor Mr. Ali Balable in Royal Embassy of Saudi Arabia Cultural Bureau, Ministry of education department in London for his kindly help and fast response to help sorting out any issues throughout my PhD.



Very special thanks with respect to My great home my country **Kingdom of Saudi Arabia**, there is no country like you in this world, i swear there is nothing like you, you are above the highest clouds even if you were just empty soil. Acknowledgment and thanks are expressed to King Salman bin Abdulaziz AL-Saud, the government of Saudi Arabia.

I would like to acknowledge my sponsor scholarship provided by Saudi Arabia's 'humane king' King Abdullah Bin Abdulaziz AL-Saud (May he rest in peace) and Ministry of Higher Education of Saudi Arabia. I recognize that this research would not have been possible without the financial assistance and support from **Saudi Arabia Government**.

Thank you very much

Norah Balahmar

31st July 2018

List of Abbreviations

Abbreviation	
ΔHa	Enthalpy of Adsorption
1D, 2D, 3D	1 Dimensional , 2 Dimensional, 3 Dimensional
ACs	Activated Carbons
Ar	Argon
Ba	Barium
BET	Brunauer-Emmett-Teller
BOC	British Oxygen Company
CA	Conventional Activation
Ca	Calcium
CCS	Carbon Capture and Sequestration
CDCs	Carbide-Derived Carbons
CMS	Carbon Molecular Sieves
CNTs	Carbon Nanotubes
CO_2	Carbon Dioxide
COFs	Covalent Organic Frameworks
Cu	Copper
CVD	Chemical Vapour Deposition
DOE	The U.S. Department of Energy, USA
ESCA	Electron Spectroscopy Chemical Analysis

FA	Furfural Alcohol
FAT	Fixed Analyser Transmission
Fe	Iron
$FeCl_3$	Iron (III) Chloride
FTIR	Fourier Transform Infrared Spectroscopy
GHG	Greenhouse Gas
H_2	Hydrogen
H_2O	Water
HCl	Hydrochloric Acid
HF	Hydrofluoric Acid
HTC	Hydrothermal Carbonization
IAST	Ideal Adsorbed Solution Theory model (selectivity analysis)
ICP-OES	Inductively Coupled Plasma Optical Emission Spectroscopy
IGA	Intelligent Gravimetric Analyser
IR	Infrared spectroscopy
IUPAC	The International Union of Pure and Applied Chemistry
K	Potassium
KBr	Potassium Bromide
KOH	Potassium Hydroxide
LI	Liquid Impregnation
MCA	Mechanochemical Activation
Mg	Magnesium

Mn	Manganese
MOFs	Metal Organic Frameworks
NLDFT	Non-Local Density Function Theory
N_2	Nitrogen
Na	Sodium- a chemical element
PPY	Polypyrrole Polymer
PSA	Pressure Swing Adsorption
PSD	Pore Size Distribution
PTh	Polythiophene Polymer
PXRD	Powder X-ray Diffraction
RT	Room Temperature
SD	Sawdust
SEM	Scanning Electron Microscopy
STP	Standard Temperature and Pressure
TEM	Transmission Electron Microscopy
TGA	Thermo Gravimetric Analysis
VSA	Vacuum Swing Adsorption
XPS	X-ray Photoelectron Spectroscopy
ZTCs	Zeolite Templated Carbons
ZY	Zeolite Y
Z13X	Zeolite 13X

Table of Contents

Research Aims and Objectives ..... **i**

Abstract ..... **ii**

Thesis Structure ..... **iii**

List of Publications ..... **vi**

Poster and Presentation Sessions ..... **viii**

Posters Presentations ..... **viii**

Attendance ..... **ix**

Dedication ..... **x**

Acknowledgments ..... **xi**

List of Abbreviations ..... **xv**

Table of Contents ..... **xviii**

Chapter 1. Introduction **30**

1.1 Motivation 31

1.2 Carbon Dioxide 32

1.2.1 Possible Solutions to Control CO_2 Emission 33

1.2.2 CO_2 Capture Systems (CCS) 34

1.2.3 Current Status of CO_2 Capture and Storage Technologies 35

1.3 Hydrogen Economy 38

1.3.1 Hydrogen as a Fuel 38

1.3.2 Current Status of Hydrogen Storage Technology 41

1.3.2.1 Physical-Based Hydrogen Storages 42

1.3.2.1.1 Compressed Hydrogen Gas 42

1.3.2.1.2 Cryogenic Liquid Hydrogen 43

1.3.2.2 Material-based Hydrogen Storage 43

1.3.2.3 Gas Adsorption on Materials 44

1.3.2.3.1 Porous Materials 46

1.3.2.3.2 Classifications of Porous Materials 48

1.3.2.3.2.1 Carbon-Based Porous Materials 50

1.3.2.3.2.1.1 Activated carbons 51

1.3.2.3.2.1.2 Production of Activated Carbons 53

1.3.2.3.2.1.2.1 Physical Activation 55

1.3.2.3.2.1.2.2 Chemical Activation 55

1.3.2.3.2.1.2.3 Hydrothermal Carbonization 56

1.3.2.3.2.1.3 Effect of Activation Parameters on Activated Carbons Proprieties 57

Mechanism of KOH Activation 60

1.3.2.3.2.1.4 Doped Carbons 63

1.4 Carbon Precursors Used in This Study 66

1.4.1 Polythiophene 66

1.4.1.1 Polypyrrole 66

1.4.1.1.1.1.1 Zeolite Templated Carbons 67

1.5 The Aim of My Research.....70

1.6 References 71

Chapter 2. Methods and Characterization Techniques 83

2.1 Aim of this Chapter 84

2.2 Preparation of Activated Carbons 85

2.2.1 Conventional Chemical Activation.....85

2.2.2 Compactivation/Mechanochemical Activation 86

2.2.3 Chemical Vapour Deposition (CVD) Processes 88

2.2.4 Hydrothermal Carbonization Reactor 88

2.2.4.1 Production of Hydrochar.....89

2.3 Analytical Techniques.....90

2.3.1 Thermogravimetric Analysis (TGA) 90

2.3.2 Powder X-Ray Diffraction (PXRD) 91

2.3.3 Nitrogen Sorption Analysis 95

2.3.3.1 Textural Properties and Porosity Analysis 95

2.3.3.2 Theory of the Brunauer–Emmett–Teller (BET) Method 100

2.3.3.3 Assessment of Microporosity; Pore Volume, Pore Size and Pore Size Distribution (PSD) 101

2.3.3.4 ASAP 2020 Micromeritics Surface Characterization Analyzer .104

2.3.3.5 Micromeritics 3Flex Surface Characterization Analyzer 106

2.3.4 CHN Elemental Analysis 109

2.3.5 Electron Microscopy 111

2.3.5.1 Scanning Electron Microscopy 112

2.3.5.2 Transmission Electron Microscopy 117

2.3.6 Spectroscopy 120

2.3.6.1 X-ray Photoelectron Spectroscopy 120

2.3.6.2 Inductively Coupled Plasma Optical Emission Spectroscopy (ICP-OES) 125

2.3.6.3 Raman Spectroscopy 128

2.3.6.4 Fourier Transform Infrared (FTIR) Spectroscopy 130

2.4 Applications: Gas Sorption Measurements (H_2 and CO_2) 134

2.4.1 Gravimetric Gas Sorption Analysis 134

2.4.1.1 IGA-003 Intelligent Gravimetric Analyser 134

2.4.2 High Accuracy Gravimetric Sorption Analyzer (XEMIS) 135

2.5 Calculation 138

2.5.1 Excess and Total Hydrogen Uptake 138

2.6 References 140

Chapter 3. Templating of Carbon in Zeolites under Pressure: Synthesis of Pelletized Zeolite Templated Carbons with Improved Porosity and Packing Density for Superior Gas (CO_2 and H_2) Uptake Properties 144

3.1 Aim of this Chapter 145

3.2 Abstract 146

3.3 Introduction 147

3.4 Experimental Section 151

3.4.1 Materials and Chemicals 151

3.4.2 Material Synthesis 152

3.4.2.1 Moderate Surface Area ZTCs 152

3.4.2.2 High Surface Area ZTCs 153

3.5 Abbreviations 156

3.6 Results and Discussion 157

3.6.1 Compared Zeolite 13X Compacted *at 5 tonnes (370 MPa)* or *10 tonnes (740 MPa)* with Original Powder Samples 157

3.6.1.1 Morphology and Surface Analysis 157

3.6.1.2 Structural Ordering Analysis PXRD 161

3.6.1.3 Textural Properties and Porosity Analysis 162

3.6.2 Zeolite Templated Carbons Prepared *via* CVD 165

3.6.2.1 Purity and Thermal Stability Analysis 165

3.6.2.2 Packing Density Assessment 167

3.6.2.3 Textural Proprieties and Porosity Analysis 169

3.6.2.4 CO_2 Uptake Measurements 175

3.6.2.4.1 CO_2 Uptake at 25 ^oC 175

3.6.3 Zeolite Templated Carbons Prepared *via* Combination of Liquid Impregnation (LI) and CVD 181

3.6.3.1 Purity and Thermal Stability Analysis 181

3.6.3.2 Structural Ordering Analysis PXRD 183

3.6.3.3 Raman Spectra Analysis 185

3.6.3.4 Morphology and Surface Analysis 187

3.6.3.5 Structural Ordering Analysis Using TEM 190

3.6.3.6 Textural Properties and Porosity Analysis 192

3.6.3.7 Hydrogen Uptake Measurements 195

3.6.3.8 CO_2 Uptake Measurements 197

3.6.3.8.1 CO_2 Uptake at 25 ^oC 197

3.6.3.8.2 CO_2 Uptake at 0 ^oC 198

3.6.3.9 Working Capacity 198

3.7 Conclusions 204

3.8 References 206

Chapter 4. Polythiophene- Derived Conventional Activated Carbons and Compactivated Carbons for Gas Storage Applications 210

4.1 Aim of this Chapter 211

4.2 Abstract 212

4.3 Introduction 213

4.4 Experimental Section 215

4.4.1 Materials and Chemicals 215

4.4.2 Material Synthesis 216

4.4.2.1 Chemical Polymerization of Thiophene Using $FeCl_3$ 216

4.4.2.2 Synthesis of Polythiophene-derived Activated Carbons 219

4.4.2.2.1 Conventionally Activation 219

4.4.2.3 Compactivation 219

4.5 Abbreviations 223

4.5.1 Conventional Polythiophene Derived-Activated Carbons 223

4.5.2 Compactivated Polythiophene Derived- Carbons 223

4.6 Results and Discussion 224

4.6.1 Effects of Compaction on Polythiophene 224

4.6.1.1 Morphology and Surface Analysis 224

4.6.1.2 Structural Ordering Analysis 227

4.6.2 Polythiophene-derived Activated Carbons 228

4.6.2.1 Purity and Thermal Stability Analysis 228

4.6.2.2 Structural Ordering Analysis 230

4.6.2.3 Elemental Analysis 232

4.6.2.4 Elemental Surface Analysis 234

4.6.2.5 Morphology and Surface Analysis 236

4.6.2.6 TEM Analysis 243

4.6.2.7 Textural Properties and Porosity Analysis 250

4.6.2.8 CO_2 and H_2 Uptake Measurements 256

4.6.2.8.1 CO_2 Uptake Measurements 256

4.6.2.8.1.1 CO_2 Uptake at 0 ^oC and 20 bar 256

4.6.2.8.1.2 CO_2 Uptake at 25 ^oC 261

4.6.2.9 H_2 Uptake Measurements 264

4.6.2.9.1.1 Conclusions 271

4.7 References 272

Chapter 5. Generalized Mechanochemical Synthesis of Biomass-Derived Sustainable Carbons for High Performance CO_2 Storage.....276

5.1 Aim of this Chapter 277

5.2 Abstract.....278

5.3 Introduction 279

5.4 Experimental Section.....282

5.4.1 Materials and Chemicals 282

5.4.2 Materials Synthesis 283

5.4.2.1 Carbon Precursors.....283

5.4.2.1.1 Wood Sawdust Derived Hydrochar.....283

5.4.2.1.2 Lignin-Derived Carbonaceous Hydrochar 283

5.4.2.2 Production of KOH Activated Carbons 286

5.4.2.2.1 Mechanochemical Activation (MCA) 286

5.4.2.2.2 Conventional Activation (CA) 286

5.5 Abbreviations 289

5.5.1 Sawdust-Derived Activated Carbons 289

5.5.2 Lignin-Derived Activated Carbons.....289

5.6 Results and Discussion 290

5.6.1 Sawdust-Derived Carbons 290

5.6.1.1 Textural Properties and Porosity.....290

5.6.1.2 Structural Ordering Analysis 297

5.6.1.3 Chemical Similarity Assessment 299

5.6.1.4 Pore Channel Assessment 301

5.6.1.5 CO_2 Storage Measurements 303

5.6.1.5.1 CO_2 Storage at 25 °C 303

5.6.2 Lignin-Derived Carbons 307

5.6.2.1 Textural Properties and Porosity Analysis 307

5.6.2.2 CO_2 Storage Measurements 310

5.6.2.2.1 CO_2 Storage at 25 °C 310

5.6.2.2.2 CO_2 Storage at 0 °C 310

5.6.3 Working Capacity, Volumetric Uptake and Benchmarking 313

5.6.3.1 Working Capacity Assessment 313

5.6.3.2 Volumetric Uptake Calculation and Packing Density Assessment 314

5.7 Conclusions 323

5.8 References 325

Chapter 6. Biomass to Porous Carbon in One Step: Directly Activated Biomass for High Performance CO_2 Storage 330

6.1 Aim of this Chapter 331

6.2 Abstract 332

6.3 Introduction 333

6.4 Experimental Section 335

6.4.1 Materials and Chemicals 335

6.4.2 Material Synthesis.....336

6.4.2.1 Direct Activation 336

6.4.2.2 Conventional Activation 336

6.5 Abbreviations 338

6.6 Results and Discussion 339

6.6.1 Thermal Stability Analysis 339

6.6.2 Structural Ordering Analysis PXRD 341

6.6.3 Elemental Composition Analysis.....343

6.6.4 The Inorganic Metal Content K, Na, Ca, Fe, Mn, Ba and Mg Analysis.....344

6.6.5 Yield of Activated Carbons.....345

6.6.6 Raman Analysis 346

6.6.7 IR Spectroscopy Analysis 349

6.6.8 Morphology Analysis.....351

6.6.9 Structural Ordering Analysis TEM 361

6.6.10 Textural Proprieties and Porosity Analysis 364

6.6.11 CO_2 Uptake Measurements.....371

6.6.11.1 CO_2 Uptake Measurements at 25 ^oC.....371

6.6.11.2 CO_2 Uptake Measurements at 0 ^oC 377

6.6.12 Selectivity.....382

6.7 Conclusions.....386

6.8 References.....387

Chapter 7. Pre-mixed Precursors for Mediating the Porosity of Activated Carbons for Gas Storage (CO_2 and H_2) Applications 391

7.1 The Aim of this Chapter 392

7.2 Abstract.....393

7.3 Introduction 394

7.4 Experimental Section.....396

7.4.1 Materials and Chemicals 396

7.4.2 Materials Synthesis 397

7.4.2.1 Carbon Precursors.....397

7.4.2.1.1 Eucalyptus Wood Sawdust.....397

7.4.2.1.2 Sawdust-Derived Hydrochar 397

7.4.2.1.3 Polypyrrole.....398

7.4.2.2 Production of Activated Carbons.....400

7.4.2.2.1 Polypyrrole/Sawdust Derived Activated Carbons.....400

7.4.2.2.2 Polypyrrole/Hydrochar Derived Activated Carbons 400

7.5 Abbreviations 401

7.5.1 Polypyrrole/Sawdust Derived Carbons 401

7.5.2 Polypyrrole/Hydrochar Derived Carbons.....401

7.6 Results and Discussion 402

7.6.1 Carbon Precursors.....402

7.6.1.1 Structural Ordering 402

7.6.1.2 Morphology and Surface Analysis 404

7.6.1.3 Elemental Composition 408

7.6.2 Activated Carbons 410

7.6.2.1 Purity and Thermal Stability 410

7.6.2.2 Structural Ordering 413

7.6.2.3 Elemental Composition 416

7.6.2.4 Morphology and Surface Analysis 418

7.6.2.5 Pore Channel Ordering 438

7.6.2.6 Textural Properties and Porosity 458

7.6.2.6.1 Polypyrrole/Sawdust Derived Activated Carbons 458

7.6.2.6.2 Polypyrrole/Hydrochar Derived Activated Carbons 461

7.6.2.7 CO_2 Uptake Measurements 471

7.6.2.7.1 Polypyrrole/Sawdust Activated Carbons 471

7.6.2.7.2 Polypyrrole/Hydrochar Activated Carbons 473

7.6.2.8 Hydrogen Capacity 481

7.7 Conclusions 487

7.8 References 489

Chapter 8. Conclusion and Further Work 497

8.1 Conclusion 497

8.2 Further Work 504

Chapter 1. Introduction

1.1 Motivation

Why should CO_2 be Captured or Sequestrated?

Global Warming: Greenhouse Effect

Global warming by way of the gradual rise of the planet's temperature caused by increased emission of greenhouse gases is an environmental concern. Global warming and associated climate change concerns both need concerted efforts by researchers in order to be effectively addressed.[1-5] The most abundant greenhouse gases in the earth's atmosphere are water vapour (H_2O), which is the most abundant, carbon dioxide (CO_2), methane (CH_4) nitrous oxide (N_2O), ozone (O_3) and chlorofluorocarbons (CFCs).[2, 6] Normally, sun light and solar energy absorbed by the earth surface can escape into outer space, however, the presence of the greenhouse gases and other air pollutants lead to trapping of the sun light and solar energy causing the atmosphere to warm up as shown in **Figure 1.1**. A main cause of climate change is the use of fossil-based resources such as oil, petroleum, and coal, which release CO_2 and other greenhouse gases into the atmosphere. Carbon dioxide capture and storage (CCS) technology is considered a crucial strategy for reducing CO_2 emissions by up to 90%. Due to the increased threat of global warming, there has been considerable attention on clean energy research aimed at replacing current used fossil-based fuels, and finding alternative renewable sources or employing efficient technologies for carbon dioxide capture.[5]

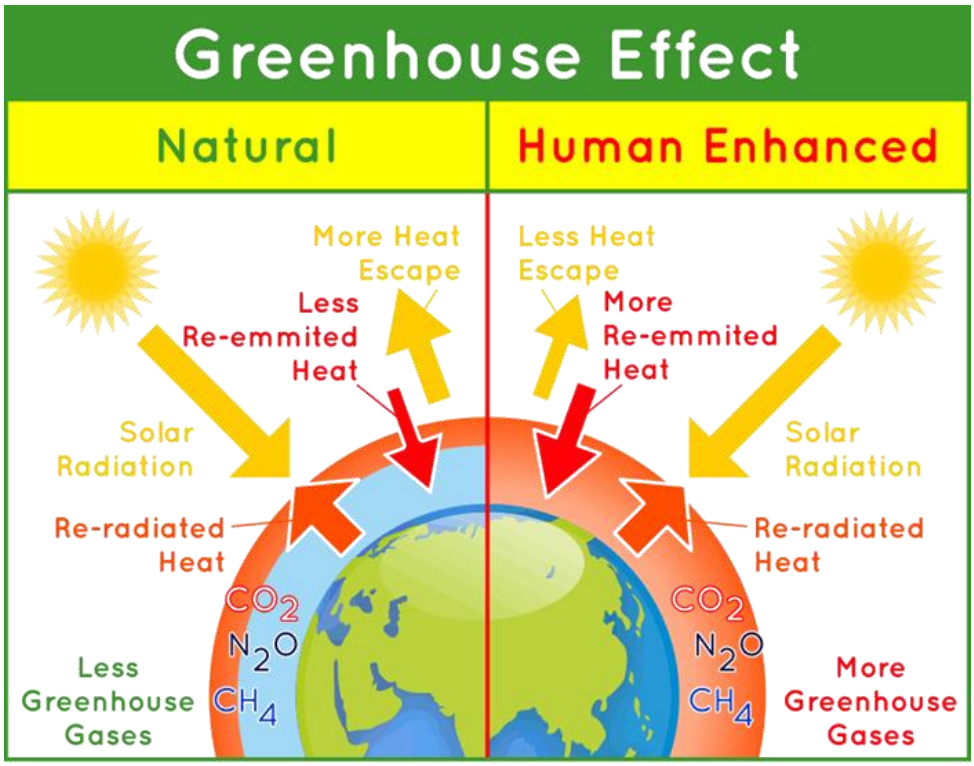


Figure 1.1: Illustration of the greenhouse effect (Global Warming).[7]

1.2 Carbon Dioxide

Carbon dioxide (CO_2) is the second most abundant greenhouse gas after water vapour and a major anthropogenic greenhouse gas.[5, 8-11] CO_2 has the ability to strongly absorb in the infrared and near-infrared and transmit the visible light, which means that more atmospheric CO_2 leads to increase the average planet temperature. Carbon dioxide is a main product of any combustion process. CO_2 sources are divided into two categories: natural sources and human sources. Currently, human use of fossil fuel-based systems for energy production are the largest source of CO_2 emissions.

1.2.1 Possible Solutions to Control CO_2 Emission

A number of approaches for capturing and storing CO_2 emissions have received intensive research attention. There are many technologies and approaches applied by different countries to tackle and control the increase of atmospheric CO_2 emissions level namely; [5, 12]

(i) Reducing the use of fossil fuel-based sources (i.e. coal, oil, petroleum and natural gas, moving to low/zero carbon emission energy sources and expanding the use of renewable energy such as solar, hydropower, wind, and biomass energy.

(ii) Appling geoengineering approaches such as afforestation and reforestation.

(iii) Appling carbon capture and storage systems (CCS) at sources of CO_2 emission.[5, 12-16] This solution requires materials that can efficiently capture and store CO_2.[13, 14, 17] A wide range of materials have been studied for application in carbon capture and storage (CCS) *via* physical adsorption and/or separation.[4, 13, 17-20] Carbon capture and sequestration (CCS) is the only available technology and the most practical approach that can reduce the long term emission of CO_2 into the atmosphere due to burning of fossil fuels as fossil fuels will continue to be a major source of energy in the foreseeable future.[21, 22] The materials studied so far, and which have received great attention, are porous carbons, [23-26] zeolites, [27-30] and metal organic frameworks (MOFs).[31-34]

The biggest challenge currently is how to demonstrate CCS effectively, safely, with competitive cost at large industrial scale. The current CO_2 capture technologies available in the market are costly, and contribute to ca. 70–80% of the total cost of a full CCS system including capture, transport and storage.[5, 35]

1.2.2 CO_2 Capture Systems (CCS)

Carbon capture and storage (CCS) technologies [3, 5, 36-41] involve three steps; capture, transport and storage. The aim is to capture up to 90% of CO_2 emitted to the atmosphere by several large-scale sources (fossil fuel-fired power plants, heavy industry), transport it (by pipeline or ship) to a suitable storage site, then finally store it in geological formations safely and permanently deep underground. There are three main systems for CO_2 capture [5, 41] (**Figure 1.2**):

1. Pre-Combustion Capture: Removal of CO_2 before fossil fuel combustion by pre-treating the fuel and converting into a clean-burning gas (a mix of separated CO_2 and H_2), *via* gasification process. The separated hydrogen is then used as fuel, or burnt to generate electricity. Pre-combustion technology is commercially mature and applied by using a number of physical and chemical separation approaches which can be easily fitted into existing power plants (See **Figure 1.2**).

2. Post-Combustion Capture: CO_2 removal from flue gas streams after fuel combustion by using a number of physical and chemical separation approaches, including chemical absorption, physical absorptions or cryogenic separation (See **Figure 1.2**).

3. Oxy-Combustion Capture: Capturing CO_2 from flue gas formed during fuel combustion by using a pure oxygen stream or enriched oxygen stream (nitrogen-free atmosphere) instead of air for combustion. This leads to a flue stream consisting mainly of concentrated CO_2, which can be easily removed and water vapour H_2O with great decrease of NO_x production (See **Figure 1.2**).

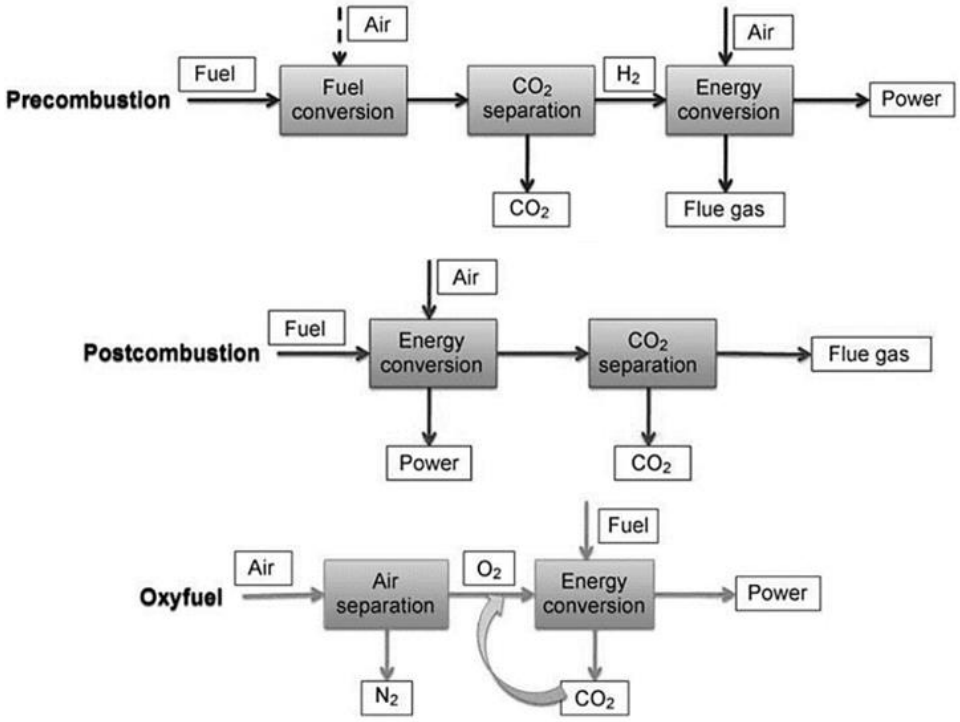


Figure 1.2: CO_2 capture systems; pre-combustion, post-combustion and oxyfuel combustion processes.[3, 42]

1.2.3 Current Status of CO_2 Capture and Storage Technologies

The search for materials that can cheaply and efficiently capture and store the CO_2 that is generated from anthropogenic sources is one of the most intensely researched areas in energy materials. Material-based developments in the storage of CO_2 is generally guided by set targets that would allow practical use of the materials in a commercially viable manner. Most CO_2 storage strategies can be classified as either chemical-based CO_2 storage or material-based CO_2 storage. **Table 1.1** presents an overview for current CO_2 capture technologies. Recently, extensive attention has been directed to developing novel adsorbents for CO_2 capture. Currently Carbon

capture and storage (CCS) by solid adsorbents is receiving a great deal of attention. The many different solid materials under investigation include; porous carbons,[23-25] zeolites [27-30] and metal organic frameworks materials (MOFs).[31-34] Carbon-based materials have received special attention due to their proprieties such as; relatively low cost, availability, ease of preparation, tunable structural, high stability (mechanical and chemical); low sensitivity to water vapor compared to other CO_2-philic materials.[2, 43, 44] Recently, studies have shown that controlling the proprieties of porous carbons can provide a very useful tool to produce tailored materials for capturing CO_2 under pre-combustion or post-combustion conditions.[12, 45-51]

Table 1.1: Overview for CO_2 capture technologies. (Adopted from [41])

Capture option	Separation technology	Method
Post-combustion	Absorption by chemical solvents [a]	• Amine-based solvent e.g. monoethanolamine (MEA),[b] diethanolamine (DEA). • Alkaline solvents, e.g. NaOH and $Ca(OH)_2$. • Ionic liquids.
	Adsorption by solid sorbents	• Amine-based solid sorbents • Alkali earth metal-based solid sorbents, e.g. $CaCO_3$. • Alkali metal carbonate solid sorbents, e.g. Na_2CO_3 and K_2CO_3. • Porous organic frameworks-polymers.
	Membrane separation	• Polymeric membranes, e.g. polymeric gas permeation membranes. [b] • Inorganic membranes, e.g. zeolites. • Hybrid membranes.
	Cryogenic separation	• Cryogenic separation
	Pressure/vacuum swing adsorption	• Zeolites. [b] • Activated carbons. [b]
Pre-combustion	Absorption by physical solvents	• Selexol, rectisol etc.
	Absorption by chemical solvents	Amine-based solvent, e.g. monoethanolamine (MEA) Ammonia.
	Adsorption by porous organic frameworks	• Porous organic frameworks membranes.
Oxyfuel-combustion	Separation of oxygen from air	• Chemical looping combustion. • Chemical looping reforming.

[a] Mature technology.
[b] Commercially available.

1.3 Hydrogen Economy

Hydrogen is the most abundant, simplest and lightest chemical elements in the universe. [52-55] Hydrogen is not usually found in nature in its pure form but is rather always combined within molecules and can be produced from a variety of sources.[52, 54, 56] Hydrogen is considered to be an ideal energy carrier and promising alternative to fossil fuels-based systems due to its light mass and very large gravimetric energy density of ca. 39 kWh kg^{-1}, which is three times higher than the most commonly used fuels such as gasoline. From an environmental view hydrogen burns cleanly with zero-CO_2 and zero-pollutant emission; the only by-products of its combustion with oxygen are water and heat. Recently, the use of hydrogen as an energy carrier has been proposed as the most promising alternative to the fossil fuel-based energy sources because whether it is burned to produce heat or reacted with air in a fuel cell to produce electricity, the only by-product is water. "Hydrogen Economy" concept was proposed in 1970 by John Bockris,[57] where hydrogen is the future solution and a low-carbon energy source to replace the current fossil fuel-based energy systems such as gasoline (transport fuel) or natural gas (heating fuel).

1.3.1 Hydrogen as a Fuel

The choice for hydrogen as a possible solution and a main future energy carrier to replace the current fuel has important advantages:[58-60] (1) The by-products of hydrogen combustion in oxygen are water and energy as heat, with zero-CO_2 emission and no pollutants. (2) Hydrogen gas is non-toxic and safe to breathe, compared to other energy sources such as nuclear energy, coal and gasoline. (3) Hydrogen is a renewable resource could be generated

via green methods. However, use of hydrogen has some challenges, chiefly; (1) In nature, hydrogen is not freely available and needs to be produced from renewable sources such as water *via* processes such as electrolysis that can require more energy than is recovered by burning it. (2) Hydrogen is highly flammable and must be handled safely (in both liquid and gas form), is a gas at ambient temperature, and thus has low density meaning that it has low volumetric energy density compared to diesel and gasoline. Indeed, this handling challenge means there is a lack of practical storage methods that have restricted its use and the development of a hydrogen economy.

The use of hydrogen as a safe, efficient and effective alternative future energy carrier with a commercial success must overcome challenges related to its production, storage and delivery. For example, hydrogen on-board storage methods for large scale mobile applications (vehicular) need to be:

1. Safe with no risk of explosion, leakage, radiation or pollution.
2. Lightweight and compact.
3. Environmentally friendly; non-toxic, not contain poisonous or polluting materials.
4. Economical; the materials used for the hydrogen storage system should be abundant and cheap.
5. Long lasting; the storage methods should have a long lifetime with the possibility for materials recycling and with high energy efficiency.

Material-based developments in the storage of hydrogen are generally guided by set targets that would allow practical use of the materials in a

commercially viable manner. The U.S. Department of Energy (DOE) has set targets for hydrogen storage systems for commercial application:[61]

1. High gravimetric and high volumetric capacity. The amount of hydrogen, is expected to be stored in a relatively light container leading to a high wt% of hydrogen in the whole system; the target is 1.8 kWh kg^{-1} (5.5 wt%). High volumetric capacity to avoid excessive volume of the system; the target is 1.3 kWh L^{-1} (40 g L^{-1} volumetric). The ultimate aim being a gravimetric uptake of 7.5 wt% and volumetric capacity of 70 g L^{-1}.

2. Reversibility and cyclability; it should be possible to load and unloaded in the storage system many times (preferably 1500 cycles) without any significant loss and changes in the system.

3. Loading/unloading time; the system should be reloadable at high rate (5 kg within 3 minutes) and also unload sufficiently fast to supply an engine or fuel cell with the desired gas flow and pressure.

4. Operating conditions should be close to ambient conditions; temperature range of -40 to 60 ^{o}C and maximum delivery pressure of 100 bar.

5. Cheap and environmental friendly storage; the materials used for the hydrogen storage system should be cheap, abundant and non-toxic for the environment.

6. The storage method should have a long lifetime with the possibility for materials recycling and with high energy efficiency.

7. Safety aspect; the risk of explosion, leakage, radiation or pollution should be considered and completely excluded by designing a safe

system.

1.3.2 Current Status of Hydrogen Storage Technology

Hydrogen has the highest energy per mass of any fuel, however, its low ambient temperature density results a low energy per unit volume, therefore requiring the development of storage methods that have potential for higher energy density. The current technologies have been investigated for hydrogen storage (**Figure 1.3**) are categorized as either (i) Physical-based storage, or (ii) Material-based storage.

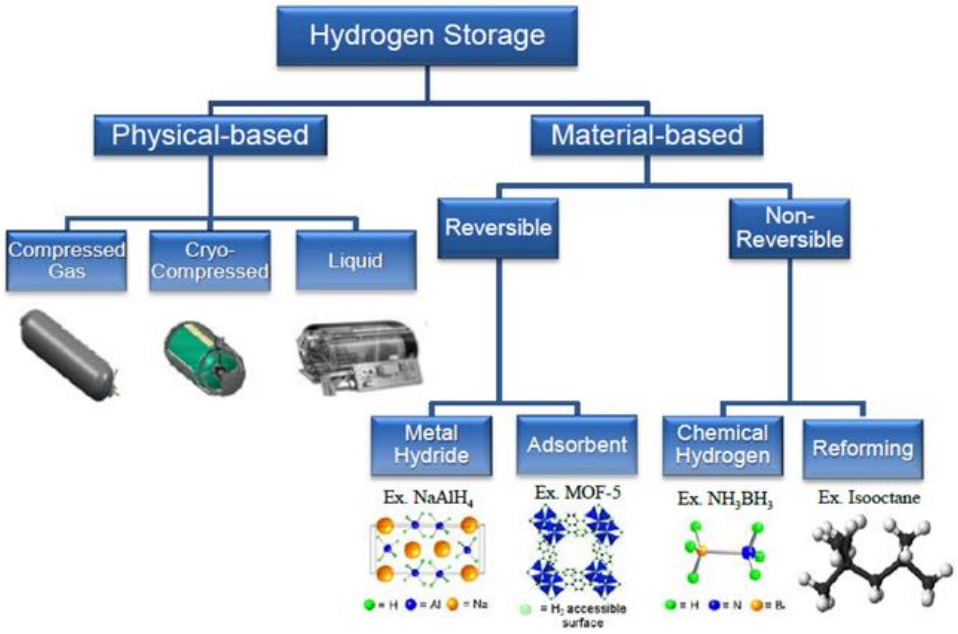


Figure 1.3: Overview of current hydrogen storage technologies.[60]

1.3.2.1 Physical-Based Hydrogen Storages

Currently, physical-based storage is the most mature technology for direct hydrogen storage, by modifying the physical state of hydrogen into gaseous or liquid form to achieve;[60, 62, 63] compressed hydrogen gas, cryo-compressed hydrogen gas and liquefied hydrogen. Each technology has its own advantages and disadvantages. Currently, the two most suitable and mature technologies of reversible hydrogen storage are; cryogenic liquid storage and compressed gas storage in high pressure gas cylinders. However, these have severe disadvantages especially in volumetric terms compared to fossil fuels-based systems. Thus the storage of hydrogen in lightweight solids and compact system for mobile application is attractive.[64]

1.3.2.1.1 Compressed Hydrogen Gas

This method has been investigated and demonstrated in fuel cell vehicles, due to the higher hydrogen densities achievable. It is the most common method used to store hydrogen physically in a gas form at high pressure system using high strength cylindrical tanks designed to withstand higher pressures. The cylindrical tanks are very heavy and usually made of steel or aluminium for pressure up to 200 bars, composites materials for pressure up to 800 bar.[62] Hydrogen can be cooled to near cryogenic temperatures to increase the volumetric energy density. This is the only technology that meets 2015 DOE targets for volumetric and gravimetric efficiency by using cold hydrogen (20.3 K or slightly above) to reach a high energy density. The main challenge is hydrogen warm-up due to heat transfer with the environment ("boil off").[62]

1.3.2.1.2 Cryogenic Liquid Hydrogen

The most common way to store hydrogen in a liquid form (liquefaction) by firstly liquefying the hydrogen to increase the volumetric density by cooling it to -253 °C. It is an attractive option since the liquefied hydrogen occupies much less space than in pressurized form. The volumetric density of liquid hydrogen is around 70 kg m^{-3} which is twice as much as pressurized at 800 bar gas.[62] The main issues of liquefaction is that it is an expensive process coupled with high energy consumption and low energy efficiency due to loss of hydrogen *via* evaporation "boil off". These disadvantages make liquid systems impractical for application in hydrogen fuel cell powered vehicles. Further Research is needed to improve liquefaction technology, as well as improved economies of scale and energy efficiency.[64]

1.3.2.2 Material-based Hydrogen Storage

Hydrogen can be stored safely and efficiently in solid state materials for both mobile and stationary applications, particularly on the surfaces of solids by adsorption or within solids by absorption. Currently, metal and complex hydrides *via* chemical adsorption in form of hydrides and porous materials *via* physical adsorption as molecular hydrogen are the main target materials. Hydrogen gas physisorbs onto a surfaces *via* very weak Van der Waals interactions, with enthalpy of adsorption, ΔHa, between 4-10 $KJmol^{-1}$. Due to the weak adsorption interaction, low temperatures (cryogenic) are needed to adsorbed significant amount of H_2 gas.[64]

1.3.2.3 Gas Adsorption on Materials

Adsorption (surface adsorption) of an adsorbate (liquid, or gas) on the surface of an adsorbent (a solid or liquid) falls into two broad categories;[65] physisorption and chemisorption. Hydrogen adsorbs on materials *via* three mechanisms depending on the nature of forces between adsorbate and adsorbent: physical adsorption, chemical adsorption, and Intermediate between physisorption and chemisorption (**Figure 1.4**).

Physisorption is also known as Vander Waal's adsorption and occurs when a gas molecule or liquid (the adsorptive) is in contact with a solid surface (the adsorbent). No chemical reaction occurs and the adsorbate/adsorbent interaction is mainly due to the van der Waals force/bonding. Physisorption is fully reversible and can be an extremely fast. Through this sorption process hydrogen gas can be adsorbed/desorbed during several cycles without any losses. Cryogenic temperatures must be applied to obtain reasonable hydrogen storage capacity due to the weak adsorption interaction. Thus, materials with very high specific surface area are desirable. In physical adsorption, adsorbate can be easily desorbed by increasing the temperature (heating) or by decreasing the pressure.

Chemical *adsorption* is also known as Langmuir adsorption. It occurs at higher temperatures, involves chemical binding of gas molecule/solid by strong covalent bonds stronger bonding than physical bonding. Therefore only monolayer adsorption is possible and adsorption cannot be easily reversed.

Intermediate (between physisorption and chemisorption or quasi-molecular bonding occurs when the bond between H atoms in the H_2 molecule is weakened but not broken.[63]

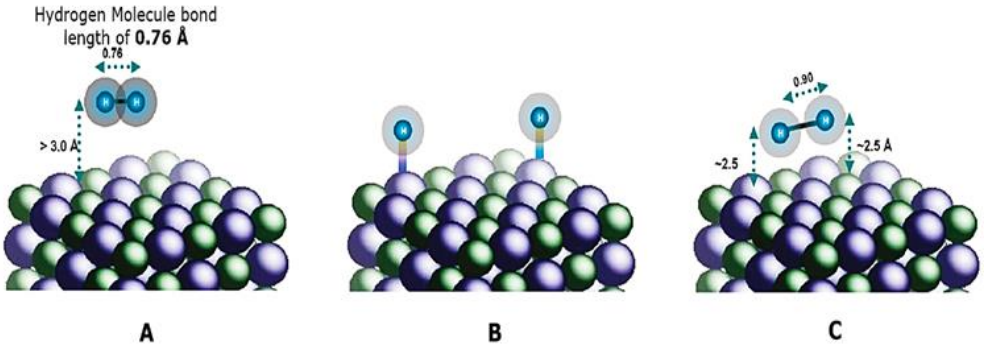


Figure 1.4: Hydrogen adsorption mechanism; **(A)** physisorption, **(B)** chemisorption, and **(C)** quasi-molecular bonding.[63]

1.3.2.3.1 Porous Materials

Porous materials have been extensively investigated as storage media for energy related gases such as hydrogen and CO_2. The focus on porous materials as stores for energy applications is driven and motivated by the need for environmental protection and demands for clean energy sources.[58, 66] The drive for environmental protection is typified by research efforts aimed at developing materials for the capture and sequestration of CO_2, while the search for cleaner energy sources requires material advances that may lead to realisation of the mooted Hydrogen Economy.[3, 13, 19, 20, 25, 32, 44, 58, 66-76] Innovative synthesis methods and the development of new types of nanoporous materials that offer improvements in overall porosity or high level control of porosity have brought significant strides in addressing the materials challenges that must be overcome in the journey towards materials-based CO_2 storage and the Hydrogen Economy.[3, 13, 20, 44, 67, 68, 77] Thus porous materials with very high surface area and/or well controlled porosity have recently come on to the research stage. The best examples of such research are illustrated by developments in metal–organic frameworks (MOFs),[78] covalent organic frameworks (COFs)[79] and porous carbons whether they be activated [44] or templated.[48, 68, 80, 81] Given the relationship between porosity and gas uptake, improvements in surface area and pore volume, and better targeting of pore size has resulted in materials with attractive gravimetric uptake for CO_2 and hydrogen; [3, 13, 20, 44, 67, 68, 82, 83] the gas uptake capacity of porous materials under any given conditions generally strongly correlates with the magnitude of the surface area and size of pore channels.[3, 13, 20, 44, 67, 68, 82, 83] Due to their more robust stability under various environments, porous carbons have retained on-going interest as gas stores even on the face of other emerging materials such as MOFs and COFs.[44, 48, 68, 80, 81] Of particular interest are zeolite templated carbons, which,

not only exhibit some of the highest reported surface area values for carbons but also offer enhanced pore size control due to the templating effect of zeolite frameworks.[81, 84-87]

Storage in porous materials compared to gaseous and liquid systems has the advantage of lower pressure hydrogen storage, increased safety, design flexibility and reasonable volumetric storage efficiency. However, the technology is not yet mature. Also, there are no imminent solutions for avoiding weight/cost penalties, and tackling thermal management issues associated with this option. Using porous materials for H_2 adsorption have a number of advantages compare to other methods, such as; high hydrogen uptake at low temperature and moderate pressures, fast kinetics of adsorption/ desorption, with no energy needed to release H_2. Among others adsorbents such as; metal organic frameworks (MOFs), zeolites etc., carbon materials offer many advantages such as; chemical stability, heat resistance, reversibility, low-cost and availability.[88, 89] Additionally, lightweight carbons with large porosity are a preferred choice to achieve the gravimetric hydrogen storage target.

1.3.2.3.2 Classifications of Porous Materials

Generally, porous materials are classified into several types based on their pore size, pore shape, and pore type but without reference to their chemical composition. According to The International Union of Pure and Applied Chemistry (IUPAC),[90, 91] porous materials are classified according to their pore size/diameter (**Table 1.2**); (i) microporous materials have small pores (2 nm); furthermore, the micropores are subdivided into two categories narrow micropores or ultra-micropores with pore diameters smaller than (0.7 nm), super-micropores with pore diameters in the range of (0.7- 2 nm), (ii) mesopores materials have pores with diameter between (2-50 nm), and (iii) macroporous materials have a pore size larger than 50 nm.

Pores have also been classified as follows: pores which communicate with the external surface are referred to as open pores like (b), (c), (d), (e) and (f) as illustrated in **Figure 1.5**. In addition pores are described as blind (i.e. dead-end, or saccafe) as they may open at one end as (b) and (f) and are accessible to molecules and ions in the surroundings. Others, as in (e) are open at two ends through pores. In contrast, closed pores as in (a) have no communication with the surroundings. While, open pores like (b), (c), (d), (e) and (f) consist of a continuous channel of communication with the external surface of the material and they are ideal for separation, catalysis and sensing applications.[90]

Pores can have various shapes and geometry, and have been classified based on geometrical shapes by Kaneko as follows: cylindrical shaped; cone shaped; ink-bottle shaped, spherical or slit shape as illustrated in **Figure 1.6**.

Table 1.2: Pore sizes systems of porous materials according to IUPAC classification.[90]

IUPAC Classification	Pore diameter (width)		Examples
	nm	Å	
Macropore	> 50	> 500	macroporous polystyrene
Mesopore	2-50	20-500	Mesopores silica
Micropore	< 2	< 20	Most common are: zeolites and activated carbons
Ultra micropore (narrow)	< 0.7	< 7	
Super micropore	0.7 - 2	7 - 20	

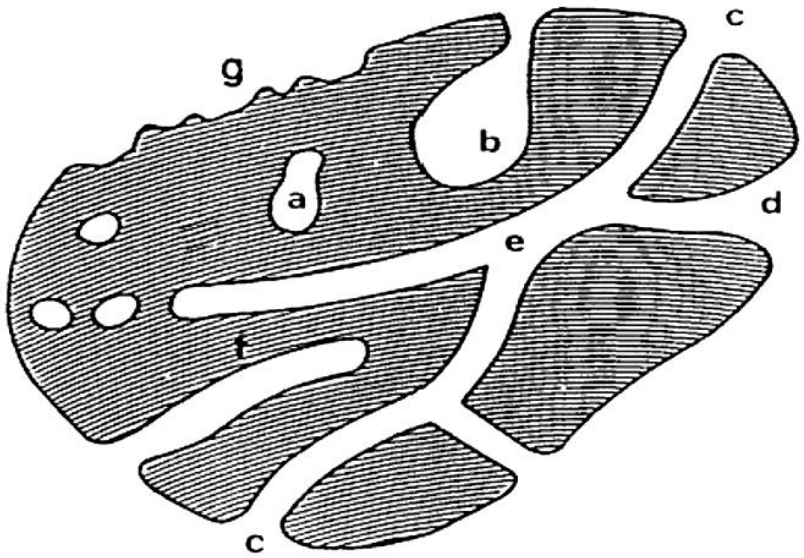


Figure 1.5: Pore classification from IUPAC (a-closed pores; b, f-pores open at one end; c, d, g-open pores; e-open at two ends through pores.[90]

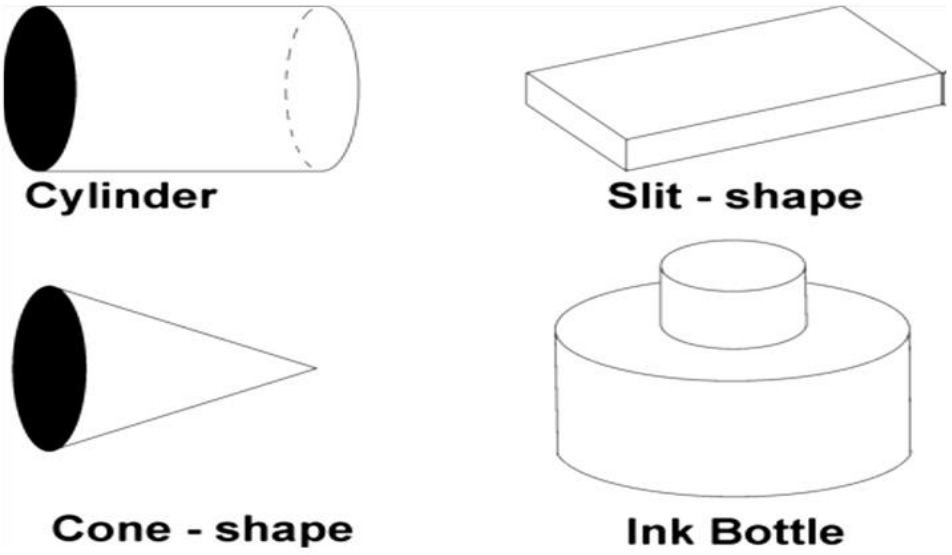


Figure 1.6: Schematic of pore shape classification based on geometry.[90]

1.3.2.3.2.1 Carbon-Based Porous Materials

Carbon-based porous materials are solid materials with voids/holes structure including activated carbons (ACs),[92, 93] carbon nanofibres,[94] templated carbons (TCs),[75, 84-86, 95-98] and multi-walled and single-walled carbon nanotubes (CNTs),[99, 100] among many others. They are considered to be the most promising for gas adsorption and separation due to their unique textural properties; low cost, high surface area and tuneable pore size, developed porosity, excellent stability, wide availability, and tunable surface chemistry.[2, 43] Many porous carbon materials have been investigated as gas stores including; activated carbons, carbon nanotubes,[99] and templated carbons.[101]

1.3.2.3.2.1.1 Activated carbons

Activated carbons (ACs) [43-45, 67, 68, 83, 102, 103] are highly porous carbonaceous materials. ACs can be produced at a relative low cost from wide range of naturally organic material with a high carbon content. ACs have been commonly used and intensively studied compared to other classes of porous materials, due to their proprieties such as; large surface area (>3000 $m^2 g^{-1}$) which allows the carbon to adsorb a wide range of compounds, and a broad range of pore sizes and large pore volume (>0.5 $cm^3 g^{-1}$), high physical and chemical stability, their wide availability, adjustable structural (porosity), tunable surface chemistry (various functional groups on the surface oxygen-containing/controllable heteroatom doping), their low-cost, light weight, existence in many varieties or forms, and ease of preparation. Activated carbons are widely used in many applications [43, 102, 104] such as; catalyst supports [44] CO_2 capture materials, gas storage materials (methane or hydrogen),[44, 83] gas separation, energy storage (e.g. supercapacitors),[44, 105] water purification and treatment, etc.[103, 106-110] ACs contain different pores systems; micropores, mesopores and macropores, as shown in **Figure 1.7**, from visible cracks and crevices to gaps and voids of molecular dimensions. Activated carbon can be made from many substances containing high carbon content such as coconut shells, coal, wood, and carbon rich polymers.[12, 93, 111] The raw materials have a major and direct influence on the properties and performance of activated carbon. For instance, activated carbons produced from coconut shells exhibit micropores, while activated carbons produced from coal have a wider range of mesopores. Furthermore, using peat or wood as the raw material results in development of an extensive structure of macroporosity. Activated carbon has different physical forms, suited to specific types of applications, such as powdered activated carbons which consists of fine particles with size of 0.045 to 0.180 mm, granulated

activated carbons consists of irregular shaped particles with size range of 0.2 to 5 mm, and extruded (cylindrical/pressed pellets) activated carbons with diameter of 1 to 5 mm, (**Figure 1.8**).[112-115]

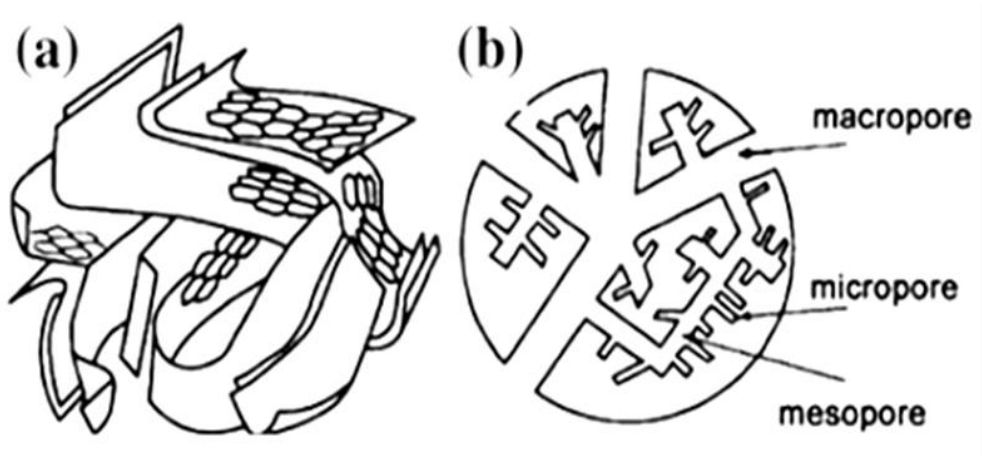


Figure 1.7: (a) 3D, **(b)** 2D schematic of ACs structure.[116]

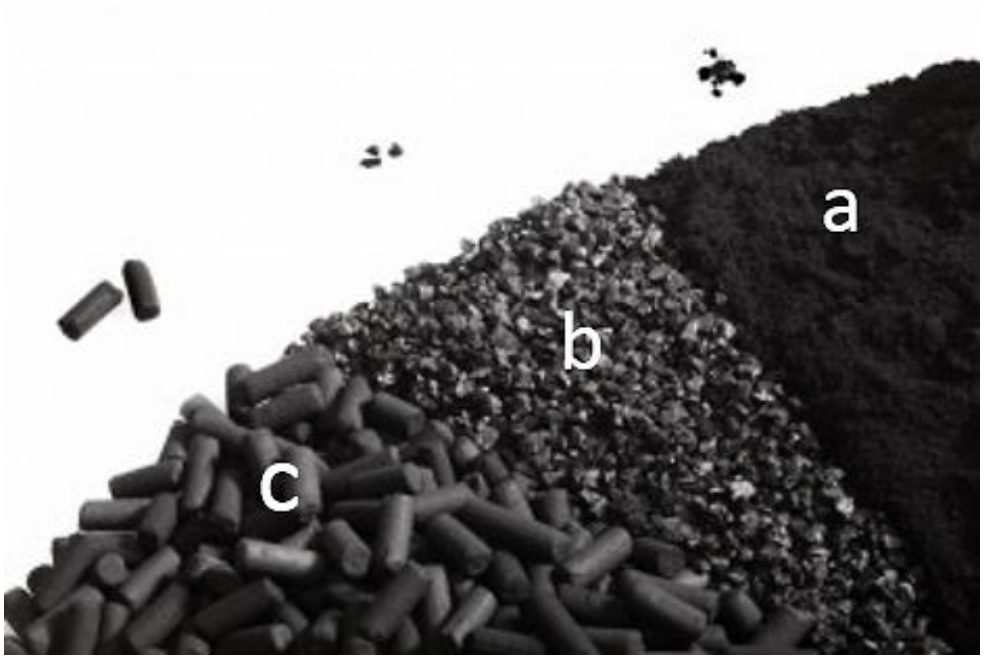


Figure 1.8: Different forms of activated carbons: **(a)** Powdered (0.045-0.180 mm), **(b)** Granulated (0.2 - 5 mm), and **(c)** Extruded/Pelletized or Cylindrical, (0.8 to 5 mm).

1.3.2.3.2.1.2 Production of Activated Carbons

ACs can be produced from a wide range of organic substances/sources which are rich in carbon such as coal, wood, sawdust, lignite coke, biochar, fruit, nutshells, bones etc. (**Figure 1.9**).[44, 117-119] ACs can be produced *via* two process;[44] (i) physical/thermal activation (ii) chemical activation and (iii) mixture of both physical and chemical activation. Both physical and chemical activation have been widely investigated for several activation agents.[120-122] Activation processes involve physical modification and thermal decomposition in a furnace, in a controlled temperature and atmosphere, which exposes the carbonaceous material (the carbon precursor is typically non-porous or lowly porous) to treatment that produces pore channels and constrained spaces in the carbonaceous material.[43] The activation develops overall porosity; a pore network and increases the surface area. The properties of the resulting carbon whether chemically or physically activated are not only depend on the activation process, but also on the precursor materials.[44]

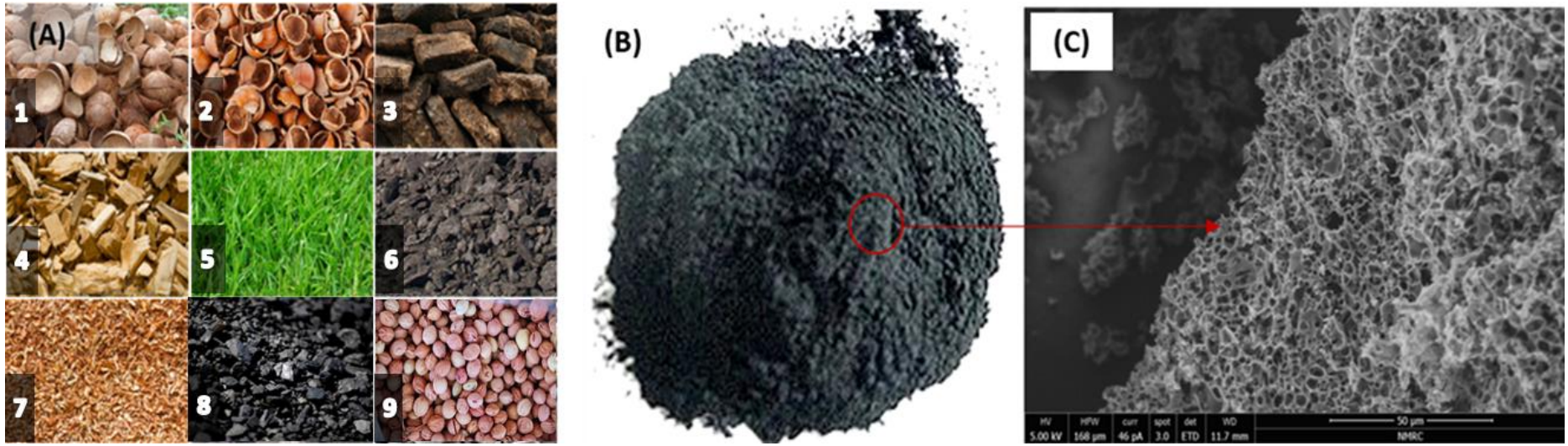


Figure 1.9: (A) Examples of natural rich-carbon materials (raw/precursors) used for activated carbon production, (1) coconut shells, (2) nuts shells, (3) peat, (4) hard wood chips, (5) grass (agricultural waste), (6) lignite coke, (7) wood sawdust, (8) coal, (9) cherry stones, **(B)** fine**-**powdered activated carbons prepared from wood sawdust using KOH, **(C) closer** look of activated carbons structure presenting in (B) using SEM analysis.

1.3.2.3.2.1.2.1 Physical Activation

Physical activation is a two steps process involving pyrolysis of carbon precursors at 400 ^{o}C – 900 ^{o}C in an inert atmosphere (usually nitrogen), to remove any non-carbon elements and the bulk of volatile matter, followed by gasification of the resulting carbon at 350 ^{o}C –1000 ^{o}C in the presence of suitable oxidizing gasifying agents such as CO_2 air or steam, or their gas mixture to develop the porosity.

1.3.2.3.2.1.2.2 Chemical Activation

Chemical activation is one of the most commonly used method to produce highly porous carbons.[44, 45, 123-127] The most commonly used activating agents are; $ZnCl_2$, H_3PO_4 and KOH. H_3PO_4 acts as dehydrating agents, while KOH acts as an oxidant. Chemical activation allows for better control of textural properties towards high surface area (up to 3600 m^2g^{-1}) with adjustable and tailored porosity.[44] The most two important features of the chemical activation for applications such as energy storage in supercapacitors or gas storage (H_2, CH_4 or CO_2), are; very high surface area (3600 m^2 g^1) and the well-developed/controlled and tailored microporosity. Those applications need materials with large surface areas with adjustable microporosity to the size of the electrolyte ions for supercapacitors or 0.7 – 1 nm for gas storage.[72, 128-136] Compared to physical activation, chemical activation has advantages as it requires only one step process. However, in chemical activation, some of the chemical activating agents used are corrosive and need to be washed off. Physical activation requires high temperature (900 ^{o}C -1500 ^{o}C), longer time (3 hours or more) for heat treatment.[44, 137, 138]

Recently, many studies have shown that KOH-activated carbons, including biomass-derived examples, can achieve some of the best CO_2 uptake under conditions (i.e., 0.1 – 1 bar and 25 °C –50 °C) relevant to industrial postcombustion capture.[17, 18, 25, 26, 46, 71-73, 139-147]

1.3.2.3.2.1.2.3 Hydrothermal Carbonization

Biomass-derived carbons are amongst the most widely used porous materials.[148-152] Biomass, which refers to any plant-derived organic matter includes agricultural crop wastes, wood wastes, grass etc. Recently, Mokaya and co-workers have reported on new synthesis routes to activated carbons generated from sustainable precursors or renewable biomass.[46, 49, 50, 76, 153, 154] The two main processes for the conversion of biomass to activateable carbonaceous matter are; (i) hydrothermal carbonisation (HTC)[155-159] and (ii) pyrolysis.[160-163] Hydrothermal carbonization proceeds *via* thermochemical decomposition and conversion of biomass into a solid residue, the so-called hydrochar, in the presence of superheated water (180 °C -250 °C) under self-generated pressure,[155-159] while pyrolysis occurs *via* processes that increase the carbon content of biomass during heating in the absence of oxygen.[160-163] HTC, discovered in 1913 by Friedrich Bergius, mimics the natural process of coal formation that converts cellulose into coal like materials. Recently, the hydrothermal carbonization process has been studied widely in great detail and received increasing considerable attention due to its efficiency, simplicity, and being an environmental friendly technology; it only involves a simple hot water treatment (as the solvent) and an organic material such as glucose, cellulose, starch or lignin.[164-171] However, in the search for sustainable and cheaper biomass-derived activated carbons it is desirable to simplify the synthesis process and in

particular to negate the need for hydrothermal carbonisation or pyrolysis prior to activation. In other words, it is desirable to directly activate biomass to activated carbons that have similar or improved yield and/or properties compared to those that are prepared *via* the conventional, and longer, two-step route incorporating HTC or pyrolysis prior to activation.

1.3.2.3.2.1.3 Effect of Activation Parameters on Activated Carbons Proprieties

There are a number of parameters which play a role in determining the properties of activated carbon, namely (i) temperature of activation, (ii) ratio of activating agent/carbon source, (iii) duration of activation, (iv) procedure of mixing (solution or solid-solid mixing),[44] (v) heating ramp rate, (vi) type of inert gas used, and (vii) the flow rate of the inert gas. These parameters as well as the reactivity of carbon precursor significantly affect the structure as well as the elemental composition of generated carbons.[45] In this thesis three parameters have been investigated; amount of activating agent, temperature of activation and the procedure of mixing (pre-mixing). In brief, the larger the amount of activating agent and higher the temperature of activation, the greater the extent of activation and widening of pores. Therefore properties of carbon can be readily tailored to specific targets by carefully controlling that amount of activating agent and temperature of activation. As for pre-mixing, it was done for the first time in this thesis.

Activation Temperature

It is known that for any given carbon precursor and activating agent combination, there is an optimum temperature for porosity development. In general, the porosity increases with temperature to a maximum and then begins to decrease with further increase of the temperature due to shrinkage or collapse of the carbon structure.[172, 173] Generally, high temperature of activation leads to enhanced textural properties (surface area and pore volume) in the resulting carbons. However, very high temperature can generate wide pore size distribution with micropores, mesopores and macropores, which can be undesirable. Low activation temperature (600 ^{o}C - 700 ^{o}C), on the other hand yields carbons with low surface area between (1000 m^2g^{-1} - 2000 m^2g^{-1}) with narrow PSD in micropore range.

Potassium Hydroxide (KOH) as Chemical Activation Agent

KOH has been studied as an activating agent to develop porosity in a range of precursor carbonaceous materials since the late 1970s when commercially available ACs, (AX21 and Maxsorb), were prepared using fossil-based carbon sources.[123, 174] KOH has been found to be more effective than other activating agents such as as $ZnCl_2$ and H_3PO_4 in creating porosity.[175, 176] Generally, KOH as activating works well with various carbon sources/precursors such as wood and nutshells, hydrothermally carbonized carbon,[44,68] polymers rich of carbon,[111,93] petroleum coke,[123] CDCs,[177, 178] zeolite templated carbons (ZTCs),[179] other forms of templated carbons [180] and graphene.[181] KOH activating is very promising because it has attractive properties/advantages such as:

(i) Ultrahigh specific high surface areas of up to 4000 m^2g^{-1} in the resulting carbon.

(ii) A significant proportion of the porosity arises from uniform micropores in the range of 1-2 nm.

(iii) High pore volume of up to 3.0 cm^3g^{-1}.

(iv)The pore structure can be tailored by varying the activating parameters such as activation temperature, KOH/carbon precursor ratio etc.

(v) Activation may be performed *via* an easy one-step process.

(vi) Lower activation temperature compared to other activating agents.

(vii) Higher carbon yields.

The amount of KOH used is one of the most important parameter that influences the porosity of the resulting carbons. For instance, high amounts of KOH may led to increased porosity, but usually at the expense of pore size uniformity, i.e., broadening of the PSD. However, control of the amount of activation agent and activation temperature are both required to achieve any given level of porosity.[182, 183]

Mixing Procedure

One major limitation of using KOH as activation agent is that in most cases the KOH and carbon precursor are both solids. In other words, the activation process between of KOH particles and carbon precursor particles is predicated initially on solid–solid interactions, which means the mixing and activation process can be slow and inefficient and some carbon particles may not be optimally activated leading to waste of KOH. Therefore, it requires higher temperature as well as higher amounts of activating agent to achieve a given level of activation and porosity. Compaction of the mixture of KOH and carbon precursor into pellets/disks rather than activating them as powder-like forms can be a solution because it leads to increase in the level

of mixing as well as increasing the level of contact between KOH particles and carbon precursor particles. Therefore, compaction reduces inter particle voids before the thermal activation treatment.[45]

Mechanism of KOH Activation

Generally, there is a complex process with several chemical reactions, which starts *via* solid–solid reactions (carbon and KOH) then proceeds *via* solid–liquid reactions including the reduction of potassium compound to form metallic K (see **Figure 1.10** and **Table 1.3**). Although the activation mechanism using KOH is a well-known method used to produce the pore network in carbons, it has not been well understood because of the large number of experimental parameters and the reactivity of different precursors used. Reactions 5, 8, 9 allow etching of the carbon framework to generate the pore network. On the other hand, reactions 2, 7, 9 form H_2O and CO_2, leads to further development of the porosity through gasification of the carbon. Reactions 5, 8, 9 generate metallic K, which intercalates into the carbon matrix resulting in expansion of the carbon lattices as shown in **Figure 1.10**. The intercalated metallic K and other K compounds are removed during washing, which generates further porosity as the expanded carbon matrix cannot return to its previous nonporous nature.

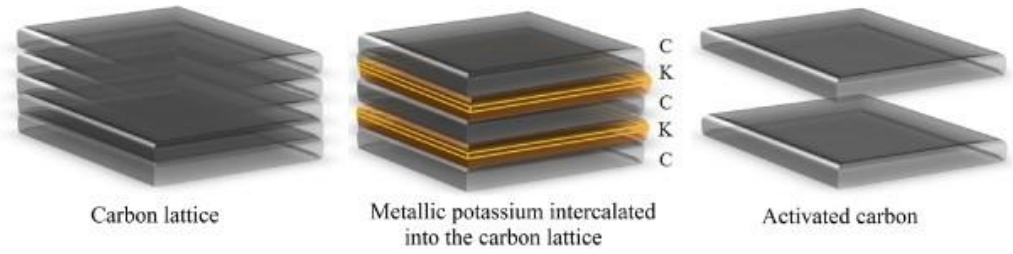


Figure 1.10: Mechanism of activation using KOH. Firstly, by the penetration of metallic K into the carbon lattices, and the removal of K from the carbon matrix.[83, 176]

Table 1.3: Mechanism of KOH activation.[83, 176]		
Explanation	Reaction	eq
At 400 °C KOH is dehydrated to transform into K_2O.	$2\ KOH \rightarrow K_2O + H_2O$	1
Carbon consumed by the reaction of carbon and H_2O with the emission of H_2.	$C + H_2O \rightarrow CO + H_2$	2
Reaction of CO with H_2O with the emission of H_2.	$CO + H_2O \rightarrow CO_2 + H_2$	3
Formation of K_2CO_3 by the reaction between K_2O and CO_2 which is produced in the reaction in eq (3).	$CO_2 + K_2O \rightarrow K_2CO_3$	4
During KOH activation at temperatures <700 °C, the reactions between KOH (activating agent) and the carbonaceous materials consist of solid–solid or solid–liquid processes that occur through stoichiometric redox reaction. At about 600 °C, KOH is completely consumed/disappears at 800 °C.	$6KOH + 2C \rightarrow 2K + 3H_2 + 2K_2CO_3$	5
At temperatures higher than 700 °C, K_2CO_3 which formed in eq (4) and (5) significantly decomposing into CO_2 and K_2O	$K_2CO_3 \rightarrow K_2O + CO_2$	6
The resulting CO_2 from eq (6) can be reduced more by C to form CO at high temperature.	$CO_2 + C \rightarrow 2CO$	7
K_2CO_3 can be reduced more by C to produce metallic K at over than 700 °C.	$K_2CO_3 + 2C \rightarrow 2K + 3CO$	8
K_2O can be reduced more by C to produce metallic K at over than 700 °C.	$K_2O + C \rightarrow 2K + CO$	9

1.3.2.3.2.1.4 Doped Carbons

Recently, functionalization of the surfaces of carbon-based materials such as activated carbons has received great attention due to the influence of such functionalization on their properties and therefore consequently on their application such as in hydrogen storage, CO_2 capture, and electrical energy storage. Doping of heteroatoms onto carbons can be achieved *via* introducing atoms such as oxygen, nitrogen, or sulfur into the carbon framework. N-doped carbons have received a great deal of research interest,[75, 144, 184, 185] However, few studies have focused on S-doped carbonaceous materials.[76, 77] N-doped Porous carbons can be prepared *via* three ways: (i) a simple route of direct carbonization of N-containing precursors at high temperatures, the nitrogen-containing precursors can be N-containing polymers such as polypyrrole (PPY) and other organic polymers; **Figure 1.11** shows different carbon precursors, (ii) using N-containing gases such as ammonia with heat treatment of porous carbons, and (iii) carbonization of mixtures of N-containing organic compounds and N-free materials. [186-188]

In case of hydrogen uptake capacity, functionalization of the surface can improve the weak interaction between H_2 gas and most porous materials. In particular, recently, the effect of doping various heteroatoms onto porous carbon on hydrogen uptake have been investigated.[86, 93, 111, 189-192] Sevilla *et. al*.[193] reported a one-step chemical activation of polythiophene polymer using KOH as activating agent to produce S-doped carbons with high surface area and large pore volume and S content of 3 – 12 wt%. The carbons had hydrogen storage capacity of up to 5.71 wt% at 20 bar and -196 ^oC. The textural properties and chemical composition (varying S content) of the carbons were tuned by modifying the activation temperature from 600 ^oC to 850 ^oC. Several studies have hinted at positive effects on

atomic hydrogen storage emanating from the presence of certain oxygen containing functional groups on the surface of carbons.[194-196] For instance, Yang *et. al.*[194, 197] reported that the hydrogen storage capacity of metal-doped carbons could be significantly enhanced by introducing surface oxygen functional groups. Also recently, Shayeganfar *et. al.* reported that oxygen-doping improves hydrogen storage capacity of pillared graphene boron nitride.[196]

In the case of CO_2 selectivity and CO_2 capturing, the introduction of nitrogen into the framework of porous carbons is thought to mimic the amine scrubbing process in enhancing the CO_2 uptake.[187] However, Sevilla *et. al.*[143] prepared a series of activated carbons samples; un-doped and N-doped, to study the effect of doping, and found that the presence of nitrogen in nitrogen-doped carbons has no influence in the CO_2 adsorption. Titirici *et. al.*[198] found that N-doping of carbons with slit-shaped pores has no significant influence in the CO_2 uptake. Moreover, Mokaya *et. al.* prepared a series of carbons samples; N-free or N-doped with closely matched porosity, in an attempt to conclusively clarify the relative influence of N-doping and pore size on the CO_2 uptake capacity at low pressure (≤1 bar). Both N-free and N-doped carbon materials, exhibited similar total surface areas (920 ± 60 m^2 g), while their micropore surface area range was even narrower (860 ± 40 m^2 g^{-1}), and found that N-doping has no positive effect on the adsorption.[187]

In contrast, most previous studies agree that CO_2 adsorption on carbons is very sensitive to and dependent on the pore size, and in particular to the slightest changes in micropore size distribution with pore size of 5−10 Å. Thus, to maximise CO_2 uptake capacity, activated carbons need to have a high surface area arising from micropores; recent studies have found that porous carbon materials with micropores ≤ 7–9 Å show better CO_2 uptakes

than those with pores ≥ 9 Å. The pore size of activated carbons can be tailored towards micropores by varying the carbonizing and activating processes.[153]

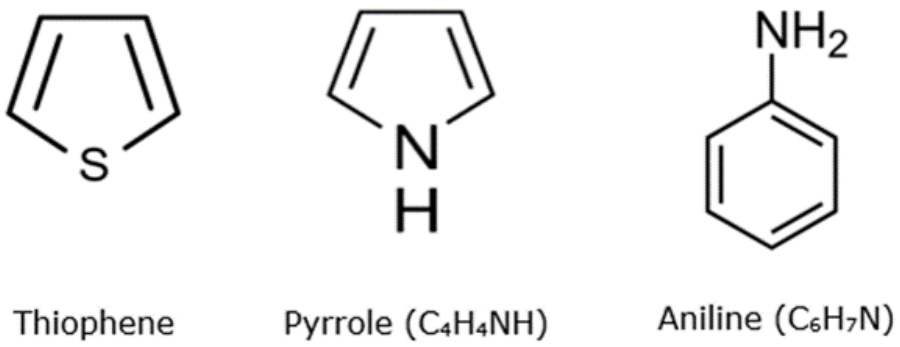


Figure 1.11: Shows chemical structures of thiophene, pyrrole, and aniline.

In my thesis, doped effects have not been investigated due to the low percentage of sulfur and nitrogen doping contents in both PTh-based activated carbons (**Chapter 4**) and PPY-based activated carbons (**Chapter 7**).

1.4 Carbon Precursors Used in This Study

1.4.1 Polythiophene

Polythiophene has received extensive attention for studies in a variety of fields due to being amenable to easy structural modification, which is a desirable property for material science applications.[199-201] Polythiophene may be synthesized *via* two methods;[202] (i) electrochemically or (ii) chemically synthesis. S-doped carbons can also be simply produced by carbonization of S-rich precursors such as polythiophene, cysteine, etc.[203-205] Some previous studies have focused on S-doped porous carbons fabrication.[111, 203-205] Shin *et al.* reported the synthesis of templated mesoporous carbons containing sulphur at 4-7 wt % using thiophenemethanol as a precursor and SBA-15 as template which produced carbon with an excellent mercury sorption performance due to the high S→Hg affinity.[203] Sevilla *et al*. reported the first one-step chemical activation polythiophene to S-doped activated carbons with high surface area and large pore volume of up to 3000 m^2g^{-1}, and 1.75 cm^3g^{-1} respectively, as well as S-contents of 3 –12 wt% and hydrogen storage capacity of up to 5.71 wt% at 20 bar (77 K).[111]

1.4.1.1 Polypyrrole

Polypyrrole has found use in a number of applications due to its relative ease of preparation and environmental stability.[206-210] Polypyrrole has previously been studied as a carbon precursor.[12, 45, 72, 93, 105, 187, 211] In general, polypyrrole offers good porous carbon yields on pyrolysis as well as high porosity with high surface area >3400 m^2g^{-1} and a high packing density.[12, 45, 93] Polypyrrole can be synthesized chemically [212] by oxidative

polymerization of pyrrole monomer or electrochemically.[200, 213] The use of polypyrrole for activated carbon synthesis has recently attracted attention. For example, Mokaya and co-workers [12] used polypyrrole as a carbon precursor to activated carbon with ultra-high surface area in the range of 2800–4000 m^2 g^1 and large pore volume in the range of 2.5 – 3.6 cm^3 g^1, with up to 95% mesoporosity and a near total absence of micropores. The mesoporous carbons were found to be ideal for CO_2 uptake under conditions that closely mimic pre-combustion CO_2 capture and storage, i.e., 25 ^oC and pressure range of 20-50 bar. The gravimetric (mmol g^{-1}) CO_2 uptake capacities were amongst the highest ever reported for porous carbons; up to 28 (20 bar), 37 (30 bar), 46 (40 bar) and 55 (50 bar). The high gravimetric CO_2 uptake of the mesoporous carbons in combination with their packing density (0.25–0.4 gcm^{-3}) offered colossal volumetric uptake (in gl^{-1}) of up to 480 (20 bar), 640 (30 bar), 780 (40 bar) and 930 (50 bar). Due to their mesoporosity, the carbons were highly suited, in terms of the CO_2 adsorption capacity and selectivity over H_2, as materials for hydrogen purification under syngas flow conditions.[12]

1.4.1.1.1.1.1 Zeolite Templated Carbons

Zeolite templated carbons (ZTCs) have attracted particular interest due to their proprieties such as high surface area and micropore structure, which are both helpful for enhancing hydrogen storage. Considerable efforts in exploiting the tuneable properties of zeolites to produce carbon materials with increased hydrogen adsorption are currently ongoing. The first to report on ZTCs for hydrogen storage was Mokaya and co-workers.[191] The prepared carbons exhibited a hydrogen storage capacity of 4.5 wt% at -196 ^oC and 20 bar. Later Mokaya and co-workers [85] prepared high surface area carbons *via*

a CVD process using zeolite β as template and acetonitrile as carbon precursor, achieving 6.9 wt% hydrogen storage at 77 K and 20 bar which was the highest uptake ever reported for templated carbon materials, and porous carbons in general. Later, Mokaya and co-workers [214] also successfully generated ultrahigh surface area ZTCs with a remarkable hydrogen uptake of 7.3 wt% (at 20 bar and 77 K), via a two-step nanocasting process involving (i) liquid impregnation of zeolite 13X with furfural alcohol followed by (ii) chemical vapour deposition (CVD) of ethylene at 700 °C.

ZTCs are prepared by the thermal treatment of a zeolite, in which a carbon precursor fills the zeolite's porous to adopt its reciprocal structure.[81] Following the removal of the zeolite template *via* selective etching, the resulting carbon structure exhibits a network of pore channels that are inversely replicated from the zeolite.[215-222] More generally, the synthesis of templated carbons involves the following four stages;

(i) Pre-treatment/preparation of the porous inorganic template by drying to open the pores or remove impurities.

(ii) Introduction of a suitable carbon precursor such as furfuryl alcohol FA, acetonitrile, into the template pores by liquid impregnation or chemical vapour deposition CVD or combination of both liquid impregnation and chemical vapour deposition CVD.

(iii) Carbonisation of the carbon precursor to generate inorganic/ organic composite at a specific temperature.

(iv) Finally, template removal by dissolution in an alkali (NaOH) or acidic media such as HF or HCI. **Figure 1.12** illustrates a typical nanocasting technique using zeolite Y as a hard template.[222, 223]

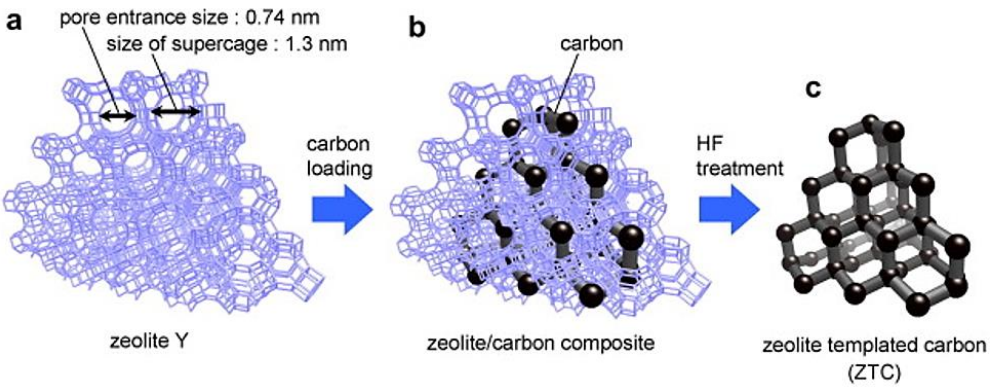


Figure 1.12: Typical nanocasting technique using zeolite Y as a hard template. (a) Zeolite Y template crystal structure, (b) composite (zeolite/carbon), and (c) framework structure of liberate carbon after zeolite etching in HF acid.[222]

1.5 The Aim of My Research

The first aim was to increase the volumetric storage capacity of carbons for energy related gases. At the present time, the materials with the highest surface area generally tend to have low packing density and therefore low volumetric uptake. Enhancements in packing density and consequently volumetric storage capacity of porous materials may be achieved by material densification or compaction. In my thesis, the effect of compactivation (i.e., mechanochemical synthesis approach) to increase packing density and therefore high volumetric uptake was explored with respect gas (CO_2 and H_2) storage.

The second aim was to find new simpler routes to activated carbons. In the search for sustainable and cheaper biomass-derived activated carbons it is desirable to simplify the synthesis process and in particular to negate the need for hydrothermal carbonisation or pyrolysis prior to activation. In other words, it is desirable to directly activate biomass to activated carbons that have similar or improved yield and/or properties compared to those that are prepared *via* the conventional, and longer, two-step route incorporating HTC (HTC + activation) or pyrolysis prior to activation.

This thesis also aimed to generate activated carbons from sythetic polymers e.g. polythiophene and plolypyrrole as S-doped carbons or N-doped carbon respectively.

1.6 References

1. D. B. Dell'Amico, F. Calderazzo, L. Labella, F. Marchetti and G. Pampaloni, *Chem. Rev.*, 2003, **103**, 3857-3897.

2. V. Jiménez, A. Ramírez-Lucas, J. A. Díaz, P. Sánchez and A. Romero, *Environ. Sci. Technol.*, 2012, **46**, 7407-7414.

3. D. M. D'Alessandro, B. Smit and J. R. Long, *Angew. Chem. Int. Ed.*, 2010, **49**, 6058-6082.

4. A. Samanta, A. Zhao, G. K. H. Shimizu, P. Sarkar and R. Gupta, *Ind. Eng. Chem. Res.*, 2012, **51**, 1438-1463.

5. D. Y. C. Leung, G. Caramanna and M. M. Maroto-Valer, *Renew. Sust. Energ. Rev.*, 2014, **39**, 426-443.

6. M. Mikkelsen, M. Jorgensen and F. C. Krebs, *Energy Environ. Sci.*, 2010, **3**, 43-81.

7. Green house effect, https://www.quora.com/What-does-global-warming-mean, (accessed 28/5/2018).

8. R. Thiruvenkatachari, S. Su, H. An and X. X. Yu, *Prog. Energy Combust. Sci.*, 2009, **35**, 438-455.

9. T. L. P. Dantas, F. M. T. Luna, I. J. Silva, A. E. B. Torres, D. C. S. de Azevedo, A. E. Rodrigues and R. Moreira, *Chem. Eng. J.*, 2011, **172**, 698-704.

10. F. T. Zangeneh, S. Sahebdelfar and M. T. Ravanchi, *J. Nat. Gas Chem.*, 2011, **20**, 219-231.

11. J. Amouroux, P. Siffert, J. P. Massue, S. Cavadias, B. Trujillo, K. Hashimoto, P. Rutberg, S. Dresvin and X. H. Wang, *Prog. Nat. Sci.*, 2014, **24**, 295-304.

12. M. Cox and R. Mokaya, *Sustainable Energy & Fuels*, 2017, **1**, 1414-1424.

13. S. Choi, J. H. Drese and C. W. Jones, *ChemSusChem*, 2009, **2**, 796-854.

14. M. E. Boot-Handford, J. C. Abanades, E. J. Anthony, M. J. Blunt, S. Brandani, N. Mac Dowell, J. R. Fernández , M. C. Ferrari, R. Gross, J. P. Hallett, R. S. Haszeldine, P. Heptonstall, A. Lyngfelt, Z. Makuch, E. Mangano, R. T. J. Porter, M. Pourkashanian, G. T. Rochelle, N. Shah, J. G. Yao and P. S. Fennell, *Energy Environ. Sci.*, 2014, **7**, 130-189.

15. K. Z. House, A. C. Baclig, M. Ranjan, E. A. van Nierop, J. Wilcox and H. J. Herzog, *Proc. Natl. Acad. Sci. U.S.A.*, 2011, **108**, 20428-20433.

16. H. J. Schellnhuber, *Proc. Natl. Acad. Sci. U.S.A.*, 2011, **108**, 20277-20278.

17. T. C. Drage, C. E. Snape, L. A. Stevens, J. Wood, J. W. Wang, A. I. Cooper, R. Dawson, X. Guo, C. Satterley and R. Irons, *J. Mater. Chem.*, 2012, **22**, 2815-2823.

18. G. T. Rochelle, *Science*, 2009, **325**, 1652-1654.

19. S. P. Wang, S. L. Yan, X. B. Ma and J. L. Gong, *Energy Environ. Sci.*, 2011, **4**, 3805-3819.

20. Q. A. Wang, J. Z. Luo, Z. Y. Zhong and A. Borgna, *Energy Environ. Sci.*, 2011, **4**, 42-55.

21. J. Wilcox, *Carbon Capture*, Springer, New York, 2012.

22. B. Smit, J. R. Reimer, C. M. Oldenburg and I. C. Bourg, *Introduction to Carbon Capture and Sequestration*, Imperial College Press, London, 2014.

23. J. P. Marco-Lozar, M. Kunowsky, F. Suárez-García, J. D. Carruthers and A. Linares-Solano, *Energy Environ. Sci.*, 2012, **5**, 9833-9842.

24. G. P. Hao, W. C. Li, D. Qian and A. H. Lu, *Adv. Mater.*, 2010, **22**, 853–857.

25. J. Silvestre-Albero, A. Wahby, A. Sepúlveda-Escribano, M. Martínez-Escandell, K. Kaneko and F. Rodríguez- Reinoso, *Chem. Commun.*, 2011, **47**, 6840-6842.

26. M. Sevilla and A. B. Fuertes, *J. Colloid Interface Sci.*, 2012, **366**, 147-154.

27. M. R. Hudson, W. L. Queen, J. A. Mason, D. W. Fickel, R. F. Lobo and C. M. Brown, *J. Am. Chem. Soc.*, 2012, **134**, 1970-1973.

28. R. V. Siriwardane, M. S. Shen and E. P. Fisher, *Energy Fuels*, 2005, **19**, 1153-1159.

29. J. Merel, M. Clausse and F. Meunier, *Ind. Eng. Chem. Res.*, 2008, **47**, 209-215.

30. R. V. Siriwardane, M. S. Shen, E. P. Fisher and J. A. Poston, *Energy Fuels*, 2001, **15**, 279-284.

31. Z. J. Zhang, Z. Z. Yao, S. C. Xiang and B. L. Chen, *Energy Environ. Sci.*, 2014, **7**, 2868-2899.

32. K. Sumida, D. L. Rogow, J. A. Mason, T. M. McDonald, E. D. Bloch, Z. R. Herm, T. H. Bae and J. R. Long, *Chem. Rev.*, 2012, **112**, 724-781.

33. A. R. Millward and O. M. Yaghi, *J. Am. Chem. Soc.*, 2005, **127**, 17998-17999.

34. Q. Y. Yang, C. L. Zhong and J. F. Chen, *J. Phys. Chem. C*, 2008, **112**, 1562-1569.

35. E. Blomen, C. Hendriks and F. Neele, *Greenhouse Gas Control Technol.*, 2009, **1**, 1505-1512.

36. E. I. Koytsoumpa, C. Bergins and E. Kakaras, *J. Supercrit. Fluids*, 2018, **132**, 3-16.

37. E. G. Hertwich, M. Aaberg, B. Singh and A. H. Stromman, *Chin. J. Chem. Eng.*, 2008, **16**, 343-353.

38. D. Weisser, *Energy*, 2007, **32**, 1543-1559.

39. P. Zapp, A. Schreiber, J. Marx, M. Haines, J. F. Hake and J. Gale, *Int. J. Greenhouse Gas Control*, 2012, **8**, 12-21.

40. P. Markewitz, W. Kuckshinrichs, W. Leitner, J. Linssen, P. Zapp, R. Bongartz, A. Schreiber and T. E. Muller, *Energy Environ. Sci.*, 2012, **5**, 7281-7305.

41. R. M. Cuéllar- Franca and A. Azapagic, *J. CO_2 Util.*, 2015, **9**, 82-102.

42. P. H. M. Feron and C. A. Hendriks, *Oil Gas Sci. Technol.*, 2005, **60**, 451-459.

43. M. a. R. Reinoso, *Activated Carbon*, 2006.

44. M. Sevilla and R. Mokaya, *Energy Environ. Sci.*, 2014, **7**, 1250-1280.

45. B. Adeniran and R. Mokaya, *Nano Energy*, 2015, **16**, 173-185.

46. W. Sangchoom and R. Mokaya, *ACS Sustainable Chem. Eng.*, 2015, **3**, 1658-1667.

47. N. Balahmar, A. C. Mitchell and R. Mokaya, *Adv. Energy Mater.*, 2015, **5**.

48. A. Almasoudi and R. Mokaya, *J. Mater. Chem. A*, 2014, **2**, 10960-10968.

49. C. Robertson and R. Mokaya, *Microporous Mesoporous Mater.*, 2013, **179**, 151-156.

50. E. Haffner-Staton, N. Balahmar and R. Mokaya, *J. Mater. Chem. A*, 2016, **4**, 13324-13335.

51. B. Adeniran and R. Mokaya, *J. Mater. Chem. A*, 2015, **3**, 5148-5161.

52. M. Balat, *Int. J. Hydrogen Energy*, 2008, **33**, 4013-4029.

53. Hydrogen Basics, http://www.fsec.ucf.edu/en/consumer/hydrogen/basics/introduction.htm, (accessed 17/6/2018).

54. P. P. Edwards, V. L. Kuznetsov, W. I. F. David and N. P. Brandon, *Energy Policy*, 2008, **36**, 4356-4362.

55. K. T. Møller , T. R. Jensen, E. Akiba and H. W. Li, *Prog. Nat. Sci.*, 2017, **27**, 34-40.

56. S. Sharma and S. K. Ghoshal, *Renew. Sust. Energy Rev.*, 2015, **43**, 1151-1158.

57. J. O. M. Bockris *Environmental Chemistry, The Hydrogen Economy Chapter*, Springer, 1977.

58. L. Schlapbach and A. Züttel, *Nature*, 2001, **414**, 353-358.

59. A. Züttel, P. Sudan, P. Mauron, T. Kiyobayashi, C. Emmenegger and L. Schlapbach, *Int. J. Hydrogen Energy*, 2002, **27**, 203-212.

60. Hydrogen storage, https://www.energy.gov/eere/fuelcells/hydrogen-storage, (accessed 28/5/2018).

61. U. S. D. o. E. Website:, https://www1.eere.energy.gov/hydrogenandfuelcells/storage/current_technology.html.).

62. Hydrogen Production and Storage: R&D Priorities and Gaps,OECD/IEAO, 2006, https://www.iea.org/publications/freepublications/publication/hydrogen.pdf).

63. P. Jena, *J. Phys. Chem. Lett.*, 2011, **2**, 206-211.

64. B. Sakintuna, F. Lamari-Darkrim and M. Hirscher, *Int. J. Hydrogen Energy*, 2007, **32**, 1121-1140.

65. A. H. Berger and A. S. Bhown, *Energy Procedia*, 2011, **4**, 562-567.

66. J. A. Turner, *Science*, 1999, **285**, 687-689.

67. L. L. Zhang and X. S. Zhao, *Chem. Soc. Rev.*, 2009, **38**, 2520-2531.

68. L. Wei and G. Yushin, *Nano Energy*, 2012, **1**, 552-565.

69. H. Furukawa, N. Ko, Y. B. Go, N. Aratani, S. B. Choi, E. Choi, A. O. Yazaydin, R. Q. Snurr, M. O'Keeffe, J. Kim and O. M. Yaghi, *Science*, 2010, **329**, 424-428.

70. A. O. Yazaydin, A. I. Benin, S. A. Faheem, P. Jakubczak, J. J. Low, R. R. Willis and R. Q. Snurr, *Chem. Mater.*, 2009, **21**, 1425-1430.

71. M. Sevilla and A. B. Fuertes, *Energy Environ. Sci.*, 2011, **4**, 1765-1771.

72. M. Sevilla, P. Valle-Vigon and A. B. Fuertes, *Adv. Funct. Mater.*, 2011, **21**, 2781-2787.

73. V. Presser, J. McDonough, S. H. Yeon and Y. Gogotsi, *Energy Environ. Sci.*, 2011, **4**, 3059-3066.

74. E. Masika and R. Mokaya, *RSC Adv.*, 2013, **3**, 17677-17681.

75. Y. D. Xia, R. Mokaya, G. S. Walker and Y. Q. Zhu, *Adv. Energy Mater.*, 2011, **1**, 678-683.

76. M. Sevilla, A. B. Fuertes and R. Mokaya, *Energy Environ. Sci.*, 2011, **4**, 1400-1410.

77. A. W. C. van den Berg and C. O. Arean, *Chem. Commun.*, 2008, 668-681.

78. H. Furukawa, K. E. Cordova, M. O'Keeffe and O. M. Yaghi, *Science*, 2013, **341**, 974.

79. Y. H. Xu, S. B. Jin, H. Xu, A. Nagai and D. L. Jiang, *Chem. Soc. Rev.*, 2013, **42**, 8012-8031.

80. Y. D. Xia, Z. X. Yang and R. Mokaya, *Nanoscale*, 2010, **2**, 639-659.

81. H. Nishihara and T. Kyotani, *Adv. Mater.*, 2012, **24**, 4473-4498.

82. Y. D. Xia, Z. X. Yang and Y. Q. Zhu, *J. Mater. Chem. A*, 2013, **1**, 9365-9381.

83. J. C. Wang and S. Kaskel, *J. Mater. Chem.*, 2012, **22**, 23710-23725.

84. T. Kyotani, T. Nagai, S. Inoue and A. Tomita, *Chem. Mater.*, 1997, **9**, 609-615.

85. Z. X. Yang, Y. D. Xia and R. Mokaya, *J. Am. Chem. Soc.*, 2007, **129**, 1673-1679.

86. Y. D. Xia, G. S. Walker, D. M. Grant and R. Mokaya, *J. Am. Chem. Soc.*, 2009, **131**, 16493-16499.

87. Y. D. Xia, R. Mokaya, D. M. Grant and G. S. Walker, *Carbon*, 2011, **49**, 844-853.

88. M. Jordá-Beneyto, D. Lozano-Castelló , F. Suárez-García , D. Cazorla-Amorós and A. Linares-Solano, *Microporous Mesoporous Mater.*, 2008, **112**, 235-242.

89. G. Sethia and A. Sayari, *Energy Fuels*, 2014, **28**, 2727-2731.

90. B. D. Zdravkov, J. J. Cermak, M. Sefara and J. Janku, *Cent. Eur. J. Chem.*, 2007, **5**, 385-395.

91. J. Rouquerol, D. Avnir, C. W. Fairbridge, D. H. Everett, J. H. Haynes, N. Pernicone, J. D. F. Ramsay, K. S. W. Sing and K. K. Unger, *Pure Appl. Chem.*, 1994, **66**, 1739-1758.

92. M. Sevilla, N. Alam and R. Mokaya, *J. Phys. Chem. C*, 2010, **114**, 11314-11319.

93. M. Sevilla, R. Mokaya and A. B. Fuertes, *Energy Environ. Sci.*, 2011, **4**, 2930-2936.

94. A. C. Dillon, K. M. Jones, T. A. Bekkedahl, C. H. Kiang, D. S. Bethune and M. J. Heben, *Nature*, 1997, **386**, 377-379.

95. N. Alam and R. Mokaya, *Energy Environ. Sci.*, 2010, **3**, 1773-1781.

96. Z. X. Ma, T. Kyotani, Z. Liu, O. Terasaki and A. Tomita, *Chem. Mater.*, 2001, **13**, 4413-4415.

97. Z. X. Ma, T. Kyotani and A. Tomita, *Chem. Commun.*, 2000, 2365-2366.

98. T. Kyotani, Z. X. Ma and A. Tomita, *Carbon*, 2003, **41**, 1451-1459.

99. C. Liu, Y. Y. Fan, M. Liu, H. T. Cong, H. M. Cheng and M. S. Dresselhaus, *Science*, 1999, **286**, 1127-1129.

100. A. La Torre, G. A. Rance, J. El Harfi, J. N. Li, D. J. Irvine, P. D. Brown and A. N. Khlobystov, *Nanoscale*, 2010, **2**, 1006-1010.

101. N. Alam and R. Mokaya, *Microporous Mesoporous Mater.*, 2011, **144**, 140-147.

102. Activated Carbon and its Applications, https://www.donau-carbon.com/getattachment/76f78828-2139-496f-9b80-6b6b9bdc6acc/aktivkohle.aspx, (accessed 17/6/2018).

103. S. Wong, N. Ngadi, I. M. Inuwa and O. Hassan, *J. Clean. Prod.*, 2018, **175**, 361-375.

104. J. Romanos, M. Beckner, T. Rash, L. Firlej, B. Kuchta, P. Yu, G. Suppes, C. Wexler and P. Pfeifer, *Nanotechnology*, 2012, **23**, 015401.

105. L. Wei, M. Sevilla, A. B. Fuertes, R. Mokaya and G. Yushin, *Adv. Funct. Mater.*, 2012, **22**, 827-834.

106. F. a. Çeçen and Ö. Aktas, *Activated Carbon for Water and Wastewater Treatment: Integration of Adsorption and Biological Treatment*, 2012, 1-388.

107. D. Mohan and C. U. Pittman, *J. Hazard. Mater.*, 2007, **142**, 1-53.

108. T. Otowa, Y. Nojima and T. Miyazaki, *Carbon*, 1997, **35**, 1315-1319.

109. J. Rivera-Utrilla, M. Sánchez- Polo, V. Gomez-Serrano, P. M. Alvarez, M. C. M. Alvim-Ferraz and J. M. Dias, *J. Hazard. Mater.*, 2011, **187**, 1-23.

110. E. N. El Qada, S. J. Allen and G. M. Walker, *Chem. Eng. J.*, 2008, **135**, 174-184.

111. M. Sevilla, A. B. Fuertes and R. Mokaya, *Int. J. Hydrogen Energy*, 2011, **36**, 15658-15663.

112. Different types of activated carbon, http://www.haycarb.com/activated-carbon, (accessed 15/10/2018).

113. Different types of activated carbon, http://www.oxbowactivatedcarbon.com/knowledgecenter/38, (accessed 13/10/2018).

114. Different types of activated carbon, http://www.redwhitechem.com/articles/types-of-activated-carbon.html, (accessed 12/10/2018).

115. Types of activated carbon, http://www.acarbons.com/what-is-pelletized-activated-carbon-and-what-it-is-used-for/, (accessed 12/10/2018).

116. F. Rodríguez-reinoso, *Carbon*, 1998, **36**, 159-175.

117. F. S. Baker, Miller, C. E., Repik, A. J., and Tolles, E. D., Kirk-Othmer, *Encyclopedia of Chemical Technology*, John Wiley & Sons, 1992.

118. O. Ioannidou and A. Zabaniotou, *Renew. Sust. Energy Rev.*, 2007, **11**, 1966-2005.

119. K. Y. Foo and B. H. Hameed, *Adv. Colloid Interface Sci.*, 2009, **152**, 39-47.

120. F. Caturla, M. Molina-Sabio and F. Rodríguez-Reinoso, *Carbon*, 1991, **29**, 999-1007.

121. F. Rodríguez-Reinoso and M. Molina-Sabio, *Carbon*, 1992, **30**, 1111-1118.

122. F. Rodríguez-Reinoso, M. Molina-Sabio and M. T. González, *Carbon*, 1995, **33**, 15-23.

123. T. Otowa, R. Tanibata and M. Itoh, *Gas Sep. Purif.*, 1993, **7**, 241-245.

124. R. Z. Bai, M. L. Yang, G. S. Hu, L. Q. Xu, X. Hu, Z. M. Li, S. L. Wang, W. Dai and M. H. Fan, *Carbon*, 2015, **81**, 465-473.

125. L. Q. Xu, L. P. Guo, G. S. Hu, J. H. Chen, X. Hu, S. L. Wang, W. Dai and M. H. Fan, *RSC Adv.*, 2015, **5**, 37964-37969.

126. M. L. Yang, L. P. Guo, G. S. Hu, X. Hu, J. Chen, S. W. Shen, W. Dai and M. H. Fan, *Ind. Eng. Chem. Res.*, 2016, **55**, 757-765.

127. X. P. Zhu, Y. Fu, G. S. Hu, Y. Shen, W. Dai and X. Hu, *Water Air and Soil Pollut.*, 2013, **224**, 12.

128. M. G. Nijkamp, J. Raaymakers, A. J. van Dillen and K. P. de Jong, *Appl. Phys. A: Mater. Sci. Process.*, 2001, **72**, 619-623.

129. I. Cabria, M. J. López and J. A. Alonso, *Carbon*, 2007, **45**, 2649-2658.

130. R. Ströbel, J. Garche, P. T. Moseley, L. Jörissen and G. Wolf, *J. Power Sources*, 2006, **159**, 781-801.

131. Y. Gogotsi, C. Portet, S. Osswald, J. M. Simmons, T. Yidirim, G. Laudisio and J. E. Fischer, *Int. J. Hydrogen Energy*, 2009, **34**, 6314-6319.

132. G. Yushin, R. Dash, J. Jagiello, J. E. Fischer and Y. Gogotsi, *Adv. Funct. Mater.*, 2006, **16**, 2288-2293.

133. J. Chmiola, G. Yushin, Y. Gogotsi, C. Portet, P. Simon and P. L. Taberna, *Science*, 2006, **313**, 1760-1763.

134. J. Chmiola, C. Largeot, P. L. Taberna, P. Simon and Y. Gogotsi, *Angew. Chem. Int. Ed.*, 2008, **47**, 3392-3395.

135. J. Chmiola, G. Yushin, R. Dash and Y. Gogotsi, *J. Power Sources*, 2006, **158**, 765-772.

136. E. Raymundo- Piñero , K. Kierzek, J. Machnikowski and F. Béguin, *Carbon*, 2006, **44**, 2498-2507.

137. A. N. A. El-Hendawy, A. J. Alexander, R. J. Andrews and G. Forrest, *J. Anal. Appl. Pyrolysis*, 2008, **82**, 272-278.

138. P. Nowicki, R. Pletrzak and H. Wachowska, *Fuel*, 2008, **87**, 2037-2040.

139. J. D. Figueroa, T. Fout, S. Plasynski, H. McIlvried and R. D. Srivastava, *Int. J. Greenhouse Gas Control*, 2008, **2**, 9-20.

140. H. Q. Yang, Z. H. Xu, M. H. Fan, R. Gupta, R. B. Slimane, A. E. Bland and I. Wright, *J. Environ. Sci.*, 2008, **20**, 14-27.

141. M. Nandi, K. Okada, A. Dutta, A. Bhaumik, J. Maruyama, D. Derks and H. Uyama, *Chem. Commun.*, 2012, **48**, 10283-10285.

142. X. Q. Fan, L. X. Zhang, G. B. Zhang, Z. Shu and J. L. Shi, *Carbon*, 2013, **61**, 423-430.

143. M. Sevilla, J. B. Parra and A. B. Fuertes, *ACS Appl. Mater. Interfaces*, 2013, **5**, 6360-6368.

144. M. Saleh, V. Chandra, K. C. Kemp and K. S. Kim, *Nanotechnology*, 2013, **24**, 8.

145. H. R. Wei, S. B. Deng, B. Y. Hu, Z. H. Chen, B. Wang, J. Huang and G. Yu, *ChemSusChem*, 2012, **5**, 2354-2360.

146. N. P. Wickramaratne and M. Jaroniec, *J. Mater. Chem. A*, 2013, **1**, 112-116.

147. N. P. Wickramaratne and M. Jaroniec, *ACS Appl. Mater. Interfaces*, 2013, **5**, 1849-1855.

148. J. Chen, J. Yang, G. S. Hu, X. Hu, Z. M. Li, S. W. Shen, M. Radosz and M. H. Fan, *ACS Sustainable Chem. Eng.*, 2016, **4**, 1439-1445.

149. L. P. Guo, J. Yang, G. S. Hu, X. Hu, L. L. Wang, Y. F. Dong, H. DaCosta and M. H. Fan, *ACS Sustainable.Chem. Eng.*, 2016, **4**, 2806-2813.

150. J. Yang, L. M. Yue, X. Hu, L. L. Wang, Y. L. Zhao, Y. Y. Lin, Y. Sun, H. DaCosta and L. P. Guo, *Energy Fuels*, 2017, **31**, 4287-4293.

151. M. L. Yang, L. P. Guo, G. S. Hu, X. Hu, L. Q. Xu, J. Chen, W. Dai and M. H. Fan, *Environ. Sci. Technol.*, 2015, **49**, 7063-7070.

152. A. S. Ello, L. K. C. de Souza, A. Trokourey and M. Jaroniec, *Microporous Mesoporous Mater.*, 2013, **180**, 280-283.

153. H. M. Coromina, D. A. Walsh and R. Mokaya, *J. Mater. Chem. A*, 2016, **4**, 280-289.

154. M. Sevilla, W. Sangchoom, N. Balahmar, A. B. Fuertes and R. Mokaya, *ACS Sustainable. Chem. Eng.*, 2016, **4**, 4710-4716.

155. M. M. Titirici and M. Antonietti, *Chem. Soc. Rev.*, 2010, **39**, 103-116.

156. B. Hu, K. Wang, L. H. Wu, S. H. Yu, M. Antonietti and M. M. Titirici, *Adv. Mater.*, 2010, **22**, 813-828.

157. M. Sevilla and A. B. Fuertes, *Carbon*, 2009, **47**, 2281-2289.

158. M. M. Titirici, R. J. White, C. Falco and M. Sevilla, *Energy Environ. Sci.*, 2012, **5**, 6796-6822.

159. J. A. Libra, K. S. Ro, C. Kammann, A. Funke, Y. N. N. D. Berge, M. M. Titirici, C. Fùnher, J. K. O. Bens and and K. H. Emmerich, *Biofuels*, 2011, **2**, 71-106.

160. F. Shafizadeh, *J. Anal. Appl. Pyrolysis*, 1982, **3**, 283-305.

161. A. Demirbas and G. Arin, *Energy Sources*, 2002, **24**, 471-482.

162. M. X. Fang, D. K. Shen, Y. X. Li, C. J. Yu, Z. Y. Luo and K. F. Cen, *J. Anal. Appl. Pyrolysis*, 2006, **77**, 22-27.

163. A. V. Bridgwater, D. Meier and D. Radlein, *Org. Geochem.*, 1999, **30**, 1479-1493.

164. Y. P. Guo and D. A. Rockstraw, *Carbon*, 2006, **44**, 1464-1475.

165. E. Gonzalez-Serrano, T. Cordero, J. Rodriguez-Mirasol, L. Cotoruelo and J. J. Rodriguez, *Water Res.*, 2004, **38**, 3043-3050.

166. J. Hayashi, A. Kazehaya, K. Muroyama and A. P. Watkinson, *Carbon*, 2000, **38**, 1873-1878.

167. J. Rodríguez -Mirasol, J. Bedia, T. Cordero and J. J. Rodríguez, *Sep. Sci. Technol.*, 2005, **40**, 3113-3135.

168. V. Fierro, V. Torné-Fernández and A. Celzard, *Microporous Mesoporous Mater.*, 2006, **92**, 243-250.

169. L. Khezami, A. Chetouani, B. Taouk and R. Capart, *Powder Technol.*, 2005, **157**, 48-56.

170. E. Gonzalez-Serrano, T. Cordero, J. Rodríguez-Mirasol and J. J. Rodríguez, *Ind. Eng. Chem. Res.*, 1997, **36**, 4832-4838.

171. J. Rodríguez-Mirasol, T. Cordero and J. J. Rodríguez, *Carbon*, 1993, **31**, 87-95.

172. H. S. Teng and L. Y. Hsu, *Ind. Eng. Chem. Res.*, 1999, **38**, 2947-2953.

173. M. Jagtoyen and F. Derbyshire, *Carbon*, 1998, **36**, 1085-1097.

174. A. N. Wennerberg and T. M. O'Grady *US Pat.*, 1978.

175. H. S. Teng, Y. C. Lin and L. Y. Hsu, *J. Air Waste Manage.*, 2000, **50**, 1940-1946.

176. J. Romanos, M. Beckner, T. Rash, L. Firlej, B. Kuchta, P. Yu, G. Suppes, C. Wexler and P. Pfeifer, *Nanotechnology*, 2012, **23**, 7.

177. M. Sevilla, R. Foulston and R. Mokaya, *Energy Environ. Sci.*, 2010, **3**, 223-227.

178. S. Yeon, S. Osswald, Y. Gogotsi, J. P. Singer, J. M. Simmons, J. E. Fischer, M. A. Lillo-Ródenas and Á. Linares-Solano, *J. Power Sources*, 2009, **191**, 560-567.

179. M. Sevilla, N. Alam and R. Mokaya, *J. Phys. Chem.*, 2010, **114**, 11314-11319.

180. A. Almasoudi and R. Mokaya, *J. Mater. Chem.*, 2012, **22**, 146-152.

181. Y. W. Zhu, S. Murali, M. D. Stoller, K. J. Ganesh, W. W. Cai, P. J. Ferreira, A. Pirkle, R. M. Wallace, K. A. Cychosz, M. Thommes, D. Su, E. A. Stach and R. S. Ruoff, *Science*, 2011, **332**, 1537-1541.

182. M. Molina-Sabio and F. Rodŕiguez-Reinoso, *Colloids Surf. A Physicochem. Eng. Asp.*, 2004, **241**, 15-25.

183. D. Lozano- Castelló, M. A. Lillo- Ródenas, D. Cazorla- Amorós and A. Linares-Solano, *Carbon*, 2001, **39**, 741-749.

184. W. Z. Shen and W. B. Fan, *J. Mater. Chem. A*, 2013, **1**, 999-1013.

185. J. P. Paraknowitsch and A. Thomas, *Macromol. Chem. Phys.*, 2012, **213**, 1132-1145.

186. L. Singoredjo, F. Kapteijn, J. A. Moulijn, J. M. Martinmartinez and H. P. Boehm, *Carbon*, 1993, **31**, 213-222.

187. B. Adeniran and R. Mokaya, *Chem. Mater.*, 2016, **28**, 994-1001.

188. E. Raymundo-Pinero, D. Cazorla-Amoros, A. Linares-Solano, J. Find, U. Wild and R. Schlogl, *Carbon*, 2002, **40**, 597-608.

189. T. S. Blankenship and R. Mokaya, *Energy Environ. Sci.*, 2017, **10**, 2552-2562.

190. X. B. Zhao, B. Xiao, A. J. Fletcher and K. M. Thomas, *J. Phys. Chem. B*, 2005, **109**, 8880-8888.

191. Z. X. Yang, Y. D. Xia, X. Z. Sun and R. Mokaya, *J. Phys. Chem. B*, 2006, **110**, 18424-18431.

192. E. Masika, R. A. Bourne, T. W. Chamberlain and R. Mokaya, *ACS Appl. Mater. Interfaces*, 2013, **5**, 5639-5647.

193. M. Sevilla and A. B. Fuertes, *Microporous Mesoporous Mat.*, 2012, **158**, 318-323.

194. Z. Wang, F. H. Yang and R. T. Yang, *J. Phys. Chem. C*, 2010, **114**, 1601-1609.

195. Q. X. Li and A. D. Lueking, *J. Phys. Chem. C*, 2011, **115**, 4273-4282.

196. F. Shayeganfar and R. Shahsavari, *Langmuir*, 2016, **32**, 13313-13321.

197. L. F. Wang, F. H. Yang, R. T. Yang and M. A. Miller, *Ind. Eng. Chem. Res.*, 2009, **48**, 2920-2926.

198. K. V. Kumar, K. Preuss, L. H. Lu, Z. X. Guo and M. M. Titiricit, *J. Phys. Chem. C*, 2015, **119**, 22310-22321.

199. F. Xu, D. C. Wu, R. W. Fu and B. Q. Wei, *Mater. Today*, 2017, **20**, 629-656.

200. Terje A. Skotheim and J. Reynolds, *Handbook of Conducting Polymers, 4th Edition*, Taylor and Francis group, 2007.

201. T. Yamamoto, *Npg Asia Mater.*, 2010, **2**, 54-60.

202. V. Gupta and N. Miura, *Electrochem. Commun.*, 2005, **7**, 995-999.

203. Y. S. Shin, G. Fryxell, W. Y. Um, K. Parker, S. V. Mattigod and R. Skaggs, *Adv. Funct. Mater.*, 2007, **17**, 2897-2901.

204. C. H. Choi, S. H. Park and S. I. Woo, *Green Chem.*, 2011, **13**, 406-412.

205. G. Hasegawa, K. Kanamori, K. Nakanishi and T. Hanada, *Carbon*, 2010, **48**, 1757-1766.

206. Z. L. Yang, W. B. Hou, Z. P. Liu, L. Y. Huang and X. G. Peng, *Chem. J. Chinese Universities*, 2002, **23**, 2014-2016.

207. S. Machida, S. Miyata and A. Techagumpuch, *Synth. Met.*, 1989, **31**, 311-318.

208. M. Satoh, K. Kaneto and K. Yoshino, *Synth. Met.*, 1986, **14**, 289-296.

209. L. X. Wang, X. G. Li and Y. L. Yang, *React. Funct. Polym.*, 2001, **47**, 125-139.

210. M. Chougule, S. Pawar, P. Godse, R. Mulik, Shashwati Sen and V. Patil, *SNL*, 2011, **1**.

211. A. B. Fuertes and T. A. Centeno, *J. Mater. Chem.*, 2005, **15**, 1079-1083.

212. S. P. Armes, *Synth. Met.*, 1987, **20**, 365-371.

213. A. F. Diaz, K. K. Kanazawa and G. P. Gardini, *J. Chem. Soc. Chem. Commun.*, 1979, 635-636.

214. E. Masika and R. Mokaya, *Prog. Nat. Sci.*, 2013, **23**, 308-316.

215. C. D. Liang, Z. J. Li and S. Dai, *Angew. Chem. Int. Ed.*, 2008, **47**, 3696-3717.

216. R. Ryoo, S. H. Joo, M. Kruk and M. Jaroniec, *Adv. Mater.*, 2001, **13**, 677-681.

217. J. Lee, J. Kim and T. Hyeon, *Adv. Mater.*, 2006, **18**, 2073-2094.

218. H. F. Yang and D. Y. Zhao, *J. Mater. Chem.*, 2005, **15**, 1217-1231.

219. M. Tiemann, *Chem. Mater.*, 2008, **20**, 961-971.

220. A. H. Lu and F. Schüth, *Adv. Mater.*, 2006, **18**, 1793-1805.

221. Z. X. Wu, Y. Meng and D. Y. Zhao, *Microporous Mesoporous Mater.*, 2010, **128**, 165-179.

222. H. Nishihara, Q. H. Yang, P. X. Hou, M. Unno, S. Yamauchi, R. Saito, J. I. Paredes, A. Martínez-Alonso, J. M. D. Tascón, Y. Sato, M. Terauchi and T. Kyotani, *Carbon*, 2009, **47**, 1220-1230.

223. P. Pachfule, B. P. Biswal and R. Banerjee, *Chem. Eur. J.*, 2012, **18**, 11399-11408.

Chapter 2. Methods and Characterization Techniques

2.1 Aim of this Chapter

This chapter divided into three parts:

- Synthesis tools and equipment used for material preparation.
- Analytical techniques used to investigate and characterize the generated materials and their properties.
- Gas (H_2 and CO_2) sorption measurements and calculations used to determine excess hydrogen uptake, packing density and bulk density of generated materials.

2.2 Preparation of Activated Carbons

2.2.1 Conventional Chemical Activation

Chemical activation is one of the most commonly used methods for the preparation of highly porous carbonaceous materials commonly referred to as activated carbons.[1, 2] In this study, chemical activation was performed as follows; A mixture containing the activating agent and carbon precursor at the desired activating agent/carbon ratio (*i.e.* 2:1 or 3:1 or 4:1 etc) was ground together with a pestle and mortar to obtain a homogeneous mixture which was loaded (as is in powder form or as pellets/discs after compaction) onto an alumina boat (**Figure 2.1**) and then placed in tubular furnace with digital control (Manufactured by Sigma scientific, carbolite 301 controller), (**Figure 2.2**) under a flow of nitrogen gas. The furnace was then heated (at a ramp rate of 3, 5 or 10 ^{o}C min^{-1}) to a temperature of between 600 ^{o}C and 900 ^{o}C and held at the target temperature for 1 hour. Following cooling under a flow of nitrogen, the resulting carbonaceous matter was recovered and washed with HCl at room temperature until all inorganic impurities were removed. The final activated carbon was then dried in an oven at 120 ^{o}C.



Figure 2.1: Alumina boat loaded with activation mixture.

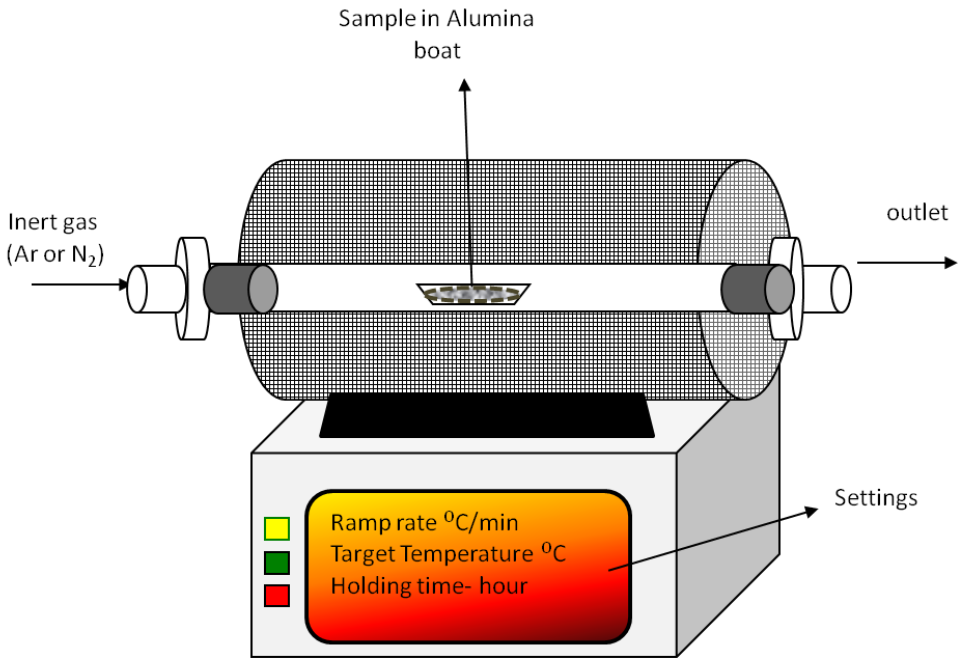


Figure 2.2: Schematic of a typical tubular horizontal furnace and setup up (i.e. gases, holding time, ramp rate, and target temperatures) used for chemical activation and chemical vapour deposition (CVD) procedures.

2.2.2 Compactivation/Mechanochemical Activation

Compactivation or mechanochemical activation [2-4] involves mechanically mixing and compacting the powdered starting materials (activating agent and carbon precursor) prior to activation. The activation mixture is compacted in a 1.3 cm die (**Figure 2.3**) to form a flat pellet or disc prior to activation. The activating agent (KOH) and carbon precursor were mixed at the desired ratio and ground together to obtain a homogeneous mixture. The mixture was then placed into an evacuable 1.3 cm die (**Figure 2.3**) and compacted for 10 minutes at ambient temperature at a load of either 5 tonnes (equivalent to 370 MPa) or 10 tonnes (equivalent to 740 MPa) using a manual hydraulic adjustable laboratory pellet press (**Figure 2.4**). The

pellet/disc was then activated as described above, except that *no stirring* was used during the washing (with HCl) step.

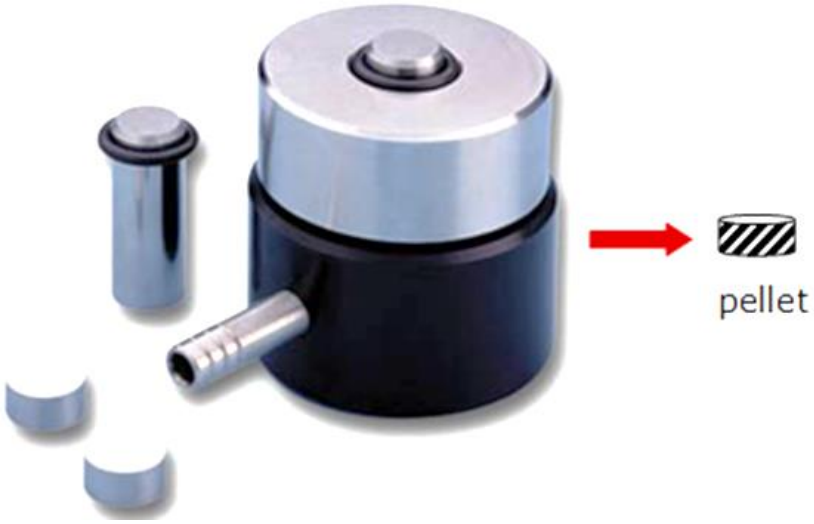


Figure 2.3: Evacuable 1.3 cm die and disc/pellet making accessories.



Figure 2.4: Manual hydraulic pellet press used to make compacted pellets/discs.

2.2.3 Chemical Vapour Deposition (CVD) Processes

In CVD processes, the substrate is exposed to one or more volatile precursors, which react and/or decompose on the substrate surface to produce the desired deposit. In this study, a tubular furnace (**Figure 2.2**) was used for formation of porous carbonaceous nanostructured materials. Typically, the hard templates (zeolite Y or zeolite 13X) were placed in an alumina boat and inserted into the tubular furnace and then were exposed to a flow of ethylene as carbon precursor. CVD experiment conditions are varied (ramp rate, temperature, holding time). See **Chapter 3**, **section 3.4**.

2.2.4 Hydrothermal Carbonization Reactor

The hydrothermal reactor used consists of two parts; an outer high quality stainless steel jacket, and an inner thick walled Teflon-lined polytetrafluoroethylene (PTFE) insert (**Figure 2.5**).



Figure 2.5: Hydrothermal synthesis autoclave reactor (manufactured by Parr Instrument Company, vessel number 4744, size 45 ml with maximum temperature of 250 ^{o}C and pressure of 1800 psig); stainless steel jacket part, and inner Teflon lined Teflon/PTFE chamber (white).

2.2.4.1 Production of Hydrochar

Hydrothermal carbonization proceeds *via* thermochemical decomposition of biomass into so-called hydrochar in the presence of superheated water.[5, 6] The wood sawdust (biomass) was converted to hydrochar as follows; an aqueous dispersion of biomass (sawdust) at a concentration of 320 gL^{-1} (6.4 g of sawdust in 20 ml of water) was placed in a stainless steel reactor (**Figure 2.5** and **Figure 2.6**) and heated up to 250 ^{o}C for 2 hours at ramp temperature of 5 ^{o}C/minute in laboratory muffle furnace. The resulting black-brownish solid (the hydrochar) was recovered by filtration and washed thoroughly with distilled water and then dried at 120 ^{o}C for 4 h.[3]



Figure 2.6: Photographic images of hydrothermal carbonisation procedure for hydrochar formation.

2.3 Analytical Techniques

2.3.1 Thermogravimetric Analysis (TGA)

Thermogravimetric analysis (TGA) [7-10] is an essential laboratory technique, which is used widely to determine the thermal and/or oxidative stabilities of materials as well as their compositional properties, impurity levels, moisture and volatiles content. TGA works by measuring the amount and rate of change in the mass of a material as a function of temperature (heating) or time under a controlled temperature program and atmosphere (inert or oxidizing atmosphere). TGA is used to characterize materials that exhibit either mass loss or loss due to volatiles/moistures, dehydration, decomposition or oxidation. TGA data can also be used in kinetic studies of reactive chemicals, to predict product performance and chemical degradation characteristics. Thermogravimetric analyser typically consists of:[11] (i) a pan (sample holder) usually made from alumina or platinum supported by a precision microbalance and located inside an electrically heated furnace. (ii) purge gas controls with the gas flowing over the sample and exiting through an exhaust and (iii) a computer with a programme used to control temperature (heating or cooling), ramp rate (fixed or varied), gas flow rates, and other functions.

Method

In this study, TGA analysis was performed using a TA Instruments SDT Q600 SDTQ600 analyser under flowing air conditions (100 mL min^{-1}).

2.3.2 Powder X-Ray Diffraction (PXRD)

Powder X-Ray Diffraction (PXRD) [12-16] is one of the most efficient, useful, and non-destructive analytical techniques. XRD is used to characterize and identify unknown crystalline solid materials and provides information about the crystal structure (molecular structure) down to the atomic level. XRD is based on constructive interference of monochromatic X-rays with crystalline materials made possible by the fact that the wavelength of X-rays are similar to the distance between atoms. The scattering of X-rays from atoms produce a diffraction pattern that contains information about the atomic arrangement in a crystal. In case of a crystalline material the diffraction pattern shows a series sharp peaks.

X-ray diffraction principle is described by Bragg's law which relates the wavelength of incident x-rays to the diffraction angle and the lattice spacing in a crystalline sample. The comparable size of the X-ray wavelength and the interplanar spacing (denoted as *d*) causes a crystal to diffract X-rays passing through it. The diffracted radiation reflected from the surface of a crystalline material may be in phase or out of phase, which corresponds to either constructive or destructive interference respectively, depending on the angle of incidence and interplanar spacing. The regular array of lattice points that make up the crystal structure provides the conditions for constructive interference that are described by Bragg's law equation below and **Figure 2.7**.[17, 18]

$$n\lambda = 2d_{hkl}\,\mathrm{Sin}\theta \qquad \textbf{Equation 2.1}$$

Where

n	is a positive integer 1, 2, 3 etc
λ	is wavelength of the incident X-ray radiation
d_{hkl}	is the lattice distance (the interlayer spacing distance of the lattice where hkl refers to Miller indices used to identify planes of atoms)
θ	is the diffraction angle between the transmitted and scattered beam directions.

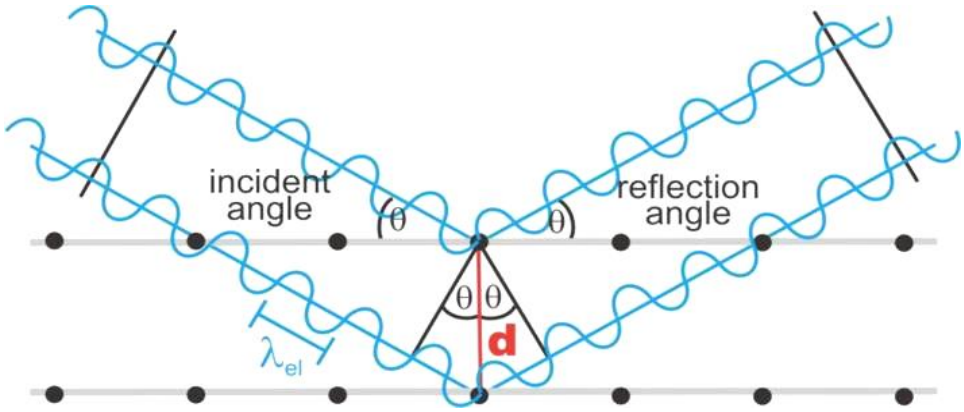


Figure 2.7: Schematic of X-ray Diffraction.[17]

A typical powder x-ray diffraction instrument mainly consists of three basic components: an X-ray tube, a sample holder, and an X-ray detector. Typically, 10 to 20 mg of powdered sample is placed on a zero background/diffraction plate (**Figure 2.8**).

Method

In this study, Measurements were performed using a PANalytical X'Pert PRO diffractometer with Cu-Kα (**Figure 2.9**). The X-ray generator was set to 40 kV and 40 mA, with step size of 0.02° and step time of 2s to 30s for values of 2θ between 2° and 60°. XRD profiles were collected in air at room temperature.



Figure 2.8: Photographic images of Zero background/diffraction plate with and without sample for XRD sample (holder).

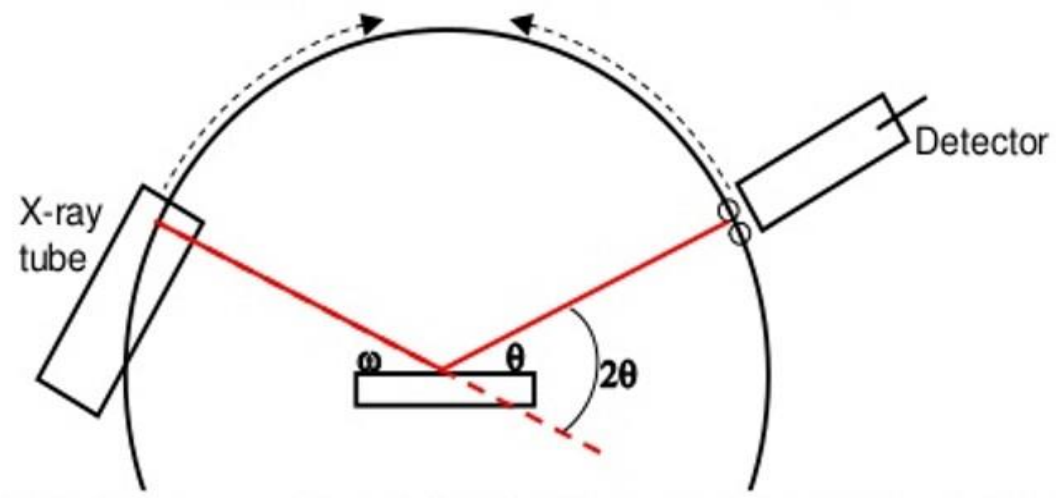


Figure 2.9: Schematic of a PANalytical X'Pert PRO diffractometer, where ω is the incident angle between the X-ray source and the sample. 2θ is the diffraction angle between the incident beam and the detector. The incident angle ω is always half of the detector angle 2θ.

2.3.3 Nitrogen Sorption Analysis

2.3.3.1 Textural Properties and Porosity Analysis

Gas sorption (adsorption/desorption) is the most common method for characterising porous solid materials so as to determine their surface area, pore volume and pore size distribution (PSD). The analysis is performed in an enclosed space by firstly degassing (heating) the sample under vacuum then exposing it to an inert gas (usually nitrogen). The amount of gas adsorbed is recorded as a function of the applied pressure at constant temperature resulting in a sorption isotherm.

The type of sorption isotherm is determined by the pore size and surface area of the material and is usually one or a combination of six categories (I to VI) of gas isotherm types defined by the International Union of Pure and Applied Chemistry IUPAC (**Figure 2.10**), namely; [19]

- **Type I isotherm:** Exhibited by microporous materials with relatively small external surfaces (e.g., some activated carbons, molecular sieve zeolites). The uptake is limited by the accessible micropore volume rather than by the internal surface area.

- **Type II isotherm:** Given by non-porous or macroporous materials. In this isotherm type monolayer coverage is completed and multilayer adsorption occur at high relative pressure. B point (**Figure 2.10**) indicates the stage at which monolayer coverage is completed and multilayer adsorption about to begin.

- **Type III isotherm:** Observed for non-porous and macroporous solid adsorbents. There is no identifiable monolayer formation; the interactions between adsorbent and adsorbate are relatively weak

which leads to low uptake at low relative pressure. This type gives a gradual curvature and indistinct point B.

- **Type IV isotherm:** Given by mesoporous adsorbent materials. The adsorption behaviour in mesoporous is determined by the adsorbent adsorptive interactions and also by the interactions between the molecules in the condensed state. A characteristic feature of the Type IV isotherm are its hysteresis loop, which is associated with capillary condensation taking place in mesopores, and the limiting uptake over a range of high P/P_o.

  Type V isotherm: A rare isotherm type with shape similar to type III due to relatively weak interactions between adsorbent and adsorbate which lead to low uptake at low relative pressure.

- **Type VI isotherm:** Stepwise and representative of layer by layer adsorption on non-porous solids with highly uniform surface.

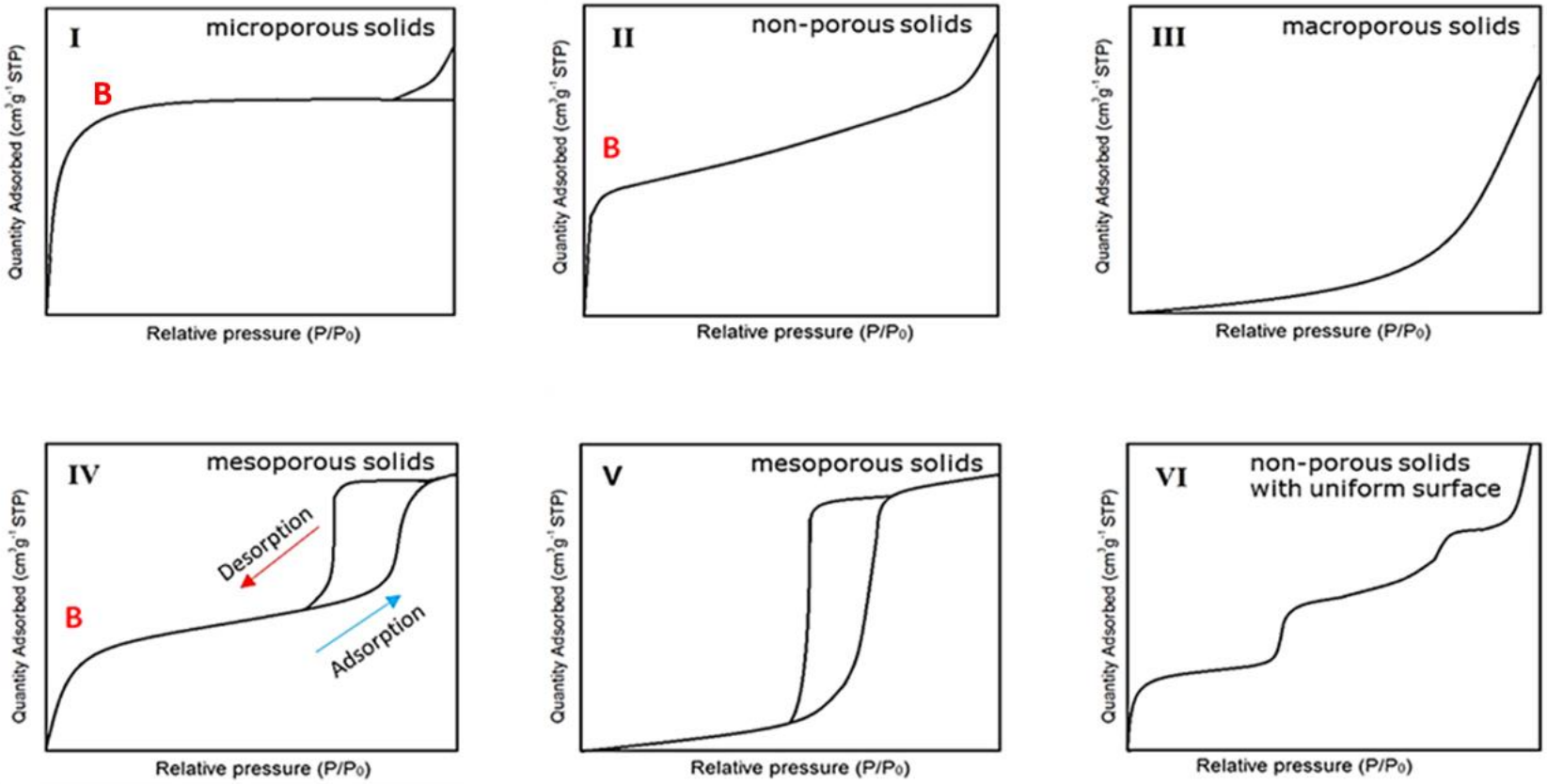


Figure 2.10: The six types of adsorption/desorption isotherms based on IUPAC classifications of isotherms. **B** point indicating the end of monolayer with simultaneous onset of multilayer coverage.[20]

Hysteresis Loops

The phenomena of hysteresis is usually related to the effect of thermodynamic or network effects or combination of both.[21] If larger pores have access to the surrounding *via* smaller pores, the pressure firstly needs to be low enough to evacuate the small pores before the adsorbate can escape from larger pores. In more details, the description of each classification of hysteresis loops according to the IUPAC are discussed into four different types below (**Figure 2.11**). The description of each classification of the hysteresis loops is as discussed below;

- **H1-type:** The shape of this hysteresis is parallel, almost vertical adsorption and desorption branches and are characteristic of highly ordered materials with cylindrical pores.

- **H2-type:** The shape of this hysteresis type is triangular in shape and has a less steep adsorption branch than H1-type loops but has similar, almost vertical, desorption branch. These kinds of loops are indicative of materials with poor pore connectivity or those with pores that are ink-bottle shaped.

- **H3-type:** This shape do not tend to level off at pressures approaching saturation pressure and are said to be associated with materials with plate-like particles and slit-like pores.

- **H4-type:** This kind of shape has parallel, almost horizontal branches and often occurs for materials with narrow slit-like pores and most common for materials possessing larger mesoporous within the matrix of smaller micropores.

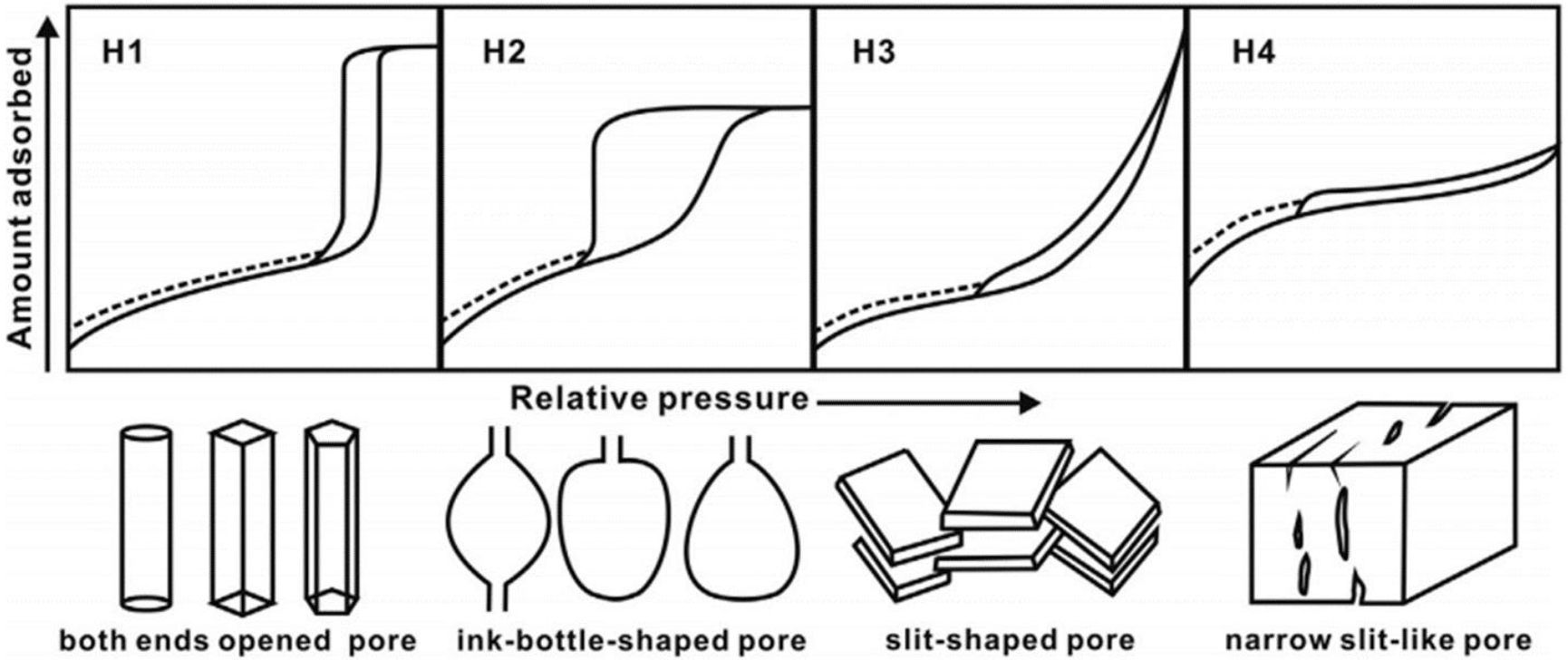


Figure 2.11: IUPAC Classification of hysteresis loops with their corresponding pore shapes.[22]

2.3.3.2 Theory of the Brunauer–Emmett–Teller (BET) Method

Specific Surface Area

BET theory is an important analysis and currently it is a standard technique used widely to calculate the specific surface area of solids by physical adsorption results from relatively weak forces (Van der Waals forces) between gas molecules adsorbate on the surface of the solid adsorbent corresponding to a layer on the surface by using the gas adsorption isotherm data. The determination is usually carried out at the temperature of liquid nitrogen (-196 ^{o}C). The amount of gas adsorbed corresponding to a monomolecular layer on the surface. The model of BET theory is that the adsorptive starts to adsorb on the strong energy sites on the surface first, then as the pressure increased, the adsorptive adsorbs on the next energy level sites. The model also takes account of the 2nd layer, 3rd layer and higher layer adsorption. BET theory [23-25] of multi-layer adsorption (**Figure 2.12**), and an extension of Langmuir model (theory of the monolayer adsorption) which at higher pressure and high coverage fails to provide accurate explanations and experimental results. BET theory was originally derived by Brunauer, Emmett and Teller (BET). In 1938, Brunauer, Emmett, and Teller (BET) analysed the first adsorption isotherm using liquid nitrogen (-196 ^{o}C) considering multi-layer adsorption. The BET equation can be written as follows: [21]

$$\frac{P}{V_A(P_o-P)} = \frac{1}{Vm\ C} + \left[\frac{C-1}{Vm\ C}\right] \mathrm{X}\ \frac{P}{P_o} \qquad \textbf{Equation 2.2}$$

Where

V_A	is the volume of monolayer gas adsorbed.
Vm	is the volume of gas adsorbate.
P	is the pressure of the gas when the volume is Vm.
P_o	is the saturation pressure at a given temperature (101.3kPa for N_2 at 77K).
C	is the BET constant parameter related to the heat of adsorption and represents the surface interaction energy, so it must be a positive value.

The BET plot of $P/V(P_o-P)$ against P/P_o gives straight line (y= mx+c) where m and c are constants, usually in the pressure range of specified partial pressure (P/P_o= 0.06 - 0.22) range of the isotherm is selected and the isotherm data is used to calculate the BET surface area range. The resultant straight line with V_m and C refers to $((C-1)/V_m C)$ and the y-intercept correspond to $(1/V_m C)$ respectively.

2.3.3.3 Assessment of Microporosity; Pore Volume, Pore Size and Pore Size Distribution (PSD)

The total pore volume can be calculated from the amount of gas adsorbed at a relative pressure close to the saturation vapour pressure when the pores are filled completely by converting the adsorbed amount to the corresponding volume of the liquid adsorbate at the temperature of the adsorption measurement.

The thickness plot (t-plot) method is used for micropore volume evaluation and microporous area. This method is based on plotting the volume of gas adsorbed against the adsorbate molecular thickness.

The pore size distribution (PSD) gives an indication of whether the sample is micro or mesoporous. This may be obtained from the adsorption branch of the isotherms using the Non-Local Density functional theory (NLDFT method); provides a microscopic treatment of sorption phenomena in micro-and mesoporous on a molecular level, i.e. based on statistical mechanics. Briefly, the PSD evaluation is based on the theoretical isotherms calculated for individual pores of a given adsorbate–adsorbent system. These isotherms, which constitute the so-called kernel, are generated using the NLDFT where the fundamental molecular parameters characterizing the gas–gas and gas–solid interactions of the adsorption system are utilized. Mathematical procedure used for PSD calculation can be described as fitting a combination of the theoretical isotherms to the experimental data. The obtained PSD represents volumetric contributions of pores with different sizes whose theoretical isotherms best fit the experimental data.

Isotherms are constructed, i.e. a plot of partial pressure relative to the saturation pressure (P/P_o) against volume of adsorbate adsorbed by a porous material. Nitrogen is used at its boiling point as the adsorbate. The amount adsorbed by an evacuated sample is then measured by gradually increasing the pressure from $P/P_o = 0$ up to the saturation pressure, i.e. $P/P_o = 1.0$. This procedure acts to measure the adsorption branch of the isotherm. On the other hand, desorption branch is measured by proceeding to decrease the pressure back to $P/P_o = 0$, before allowing sample to return to atmospheric pressure.

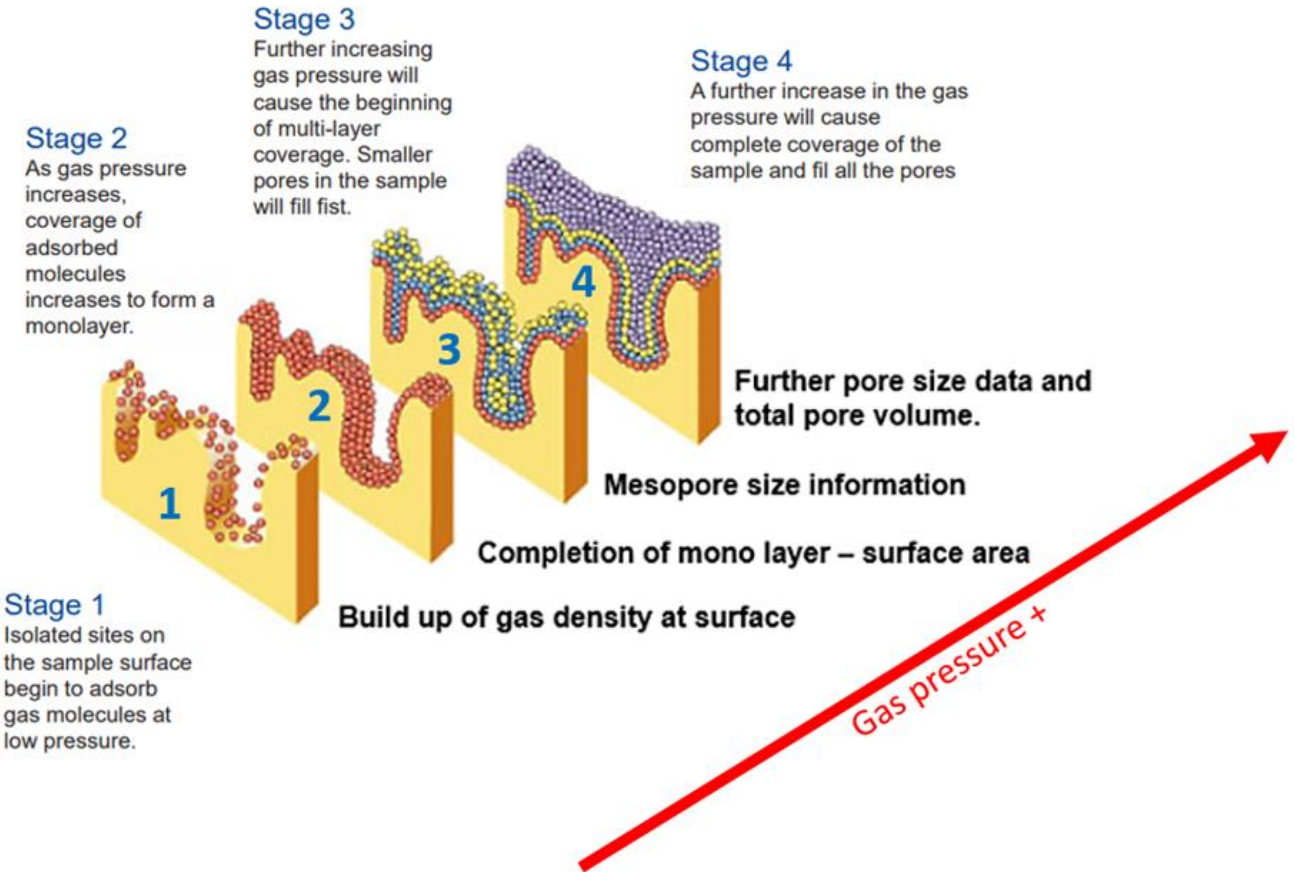


Figure 2.12: Stages of gas adsorption experiment.

Physical Proprieties: Surface Area and Porosity Measurement

it is an important analysis used to provide specific surface area (by calculating the amount of adsorbate gas corresponding to a monomolecular layer on the surface of material) and porosity of materials with a wide variety such as catalysts, zeolites, MOFs etc., by nitrogen adsorption measured as a function of relative pressure. In this study, two instruments were used; ASAP 2020 Micromeritics surface characterization analyzer and 3Flex surface characterization analyzer.

2.3.3.4 ASAP 2020 Micromeritics Surface Characterization Analyzer

ASAP 2020 Micromeritics surface characterization analyzer [26, 27] (**Figure 2.13**) is a two independent vacuum stations intelligent degas system or fully automated degassing with precisely controlled heating profiles and one analysis station. This technique used physical adsorption of a gas to determine surface area and porosity of porous solids materials (i.e. activated carbons). Firstly, the sample loaded into a tube (**Figure 2.15**) for pre-treatment including; heating (degassing) in conjunction with vacuum to remove moistures and impurities from the surface of the powder sample by applying elevated temperature (up to 250 ^{o}C) which does not cause any structural change to the sample. The material is then cooled to cryogenic temperatures. An adsorptive a probe gas (commonly nitrogen is added to the material at controlled pressure increments. After each dose of adsorptive, the pressure is equilibrated and the quantity adsorbed is

calculated. After the area is covered by adsorbed gas molecules, the surface area can be calculated/measured usually using the Brunauer-Emmett-Teller (BET) method [24, 28] which employs the nitrogen adsorption at different pressures at the temperature of liquid nitrogen (77 K). The total pore volume is estimated from the amount of nitrogen adsorbed at the highest relative pressure, pore size distribution can be calculated using Non Local Density Functional Theory method (NLDFT). At the end a vacuum is applied and the gas removed, which may result in hysteresis behaviour. The relative pressure and quantity of gas adsorbed are measured to give an adsorption isotherm, which depends on the nature of the material.



Figure 2.13: ASAP 2020 Micromeritics surface and porosity characterization analyzer.

2.3.3.5 Micromeritics 3Flex Surface Characterization Analyzer

The 3Flex [29, 30] (Physisorption) is similar in function to ASAP 2020 Micromeritics surface characterization analyzer but with three fully automated analysis ports instrument, capable of high-performance physisorption (mesopore and micropore) and chemisorption analyses with superior accuracy, resolution and data reduction. Its advanced manifold design and embedded control provide an ultra-stable environment for pressure and temperature measurements, extending the limits of resolution, a new advanced dosing method that allows you to mix both pressure and volume increments, ultra-clean manifold design features hard-seal valves and metal seals to provide high chemical resistivity, ease of evacuation, and lowest outgassing rate in the industry. The 3Flex is ideally suited for the characterization of different materials such as; MOFs, zeolites, activated carbons, adsorbents and a wide variety of porous and non-porous materials. 3Flex can characterize three samples at the same time with three different adsorptive (conditions) with just a single click.

Sample Preparation

Sample preparation for both BET 2020 and the 3Flex are the same (**Figure 2.15**). Firstly, at least 50-100 mg of clean carbons dried overnight in the oven at 150 ^{o}C loaded into a tube and then evacuated overnight under vacuum at 200 ^{o}C for 12 h before analysis to remove the physisorbed species (water/moistures) from the adsorbent without causing any irreversible changes to the surface or to the solid structure by control the out-gassing conditions (such as the heating temperature/time, the change in pressure over the adsorbent).

Method

In this study, nitrogen sorption isotherms and textural properties of carbon materials were determined at 77K (-196 ^{o}C) using a Micrometrics ASAP 2020 sorptometer (**Figure 2.13**) or Micromeritics 3Flex surface characterization analyzer (**Figure 2.14**). The surface area of carbons was calculated using the BET equation applied to adsorption data in the relative pressure (P/P_o) range of 0.01–0.22 and total pore volume was calculated from the amount of nitrogen adsorbed at relative pressure (P/P_o= 0.99). The micropore surface area and micropore volume were estimated by t-plot analysis. The pore size distributions were obtained *via* a Non-Local Density Function Theory (NLDFT) method using nitrogen adsorption data.



Figure 2.14: Micromeritics 3Flex surface characterization analyzer (three-station instrument).



Figure 2.15: Photographic image of Micromeritics surface sample tube holder.

2.3.4 CHN Elemental Analysis

Elemental Microanalysis [31, 32] is a quick, straightforward, accurate and cost-effective technique used to provide information on the purity and composition of samples by providing a precise and accurate analysis of a sample's percentage carbon, hydrogen and nitrogen content. Combustion of the accurately weighed sample (typically 2 mg) held in a tin container placed inside the autosampler drum where they are purged with a continuous flow of helium and then dropped at present intervals into a vertical quartz tube maintained occurs in a high temperature furnace (975 °C) (combustion reactor) under pure oxygen gas. The combustion products are carried through the analytical system by a flow of helium gas then pass over suitable reagents in the combustion tube to ensure complete oxidation and removal of undesirable by-products such as sulphur, phosphorus and halogen gases. In the reduction tube which maintained at 625 °C, oxides of nitrogen are converted to molecular nitrogen and residual oxygen is removed. The sample gases are then thoroughly homogenized to a precise volume, temperature and pressure in the mixing volume. This mixture is then released and detected by thermal conductivity detector.[32]

Between the first of three pairs of thermal conductivity cells, an absorption trap removes water from the sample gas. The differential signal read before and after the trap reflects the water concentration and, therefore, the amount of hydrogen in the original sample. A similar measurement is made of the signal output of a second pair of thermal conductivity cells, between which a trap removes carbon dioxide, thus determining the carbon content. The remaining gas now consists only of helium and nitrogen. This gas passes through a thermal conductivity cell and the output signal is compared to a

reference cell through which pure helium flows. This gives the nitrogen concentration

Sample Preparation

Typically 2 mg of fine, dry, and clean powdered carbons (free of moistures dust, and hair), needed for a duplicate run.

Method

In this study, The Elemental Microanalysis for C, H and N for carbons performed using a model Carlo Erba CE-118 Elemental Analyzer (**Figure 2.16**).



Figure 2.16: Carlo Erba CE-118 Elemental Analyzer.[32]

2.3.5 Electron Microscopy

In this study, the two types of electron microscope were used: Scanning Electron Microscope (SEM), and Transmission Electron Microscope (TEM).

In electron microscopy, a highly energetic beam of electrons hits the surface of solid specimens to a few microns depth, which leads to elastic and inelastic scattering of electrons comprising of; (i) secondary electrons (SE), (ii) backscattered electrons (BSD), Auger electrons, (iii) characteristic X-rays, (iv) photons, light and heat, as shown in **Figure 2.17**.

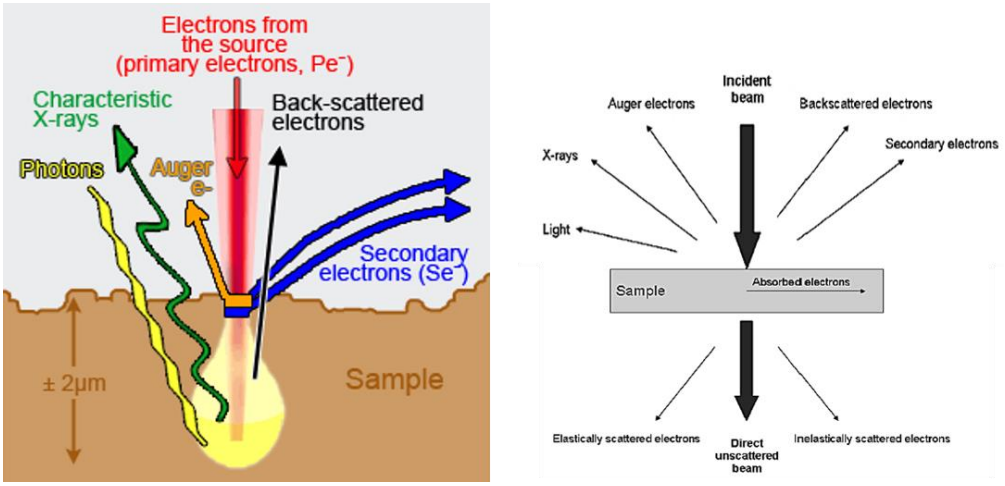


Figure 2.17: Schematic showing how a highly energetic electron beam interacts/behaves with the sample in an electron microscope.[33]

2.3.5.1 Scanning Electron Microscopy

Scanning Electron Microscopy (SEM) [34-36] is used to scan the surface structure/topography of solid samples with high resolution of ca. 1-20 nm. The maximum resolution obtained of SEM depends on many factors such as sample preparation, the electron spot size, and interaction volume between the electron beam and the sample. SEM microscope consists of four basic components (**Figure 2.18**);

(i) An electron gun, located at the top of the SEM column to produce an incident beam of stable, highly energetic accelerated electrons.

(ii) Vacuum system, which consists of various pumps to keep the system under high vacuum which help to minimizes interaction between the electrons and gaseous species before hitting the specimen.

(iii) A series of several lenses; electromagnetic lenses, objective lens and condenser lenses, and apertures, each with its function and all used to maximize the efficiency of SEM.

(iv) Detectors, including Secondary Electron Detector (SED), Backscatter Detector, Diffracted Backscatter Detector (EBSD), X-ray Detector (EDS) etc.

(v) Computer; to control the system, display and view the images.

Samples Preparation

In this study, the sample preparation required depends on whether it is electrically conducting or not. Electrically conductive samples, such as carbons, only require minimal sample preparation; a small amount of the fine powder sample was directly mounted on an aluminium stub with double-

sided adhesive carbon tape (**Figure 2.19**). Non-conductive (or poorly conductive) non-coated samples such as sawdust biomass, were firstly coated before imaging with an ultra-thin (<15 nm) conductive metal coating of an electrically-conducting material such as platinum or gold using sputter coater[37] (**Figure 2.20** and **Figure 2.21**).

Method

In this study, scanning electron microscopy images were obtained using FEI Quanta 650 ESEM instrument (**Figure 2.22** and **Figure 2.23**) and JEOL 6490 instrument,[38] at room temperature, and voltage of 5 kV or 10 kV. FEI Quanta 650 ESEM instrument and JEOL 6490 instrument both setup to work in air.

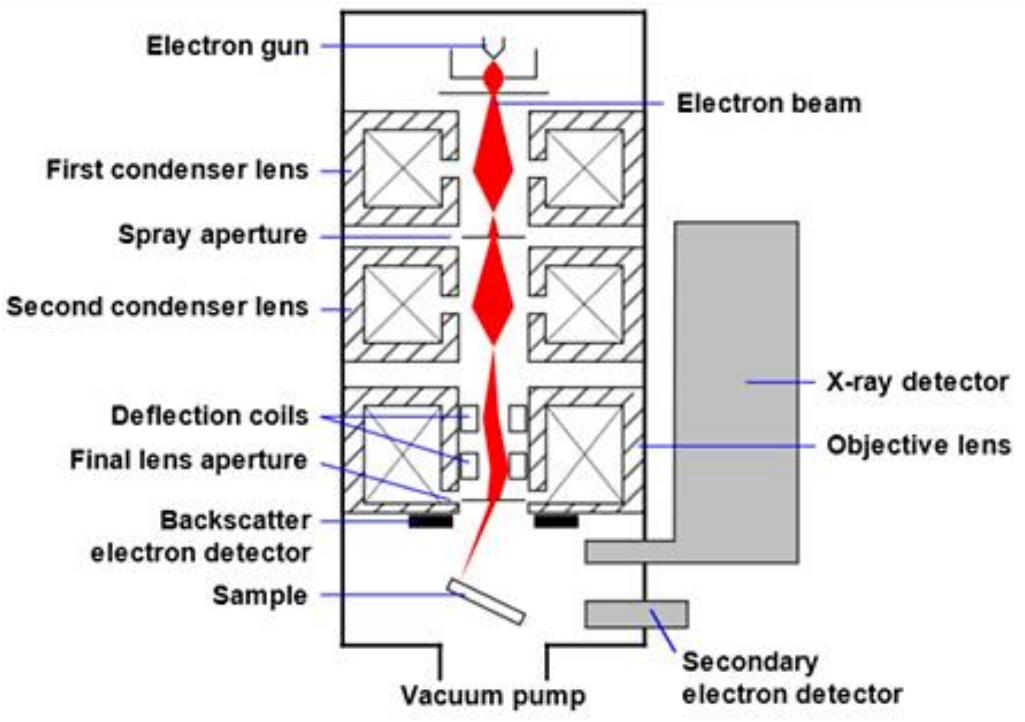


Figure 2.18: Schematic diagram of typical Scanning Electron Microscopy (SEM).

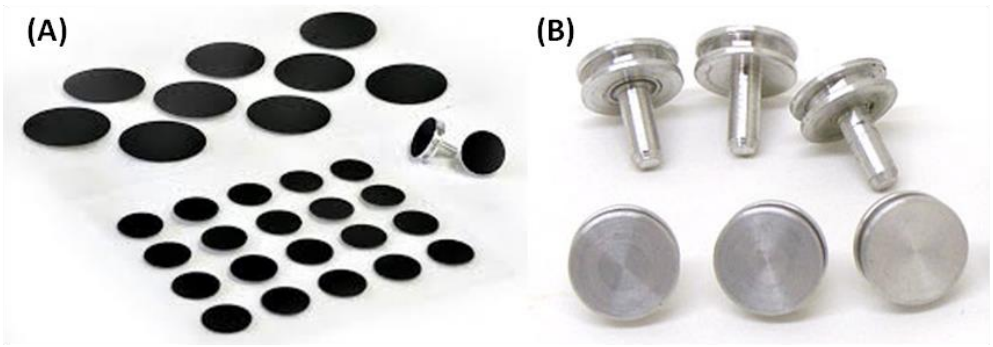


Figure 2.19: (A) Double-sided adhesive carbon tape, **(B)** SEM specimen aluminium stubs.

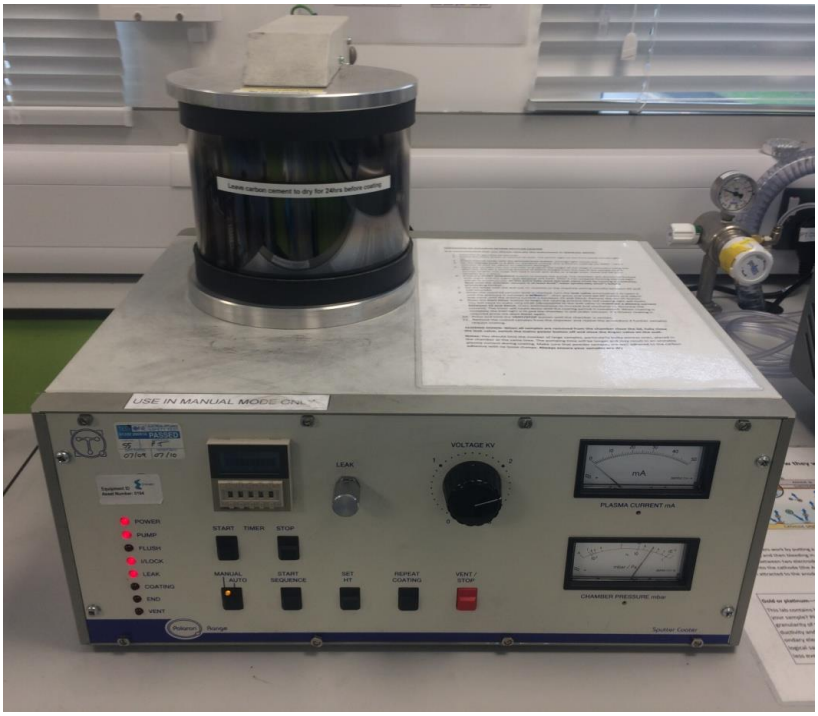


Figure 2.20: Photographic image of sputter coater at Nanoscale and Microscale Research Centre (NMRC) at University of Nottingham. An argon plasma is used in a vacuum chamber to sputter particles of metal from the targets which form a thin (<15 nm) layer on the sample.

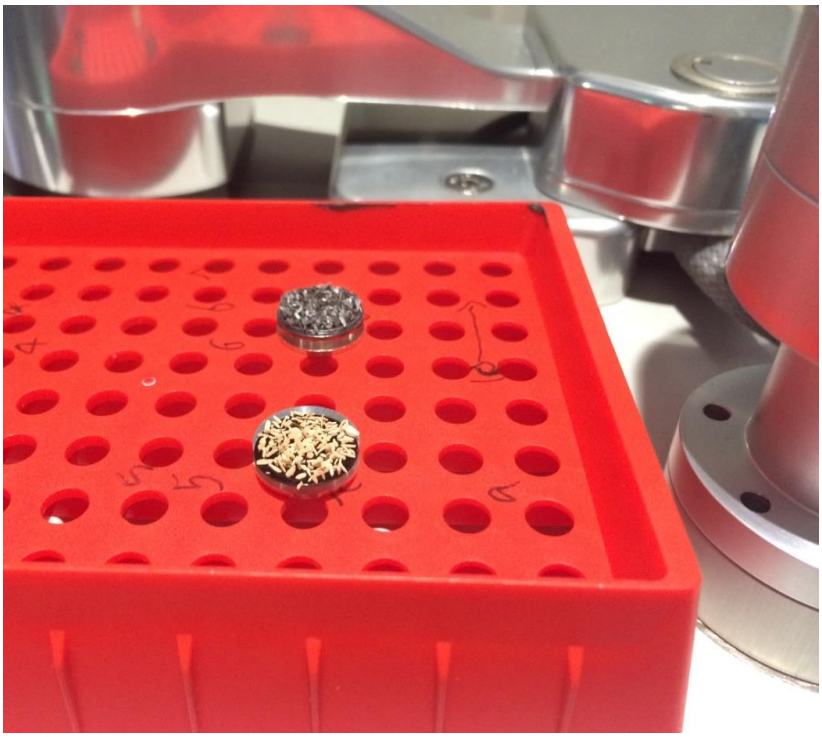


Figure 2.21: Photographic image of wood sawdust (non-conducting sample) before and after conductive thin platinum coating.

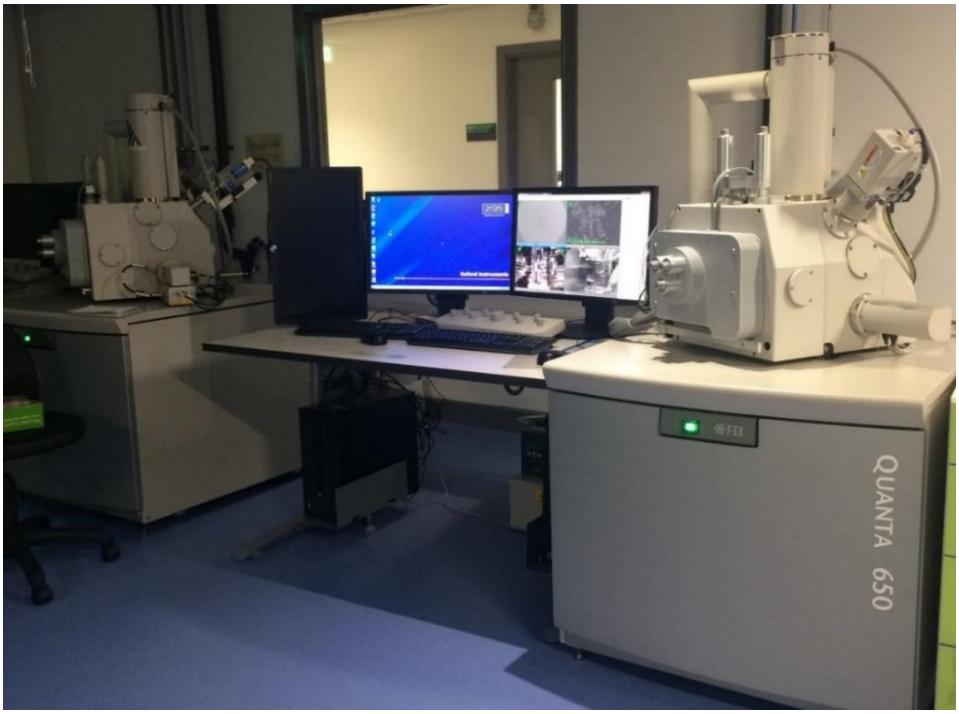


Figure 2.22: Photographic image of FEI Quanta 650 ESEM at Nanoscale and Microscale Research Centre (NMRC) at University of Nottingham.

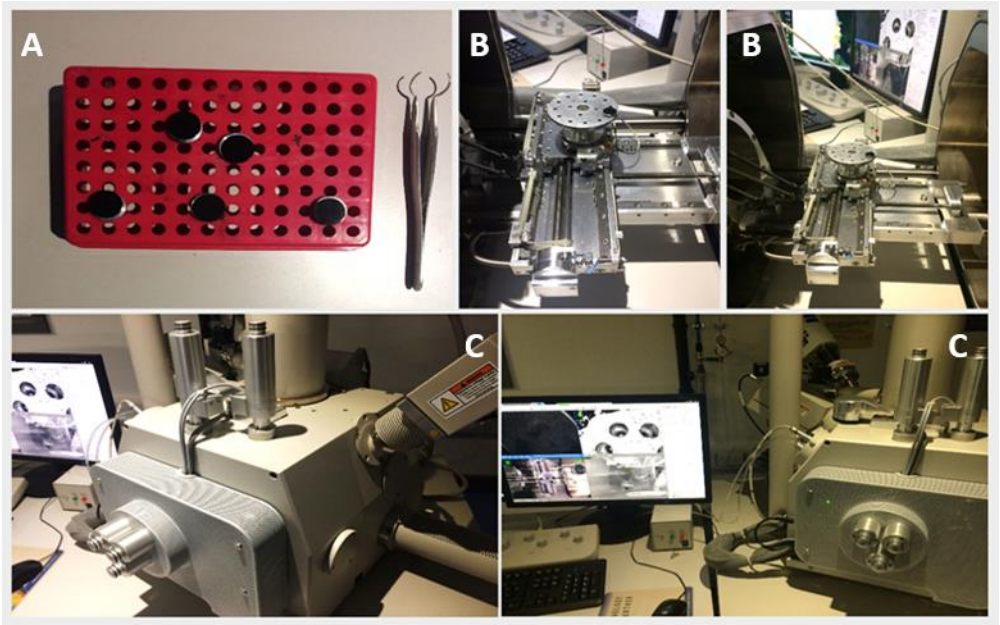


Figure 2.23: Photographic images showing SEM samples preparation **(A)**, ESEM sample chamber **(B)**, and FEI Quanta 650 ESEM instrument **(C)**, at Nanoscale and Microscale Research Centre (NMRC) at University of Nottingham.

2.3.5.2 Transmission Electron Microscopy

Transmission electron microscopy (TEM) [35, 39, 40] is a very powerful technique for material science development and nano-technologies research. It images thin or ultrathin specimens (ideally ≤ 100 nm thick) by exposing them directly to a highly energetic monochromatic electron beam. The quality of TEM images depends largely on sample preparation, the accuracy of the mechanical and electrical adjustments. Resolution in TEM performance is affected and limited by the spherical aberration effect. However, a new generation of microscopes have been developed and designed with aberration correctors to minimize spherical aberration to increase the resolution. For example, development of high resolution TEM (HRTEM) has achieved images with resolution of <5 nm at magnifications >50 million times.

Sample Preparation

Samples were prepared for TEM by dispersing a finely ground sample suspended in isopropanol or methanol. Several drops of the mixture were then dispersed onto Lacey-carbon support film on copper grid (**Figure 2.24**) to obtain thin specimen, which were dried under ambient conditions prior to analysis.

Method

Transmission electron microscopy (TEM) images were obtained using a Field Emission Electron Gun Transmission electron microscopy JEOL 2100 FEG-TEM instrument (**Figure 2.25** and **Figure 2.26**) operating at 200 kV equipped with a Gatan Orius CCD for imaging.

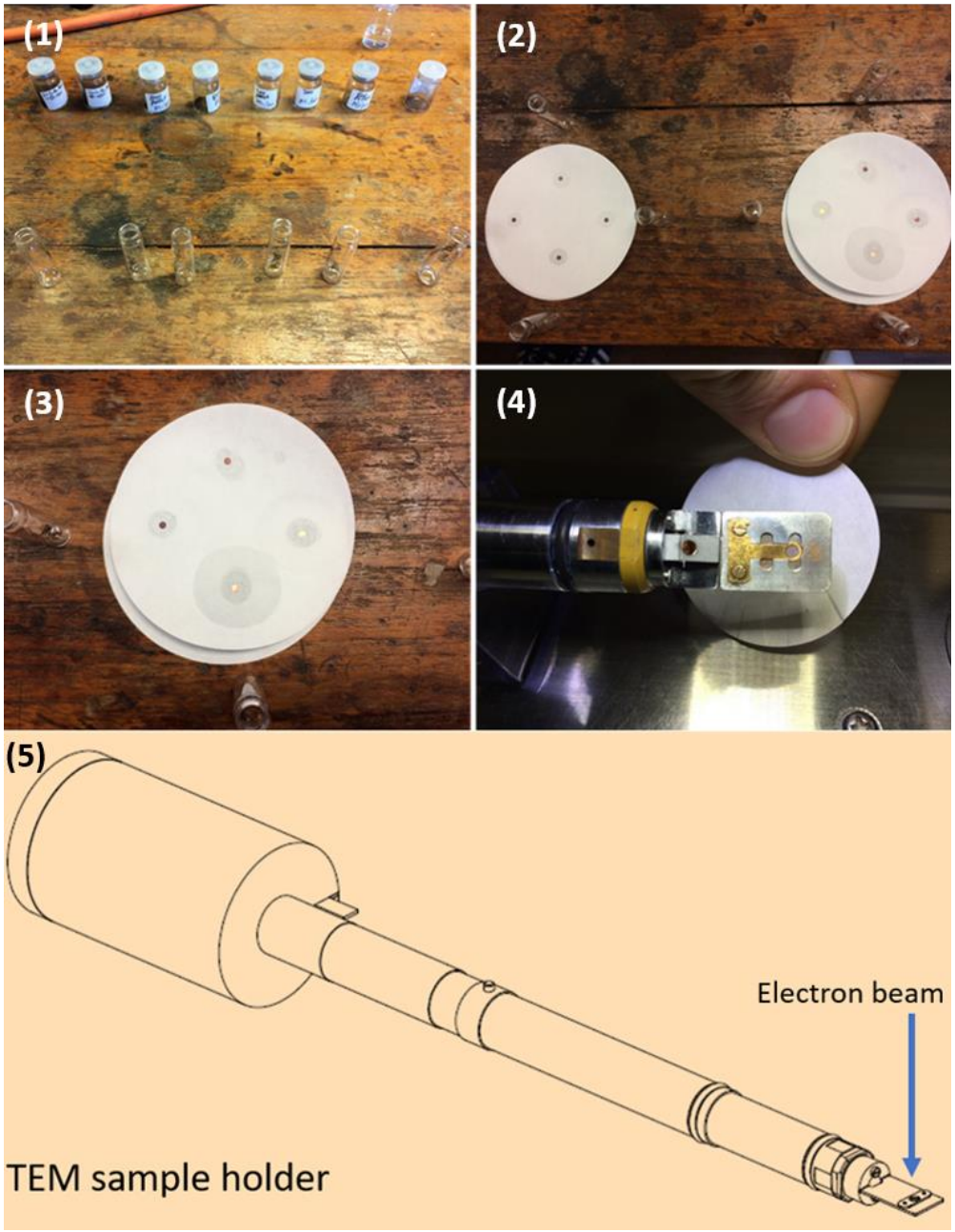


Figure 2.24: Photographic images of TEM sample preparation steps; **(1)** a finely ground sample suspended in isopropanol or methanol, **(2)** several drops of the mixture were then dispersed onto Lacey-carbon support film on copper grid, **(3)** sample dried under ambient conditions prior to analysis, **(4)** load/screw a TEM grid on the grid holder, and **(5)** showing TEM sample holder with loaded sample and beam position.

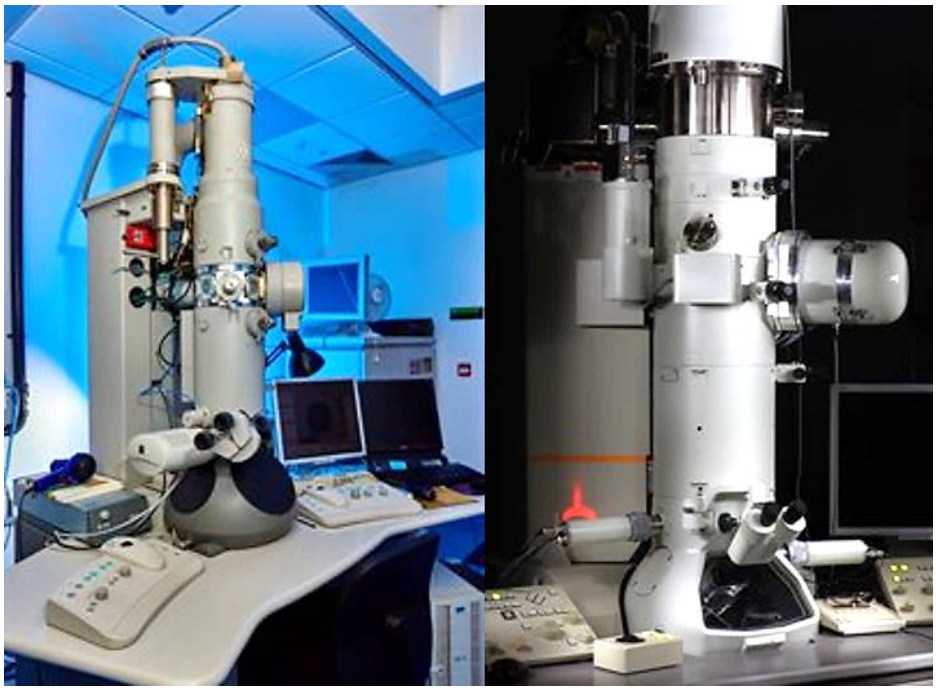


Figure 2.25: Photographic images of JEOL 2100 FEG-TEM instrument at Nanoscale and Microscale Research Centre (NMRC) at University of Nottingham.

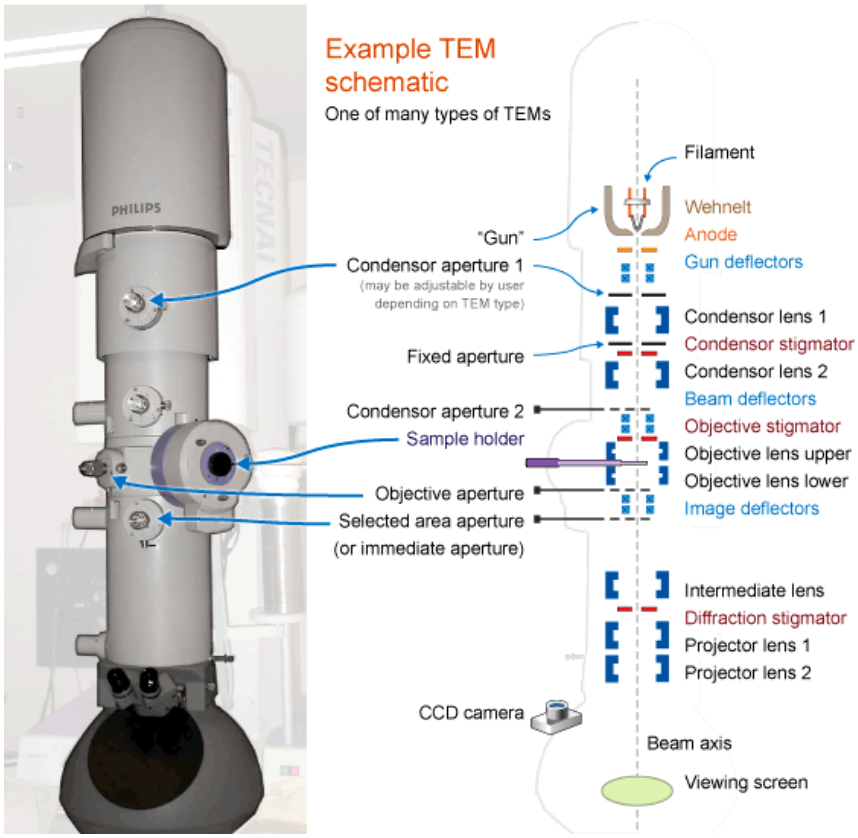


Figure 2.26: Schematic diagram of internal structure of Transmission Electron Microscopy (TEM).[40]

2.3.6 Spectroscopy

2.3.6.1 X-ray Photoelectron Spectroscopy

X-ray Photoelectron Spectroscopy XPS [41-43] is an elemental surface analysis technique, with average analysis depth of less than 5 nm (**Figure 2.27**) and is therefore useful for the compositional analysis of ultra-thin layers and thin micro-scale sample features. It provides valuable quantitative and chemical state information from the surface of all the elements with an atomic number (Z= 3) (lithium) and above. However, XPS is not able to detect hydrogen and helium elements (Z= 1) or helium (Z= 2). XPS is also known as electron spectroscopy for chemical analysis (ESCA) because it has also the ability to identify chemical status of elements on the surface. XPS based on the photoelectric effect, i.e., emission of electron following excitation of core level electrons by photons. XPS can measure the elemental composition, chemical state and electronic state of the elements in a material. XPS is mostly used because of it's relative simple use and ease of data interpretation.[41] XPS provides information about the structures of surface layers or thin films where surface or thin film composition plays a critical role in performance such as in nanomaterials, photovoltaics, catalysis, corrosion, electronic devices, surface treatments, and thin film coatings. **Figure 2.28** shows the basics of XPS.

Typically, XPS works by bombarding the atoms (core-levels) in the surface of the sample by a beam of monochromatic and energetic x-rays (photons with enough energy *hv*) which absorbed by core (inner shell) in atom, led to ionization (by removing of one of these valence electrons) and the emission of a core (inner shell) electron in order to emit photoelectrons with kinetic energy with E_K from the surface (the kinetic energy of the electron depends on the photon energy (*hv*) and the binding energy (*BE*) of the electron. From

the top 1-10 nm of the material surface (**Figure 2.27**), leading to ionization and the emission of core (inner shell) electrons. The energy of emitted photoelectrons is measured by electron analyser from the position and intensity of the peaks in an energy spectrum, the elemental identity, chemical state, and quantitative information of a detected element can be determined.

The energy of a photon is given by the Einstein relation:

$$E_B = hv - E_K - W \qquad \textbf{Equation 2.3}$$

Where

hv	is the energy of x-ray photon (1486.6 eV for monochromatic ALKα)
E_K	is the kinetic energy of photoelectron
W	is the work function induced by the analyser (about 4-5 eV)

Sample Preparation

Practically about 5-10 mg of powdered dried clean carbons (no pre-treatment required).

Method

In this study**,** the sample analysis is conducted in a vacuum chamber, under the best vacuum conditions achievable (10^{-9} Torr) using a Kratos Liquid Phase Photoelectron Spectroscopy (LIPPS) (**Figure 2.29**) or a Kratos AXIS ULTRA (**Figure 2.30**) both with a monochromated Al Kα X-ray source radiation (*hv* =1486.6 eV) operated at 10 mA emission current and 12 kV anode potential used. Fixed analyser transmission mode (FAT) was used, with pass energies of 160 eV or 80 eV for survey scans and 20 eV for high

resolution scans. The magnetic immersion lens system allows the area of analysis to be defined by apertures, a slot aperture of 300 x 700 μm for wide/survey scans and aperture of 110 μm for high resolution scans. The take-off angle for photoelectron analyser was 90 degrees and acceptance angle of 30 degrees (in magnetic lens modes). Obtained data was analysed using CASAXPS software with Kratos sensitivity factors to determine atomic values (%) from the peak areas.

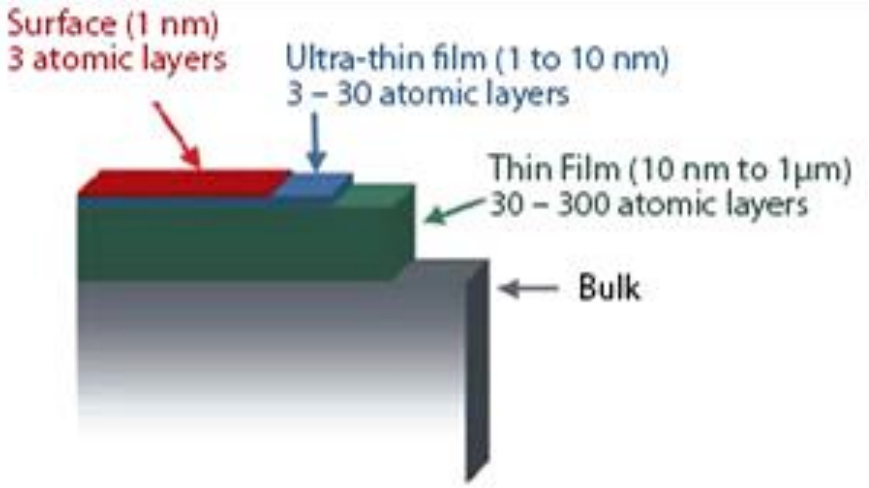


Figure 2.27: Showing the materials layer.[42]

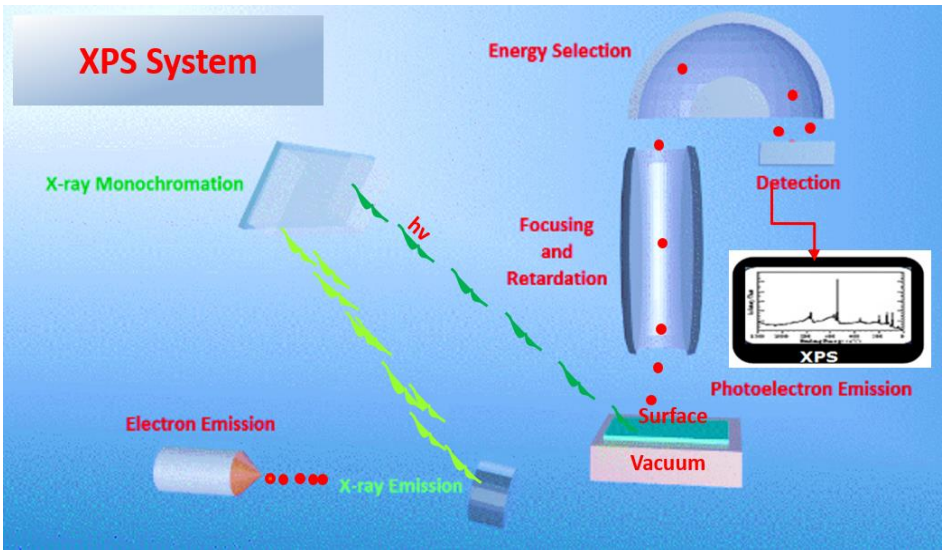


Figure 2.28: Schematic of basic components of XPS system.[42]



Figure 2.29: Photographic image of Kratos Liquid Phase Photoelectron Spectroscopy (LIPPS) at Nanoscale and Microscale Research Centre (NMRC) at University of Nottingham.[44]



Figure 2.30: Photographic image of KRATOS Axis Ultra Spectrometer XPS at Nanoscale and Microscale Research Centre (NMRC) at University of Nottingham.

2.3.6.2 Inductively Coupled Plasma Optical Emission Spectroscopy (ICP-OES)

Inductively coupled plasma - optical emission spectrometer (ICP-OES) is one of the most powerful techniques for determining elemental composition. [45-49] ICP-OES is composed of two parts; the ICP emission and the optical spectrometer. The technique can be used to quantitatively identify a wide range of elements such as K, Na, Ca, Fe, Mn, Ba and Mg, and is suitable for trace analysis of metal elements (0.0002 ppm -1000 ppm) and a limited number of non-metallic elements such as S and P. The system of ICP-OES generally consists of three parts; sample introduction system, plasma generator, and spectrometer (**Figure 2.31**).

Sample Preparation

Approximately 10 mL of aqueous solution typically in 2 -10% nitric acid/or other suitable acid such as HCl. The solid sample is fully dissolved *via* digestion to ensure that there are no particles that can easily clog the tip of the nebulizer. The solubilized sample solution is injected into the instrument by nebulizer into the spray chamber and carried by argon gas into a torch heated to approximately 10,000 °C. Standard reference samples of known concentration are used to allow unknowns to be determined.

Method

In this study, a Perkin Elmer Optima 2000 DV ICP-OES with S10 auto-sampler ICP-OES (**Figure 2.32**) was used. The spectrometer was pre-set to measure emitted light at specific wavelengths. The sample solution was introduced by peristaltic pump through a nebuliser and into the argon plasma flame. The flame was ignited and maintained by way of a high power RF circuit. The intensity of the emitted light at specific wavelengths is proportional to the concentration of sample; therefore, calibration of the instrument with samples of known concentration allows unknowns to be determined. [47]

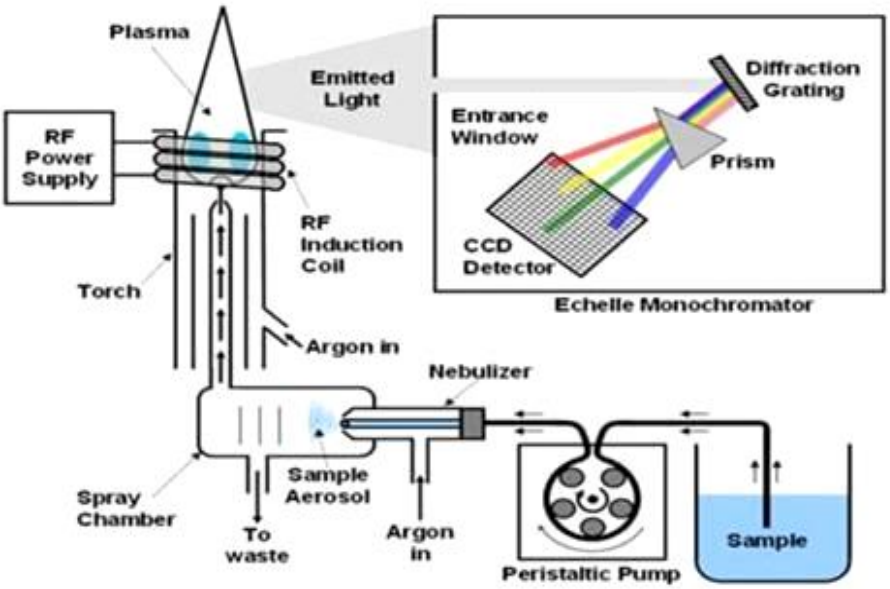


Figure 2.31: Schematic of the inductively coupled plasma- optical emission spectrometer ICP-OES.



Figure 2.32: Photographic image of MODEL Optima 2000 DV ICP-OES with S10 autosampler manufactured by Perkin Elmer.

2.3.6.3 Raman Spectroscopy

Raman spectroscopy [50-53] is an invaluable analytical tool that can study solid, liquid and gas samples. Raman is a molecular spectroscopy is based on inelastic scattering of monochromatic light, usually from a laser source and detects vibrations involving a change in polarizability. Raman is commonly used for molecular finger printing as well as monitoring changes in molecular bond structure (e.g. state changes and stresses and strains). It used to determine the chemical identity and state of a sample by its unique vibrational (molecular) modes.

Raman spectroscopy is named in the honor of its inventor Sir Chandrasekhara Venkata Raman. The principle of Raman technique is normally measuring the interaction between a monochromatic light source (laser beam) in the ultraviolet range (UV), visible or near infrared (NIR) range which have low energy, used to illuminate the sample and absorbed by the sample and lead to vibrational (and other low-frequency) modes of the molecular systems being analysed. The laser light and then photons reemitted from the sample with altered frequency (shifted up or down) compare to the original monochromatic frequency, this phenomenon called the Raman effect. Raman Effect is that frequency of a small fraction of scattered radiation is different from frequency of the original incident radiation. This shift gives information about vibrational, rotational and other low frequency transitions in molecules. The scattered light from the sample is collected with a lens then sent through interference filter or spectrophotometer to obtain Raman spectrum. This change in frequency can be recorded and plotted against the scattered light intensity. Therefore Raman scattering gives rise to reductions or gains in light frequencies that correspond very sensitively to the molecular structure of the material and its state.

Sample Preparation

Raman spectroscopy requires little to no sample preparation and is insensitive to aqueous absorption bands.

Method

Raman spectra were recorded using a Horiba–Jobin–Yvon LabRAM Raman microscope with a 532 nm laser operating at ca. 4 mW (10%) and a 600 lines per mm grating. Spectra were collected by averaging 8 acquisitions of 60s duration. The Raman shift was calibrated using the rayleigh peak and the 520.7 cm^{-1} Si line from a Si (100) reference sample.

2.3.6.4 Fourier Transform Infrared (FTIR) Spectroscopy

Fourier Transform Infrared (FTIR) Spectroscopy [54, 55] provides information of functional groups presence such as C=C, C=O, O–H, and C–H. It used to determine the structure of molecules as well as to quantitate components of an unknown mixture. It is very useful to confirm purity or impurities. The method consists of a beam containing many light frequencies at once and measures how much of that beam is absorbed by the sample. Molecular bonds vibrate at various frequencies depending on the elements and the type of bonds. For any given bond, there are several specific frequencies at which it can vibrate. According to quantum mechanics, these frequencies correspond to the ground state (lowest frequency) and several excited states (higher frequencies).

Sample Preparation

In this study, spectrophotometric-grade KBr was used, which is transparent to infrared radiation. The KBr was dried overnight at 100 ^{o}C to remove any adsorbed water or volatiles and then stored in a desiccator. 1.5 mg of dry carbon sample was mixed with 400 mg of spectrophotometric-grade KBr and ground to a fine homogeneous powder (**Figure 2.33** and **Figure 2.35**), which was then placed in a stainless steel die (**Figure 2.34**) and sufficient high pressure applied (a load of 6 to 7 tonnes on the press gauge) using manual hydraulic adjustable laboratory pellet press (**Figure 2.4**), to form a transparent thin and flat pellet/disk with approximately no more than 0.5 – 1.5 mm thickness to allow the light to pass through to the detector (**Figure**

2.37). In this study, IR spectra were obtained on a Bruker optics TENSOR 27 series FT-IR spectrometer (**Figure 2.35**).

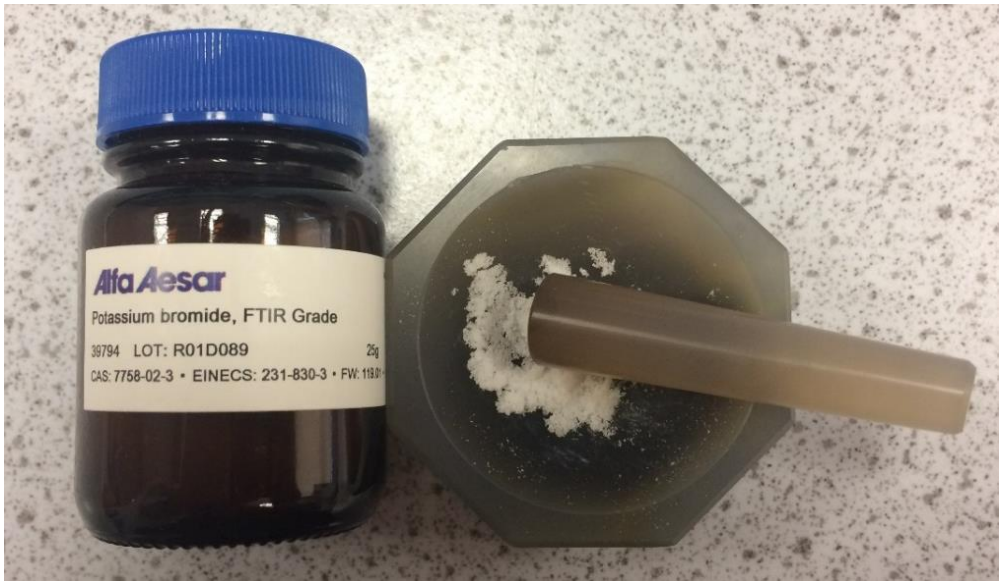


Figure 2.33: Photographic image of agate mortar and pestle used to produce fine/homogenous mixture of KBr with the sample.

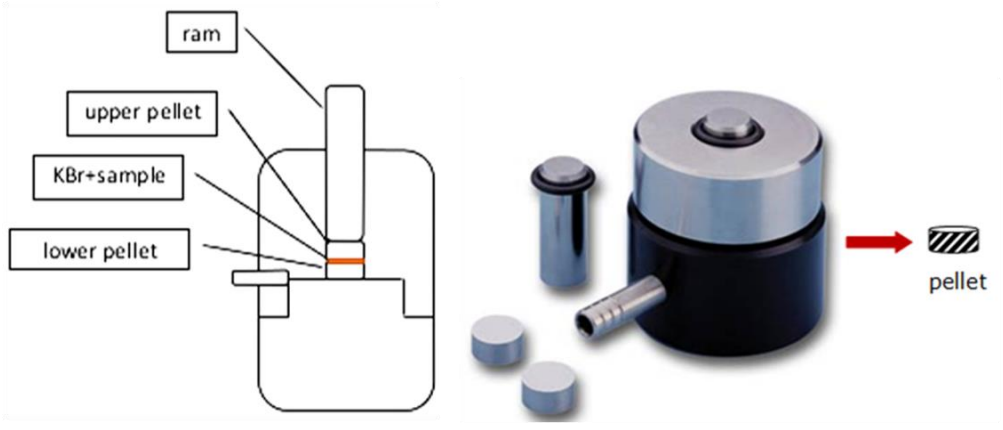


Figure 2.34: An evacuable 1.3 cm die used to produce transparent pellets/disks of KBr/sample mixture. Schematic of cross section of an evacuable 1.3 cm die (used for compaction of KBr/sample mixture.

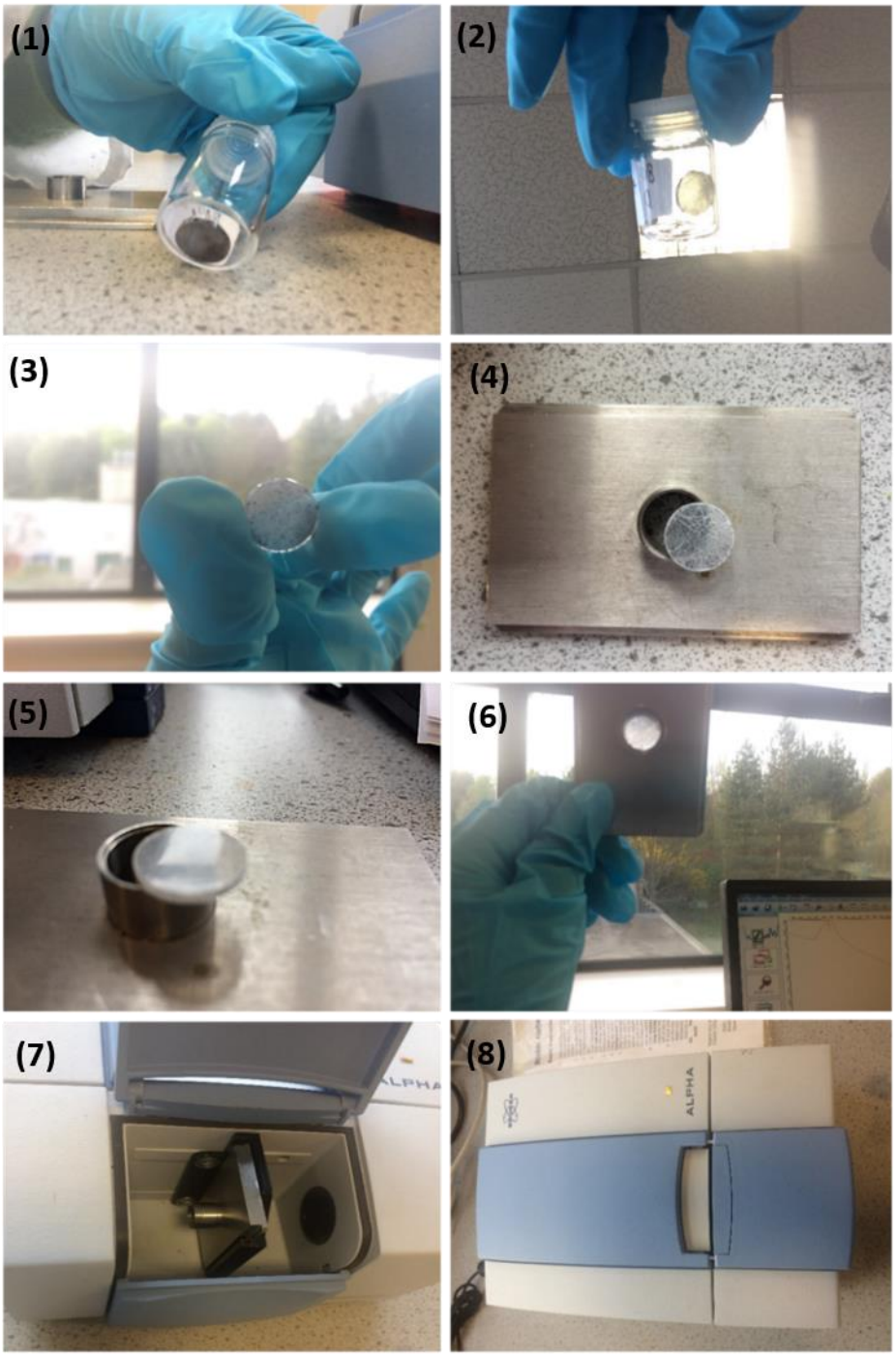


Figure 2.35: Photographic images showing different KBr/carbon pellets preparation: **(1)** opaque pellet which is useless, **(2)** and **(3)** excellent transparent pellet, **(4)** flaking pellet not preferable, **(5)** and **(6)** are translucent pellet which are ok, **(7)** KBr/carbon pellet position in (FTIR) spectroscopy, and **(8)** FTIR spectroscopy.

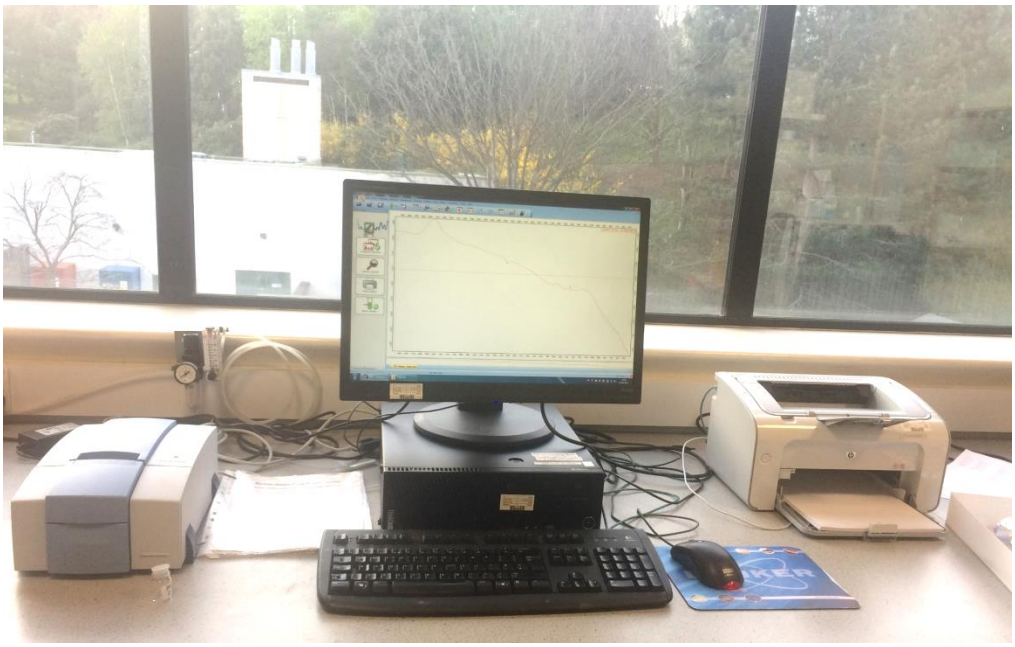


Figure 2.36: Photographic image of transmission potassium bromide (KBr)-pellet FTIR spectroscopy.

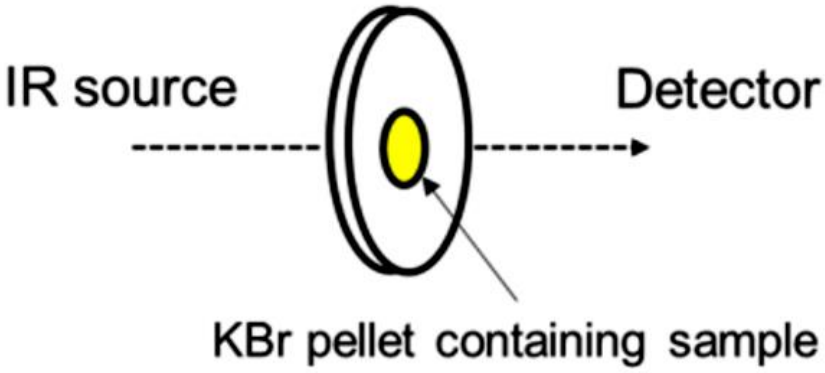


Figure 2.37: Schematic of IR radiation the light pass through the pellet then reach the detector in Fourier Transform Infrared (FTIR) spectroscopy (bulk measurements). [55]

2.4 Applications: Gas Sorption Measurements (H_2 and CO_2)

2.4.1 Gravimetric Gas Sorption Analysis

This technique based on physisorption which is interaction between gas and a solid *via* weak Van der Waals forces. The ads/des gas recording of gravimetric methods used to determine gas storage capacity on solid surface at controlled pressure and temperature. The amount of adsorbed gas (CO_2 or H_2) at changing pressure is measured as a function of the applied pressure and the corresponding isotherm is produced. Many materials can be analysed using this technique such as; carbons, zeolites, and polymers, among others. In this study, tow instruments used IGA-003 Intelligent Gravimetric Analyser and High accuracy gravimetric sorption analyzer (XEMIS).

2.4.1.1 IGA-003 Intelligent Gravimetric Analyser

A typical IGA-003 Intelligent Gravimetric Analyser [56, 57] is shown in **Figure 2.38**. According to the manufacturer (Hiden Isochema, 2015), automated measurements of adsorption/desorption isotherms in IGA system is performed with precise temperature and pressure control. The instruments can also be used to accurately measure and determine multi-component gas and/or vapour sorption-desorption processes at high pressure ranging from vacuum to high pressure (20 bar maximum), at temperatures ranging from -196 °C to 1000 °C, by measurement of mass change, pressure and temperature in diverse operating conditions and by using different dynamic flow of gases mixed or separate such as carbon dioxide, hydrogen, and methane.

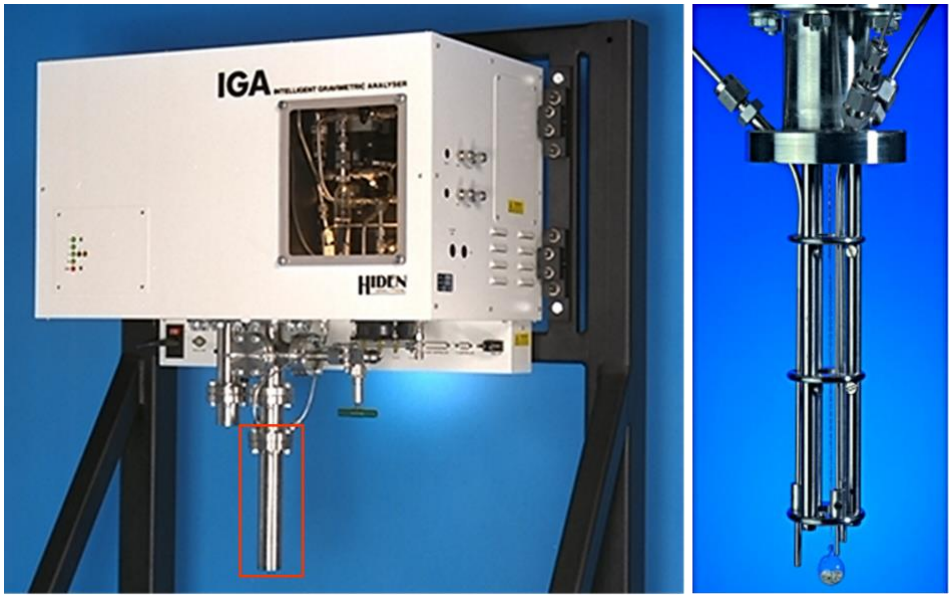


Figure 2.38: Intelligent Gravimetric Analyzer (IGA-003), sample chamber and sample holder position (red box).

2.4.2 High Accuracy Gravimetric Sorption Analyzer (XEMIS)

The XEMIS [58, 59] (**Figure 2.39**) is a high accuracy sorption gravimetric instrument that can accurately measure the uptake of gases by materials under a wide ranging combination of temperature and pressure conditions. The XEMIS can operate under wide-ranging experimental conditions; temperatures to 773 K and pressures up to 200 bar, which allows gravimetric sorption testing at high pressures and high temperatures.

Sample Preparation

About 10 to 100 mg of the sample were dried in an oven for 24 h at 120 °C then loaded into the analyser. The samples were firstly evacuated at up to 10^{-7} bar under heating (200-250 °C) overnight before measurements were performed in the pressure range of 0-20 bar for an IGA-001 Intelligent Gravimetric Analyzer and 0-200 bar for the XEMIS analyzer. Carbon density of 1.5 $cm^3\ g^{-1}$ was used for buoyancy correction of adsorbed gas. This carbon density had previously been determined from helium sorption data obtained using the IGA at a pressure of up to 20 bar at 0 °C.

CO_2 Uptake Measurements

CO_2 uptakes were performed using high purity CO_2 gas (99.9999%). CO_2 uptake isotherms were measured at room temperature (25 °C) using water bath and at 0 °C (using ice bath).

Hydrogen Uptake Measurements

Hydrogen uptake were performed using established procedures,[60-62] with high purity (99.9999%) hydrogen gas in the pressure range of 0–20 bar using IGA-003 Intelligent Gravimetric Analyser or 0-200 bar using XEMIS analyser. The hydrogen adsorption data was corrected for buoyancy effects with carbon density of 1.5 g cm^{-3} and hydrogen density of 0.04 g cm^{-3} for total uptake and 0 g cm^{-3} for excess uptake (see calculation section).



Figure 2.39: XEMIS sorption analyzer.

2.5 Calculation

2.5.1 Excess and Total Hydrogen Uptake

The hydrogen uptake measurements provided the excess hydrogen uptake,[63] which is the amount of hydrogen adsorbed in the carbons above that which would have been stored in the pores under similar conditions (temperature and pressure) assuming that there is zero energy of interaction between the hydrogen and the carbon pore walls. The total uptake is calculated from the excess storage by taking into account the amount of hydrogen compressed into the carbon pore volume space. The used gravimetric method measured the excess hydrogen uptake (θ_{Exc}) from which the total storage (wt %) (θ_T) was calculated from the equation below:

$$\Theta_T = \Theta_{Exc} + \frac{100 \text{ X } d_{H2} \text{ X } V_T}{1 + (d_{H2} \text{ X } V_T)} \qquad \textbf{Equation 2.4}$$

Where

Θ_T	Total hydrogen uptake (wt %)
Θ_{Exc}	Excess hydrogen uptake (wt %)
d_{H_2}	Density (gcm^{-3}) of compressed hydrogen gas at the relevant temperature and pressure. The density was obtained from the National Institute of Standards and Technology (NIST) (website http://www.nist.gov/)
V_T	Pore volume (cm^3g^{-1}) of the carbon, which obtained from Nitrogen sorption analysis (BET).

The excess volumetric uptake capacity ($v\theta_{Exc}$), in g L^{-1}, was obtained using the equation;

$$v\theta_{Exc} = \theta_{Exc} \, X \, d_{carbon} \qquad \textbf{Equation 2.5}$$

Where, d_{carbon} = packing density of the carbon

The total volumetric uptake capacity ($v\theta_T$), in g L^{-1}, was obtained using the equation;

$$v\Theta_T = \Theta_T \ \mathbf{X} \ \boldsymbol{d_{carbon}} \qquad \textbf{Equation 2.6}$$

Where; d_{carbon} = packing density of the carbon.

The packing density of powder samples was determined by pressing a given amount of carbon in a 1.3 cm die at pressure of 7 MPa for 10 minutes. Alternatively similar values can be obtained using the general equation;

$$\boldsymbol{\rho_d} = \left(\frac{\mathbf{1}}{\boldsymbol{\rho_s}} + \boldsymbol{V_T}\right)^{-\mathbf{1}} \qquad \textbf{Equation 2.7}$$

Where

ρ_s	is skeletal density
V_T	is total pore volume

The hydrogen uptake was calculated on the basis of a density of 1.5 g cm^{-3} for the carbons.

2.6 References

1. M. Sevilla and R. Mokaya, *Energy Environ. Sci.*, 2014, **7**, 1250-1280.

2. B. Adeniran and R. Mokaya, *Nano Energy*, 2015, **16**, 173-185.

3. N. Balahmar, A. C. Mitchell and R. Mokaya, *Adv. Energy Mater.*, 2015, **5**.

4. M. Cox and R. Mokaya, *Sustainable Energy & Fuels*, 2017, **1**, 1414-1424.

5. M. Sevilla and A. B. Fuertes, *Carbon*, 2009, **47**, 2281-2289.

6. M. Sevilla, J. A. Maciá-Agulló and A. B. Fuertes, *Biomass Bioenergy*, 2011, **35**, 3152-3159.

7. F. W. Fifield and D. Kealey, *Principles and Practice of Analytical Chemistry, 4th Edition*, Blackie Academic & Professional, an Imprint of Chapman and Hall, Glasgow, 1995.

8. SDT Q600, TGA, http://www.mtm.kuleuven.be/equipment/dsc_and_tga/dsc_and_tga , (accessed 12/12/2017).

9. TGA analysis, http://www.andersonmaterials.com/tga.html, (accessed 12/12/2017).

10. https://equipment.nottingham.ac.uk/browse/ou-20-Chemistry/category-1-Characterisation+%26+Measurement/item/thermogravimetric-analyser-q600-/303, Thermogravimetric analyser-Q600, (accessed 12/12/2017).

11. Thermogravimetric Analysis, https://www.perkinelmer.com/lab-solutions/resources/docs/faq_beginners-guide-to-thermogravimetric-analysis_009380c_01.pdf, (accessed 20/2/2018).

12. C. Hammond, *The Basics of Crystallography and Diffraction*, Oxford University Press, 2011.

13. J. R. A. Clearfield, and N.i Bhuvanesh, *Principles and Applications of Powder Diffraction*, 2008.

14. E. P. Bertin, *Principles and Practice of X-ray Spectrometric Analysis*, 1970

15. M. M. Woolfson, *An Introduction to X-ray Crystallography*, Cambridge University Press, 1997.

16. V. Pecharsky and P. Zavalij, *Fundamentals of Powder Diffraction and Structural Characterization of Materials. 2nd Edition*, 2009.

17. Bragg's Law of Diffraction, http://www.microscopy.ethz.ch/bragg.htm, (accessed 20/12/2017).

18. X-ray Powder diffraction, https://serc.carleton.edu/research_education/geochemsheets/techniques/XRD.html, (accessed 12/12/2017).

19. K. S. W. Sing, D. H. Everett, R. A. W. Haul, L. Moscou, R. A. Pierotti, J. Rouquerol and T. Siemieniewska, *Pure Appl. Chem.*, 1985, **57**, 603-619.

20. Adsorption Isotherms, http://www.microtrac-bel.com/en/tech/bel/seminar02.html, (accessed 27/2/2018).

21. F. Rouquerol, J. R. and and K. Sing, *Adsorption by Powders and Porous Solids Principles, Methodology and Applications, 2nd Edition*, Academic Press, London, 1999.

22. X. Tang, Z. Jiang, Z. Li, Z. Gao, Y. Bai, S. Zhao and J. Feng, *J. Nat. Gas Sci. Eng.*, 2015, **23**, 464-473.

23. A. V. Neimark, P. I. Ravikovitch, M. Grun, F. Schuth and K. K. Unger, *J. Colloid Interface Sci.*, 1998, **207**, 159-169.

24. S. Brunauer, P. H. Emmett and E. Teller, *J. Amer. Chem. Soc.*, 1938, **60**, 309-319.

25. BET theory, http://www.microtrac-bel.com/en/tech/bel/seminar07.html, (accessed 27/2/2017).

26. BET Micromeritics surface area and porosity analyzer, http://www.micromeritics.com/Product-Showcase/Surface-Area.aspx, (accessed 1/1/2018).

27. Surface Area and Porosity Analyzer (ASAP)2020, https://equipment.nottingham.ac.uk/search/item/304/physisorption-analyzer.html?q=bet, (accessed 1/1/2018).

28. C. A. Nunes and M. C. Guerreiro, *Quim. Nova*, 2011, **34**, 472-U309.

29. 3Flex surface characterization analyzer, http://www.micromeritics.com/Repository/Files/3flex_brochure_2016_v8.pdf, (accessed 22/12/2017).

30. 3Flex surface characterization analyzer, https://www.azom.com/article.aspx?ArticleID=11661, (accessed 12/3/2018).

31. CHN Microanalysis, http://midwestlab.com/wp-content/uploads/2013/11/CHN_Analysis.pdf, (accessed 22/12/2017).

32. CHN Elemental Analyser, https://equipment.nottingham.ac.uk/browse/ou-20-Chemistry/item/chn-elemental-analyser/211, (accessed 23/12/2017).

33. High energetic electron beam interactions with the sample in an electron microscope,

https://sites.google.com/site/itfinalkmitl/information-from-sem, (accessed 3/6/2018).

34. Scanning Electron Microscopy (SEM), http://www.nottingham.ac.uk/nmrc/facilities/emsuite/sem.aspx, (accessed 30/12/2017).

35. P. J. Goodhew, F. J. H. and and R. Beanland, *Electron Microscopy and Analysis, 3rd Edition*, Taylor & Francis Group, London, 2001.

36. Scanning Electron Microscopy (SEM), http://www.ammrf.org.au/myscope/sem/introduction/, (accessed 21/2/2018).

37. Gold and Platinum Sputter Coaters, https://www.nottingham.ac.uk/nmrc/facilities/emprep.aspx, (accessed 4/3/2018).

38. Electron Microscopes, https://www.nottingham.ac.uk/isac/news-items/new-electron-microscopes.aspx, (accessed 4/1/2018).

39. Transmission Electron Microscopy, http://www.nottingham.ac.uk/nmrc/facilities/emsuite/tem.aspx, (accessed 30/12/2017).

40. Transmission Electron Microscopy (TEM), http://www.ammrf.org.au/myscope/tem/introduction/, (accessed 21/2/2018).

41. J. W. J.F. Watts, *An Introduction to Surface Analysis by XPS and AES*, Wiley, 2003.

42. X-ray Photoelectron Spectroscopy XPS, https://xpssimplified.com/whatisxps.php, (accessed 23/12/2017).

43. X-Ray Photoelectron Spectroscopy (XPS), https://www.nottingham.ac.uk/isac/facilities/xps.aspx, 23/12/2017).

44. X-ray Photoelectron Spectroscopy (XPS), https://www.nottingham.ac.uk/nmrc/facilities/xps/x-ray-photoelectron-spectroscopy-xps.aspx, (accessed 6/3/2018).

45. F. Rouessac and A. Rouessac, *Chemical Analysis, Modern Instrumentation Methods and Techniques, 2nd Edition*.

46. F. W. Fifield and D. Kealey, *Principles and Practice of Analytical Chemistry, 4th Edition*, Blackie Academic & Professional, an Imprint of Chapman and Hall, Glasgow, 1995.

47. The inductively coupled plasma - optical emission spectrometer (ICP-OES), https://equipment.nottingham.ac.uk/browse/ou-20-Chemistry/item/inductively-coupled-plasma-optical-emission-spectrometer/213, (accessed 23/12/2017).

48. The inductively coupled plasma-optical emission spectrometer (ICP-OES), http://www.chemiasoft.com/chemd/node/52, (accessed 22/12/2017).

49. The inductively coupled plasma-optical emission spectrometer (ICP-OES), https://web.archive.org/web/20120526165604/http://www.wfu.edu/chemistry/courses/jonesbt/334/icpreprint.pdf, (accessed 8/3/2018).

50. G. D. Ewen Smith, *Modern Raman Spectroscopy: A Practical Approach*, John Wiley & Sons Ltd, 2005.

51. RAMAN Spectroscopy, http://www.nottingham.ac.uk/nmrc/facilities/raman/raman-spectroscopy.aspx, (accessed 30/12/2017).

52. RAMAN Spectroscopy, http://bwtek.com/raman-introduction-to-raman-spectroscopy/, (accessed 30/12/2017).

53. Raman Spectroscopy, http://www.renishaw.com/en/a-basic-overview-of-raman-spectroscopy--25805, (accessed 4/1/2018).

54. FTIR Spectrometer, https://chem.libretexts.org/Core/Physical_and_Theoretical_Chemistry/Spectroscopy/Vibrational_Spectroscopy/Infrared_Spectroscopy/How_an_FTIR_Spectrometer_Operates, (accessed 30/12/2017).

55. Y. Y. Chen, C. N. Zou, M. Mastalerz, S. Y. Hu, C. Gasaway and X. W. Tao, *Int. J. Mol. Sci.*, 2015, **16**, 30223-30250.

56. Intelligent Gravimetric Analyzer (IGA-003), https://hidenisochema.com/hiden-products/iga-003/, (accessed 12/12/2017).

57. Intelligent Gravimetric Analyser (IGA-003), https://equipment.nottingham.ac.uk/search/item/305/intelligent-gravimetric-analyser.html?q=IGA, (accessed 23/12/2017).

58. High accuracy gravimetric sorption analyzer (XEMIS), https://hidenisochema.com/ hiden -products/xemis/, (accessed 12/12/2017).

59. Hiden Isochema XEMIS, https://www.azom.com/equipment-details.aspx?EquipID=3478, (accessed 12/12/2017).

60. Z. X. Yang, Y. D. Xia, X. Z. Sun and R. Mokaya, *J. Phys. Chem. B*, 2006, **110**, 18424-18431.

61. M. Sevilla, A. B. Fuertes and R. Mokaya, *Energy Environ. Sci.*, 2011, **4**, 1400-1410.

62. M. Sevilla, R. Mokaya and A. B. Fuertes, *Energy Environ. Sci.*, 2011, **4**, 2930-2936.

63. T. S. Blankenship, N. Balahmar and R. Mokaya, *Nat. Commun.*, 2017, **8**, 12.

Chapter 3. Templating of Carbon in Zeolites under Pressure: Synthesis of Pelletized Zeolite Templated Carbons with Improved Porosity and Packing Density for Superior Gas (CO_2 and H_2) Uptake Properties

3.1 Aim of this Chapter

A main motivation of this chapter is:

- To increase the packing density of the final zeolite templated carbons ZTCs for high volumetric gas uptake.

- To study and probe the properties and effects of post-synthesis compaction/pelletization of zeolite templated carbons ZTCs generated from zeolites pressed into pellets at high pressure and pelletized ZTCs prepared *via* a combination of liquid impregnation and CVD on and the consequences of such compaction on porosity, densification and both gravimetric and volumetric gas (CO_2 and hydrogen) uptake.

3.2 Abstract

This chapter explores the use of compacted zeolite pellets as templates for the preparation of pelletized zeolite templated carbons (ZTCs). The effects of zeolite compaction before use as hard templates were investigated through the compression of powder forms of zeolites at 370 MPa (equivalent to 5 tonnes) or 740 MPa (equivalent to 10 tonnes) prior to their use as templates. The resulting carbon samples were compared to compacted conventionally templated (with powdered zeolites) ZTCs. The use of compacted zeolite pellets results in pelletized ZTCs that simultaneously exhibit higher porosity and higher packing density, which translates to highly enhanced volumetric gas (CO_2 and hydrogen) uptake. For CVD-derived samples, the pelletized ZTCs achieve 10% higher surface area than powdered samples (and reach > 2000 $m^2\ g^{-1}$) despite their packing density increasing from *ca.* 0.55 to 0.85 g cm^{-3}, which means that the surface area per unit volume increases by *ca.* 60% from between 1000 $m^2\ cm^{-3}$ and 1100 $m^2\ cm^{-3}$ for the powdered ZTCs to *ca.* 1670 $m^2\ cm^{-3}$ for pelletized samples. Thus their volumetric CO_2 uptake at 25 ^oC increases by 140% and 85% at 1 bar and 20 bar, respectively, compared to powdered ZTCs. Pelletized ZTCs prepared *via* a combination of liquid impregnation and CVD achieve much higher surface area of 3000 m^2g^{-1} (compared to 2700 m^2g^{-1} for powder samples) despite an increase in packing density from 0.44 to 0.69 g cm^{-3}, resulting in a surface area per unit volume rise of 75% from 1189 $m^2\ cm^{-3}$ to 2085 $m^2\ cm^{-3}$. The high surface area pelletized ZTCs have an attractive gravimetric hydrogen uptake of 6.6 wt% (5.5 wt% for powdered sample) at 20 bar and -196 ^oC, and reach a volumetric hydrogen storage capacity of 46 g L^{-1} (24 g L^{-1} for powder sample). For CO_2 uptake at 25 ^oC and at 20 bar, the volumetric uptake of the high surface area pelletized ZTC is nearly twice that of the powdered sample; 668 g L^{-1} compared to 360 g L^{-1}.

3.3 Introduction

Porous materials have been extensively investigated as storage media for energy related gases such as hydrogen and CO_2. The focus on porous materials as stores for energy applications is driven and motivated by the need for environmental protection and demands for clean energy sources.[1, 2] The drive for environmental protection is typified by research efforts aimed at developing materials for the capture and sequestration of CO_2, while the search for cleaner energy sources requires material advances that may lead to realisation of the mooted Hydrogen Economy.[1-19] Innovative synthesis methods and the development of new types of nanoporous materials that offer improvements in overall porosity or high level control of porosity have brought significant strides in addressing the materials challenges that must be overcome in the journey towards materials-based CO_2 storage and the Hydrogen Economy.[3-8, 20] Thus porous materials with very high surface area and/or well controlled porosity have recently come on to the research stage. The best examples of such research are illustrated by developments in metal–organic frameworks (MOFs), [21] covalent organic frameworks (COFs) [22] and porous carbons whether they be activated[4] or templated.[5, 23-25] Given the relationship between porosity and gas uptake, improvements in surface area and pore volume, and better targeting of pore size has resulted in materials with attractive gravimetric uptake for CO_2 and hydrogen; [3-8, 26, 27] the gas uptake capacity of porous materials under any given conditions generally strongly correlates with the magnitude of the surface area and size of pore channels.[3-8, 26, 27] Due to their more robust stability under various environments, porous carbons have retained on-going interest as gas stores even on the face of other emerging materials such as MOFs and COFs.[4, 5, 23-25] Of particular interest are zeolite templated carbons, which, so far, not only exhibit some of the highest

reported surface area values for carbons but also offer enhanced pore size control due to the templating effect of zeolite frameworks.[24, 28-31]

Material-based developments in the storage of CO_2 and hydrogen are generally guided by set targets that would allow practical use of the materials in a commercially viable manner. Examples of such targets include those of the United States Department of Energy (DOE) which, for hydrogen storage, currently stipulate a whole system uptake of 5.5 wt% (gravimetric) and 40 g L^{-1} (volumetric), with the ultimate aim being a gravimetric uptake of 7.5 wt% and volumetric capacity of 70 g L^{-1}.[32] Therefore, there is need to not only increase the gravimetric uptake of porous materials but even more importantly, to improve the volumetric storage capacity. Recent trends in the development of porous materials for CO_2 and hydrogen storage have mainly emphasised porosity changes that allow improvements in the gravimetric uptake.[3-19] This has included preparation of ultra-high surface area nanostructures for gas uptake at high pressures [21, 22] and on the other hand, synthesis of highly microporous materials for CO_2 uptake at low pressure.[7, 33-39] Unfortunately, at the present time, the materials with the highest surface area generally tend to have low packing density and therefore low volumetric uptake. Enhancements in packing density and consequently volumetric storage capacity of porous materials may be achieved by material densification or compaction. However, for most porous materials, attempts at densification generally fail to achieve the desired outcome due to the fact that increase in packing density causes a decrease in porosity due to the inherent mechanical instability of most nanostructures. Densification *via* compaction, therefore, generally results in drastic decrease in both the porosity (surface area and pore volume) and gravimetric uptake of CO_2 and hydrogen. In this regard, whilst porous carbons are generally mechanically robust and can withstand moderate densification, MOFs and

COFs on the other hand, have low mechanical stability and are easily destroyed with loss of porosity even at low compaction pressures.[40-43]

Examples of porous solids with varying mechanical stability and amenability to compaction include; activated carbons compacted at 40 MPa that reach a packing density of 0.5 g cm^{-3} and hydrogen storage capacity of 20 g L^{-1} (at -196 ^{o}C and 40 bar),[40, 41] monolithic forms of activated carbon with packing density of 0.7 g cm^{-3} that achieve a total volumetric hydrogen uptake capacity of 39 g L^{-1} at -196 ^{o}C and 44 bar,[44] compacted activated carbon with a packing density of 0.72 g cm^{-3} with volumetric hydrogen uptake capacity of 41 g L^{-1} at -196 ^{o}C and 60 bar.[45] More recently, Mokaya and co-workers have shown that so-called compactivated carbons, which are prepared *via* a mechanochemical approach involving compaction of carbonaceous matter before activation, show improvements in porosity and may be densified to higher packing density than conventionally activated carbons and therefore show attractive volumetric gas (CO_2 and hydrogen) uptake.[46] On the other hand, compaction of MOFs yields less promising results; compaction of a MOF-5, achieves an uptake of *ca.* 16 g L^{-1} (at -196 ^{o}C and pressure of between 40 and 60 bar).[45, 47] Other examples of MOF densification include those of; (i) Chahine and co-workers (38 and 48 g L^{-1} at 50 and 130 bar, respectively, and -196 ^{o}C for densified MOF-177),[48] (ii) Muller and co-workers (38 and 48 g L^{-1} at 50 and 80 bar, respectively, and -196 ^{o}C for densified MOF-5),[49] Siegel and co-workers (38 and 43 g L^{-1}, respectively, at 50 bar and 100 bar and -196 ^{o}C for densified MOF-5).[50] Much less work has been reported on the effects of densification of porous materials on their volumetric CO_2 uptake; Marco-Lozar and co-workers have reported on activated carbon monoliths that have high packing density and volumetric CO_2 uptake,[51] while Mokaya and co-workers have achieved improvements in volumetric uptake of activated carbons *via* a mechanochemical activation (so-called compactivation) route.[52]

Zeolites, which are known to have high mechanical stability, have in the recent past been extensively studied for carbon templating, as they offer a wide range of porous structures for carbon materials to adopt with a high level of structural ordering.[23, 24] Zeolite-templated carbons (ZTCs) are prepared by the carbonisation of a zeolite, in which a carbon precursor fills the zeolite's porous framework to adopt its reciprocal structure.[24] Following the removal of the zeolite template *via* selective etching, the resulting carbon structure exhibits a network of pore channels that are inversely replicated from the zeolite. Past efforts to increase the volumetric gas uptake of ZTCs include the densification of zeolite Y-templated carbon by Kyotani and co-workers *via* hot-pressing at 300 ^{o}C and 147 MPa, which achieved packing density of between 0.7 g cm^{-3} and 0.9 g cm^{-3}.[53] More recently, Mokaya and co-workers have shown that ZTCs have excellent mechanical stability and are amenable to densification to packing density of *ca.* 0.72 g cm^{-3} and consequently a rise in volumetric hydrogen storage capacity from 30 g L^{-1} to values greater than 50 g L^{-1} at 20 bar and -196 ^{o}C.[54] However, despite the excellent mechanical stability of the ZTCs, there was a loss of porosity on compaction.[54] It is therefore of interest to explore other possible densification routes for this robust group of templated porous carbons. Motivated by the known high mechanical stability of zeolites, this chapter explores the effect of templating ZTCs from compacted zeolite pellets. This is the first time that compacted zeolites, in the form of pellets, have been used as templates for nanostructured carbon, and represents an entirely new approach to the synthesis of ZTCs. An added attraction of this new approach is that, importantly, it has the potential to generate densified ZTCs.

This chapter reports on the properties of compacted pelletized zeolite templated carbons generated from zeolites pressed into pellets at high pressure and the consequences of such compaction on porosity, densification and both gravimetric and volumetric gas (hydrogen and CO_2) uptake.

3.4 Experimental Section

This section presents a detailed description of the materials and chemicals, experimental procedures, and approach used in **Chapter 3**.

3.4.1 Materials and Chemicals

The list of chemicals/materials used with their sources and purity are presented below in **Table 3.1.**

Table 3.1: List of chemical reagents/materials used in the experiment.

Chemical/Material	Source/Manufacturer	Purity/Concentration
Furfural alcohol (FA)	Aldrich	99%
Hydrochloric acid (HCl)	Fisher Scientific	37%
Hydrofluoric acid (HF)	Acros Organics	(37%) Solution in water
Zeolite Y	Zeolyst International	-
Zeolite 13X	Alfa Aesar	-
Argon compressed gas (Cylinder)	BOC Ltd	99%
Acetonitrile solvent	Fisher Scientific	High purity 99%
Ethylene/Argon compressed gas (Cylinder)	BOC Ltd	10% Ethylene/Argon gas (by volume)

3.4.2 Material Synthesis

To test the full range of applicability of the proposed synthesis route, the ZTCs were prepared *via* two synthesis regimes that generate carbons with either moderate surface area or high surface area.

3.4.2.1 Moderate Surface Area ZTCs

Conventionally templated (i.e., powder) ZTCs were prepared as follows; 0.5 g of dry zeolite (13X or Y) was heated at a ramp rate of 10 ^{o}C min^{-1} to 700 ^{o}C under nitrogen flow. Chemical vapour deposition was then performed for 3 h at 700 ^{o}C with a flow of nitrogen saturated with acetonitrile, following which the gas flow was switched to nitrogen only and the temperature increased at a ramp rate of 10 ^{o}C min^{-1} to 900 ^{o}C and held for 3 h, followed by cooling to room temperature under nitrogen flow (**Figure 3.1**). The resulting zeolite/carbon composite was treated sequentially in 10% hydrofluoric acid (HF) at room temperature, washed in distilled water and then refluxed (at 60 ^{o}C) in concentrated hydrochloric acid (HCL). The final carbon was then repeatedly washed with distilled water and dried at 60 ^{o}C for 12 h to yield *ca.* 0.1 g ZTC. Denoted as CZ13X or CZY for templating with zeolite 13X or zeolite Y, respectively. (See abbreviations section **Table 3.2**).

To probe the effects of post-synthesis compaction, *ca.* 40 mg of both CZ13X and CZY were compacted into pellets at a load of 5 tonnes (equivalent to 370 MPa of compaction pressure) on a 1.3 cm diameter die. The compacted samples were denoted as C5-CZ13X and C5-CZY, respectively. (See abbreviations section).

To explore the effects of templating with compacted zeolite pellets, 0.5 g zeolite 13X or 0.23 g of zeolite Y was compacted into a pellet at a load of 5

tonnes (equivalent to 370 MPa of compaction pressure) on a 1.3 cm diameter die. The compaction increased the zeolite density by nearly 50% from 0.7 g cm^{-3} to 1.08 g cm^{-3}. The carbon templating process was carried out as described before for powder samples except that the resulting zeolite/carbon composites were placed in HF and HCl acids as described above but with *no agitation* so as to preserve a compact pelletized nature. The washing cycle was repeated until the zeolite framework was etched out. The final carbons denoted as CZ13XP and CZYP from zeolite 13X and zeolite Y, respectively (see abbreviations section **Table 3.2**), were washed with deionized water and dried at 100 ^{o}C. The yield of carbon for the pelletized ZTCs was similar to that of the conventionally templated powder samples.

3.4.2.2 High Surface Area ZTCs

High surface area ZTCs were prepared as follows; 0.6 g zeolite 13X (powder or compacted into a pellet *at 10 tonnes* equivalent to 740 MPa) was dried in a furnace at 300 ^{o}C for 12 h before being impregnated, *via* the incipient wetness method, with furfural alcohol (FA). Typically, several droplet of furfural alcohol (FA) added to zeolite 13X (powder or pellets) at room temperature until zeolite become fully wet and show homogeneous FA/zeolite. The resulting FA/zeolite composite, in an alumina boat, was heated under argon flow at 80 ^{o}C for 24 h followed by further heating at 150 ^{o}C for 8 h. The temperature was then raised at a ramp rate of 5 ^{o}C min^{-1} to 700 ^{o}C and held for 3 h under argon flow. The resulting zeolite/carbon composite was then exposed to further carbon deposition *via* CVD with ethylene gas (10% in argon by volume) at 700 ^{o}C for 3 h. The gas flow was then switched to argon only and the temperature raised to 900 ^{o}C and held for 3 h followed by cooling under argon to room temperature (**Figure 3.2**).

The resulting zeolite/carbon composites were washed in 10% hydrofluoric acid (HF) for 24 h and then refluxed in concentrated hydrochloric acid (HCl) for 6 h. *No stirring* was applied during washing of the compact pelletized sample. The final carbon material, denoted as CZ13XFAET (powder) or CZ13XFAETP (compacted pellets), (see abbreviations section **Table 3.2**), was washed with deionized water and dried at 100 ^{o}C for 24 h.

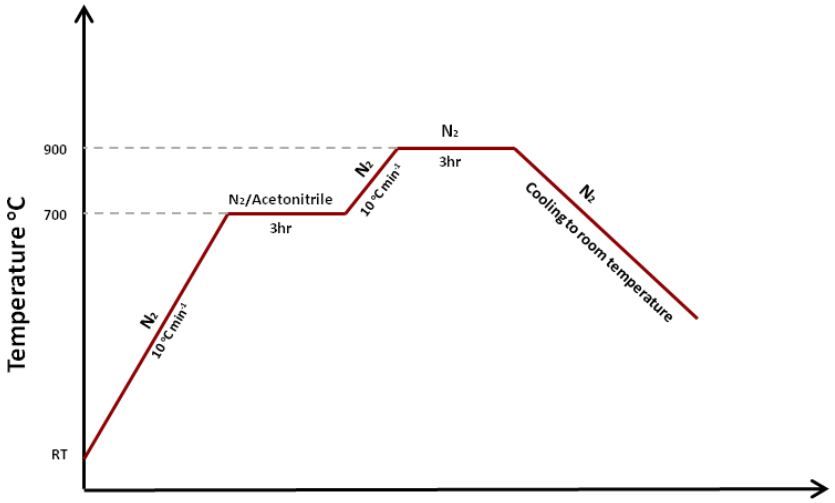


Figure 3.1: A plot representing the temperature programme used to prepare moderate surface area ZTCs.

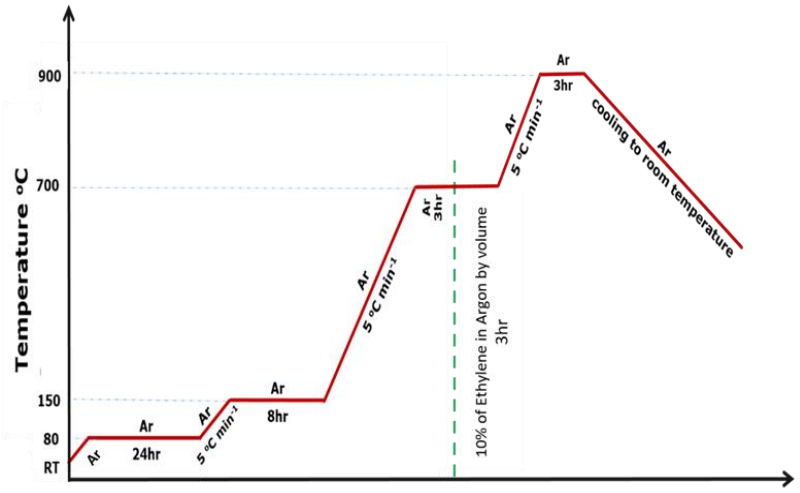


Figure 3.2: A plot representing the temperature programme used to prepare high surface area ZTCs.

3.5 Abbreviations

Table 3.2 shows a list of sample abbreviations for samples prepared using ***Zeolite X*** and ***Zeolite Y***.

Table 3.2: List of ZTCs samples abbreviations.

Moderate Surface Area ZTCs			
Zeolite Type	Conventionally Templated Carbons (powder)	Post-Compacted Templated Carbons (pellets) *@5 tonnes* (*370 MPa*)	Pre-Compacted Templated Carbons (pellets) *@5 tonnes* (*370 MPa*)
Zeolite 13X	CZ13X	C5-CZ13X	CZ13XP
Zeolite Y	CZY	C5-CZY	CZYP
High Surface Area ZTCs			
Zeolite Type	Conventionally Templated Carbons (powder)	Compacted Zeolite (pellets) *@10 tonnes* (*740 MPa*)	
Zeolite 13X	CZ13XFAET	CZ13XFAETP	

3.6 Results and Discussion

3.6.1 Compared Zeolite 13X Compacted *at 5 tonnes (370 MPa)* or *10 tonnes (740 MPa)* with Original Powder Samples

Prior to their use as templates, the nature of compacted zeolites was ascertained with respect to their morphology, structural ordering and porosity. This was achieved by comparing samples of zeolite 13X compacted *at 5 tonnes* (equivalent to 370 MPa) or *at 10 tonnes* (equivalent to 740 MPa) with original powder samples.

3.6.1.1 Morphology and Surface Analysis

SEM micrographs images (**Figure 3.3**, **Figure 3.4** and **Figure 3.5**) show that whilst powder samples of zeolite 13X have well dispersed and 'free flowing' standalone particles (**Figure 3.3**), compaction causes aggregation of the particles and that the extent of aggregation increases at higher compaction pressure (**Figure 3.4** and **Figure 3.5**) for *5 tonnes* and *10 tonnes,* respectively. Individual zeolite particles are still observed in the compacted zeolites but mainly as part of larger aggregates. The compaction, clearly, leads to a decrease in interparticle voids, which manifest in the form of higher packing density.

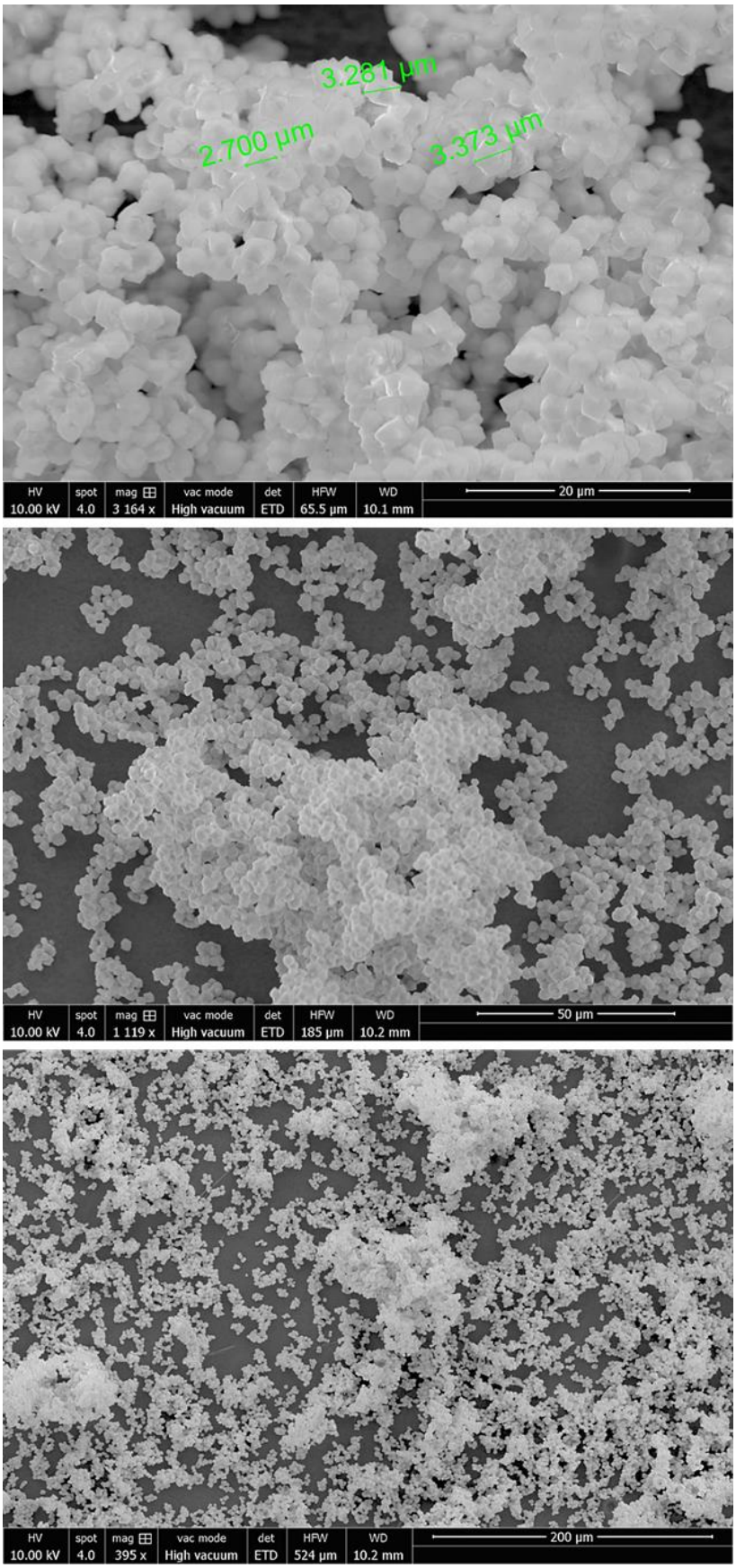


Figure 3.3: SEM micrographs images of powdered Zeolite 13X.

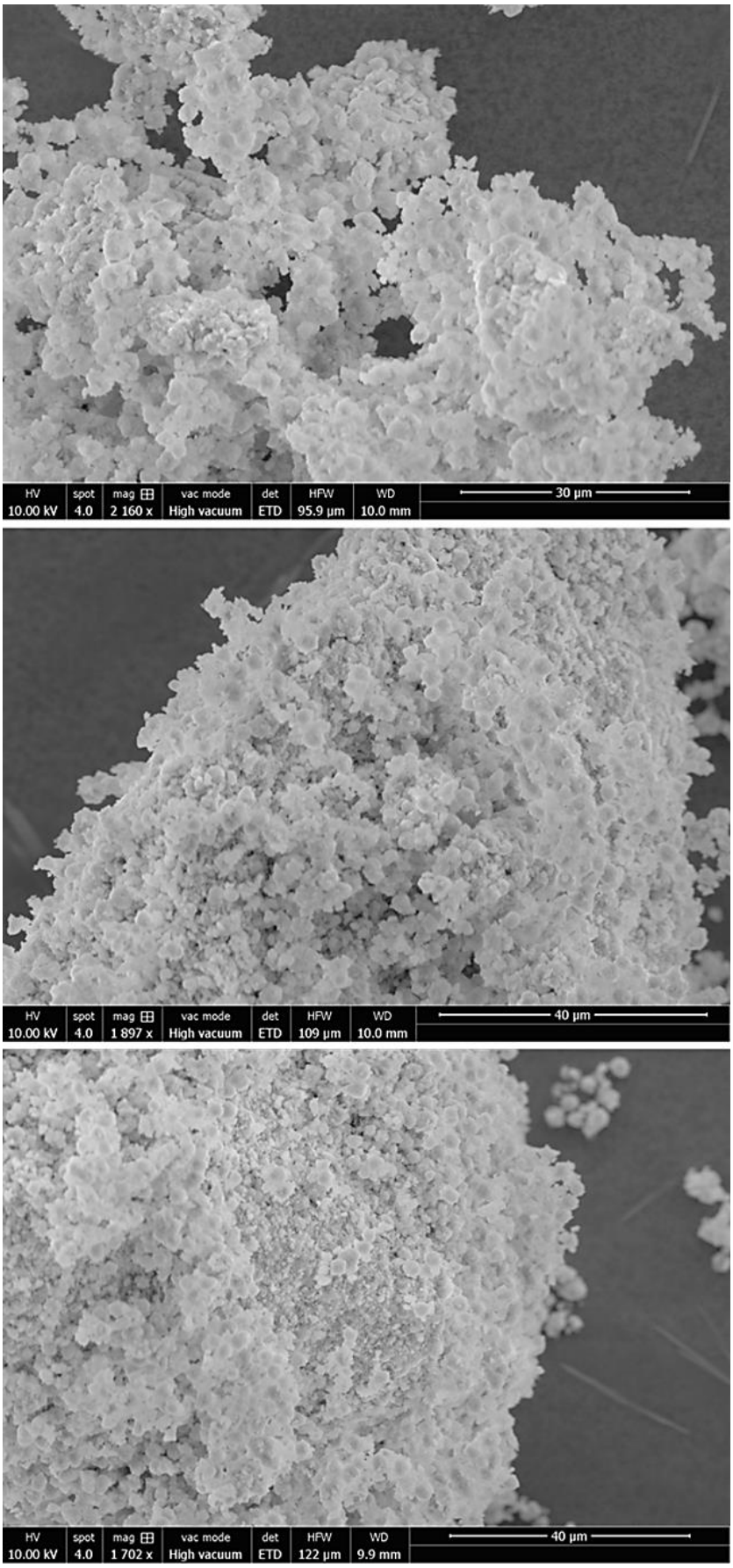


Figure 3.4: SEM micrographs images of Zeolite 13X compacted *at 5* tonnes (equivalent to 370 MPa).

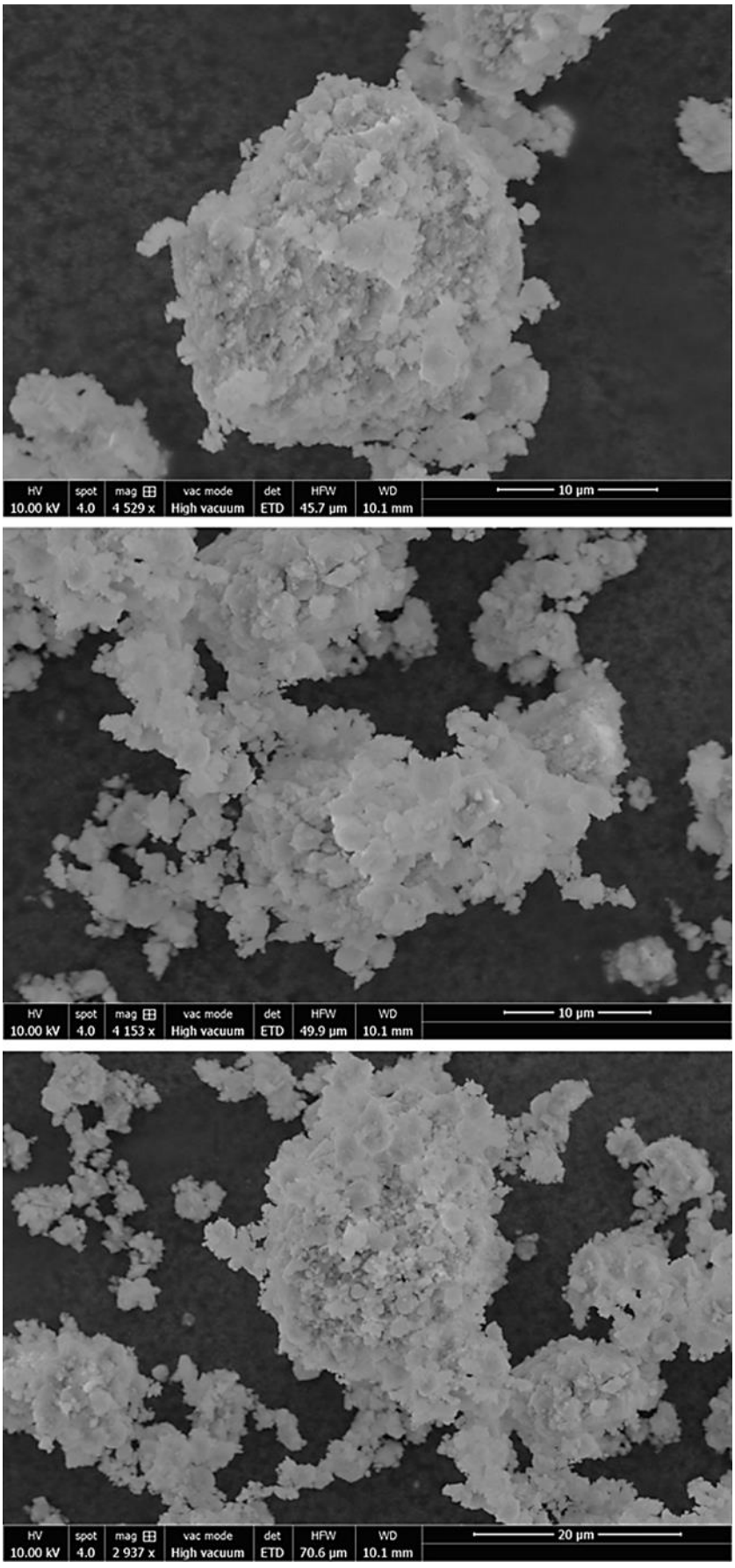


Figure 3.5: SEM micrographs images of Zeolite 13X compacted *at 10* tonnes (equivalent to 740 MPa).

3.6.1.2 Structural Ordering Analysis PXRD

The compaction and change in packing density does not have any significant effect of the structural ordering of the zeolite as shown by XRD patterns (**Figure 3.6**). The XRD patterns of the powder and compacted *at 10 tonnes* (equivalent to 740 MPa) zeolite samples are similar, which confirms the mechanically robust nature of the zeolites.

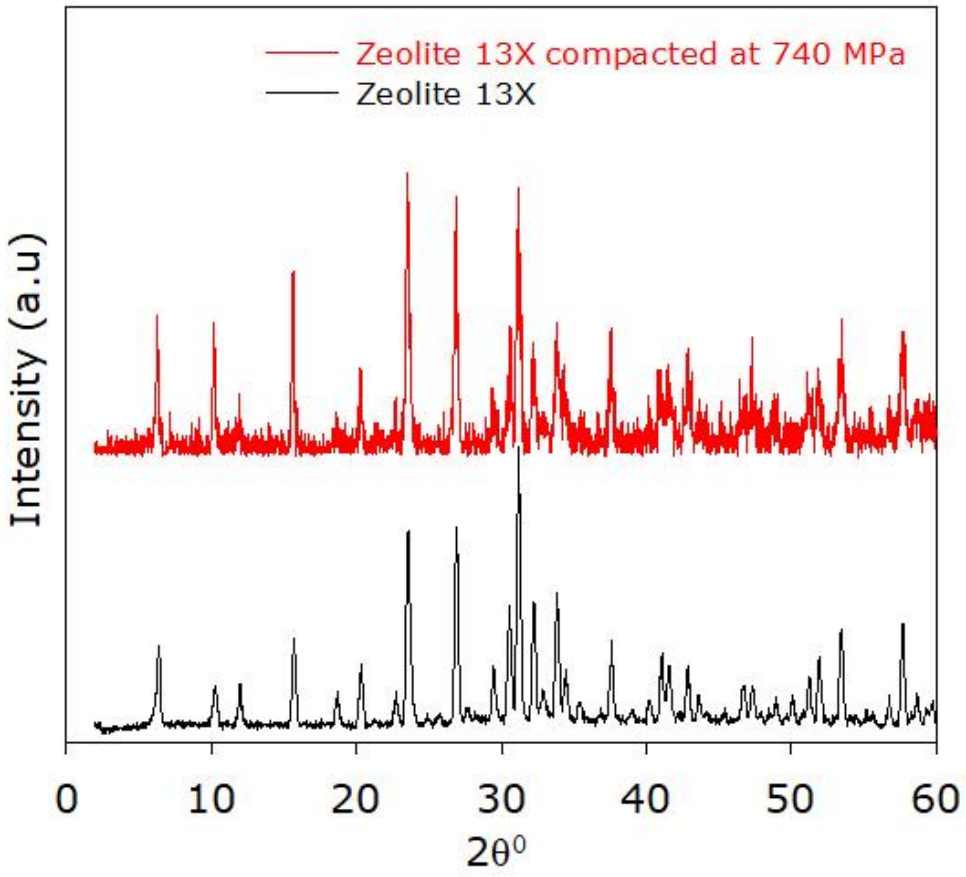


Figure 3.6: Powder XRD patterns of zeolite 13X before and after compaction *at 10 tonnes* (equivalent to 740 MPa). The XRD patterns remain unchanged, which indicates that the structural ordering of the zeolite is preserved after compaction.

3.6.1.3 Textural Properties and Porosity Analysis

The porosity of the zeolites remains largely unchanged after compaction *at 10 tonnes* (equivalent to 740 MPa), according to nitrogen porosity analysis (**Figure 3.7**). The nitrogen sorption isotherms and pore size distribution curves (**Figure 3.7 A** and **Figure 3.7 B**), are similar for powder and compacted zeolites. The textural properties and pore size of the zeolites remain unchanged by the compaction (**Table 3.3**).

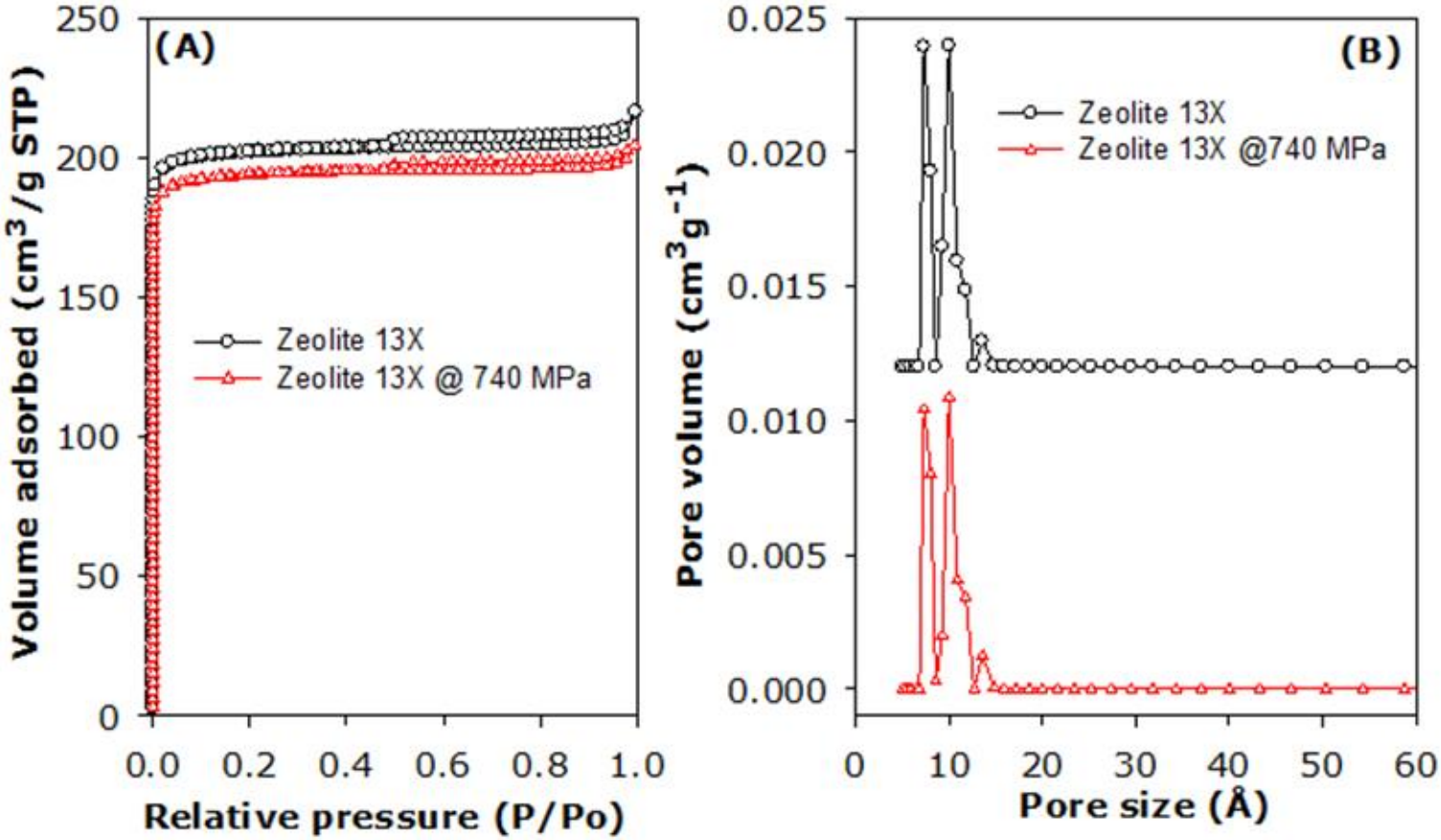


Figure 3.7: (A) Nitrogen sorption isotherms and **(B)** Corresponding pore size distribution (PSD) curves of ***Zeolite 13X*** before (powder) and after compaction *at 10 tonnes* (equivalent to *740 MPa*).

Table 3.3: Textural properties of ***Zeolite 13X*** before (powder) and after compaction at *10 tonnes* (740 MPa).

Sample	Surface area [a] ($m^2\ g^{-1}$)	Pore Volume [b] ($cm^3\ g^{-1}$)	Pore size [c] (Å)
Z13X	717 (705)	0.33 (0.31)	7.5/10
Z13X@*740 MPa* [d]	692 (680)	0.32 (0.30)	7.5/10

[a] The values in the parenthesis refer to micropore surface area
[b] The values in the parenthesis refer to micropore volume.
[c] pore size distribution maxima obtained from NLDFT analysis.
[d] *740 MPa* equivalent to 10 tonnes.

3.6.2 Zeolite Templated Carbons Prepared *via* CVD

It has previously been shown that powder forms of zeolite 13X and zeolite Y may be used as templates for the formation of ZTCs with moderate surface area *via* a chemical vapour deposition route CVD.[55, 56] In the present study powder zeolites were used as control (baseline) experiments.

3.6.2.1 Purity and Thermal Stability Analysis

Thermogravimetric analysis (TGA) was performed to confirm that the compacted zeolite pellets generated purely carbonaceous ZTCs. **Figure 3.8** shows TGA curves of zeolite Y, pelletized zeolite Y/carbon composite and the final pelletized ZTC (CZYP). The air dried zeolite Y shows a mass loss of *ca.* 20 wt% up to 300 ^{o}C due to loss of water, and thereafter remains thermally stable up to 1000 ^{o}C. The zeolite/carbon composite shows a mass loss of *ca.* 30 wt% between 450 ^{o}C and 630 ^{o}C, which is attributable to the combustion of the carbon component.[55, 56] The pelletized CZYP carbon shows one main mass loss event due to carbon burn off, which commences at *ca.* 440 ^{o}C and is complete at 630 ^{o}C. The TGA curve for the CZYP carbon shows that the pelletized ZTC is virtually zeolite free, with a residual mass typically less than 1 wt% at 1000 ^{o}C. Thus, the use of compacted zeolite pellets as template offers no major variation in terms of carbon yield, thermal stability and etching of the zeolite framework.

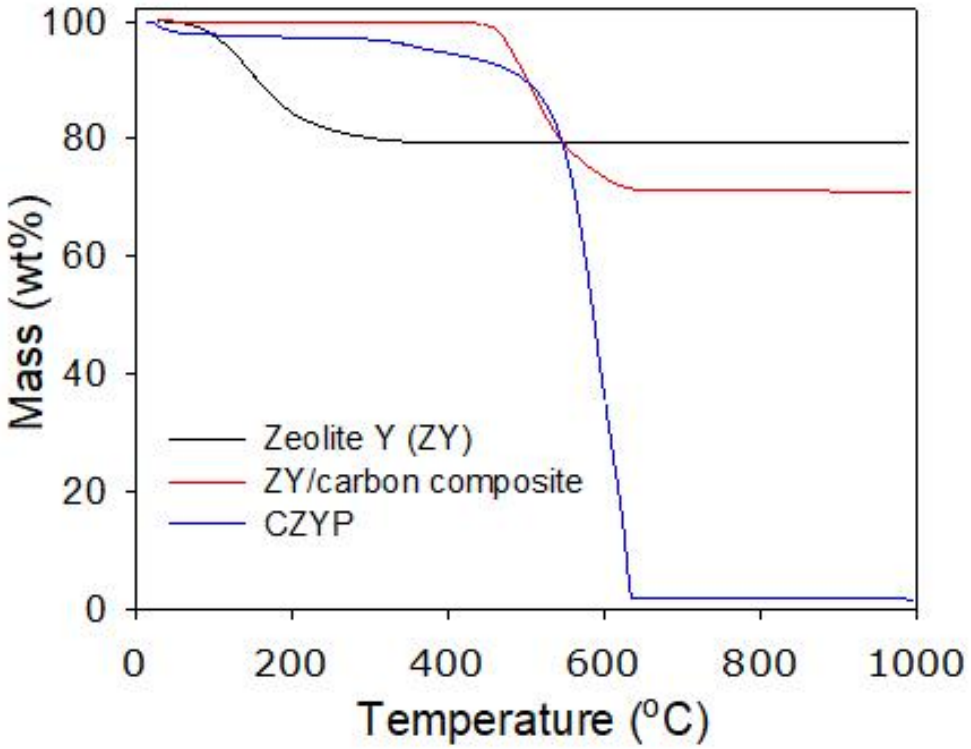


Figure 3.8: Thermogravimetric analysis curves of zeolite Y, zeolite Y/carbon composite and carbon CZYP.

3.6.2.2 Packing Density Assessment

A main motivation of the present work is to increase the packing density of the final ZTCs. The packing density of ZTCs may be increased by direct compaction of the carbons.[54] In the present study, it is the zeolite that is compacted prior to use as a template for the formation of ZTCs. As mentioned before, the packing density of the zeolite templates increased by *ca.* 50% from 0.7 g cm^{-3} to 1.08 g cm^{-3}. The increase in zeolite packing density arises from compaction into smaller volume and the removal of any large interparticle voids. In this work, it has been ascertained that the overall surface area and pore volume of the zeolite remained unaffected by the compaction. It is expected that the use of such compacted zeolites should yield pelletized forms of ZTCs that replicate the lack of large interparticle voids from the zeolite, with the overall effect being an increase in packing density. To retain pellet forms of ZTC, the steps involving washing of the zeolite/carbon composites in acid (HF and HCl) were performed without any agitation. However, in order to allow analysis, the pellet forms of ZTCs that emerged from the compacted zeolite pellets were loosely broken up. It emerged straight away, as shown in **Figure 3.9 A** that the ZTCs derived from compacted zeolites had a significantly higher packing density and were much less fluffy.

Figure 3.9. **B** shows equivalent amounts with respect to mass (i.e., 0.1 g) of CZ13XP and CZ13X. **Figure 3.9 A** indicates that the pelletized CZ13XP sample is less fluffy and more compact, which is confirmed in **Figure 3.9 B** where it occupies about half the volume of the powder CZ13X sample. The packing density values determined for the CVD-derived ZTCs (following a gentle compaction at load of 74 MPa),[54] are given in **Table 3.4**. The packing density of the ZTC derived from zeolite 13X increases from 0.53 g cm^{-3} for powdered zeolite templating (CZ13X) to 0.82 g cm^{-3} for the carbon from the

compacted zeolite template (CZ13XP), which is an increase of *ca.* 55%. A similar increase was observed for the ZTCs derived from zeolite Y, i.e., from 0.55 g cm^{-3} for CZY to 0.88 g cm^{-3} for CZYP, a rise in packing density of *ca.* 60%. It is noteworthy that the packing density of the powdered ZTCs could also be increased by direct compaction *at 370 MPa* to 0.65 g cm^{-3} (C5-CZ13X) and 0.71 g cm^{-3} (C5-CZY). However, these packing density values are still somewhat lower than those of analogous ZTCs derived from compacted zeolite pellets.

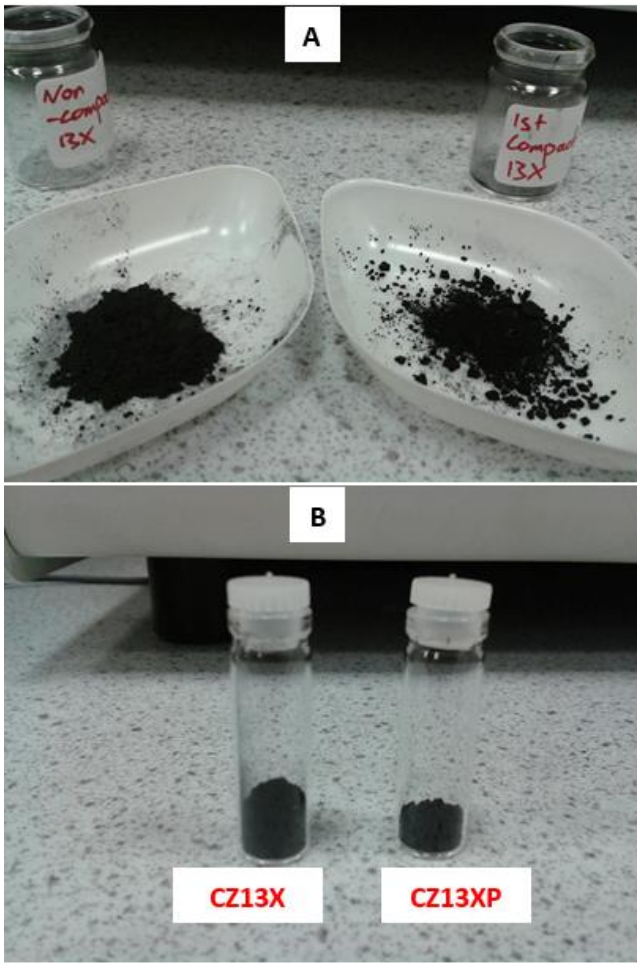


Figure 3.9: Photographic images **(A)** and **(B)** of CVD-derived ZTCs templated by powdered zeolite 13X (CZ13X) and compacted (at *5* tonnes equivalent to 370 MPa) zeolite 13X pellet (CZ13XP). The image in **(A)** show the pelletized CZ13XP sample is less fluffy and more compact than powdered sample (CZ13X), **(B)** show equal (0.1 g) amounts of ZTC and illustrate differences in packing density.

3.6.2.3 Textural Proprieties and Porosity Analysis

Figure 3.10 A and **Figure 3.11 A** shows the nitrogen sorption isotherms of the CVD derived ZTCs templated by powder or compacted pellets forms of zeolite 13X or zeolite Y, respectively. In each case, also shown is the nitrogen sorption isotherm of the equivalent directly compacted ZTC. In all cases, the isotherms are type *I*, as the nitrogen uptake is highest at low relative pressures ($P/P_o < 0.1$), which is typical for carbons that adopt the structural ordering of zeolites.[55, 56] The shape of the isotherm for the pelletized ZTC samples (CZ13XP and CZYP) is identical to that of the powder analogues (CZ13X and CZY) except that the pelletized samples have higher nitrogen sorption. A higher nitrogen sorption hints at enhancement of porosity in the pelletized ZTCs. Such an enhancement is particularly clear for CZYP compared to CZY (**Figure 3.11 A**). It is also clear, based on the amount of nitrogen sorbed that in both cases, direct compaction (samples C5-CZ13X and C5-CZY) leads to a decrease in porosity. This would suggest an advantage of the use of compacted zeolite pellets as templates over direct compaction of already prepared ZTCs with respect to retention of high porosity.

The textural parameters of the CVD-derived ZTCs are summarised in **Table 3.4**. It is noteworthy that despite their higher packing density, the surface area of pelletized ZTCs templated by compacted zeolite pellets is still comparable or higher than that of analogous conventional powder samples. The surface area of CZ13X is 1927 $m^2\ g^{-1}$ compared to 2038 $m^2\ g^{-1}$ for the pelletized CZ13XP sample, while for zeolite Y templated carbons the pelletized CZYP sample has a significantly higher surface area (1897 $m^2\ g^{-1}$) compared to 1654 $m^2\ g^{-1}$ for the analogous powder ZTC (CZY). The micropore surface area of the pelletized ZTCs is between 25% and 40% higher than that of powder samples. Furthermore, both the total and

micropore surface area of pelletized ZTCs is much higher than that of directly compacted C5-ZTC samples. Similar trends in pore volume are observed with the pelletized ZTCs exhibiting higher total and micropore volume (**Table 3.4**). The proportion of micropore surface area increased from *ca.* 60% for powder samples to 75–80% for the pelletized ZTCs. The improvement in both the packing density and porosity for the pelletized ZTCs means that the surface area per unit volume increased by *ca.* 60% from between 1000 m^2 cm^{-3} and 1100 m^2 cm^{-3} for the powder and directly compacted ZTCs to *ca.* 1670 m^2 cm^{-3} for pelletized samples (**Table 3.4**).

The PSD curves in **Figure 3.10 B** and **Figure 3.11 B** and the wide pore size curves in **Figure 3.12** and **Figure 3.13**, and pore size data in **Table 3.4** indicate that use of a compacted zeolite pellets as templates has little effect on the pore size.

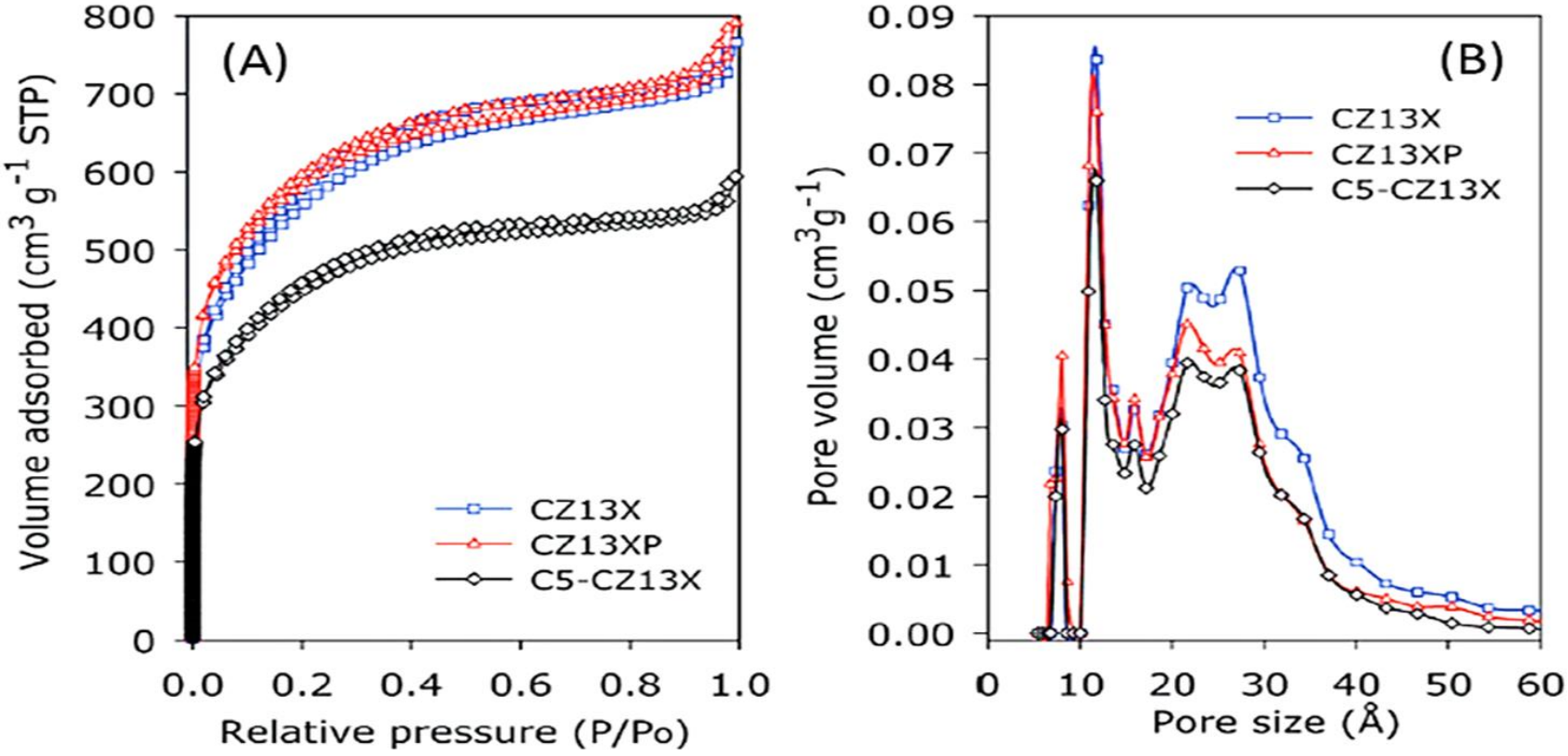


Figure 3.10: (A) Nitrogen sorption isotherms and **(B)** Corresponding pore size distribution (PSD) curves of zeolite templated carbons prepared *via* a CVD route using powder (C13X) or compacted pellets (C13XP) of ***Zeolite 13X*** as hard template. Sample C5-CZ13X is a directly compacted (at 370 MPa) form of CZ13X. The nitrogen sorption isotherm and PSD curve of the equivalent directly (i.e., post-templating) compacted ZTC (C5-CZ13X) shown for comparison purposes.

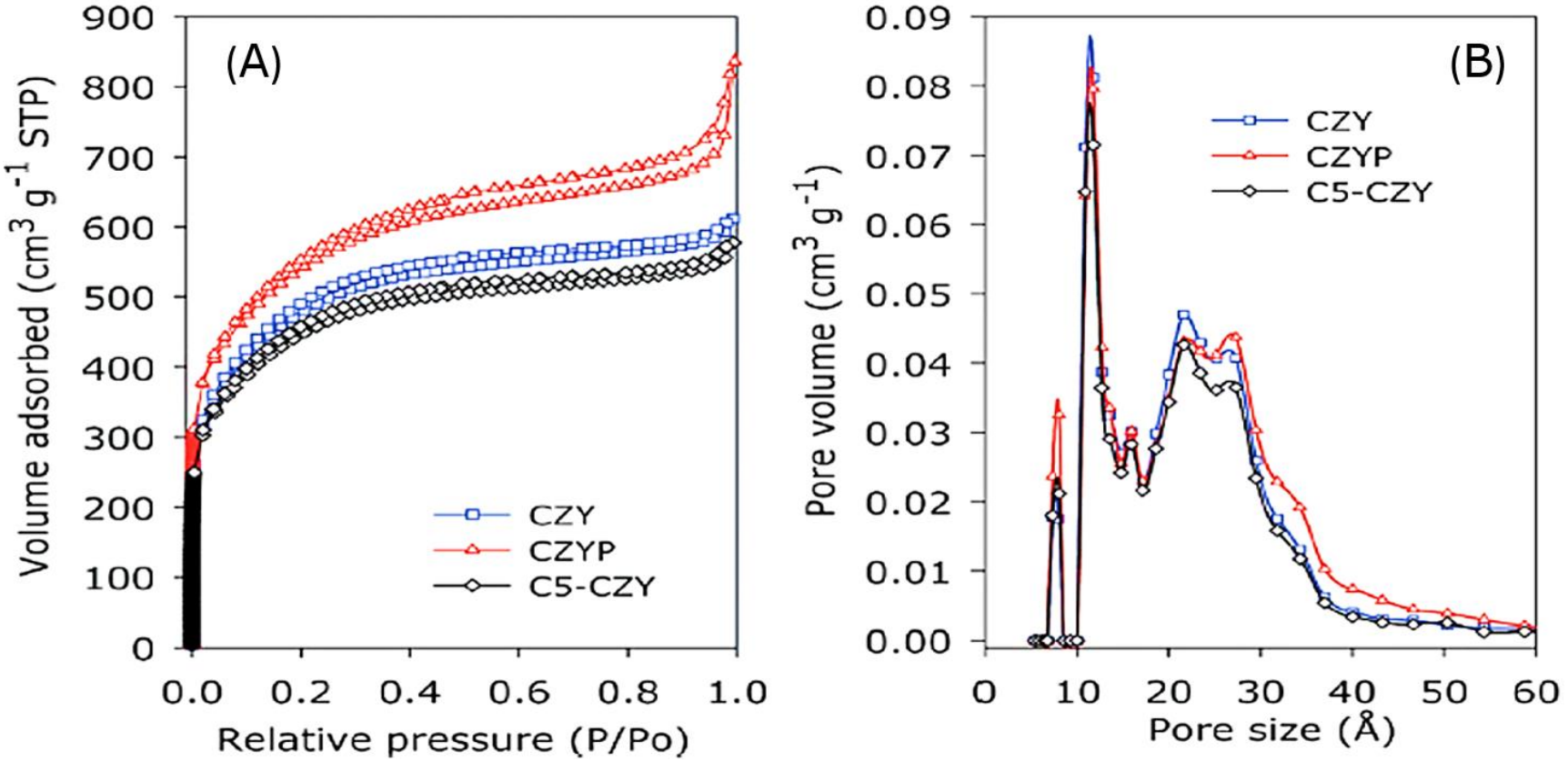


Figure 3.11: **(A)** Nitrogen sorption isotherms and **(B)** Corresponding pore size distribution (PSD) curves of CVD-ZTC templated by powder or compacted pellets of ***Zeolite Y***. Sample C5-CZY is a directly compacted (at 370 MPa) from of CZY. The nitrogen sorption isotherm and PSD curve of the equivalent directly (i.e., post-templating) compacted ZTC (C5-CZY) shown for comparison purposes.

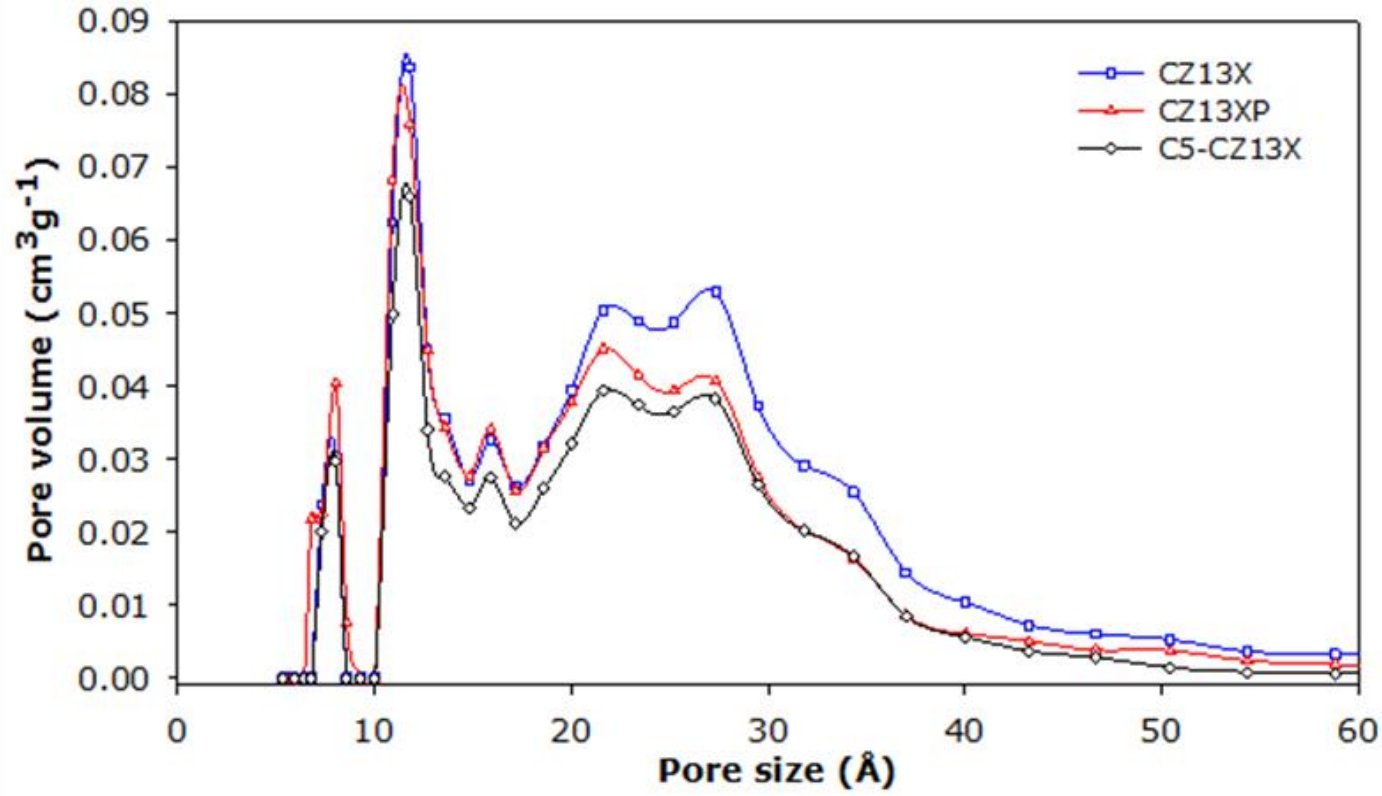


Figure 3.12: Wider pore size distribution curves of zeolite templated carbons prepared *via* a CVD route using powder (C13X) or compacted pellets (C13XP) of ***Zeolite 13X*** as hard template. Sample C5-CZ13X is a directly compacted (*at 370 MPa*) form

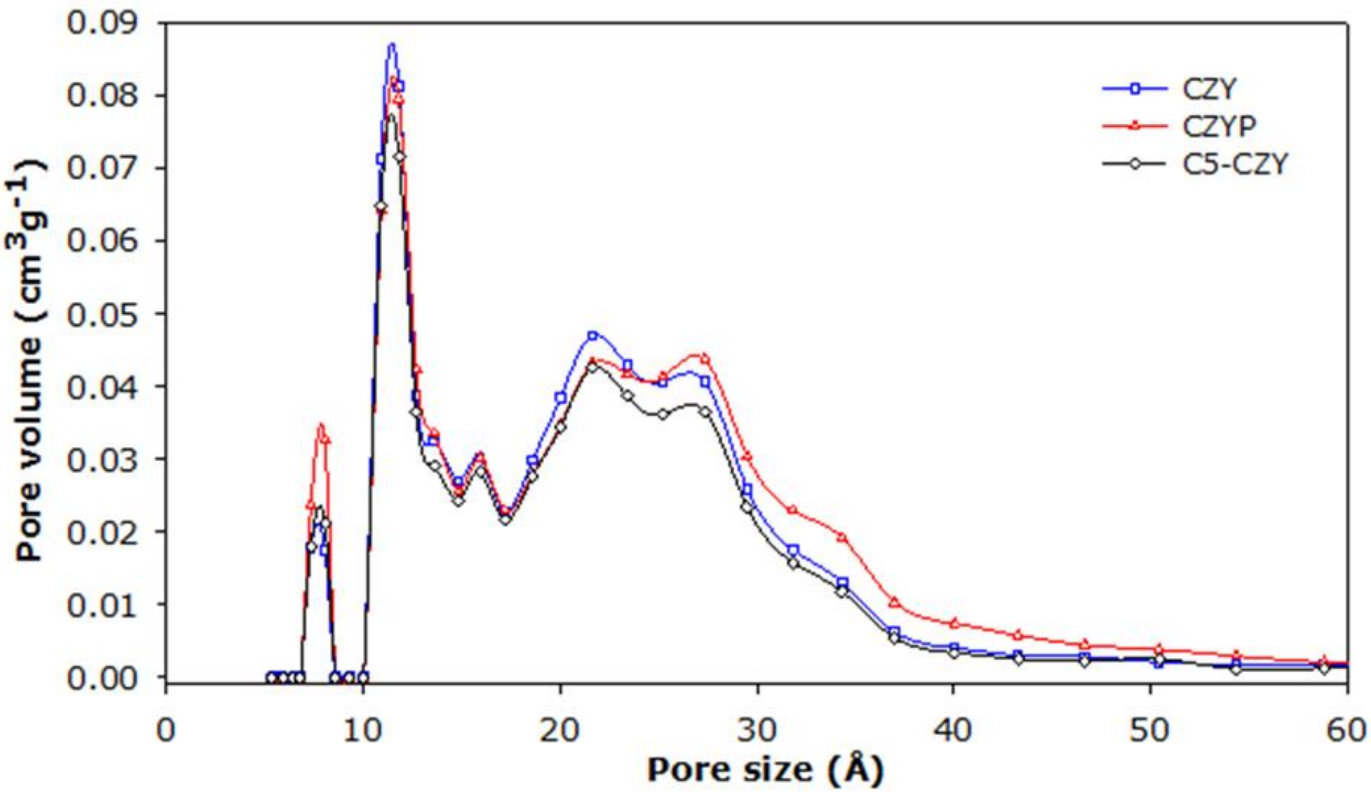


Figure 3.13: Wider pore size distribution curves of zeolite templated carbons prepared *via* a CVD route using powder (CZY) or compacted pellets (CZYP) of ***Zeolite Y*** as hard template. Sample C5-CZY is a directly compacted (*at 370 MPa)* form of CZY.

3.6.2.4 CO_2 Uptake Measurements

3.6.2.4.1 CO_2 Uptake at 25 ^oC

The CO_2 uptake properties of the CVD-derived carbons explored in an effort to illustrate the benefits that may arise from the higher packing density of the pelletized ZTCs. The CO_2 uptake was determined *at 25 ^oC* and the pressure range 0–20 bar. **Figure 3.14 A** and **Figure 3.14 B** compares the CO_2 uptake isotherms of ZTCs prepared from compacted zeolites (CZ13XP and CZYP) to analogous samples that were directly compacted (C5-CZ13X and C5-CZY). We note that direct compaction did not affect the gravimetric CO_2 storage capacity under our measurement conditions. The CO_2 uptake at 1 bar and 20 bar summarized in **Table 3.4**.

The CO_2 uptake of the pelletized ZTCP carbons is at all pressures higher than that of equivalent powder samples whether compacted or not. At 1 bar, the CO_2 uptake of sample CZ13XP is 2.8 mmol g^{-1} compared to 1.9 mmol g^{-1} for CZ13X and C5-CZ13X, which represents a nearly 50% enhancement in storage capacity for the pelletized ZTCP sample. For the zeolite Y templated carbons the CO_2 uptake of the ZTCP sample (CZYP) is 56% higher at 2.6 mmol g^{-1} compared to 1.6 mmol g^{-1} for the powdered (CZY) and directly compacted (C5-CZY) samples. A similar trend is observed at 20 bar where the CO_2 uptake of the pelletized ZTCP samples is between 15% and 20% higher than that of analogous powdered or directly compacted samples. We ascribe the enhancement in CO_2 uptake for the pelletized ZTC samples at 1 bar to their higher levels of micropore surface area. For example, the micropore surface area of pelletized CZ13XP is 1601 m^2 g^{-1} compared to 1140 m^2 g^{-1} for the powdered CZ13X sample, or 1197 m^2 g^{-1} for the compacted C5-CZ13X sample.

Additionally, the micropore surface area as a proportion of the total surface area is 79% for pelletized CZ13XP compared to 59% for the powdered CZ13X sample. Likewise, for pelletized CZYP, the micropore surface area is higher at 1413 m^2 g^{-1} compared to 1143 m^2 g^{-1} for the powdered CZY sample, or 1275 m^2 g^{-1} for the analogous compacted C5-CZY sample. Additionally, the micropore surface area as a proportion of the total surface area is 75% for pelletized CZYP compared to 69% for the powdered CZY sample. This finding is consistent with the fact that the CO_2 uptake at low pressure (1 bar) is very dependent on the pore size of the carbons.[33-39] On the other hand, the greater CO_2 uptake of the pelletized samples at 20 bar may be ascribed to their higher overall surface area and pore volume. It is known that the CO_2 uptake of porous carbons at high pressure (such as 20 bar) is determined by the total surface area.[33-39]

Thus, purely on the basis of gravimetric CO_2 uptake, the porosity enhancements derived from templating with compacted zeolite pellets are evident. However, of greater significance is the improvement in volumetric CO_2 uptake as shown in **Table 3.4**, **Figure 3.15 A** and **Figure 3.15 B**, arising from the higher packing density of the pelletized ZTCs. At 1 bar, the volumetric CO_2 uptake of sample CZ13XP is 101 g L^{-1}, which is 130% higher than 44 g L^{-1} for the powder sample CZ13X, and 87% higher than 54 g L^{-1} for the directly compacted C5-CZ13X carbon (**Figure 3.15 A**). For the ZTCs templated by zeolite Y (**Figure 3.15 B**), the volumetric CO_2 uptake of the pelletized ZTCP sample (CZYP) is 97 g L^{-1}, which is 137% higher than that of CZY (41 g L^{-1}), and nearly double that of the directly compacted C5-CZY sample (50 g L^{-1}). The low pressure volumetric CO_2 uptake enhancements of between 85% and 140% arise from the higher micropore surface area of the pelletized ZTCP samples and their greater packing density. A similar trend is observed at 20 bar although the enhancements in volumetric CO_2 uptake are

lower at between 40% and 85%. It is noteworthy that a volumetric uptake of up to 531 g L^{-1} is achieved for sample CZYP at 20 bar and 25 ^{o}C (**Figure 3.15 B**).

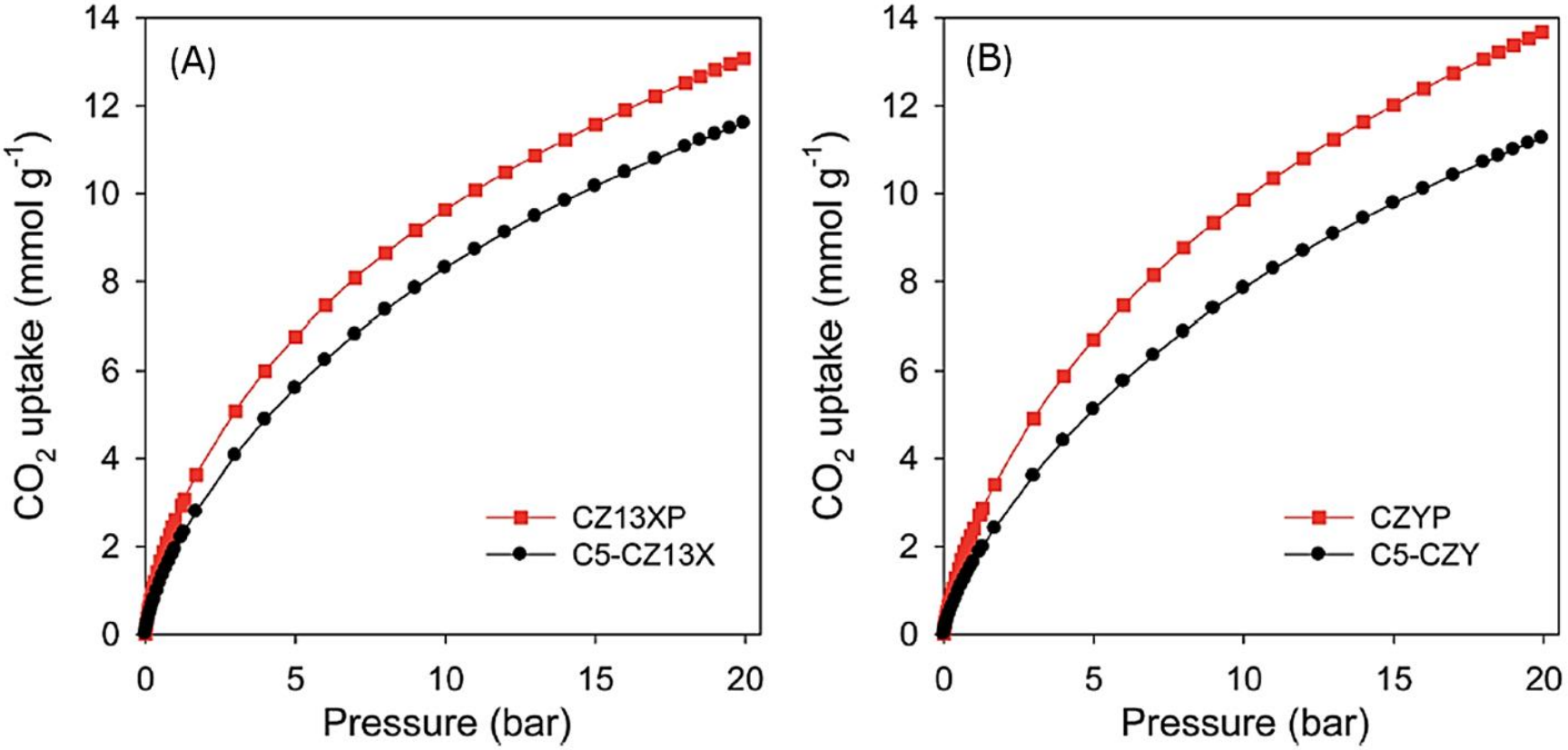


Figure 3.14: CO_2 uptake isotherms ***at 25 °C*** and 0–20 bar for variously prepared zeolite templated carbons; CZ13XP and CZYP were templated by compacted zeolite pellets, while C5-CZ13X and C5-CZY are directly compacted forms of conventionally synthesised powder samples. **(A)** For the ZTCs templated by ***Zeolite13X*** and **(B)** For the ZTCs templated by ***Zeolite Y.***

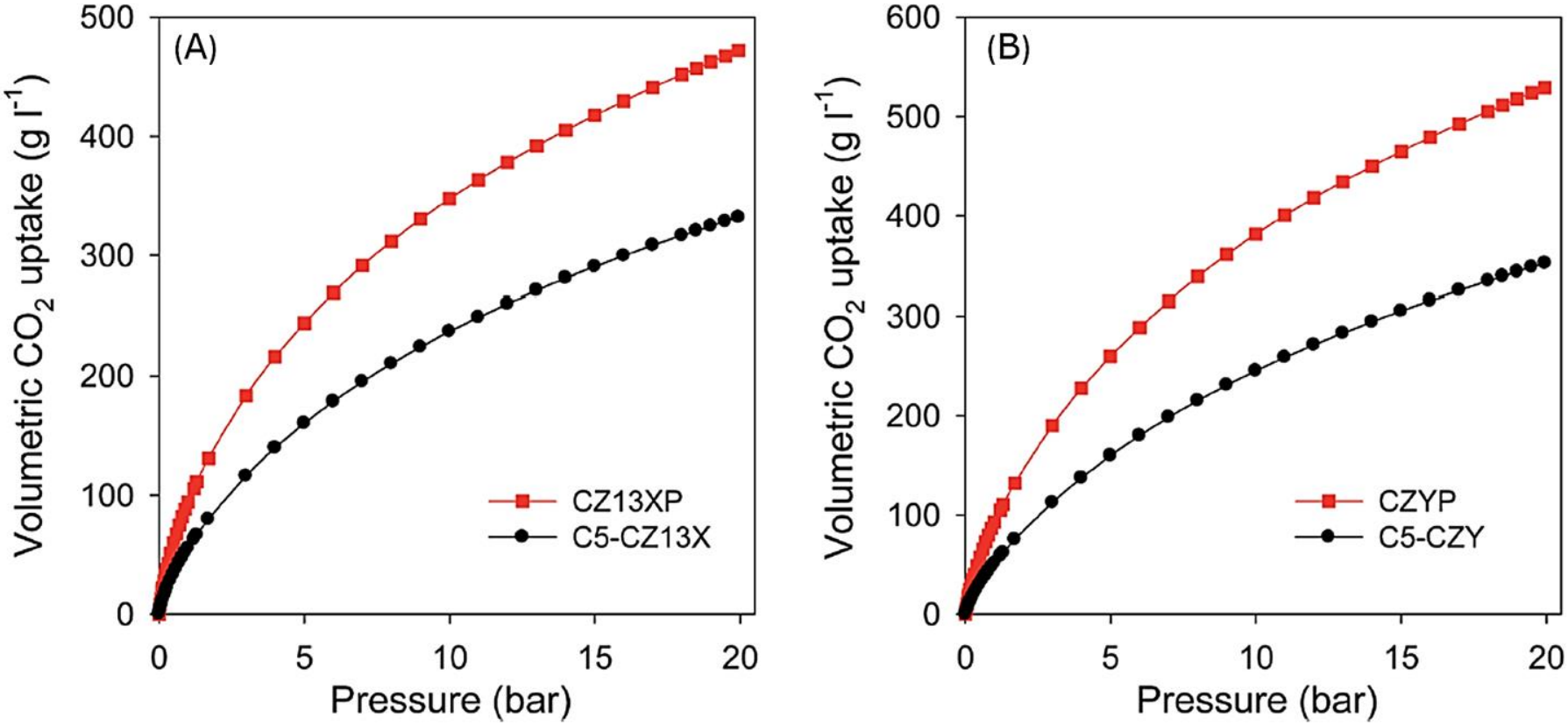


Figure 3.15: Volumetric CO_2 uptake ***at 25 °C*** and 0–20 bar for various zeolite templated carbons; CZ13XP and CZYP were templated by compacted zeolite pellets, while C5-CZ13X and C5-CZY are directly compacted forms of conventionally synthesised powder samples. **(A)** For the ZTCs templated by ***Zeolite13X*** and **(B)** For the ZTCs templated by ***Zeolite Y***.

Table 3.4: Packing density, textural properties and CO_2 uptake of CVD-derived zeolite templated carbons templated by powdered or compacted pellets of ***Zeolite 13X*** or ***Zeolite Y***.

Sample	Packing density ($g\ cm^{-3}$)	Surface area [a] ($m^2\ g^{-1}$)	Pore volume [b] ($cm^3\ g^{-1}$)	Pore size [c] (Å)	V/S [d] ($m^2\ cm^{-3}$)	CO_2 uptake [e, f] ($mmol\ g^{-1}$)	
						1 bar	20 bar
CZ13X	0.53	1927 (1140)	1.19 (0.53)	7.5/12/24	1021	1.9 (44)	11.6 (271)
CZ13XP	0.82	2038 (1601)	1.22 (0.75)	7.5/12/24	1671	2.8 (101)	13.1 (473)
C5-CZ13X	0.65	1578 (1197)	0.92 (0.56)	7.5/12/24	1026	1.9 (54)	11.6 (332)
CZY	0.58	1654 (1143)	0.95 (0.53)	8/11.5/24	959	1.6 (41)	11.2 (286)
CZYP	0.88	1897 (1413)	1.29 (0.66)	8/11.5/24	1670	2.5 (97)	13.7 (531)
C5-CZY	0.71	1575 (1275)	0.89 (0.60)	8/11.5/24	1118	1.6 (50)	11.3 (353)

[a] The values in the parenthesis refer to micropore surface area.
[b] The values in the parenthesis refer to micropore volume.
[c] Pore size distribution maxima obtained from NLDFT analysis.
[d] Surface area per unit volume.
[e] CO_2 uptake *at 25 °C* and various pressures (i.e., 1 bar and 20 bar).
[f] The values in parenthesis are volumetric CO_2 uptake in $g\ L^{-1}$.

3.6.3 Zeolite Templated Carbons Prepared *via* Combination of Liquid Impregnation (LI) and CVD

Zeolite templated carbons with high surface area may be prepared *via* a synthesis route that combines liquid impregnation (LI) of a carbon precursor and CVD.[18, 23, 30, 31, 54] In order to fully explore our 'templating under pressure route' we extended the use of compacted zeolite pellets as templates to the synthesis of ZTCs *via* both LI and CVD.

3.6.3.1 Purity and Thermal Stability Analysis

Firstly, thermogravimetric analysis performed to confirm that fully carbonaceous ZTC carbons were generated from both powder (sample CZ13XFAET) and compacted (CZ13XFAETP) zeolites (**Figure 3.16**).

According to thermogravimetric analysis (**Figure 3.16**) both the pelletized (CZ13XFAETP) and powder (CZ13XFAET) ZTCs are very dry and show no mass loss below 300 ^{o}C. At higher temperature (400 ^{o}C – 600 ^{o}C), both ZTCs show a sharp mass loss due to carbon burn-off. The sharp mass loss due to carbon burn off suggests that the templated carbons are mainly one phase materials, which is an indication that the carbonaceous matter of the ZTCs is formed within the zeolite pore channels rather than both within the pores and outside as the latter carbon would be graphitic and thus have a higher burn-off temperature. The ZTCs show virtually no residual mass after 800 ^{o}C, confirming that they are zeolite free. The use of compacted zeolite 13X pellets as template for the LI + CVD nanocasting route does not appear to have any effect on the thermal properties of the ZTCs.

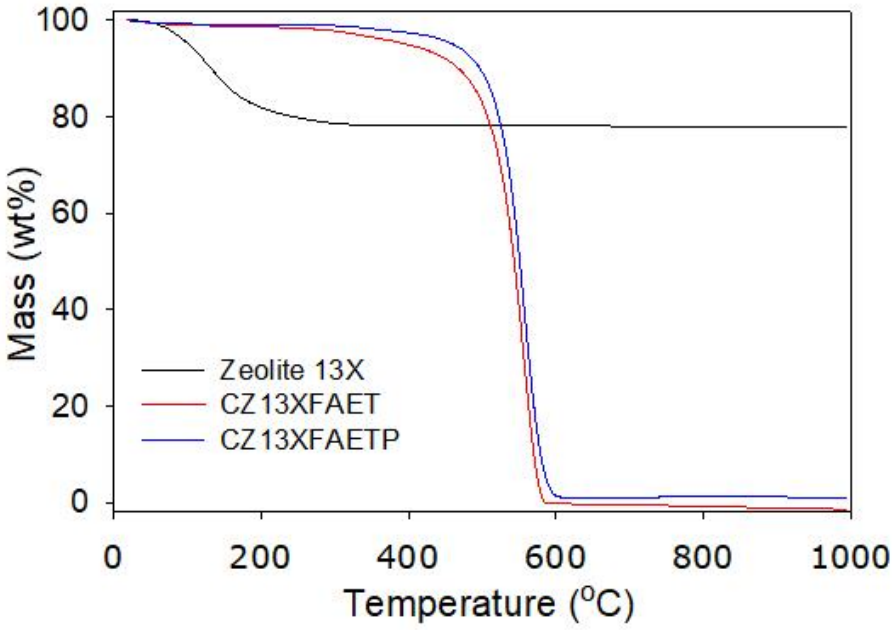


Figure 3.16: Thermogravimetric analysis (TGA) curves of zeolite 13X, and zeolite templated carbons prepared *via* a route that combines liquid impregnation (LI) and CVD using powder (CZ13XFAET) or compacted pellets (CZ13XFAETP) of Zeolite 13X as hard template. The TGA was performed under flowing air conditions.

3.6.3.2 Structural Ordering Analysis PXRD

The nature of carbon was confirmed by powder XRD patterns shown in **Figure 3.17**. The XRD pattern of the pelletized CZ13XFAETP carbon exhibits a sharp peak at 2θ= 7°, which is similar to that present in zeolite 13X (**Figure 3.17**). The peak suggest a d-spacing of *ca.* 1.4 nm, which is comparable to that of zeolite 13X, and indicates microporous structural ordering replicated from the zeolite template.[18, 23, 30, 31, 54] The XRD pattern also shows very broad features at 2θ= 25° and 44°, which, if they were sharp would be (002) and (101) diffractions from graphitic carbon. The broad nature of these features confirms that the carbon is amorphous in nature. This finding is consistent with the carbon being formed (templated) within the zeolite pore channels; given the narrow pores of zeolite 13X, it is impossible to form stacking structures within the pores and therefore the expectation is that the resultant carbon will comprise a single graphene sheet without any stacking and are thus be largely non-graphitic.[57, 58]

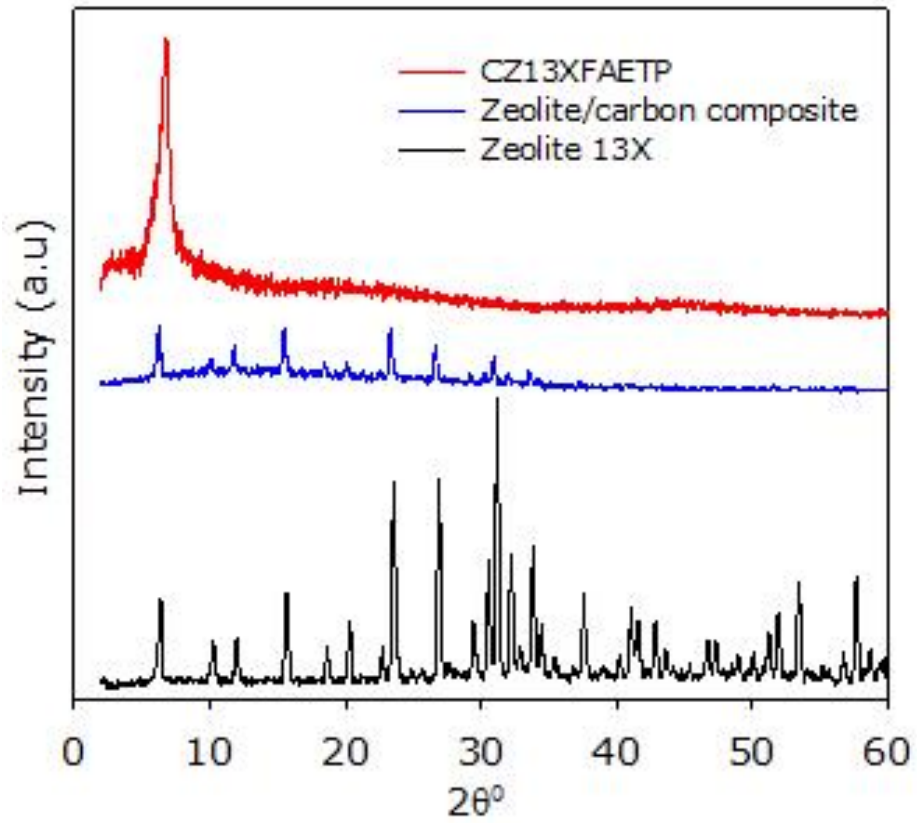


Figure 3.17: Powder XRD patterns of zeolite 13X, zeolite 13X/carbon composite and the final CZ13XFAETP carbon.

3.6.3.3 Raman Spectra Analysis

PXRD analysis view is consistent with the Raman spectra of the templated carbons (**Figure 3.18**). The carbons exhibit bands at *ca.* 1344 cm^{-1} and 1595 cm^{-1} that are, respectively, the so-called D-peak (disordered carbon) and the G-peak (graphitic domains). The ratio of peak area of the D-peak to G-peak (ID/IG), based on the two-band fitting model is 0.83 for the conventional powdered CZ13XFAET sample and 0.87 for the pelletized CZ13XFAETP carbon.

The ID/IG ratio is in a range expected for non-graphitic carbon and also confirms that pelletization does not affect the level of graphitisation in the templated carbons. The absence of graphitisation means it is instead likely that single nanographene-like sheets are formed in the zeolite 13X pores, curved with a bucky bowl resemblance to replicate the inner-cavities of the spherical pores of the zeolite framework.[57] The presence of sharp peaks in the pattern of the zeolite/carbon composite (**Figure 3.17**) is evidence that the zeolite framework is not destroyed and its structural ordering is not altered during the templating process despite a priori compaction of the zeolite *at 740 MPa*. The filling of the carbon into the zeolite pores reduces phase contrast scattering resulting in some zeolite peaks being lost or reduced in intensity in the XRD pattern of the composite.

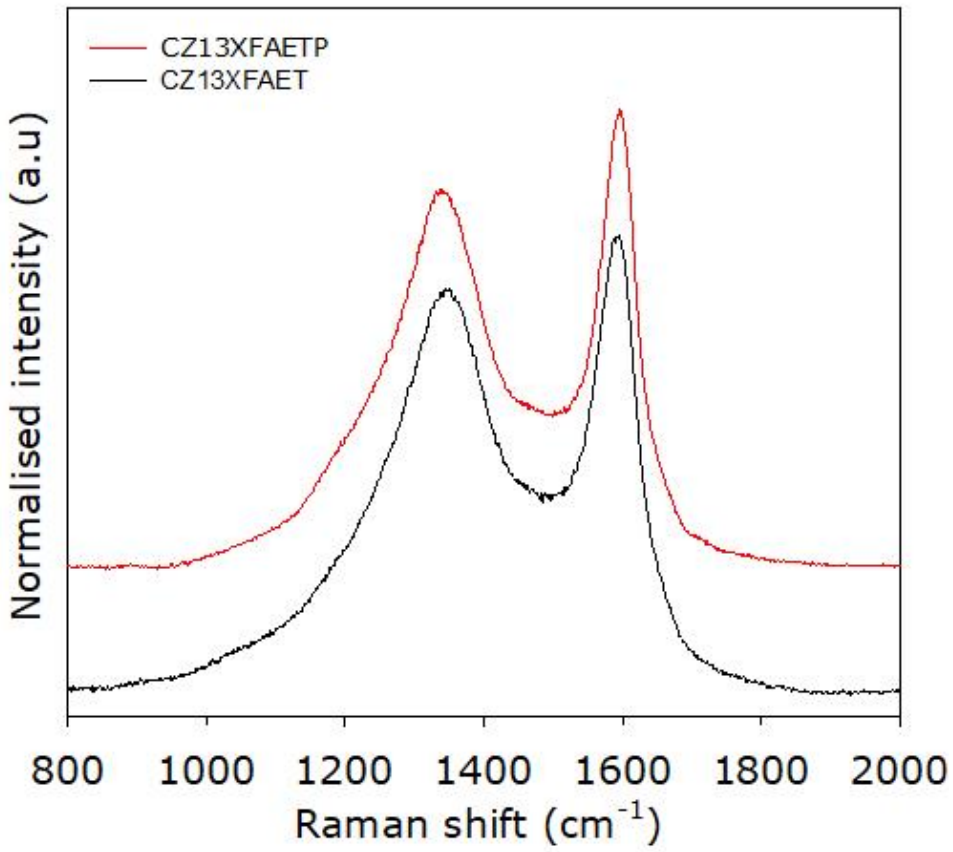


Figure 3.18: Raman spectra of zeolite templated carbons prepared *via* a route that combines liquid impregnation and CVD using powder (CZ13XFAET) or compacted pellets (CZ13XFAETP) of ***Zeolite 13X*** as hard template.

3.6.3.4 Morphology and Surface Analysis

The replication process was explored by observing SEM micrographs images of the powder (CZ13XFAET) and pelletized (CZ13XFAETP) samples. In both cases (**Figure 3.19**), the morphology of the templated carbons is similar to that of the zeolite particles shown in **Figure 3.3** and **Figure 3.4**. The morphology of the zeolite 13X template, whether in powder or pellet form, was evidently replicated in the carbon materials, which is necessary for a templating process wherein the carbon precursor must be transformed into a carbon framework within the zeolite pore channels. It is also clear that the individual particle size of the carbons is similar to that of the zeolite, an observation that precludes excessive deposition of carbon on the external surface of zeolites. It is noteworthy that the aggregated particles of the compacted zeolite (**Figure 3.4**) are replicated in the pelletized CZ13XFAETP sample (**Figure 3.19** and **Figure 3.20**). This is consistent with the increase in packing density observed not only for the compacted zeolite 13X but also the pelletized zeolite templated carbon.

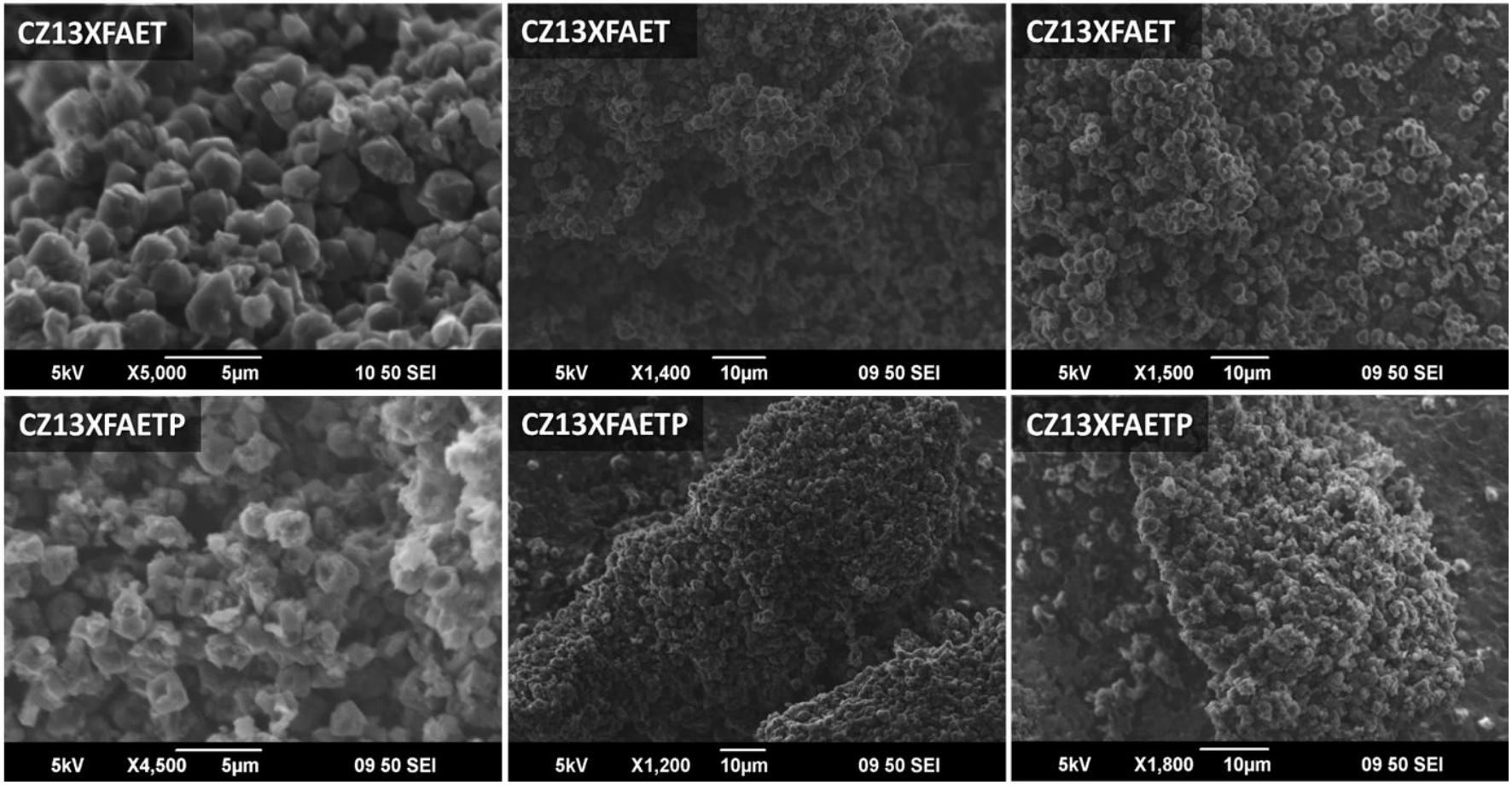


Figure 3.19: Representative SEM micrographs images of zeolite templated carbons templated by powder (CZ13XFAET) or compacted pellets (CZ13XFAETP) of ***Zeolite 13X.***

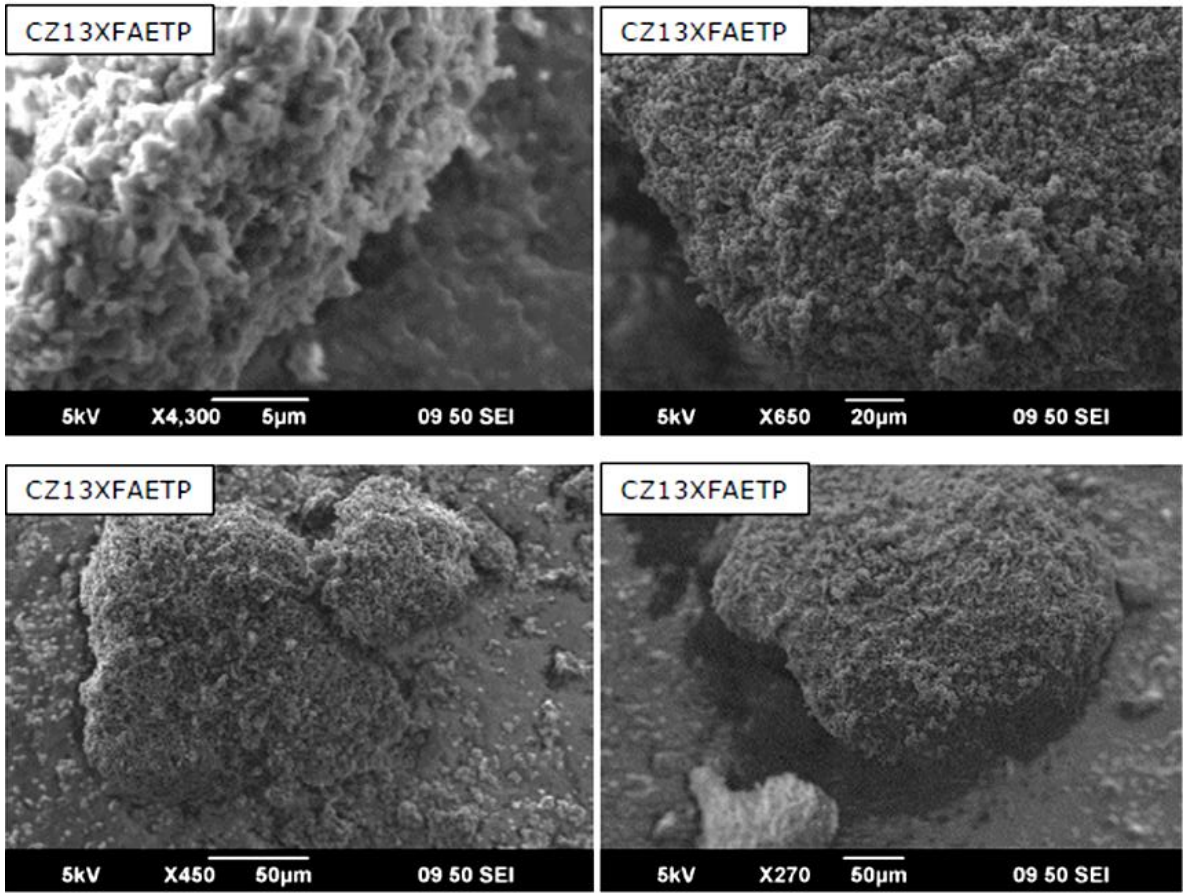


Figure 3.20: SEM micrographs images of zeolite templated carbons templated by compacted pellets (CZ13XFAETP) of ***Zeolite 13X***.

3.6.3.5 Structural Ordering Analysis Using TEM

TEM analysis used to confirm that zeolite structural ordering was replicated in the templated carbons as shown by the TEM micrographs images in **Figure 3.21**. A high level of structural ordering is observed for both the powder (CZ13XFAET) and pelletized (CZ13XFAETP) ZTCs. The TEM micrographs images indicate a pore channel size of 10–15 Å, which is in agreement with porosity studies discussed in textural properties and porosity analysis section.

The TEM micrographs images also show that there is a minor amount of graphitic/turbostratic carbon deposited as thin layers on the surface of the carbon particles but that the bulk of the carbons are amorphous as per their XRD patterns (**Figure 3.17**). Pelletization does not, therefore, have any significant effects on both the morphology and structural ordering of the ZTCs.

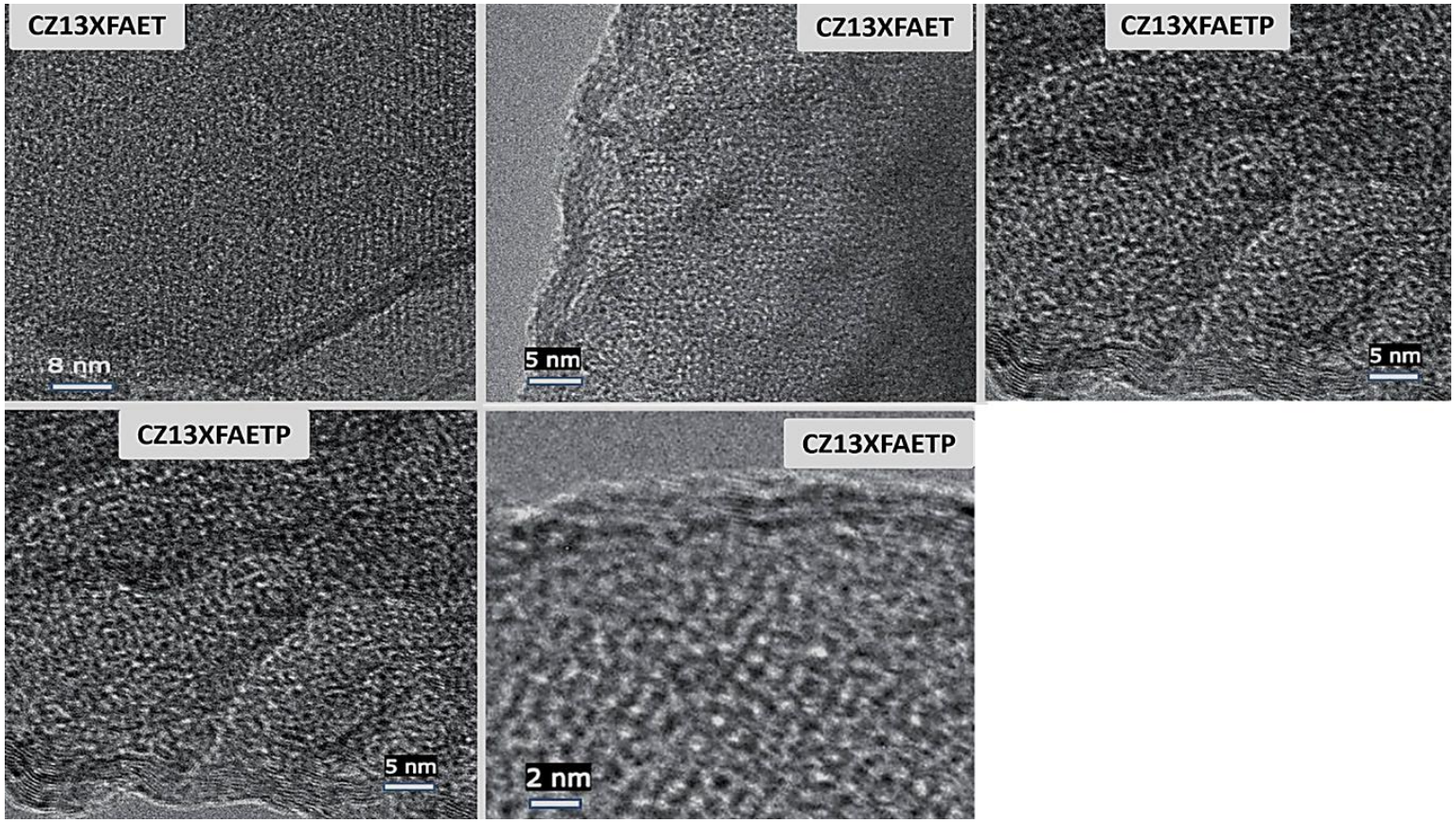


Figure 3.21: Representative TEM micrographs images of zeolite templated carbons templated by powder (CZ13XFAET) or compacted pellets (CZ13XFAETP) of ***Zeolite 13X***.

3.6.3.6 Textural Properties and Porosity Analysis

The nitrogen sorption isotherms for the pelletized and powder ZTCs are shown in **Figure 3.22 A**. Both sorption isotherms are mainly type *I*, with a high nitrogen uptake in the low relative pressure ($P/P_o \leq 0.1$) region. It is however clear that the pelletized sample has higher nitrogen sorption due to enhanced porosity. The textural properties of the ZTCs are summarized in **Table 3.5**. The powder (CZ13XFAET) ZTC has total surface area of 2702 m^2 g^{-1} and micropore area of 2342 m^2 g^{-1}, which is typical of well-ordered zeolite templated carbons.[18, 23, 30, 31, 54] The pelletized sample (CZ13XFAETP), on the other hand, has total surface area of 3021 m^2 g^{-1} and micropore area of 2448 m^2 g^{-1}. Thus compaction of the zeolite prior to use as template engenders a 12% increase in total surface area, while the micropore surface area shows a more modest rise of 5%.

PSD curves of the two high surface area ZTCs (the powder (CZ13XFAET), and the pelletized sample (CZ13XFAETP) are presented in **Figure 3.22 B**, and the pore size maxima values are summarised in **Table 3.5**. The average pore width of the ZTCs is 12 Å, along with a minor distribution of smaller pores at 7.5 Å. The pore channels are smaller and more sharply distributed than those of the CVD-derived ZTCs (**Table 3.4**), which suggest a high level of zeolite-like structural ordering.[18, 23, 30, 31, 59, 60] Compaction of the zeolite prior to use as a template, therefore, has no effect on the PSD, similar to what is observed for CVD-derived ZTCs as discussed above. The high surface area and pore volume of the pelletized CZ13XFAETP sample is very attractive given that it has a packing density of 0.69 compared to 0.44 g cm^{-3} for the conventionally templated CZ13XFAET sample, which is an increase in packing density of *ca.* 57%. This means that the surface area per unit volume

rises by 75% from 1189 m^2 cm^{-3} for powdered CZ13XFAET to 2085 m^2 cm^{-3} for the pelletized CZ13XFAETP sample.

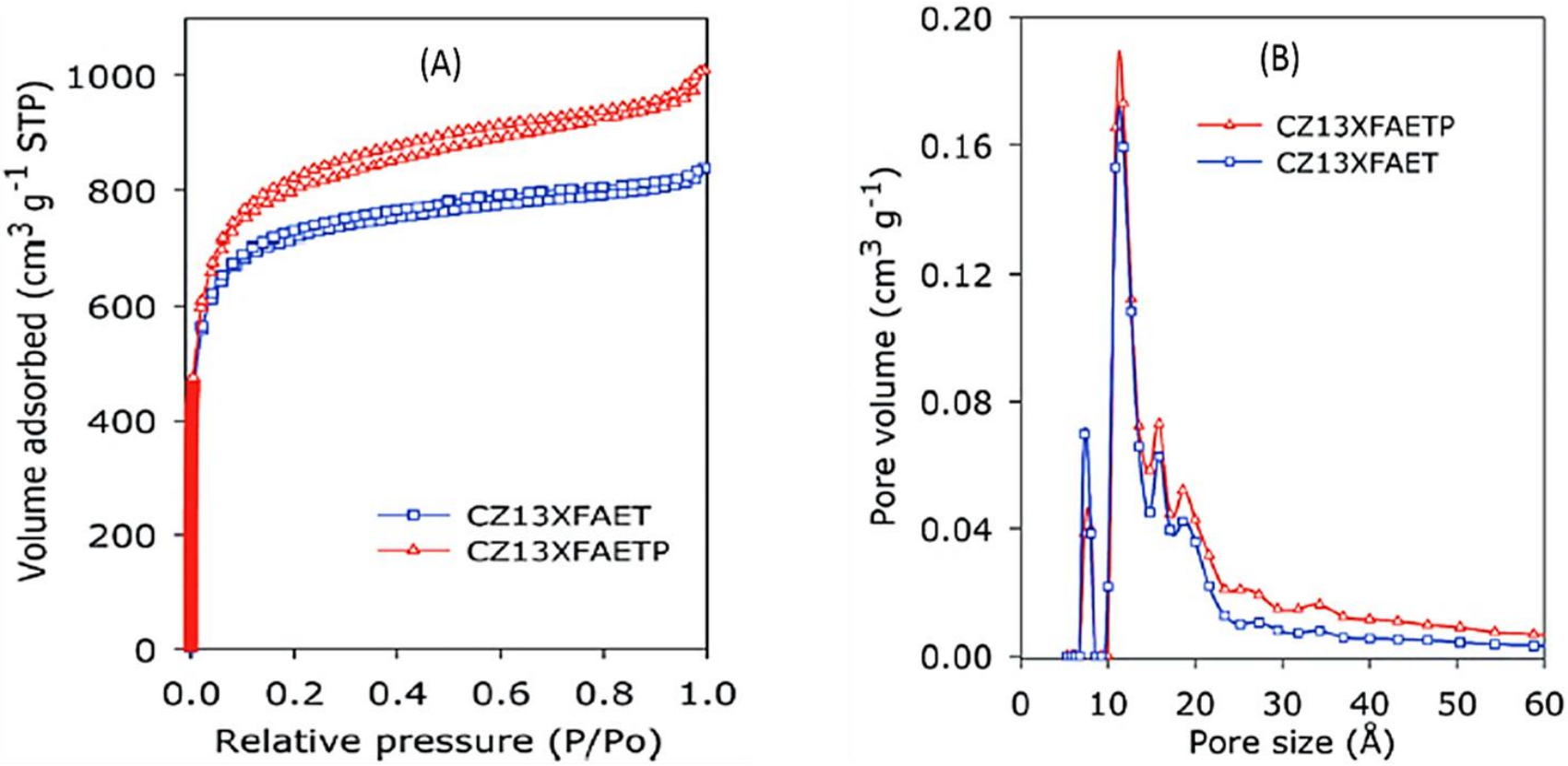


Figure 3.22: (A) Nitrogen sorption isotherms and **(B)** Corresponding pore size distribution (PSD) curves of zeolite templated carbons prepared *via* a route that combines liquid impregnation and CVD using powder (CZ13XFAET) or compacted pellets (CZ13XFAETP) of ***Zeolite 13X*** as hard template.

3.6.3.7 Hydrogen Uptake Measurements

Given the high surface area of the ZTCs prepared *via* the LI + CVD route, we assessed their gas uptake for both hydrogen and CO_2. The total and excess hydrogen uptake isotherms of the powder and pelletized ZTCs are shown in **Figure 3.23 A** and **Figure 3.23 B** and the storage capacity at 20 bar (and at -196 ^oC under a liquid nitrogen bath) is stated in **Table 3.5**. The hydrogen uptake was corrected for buoyancy effect as previously described.[29, 30] The hydrogen uptake was calculated based on skeletal density of 1.5 g cm^{-3} for the carbons, which was determined from helium sorption data obtained using the IGA at a pressure of up to 20 bar *at 0 ^oC*.

At a pressure of 20 bar, the pelletized ZTC (CZ13XFAETP) has total hydrogen uptake capacity of 6.6 wt% compared to 5.5 wt% for the powder CZ13XFAET sample. The excess hydrogen uptake at 20 bar follows a similar trend; 5.5 wt% for CZ13XFAETP and 4.7 wt% for CZ13XFAET. The gravimetric hydrogen uptake values are as expected for high surface area zeolite-templated carbons ZTCs.[28, 30, 54] The motivation for this work was to generate materials with a high volumetric gas uptake. **Figure 3.23 B** shows both the excess and total volumetric hydrogen uptake calculated on the basis of a packing/bulk density of 0.44 g cm^{-3} for CZ13XFAET and 0.69 g cm^{-3} for CZ13XFAETP. The ZTCs have total volumetric hydrogen uptake (at 20 bar and -196 ^oC) of 24 g L^{-1} and 46 g L^{-1} for CZ13XFAET and CZ13XFAETP, respectively. Thus the total volumetric hydrogen uptake (at 20 bar) of the powdered ZTC is nearly doubled from 24 g L^{-1} to 46 g L^{-1} by performing the templating process with compacted zeolite pellets as template. Such a volumetric hydrogen uptake, at the relatively pressure of 20 bar, is amongst the highest ever reported for any porous material, including densified carbons and MOFs.[25, 40, 44-50, 54, 61-69]

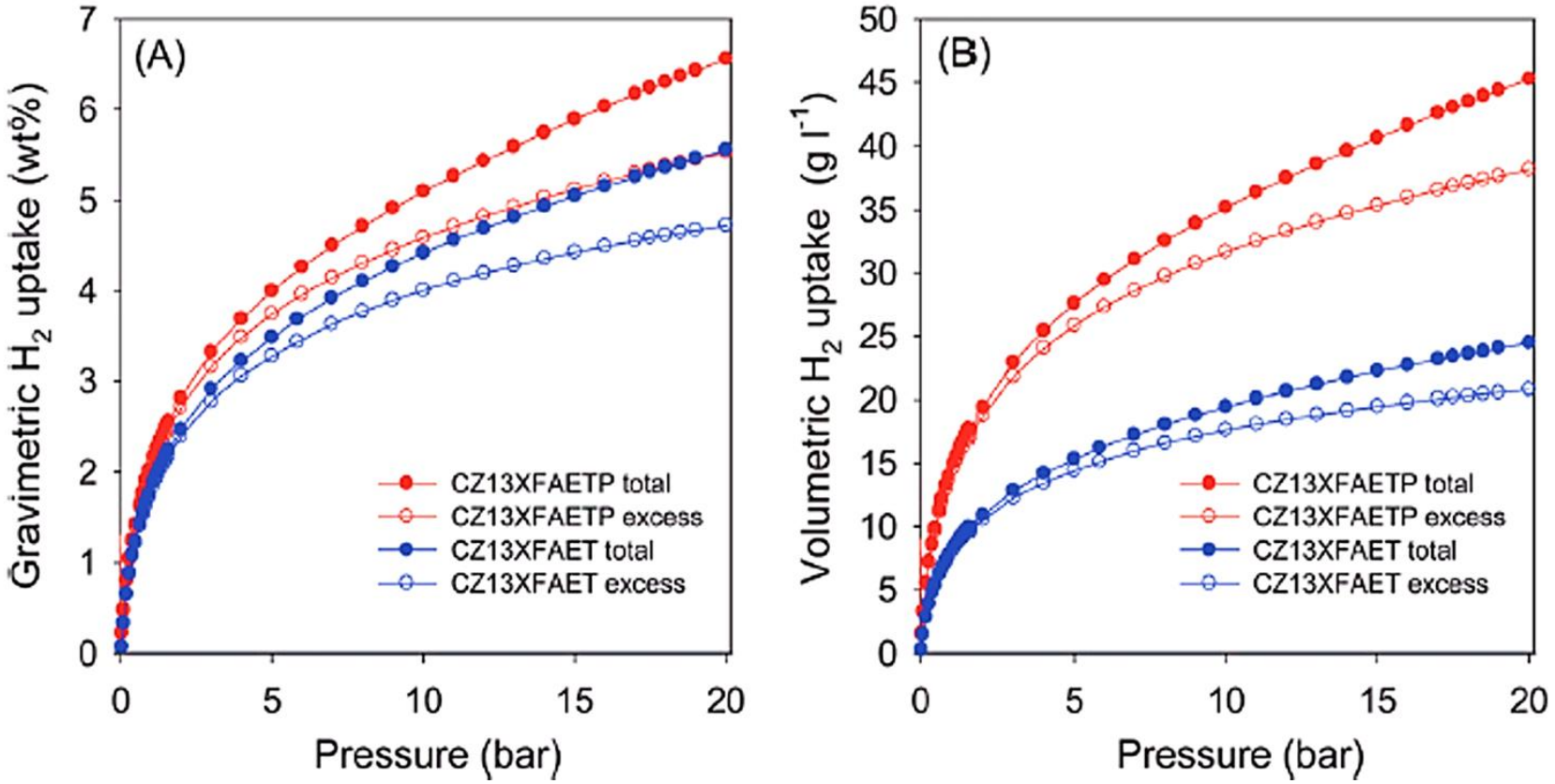


Figure 3.23: (A) Gravimetric (excess and total) and **(B)** Volumetric (excess and total) hydrogen uptake isotherms at -196 °C of zeolite templated carbons templated by powder (CZ13XFAET) or compacted pellets (CZ13XFAETP) of ***Zeolite 13X***.

3.6.3.8 CO_2 Uptake Measurements

3.6.3.8.1 CO_2 Uptake at 25 ^oC

The CO_2 uptake isotherms, obtained *at 25 ^oC*, for the ZTCs prepared *via* the CVD + LI route are shown in **Figure 3.24** and the storage capacity at 1 bar and 20 bar is given in **Table 3.5**.

The gravimetric uptake capacity *at 25 ^oC* and 1 bar (**Figure 3.24 A**) is similar for both the powder CZ13XFAET (2.5 mmol g^{-1}) and pelletized samples CZ13XFAETP (2.6 mmol g^{-1}). This is simply a reflection of the fact that low pressure CO_2 uptake is dependent on pore size and level of microporosity, variables that are similar for the two samples (**Table 3.5**). The higher surface area of the pelletized ZTC is reflected by the greater CO_2 uptake capacity at 20 bar of 22 mmol g^{-1} compared to 18.6 mmol g^{-1} for the powder sample, which is an increase of *ca.* 20%. More importantly, as shown in **Figure 3.24 B**, the volumetric CO_2 uptake of the pelletized sample is far superior due to higher packing density. For example at 1 bar, CZ13XFAETP has an uptake of 79 g L^{-1}, which is 65% higher than that of CZ13XFAET (48 g L^{-1}). The superior volumetric uptake capacity of the pelletized sample increases at higher pressure such that at 20 bar it is nearly twice that of the powdered sample; 668 g L^{-1} compared to 360 g L^{-1}.

3.6.3.8.2 CO_2 Uptake at 0 ^oC

A similar trend is observed for CO_2 uptake *at 0 ^oC* with slightly higher gravimetric uptake for the pelletized sample but much higher volumetric capacity (**Table 3.6**) and (**Figure 3.25**).

Templating of high surface area ZTCs with compacted zeolites therefore offers advantages with respect to the gravimetric and volumetric uptake of CO_2.

3.6.3.9 Working Capacity

Another critical measure of CO_2 uptake capacity is the so-called working capacity, which is especially relevant for pressure swing adsorption (PSA) processes that enable regeneration of the storage material. Comparing the CO_2 uptake at 20 bar (charging pressure) and atmospheric pressure (discharge/material regeneration pressure), the working capacity of the ZTCs is 19.4 and 16.1 mmol CO_2 per g for CZ13XFAETP and CZ13XFAET, respectively. The gravimetric working capacity of 19.4 mmol g^{-1} for the pelletized sample is comparable to the best adsorbents reported so far (**Table 3.7**). However, when the packing density of the adsorbents is taken into account to calculate the volumetric uptake, the pelletized ZTC sample outperforms all currently available benchmark materials The volumetric working capacity of CZ13XFAETP is 589 g L-1 (or 300 cm^3 cm^{-3}), which is higher than that of the best previously reported value of 529 g L^{-1} (269 cm^3 cm^{-3}) for mesophase pitch-derived activated carbon.

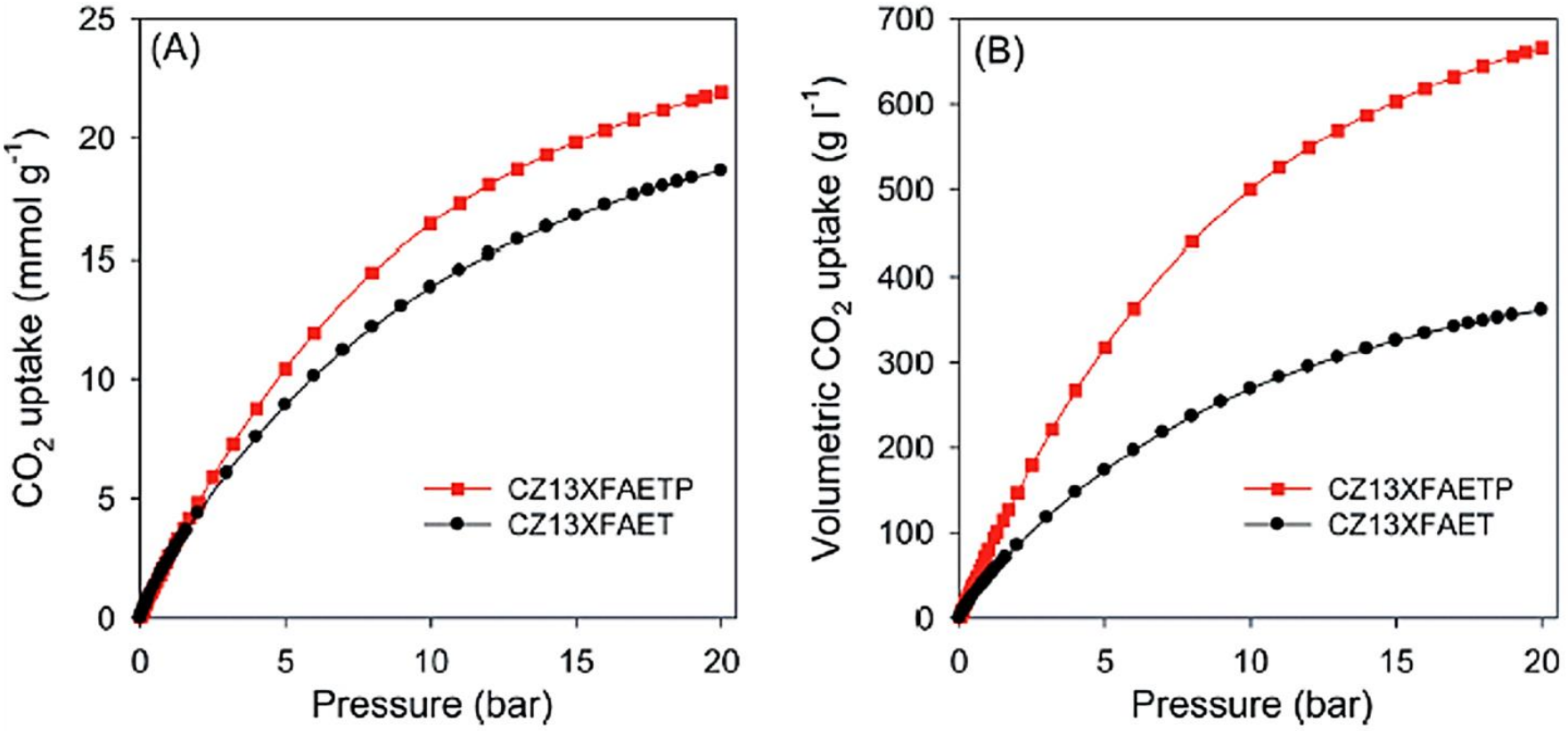


Figure 3.24: (A) Gravimetric CO_2 uptake and **(B)** Volumetric CO_2 uptake ***at 25 °C*** and 0-20 bar for zeolite templated carbons templated by powder (CZ13XFAET) or compacted pellets (CZ13XFAETP) of ***Zeolite 13X***.

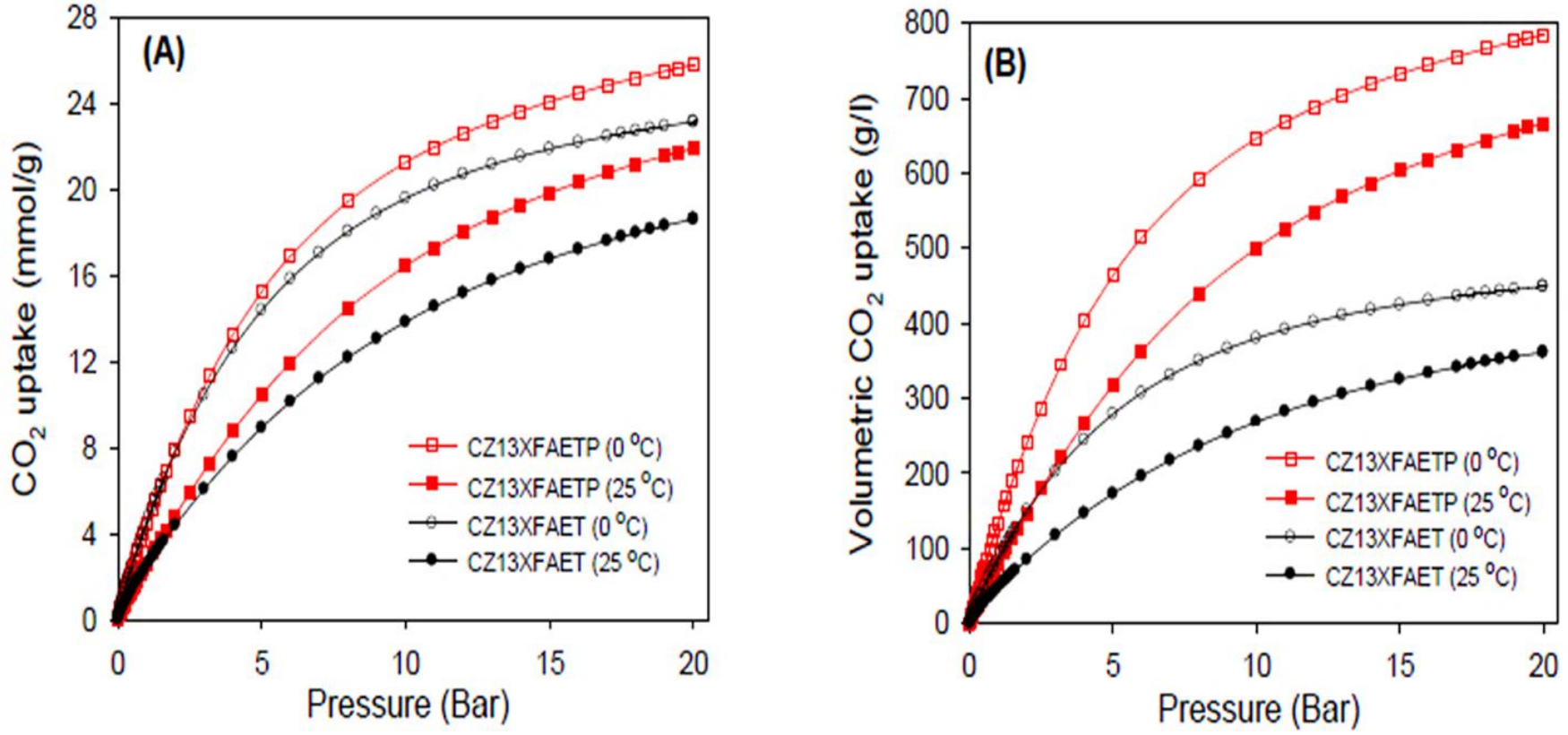


Figure 3.25: (A) Gravimetric and **(B)** Volumetric CO_2 uptake ***at 0 °C*** or ***25 °C*** and 0-20 bar for zeolite templated carbons templated by powder (CZ13XFAET) or compacted pellets (CZ13XFAETP) of ***Zeolite 13X***.

Table 3.5: Textural properties and gas (CO_2 and hydrogen) uptake of zeolite templated carbons templated by powder or compacted pellets of ***Zeolite 13X***.

Sample	Surface area [a] ($m^2\ g^{-1}$)	Pore volume [b] ($cm^3\ g^{-1}$)	Pore size [c] (Å)	CO_2 uptake [d] (mmol g^{-1})		H_2 uptake [e]	
				1 bar	20 bar	(wt %)	(g L^{-1}) [f]
CZ13XFAET	2702 (2341)	1.30 (0.95)	7.5/12	2.5 (48)	18.6 (360)	5.5 (4.7)	24 (21)
CZ13XFAETP	3021 (2448)	1.56 (1.00)	7.5/12	2.6 (79)	22.0 (668)	6.6 (5.5)	46 (38)

[a] The values in the parenthesis refer to micropore surface area.
[b] The values in the parenthesis refer to micropore volume.
[c] Pore size Distribution maxima obtained from NLDFT analysis.
[d] CO_2 uptake *at 25 °C* and various pressures (i.e., 1 bar and 20 bar); the values in parenthesis are volumetric CO_2 uptake in g L^{-1}.
[e] Gravimetric (wt%) and volumetric (g L^{-1}) H_2 uptake at -196 °C and 20 bar; the values in parenthesis are excess H_2 uptake.
[f] Packing/bulk density of 0.44 g cm^{-3} for CZ13XFAET and 0.69 g cm^{-3} for CZ13XFAETP.

Table 3.6: CO_2 uptake ***at 0 °C*** for zeolite templated carbons templated by powder (CZ13XFAET) or compacted pellets (CZ13XFAETP) of ***Zeolite 13X***.

Sample	CO_2 uptake [a, b] (mmol g^{-1})		Working capacity [b, c] (mmol g^{-1})
	1 bar	20 bar	
CZ13XFAET	4.3 (83)	23.2 (449)	18.9 (366)
CZ13XFAETP	4.5 (137)	26.0 (789)	21.5 (652)

[a] CO_2 uptake *at 0 °C* and various pressures (i.e., 1 bar and 20 bar).
[b] The values in the parenthesis are volumetric CO_2 uptake in g L^{-1}.
[c] Defined as the difference of storage capacity between 20 bar and 1 bar.

Table 3.7: CO_2 uptake ***at 25 °C*** and 20 bar and working capacity for PSA (20 bar to 1 bar) for powder (CZ13XFAET) and pelletized (CZ13XFAETP) ZTCs compared to top-performing materials reported in the literature.

Sample	Packing density (g cm^{-3})	CO_2 uptake [a] (mmol g^{-1})	Working capacity for PSA system [b]			References
			(mmol g^{-1})	(g L^{-1})	(cm^3 cm^{-3})	
CZ13XFAETP	0.69	22.0	19.4	589	300	This work
CZ13XFAET	0.44	18.6	16.1	312	159	This work
VR-5 (AC from mesophase pitch)	0.47	26.8	22.0	455	232	16
VR-93 (AC from mesophase pitch)	0.47	30.4	25.6	529	269	16
VR5-4:1 (AC from mesophase pitch)	0.47	22.0	19.4	401	204	70
Maxsorb (commercial AC)	0.29	19.0	16.9	216	110	71
HPC5b2-1100 (hierarchical carbon)	-	20.8	17.1	-	-	72
MOF-5	0.31[c]	19.3	18.5	252	128	48, 69, 72
MOF-177	0.21[d]	28.1	27.1	250	127	49, 50, 73

[a] CO_2 uptake *at 25 °C* and at 20 bar.
[b] Defined as the difference of storage capacity between 20 bar and 1 bar.
[c] Packing (or pellet) density according to reference [69] and reference [72].
[d] Packing density according to reference [50] and reference [49].

3.7 Conclusions

A nanocasting process that utilizes compacted zeolite pellets as hard templates has been employed to generate pelletized zeolite template carbons (ZTCs) with moderate to high surface area and pore volume. The use of compacted zeolite pellets (following compression of powder forms of zeolites at *370 MPa* or *740 MPa*) rather than powdered forms of zeolites generates pelletized ZTCs with higher porosity and higher packing density. The rise in porosity and packing density does not, however, affect the pore size and pore size distribution. The higher porosity and packing density for the pelletized ZTCs translates to highly enhanced volumetric gas (CO_2 and hydrogen) uptake.

For CVD-derived samples that exhibit moderate porosity, the pelletized ZTCs have surface area of *ca.* 2000 $m^2\ g^{-1}$, which is 10% higher than for powder samples, despite an increase in packing density from *ca.* 0.55 g cm^{-3} to 0.85 g cm^{-3}. This means that the surface area per unit volume rises by *ca.* 60% from between 1000 $m^2\ cm^{-3}$ and 1100 $m^2\ cm^{-3}$ for the powder ZTCs to 1670 $m^2\ cm^{-3}$ for pelletized samples. For the CVD-derived samples, the volumetric CO_2 uptake at 25 ^oC increases by 140% and 85% at 1 bar and 20 bar respectively, to reach 101 g L^{-1} (at 1 bar) and 531 g L^{-1} (at 20 bar).

Pelletized ZTCs prepared *via* a combination of liquid impregnation and CVD achieve much higher surface area above 3000 $m^2\ g^{-1}$ (compared to 2700 $m^2\ g^{-1}$ for powder samples). The increase in surface area occurs despite a simultaneous rise in packing density from 0.44 g cm^{-3} to 0.69 g cm^{-3}. The overall effect of this is that the surface area per unit volume rises by 75% from 1189 $m^2\ cm^{-3}$ to 2085 $m^2\ cm^{-3}$ for the pelletized sample. The high surface area pelletized ZTCs have attractive gravimetric hydrogen uptake of 6.6 wt% (5.5 wt% for powder sample) at 20 bar and -196 ^oC, and due to

their higher packing density have exceptional volumetric hydrogen storage capacity of 46 g L^{-1} (24 g L^{-1} for powder sample). For CO_2 uptake (at 25 ^oC and 20 bar), the volumetric uptake of the high surface area pelletized ZTC is close to double that of the analogous powder sample, i.e., 668 g L^{-1} compared to 360 g L^{-1}.

In all cases, the pelletized carbon samples also have higher gravimetric and volumetric gas uptake compared to directly compacted conventionally templated (with powdered zeolites) ZTCs. This study, and the findings herein described, present an entirely new route to microporous templated carbons and also break new ground with respect to levels of volumetric hydrogen uptake achievable for templated porous carbons. The findings add new insights in the development of carbonaceous materials with enhanced properties for the storage of energy related gases. The pelletized ZTCs may also be used for storage of other gases such as methane, acetylene and natural gas.

3.8 References

1. L. Schlapbach and A. Züttel, *Nature*, 2001, **414**, 353-358.

2. J. A. Turner, *Science*, 1999, **285**, 687-689.

3. L. L. Zhang and X. S. Zhao, *Chem. Soc. Rev.*, 2009, **38**, 2520-2531.

4. M. Sevilla and R. Mokaya, *Energy Environ. Sci.*, 2014, **7**, 1250-1280.

5. L. Wei and G. Yushin, *Nano Energy*, 2012, **1**, 552-565.

6. S. Choi, J. H. Drese and C. W. Jones, *ChemSusChem*, 2009, **2**, 796-854.

7. Q. A. Wang, J. Z. Luo, Z. Y. Zhong and A. Borgna, *Energy Environ. Sci.*, 2011, **4**, 42-55.

8. D. M. D'Alessandro, B. Smit and J. R. Long, *Angew. Chem. Int. Ed.*, 2010, **49**, 6058-6082.

9. S. P. Wang, S. L. Yan, X. B. Ma and J. L. Gong, *Energy Environ. Sci.*, 2011, **4**, 3805-3819.

10. K. Sumida, D. L. Rogow, J. A. Mason, T. M. McDonald, E. D. Bloch, Z. R. Herm, T. H. Bae and J. R. Long, *Chem. Rev.*, 2012, **112**, 724-781.

11. H. Furukawa, N. Ko, Y. B. Go, N. Aratani, S. B. Choi, E. Choi, A. O. Yazaydin, R. Q. Snurr, M. O'Keeffe, J. Kim and O. M. Yaghi, *Science*, 2010, **329**, 424-428.

12. A. O. Yazaydin, A. I. Benin, S. A. Faheem, P. Jakubczak, J. J. Low, R. R. Willis and R. Q. Snurr, *Chem. Mater.*, 2009, **21**, 1425-1430.

13. M. Sevilla and A. B. Fuertes, *Energy Environ. Sci.*, 2011, **4**, 1765-1771.

14. M. Sevilla, P. Valle-Vigon and A. B. Fuertes, *Adv. Funct. Mater.*, 2011, **21**, 2781-2787.

15. V. Presser, J. McDonough, S. H. Yeon and Y. Gogotsi, *Energy Environ. Sci.*, 2011, **4**, 3059-3066.

16. J. Silvestre-Albero, A. Wahby, A. Sepúlveda-Escribano, M. Martínez-Escandell, K. Kaneko and F. Rodríguez- Reinoso, *Chem. Commun.*, 2011, **47**, 6840-6842.

17. E. Masika and R. Mokaya, *RSC Adv.*, 2013, **3**, 17677-17681.

18. Y. D. Xia, R. Mokaya, G. S. Walker and Y. Q. Zhu, *Adv. Energy Mater.*, 2011, **1**, 678-683.

19. M. Sevilla, A. B. Fuertes and R. Mokaya, *Energy Environ. Sci.*, 2011, **4**, 1400-1410.

20. A. W. C. van den Berg and C. O. Arean, *Chem. Commun.*, 2008, 668-681.

21. H. Furukawa, K. E. Cordova, M. O'Keeffe and O. M. Yaghi, *Science*, 2013, **341**, 974.

22. Y. H. Xu, S. B. Jin, H. Xu, A. Nagai and D. L. Jiang, *Chem. Soc. Rev.*, 2013, **42**, 8012-8031.

23. Y. D. Xia, Z. X. Yang and R. Mokaya, *Nanoscale*, 2010, **2**, 639-659.

24. H. Nishihara and T. Kyotani, *Adv. Mater.*, 2012, **24**, 4473-4498.

25. A. Almasoudi and R. Mokaya, *J. Mater. Chem. A*, 2014, **2**, 10960-10968.

26. Y. D. Xia, Z. X. Yang and Y. Q. Zhu, *J. Mater. Chem. A*, 2013, **1**, 9365-9381.

27. J. C. Wang and S. Kaskel, *J. Mater. Chem.*, 2012, **22**, 23710-23725.

28. T. Kyotani, T. Nagai, S. Inoue and A. Tomita, *Chem. Mater.*, 1997, **9**, 609-615.

29. Z. X. Yang, Y. D. Xia and R. Mokaya, *J. Am. Chem. Soc.*, 2007, **129**, 1673-1679.

30. Y. D. Xia, G. S. Walker, D. M. Grant and R. Mokaya, *J. Am. Chem. Soc.*, 2009, **131**, 16493-16499.

31. Y. D. Xia, R. Mokaya, D. M. Grant and G. S. Walker, *Carbon*, 2011, **49**, 844-853.

32. U.S. Department of Energy, https://www1.eere.energy.gov/hydrogenandfuelcells/storage/current_technology.html., 12/10/2017).

33. B. Adeniran and R. Mokaya, *Chem. Mater.*, 2016, **28**, 994-1001.

34. M. Sevilla, J. B. Parra and A. B. Fuertes, *ACS Appl. Mater. Interfaces*, 2013, **5**, 6360-6368.

35. B. Adeniran and R. Mokaya, *J. Mater. Chem. A*, 2015, **3**, 5148-5161.

36. K. V. Kumar, K. Preuss, L. H. Lu, Z. X. Guo and M. M. Titiricit, *J. Phys. Chem. C*, 2015, **119**, 22310-22321.

37. B. Adeniran, E. Masika and R. Mokaya, *J. Mater. Chem. A*, 2014, **2**, 14696-14710.

38. H. M. Coromina, D. A. Walsh and R. Mokaya, *J. Mater. Chem. A*, 2016, **4**, 280-289.

39. W. Sangchoom and R. Mokaya, *ACS Sustainable Chem. Eng.*, 2015, **3**, 1658-1667.

40. J. P. Marco-Lozar, J. Juan-Juan, F. Suárez-García, D. Cazorla-Amorós and A. Linares-Solano, *Int. J. Hydrogen Energy*, 2012, **37**, 2370-2381.

41. J. Juan-Juan, J. P. Marco-Lozar, F. Suárez-García, D. Cazorla-Amorós and A. Linares-Solano, *Carbon*, 2010, **48**, 2906-2909.

42. K. W. Chapman, G. J. Halder and P. J. Chupas, *J. Am. Chem. Soc.*, 2009, **131**, 17546-17547.

43. J. Alcañiz-Monge, G. Trautwein, M. Pérez-Cadenas and M. C. Román-Martínez, *Microporous Mesoporous Mater.*, 2009, **126**, 291-301.

44. M. Jordá-Beneyto, D. Lozano-Castelló , F. Suárez-García , D. Cazorla-Amorós and A. Linares-Solano, *Microporous Mesoporous Mater.*, 2008, **112**, 235-242.

45. L. Zhou, Y. P. Zhou and Y. Sun, *Int. J. Hydrogen Energy*, 2004, **29**, 319-322.

46. B. Adeniran and R. Mokaya, *Nano Energy*, 2015, **16**, 173-185.

47. U. Mueller, M. Schubert, F. Teich, H. Puetter, K. Schierle-Arndt and J. Pastre, *J. Mater. Chem.*, 2006, **16**, 626-636.

48. R. Zacharia, D. Cossement, L. Lafi and R. Chahine, *J. Mater. Chem.*, 2010, **20**, 2145-2151.

49. J. J. Purewal, D. Liu, J. Yang, A. Sudik, D. J. Siegel, S. Maurer and U. Muller, *Int. J. Hydrogen Energy*, 2012, **37**, 2723-2727.

50. J. Purewal, D. G. Liu, A. Sudik, M. Veenstra, J. Yang, S. Maurer, U. Muller and D. J. Siegel, *J. Phys. Chem. C*, 2012, **116**, 20199-20212.

51. J. P. Marco-Lozar, M. Kunowsky, F. Suárez-García, J. D. Carruthers and A. Linares-Solano, *Energy Environ. Sci.*, 2012, **5**, 9833-9842.

52. N. Balahmar, A. C. Mitchell and R. Mokaya, *Adv. Energy Mater.*, 2015, **5**.

53. P. X. Hou, H. Orikasa, H. Itoi, H. Nishihara and T. Kyotani, *Carbon*, 2007, **45**, 2011-2016.

54. E. Masika and R. Mokaya, *Energy Environ. Sci.*, 2014, **7**, 427-434.

55. Z. X. Yang, Y. D. Xia, X. Z. Sun and R. Mokaya, *J. Phys. Chem. B*, 2006, **110**, 18424-18431.

56. C. Portet, Z. Yang, Y. Korenblit, Y. Gogotsi, R. Mokaya and G. Yushin, *J. Electrochem. Soc.*, 2009, **156**, A1-A6.

57. H. Nishihara, Q. H. Yang, P. X. Hou, M. Unno, S. Yamauchi, R. Saito, J. I. Paredes, A. Martínez-Alonso, J. M. D. Tascón, Y. Sato, M. Terauchi and T. Kyotani, *Carbon*, 2009, **47**, 1220-1230.

58. N. Alam and R. Mokaya, *Energy Environ. Sci.*, 2010, **3**, 1773-1781.

59. T. Kyotani, Z. X. Ma and A. Tomita, *Carbon*, 2003, **41**, 1451-1459.

60. F. O. M. Gaslain, J. Parmentier, V. P. Valtchev and J. Patarin, *Chem. Commun.*, 2006, 991-993.

61. M. Sevilla, R. Mokaya and A. B. Fuertes, *Energy Environ. Sci.*, 2011, **4**, 2930-2936.

62. H. Nishihara, P. X. Hou, L. X. Li, M. Ito, M. Uchiyama, T. Kaburagi, A. Ikura, J. Katamura, T. Kawarada, K. Mizuuchi and T. Kyotani, *J. Phys. Chem. C*, 2009, **113**, 3189-3196.

63. N. P. Stadie, J. J. Vajo, R. W. Cumberland, A. A. Wilson, C. C. Ahn and B. Fultz, *Langmuir*, 2012, **28**, 10057-10063.

64. S. S. Kaye, A. Dailly, O. M. Yaghi and J. R. Long, *J. Am. Chem. Soc.*, 2007, **129**, 14176.

65. Y. Peng, V. Krungleviciute, I. Eryazici, J. T. Hupp, O. K. Farha and T. Yildirim, *J. Am. Chem. Soc.*, 2013, **135**, 11887-11894.

66. H. Furukawa, M. A. Miller and O. M. Yaghi, *J. Mater. Chem.*, 2007, **17**, 3197-3204.

67. Y. Yan, X. Lin, S. H. Yang, A. J. Blake, A. Dailly, N. R. Champness, P. Hubberstey and M. Schröder *Chem. Commun.*, 2009, 1025-1027.

68. O. K. Farha, A. O. Yazaydin, I. Eryazici, C. D. Malliakas, B. G. Hauser, M. G. Kanatzidis, S. T. Nguyen, R. Q. Snurr and J. T. Hupp, *Nat. Chem.*, 2010, **2**, 944-948.

69. A. Dailly and E. Poirier, *Energy Environ. Sci.*, 2011, **4**, 3527-3534.

70. M. E. Casco, M. Martínez-Escandell, J. Silvestre-Albero and F. Rodríguez-Reinoso, *Carbon*, 2014, **67**, 230-235.

71. S. Himeno, T. Komatsu and S. Fujita, *J. Chem. Eng. Data*, 2005, **50**, 369-376.

72. G. Srinivas, V. Krungleviciute, Z. X. Guo and T. Yildirim, *Energy Environ. Sci.*, 2014, **7**, 335-342.

73. A. R. Millward and O. M. Yaghi, *J. Am. Chem. Soc.*, 2005, **127**, 17998-17999.

Chapter 4. Polythiophene - Derived Conventional Activated Carbons and Compactivated Carbons for Gas Storage Applications

4.1 Aim of this Chapter

The main motivation of this chapter is:

- To generate activated carbons from the polymer polythiophene as starting material, and to study the energy related gas uptake properties of the generated carbons.

- To study the effect of compactivation (i.e., mechanochemical synthesis approach) on textural properties and CO_2 capture of resulting compactivated polythiophene-derived carbons

4.2 Abstract

Activated carbons derived from a sulphur-rich polymer (polythiophene, PTh) as a carbon precursor have been successfully synthesized by one-step chemical activation using KOH as activating agent. The activation process was performed for 1 h under nitrogen atmosphere, KOH/PTh weight ratio of 2:1 and various reaction temperatures in the 600-800 ^{o}C range. Conventional activated carbons obtained at 800 ^{o}C (sample PT2800) have high surface area of up to 2035 m^2g^{-1}, pore volume of up to 1.3 cm^3g^{-1} with micropores of size 0.7 nm - 1.1 nm, and achieve excess hydrogen uptake of 4.2 wt% at -196 ^{o}C and 20 bar. Sample PT2800 also exhibits attractive excess CO_2 uptake; 21 mmol g^{-1} (at 25 ^{o}C and 40 bar), 19 mmol g^{-1} (at 25 ^{o}C and 20 bar), and 25 mmol g^{-1} (at 0 ^{o}C and at 20 bar). On the other hand, compactivated carbons, prepared *via* a route that includes compaction of the polythiophene at load of *10 tonnes* equivalent to compression pressure of 740 MPa prior to activation, exhibited higher porosity. The compactivated carbon prepared at 800 ^{o}C (sample PT2800P) has surface area and pore volume of 2250 m^2g^{-1} and 1.6 cm^3g^{-1}, respectively but with no change in the micropores size range of 0.7 nm - 1.1 nm. The higher porosity resulted in an increase in gas uptake; excess hydrogen storage capacity at -196 ^{o}C and 20 bar of 4.8 wt%, with CO_2 storage capacity of 21 mmol g^{-1} (at 25 ^{o}C and at 20 bar) and 29 mmol g^{-1} at 0 ^{o}C. Their ease of preparation and high uptake makes the polythiophene-derived carbons attractive for hydrogen and CO_2 storage.

4.3 Introduction

Activated carbons are solid highly porous carbonaceous microcrystalline materials which have been intensively studied and used widely in many applications including as adsorbents,[1] catalyst supports, gas storage materials,[1, 2] and for water purification.[3] Activated carbons have unique characteristic features and proprieties such as low-cost, light weight, ease of preparation, large surface area (>3000 $m^2 g^{-1}$) and pore volume (>0.5 $cm^3 g^{-1}$), high physical and chemical stability, wide availability, adjustable structural (porosity), tunable surface chemistry (various functional groups on the surface oxygen-containing/controllable heteroatom doping).[2, 4-8]

Recently, there has been interest in the functionalization of surfaces of activated carbons materials, which have considerably influenced their properties.[9-11] Heteroatom-doped materials can be prepared *via* simple and effective processes that involve the introduction of atoms such as N, B, P, S onto the carbon framework.[12, 13] The introduction of such heteroatoms can significantly affect the application of activated carbons in CO_2 capture,[14] hydrogen storage,[15] and electrical energy storage when the carbons are electrode in supercapacitors.[16] There are many different strategies that have been used to produce carbons with functionalized surfaces, and most of them are based on the direct reaction between carbon and different chemical agents. Another method is by using organic substances containing heteroatoms as carbon precursors such as; polythiophene, polypyrrole, acetonitrile etc. This methodology can be applied along with nanocasting techniques to generate functionalized carbon materials.[17, 18] While N-doped carbons has received extensive research interest, [9, 10] few studies have focused on S-doped carbonaceous materials.[19-22] Sevilla *et al*. reported a one-step chemical activation of polythiophene polymer using KOH as

activating agent to produce S-doped carbons with high surface area and large pore volume and S content of 3 –12 wt%. The carbons had hydrogen storage capacity of up to 5.71 wt% at 20 bar and -196 ^{o}C. The textural properties and chemical composition (varying s content) of the carbons were tuned by modifying the activation temperature from 600 ^{o}C to 850 ^{o}C.[20] The aim of this chapter was to generate activated carbons from the polymer polythiophene as starting material, and to study the energy related gas uptake properties of the generated carbons. In a departure from previous studies, this chapter also explored the effect of compactivation (i.e., mechanochemical synthesis approach) on textural properties and CO_2 capture of resulting compactivated polythiophene-derived carbons

4.4 Experimental Section

This section presents a detailed description of the materials and chemicals, experimental procedures, and approaches used in **Chapter 4**.

4.4.1 Materials and Chemicals

The list of chemicals/materials used in this chapter, their sources and purity are presented in **Table 4.1**.

Table 4.1: List of chemical reagents/materials used in the experiment.

Chemical/Material	Source	Purity/Concentration
2-Thiophenemethanol	Acros Organics	99+%
Iron(III)chloride ($FeCl_3$)	Sigma-Aldrich	97%
Potassium Hydroxide (KOH)	Fisher Scientific	-
Acetonitrile (CH_3CN)	VWR	99%
N_2 Compressed gas (Cylinder)	BOC Ltd	100%
Hydrochloric acid (HCl)	Fisher Scientific	37%

4.4.2 Material Synthesis

4.4.2.1 Chemical Polymerization of Thiophene Using $FeCl_3$

Polythiophene (PTh) was obtained *via* chemical oxidation of 2-thiophenemethanol, which is commercially available using $FeCl_3$ as an oxidant. In a typical synthesis,[18, 20] 3 g of 2-thiophenemethanol in 20 ml of acetonitrile CH_3CN, were slowly added, under vigorous stirring, to a solution of $FeCl_3$ (28.9 g) in 100 ml of acetonitrile CH_3CN. The resulting mixture was stirred for 15 h at room temperature. The obtained polymer (PTh) being deep brownish-black in colour was separated by filtration, washed with distilled water and then with acetone, and finally dried overnight at 120 ^oC (**Figure 4.1**). The PTh polymer yield before carbonization was close to 100%. **Figure 4.2** shows the synthesis steps of polythiophene-based activated carbons and structure of S-doped activated carbons.[20]

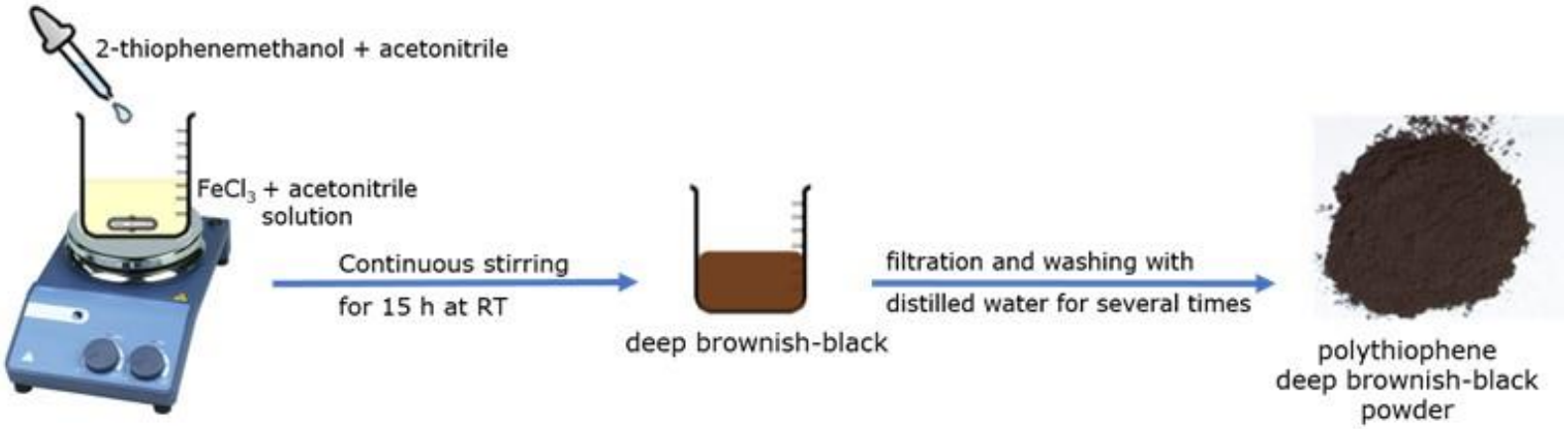


Figure 4.1: Synthetic steps of Polythiophene preparation.

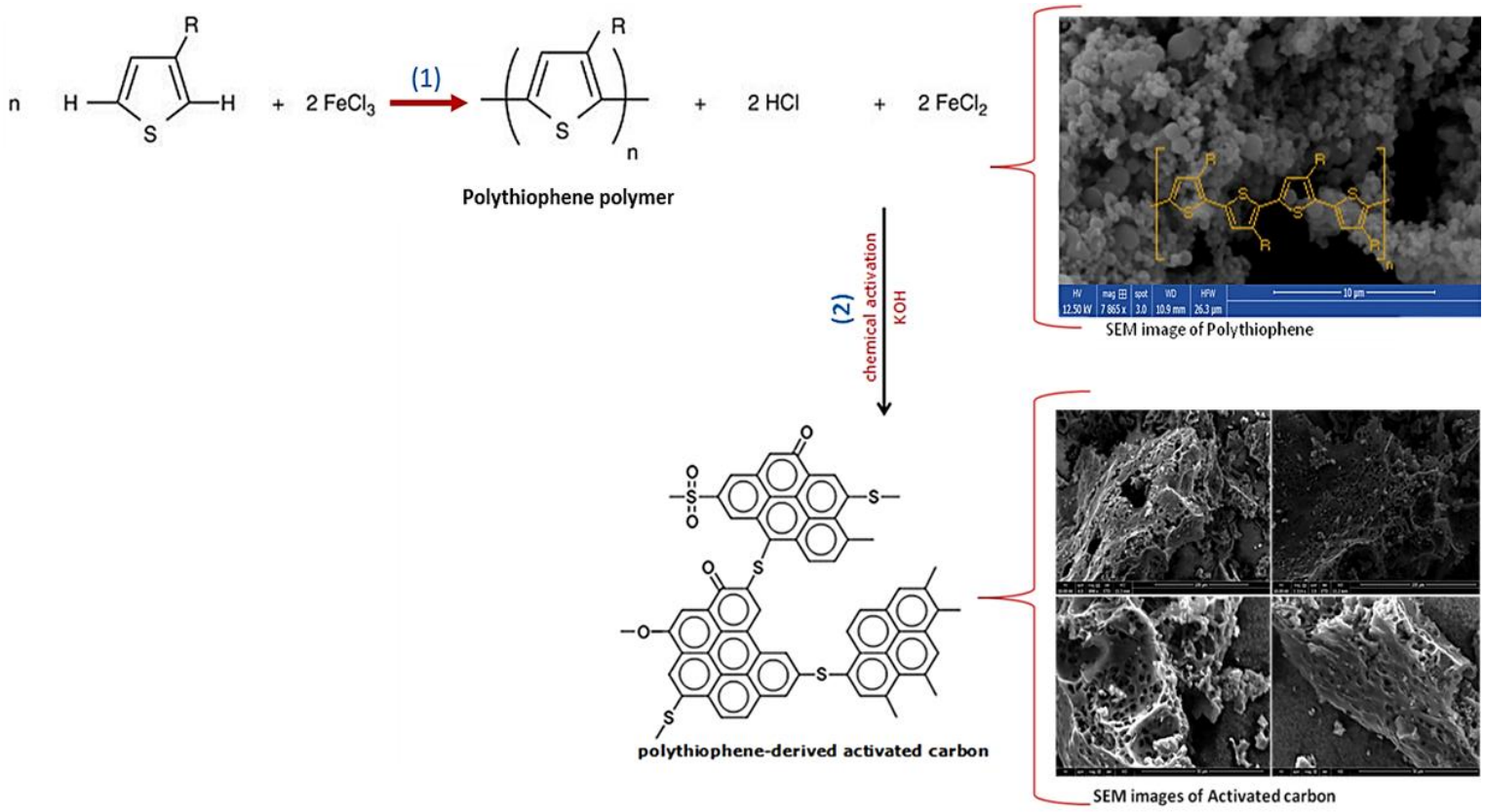


Figure 4.2: Steps of Polythiophene-derived activated carbons synthesis; **(1)** Polythiophene preparation by chemical oxidation (polymerization) using $FeCl_3$ as oxidant, **(2)** Chemical activation using KOH to generate S-doped porous activated carbons.

4.4.2.2 Synthesis of Polythiophene-derived Activated Carbons

4.4.2.2.1 Conventionally Activation

Conventionally activated carbons were prepared by mixing PTh and KOH at KOH/PTh weight ratio of 2:1. The mixture of KOH/PTh was placed into a horizontal tube furnace flushed with N_2 gas and heated up to a target temperature in the range of 600 ^oC - 800 ^oC (ramp rate: 5 ^oC min^{-1}, holding time: 1 h, under N_2 flow, see **Figure 4.3** and **Figure 4.5**. **Figure 4.2** show the steps of polythiophene-derived activated carbons synthesis and **Table 4.2** summarizes the parameters and conditions used to obtain conventionally activated carbons. The activated carbons were then thoroughly washed several times with HCl (10 wt%) under stirring at room temperature to remove any excess KOH and inorganic salts formed during the activation stage and then washed repeatedly with distilled water until neutral pH=7 was attained. Finally, the carbons were dried at 120 ^oC overnight and kept in tightly closed vials. The obtained samples were denoted as ***PT2X***. See **Table 4.3** for sample abbreviation.

4.4.2.3 Compactivation

Compactivated carbons [8, 23-25] were prepared *via* a mechanochemical approach involving compression the KOH/PTh mixture into pellets/discs prior to activation. The mixture of KOH/PTh was compacted for 10 minutes at load of *10 tonnes* equivalent to compression pressure of 740 MPa, in a 1.3 cm diameter die to obtain pellets/disks. The compacted mixture in a crucible boat was placed into a horizontal tubular furnace flushed with N_2 gas and

heated up to a target temperature in the range of 600 °C - 800 °C (ramp rate: 5 °C/min, holding time: 1h, under N_2 flow, see **Figure 4.4** and **Figure 4.5**. **Figure 4.2** show the steps of polythiophene-derived activated carbons synthesis and **Table 4.2** summarized the parameters and conditions used to obtain compactivated carbons. The activated samples were then thoroughly washed several times with HCl (10 wt%) at room temperature to remove any excess of KOH and inorganic salts formed during the activation stage and then washed repeatedly with distilled water until neutral pH=7 was attained, and finally dried at 120 °C overnight. The obtained carbons were denoted as ***PT2XP***. See **Table 4.3** for sample abbreviation.

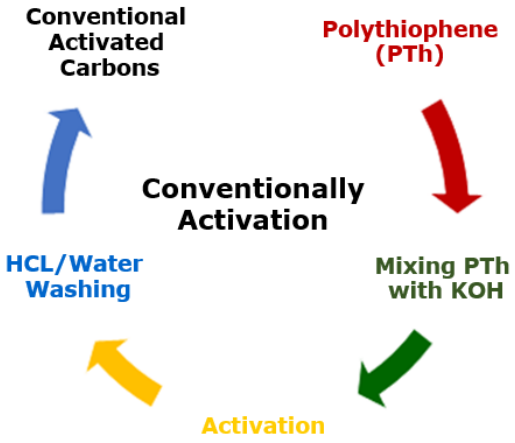


Figure 4.3: Schematic diagram of conventional activation steps.

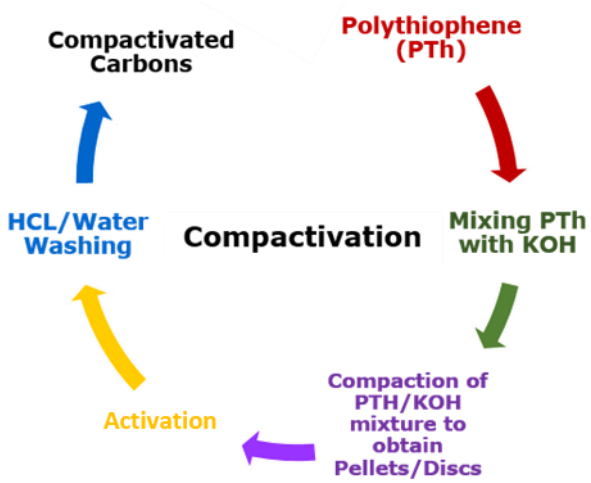


Figure 4.4: Schematic diagram of compactivation steps.

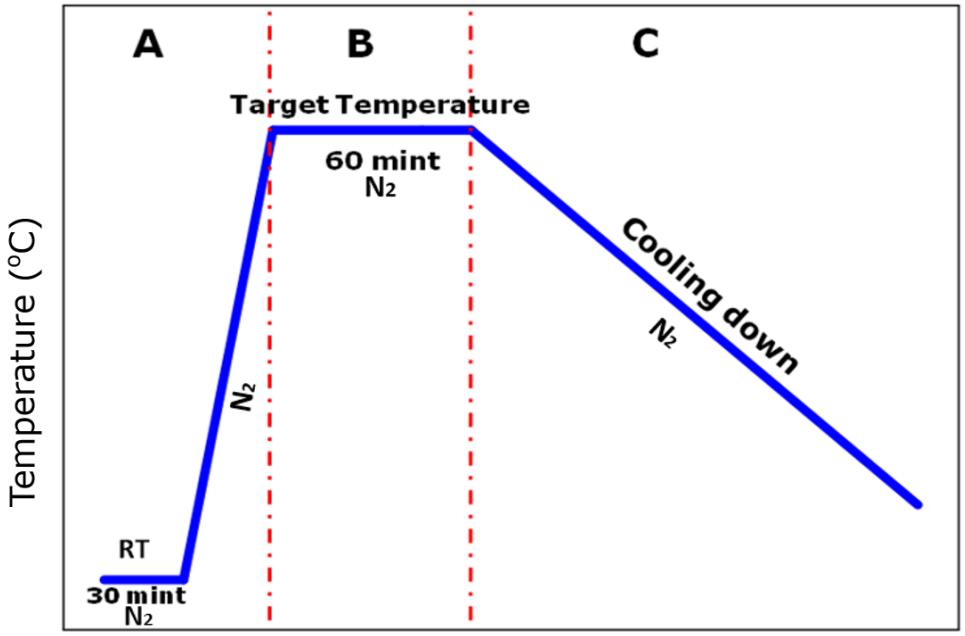


Figure 4.5: A plot representing the temperature programme used to prepare conventional activated carbons and compactivated carbons at various temperature 600 °C, 700 °C and 800 °C.

Table 4.2: Summary of Polythiophene-derived activated carbons synthesis: parameters and conditions.

Carbon Precursor	Polythiophene
Activating Agent	KOH (powder)
KOH/PTh Ratio	2:1
Target Temperature	600 °C or 700 °C or 800 °C
Ramp Rate	5 °C/minute
Activation Holding Time	1 hour
Gas/Environment	Nitrogen gas

4.5 Abbreviations

4.5.1 Conventional Polythiophene Derived-Activated Carbons

The Conventional activated carbons were denoted as ***PT2X***, where *2* corresponds to the KOH/PTh ratio (2:1) and *X* is the activation temperature (600 °C, 700 °C or 800 °C), see **Table 4.3**.

4.5.2 Compactivated Polythiophene Derived-Carbons

The compactivated carbons were denoted as ***PT2XP*** for the compaction for 10 min at 10 tonnes (equivalent to compression pressure of 740 MPa), in a 1.3 cm diameter die, where *2* corresponds to the KOH/PTh ratio (2:1), *X* is the activation temperature (600 °C, 700 °C or 800 °C), see **Table 4.3**.

Table 4.3: List of activated carbons abbreviations.

Polythiophene Derived-Activated Carbons	
Conventional Activated Carbons	Compactivated Carbons at *10 tonnes*=740 MPa
PT2600	PT2600P
PT2700	PT2700P
PT2800	PT2800P

4.6 Results and Discussion

4.6.1 Effects of Compaction on Polythiophene

The nature of the starting material polythiophene PTh was ascertained with respect to morphology, structural ordering and porosity. This was achieved by comparing polythiophene compacted *at 10 tonnes* (equivalent to compression pressure of 740 MPa), designated as PThP, with the original powder polythiophene (designated as PTh).

4.6.1.1 Morphology and Surface Analysis

Polythiophene (PTh) was investigated by scanning electron microscopy before and after compaction. The SEM micrographs images in **Figure 4.6** and **Figure 4.7** show the original powdered PTh and compacted polythiophene PThP, respectively. It can be seen that both the original powdered PTh and compacted PThP consist of spherical particles that are aggregated together, which is similar to what has been observed before.[18, 26-28] It is also evident that compaction causes greater aggregation of the particles. Nevertheless, individual particles are still observed in the compacted PThP but mainly as part of larger aggregates. The compaction, clearly, leads to a decrease in interparticle voids.

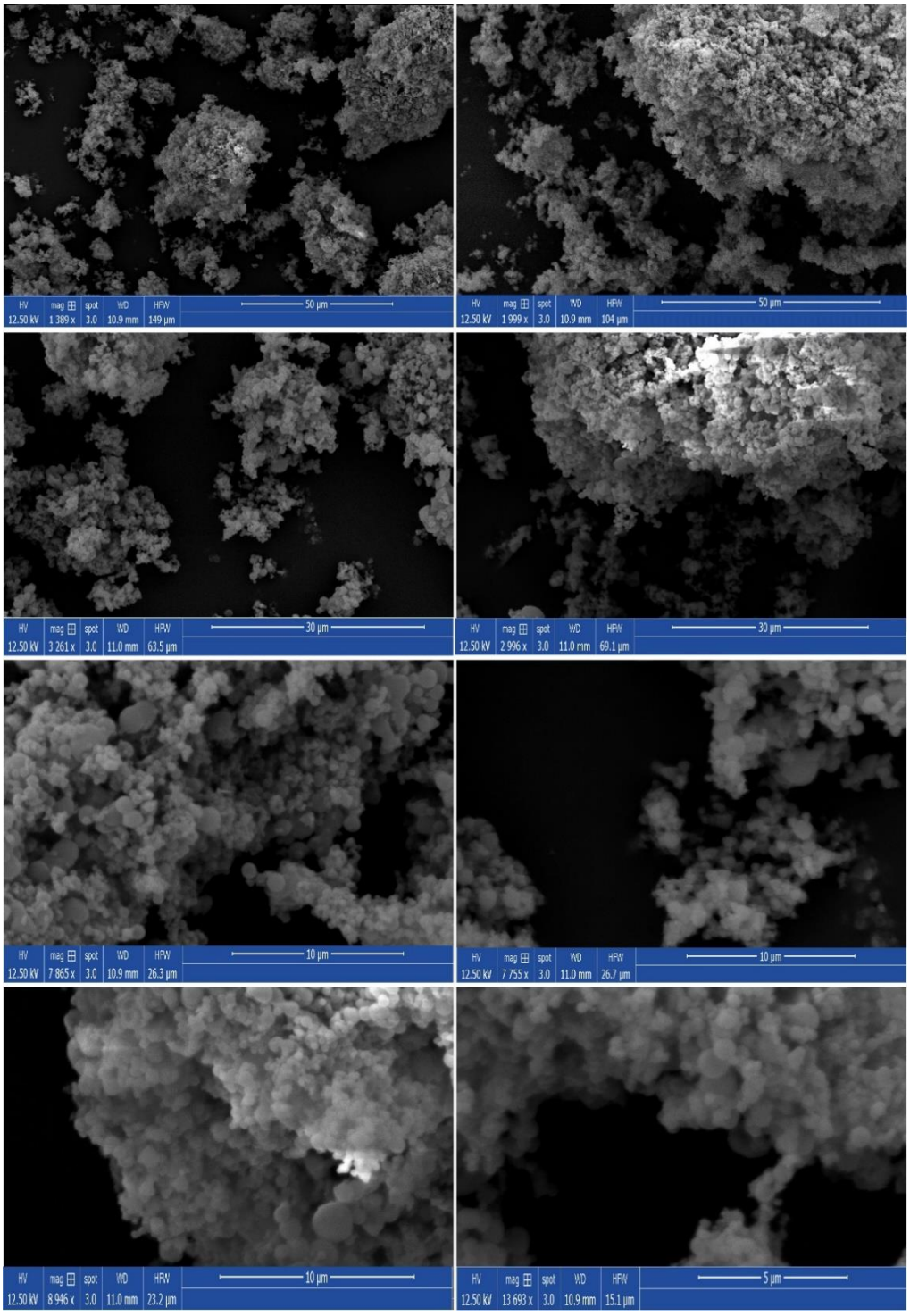


Figure 4.6: SEM micrographs images of original powdered polythiophene (PTh).

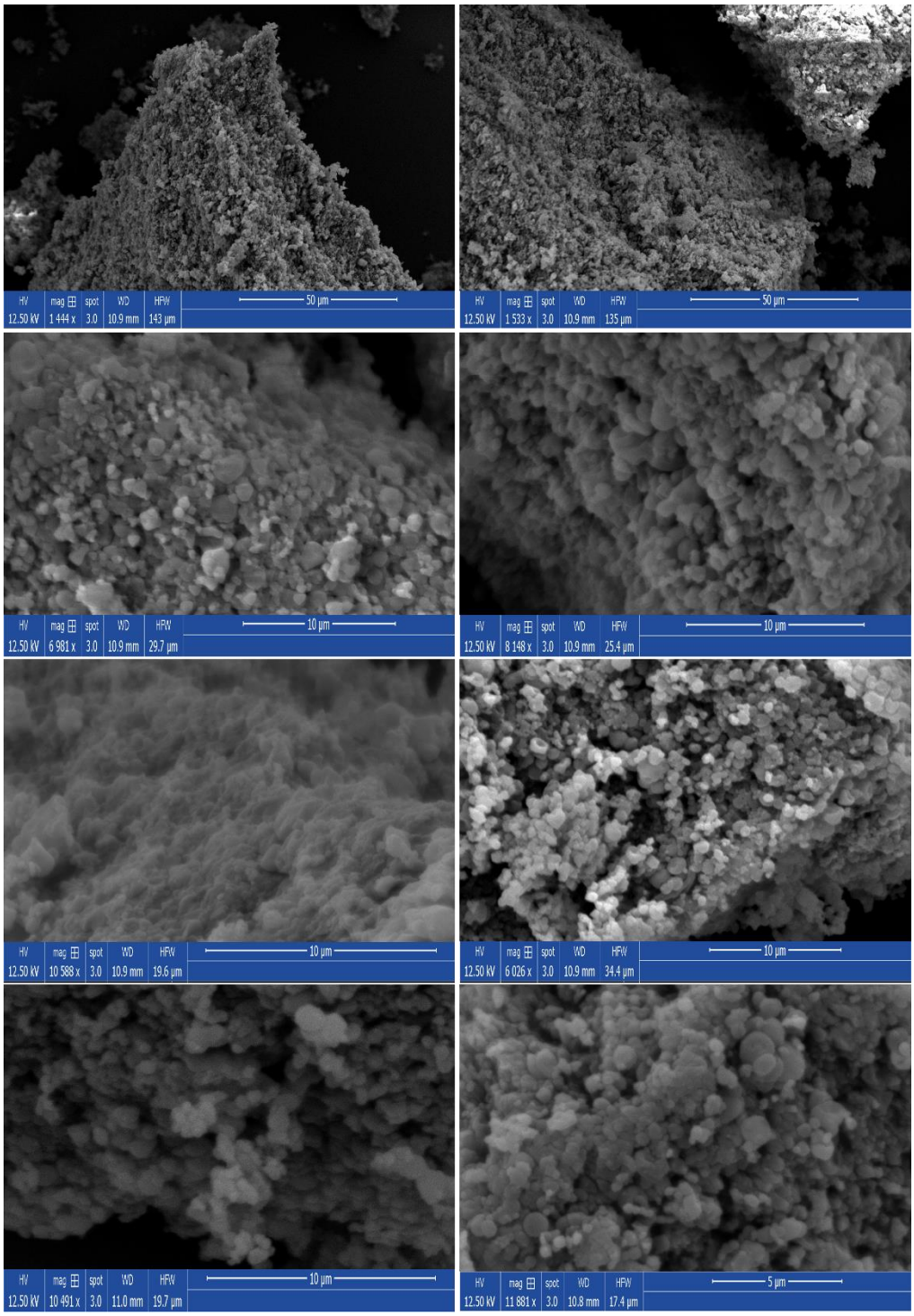


Figure 4.7: SEM micrographs images of compacted polythiophene (PThP).

4.6.1.2 Structural Ordering Analysis

Powder XRD patterns of polythiophene before (PTh) and after compaction (PThP) are shown in **Figure 4.8**. The XRD patterns are consistent with structurally disordered materials and are unaffected by compaction. This means that the structural make up PTh is preserved after compaction. The XRD patterns exhibit a very broad peak centred at 2θ= 22°, which is consistent with the amorphous nature of PTh chains.[26-30]

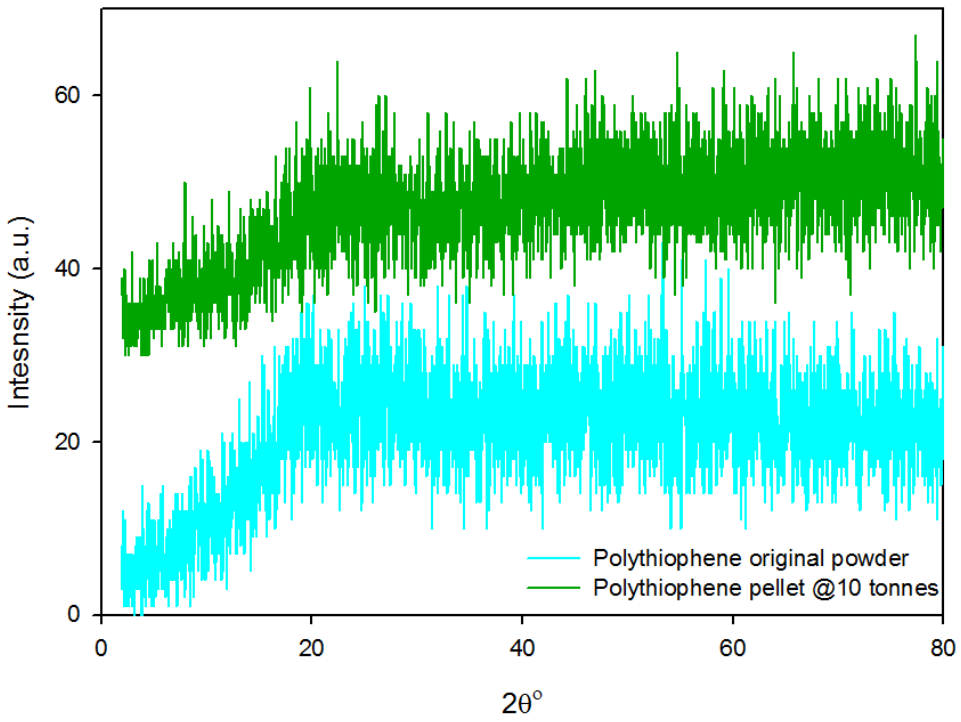


Figure 4.8: XRD patterns of polythiophene before and after compaction.

4.6.2 Polythiophene-derived Activated Carbons

4.6.2.1 Purity and Thermal Stability Analysis

Thermogravimetric analysis was performed under flowing air conditions to confirm the complete removal of iron compounds and to ascertain thermal stability. The TGA curves polythiophene-derived activated and compactivated carbons are shown in **Figure 4.9 A** and **Figure 4.9 B** respectively.

All TGA curves of conventional activated carbons (**Figure 4.9 A**), clearly show three major mass loss events. The first mass loss of ca. 10 wt% below 300 ^{o}C is ascribed to removal of water or volatiles. The second mass loss (ca. 22%) at ca. 400 ^{o}C is due to thermal decomposition of PTh.[28] Further mass loss between 400 ^{o}C and 650 ^{o}C is due to carbon burn off. The burn off temperature range is related to the thermal stability of the carbons and appears to be influenced by the activation temperature with sample PT2800 exhibiting the greatest thermal stability. Overall, the burn off temperature range for all the carbons is typical for largely amorphous porous carbons (i.e. non-graphitic). Furthermore, the TGA curves shows residual mass of ≤3 wt%, which indicates that they are essentially carbonaceous in nature.[25]

For compactivated carbons (**Figure 4.9 B**), a similar trend is observed with no much difference in thermal stability and residual mass compared to conventional activated carbons. Thus, compactivation has no effect on both the thermal stability and residual mass. PT2800P has the greater thermal stability which is related to the higher activation temperature as mentioned before.

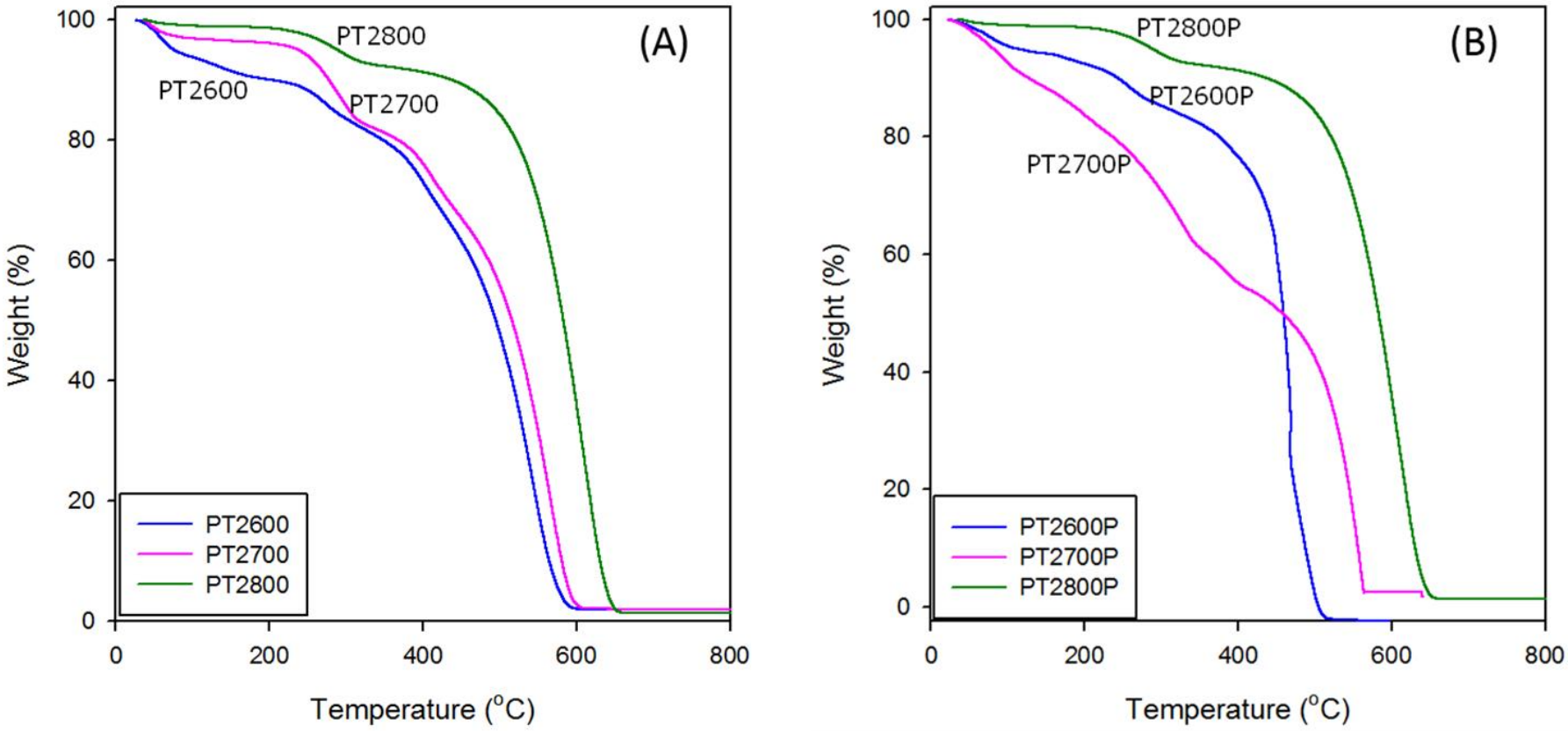


Figure 4.9: Thermogravimetric analysis curves of **(A)** Conventional activated carbons (PT2600, PT2700, and PT2800) and **(B)** Compactivated carbons (PT2600P, PT2700P, and PT2800P).

4.6.2.2 Structural Ordering Analysis

The XRD patterns of PTh, conventional activated carbons (PT2600, PT2700, and PT2800) and compactivated carbons (PT2600P, PT2700P, and PT2800P) are shown in **Figure 4.10 A** and **Figure 4.10 B** respectively. A comparison of the activated carbons (**Figure 4.10 A** and **Figure 4.10 B**) with the starting materials (**Figure 4.8**) shows that the structure of PTh has totally changed after activation. The XRD patterns of the conventional and compactivated carbons are similar to those of compactivated carbons, and both are typical of activated carbons with amorphous structure. Thus, compactivation has no effect on the level of graphitization in the activated carbons. However the activation temperature showed a clear effect. For conventional activated carbons PT2600 and PT2700 (**Figure 4.10 A**) have two broad peaks centred at $2\theta = 24^{o}$ and $2\theta = 45^{o}$ which are, respectively, due to the (002) and (100) diffractions/planes of poorly ordered (disordered) graphitic carbons.[23, 31] The broad nature of the peaks and their relatively low intensity suggests that the carbons are largely amorphous. As the temperature of activation increased from 700 ^{o}C to 800 ^{o}C in case of conventional activated carbons and from 600 ^{o}C to 800 ^{o}C in case of compactivated carbons (**Figure 4.10 B**), the intensity of peaks $2\theta = 24^{o}$ are decreased/disappears, which indicated an increase in level of graphitization as confirmed by TEM analysis. As the activating temperature increased, the crystallinity degree of the carbon materials gradually increased which led to increase the thermal stability.

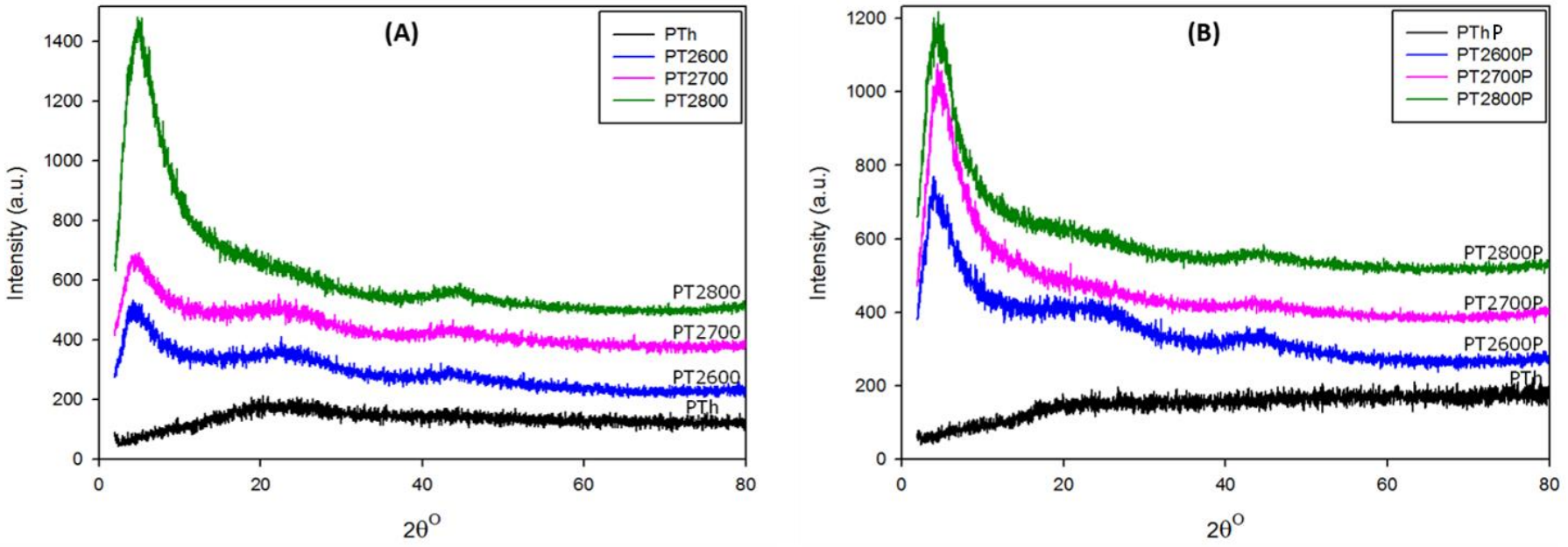


Figure 4.10: XRD patterns of **(A)** Conventional activated carbons (PT2600, PT2700, and PT2800) **(B)** Compactivated carbons (PT2600P, PT2700P, and PT2800P). XRD patterns of starting materials, PTh and PTHP are included for comparison.

4.6.2.3 Elemental Analysis

Elemental composition analysis *via* C-H-N microanalysis (excluding analysis of S) following the procedure discussed in **Chapter 2** indicated the presence of carbon, hydrogen and nitrogen content (C, H and N) in polythiophene polymer and polythiophene-derived activated carbons. Elemental composition values are given in **Table 4.4**.

Activated carbons prepared by KOH activation normally contain a variable amount of the hetero atoms such as oxygen, nitrogen, hydrogen, sulfur, depending on procedures used and carbon sources. According to the data in **Table 4.4**, there is a clear change in the elemental composition between the polythiophene and the activated carbons. As the temperature of activation increased, there is a decrease in the content of Hydrogen and nitrogen. The changes may be understood by considering that on heating, the least stable fragments of the structure (e.g. methylene and oxygen bridges) undergo decomposition leading to formation of side products of carbonization rich in hydrogen and oxygen, such as water and simple hydrocarbons. As the temperature of activation increased, there is significant increase in C content from 52% to 79.5%, which is accompanied with decrease in the content of H from 2.03% to 0.5. The highest carbon content was in sample PT2800, whereas the lowest content of carbon was in sample PT2700.

Table 4.4: Elemental analysis of starting materials PTh and polythiophene-derived activated carbons.

Sample	Chemical Composition (wt %) [a]			
	C	H	N	O+X [b]
PTh	50	2.23	0.3	47.38
PT2600	57	2.03	0.3	40.5
PT2700	52	3.2	0.3	44.5
PT2800	79.5	0.5	0.2	19.8

[a] Determined from CHN microanalysis.
[b] Oxygen concentration + X (where X are other elements) obtained by: O+X (%)= [100 –(C+H+N)].

4.6.2.4 Elemental Surface Analysis

The surface elemental content (carbon, oxygen, sulfur) of the activated carbons was investigated using XPS and the resulting values are presented in **Table 4.5.** The polythiophene polymer/starting material contains 17.6 wt% of sulfur, The lower sulfur content in the polymer is due to the presence of 24.3 wt% oxygen, which arises from the oxidative polymerization process. When polythiophene is carbonized at 800 ^{o}C, half of the sulfur is removed, while activation of the polymer causes a decrease in sulfur content from 17.56 wt% to 3.0 wt%. It is clear that, as the activating temperature increase from 600 ^{o}C to 800 ^{o}C, sulphur content decrease by 30-40%. The XPS analysis confirms the chemical composition on the surface and near surface elemental content as surface composition is important for adsorption processes. The elemental composition for all the activated carbons are comparable to what was observed before by Sevilla *et al*.[18] The elemental composition of conventional activated carbons and compactivated carbons indicate that there is no much difference in composition of samples prepared using compactivation route compared to conventional activated carbons. Thus, compactivation has no effect on elemental composition of the activated carbons. However the activation temperature showed a clear effect. As the temperature of activation increased from 600 ^{o}C to 800 ^{o}C the carbon content increased significantly at the lowest activation temperature 600 ^{o}C in PT2600 which the sulfur has been reduced to 3.0 wt%, the lower sulfur content in the polymer is due to the presence of 24.3 wt% oxygen, which arises from the oxidative polymerization process. When polythiophene is activated at the highest activation temperature 800 ^{o}C, about half of the sulfur is removed, while activation of the polymer causes a decrease in sulfur content from 17.6 wt% to 3.0 wt%. There is a decrease in sulphur content as the activation temperature increases from 600 ^{o}C to 800 ^{o}C.

Table 4.5: Chemical composition of polythiophene-derived conventional activated carbons and compactivated carbons.

Sample	Chemical Composition (wt %) [a]		
	C	**O**	**S+X** [b]
PTh	58.2	24.3	17.6
PT2600	67.2	29.9	3.0
PT2600P	71.0	26.2	2.6
PT2700	73.9	24.6	1.5
PT2700P	77.4	21.2	1.2
PT2800	80.8	14.6	0.7
PT2800P	85.2	14.1	1.1

[a] Obtained by XPS.
[b] Sulfur concentration + X (where X are other elements) obtained by: S+X (%)= [100 –(C+O)].

4.6.2.5 Morphology and Surface Analysis

SEM micrographs images for conventionally activated carbons are shown in **Figure 4.11**, **Figure 4.13**, and **Figure 4.15**, while those of compactivated carbons are shown in **Figure 4.12**, **Figure 4.14**, and **Figure 4.16**.

It is clear that the PTh spherical morphology was converted to entirely different particle morphology, with multiple corners and edges that are not in the PTh, which is consistent with previous reports.[18, 20] The resulting ACs have a sponge-like structure with highly irregular particles shape. Moreover, there is no significant difference in morphology between conventional activated carbons and compactivated carbons.

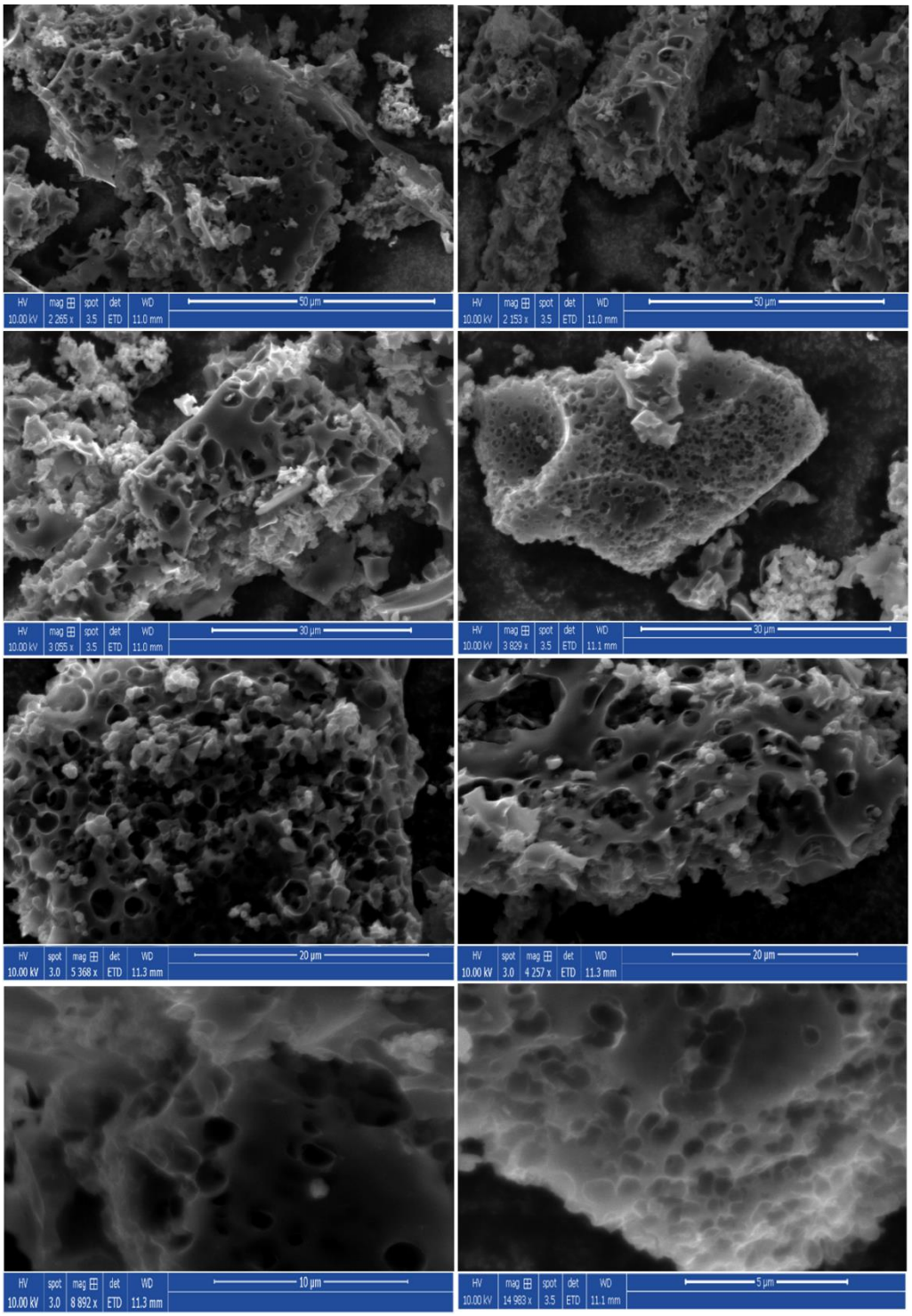


Figure 4.11: SEM micrographs images of PT2600 at high and low magnifications.

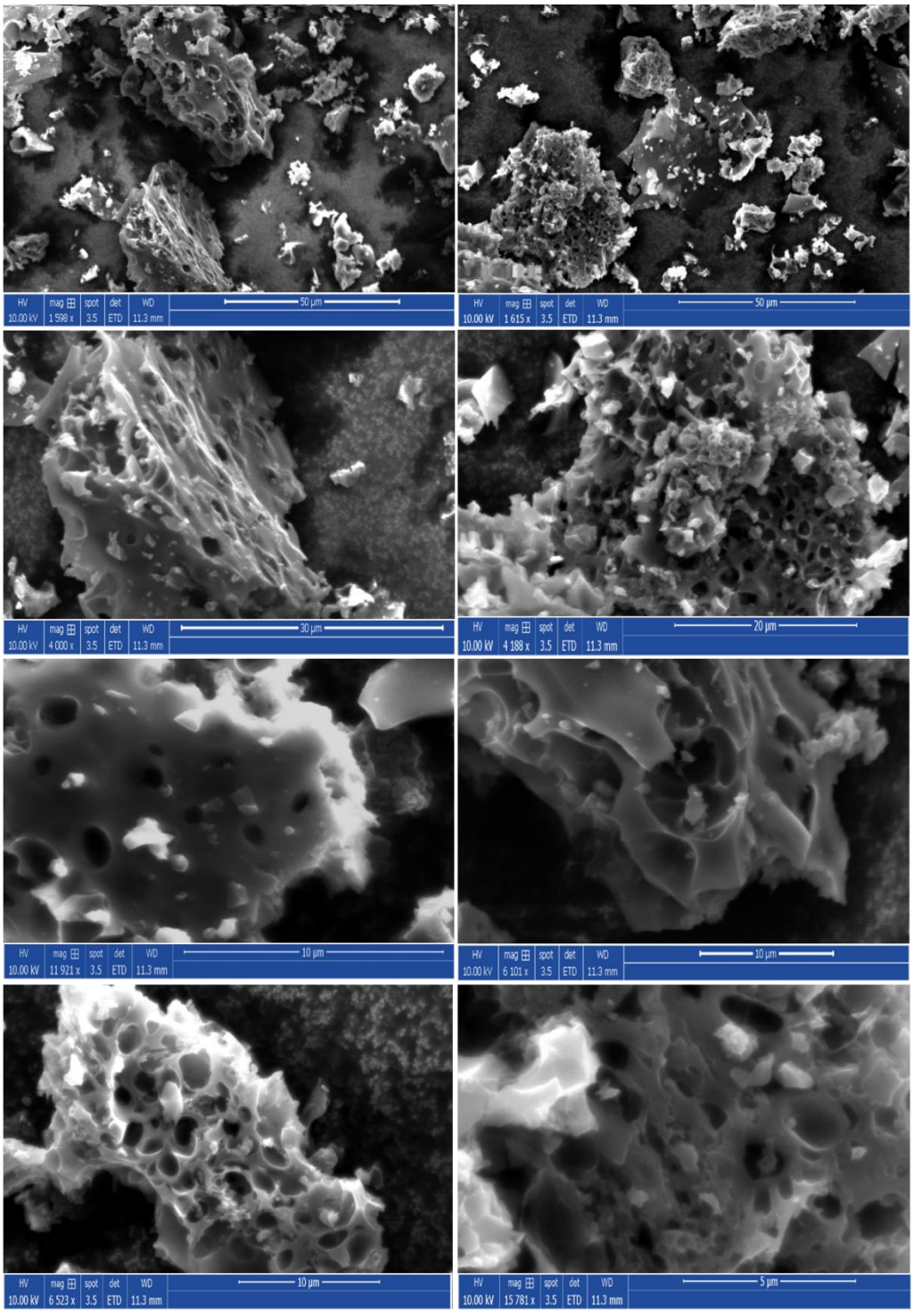


Figure 4.12: SEM micrographs images of PT2600P at high and low magnifications.

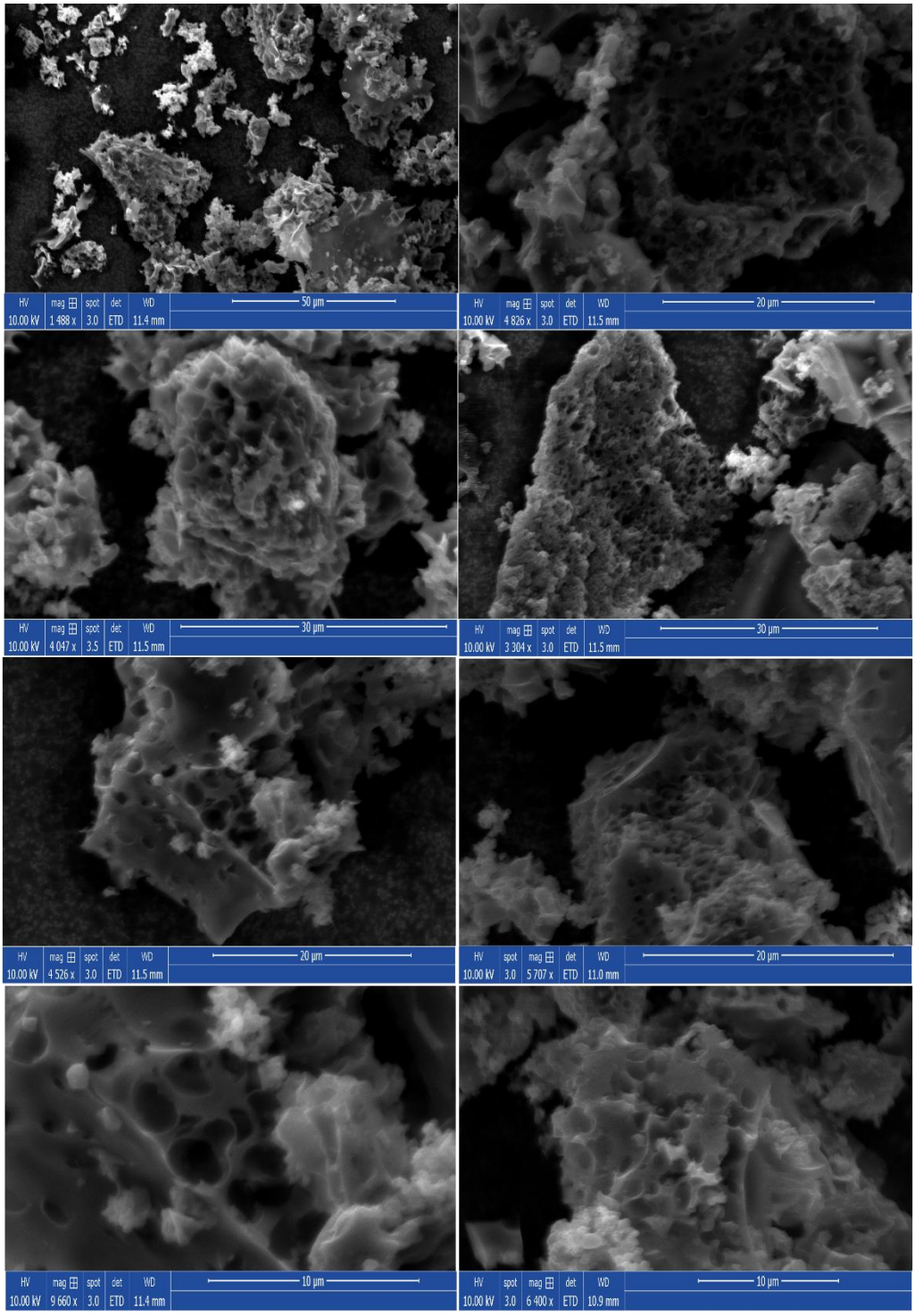


Figure 4.13: SEM micrographs images of PT2700 at high and low magnifications.

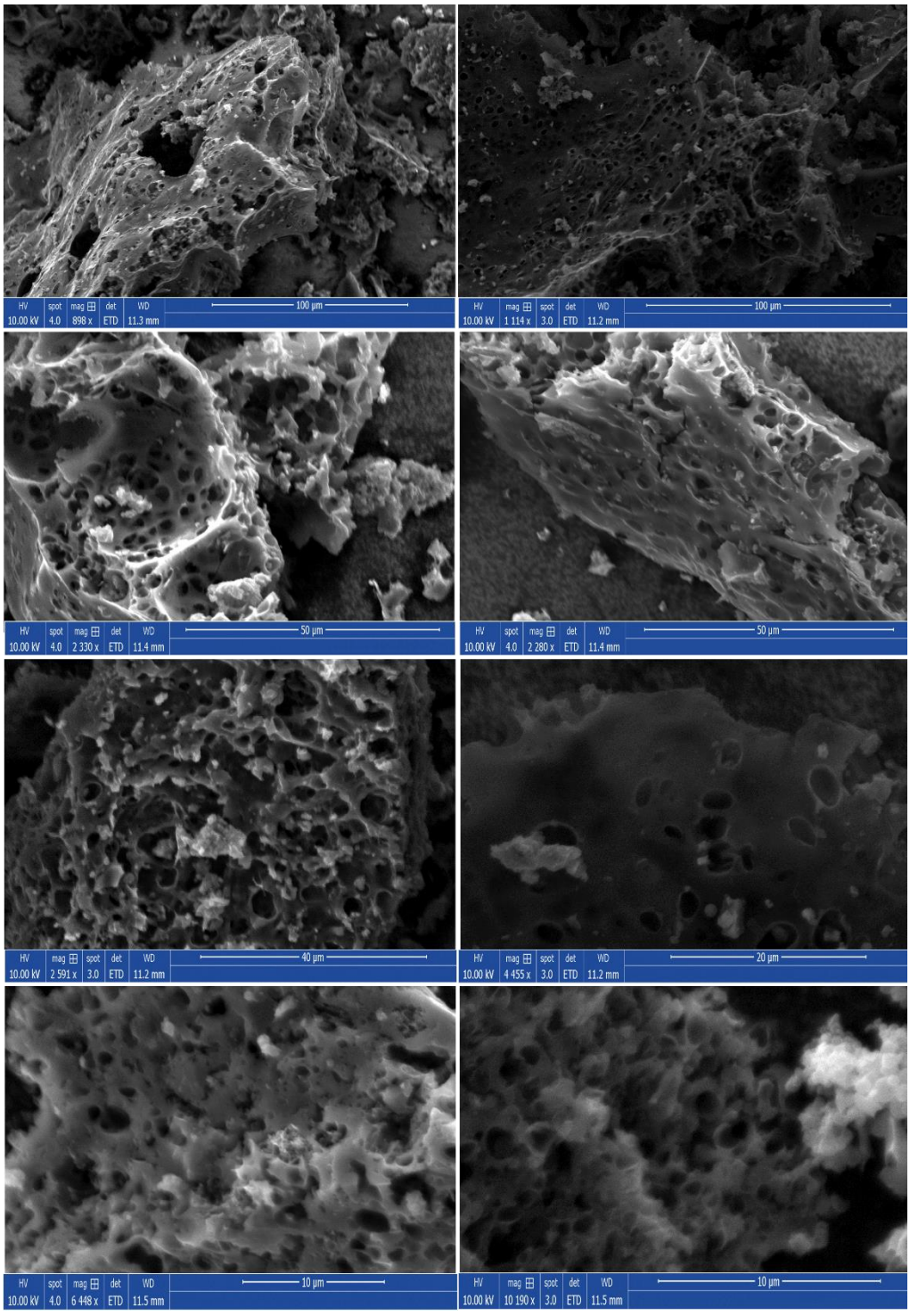


Figure 4.14: SEM micrographs images of PT2700P at high and low magnifications.

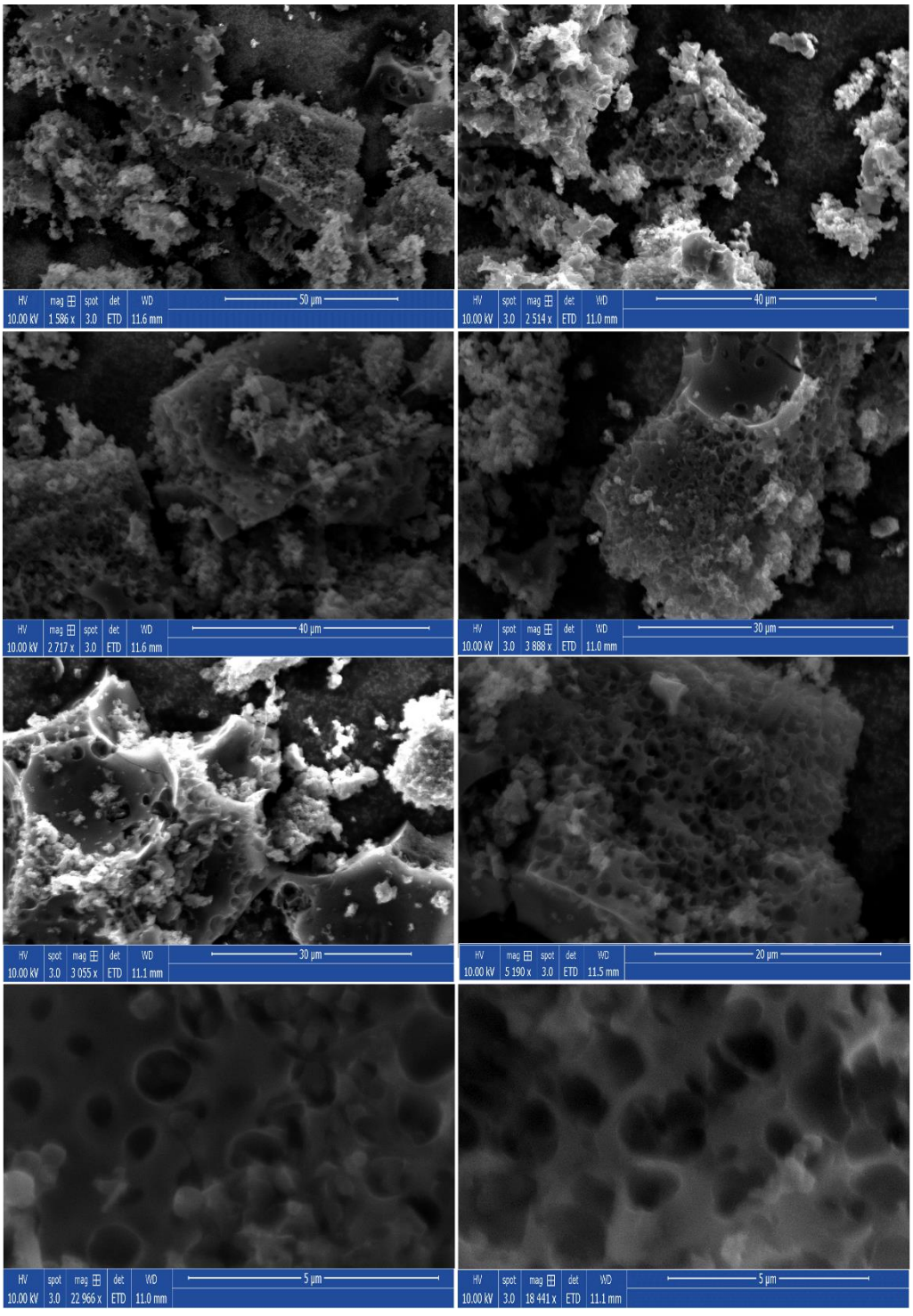


Figure 4.15: SEM micrographs images of PT2800 at high and low magnifications.

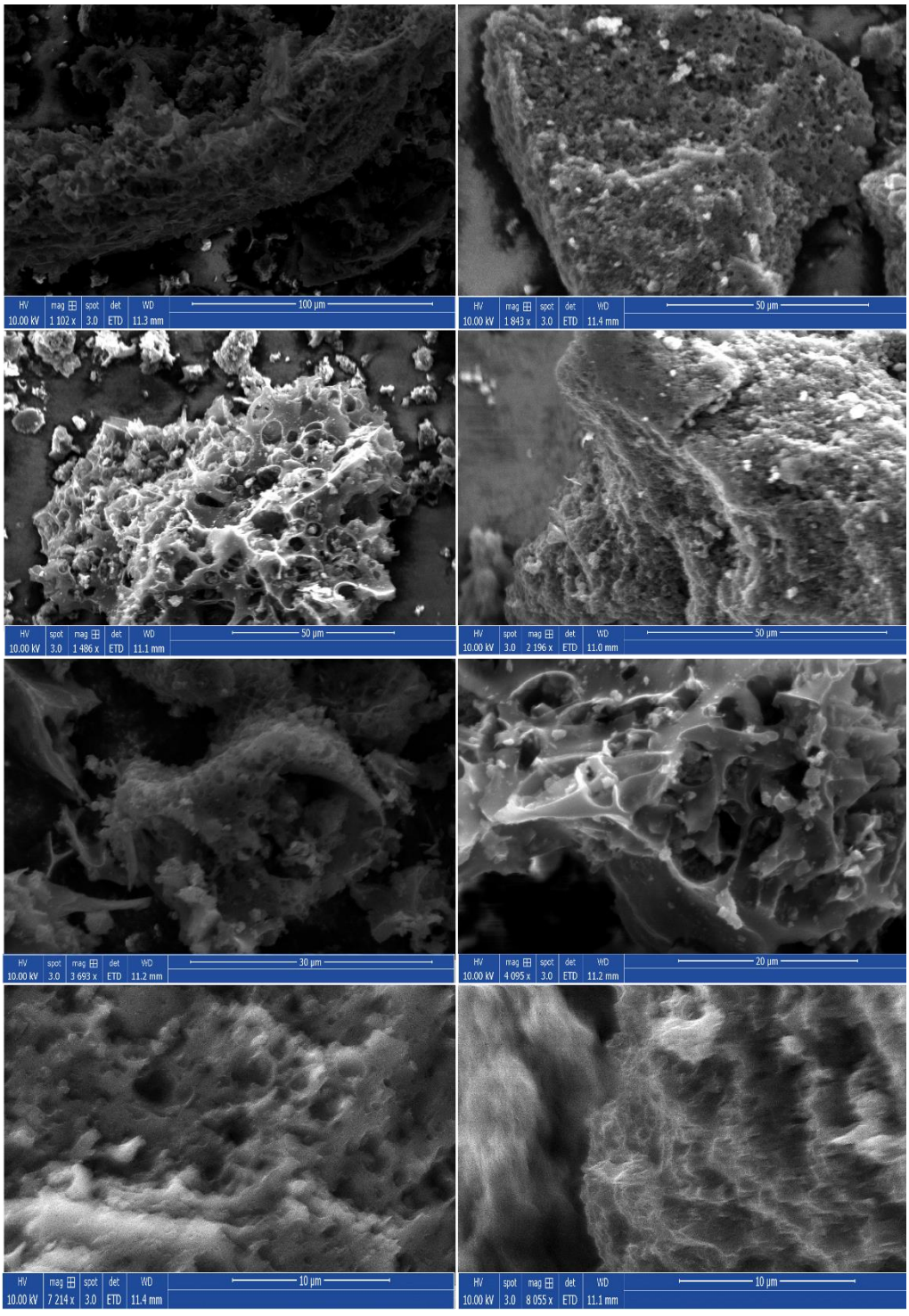


Figure 4.16: SEM micrographs images of PT2800P at high and low magnifications.

4.6.2.6 TEM Analysis

TEM micrographs images of conventional activated carbons are shown in **Figure 4.17**, **Figure 4.19**, and **Figure 4.21**, and those of compactivated carbons are shown in **Figure 4.18**, **Figure 4.20**, and **Figure 4.22**. Both conventional activated carbons and compactivated carbons have wormhole type pores that are typical for activated carbons.[18, 32, 33] It is clear that there is no difference in the pore channel type meaning that compactivation does not alter the nature of the pores. The TEM images for both sets of activated carbons show no clear evidence of the presence of graphitic domains, which is consistent with the XRD patterns **Figure 4.10**.

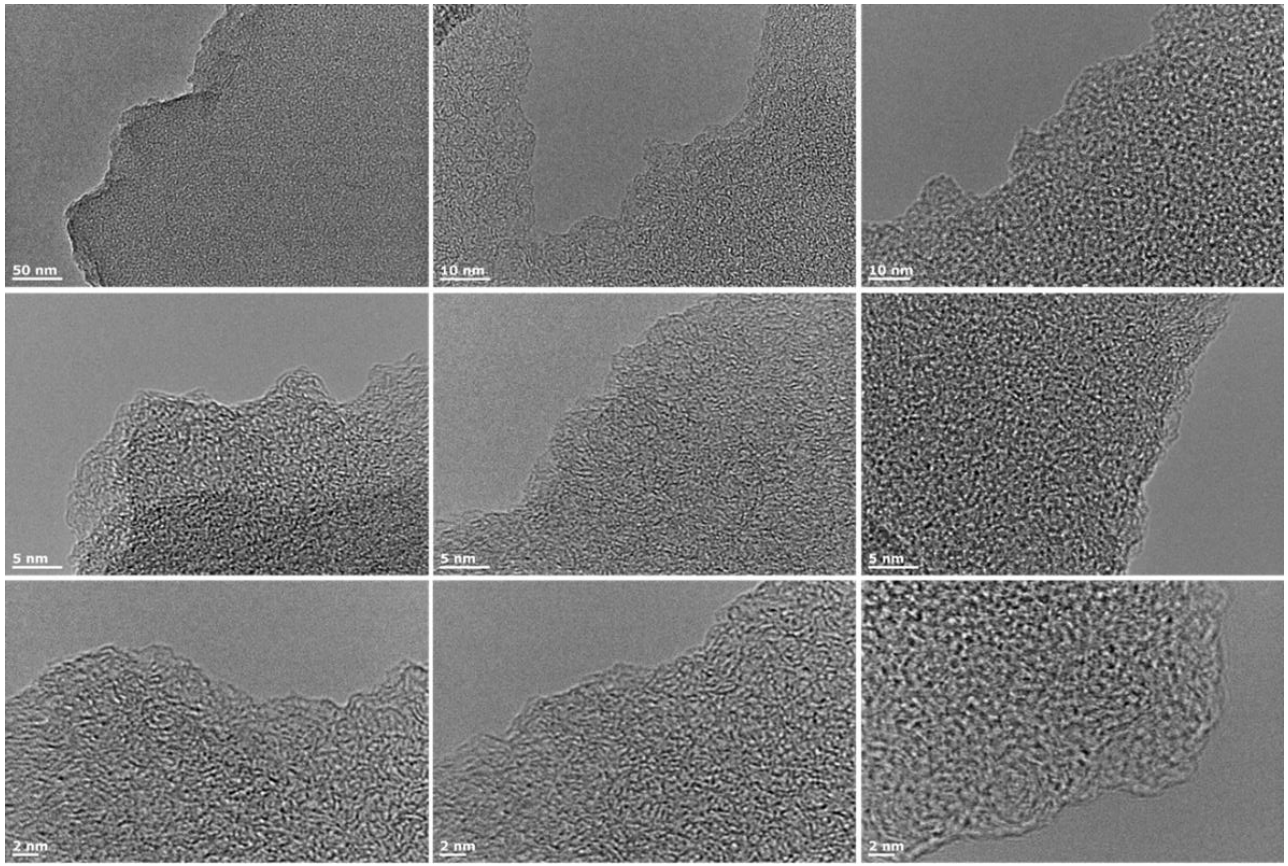


Figure 4.17: TEM micrographs images at low and high magnification of PT2600.

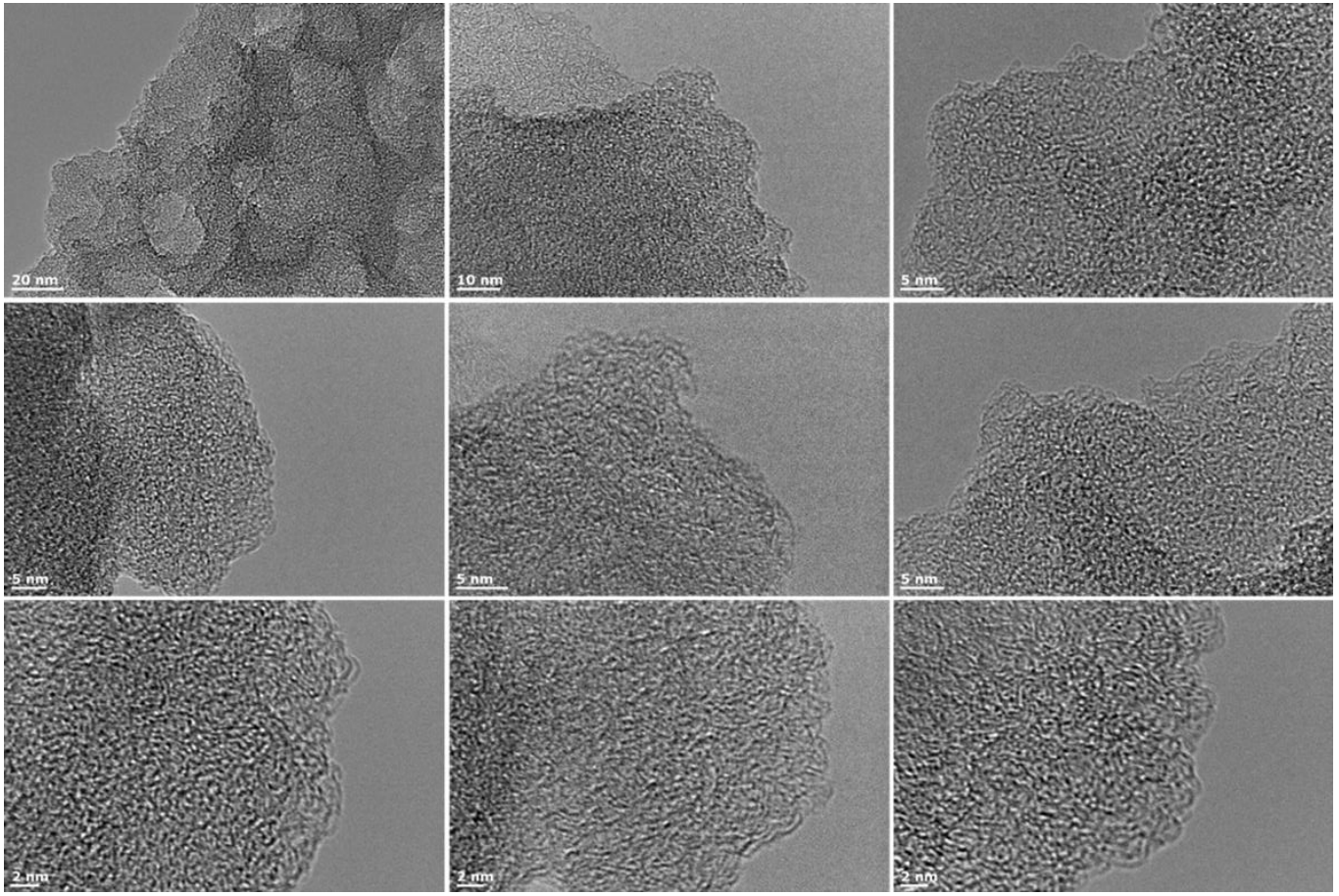


Figure 4.18: TEM micrographs images at low and high magnification of PT2600P.

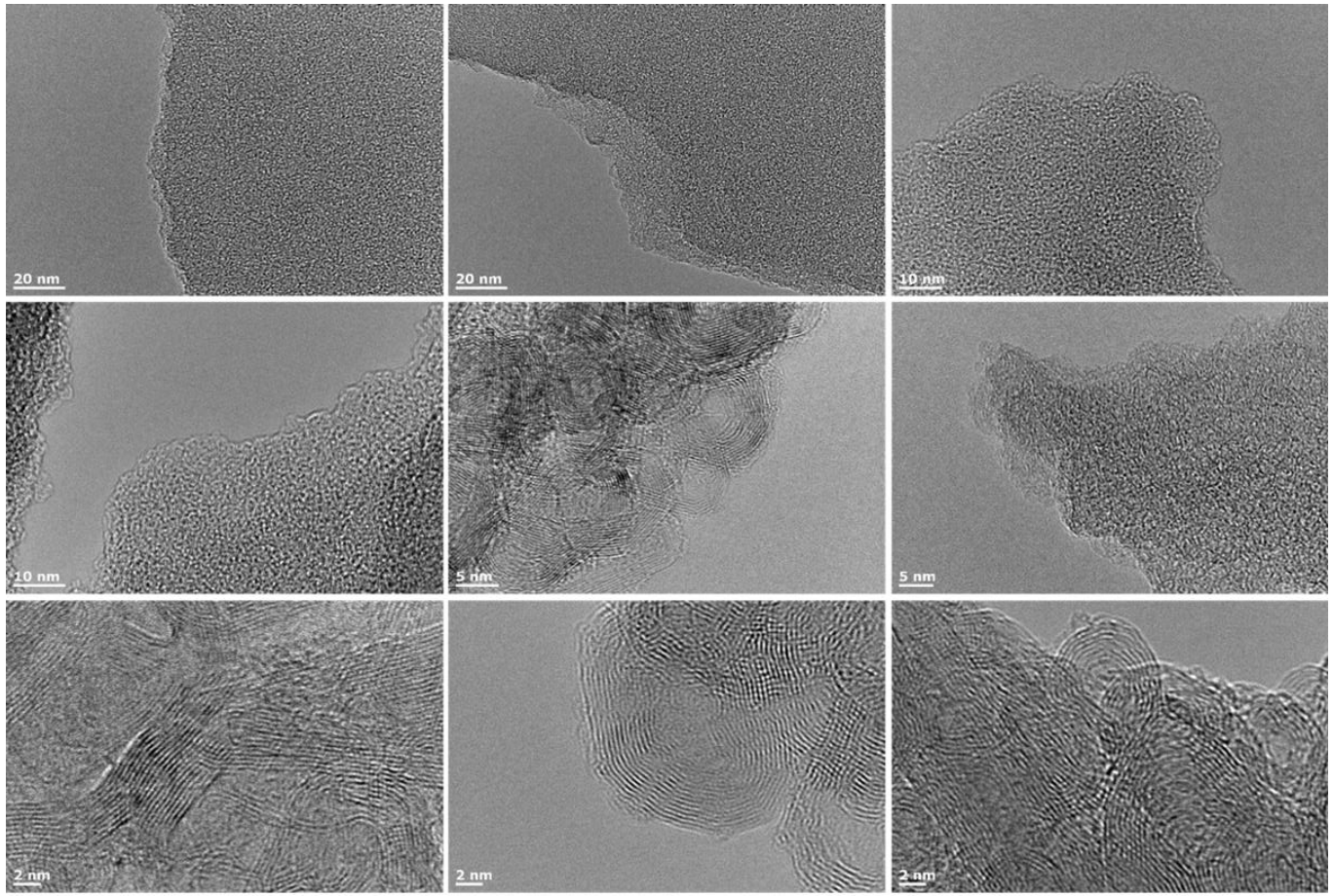


Figure 4.19: TEM micrographs images at low and high magnification of PT2700.

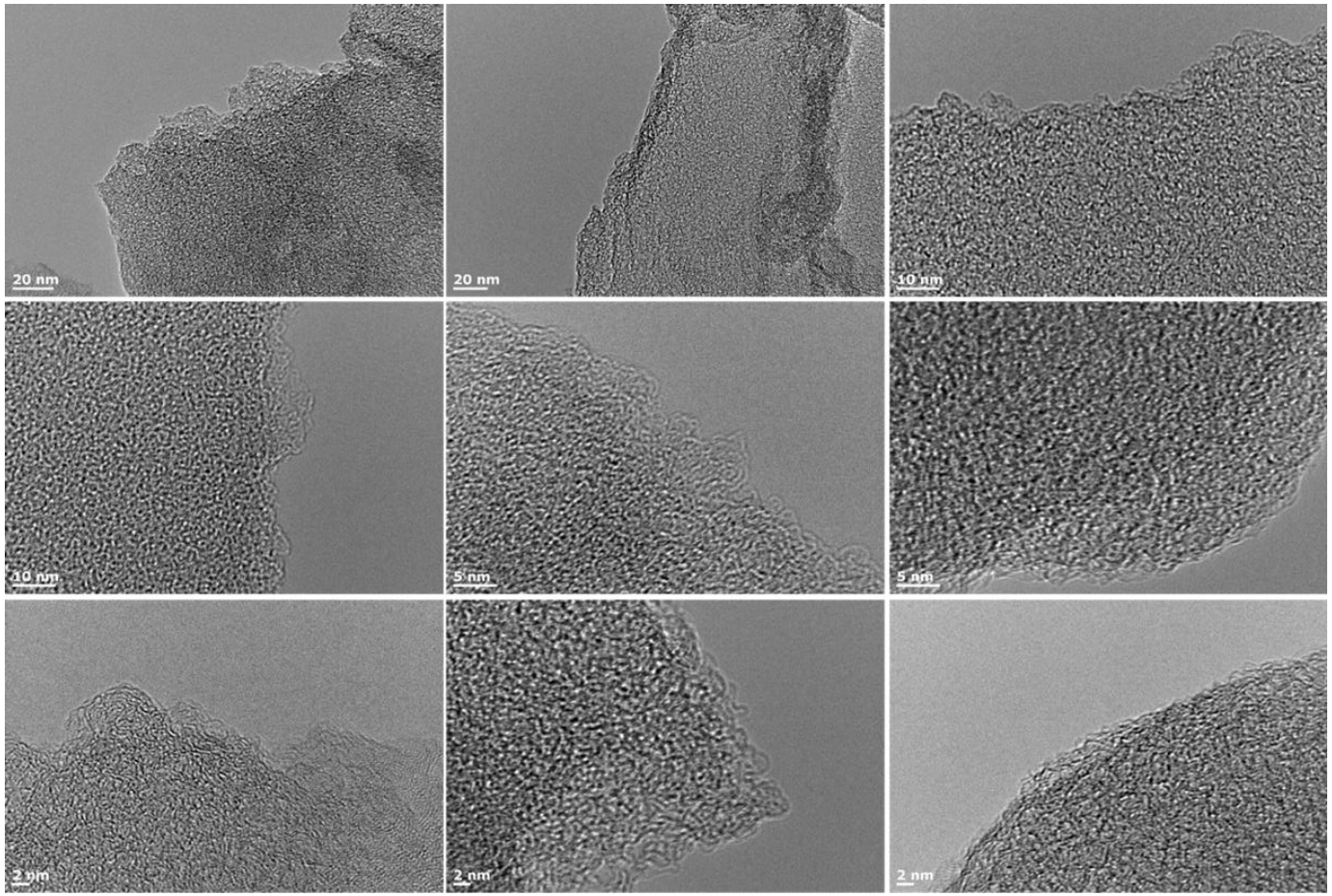


Figure 4.20: TEM micrographs images at low and high magnification of PT2700P.

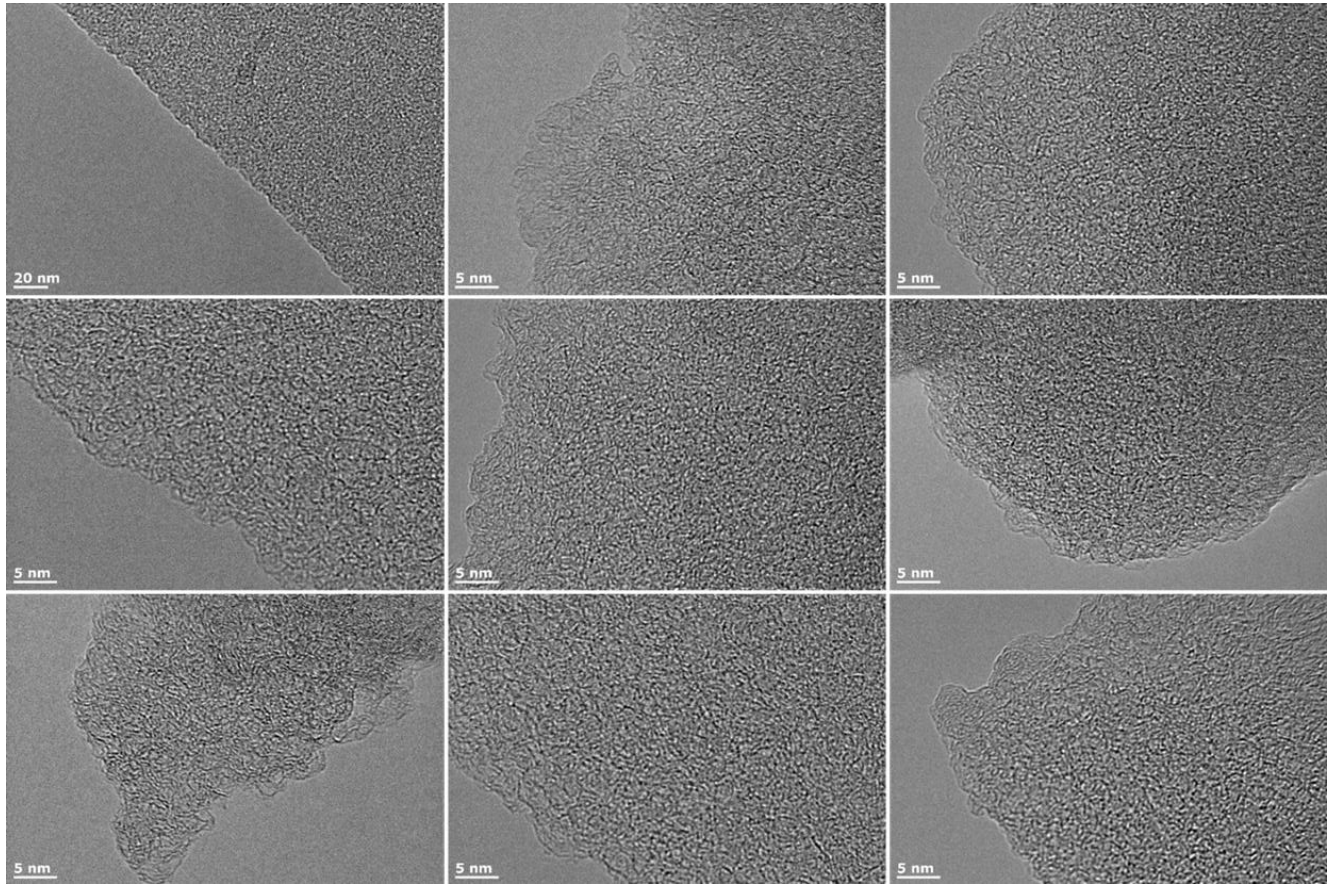


Figure 4.21: TEM micrographs images at low and high magnification of PT2800.

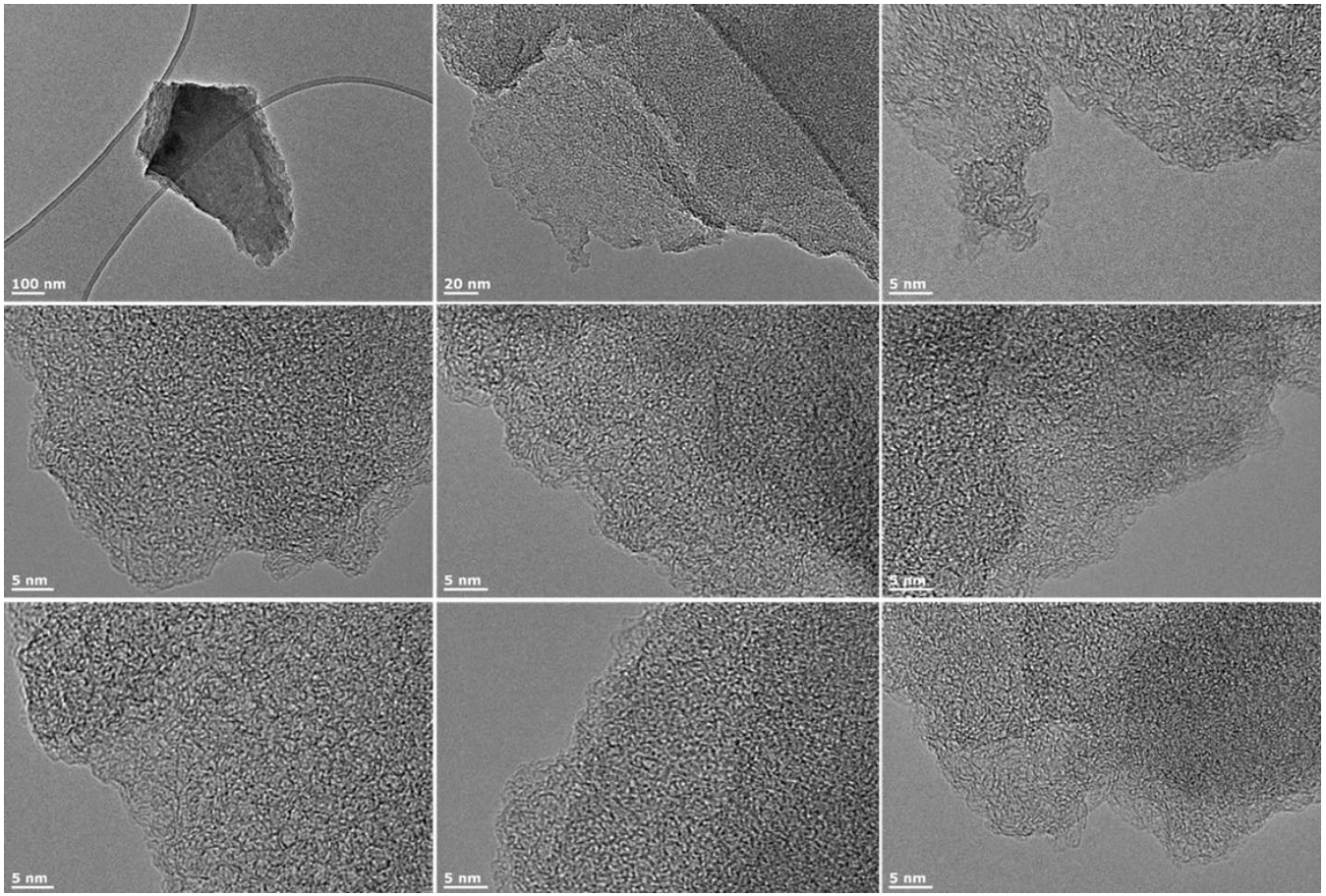


Figure 4.22: TEM micrographs images at low and high magnification of PT2800P.

4.6.2.7 Textural Properties and Porosity Analysis

The nitrogen sorption isotherms and corresponding pore size distributions (PSDs) curves for polythiophene-derived conventional activated carbons (PT2600, PT2700, and PT2800) are presented in **Figure 4.23 A** and **Figure 4.23 B**, respectively, and for compactivated carbons (PT2600P, PT2700P, and PT2800P) are presented in **Figure 4.24 A** and **Figure 4.24 B**, respectively, and the corresponding textural properties of both polythiophene-derived conventional activated carbons and compactivated carbons are summarized in **Table 4.6**.

All the isotherms of non-compacted activated carbons (**Figure 4.23 A**) are mainly type I, according to the IUPAC classification,[34] and reversible with no hysteresis. They exhibit high nitrogen uptake at the low relative pressure (P/Po≤1.0) which indicates that the carbons porosity is mainly composed of micropores and ultra-micropores. It is notable from **Table 4.6**, that all carbons exhibit high surface area in the range of 1300 m^2g^{-1} - 2035 m^2g^{-1} and high pore volumes in the range of 0.7 cm^3g^{-1} and 1.3 cm^3g^{-1}. The sample prepared at the highest temperature (PT2800) has the highest surface area of 2035 m^2g^{-1} whereas sample PT2600 which was prepared at lowest temperature has lowest surface area of 1300 m^2g^{-1} respectively. The generated porosity measured by the amount of nitrogen adsorbed, as activation temperature rises from 600 ^oC to 800 ^oC, is similar to what is known to occur for activated carbons.[7, 8, 23, 24, 32, 33, 35-42]

The nitrogen sorption isotherms for compactivated carbons displayed in **Figure 4.24 A** indicate no significant change in nitrogen isotherm shapes upon compaction. All the isotherms are reversible with no hysteresis and are mainly type I isotherm, with high nitrogen uptake at the low relative pressure (P/Po≤1.0) which indicates that the porosity of the compactivated carbons

mainly arises from micropores. The slight change of the isotherm shapes when the activation temperature raised from 600 °C to 800 °C is due to pore widening and/or in microporosity. Overall, the textural data indicate that the surface area rises from 1300 m^2 g^{-1}, 1561 m^2 g^{-1} and 2035 m^2 g^{-1} for non-compacted carbons to 2048 m^2 g^{-1}, 1933 m^2 g^{-1} and 2250 m^2 g^{-1}, for compactivated samples prepared at 600 °C, 700 °C and 800 °C, respectively. In compactivated carbons, the compression of the KOH/carbon mixture into pellets, leads to closer contact between carbon precursor (polythiophene) and activating agent (KOH) and allow for more efficient use of the KOH and thus generates higher porosity. In all cases compactivation generates higher levels of porosity, which is consistent with previous studies.[8, 23, 24, 32, 33, 35-43]

The pore size distribution curves of conventional activated carbons are presented in **Figure 4.23 B** and the pore sizes are summarized in **Table 4.6**. It is notable that most of the activated carbons exhibited micropores nature with three narrow pore size in the range of microporous and no hardly any pores ≥ 20 Å. Sample PT2600 which activated at low temperature 600 °C has three pore systems centred at in ultra-microporous range and super-microporous 7.33, 9 and 12 Å. PT2700 has only two pore systems in super-microporous range at 9 and 12Å which are also present in PT2600. PT2800 prepared at the highest temperature 800 °C has three pores maxima at 6.5, 8 and 12 Å.

The PSD curves of compactivated carbons in **Figure 4.24 B** indicate that the samples obtained at low temperature 600 ºC (PT2600P) and high temperature 800 ºC (PT2800P) have three pore maxima at 7, 9 and 12, while for sample PT2700P the pore maxima are at 6.5, 9 and 12 Å.

A comparison of **Figure 4.23 B**, **Figure 4.24 B** and **Table 4.6**, shows that; (i) modifying the activating temperature has no significant effect on PSD

apart from a slight broadening and shift towards larger pores as the activation temperature increased, and (ii) Compactivation does not significantly affect the pore size.[8, 23, 31]

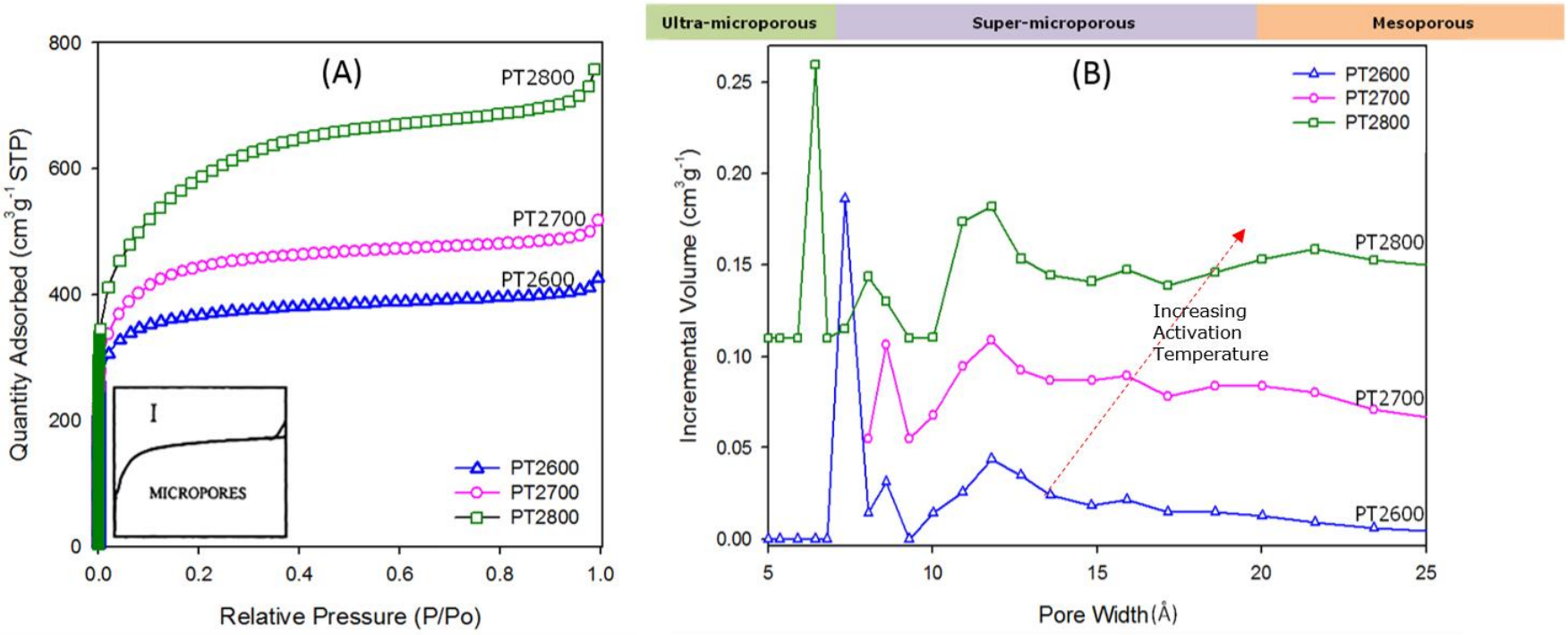


Figure 4.23: (A) N_2 isotherms (ads/des) of conventional activated carbons, and **(B)** Corresponding pore size distribution (PSD) curves.

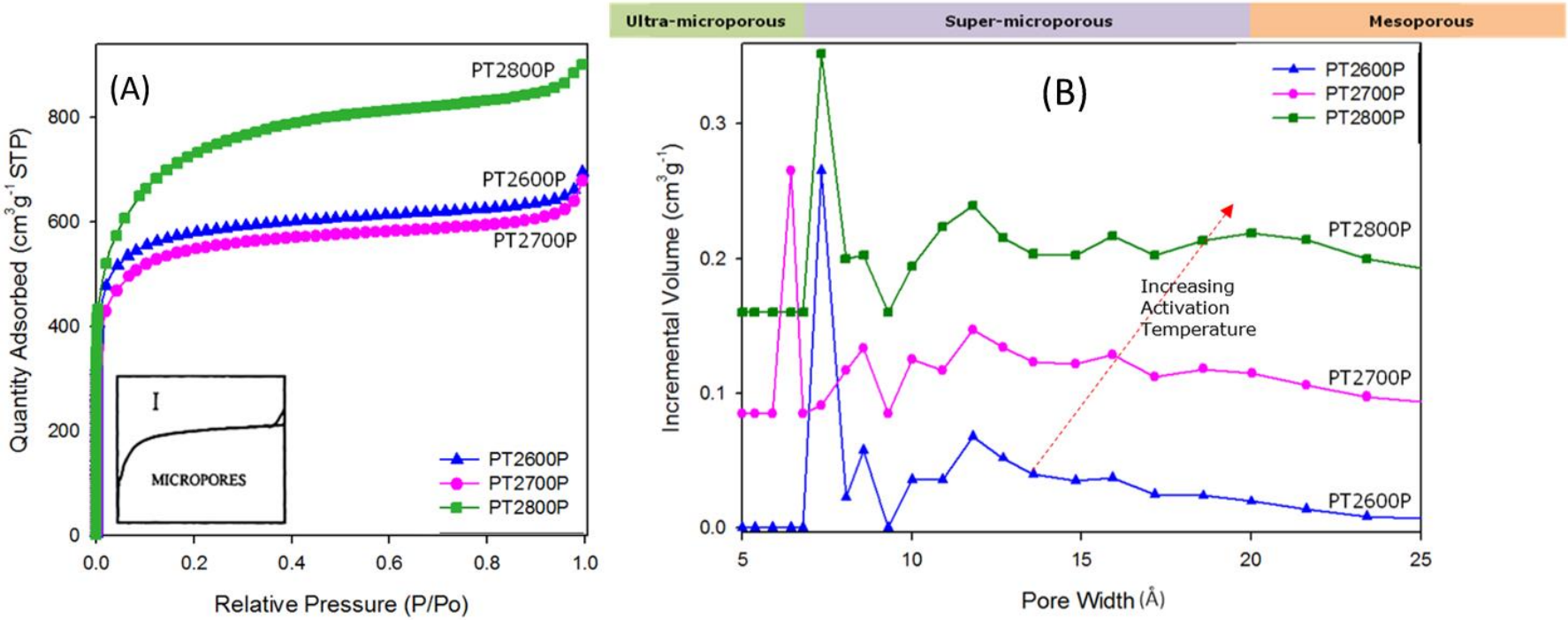


Figure 4.24: (A) N_2 sorption isotherms of compactivated carbons, and **(B)** Corresponding pore size distribution (PSD) curves.

Table 4.6: Textural properties of polythiophene-derived activated and compactivated carbons.

Sample [a]	BET Surface Area [b] (m^2g^{-1})	Pore Volume [c] (cm^3g^{-1})	Pore Size [d] (Å)
PT2600	1300 (1164)	0.70 (0.51)	7.33/8.58/11.79
PT2600P	2048 (1825)	1.10 (0.80)	7.33/8.58/11.79
PT2700	1561 (1371)	0.80 (0.61)	8.58/11.79
PT2700P	1933 (1713)	1.00 (0.75)	6.43/8.58/11.79
PT2800	2035 (1414)	1.30 (0.65)	6.43/8.04/11.79
PT2800P	2250 (1964)	1.44 (0.90)	7.33/8.58/11.79

[a] Carbons are designated as *PT2X* for conventional polythiophene-derived activated carbons, and *PT2XP* for polythiophene-derived compactivated carbons.

[b] The values in the parenthesis refer to micropore surface area.

[c] The values in the parenthesis refer to micropore volume.

[d] Pore size distribution maxima obtained from NLDFT analysis, assuming slit-shaped pores.

4.6.2.8 CO_2 and H_2 Uptake Measurements

Surface area, pore volume and pore size distribution of porous materials have great influence on gas uptake (CO_2 and H_2).[2, 6, 7, 44, 45] The effect of temperature of activation, compaction route, and S content were explored. The samples were characterized according to the experimental procedures given in **Chapter 2**, to determine CO_2 uptake at two different temperatures 0 ^oC and 25 ^oC.

4.6.2.8.1 CO_2 Uptake Measurements

4.6.2.8.1.1 CO_2 Uptake at 0 ^oC and 20 bar

The CO_2 sorption isotherms of non-compacted and compacted polythiophene-derived activated carbons as measured by gravimetric analysis (IGA), over the pressure range (of 0 – 20 bar at 0 ^oC are presented in **Figure 4.25 A** and **Figure 4.25 B** respectively, and **Table 4.7** summarises the amount of CO_2 adsorbed at various pressures (1 and 20 bar). All the CO_2 uptake isotherms of non-compacted activated carbons are completely reversible, with absence of hysteresis between the adsorption and desorption process. There is a good correlation between the CO_2 uptake capacities and textural properties (surface area and micropore volume).

For non-compacted activated carbons (**Figure 4.25 A**), the sample prepared at high activation temperature (PT2800) has the best CO_2 uptake at high pressure (20 bar) of 109.2 wt% (24.8 mmol g^{-1}) due to its high total surface area and micropore surface area by 2035 m^2g^{-1} and 1414 m^2g^{-1}, respectively. However, the sample prepared at lower activation temperature (PT2600) has

the lowest CO_2 uptake of 62.6 wt% (14.2 mmol g^{-1}) due to its low total surface area and micropore area of 1300 m^2g^{-1} and 1164 m^2g^{-1}, respectively.

For compactivated carbons, all the CO_2 uptake isotherms are fully reversible (**Figure 4.25 B**). Sample PT2800P has an excellent CO_2 uptake of 124.7 wt% (28.3 mmol g^{-1}) due to its high textural proprieties; surface area and micropore area of 2550 m^2g^{-1} and 1962 m^2g^{-1}, respectively. On the other hand, sample PT2600P has uptake of 79.92 wt% (18.2 mmol g^{-1}) at 20 bar and 0 ^oC due to its lower textural proprieties: surface area and micropore area of 2048 m^2g^{-1} and 1825 m^2g^{-1}, respectively.

In general, increasing the activation temperature led to increase in the CO_2 uptake, while using compactivation at led to improvement in the porosity and increase in the CO_2 uptake. **Figure 4.26** shows that there is no clear influence of S content on CO_2 uptake at 0 ^oC for both conventional and compactivated carbons.

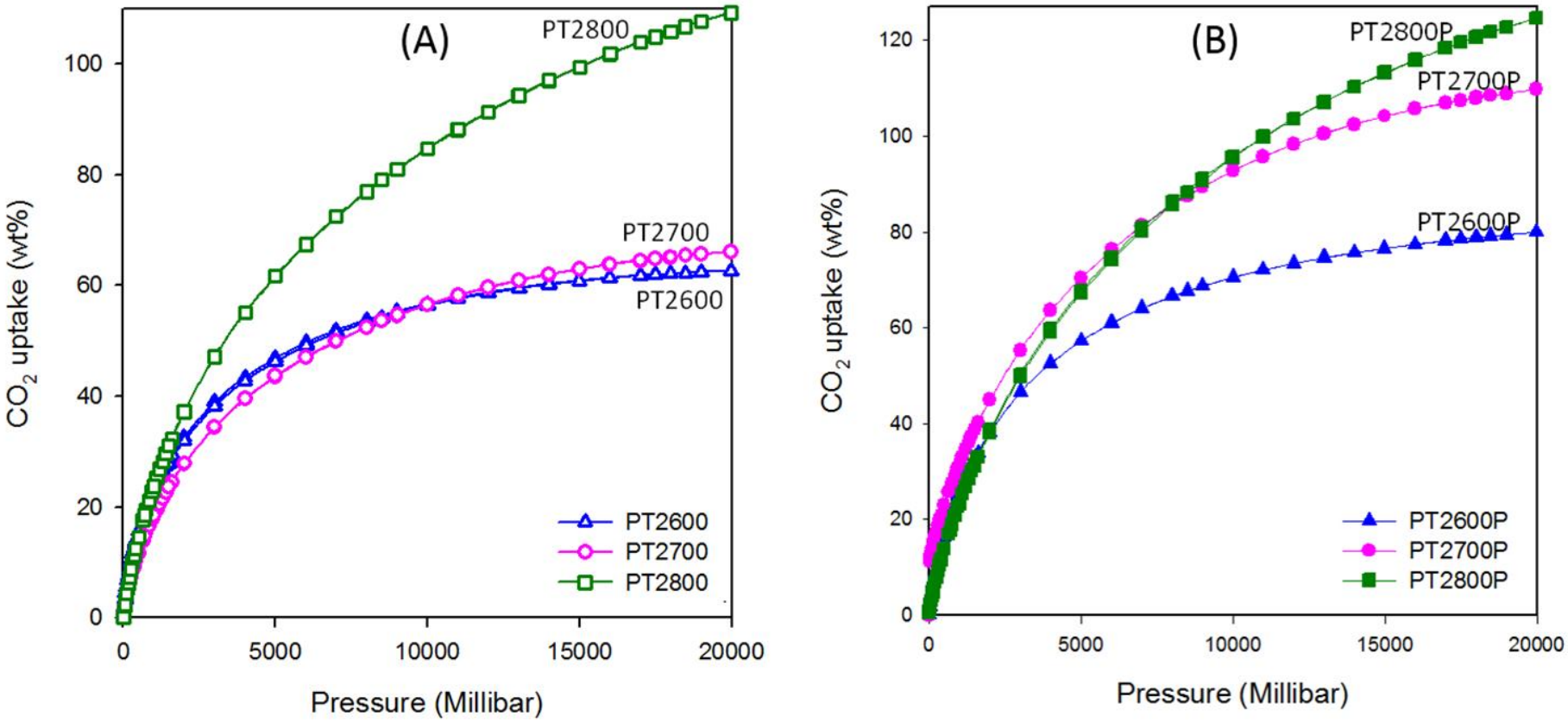


Figure 4.25: CO_2 uptake ***at 0 °C*** of **(A)** Conventional activated carbons **(B)** Compactivated.

Table 4.7: CO_2 uptake data expressed in wt% and $mmolg^{-1}$ respectively ***at 0 °C*** and 0.15 bar, 1 bar, and 20 bar for conventional carbons and compactivated carbons.

Sample	CO_2 Uptake *at 0 °C* [a]					
	0.15 bar		1 bar		20 bar	
	wt%	$mmolg^{-1}$	wt%	$mmolg^{-1}$	wt%	$mmolg^{-1}$
PT2600	7.6	1.74	24.3	5.53	62.6	14.2
PT2600P	7.3	1.66	25.7	5.8	79.9	18.2
PT2700	5.24	1.2	19.54	4.4	66.0	15.01
PT2700P	5.49	1.34	33	7.5	95.3	21.7
PT2800	6.12	1.4	25.33	5.8	109.2	24.8
PT2800P	5.75	1.31	25.28	5.75	124.6	28.3

[a] CO_2 uptake at *0 °C* and various pressures (i.e., 0.15 bar, 1 bar, 20 bar).

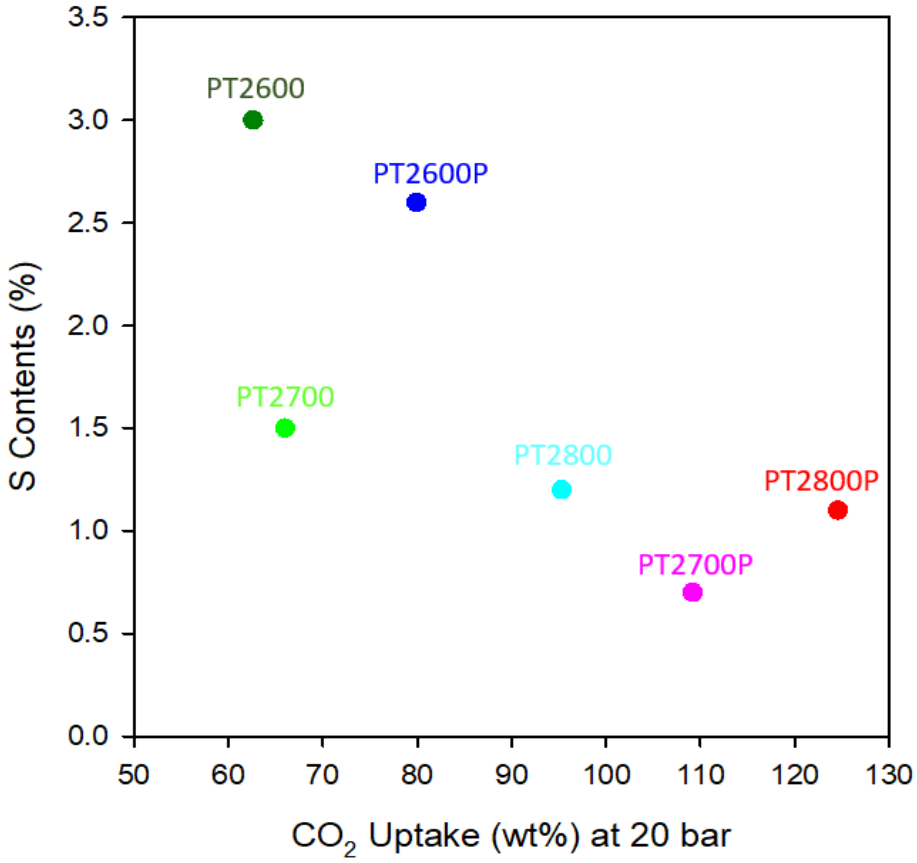


Figure 4.26: Plot showing a relation between sulphur content and CO_2 uptake ***at 20 bar and 0 °C*** of conventional activated carbons and compactivated carbons.

4.6.2.8.1.2 CO_2 Uptake at 25 °C

The CO_2 isotherms of PTh-derived conventional and compactivated carbons as measured by gravimetric over the pressure range 0–20 bar at 25 °C are presented in **Figure 4.27 A** and **B** respectively, and the corresponding CO_2 uptake values at 25 °C and at 0.15 bar, 1 bar and 20 bar are summarized in **Table 4.8**. All the CO_2 uptake isotherms are completely reversible, with near absence of hysteresis between the adsorption and desorption process and there is a good correlation between the CO_2 uptake capacities and textural properties (surface area and micropore volume). For conventional carbons (**Figure 4.27 A**), the sample prepared at the highest activation temperature (PT2800) has the best CO_2 uptake at high pressure (20 bar) of 82.5 wt% (18.8 mmol g^{-1}) due to its high surface area of 2035 m^2g^{-1} and micropore area by 1414 m^2g^{-1}. However, sample prepared at lowest activation temperature (PT2600) has lower CO_2 uptake of 54.4 wt% (12.4 mmol g^{-1}) due to its low total surface area of 1300 m^2g^{-1} and micropore area of 1164 m^2g^{-1}. At low pressure ≤1 bar, PT2600 and PT2800 both have the highest CO_2 by 15.6 and 14.9 wt%, respectively, due to their ultra-micropores of size ≤7. This is simply a reflection of the fact that low pressure CO_2 uptake is dependent on pore size and level of microporosity, and that both samples have such pores; 7.3 to 8.6 Å for PT2600, and 6.3 to 8.58 Å by for PT2800, combined with the high surface area of 1300 m^2g^{-1} and 2035 m^2g^{-1}, respectively. For compactivated carbons (**Figure 4.27**), at high pressure (20 bar) PT2800P has an excellent CO_2 uptake of 92.7 wt% (21.1 mmol g^{-1}) due to its high textural proprieties; surface area of 2550 m^2g^{-1} and micropore area of 1962 m^2g^{-1}, whereas PT2600P achieves 66.3 wt% (15.1 mmol g^{-1}) CO_2 uptake due to its low textural proprieties. For storage of CO_2 onto solid state materials at low pressure (≤1 bar), the size of pores is known to be the main factor. [38, 40, 46-59]

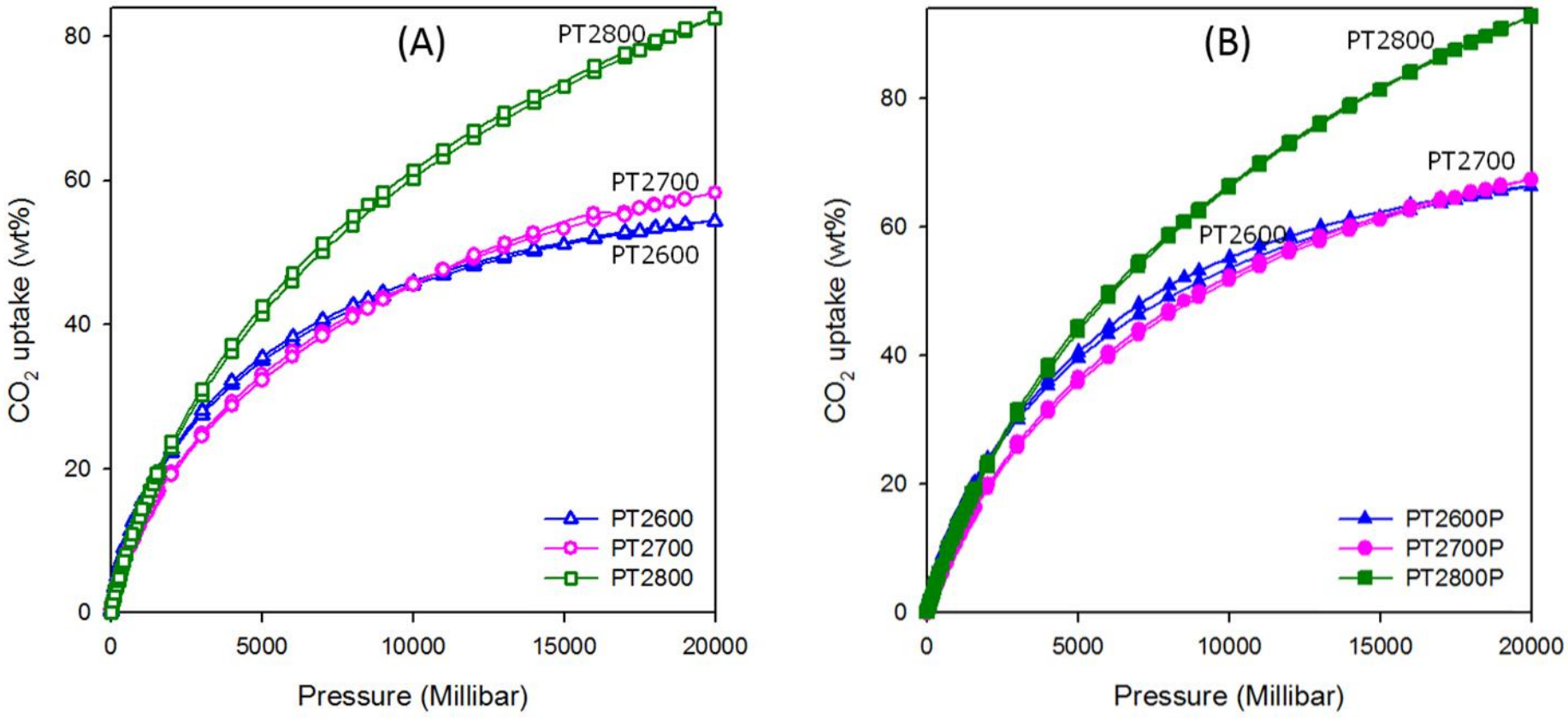


Figure 4.27: CO_2 uptake ***at 25 °C*** and at pressure range of **0-20 bar** for **(A)** Conventional activated carbons, and **(B)** Compactivated carbons.

Table 4.8: CO_2 uptake ***at 25 °C*** expressed in wt% and $mmolg^{-1}$ for conventional and compactivated carbons derived from polythiophene.

Sample	CO_2 Uptake @25 °C [a]					
	0.15 bar		1 bar		20 bar	
	wt %	$mmolg^{-1}$	wt %	$mmolg^{-1}$	wt %	$mmolg^{-1}$
PT2600	4.2	0.96	15.6	3.6	54.4	12.4
PT2600P	3.8	0.87	15.8	3.6	66.3	15.1
PT2700	3.2	0.72	13.2	3	58.2	13.2
PT2700P	4.1	0.93	14.7	3.1	82.6	18.9
PT2800	3.4	0.77	14.9	3.4	82.7	18.8
PT2800P	2.6	0.59	14.2	3.2	92.7	21.1

[a] CO_2 uptake at 25 °C and various pressures (i.e., 0.15 bar, 1 bar, and 20 bar).

4.6.2.9 H_2 Uptake Measurements

The hydrogen storage capacity of polythiophene-derived conventional activated carbons and compactivated carbons was investigated at low temperature of -196 ^oC by using a Hiden Intelligent Gravimetric Analyzer (IGA-003) in the pressure range of 0–20 bar according to the experimental procedures given in **Chapter 2**. The excess hydrogen uptake isotherms of conventional and compactivated carbons are shown in **Figure 4.28 A** and **Figure 4.28 B** respectively, and at low pressure (0-1 bar) in **Figure 4.29 A** and **Figure 4.29 B**. The corresponding excess hydrogen uptake at 1 bar and 20 bar is summarized in **Table 4.9.**

For conventional carbons (**Figure 4.28 A**), sample PT2800 and PT2700 both have moderate H_2 uptake at 20 bar of 4.2 wt% and 3.1 wt%, which is consistent with their surface area of 2035 and 1561 m^2g^{-1} respectively and pore volume of 1.30 cm^3g^{-1} and 1 cm^3g^{-1}, respectively. However, PT2600 has the lowest H_2 uptake of 2.4 wt% due to its lower surface area of 1300 m^2g^{-1} and pore volume by 0.70 cm^3g^{-1}. In addition, at low pressure (1 bar) sample PT2800 has the highest H_2 uptake of 2.2 wt% due to its high surface area by 2035 m^2g^{-1} as well as the presence of ultra-micropores of size 6.43 Å.

For compactivated carbons (**Figure 4.28 B**), sample PT2800P and PT2600P both have relatively high H_2 uptake at high pressure (20 bar) of 4.8 wt% and 3.9 wt%, respectively due to their higher surface area of 2550 m^2g^{-1} and 2048 m^2g^{-1}, respectively, and pore volume of 1.44 cm^3g^{-1} and 1.10 cm^3g^{-1}, respectively while sample PT2700P has H_2 uptake of 3.4 wt% due to its lower surface area of 1933 m^2g^{-1} and pore volume by 1 cm^3g^{-1}. For sample PT800P, it is clear the effect of compactivation combined with increasing activation temperature raises H_2 uptake to 4.8 wt%.

Figure 4.30 show a near linear relation between the BET surface area and H_2 uptake at high pressure 20 bar and -196 ^oC of conventional and compactivated carbons. However, **Figure 4.31 and Figure 4.32** show Plot showing no relation between sulfur content and H_2 uptake at 20 bar and -196 ^oC and between s contents and BET surfaces area.

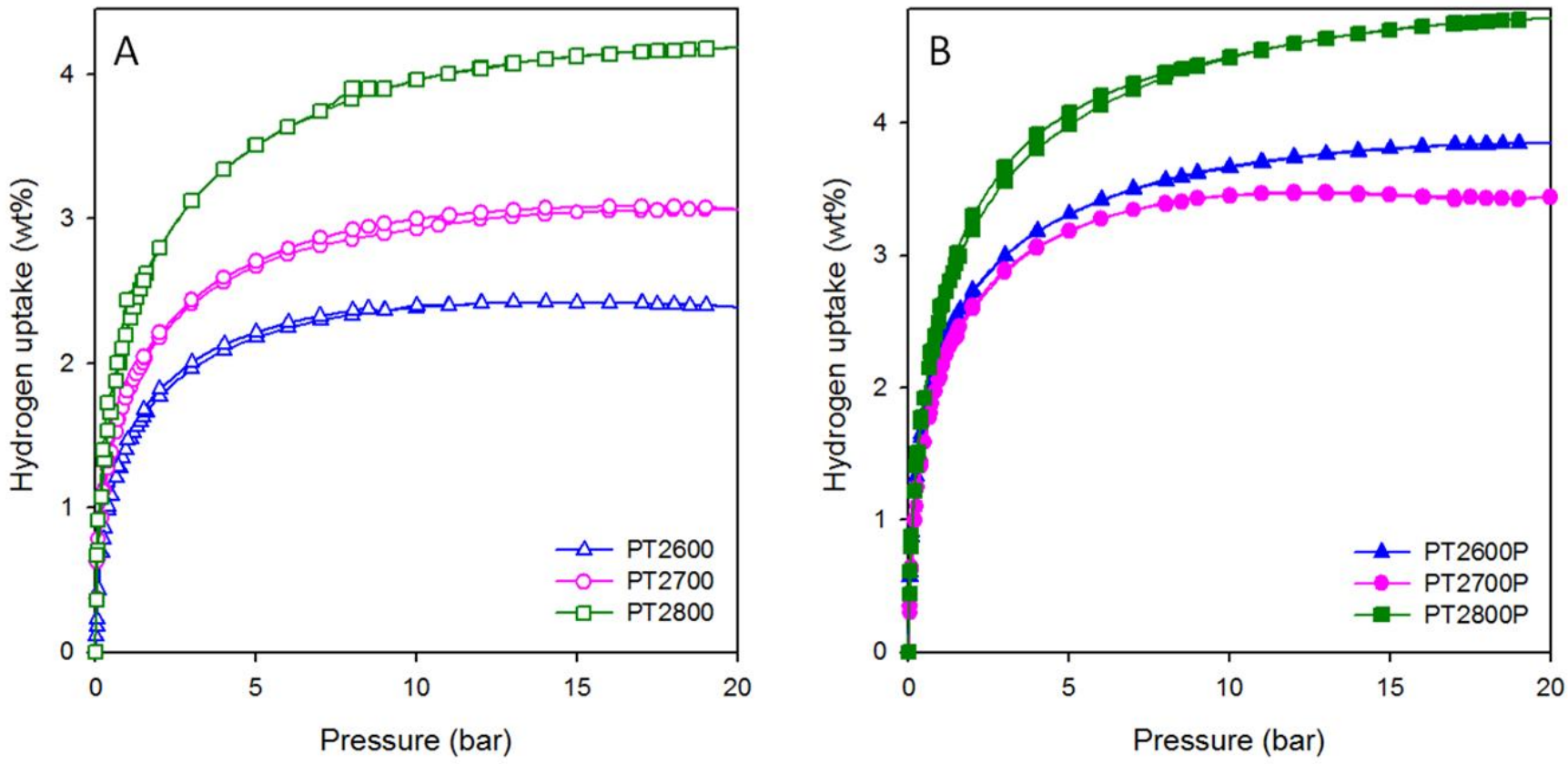


Figure 4.28: H_2 uptake ***at 20 bar*** and *at -196 °C* of **(A)** Conventional activated carbons, and **(B)** Compactivated carbons.

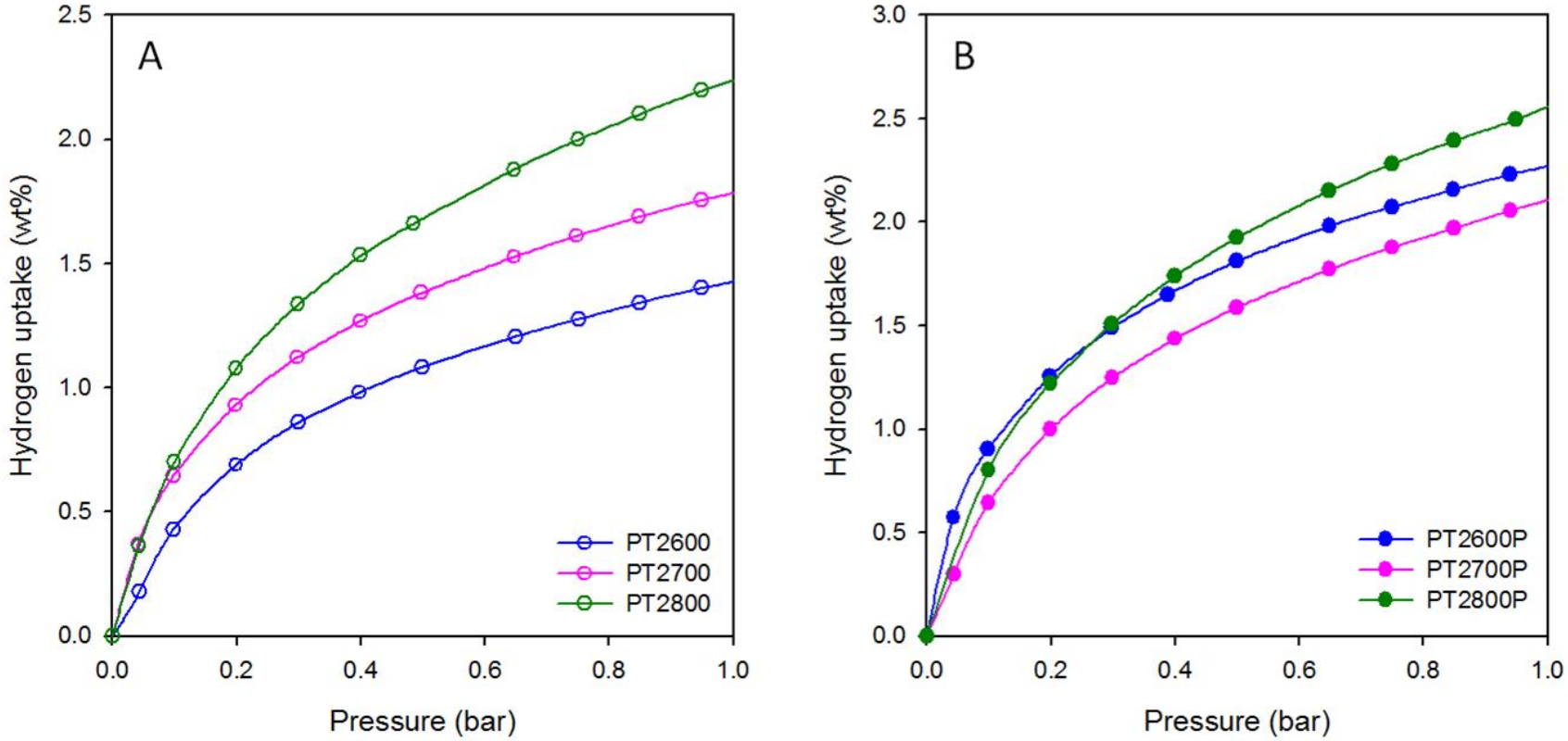


Figure 4.29: H_2 uptake ***at 1 bar*** and *at -196 °C* of **(A)** Conventional activated carbons, and **(B)** Compactivated carbons.

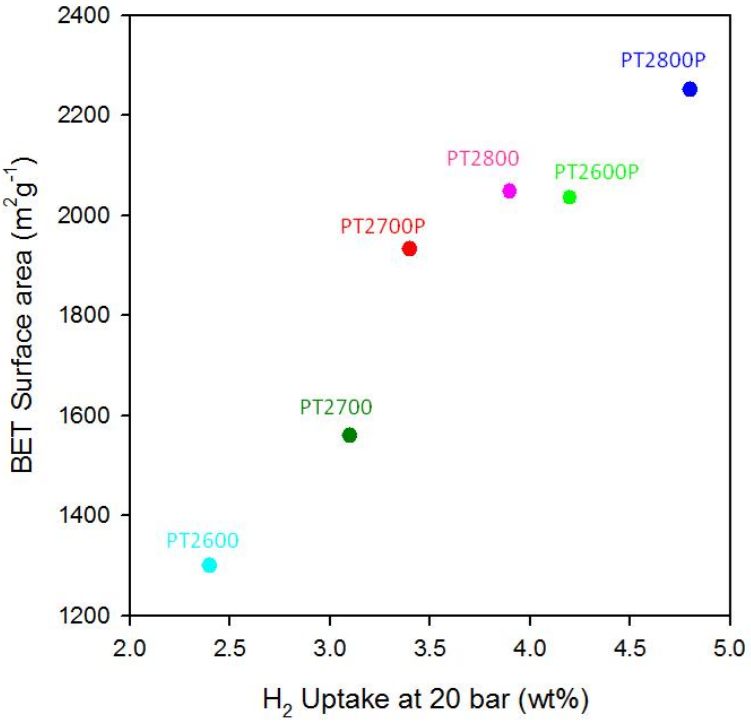


Figure 4.30: Plot showing a near linear relation between the BET surface area and H_2 uptake ***at high pressure 20 bar and -196 °C*** of conventional and compactivated carbons.

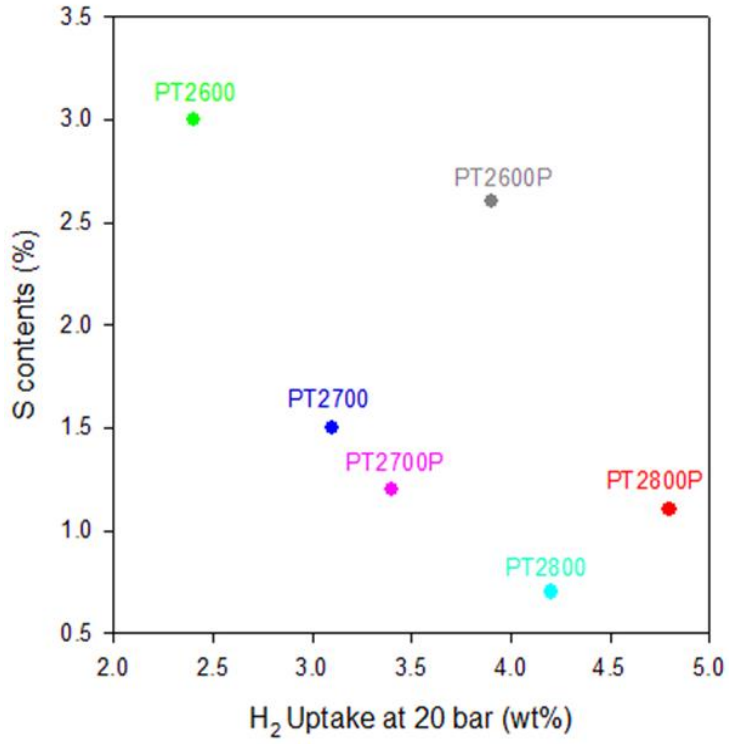


Figure 4.31: Plot showing no relation between sulfur content and H_2 uptake ***at 20 bar and -196 °C*** of conventional and compactivated carbons.

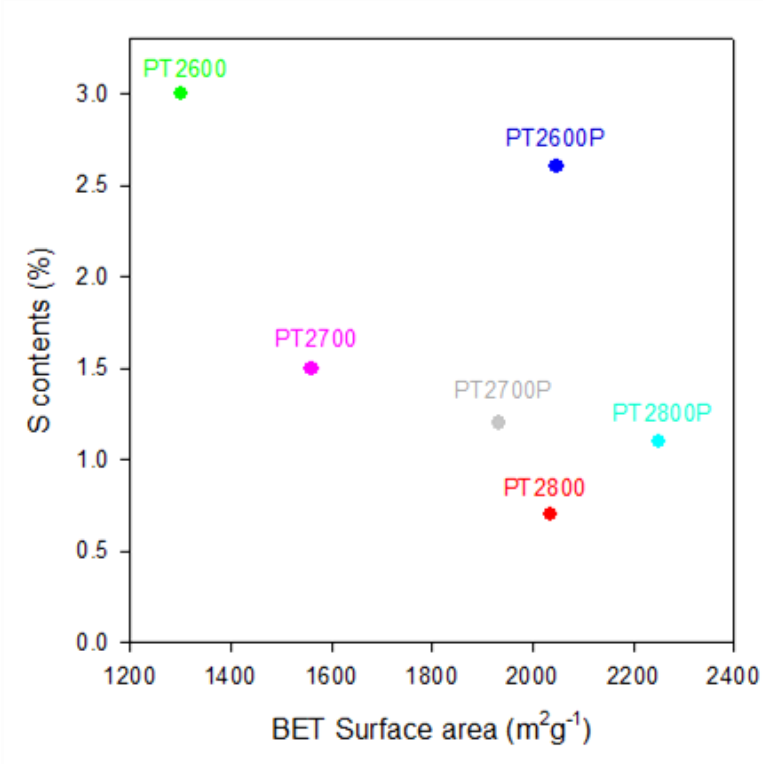


Figure 4.32: Plot showing relation between sulfur content and BET surface area of conventional and compactivated carbons.

Table 4.9: Excess H_2 uptake *at -196 °C* expressed in wt% of conventional activated carbons and compactivated carbons derived from polythiophene at various temperature 600 °C, 700 °C, and 800 °C.

Sample	H_2 Uptake (wt %)	
	1 bar	20 bar
PT2600	1.4	2.4
PT2600P	2.34	3.85
PT2700	1.8	3.1
PT2700P	2.17	3.44
PT2800	2.2	4.2
PT2800P	2.56	4.8

4.6.2.9.1.1 Conclusions

Polythiophene-derived activated carbons have been successfully obtained *via* one-step chemical activation using KOH as the activating agent and polythiophene as a carbon precursor with low KOH/PTh ratio of 2:1 to produce porous carbons. The choice of PTh which has been successfully prepared *via* easy one-step using $FeCl_3$ proves to be an excellent carbon precursor to produce cheap adsorbents with attractive textural properties such as high surface area of 2550 m^2g^{-1} and ultra-microporous nature and pore volume of 1.44 cm^3g^{-1}. Compaction before thermochemical activation leads to increase the porosity but without any significant changes in pore size and PSD compare to conventional ACs. The compaction method works for both highly activated and lowly activated carbons. The textural properties of generated ACs were tailored by modifying temperature of activation in the range of 600- 800 ^oC. Thus, an increase of temperature causes a gradual rise of surface area. in case of conventional activated carbons, sample PT2800 which was prepared at high activation temperature of 800 ^oC has high surface area of 2035 m^2g^{-1} pore volume of 1.3 cm^3g^{-1} with micropores of size 0.7- 1.1 nm with high CO_2 uptake of 90.1 wt%, and achieves excess hydrogen uptake of 4.2 wt% at -196 ^oC and 20 bar, while PT2600 obtained at low activation temperature (600 ^oC) has lower surface area by 1300 m^2g^{-1} with low CO_2 uptake by 52.4 wt%. However, in case of compactivated activated carbons, PT2800P sample has high surface area of 2250 m^2g^{-1}, pore volume of 1.6 cm^3g^{-1} with no change in the micropores size range of 0.7- 1.1 nm. The higher porosity resulted in an increase in gas uptake; excess H_2 storage capacity at -196 ^oC and 20 bar of 4.8 wt%, and CO_2 uptake of 91.8 wt%. The generated PTh-derived activated and compactivated carbons have sulphur contents of 0.7–3 wt%, but no influence of sulphur content on CO_2 capture and Hydrogen uptake was observed.

4.7 References

1. M. Sevilla and R. Mokaya, *Energy Environ. Sci.*, 2014, **7**, 1250-1280.
2. J. C. Wang and S. Kaskel, *J. Mater. Chem.*, 2012, **22**, 23710-23725.
3. T. Otowa, Y. Nojima and T. Miyazaki, *Carbon*, 1997, **35**, 1315-1319.
4. L. L. Zhang and X. S. Zhao, *Chem. Soc. Rev.*, 2009, **38**, 2520-2531.
5. L. Wei and G. Yushin, *Nano Energy*, 2012, **1**, 552-565.
6. Y. D. Xia, Z. X. Yang and Y. Q. Zhu, *J. Mater. Chem. A*, 2013, **1**, 9365-9381.
7. M. Sevilla and R. Mokaya, *Energy Environ Sci.*, 2014, **7**, 1250-1280.
8. B. Adeniran and R. Mokaya, *Nano Energy*, 2015, **16**, 173-185.
9. W. Z. Shen and W. B. Fan, *J. Mater. Chem. A*, 2013, **1**, 999-1013.
10. J. P. Paraknowitsch and A. Thomas, *Macromol. Chem. Phys.*, 2012, **213**, 1132-1145.
11. W. Kicinski, M. Szala and M. Bystrzejewski, *Carbon*, 2014, **68**, 1-32.
12. Y. D. Xia, Y. Q. Zhu and Y. Tang, *Carbon*, 2012, **50**, 5543-5553.
13. M. Sankaran and B. Viswanathan, *Carbon*, 2006, **44**, 2816-2821.
14. S. Choi, J. H. Drese and C. W. Jones, *ChemSusChem*, 2009, **2**, 796-854.
15. Y. Yurum, A. Taralp and T. N. Veziroglu, *Int. J. Hydrogn. Energy*, 2009, **34**, 3784-3798.
16. D. S. Su and R. Schlögl, *ChemSusChem*, 2010, **3**, 136-168.
17. Y. F. Jia, B. Xiao and K. M. Thomas, *Langmuir*, 2002, **18**, 470-478.
18. M. Sevilla and A. B. Fuertes, *Microporous Mesoporous Mat.*, 2012, **158**, 318-323.
19. Y. S. Shin, G. Fryxell, W. Y. Um, K. Parker, S. V. Mattigod and R. Skaggs, *Adv. Funct. Mater.*, 2007, **17**, 2897-2901.
20. M. Sevilla, A. B. Fuertes and R. Mokaya, *Int. J. Hydrogen Energy*, 2011, **36**, 15658-15663.
21. C. H. Choi, S. H. Park and S. I. Woo, *Green Chem.*, 2011, **13**, 406-412.
22. G. Hasegawa, K. Kanamori, K. Nakanishi and T. Hanada, *Carbon*, 2010, **48**, 1757-1766.

23. N. Balahmar, A. C. Mitchell and R. Mokaya, *Adv. Energy Mater.*, 2015, **5**.

24. N. Balahmar, A. M. Lowbridge and R. Mokaya, *J. Mater. Chem. A*, 2016, **4**, 14254-14266.

25. M. Cox and R. Mokaya, *Sustainable Energy & Fuels*, 2017, **1**, 1414-1424.

26. U. Olgun and M. Gülfen *RSC Adv.*, 2014, **4**, 25165-25171.

27. M. R. Karim, C. J. Lee and M. S. Lee, *J. Polym. Sci. Pol. Chem.*, 2006, **44**, 5283-5290.

28. C. Bora, R. Pegu, B. J. Saikia and S. K. Dolui, *Polym. Int.*, 2014, **63**, 2061-2067.

29. F. Wu, J. Z. Chen, R. J. Chen, S. X. Wu, L. Li, S. Chen and T. Zhao, *J. Phys. Chem. C*, 2011, **115**, 6057-6063.

30. Y. N. Li, G. Vamvounis and S. Holdcroft, *Macromolecules*, 2002, **35**, 6900-6906.

31. E. Haffner-Staton, N. Balahmar and R. Mokaya, *J. Mater. Chem. A*, 2016, **4**, 13324-13335.

32. B. Adeniran and R. Mokaya, *J. Mater. Chem. A*, 2015, **3**, 5148-5161.

33. N. Balahmar, A. S. Al-Jumialy and R. Mokaya, *J. Mater. Chem. A*, 2017, **5**, 12330-12339.

34. K. S. W. Sing, D. H. Everett, R. A. W. Haul, L. Moscou, R. A. Pierotti, J. Rouquerol and T. Siemieniewska, *Pure Appl. Chem.*, 1985, **57**, 603-619.

35. M. Sevilla, A. B. Fuertes and R. Mokaya, *Energy Environ. Sci.*, 2011, **4**, 1400-1410.

36. H. M. Coromina, D. A. Walsh and R. Mokaya, *J. Mater. Chem.*, 2016, **4**, 280-289.

37. H. M. Coromina, B. Adeniran, R. Mokaya and D. A. Walsh, *J. Mater. Chem. A*, 2016, **4**, 14586-14594.

38. B. Adeniran and R. Mokaya, *Chem. Mater.*, 2016, **28**, 994-1001.

39. W. Sangchoom and R. Mokaya, *ACS Sustainable Chem. Eng.*, 2015, **3**, 1658-1667.

40. B. Adeniran, E. Masika and R. Mokaya, *J. Mater. Chem. A*, 2014, **2**, 14696-14710.

41. M. Sevilla, W. Sangchoom, N. Balahmar, A. B. Fuertes and R. Mokaya, *ACS Sustainable. Chem. Eng.*, 2016, **4**, 4710-4716.

42. A. Almasoudi and R. Mokaya, *Microporous Mesoporous Mater.*, 2014, **195**, 258-265.

43. T. S. Blankenship and R. Mokaya, *Energy Environ. Sci.*, 2017, **10**, 2552-2562.

44. L. X. Wang, X. G. Li and Y. L. Yang, *React. Funct. Polym.*, 2001, **47**, 125-139.

45. Y. D. Xia, Z. X. Yang and R. Mokaya, *Nanoscale*, 2010, **2**, 639-659.

46. S. P. Wang, S. L. Yan, X. B. Ma and J. L. Gong, *Energy Environ. Sci.*, 2011, **4**, 3805-3819.

47. Q. A. Wang, J. Z. Luo, Z. Y. Zhong and A. Borgna, *Energy Environ. Sci.*, 2011, **4**, 42-55.

48. A. Samanta, A. Zhao, G. K. H. Shimizu, P. Sarkar and R. Gupta, *Ind. Eng. Chem. Res.*, 2012, **51**, 1438-1463.

49. J. P. Marco-Lozar, M. Kunowsky, F. Suarez-Garcia, J. D. Carruthers and A. Linares-Solano, *Energy Environ. Sci.*, 2012, **5**, 9833-9842.

50. G. P. Hao, W. C. Li, D. Qian and A. H. Lu, *Adv. Mater.*, 2010, **22**, 853–857.

51. J. Silvestre-Albero, A. Wahby, A. Sepulveda-Escribano, M. Martinez-Escandell, K. Kaneko and F. Rodriguez-Reinoso, *Chem. Commun.*, 2011, **47**, 6840-6842.

52. M. Sevilla and A. B. Fuertes, *J. Colloid Interface Sci.*, 2012, **366**, 147-154.

53. M. Sevilla and A. B. Fuertes, *Energy Environ. Sci.*, 2011, **4**, 1765-1771.

54. G. Srinivas, J. Burress and T. Yildirim, *Energy Environ. Sci.*, 2012, **5**, 6453-6459.

55. N. P. Wickramaratne and M. Jaroniec, *J. Mater. Chem. A*, 2013, **1**, 112-116.

56. N. P. Wickramaratne and M. Jaroniec, *ACS Appl. Mater. Interfaces*, 2013, **5**, 1849-1855.

57. Z. S. Zhang, J. Zhou, W. Xing, Q. Z. Xue, Z. F. Yan, S. P. Zhuo and S. Z. Qiao, *Phys. Chem. Chem. Phys.*, 2013, **15**, 2523-2529.

58. X. Q. Fan, L. X. Zhang, G. B. Zhang, Z. Shu and J. L. Shi, *Carbon*, 2013, **61**, 423-430.

59. H. R. Wei, S. B. Deng, B. Y. Hu, Z. H. Chen, B. Wang, J. Huang and G. Yu, *ChemSusChem*, 2012, **5**, 2354-2360.

60. M. R. Hudson, W. L. Queen, J. A. Mason, D. W. Fickel, R. F. Lobo and C. M. Brown, *J. Am. Chem. Soc.*, 2012, **134**, 1970-1973.

61. J. Merel, M. Clausse and F. Meunier, *Ind. Eng. Chem. Res.*, 2008, **47**, 209-215.

62. R. V. Siriwardane, M. S. Shen and E. P. Fisher, *Energy Fuels*, 2005, **19**, 1153-1159.

63. Z. J. Zhang, Z. Z. Yao, S. C. Xiang and B. L. Chen, *Energy Environ. Sci.*, 2014, **7**, 2868-2899.

64. K. Sumida, D. L. Rogow, J. A. Mason, T. M. McDonald, E. D. Bloch, Z. R. Herm, T. H. Bae and J. R. Long, *Chem. Rev.*, 2012, **112**, 724-781.

65. A. Almasoudi and R. Mokaya, *J. Mater. Chem. A*, 2014, **2**, 10960-10968.

66. C. Robertson and R. Mokaya, *Microporous Mesoporous Mater.*, 2013, **179**, 151-156.

67. H. W. Langmi, A. Walton, M. M. Al-Mamouri, S. R. Johnson, D. Book, J. D. Speight, P. P. Edwards, I. Gameson, P. A. Anderson and I. R. Harris, *J. Alloy. Compd.*, 2003, **356**, 710-715.

68. B. Panella, M. Hirscher and S. Roth, *Carbon*, 2005, **43**, 2209-2214.

69. M. Hirscher and B. Panella, *J. Alloy. Compd.*, 2005, **404**, 399-401.

Chapter 5. Generalized Mechanochemical Synthesis of Biomass-Derived Sustainable Carbons for High Performance CO_2 Storage

5.1 Aim of this Chapter

A main motivation of this chapter:

- To generate cheap and sustainable carbons (using biomass as starting material) with optimum pore size and the highest possible surface area for high performance CO_2 adsorption at low pressure, which would make them suitable absorbers in flue gas streams emitted from coal-fired power stations wherein CO_2 pressure is typically ≈0.15 bar.

- To study the effect of the mechanochemical synthesis approach on textural properties and CO_2 capture of resulting mechanochemically activated (i.e., compactivated) biomass-derived carbons.

5.2 Abstract

Novel mechanochemical activation generates biomass-derived carbons with unprecedented CO_2 storage capacity due to higher porosity than analogous conventionally activated carbons but similar pore size. The mechanochemical activation, or so-called compactivation, process involves compression, at *740 MPa*, of mixtures of activating agent (KOH) and biomass hydrochar into pellets/disks prior to thermal activation. Despite the increase in surface area and pore volume of between 25% and 75% compared to conventionally activated carbons, virtually all of the porosity of the biomass (sawdust and lignin) derived mechanochemically activated carbons is from small micropores (5.8 Å – 6.5 Å), which results in a dramatic increase in CO_2 storage capacity at 25 °C and low pressure (≤1 bar). The ambient temperature CO_2 uptake for a carbon derived from sawdust at 600 °C and a KOH/carbon ratio of 2, rises from 1.3 mmol g^{-1} to 2.0 mmol g^{-1} at 0.15 bar, and from 4.3 mmol g^{-1} to 5.8 mmol g^{-1} at 1 bar, which is the highest ever reported for carbonaceous materials. The mechanochemically activated carbons have a superior CO_2 working capacity for pressure swing adsorption and vacuum swing adsorption processes and, due to a high packing density, they exhibit excellent volumetric CO_2 uptake that is higher than for any material reported to date.

5.3 Introduction

The search for materials that can cheaply and efficiently capture and store the CO_2 that is generated from anthropogenic sources is one of the most intensely researched areas in energy materials. The CO_2 produced during the burning of fossil fuels for energy generation is considered to be a major contributor to global warming and associated climate change.[1-4] The continuing reliance on fossil fuels means that it is critically important to find avenues to diminish the level of CO_2 emissions but also to more efficiently capture and store the emitted CO_2. This has spawned much research aimed at finding and developing solid state CO_2 absorber-based technology that can replace the current expertise, which is based on energy inefficient absorption-regeneration processes with liquid amine-based absorbents;[5-8] the better efficiency of solid state absorbents is related to the ease (with respect to energy penalty) of their regeneration *via* energy efficient pressure or temperature swing changes. Porous solid state materials, namely, zeolites,[9-12] metal organic frameworks (MOFs),[13-16] covalent organic frameworks (COFs) [13-16] and carbons [17-24] are currently the most studied CO_2 absorbers for post-combustion capture and storage. Of the three classes of porous materials, carbons are attractive due to their abundance, low cost, and rich availability in activated [17-32] or templated [33-52] form.

Activated carbons are particularly attractive as they may be prepared from biomass *via* valorisation processes that convert low value waste into valuable carbonaceous materials.[22] Recent studies have shown that KOH activated carbons, including biomass-derived examples, can achieve some of the best CO_2 uptake under conditions (i.e., 0.1–1 bar and 25°C –50 °C) relevant to industrial post-combustion capture.[5-8, 17-32] It is now well established that pore size is the main factor that determines CO_2 uptake of activated carbons

under post-combustion capture conditions.[17-32, 47-52] The critical importance of pore size arises from the fact that the CO_2-carbon interaction emanates from short-range attractive forces which are maximized when CO_2 adsorption takes place in very narrow pores where overlapping potential fields from neighbouring walls exert a positive influence. For slit-shaped pores, such as those present in activated carbons, enhancement of the adsorption potential may be maximized for micropore widths that are two times the diameter of the CO_2 molecule,[53] which translates to an optimal pore size of 6–7 Å. Such pores can be obtained in lowly or mildly activated carbons prepared at KOH/carbon ratio of 2 and between 600 °C and 700 °C.[5-8, 17-32, 47-52, 54] Indeed, to date, such activated carbons are among materials that show the highest CO_2 uptake at 25 °C and low pressure (up to 1 bar).[5-8, 17-32, 47-52] Conversely, though, such lowly activated carbons tend to have low surface area, which limits the maximum amount of CO_2 that they can store. For this reason, there appears to be a limit on the amount of CO_2 that can be stored by biomass-derived or other activated carbons at 25 °C of ≈1.5 mmol g^{-1} at 0.15 bar and 4.5 mmol g^{-1} at 1 bar. [5-8, 17-32, 47-52, 55-63]

Increase in surface area can be achieved at higher activation levels (higher KOH amounts or temperature), but the pore size also expands, which results in a decrease in CO_2 capture efficiency.[17-32] Thus at present the maximum post-combustion CO_2 capture capacity of activated carbons appears to be limited by the inability to increase the surface area of carbons with the optimum 6–7 Å pores. It is likely that higher surface area activated carbons with 6–7 Å pores would perform as well as or better than the current state of-the-art materials, namely, amine functionalized MOFs,[9-16, 64-66] or bare metal site containing MOFs, [9-16] but would have the advantage of weaker binding of the CO_2 and therefore easier and less cost-intensive regeneration processes.

In an attempt to address this conundrum between CO_2 uptake, surface area and pore size, this chapter considers the following questions; (i) how efficiently is the KOH used during the activation process given that, at the initial stages, the process relies on solid/solid interactions between the carbon and KOH; where mechanical mixing of KOH and carbon is used, the resulting scenario cannot exclude poor KOH/carbon contact with the possibility that some of the KOH may be inefficiently utilized, (ii) might closer contact between biomass carbon precursors and activating agent allow for more efficient use of the KOH and thus generate higher surface area but without pore size expansion, and (iii) could closer contact be engendered *via* a mechanochemical approach involving compression the KOH/carbon mixture into pellets/disks, so as to remove interparticle voids and increase contact between the particles of the KOH and carbon precursor, prior to the thermal activation process.

This chapter reports on the use of biomass as starting material for such a mechanochemical synthesis approach and the effect on textural properties and CO_2 capture of resulting mechanochemically activated (i.e., compactivated) biomass-derived carbons. The CO_2 uptake data in this study targets post-combustion capture wherein it is assumed that flue gas streams contain a mix of N_2 (70% – 75%), CO_2 (15% – 16%), and water (5% – 7%).[6, 67] The motivation of the study is to generate cheap and sustainable carbons with optimum pore size and the highest possible surface area for high performance CO_2 adsorption at low pressure, which would make them suitable absorbers in flue gas streams emitted from coal-fired power stations wherein CO_2 pressure is typically ≈0.15 bar.[6, 67]

5.4 Experimental Section

This section presents a detailed description of the materials and chemicals, experimental procedures, and approach used in **Chapter 5**.

5.4.1 Materials and Chemicals

The list of chemicals/materials used, their sources and purity are presented in **Table 5.1**.

Table 5.1: List of chemical reagents/materials used in the experiment.

Chemical/Material	Source	Purity/Concentration
Biomass	eucalyptus wood sawdust	-
Lignin (lignin waste)	Borregaard LignoTech	-
Potassium hydroxide (KOH)	Fisher Scientific	-
N_2 Compressed gas (Cylinder)	BOC Ltd	100%
Hydrochloric acid (HCl)	Fisher Scientific	37%

5.4.2 Materials Synthesis

5.4.2.1 Carbon Precursors

5.4.2.1.1 Wood Sawdust Derived Hydrochar

Wood sawdust derived hydrochar was prepared as follows; an aqueous dispersion of sawdust at a concentration of 320 g L^{-1} (6.4 g of sawdust in 20 ml of water) was placed in a stainless steel autoclave and heated up to 250 ^{o}C and maintained at the target temperature for 2 h (**Figure 5.1**). The resulting solid (hydrochar) product was recovered by filtration and washed thoroughly with distilled water and then dried at 120 ^{o}C for 4 h. The elemental composition of the wood sawdust-derived hydrochar presented in **Table 5.2**.

5.4.2.1.2 Lignin-Derived Carbonaceous Hydrochar

Lignin-derived carbonaceous hydrochar was obtained from hydrothermal treatment of lignin in an autoclave in high temperature water (300 ^{o}C – 390 ^{o}C). The resulting solid hydrochar was recovered by filtration and washed thoroughly with distilled water and then dried at 120 ^{o}C for 4 h. The elemental composition of the lignin-derived hydrochar presented in **Table 5.2**.



Figure 5.1: A stainless steel autoclave used for hydrothermal treatment to convert Sawdust to hydrochar.

Table 5.2: The elemental composition of hydrochar derived from eucalyptus wood sawdust and lignin.

Sample	Elemental composition (wt %)		
	C [a]	H [a]	O + X [b]
Eucalyptus wood sawdust-derived hydrochar	69.3	6.8	23.9
Lignin-derived hydrochar	66.6	5.1	28.3

[a] Obtained from CHN analysis.
[b] Obtained as follows: Oxygen content + X (where X are other elements) (%)= [100 – (C+H+N)]

5.4.2.2 Production of KOH Activated Carbons

5.4.2.2.1 Mechanochemical Activation (MCA)

The carbon precursor was thoroughly mixed with KOH at KOH/carbon precursor weight ratio of 2 in an agate mortar. The KOH/carbon precursor mixtures were then compacted for 10 min at load of 10 tonnes (equivalent to compression pressure of *740 MPa*) in a 1.3 cm diameter die. The resulting pellets were placed in an alumina boat, in a horizontal furnace and heat treated to the target activation temperature (600 ^{o}C or 650 ^{o}C) at heating ramp rate of 3 ^{o}C min^{-1} under a nitrogen gas flow and held at the activation temperature for 1 h (**Figure 5.2** and **Figure 4.5**). The resulting compactivated MCA carbons were then thoroughly washed several times with 10 wt% HCl to remove any inorganic salts, and then with distilled water until neutral pH. *No stirring* was used during the washing step. Finally, the carbons were dried in an oven at 120 ^{o}C for 3 h. Abbreviations are in **Table 5.4** for sawdust-derived activated carbons and **Table 5.5** for lignin-derived activated carbons. **Table 5.3** summarized the parameters and conditions used for synthesis.

5.4.2.2.2 Conventional Activation (CA)

Conventionally activated carbons were prepared as described above but without the mechanical compaction step (**Figure 5.2** and **Figure 4.5**) and *stirring* was used during the acid washing step (HCl). Abbreviations are in **Table 5.4** for sawdust-derived activated carbons and **Table 5.5** for lignin-derived activated carbons. **Table 5.3** summarized the parameters and conditions used for synthesis.

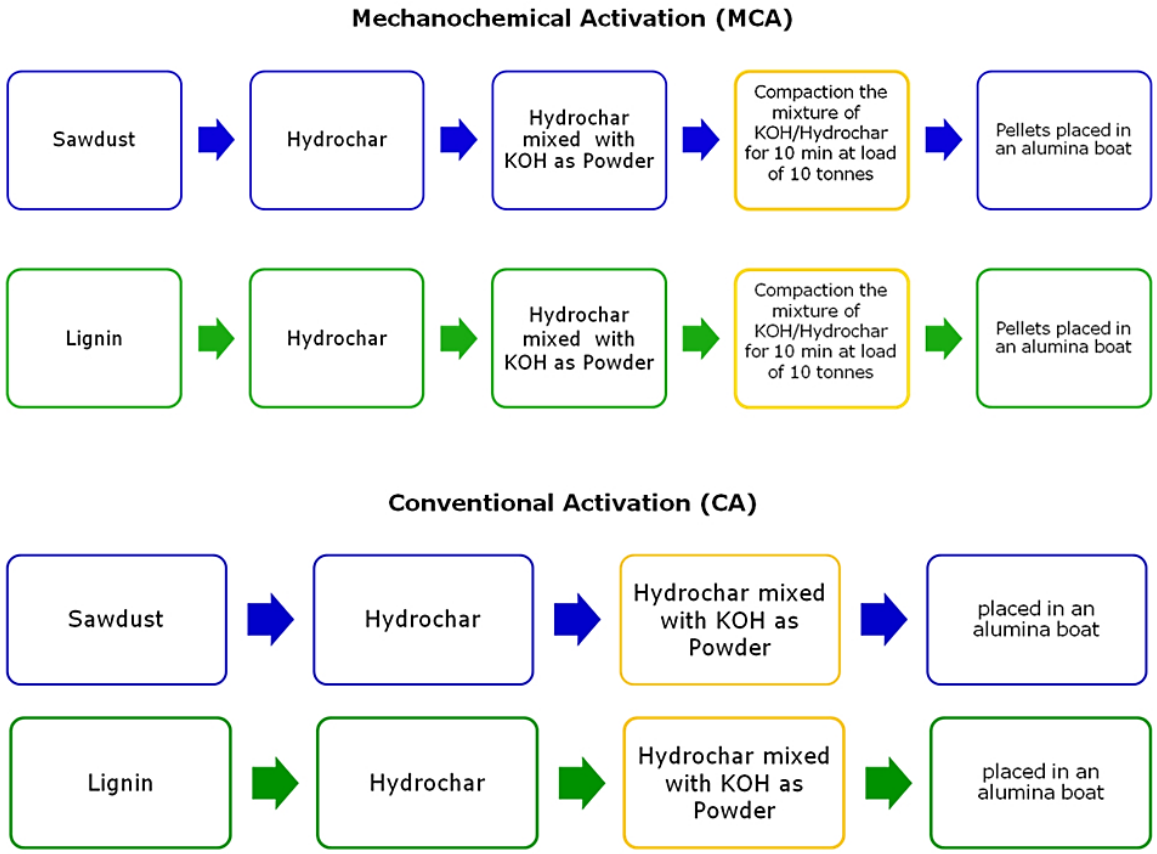


Figure 5.2: Schematic representation showing the mechanochemical activation route (MCA) and conventional activation route (CA) used to prepare compactivated carbons and conventionally activated carbons, respectively.

Table 5.3: Summary of ACs synthesis: parameters and conditions.

Carbon Precursors	Eucalyptus wood sawdust-derived hydrochar
	Lignin-derived hydrochar
Activating Agent	KOH (powder)
KOH Ratio	KOH/sawdust-derived hydrochar 2:1 KOH/lignin-derived hydrochar 2:1
Activation Temperature	600 ^{o}C or 650 ^{o}C
Ramp Rate	3 ^{o}C/min
Process Hold Time	1 hour
Gas/Environment	Nitrogen flow

5.5 Abbreviations

5.5.1 Sawdust-Derived Activated Carbons

Sawdust-derived mechanochemically activated carbons were designated as SD2xP and conventionally activated carbons were designated as SD2x, where *x*= 600 °C or 650 °C and a KOH/Sawdust-derived hydrochar at ratio of 2. See **Table 5.4** for samples abbreviations.

Table 5.4: Abbreviations of Sawdust-derived activated carbons.

Activation Conditions	Conventionally Activated Carbons CA	Mechanochemically Activated Carbons/ Compactivated @10 tonnes=740 MPa MCA
Activation at 600 °C KOH/Precursor at ratio of 2:1	SD2600	SD2600P
Activation at 650 °C KOH/Precursor at ratio of 2:1	SD2650	SD2650P

5.5.2 Lignin-Derived Activated Carbons

Mechanochemically activated carbons were designated as L2xP and conventionally activated carbons were designated as L2x, where *x*= 600 °C or 650 °C and a KOH/Lignin-derived hydrochar at ratio of 2. See for **Table 5.5** samples abbreviations.

Table 5.5: Abbreviations of Lignin-derived activated carbons.

Activation Conditions	Conventionally Activated Carbons CA	Mechanochemically Activated Carbons /Compactivated @10 tonnes=740 MPa MCA
Activation at 600 °C KOH/Precursor at ratio of 2:1	L2600	L2600P

5.6 Results and Discussion

5.6.1 Sawdust-Derived Carbons

5.6.1.1 Textural Properties and Porosity

The nitrogen sorption isotherms and corresponding pore size distribution (PSD) curves of the sawdust-derived carbons are shown in **Figure 5.3** and **Figure 5.4**, respectively.

In both cases, the nitrogen sorption isotherms of the MCA carbons show higher nitrogen adsorption compared to the equivalent CA carbons. As expected for carbons activated at such lowly temperatures (600 – 650 °C) and KOH/carbon ratio of 2, both pairs of carbons are highly microporous and as such the isotherms show significant nitrogen adsorption at very low relative pressure ($P/P_o < 0.01$).

The textural parameters of the CA and MCA carbons in **Table 5.6** confirm the higher surface area and pore volume of the later. The surface area and pore volume of the MCA carbons are typically 25% higher than for equivalent CA carbons. Thus, the surface area of the sample activated at 600 °C increases from 866 $m^2\ g^{-1}$ to 1066 $m^2\ g^{-1}$, while at 650 °C, the increase is from 1039 $m^2\ g^{-1}$ to 1313 $m^2\ g^{-1}$. This means that at KOH/carbon ratio of 2, the MCA route achieves surface area that, within our activation set up, requires conventional activation at 650 °C. Nevertheless, it is clear in **Figure 5.3** that the shape of the isotherms for the MCA carbons is similar to that of the CA carbons despite the higher porosity of the former. This is a reflection of the fact that there is little change in PSD and extent of microporosity between the two pairs of samples. This is confirmed by the PSD curves in **Figure 5.4 a** and **Figure 5.4 b** which show that the size of pore channels

generated in the MCA and CA carbons is largely similar. Rather than pore expansion, there is in contrast a slight contraction of the main pores for the MCA carbons from 6.8 Å to 5.9 Å for 600 °C samples, and 7 Å to 6.5 Å for samples activated at 650 °C (**Table 5.6**). This is a counterintuitive observation given that higher porosity in activated carbons is typically accompanied by enlargement of pore size.[17-32, 54]

Overall, however, the pore size distribution is comparable for both sets of samples; in both cases there is a small proportion of pores of size 8.5 Å and minor presence of 11.5 Å pores (**Figure 5.4** and **Table 5.6**) and no other pores are observed (**Figure 5.5**). The MCA route, therefore, achieves higher surface area but without any undesirable effects of pore size expansion. Furthermore, as shown in **Table 5.6**, the proportion of microporosity, according to t-plot analysis (**Figure 5.6**) is similar for both sets of samples, i.e., ≈94% of surface area and 85% (at 600 °C) and 80% (at 650 °C) of pore volume. It is likely that the higher porosity for MCA carbons arises from more efficient KOH usage due to minimizing of the interparticle voids *via* compaction.

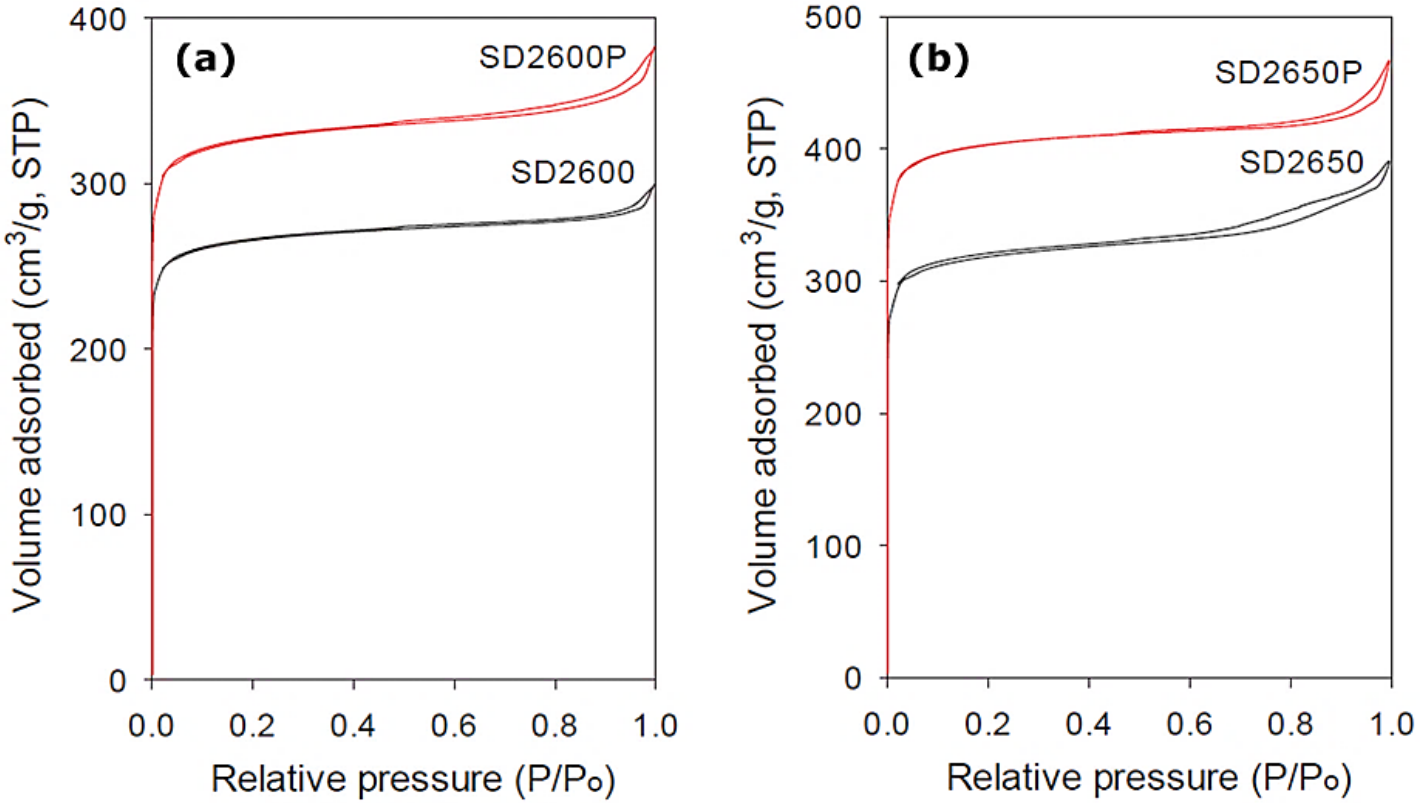


Figure 5.3: Nitrogen sorption isotherms of Sawdust-derived mechanochemically activated carbons (SD2xP) and conventionally activated carbons (SD2x) **(a)** prepared at x= 600 °C and a KOH/carbon ratio of *2* and (b) prepared at x= 650 °C and a KOH/carbon ratio of *2*.

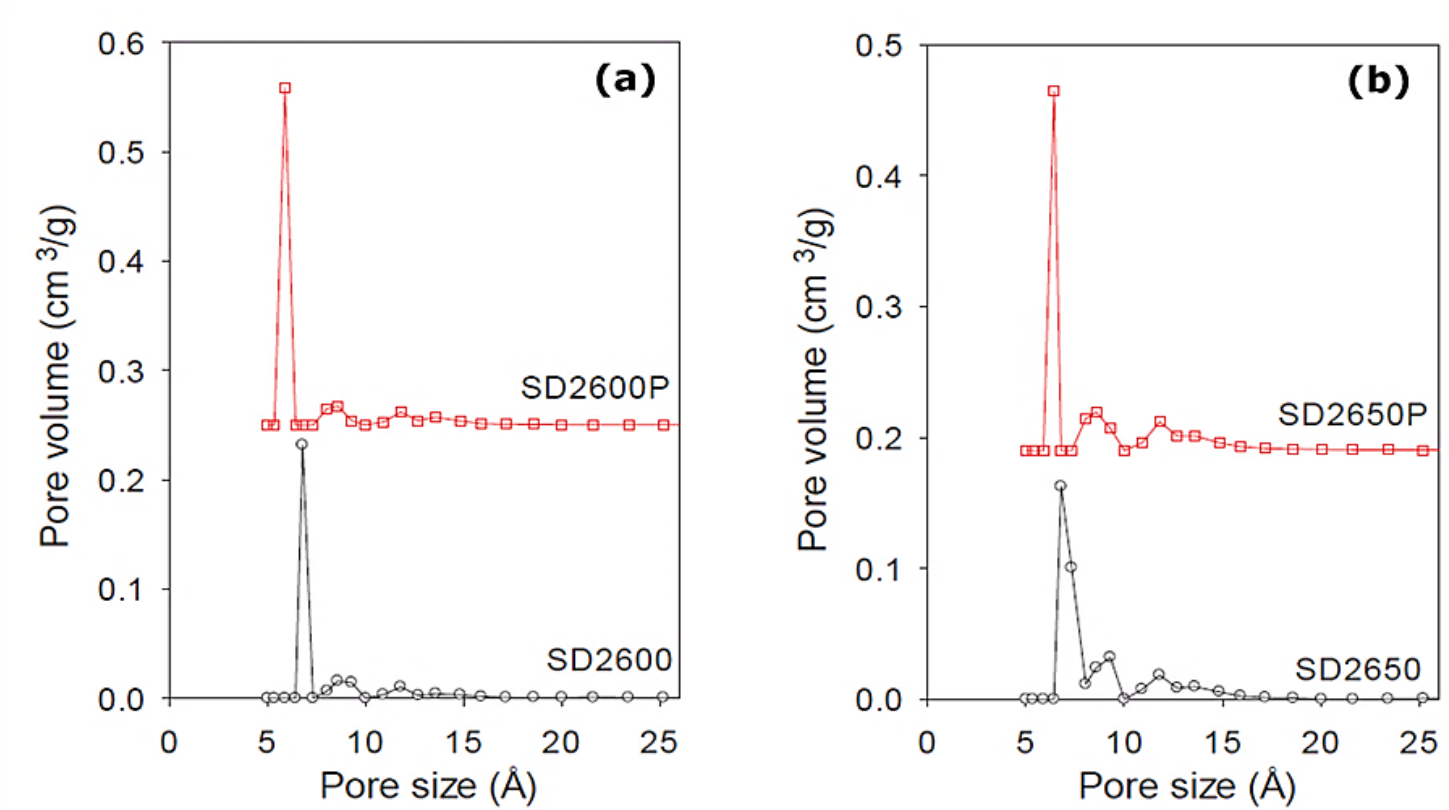


Figure 5.4: Pore size distribution (PSD) curves of Sawdust-derived mechanochemically activated carbons (SD2xP) and conventionally activated carbons (SD2x) **(a)** prepared at x= 600 °C and a KOH/carbon ratio of *2* and **(b)** prepared at x= 650 °C a KOH/carbon ratio of *2*.

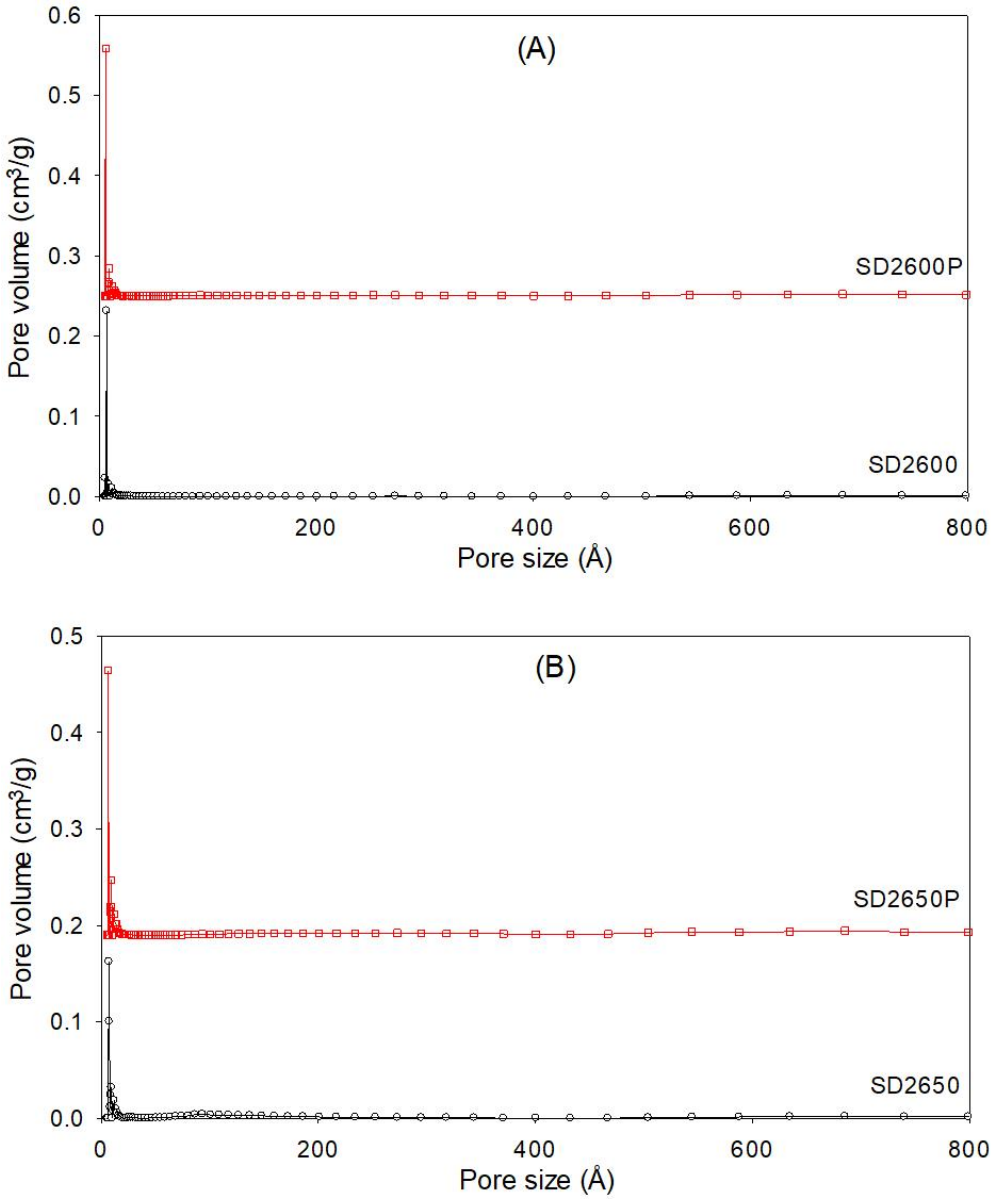


Figure 5.5: Wide pore size distribution of mechanochemically activated carbons (SD2600P and SD2650P) and conventionally activated carbons (SD2600 and SD2650) derived from sawdust **(A)** at 600 °C or **(B)** at 650 °C, and KOH/carbon ratio of *2*.

Table 5.6: Textural properties and CO_2 uptake of conventionally activated carbons and mechanochemically activated carbons derived from sawdust and lignin.

Sample	Surface area [a] [$m^2\ g^{-1}$]	Pore volume [b] [$cm^3\ g^{-1}$]	Pore size [c] [Å]	CO_2 uptake [d] [mmol g^{-1}]		
				0.15 bar	1 bar	20 bar
SD2600	866 (823)	0.46 (0.39)	6.8	1.3	4.3	8.6
SD2600P	1066 (1007)	0.59 (0.48)	5.9	2.0	5.8	10.5
SD2650	1039 (970)	0.60 (0.46)	7/8.5	1.2	4.1	9.8
SD2650P	1313 (1258)	0.72 (0.60)	6.5/8.5	1.5	5.3	11.6
L2600	1277 (1204)	0.59 (0.53)	6/7/9/12	0.5 (1.3) [e]	3.3 (5.3) [e]	10.4 (11.5) [e]
L2600P	2224 (2089)	1.02 (0.91)	6/7/9/12	1.2 (2.3) [e]	4.5 (7.3) [e]	12.8 (14.6) [e]

[a] Micropore surface area.
[b] Micropore volume.
[c] Main pore size distribution maxima obtained from NLDFT analysis.
[d] CO_2 uptake at *25 °C* and at pressure of 0.15 bar, 1 bar, and 20 bar.
[e] The values in parentheses are CO_2 uptake *at 0 °C*.

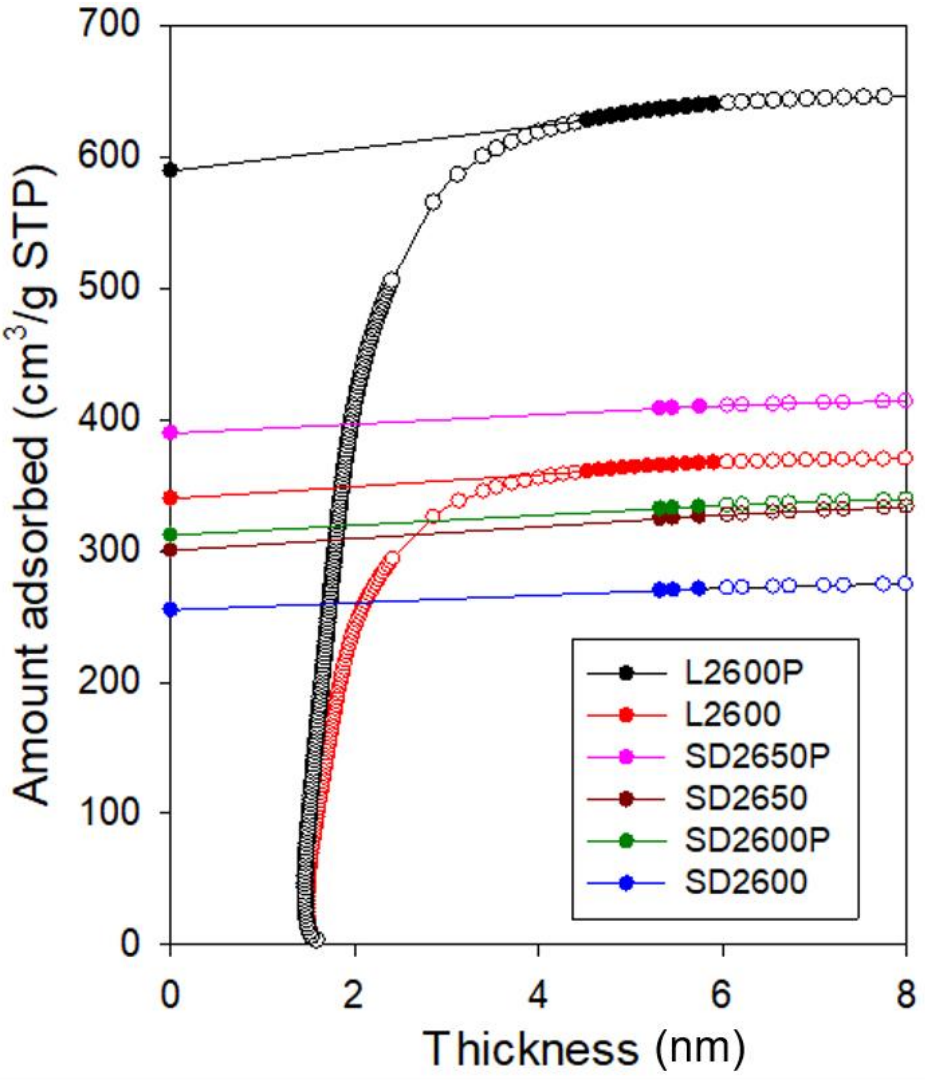


Figure 5.6: T-plot analysis curves for determining microporosity from nitrogen sorption data.

5.6.1.2 Structural Ordering Analysis

According to powder X-ray diffraction (XRD) analysis (**Figure 5.7**) there are subtle differences in the nature of the MCA and CA carbons with respect to their apparent levels of graphitization especially for samples activated at 600 °C. The peaks that indicate graphitization in a carbon are expected at 2θ= 22° for the (002) diffraction and at 2θ= 43° for the (101) diffraction. Although the peak expected at 2θ = 22° is not clearly observed due to being masked by the gradient of the baseline, the graphitic diffraction bands are only really observed for carbons activated at 600 °C, wherein (**Figure 5.7**) the CA sample (SD2600) exhibits peaks with somewhat higher intensity compared to the MCA sample (SD2600P). This suggests that the MCA samples are less graphitic compared to CA samples, which is consistent with their higher surface area and overall porosity.

For samples activated at 650 °C, the difference in graphitization between the MCA and CA samples is less clear (**Figure 5.7**). Nevertheless, the graphitic peaks are very broad, which indicates that both sets of sawdust-derived samples mainly contain amorphous carbon but with some small amounts of disordered turbostratic domains.

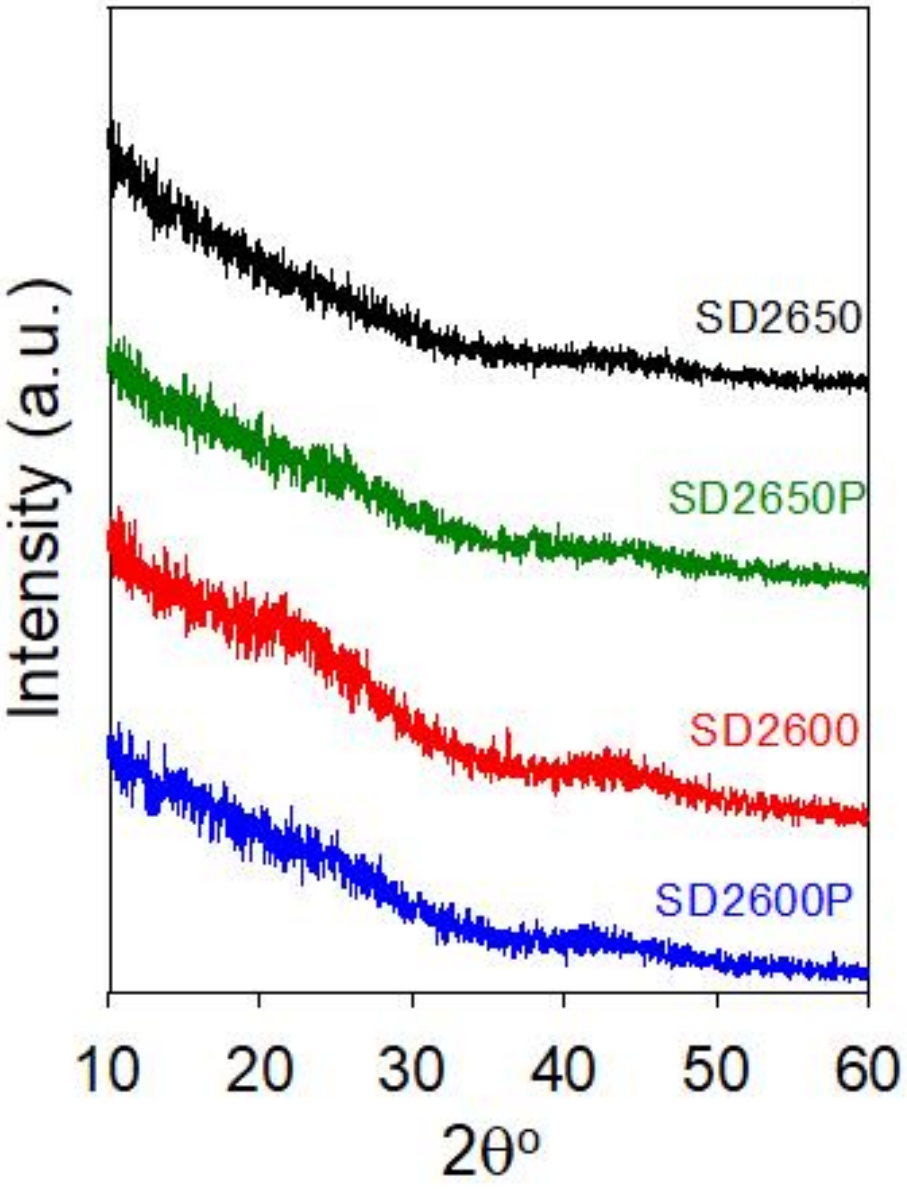


Figure 5.7: Powder XRD patterns of mechanochemically activated carbons (SD2600P and SD2650P) and conventionally activated carbons (SD2600 and SD2650) derived from sawdust.

5.6.1.3 Chemical Similarity Assessment

The chemical similarity between the MCA and CA carbons probed by performing infra-red (IR) spectroscopy analysis. The IR spectra of both sets of samples were found to be typical for activated carbons [68] (**Figure 5.8**).

The spectra show the C–OH stretch band at ≈3400 cm^{-1} and at least three other peaks; at 1240–1250 cm^{-1} (C–O), 1585–1600 cm^{-1} (C=C), and ≈1700 cm^{-1} (C=O), which are consistent with the fact that the activated carbons are carbon-rich with low amounts of H. Indeed, compared to the IR spectra of the hydrochar,[69] no any C–H peaks were observed.[69] The IR spectra also confirm that both the CA and MCA carbons do not possess any adventitious organic molecules. More importantly, the IR spectra of the CA and MCA carbons are virtually identical, which indicates that the mechanochemical route does not alter the chemical composition of the carbons.

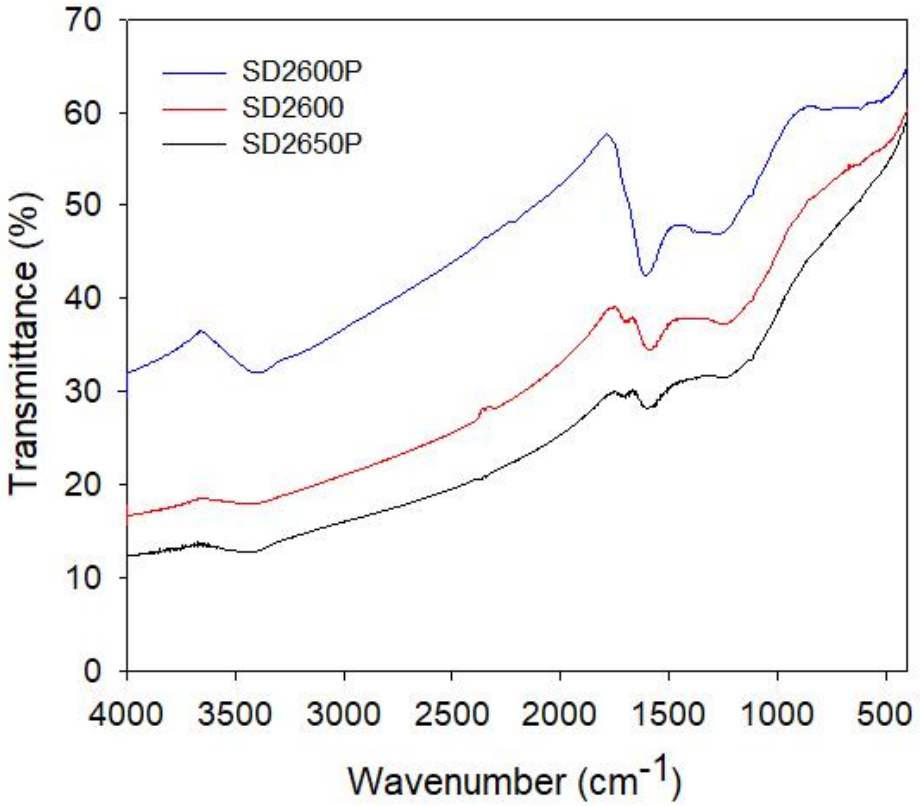


Figure 5.8: FTIR spectra of mechanochemically activated carbons (SD2600P and SD2650P) and conventionally activated carbons (SD2600) derived from sawdust.

5.6.1.4 Pore Channel Assessment

According to transmission electron microscopy (TEM) micrograph images (**Figure 5.9**) the level of pore channel order/disorder is similar for both sets of samples. The TEM micrograph images of sample SD2600P and SD2600 show pore channels of size 6–7 Å, which is in agreement with the porosity data (**Figure 5.4** and **Table 5.6**). Also, despite inclusion of a compression step for the compactivated MCA carbons, the particle morphology was similar to that of CA carbons and comparable to other types of activated carbons generated *via* KOH activation, i.e., irregular shaped particles with large conchoidal cavities and smooth surfaces.[69] Indeed, such morphology has previously been noted to be common for activated samples regardless of the hydrochar precursor from which they are derived.[69]

The overall picture that emerges from XRD analysis, IR spectra analysis, and TEM micrograph images is that, although the mechanochemical synthesis route significantly increases the surface area, there are hardly any changes to the nature and ordering of the carbon except for a slight decrease in the apparent level of graphitization, compared to conventionally activated carbons.

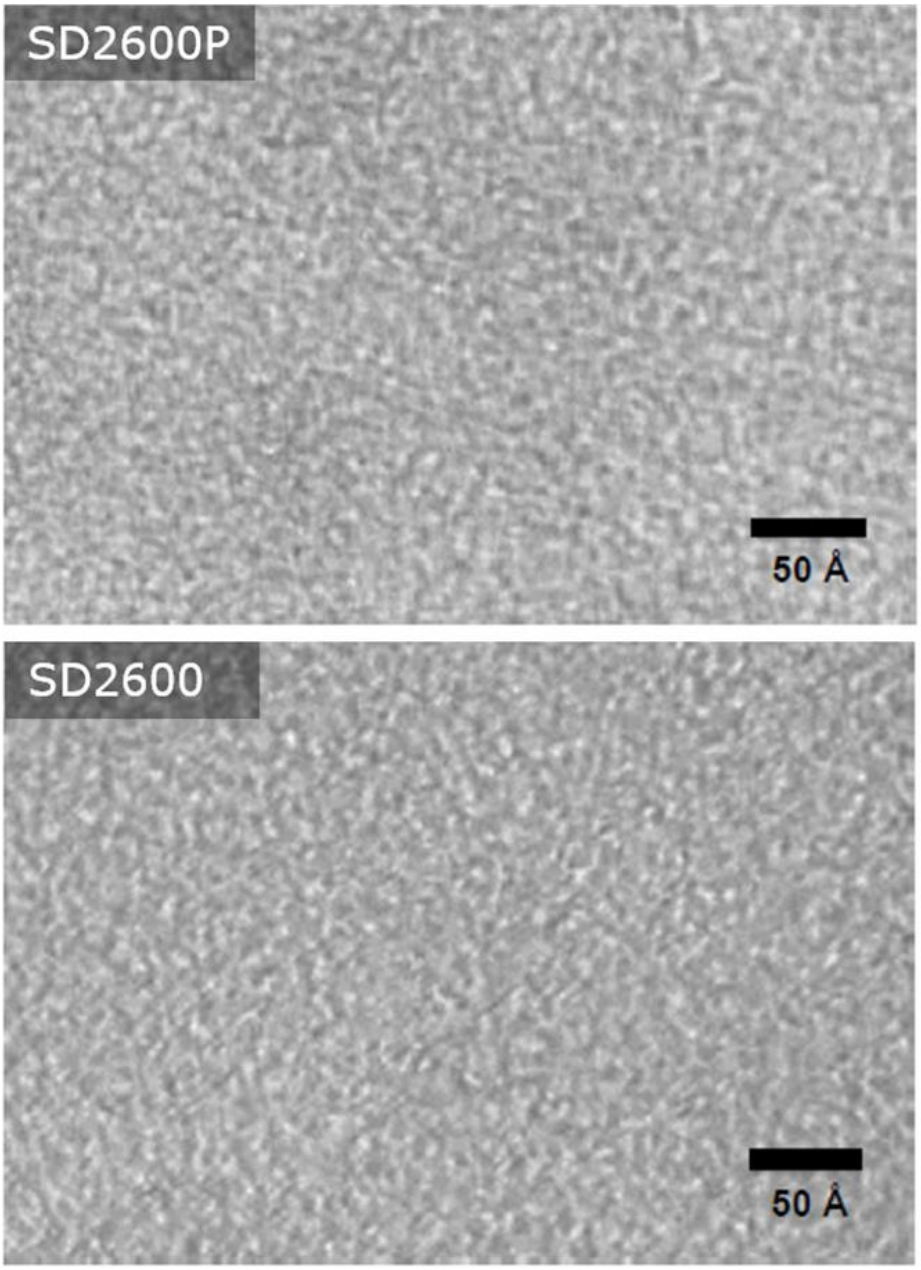


Figure 5.9: TEM micrograph images of mechanochemically activated carbons (SD2600P) and conventionally activated carbons (SD2600) derived from sawdust.

5.6.1.5 CO_2 Storage Measurements

5.6.1.5.1 CO_2 Storage at 25 °C

The CO_2 uptake capacity of the sawdust-derived compactivated MCA carbons and conventionally activated carbons CA was measured *at 25 °C* and pressure range of 0–20 bars. The CO_2 uptake isotherms are shown in **Figure 5.10** and the storage capacity at 0.15 bar, 1 bar and 20 bars is summarized in **Table 5.6**. It is quite clear that the higher surface area of the mechanochemically activated carbons results in a dramatic increase in CO_2 uptake (**Figure 5.10** and **Figure 5.11**). At 1 bar the uptake of conventionally activated SD2600 sample is 4.3 mmol g^{-1}, which is comparable to the best biomass-derived carbon materials reported so far.[17-32, 47-52, 55-63] Indeed, CO_2 uptake of 4.3 mmol g^{-1} , at 25 °C and 1 bar, is comparable to one of the highest values reported so far allowing for the lower surface area of our sample.[23, 24] On the other hand, the compactivated or mechanochemically activated SD2600P carbon has a much higher uptake of 5.8 mmol g^{-1}, which is a 35% increase compared to the conventional SD2600 sample. As far as we know a CO_2 uptake of 5.8 mmol g^{-1} (at 25 °C and 1 bar) is the highest ever reported for any biomass derived carbon or indeed any porous purely carbon material.[17-32, 47-52, 55-63]

At 0.15 bar, a pressure that is particularly relevant for CO_2 capture from postcombustion flue gas streams, the uptake of the mechanochemically activated SD2600P carbon is 2.0 mmol g^{-1}, which is much higher than 1.3 mmol g^{-1} for the conventionally activated SD2600 sample. This represents a remarkable 54% increase in CO_2 uptake capacity. At pressure of 20 bars, the increase in CO_2 uptake is a more modest 22% from 8.6 mmol g^{-1} for SD2600 to 10.5 mmol g^{-1} for SD2600P. We believe that the remarkable increase in CO_2 uptake at low pressure (0.15 bar and 1 bar) is

due to both the slight optimization of pore size (from 6.8 Å to 5.9 Å) and the increase in surface area. Similar trends in CO_2 storage are observed for the samples activated at 650 °C (**Table 5.6**) although the overall uptake values achieved are lower, which is ascribed to the fact that these samples have a slightly higher proportion of larger pores compared to those prepared at 600 °C (**Figure 5.4 a** and **Figure 5.4 b**).

At 0.15 and 1 bar the uptake increases from 1.2 mmol g^{-1} and 4.1 mmol g^{-1}, respectively for SD2650 to 1.5 mmol g^{-1} and 5.3 mmol g^{-1}, respectively for the mechanochemically activated SD2650P sample; the rises are 25% and 29% at 0.15 bar and 1 bar, respectively. It is noteworthy that the 5.3 mmol g^{-1} CO_2 uptake of SD2650P at 1 bar is still higher than any previously reported biomass or otherwise derived carbon.[17-32, 47-52, 55-63] Indeed, the uptake of the mechanochemically activated SD2600P and SD2650P samples is better than that of current benchmark template [47-52] or activated carbons,[17-32, 55-63, 70] including those derived from sawdust,[23, 24] petroleum pitch [61] and even N-doped carbons.[20, 62, 71, 72] It is interesting to note that despite a higher surface area, the low pressure uptake of sample SD2650P is lower than that of SD600P (**Figure 5.11**), which is due to the slightly larger pore size of the former (**Table 5.6**).

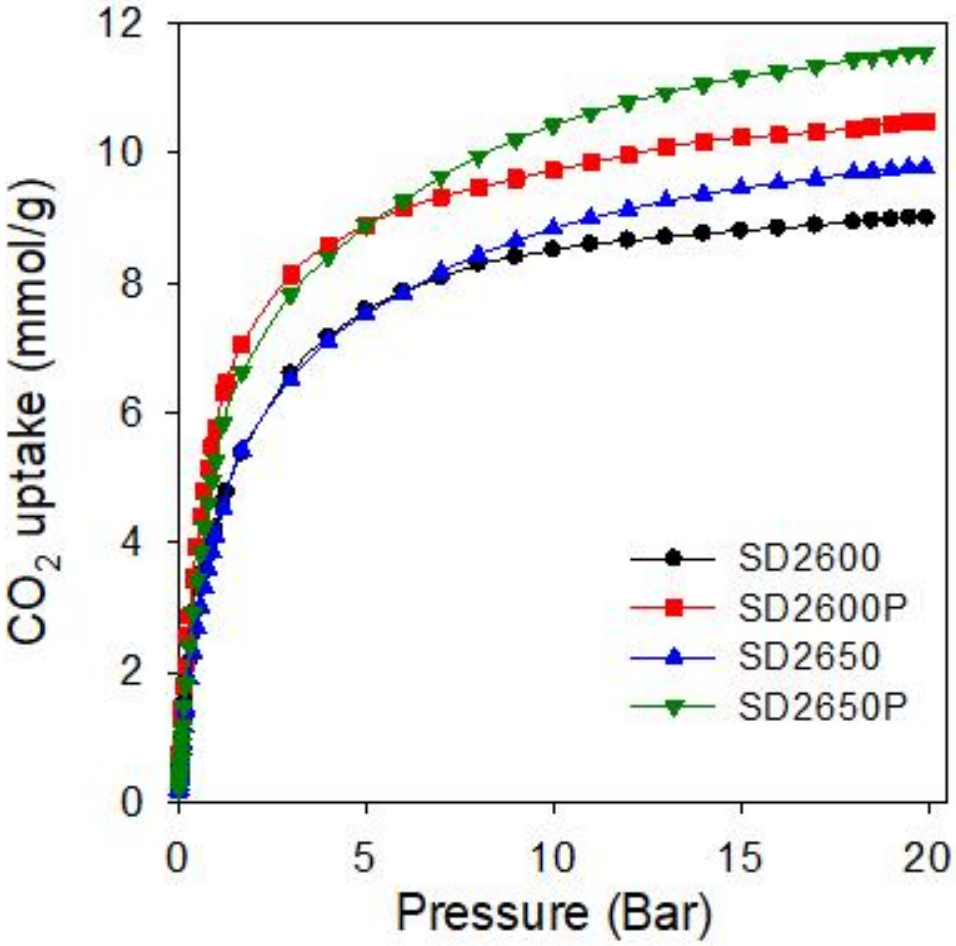


Figure 5.10: CO_2 uptake isotherms ***at 25 °C*** and pressure range **0-20 bar** for sawdust-derived mechanochemically activated carbons (SD2xP) and conventionally activated carbons (SD2x) prepared at x= 600 °C or 650 °C and a KOH/carbon precursor ratio of *2*.

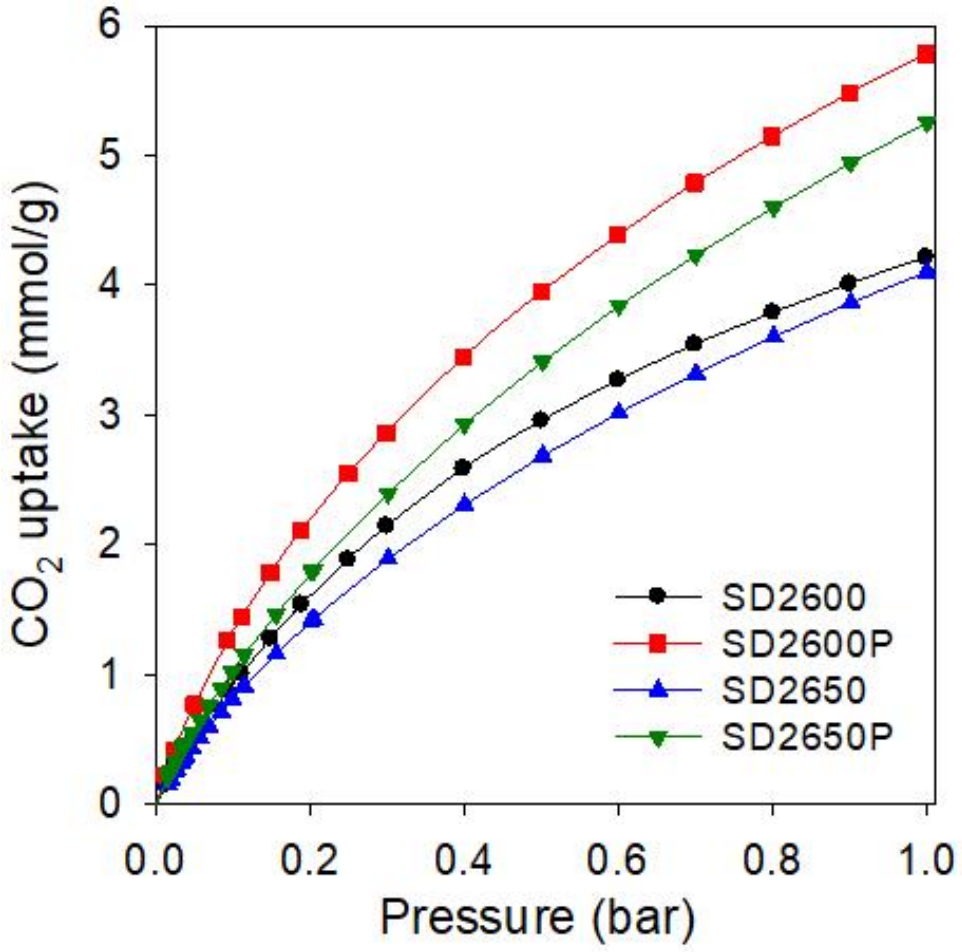


Figure 5.11: CO_2 uptake isotherms ***at* 25 °C** and pressure range **0-1 bar** for sawdust-derived mechanochemically activated carbons (SD2xP) and conventionally activated carbons (SD2x) prepared at x= 600 °C or 650 °C and KOH/carbon ratio of *2.*

5.6.2 Lignin-Derived Carbons

5.6.2.1 Textural Properties and Porosity Analysis

To test the general applicability of the mechanochemical activation process, we also prepared mechanochemically activated carbons from lignin-derived hydrochar. Lignin is one of the most abundant carbonaceous materials but is known to exhibit low reactivity with respect to activation. [73, 74]

Figure 5.12 a and **Figure 5.12 b** show the nitrogen sorption isotherm and the PSD distribution curves of the conventionally activated (L2600) and mechanochemically activated (L2600P) lignin-derived samples, respectively. Both samples present similarly shaped type *I* isotherms consistent with highly microporous materials with the amount of nitrogen adsorbed being much higher for the compactivated MCA sample (L2600P). As shown in **Table 5.6**, sample L2600 has a surface area and pore volume of 1277 $m^2 g^{-1}$ and 0.59 $cm^3 g^{-1}$, respectively, while the surface area and pore volume of the mechanochemically activated L2600P sample is 75% higher at 2224 $m^2 g^{-1}$ and 1.02 $cm^3 g^{-1}$, respectively. Despite this large increase in surface area, the level of microporosity (**Table 5.6**), according to t-plot analysis (**Figure 5.6**) is similar for both samples, i.e., 94% of surface area and 90% of pore volume.

There is clearly no change to the PSD distribution (**Figure 5.12 b**) or pore size (**Table 5.6**) The pore size distribution of the two lignin-derived carbons is identical (**Figure 5.12 b** and **Figure 5.13**) despite the much higher surface area and pore volume of the mechanochemically activated sample. This confirms that mechanochemical activation increases the efficiency of the KOH in generating porosity in the lignin-derived hydrochar but without compromising on the size of pores created.

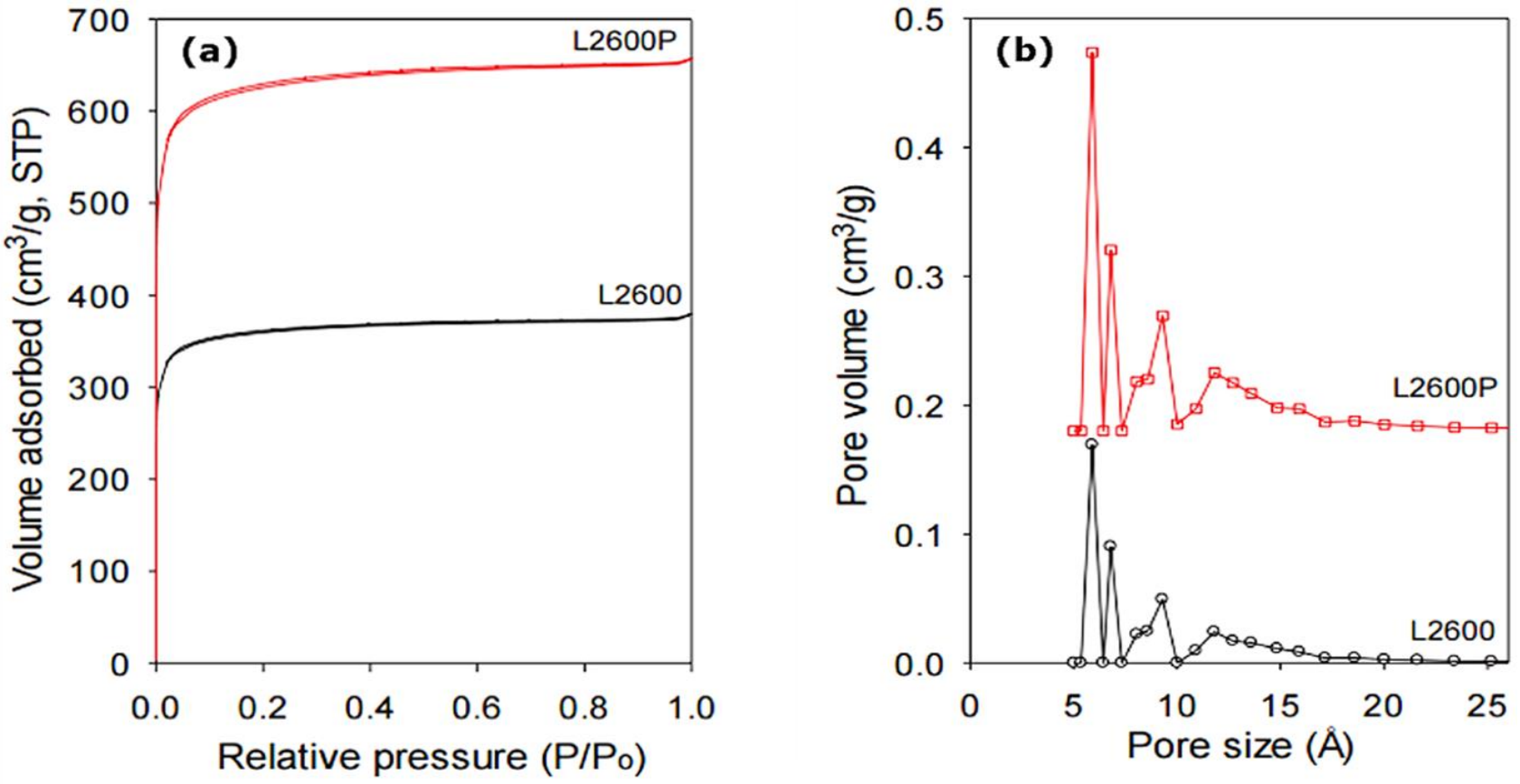


Figure 5.12: (a) Nitrogen sorption isotherms and **(b)** corresponding pore size distribution curves of lignin-derived conventionally activated (L2600) and mechanochemically activated carbons (L2600P) prepared 600 °C and a KOH/carbon ratio of *2*. The PSD curve of the L2600P is offset (y -axis) by 0.18 $cm^3\ g^{-1}$.

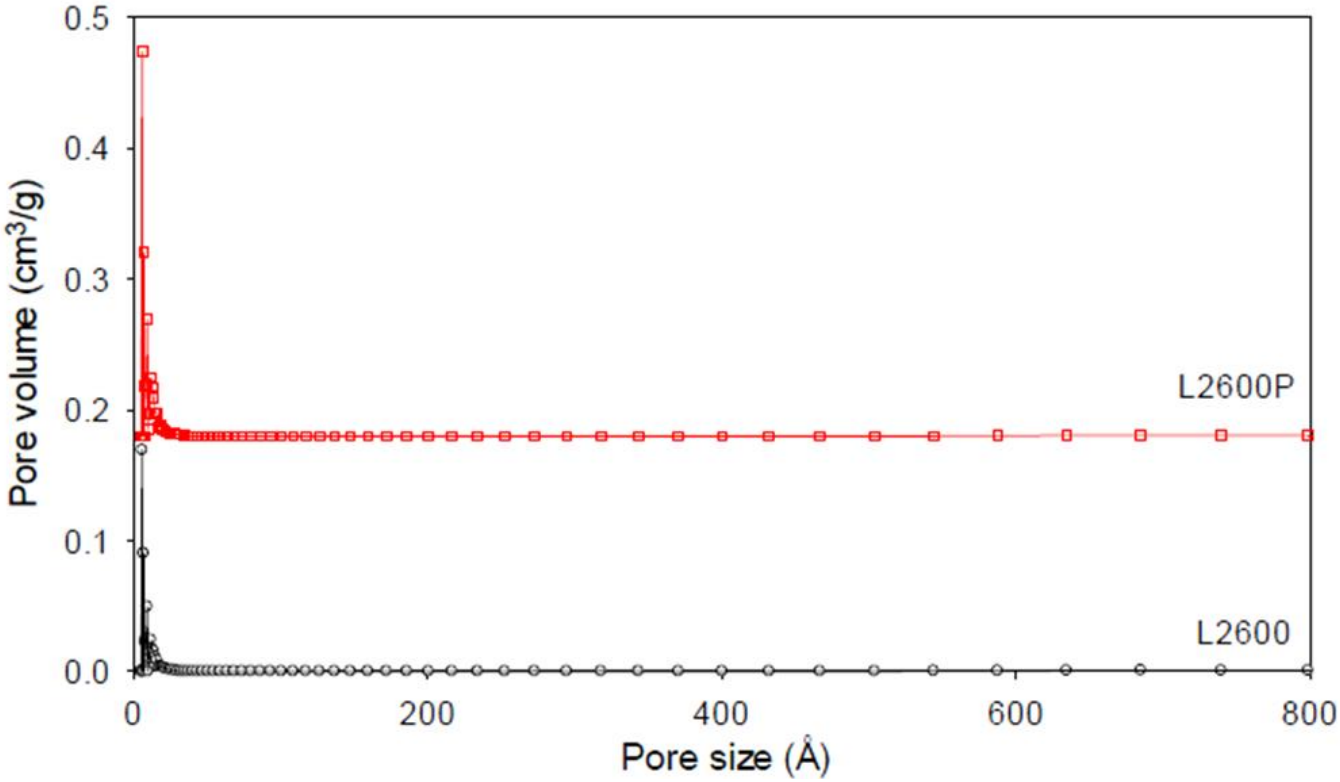


Figure 5.13: Wide pore size distribution of mechanochemically (L2600P) and conventionally activated carbons (L2600) derived from lignin at 600 °C and KOH/carbon ratio of *2*.

5.6.2.2 CO_2 Storage Measurements

The mechanochemically activated L2600P sample exhibits much higher CO_2 storage as shown in **Figure 5.14** and **Table 5.6**.

5.6.2.2.1 CO_2 Storage at 25 °C

At 25 °C (**Figure 5.14** and **Table 5.6**) and pressure of 0.15 bar, there is a 140% increase in CO_2 uptake from 0.5 mmol g^{-1} for sample L2600 to 1.2 mmol g^{-1} for L2600P. At 1 bar, there is a 40% increase in CO_2 uptake from 3.3 mmol g^{-1} for sample L2600 to 4.6 mmol g^{-1} for sample L2600P. At 20 bars, the increase (23%) is less dramatic from 10.4 mmol g^{-1} to 12.8 mmol g^{-1}.

5.6.2.2.2 CO_2 Storage at 0 °C

A similar trend in increase of CO_2 uptake for sample L2600P over L2600 is observed at 0 °C (**Figure 5.15** and **Table 5.6**). At 0.15 bar, there is a 77% increase from 1.3 mmol g^{-1} for sample L2600 to 2.3 mmol g^{-1} for L2600P. At 1 and 20 bars, the CO_2 uptake of the mechanochemically activated L2600P is higher by 37% and 27%, respectively. The trends indicate that surface area can play a significant role in determining CO_2 storage at low pressure (≤1 bar) as long as the pore size is optimized. The low pressure (≤1 bar) CO_2 uptake of lignin-derived samples is lower than that of sawdust-derived samples due to the presence of a greater proportion of larger pores in the lignin-derived samples.

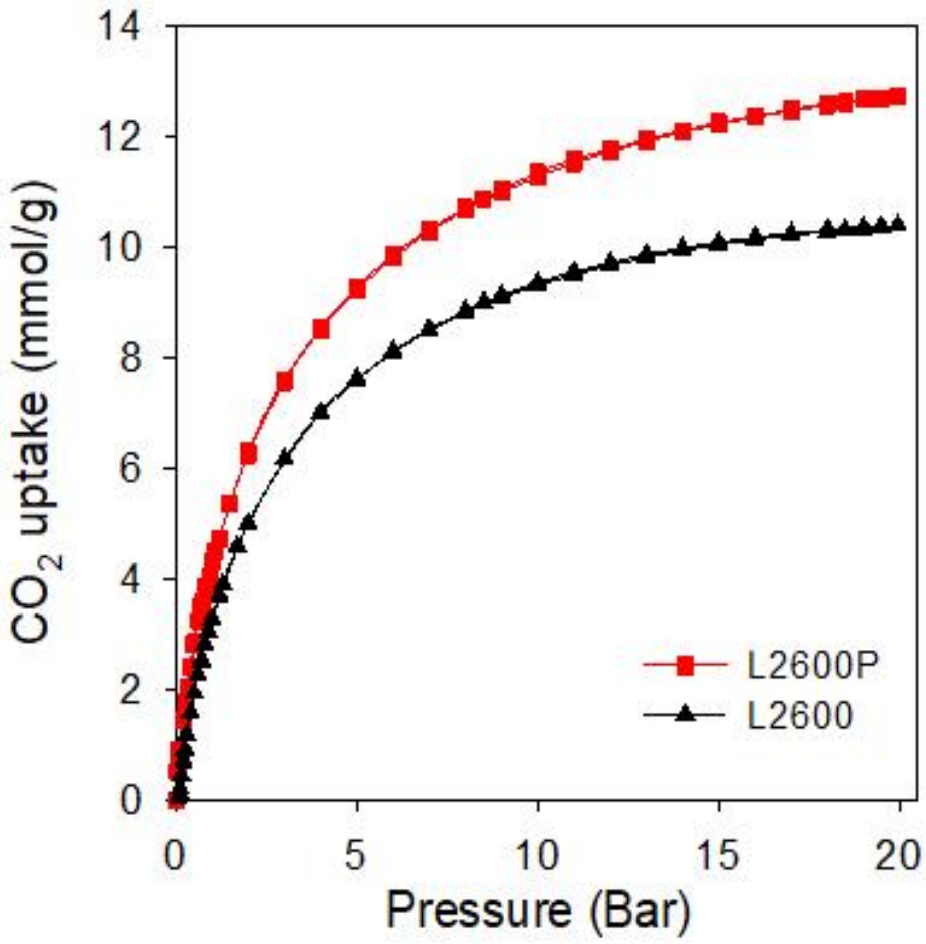


Figure 5.14: CO_2 uptake isotherms ***at 25 °C*** and pressure range **0-20 bar** for lignin-derived mechanochemically activated carbons (L2600P) and conventionally activated carbons (L2600) prepared at 600 °C and a KOH/carbon precursor ratio of *2*.

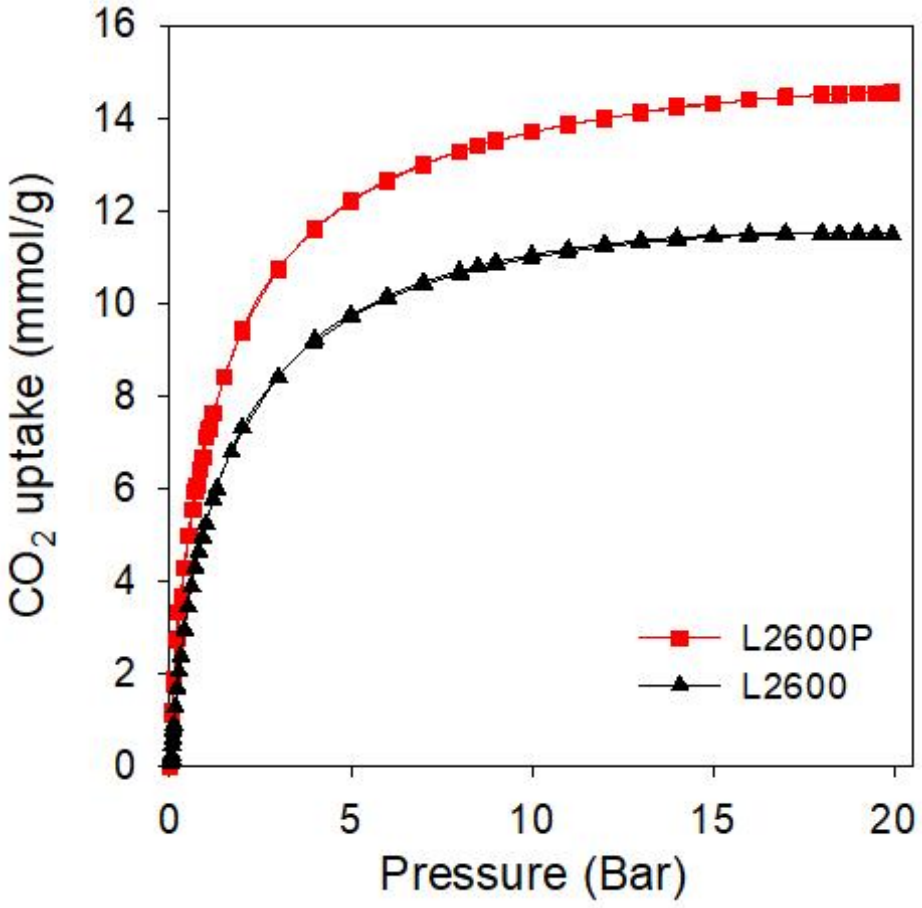


Figure 5.15: CO_2 uptake isotherms ***at 0 °C*** and pressure range **0-20 bar** for lignin-derived mechanochemically activated carbons (L2600P) and conventionally activated carbons (L2600) prepared at 600 °C and KOH/carbon precursor ratio of *2*.

5.6.3 Working Capacity, Volumetric Uptake and Benchmarking

The CO_2 uptake data discussed before show that mechanochemical activation results in a dramatic rise in gravimetric CO_2 storage capacity. The biomass-derived carbons in this study were found to have good regeneration and recyclability in a manner similar to that previously reported for comparable activated carbons prepared from a variety of biomass and other carbon sources.[17-32] Several considerations are of particular interest and relevance for solid-state adsorbents, namely: (i) the mode of CO_2 uptake from postcombustion flue gas streams, (ii) regeneration of the solids to sequester the CO_2 and recycle the adsorbent and (iii) volumetric uptake. Adsorption and regeneration may be achieved through pressure swing operations *via* either pressure swing adsorption (PSA) or vacuum swing adsorption (VSA) processes.[75-77] It is therefore of interest to assess the performance of the mechanochemically activated carbons in typical PSA and VSA processes so as to determine their so-called working capacity. For PSA, we postulate adsorption at 6 bars and desorption at 1 bar, while for VSA an adsorption pressure of 1.5 bar and evacuation at 0.05 bar.[78]

5.6.3.1 Working Capacity Assessment

The assessment of working capacity was done for CO_2 capture in two scenarios, namely, from a pure CO_2 stream and from a flue gas stream in which CO_2 is assumed to constitute ≈20% of the gas flow. The later was performed in order to assess CO_2 adsorption at pressures that mimic real postcombustion flue gas stream conditions.[6, 67] The gravimetric working

capacity data are presented in **Table 5.7** for sawdust-derived samples compared to three current benchmark materials, namely, two high performing MOFs (Mg-MOF-74 and HKUST-1),[79] and zeolite NaX.[80] For a pure CO_2 stream, the PSA working capacity of both mechanochemically activated and activated carbons ranges between 3.4 mmol g^{-1} and 4.0 mmol g^{-1} and is comparable to that of Mg-MOF-74 but lower than for HKUST-1 and much higher than for zeolite NaX. For flue gas conditions, the PSA uptake of the carbons is between 3 mmol g^{-1} and up to 4.1 mmol g^{-1} for samples SD2600P and SD2650P, which almost matches that of HKUST-1 (4.5 mmol g^{-1}). On the other hand, the VSA uptake of the mechanochemically activated carbons is very attractive; For sample SD2600P it reaches 6.0 mmol g^{-1} and 2.9 mmol g^{-1}, under pure CO_2 and flue gas conditions, respectively, which is comparable or better than that of Mg-MOF-74 and HKUST1.[79] The mechanochemical activation route clearly provides a route to lowly activated carbons with enhanced porosity with respect to surface area and pore volume and associated superior gravimetric CO_2 uptake. Whilst the gravimetric uptake is a good measure of performance for CO_2 storage, it is also important to assess the volumetric uptake. Knowledge of the volumetric uptake is essential given that for CO_2 capture under flue gas stream conditions, the adsorbent is packed into a column with spatial restrictions and therefore the amount of CO_2 stored per given space (volume) should be maximized.

5.6.3.2 Volumetric Uptake Calculation and Packing Density Assessment

To calculate the volumetric uptake, firstly the packing density of the carbons was determined using established procedures.[81] The packing density of the

mechanochemically activated and activated carbons derived from sawdust was in the range 0.81 g cm^{-3} – 0.95 g cm^{-3}, values of which are consistent with previous reports for similarly treated activated carbons of comparable porosity (i.e., surface area and pore volume).[81, 82] The volumetric CO_2 uptake is shown in **Figure 5.16** and the packing density values and uptakes at various pressures are summarized in **Table 5.8**. The volumetric CO_2 uptake of the mechanochemically activated samples is enhanced over that of the conventionally activated carbons, and is also superior to that of carbon monoliths (sample A1) and activated carbon monoliths (samples A3–36), which are the current benchmark materials.[82] At 0.15 bar, which is the uptake pressure that most closely matches conditions of postcombustion CO_2 capture, the compactivated MCA sample SD2600P has volumetric CO_2 uptake of 80 g L^{-1} compared to 54 g L^{-1} for conventionally activated CA sample SD2600 (i.e., a 48% increase). The uptake of SD2600P is also much higher than the 30–40 g L^{-1} achieved by carbon monoliths (sample A1) and activated carbon monoliths (samples A3–36).[82] At an uptake pressure of 1 bar, sample SD2600P can capture 242 g L^{-1} compared to 178 g L^{-1} for sample SD2600, and 130–160 g L^{-1} for carbon monoliths (sample A1) and activated carbon monoliths (samples A3–36).[82] As similar trend is observed for sample SD2650P and SD2650 (**Table 5.8**). The higher CO_2 uptake of the mechanochemically activated carbons at low pressure coupled with the generally higher packing density for carbonaceous materials means that their volumetric uptake (at pressure of ≤1 bar) is much higher when compared to a high surface area metal organic framework (MOF210) which has apparent CO_2 volumetric storage of 4 g L^{-1} and 10 g L^{-1} at 0.15 bar and 1 bar, respectively.[83] The higher volumetric CO_2 uptake of the mechanochemically activated carbons is maintained over the pressure range 1–10 bar as shown in **Figure 5.16** and **Table 5.8**.

To date, the most promising porous material with respect to low pressure (≤1 bar) CO_2 uptake at 25 °C is Mg-MOF-74, a magnesium-containing metal organic framework that possess bare metal (Mg) sites.[79, 84-86] It is thought that CO_2 uptake in Mg-MOF-74 is enhanced due to strong Mg–O links between the MOF surface and CO_2 molecules.[79, 82-86] We thus compared the CO_2 uptake of the mechanochemically activated carbons with Mg-MOF-74 (**Figure 5.17**). The gravimetric CO_2 uptake of Mg-MOF-74 is 5.7 and 8.0 mmol g^{-1} at 0.15 and 1 bar, respectively, compared to 2.0 and 5.8 mmol g^{-1}, respectively, for SD2600P, which is the best performing sawdust-derived sample (**Figure 5.17**). On the other hand, the volumetric uptake of SD2600P and Mg-MOF-74 are much more closely matched (**Figure 5.18**), as shown in **Table 5.8**; using the "tapped density" of 0.41 g cm^{-3} for Mg-MOF-74,[85] it has a volumetric uptake of 103 g L^{-1} at 0.15 bar compared to 80 g L^{-1} for sample SD2600P. However, at 1 bar, the volumetric uptake of SD2600P (242 g L^{-1}) surpasses that of Mg-MOF-74 (144 g L^{-1}). More importantly, as shown in **Table 5.7**, the volumetric working capacity of the mechanochemically activated carbons for PSA and VSA processes is generally higher than that of the best available benchmark materials. The packing density used for calculating the volumetric working capacity of the mechanochemically activated carbons and Mg-MOF-74 is already stated above, while we used packing density of 0.63 g cm^{-3} for zeolite NaX,[79] and 0.43 g cm^{-3} as "tapping density" for HKUST-1.[85]

It is clear that the volumetric working capacity of the mechanochemically activated carbons significantly outperforms that of zeolite NaX and the MOF materials. For a pure CO_2 stream, the PSA volumetric working capacity of both mechanochemical activated and conventional activated carbons ranges between 142 g L^{-1} and 153 g L^{-1} and is thus higher than for Mg-MOF-74 (63 g L^{-1}) and comparable to HKUST-1 (147 g L^{-1}). This is a very

attractive performance given that HKUST-1 has recently been identified as one of the best performing materials under those conditions.[79] The best performing carbon, SD2600P, for a pure CO_2 stream, has exceptional VSA volumetric working capacity of 251 g L^{-1} compared to 121 g L^{-1}, 70 g L^{-1} and 78 g L^{-1} for HKUST-1, Mg-MOF-74, and zeolite NaX, respectively. A similar trend is observed for VSA under flue gas conditions (**Table 5.7**). For PSA under flue gas conditions, the volumetric working capacity of SD2600P is 171 g L^{-1} which is at least twice as much as for the acknowledged best performer HKUST-1 (85 g L^{-1}) [79] and much higher than for zeolite NaX (50 g L^{-1}) and Mg-MOF-74 (38 g L^{-1}). The porosity and CO_2 uptake data reveal that mechanochemical activation, or so-called compactivation, offers benefits arising from enhanced surface area without compromising or changing pore size. We postulate that solid–solid interactions between carbon and KOH, during the early stages of the thermal treatment step, are maximized by the decrease of interparticle spaces occasioned by the compaction.

Mechanochemical activation, while offering benefits, does require a compaction step compared to conventional activation. However, the compaction step should not present obstacles as it can be included in a manner similar to that of pelletisation processes used in the preparation of granules or pellets of activated carbon.

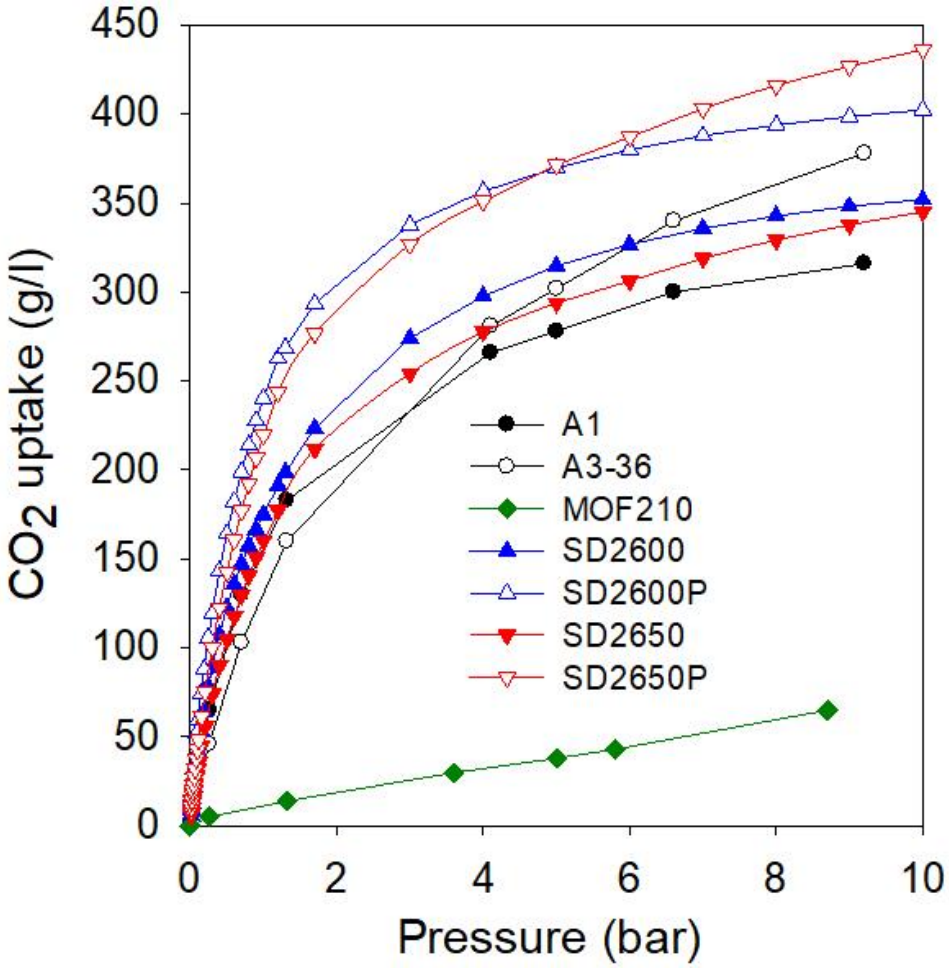


Figure 5.16: Volumetric CO_2 uptake *at 25 °C* for sawdust-derived mechanochemically activated carbons (SD2xP) and conventionally activated carbons (SD2x) prepared at x=600 °C or 650 °C and a KOH/carbon precursor ratio of *2*, compared with benchmark carbon and MOF materials. Data for carbons monoliths A1 and A3-36 which are generated by pyrolysis of a Polyvinylidene chloride copolymer (PVDC), (A1 submitted to a higher degree of activation in nitrogen than sample A3), was obtained from reference [80]. Data for MOF-210 was obtained from reference [81].

Table 5.7: Gravimetric and volumetric working capacity for pressure swing adsorption (PSA) and vacuum swing adsorption (VSA) of CO_2 on sawdust-derived mechanochemically activated carbons (SD2xP) and conventionally activated carbons (SD2x) and benchmark porous materials *at ≈25 °C* for a pure CO_2 gas stream and a 20% partial CO_2 pressure flue gas. The values in parentheses are volumetric uptake (in g L^{-1}).

Sample	Pure CO_2 uptake [a] (mmol g^{-1})		Flue gas CO_2 uptake [b] (mmol g^{-1})		Reference
	PSA	VSA	PSA	VSA	
SD2600	3.7 (153)	4.6 (190)	3.0 (124)	2.1 (87)	This work
SD2600P	3.4 (142)	6.0 (251)	4.1 (171)	2.9 (121)	This work
SD2650	3.8 (149)	4.6 (180)	3.1 (121)	1.9 (74)	This work
SD2600P	4.0 (143)	5.7 (213)	4.0 (143)	2.4 (86)	This work
HKUST-1	7.8 (147)	6.4 (121)	4.5 (85)	1.6 (30)	[75-77]
Mg-MOF-74	3.5 (63)	3.9 (70)	2.1 (38)	4.1 (74)	[75-77]
NaX	1.6 (44)	2.8 (78)	1.8 (50)	2.5 (69)	[78]

[a] 1 bar -6 bar for PSA; 0.05 bar -1.5 bar for VSA.
[b] 0.2 bar -1.2 bar for PSA; 0.01 bar - 0.3 bar for VSA.

Table 5.8: Packing density and volumetric CO_2 uptake ***at 25 ºC*** for sawdust-derived mechanochemically activated carbons (SD2xP) and conventionally activated carbons (SD2x) prepared at x = 600 °C or 650 °C and KOH/carbon precursor ratio of *2*. Uptake data for benchmark carbon and metal organic framework (MOF) materials shown for comparison.

Sample	Packing density [gcm^{-3}]	Volumetric CO_2 uptake [gL^{-1}]				Reference
		0.15 bar	1 bar	5 bar	9 bar	
SD2600	0.94	54	178	315	348	This work
SD2600P	0.95	80	242	370	399	This work
SD2650	0.89	47	161	294	338	This work
SD2650P	0.81	54	189	371	427	This work
Carbon A1 [a]	1.00 [a]	38	157	278	316	Data from [82]
Carbon A3-36 [a]	0.87 [a]	27	128	302	378	Crystal density from [82]
MOF210 [b]	0.25 [c]	4	10	38	65	Data from [83, 83]
Mg-MOF-74 [d]	0.41[e]	103	144	-	-	Tapping density from [84,85]

[a] Data from reference [82].
[b] Data from reference [83].
[c] Crystal density of MOF210 from reference [83].
[d] Data from reference [84].
[e] "Tapping density" of Mg-MOF-74 from reference [85].

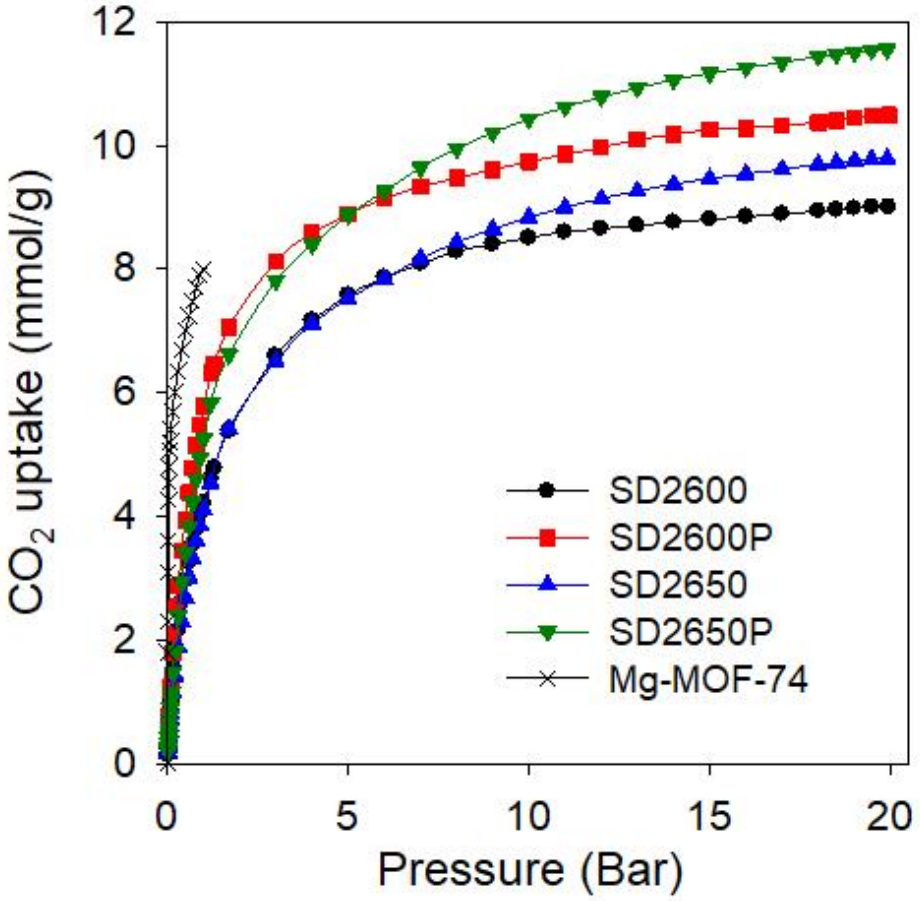


Figure 5.17: CO_2 uptake isotherms ***at 25 °C*** and pressure range **0-20 bar** for sawdust-derived mechanochemically activated carbons (SD2xP) and conventionally activated carbons (SD2x) prepared at x= 600 or 650 °C and KOH/carbon ratio of *2* compared to Mg-MOF-74. Data for Mg- MOF-74 was obtained from reference [84].

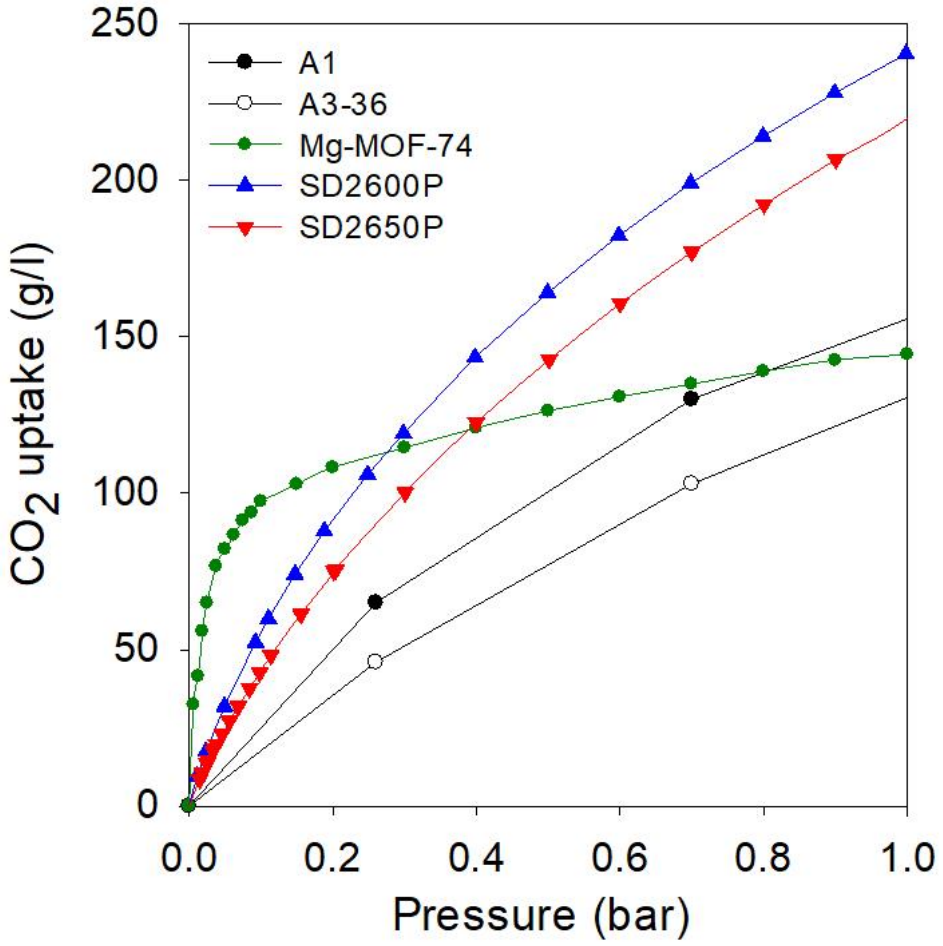


Figure 5.18: CO_2 volumetric uptake ***at 25 ºC*** and pressure range **0-1 bar** for sawdust-derived mechanochemically activated carbons (SD2xP) prepared at x= 600 ºC or 650 ºC and KOH/carbon precursor ratio of *2* compared to benchmark carbons (A1 and A3-36) and Mg-MOF-74. Data for carbons A1 and A3-36 was obtained from reference [82] while data for Mg-MOF-74 is from reference [84].

5.7 Conclusions

The work reported in this chapter describes a mechanochemical activation route that enables the production of lowly compactivated biomass derived carbons that exhibit enhanced surface area and pore volume compared to conventionally activated carbons prepared under similar conditions (i.e., temperature and KOH/carbon ratio) but without compromising the pore size or pore size distribution. The mechanochemical activation process is based on compaction, *at 740 MPa*, of powder mixtures of activating agent (KOH) and biomass hydrochar (at KOH/hydrochar ratio of 2) into pellets/disks prior to thermal activation at 600 °C or 650 °C. The surface area and pore volume of the biomass (wood sawdust and lignin) derived mechanochemically activated carbons is higher by between 25% and 75% compared to conventionally activated carbons. Despite their higher porosity, the mechanochemically activated carbons possess mainly small micropores (5.8 Å – 6.5 Å) similar to those of equivalent conventionally activated samples that nevertheless have lower surface area and pore volume. The increase in surface area arising from such small micropores results in a dramatic increase in CO_2 storage capacity at 25 °C and low pressure (≤1 bar). For sawdust-derived mechanochemically activated carbons prepared at 600 °C and KOH/carbon ratio of 2, the CO_2 uptake at 25 °C rises from 1.3 mmol g^{-1} to 2.0 mmol g^{-1} at 0.15 bar, and from 4.3 mmol g^{-1} to 5.8 mmol g^{-1} at 1 bar, which is the highest reported for carbonaceous materials. Also, due to their lowly activated nature, they have high packing density and therefore exhibit excellent volumetric CO_2 uptake (80 g L^{-1} and 242 g L^{-1} at 0.15 bar and 1 bar, respectively) that is higher than for any material reported to date. Furthermore, the mechanochemically activated carbons exhibit

superior CO_2 working capacity (both gravimetric and volumetric) for PSA and VSA processes.

5.8 References

1. R. S. Haszeldine, *Science*, 2009, **325**, 1647-1652.

2. V. Scott, S. Gilfillan, N. Markusson, H. Chalmers and R. S. Haszeldine, *Nat. Climate Change*, 2013, **3**, 105-111.

3. K. S. Lackner, S. Brennan, J. M. Matter, A. H. A. Park, A. Wright and B. van der Zwaan, *Proc. Natl. Acad. Sci U.S.A.*, 2012, **109**, 13156-13162.

4. P. Markewitz, W. Kuckshinrichs, W. Leitner, J. Linssen, P. Zapp, R. Bongartz, A. Schreiber and T. E. Muller, *Energy Environ. Sci.*, 2012, **5**, 7281-7305.

5. G. T. Rochelle, *Science*, 2009, **325**, 1652-1654.

6. J. D. Figueroa, T. Fout, S. Plasynski, H. McIlvried and R. D. Srivastava, *Int. J. Greenhouse Gas Control*, 2008, **2**, 9-20.

7. H. Q. Yang, Z. H. Xu, M. H. Fan, R. Gupta, R. B. Slimane, A. E. Bland and I. Wright, *J. Environ. Sci.*, 2008, **20**, 14-27.

8. T. C. Drage, C. E. Snape, L. A. Stevens, J. Wood, J. W. Wang, A. I. Cooper, R. Dawson, X. Guo, C. Satterley and R. Irons, *J. Mater. Chem.*, 2012, **22**, 2815-2823.

9. A. Samanta, A. Zhao, G. K. H. Shimizu, P. Sarkar and R. Gupta, *Ind. Eng. Chem. Res.*, 2012, **51**, 1438-1463.

10. S. Choi, J. H. Drese and C. W. Jones, *ChemSusChem*, 2009, **2**, 796-854.

11. Q. A. Wang, J. Z. Luo, Z. Y. Zhong and A. Borgna, *Energy Environ. Sci.*, 2011, **4**, 42-55.

12. D. M. D'Alessandro, B. Smit and J. R. Long, *Angew. Chem. Int. Ed.*, 2010, **49**, 6058-6082.

13. K. Sumida, D. L. Rogow, J. A. Mason, T. M. McDonald, E. D. Bloch, Z. R. Herm, T. H. Bae and J. R. Long, *Chem. Rev.*, 2012, **112**, 724-781.

14. J. Liu, P. K. Thallapally, B. P. McGrail and D. R. Brown, *Chem. Soc. Rev.*, 2012, **41**, 2308-2322.

15. N. Huang, X. Chen, R. Krishna and D. L. Jiang, *Angew. Chem. Int. Ed.*, 2015, **54**, 2986-2990.

16. N. Huang, R. Krishna and D. L. Jiang, *J. Am. Chem. Soc.*, 2015, **137**, 7079-7082.

17. V. Presser, J. McDonough, S. H. Yeon and Y. Gogotsi, *Energy Environ. Sci.*, 2011, **4**, 3059-3066.

18. M. Sevilla, P. Valle-Vigon and A. B. Fuertes, *Adv. Funct. Mater.*, 2011, **21**, 2781-2787.

19. M. Nandi, K. Okada, A. Dutta, A. Bhaumik, J. Maruyama, D. Derks and H. Uyama, *Chem. Commun.*, 2012, **48**, 10283-10285.

20. J. Silvestre-Albero, A. Wahby, A. Sepúlveda-Escribano, M. Martínez-Escandell, K. Kaneko and F. Rodríguez- Reinoso, *Chem. Commun.*, 2011, **47**, 6840-6842.

21. X. Q. Fan, L. X. Zhang, G. B. Zhang, Z. Shu and J. L. Shi, *Carbon*, 2013, **61**, 423-430.

22. W. Sangchoom and R. Mokaya, *ACS Sustainable Chem. Eng.*, 2015, **3**, 1658-1667.

23. M. Sevilla and A. B. Fuertes, *Energy Environ. Sci.*, 2011, **4**, 1765-1771.

24. M. Sevilla, J. B. Parra and A. B. Fuertes, *ACS Appl. Mater. Interfaces*, 2013, **5**, 6360-6368.

25. G. Srinivas, J. Burress and T. Yildirim, *Energy Environ. Sci.*, 2012, **5**, 6453-6459.

26. N. P. Wickramaratne and M. Jaroniec, *J. Mater. Chem. A*, 2013, **1**, 112-116.

27. N. P. Wickramaratne and M. Jaroniec, *ACS Appl. Mater. Interfaces*, 2013, **5**, 1849-1855.

28. M. Sevilla and A. B. Fuertes, *J. Colloid Interface Sci.*, 2012, **366**, 147-154.

29. H. R. Wei, S. B. Deng, B. Y. Hu, Z. H. Chen, B. Wang, J. Huang and G. Yu, *ChemSusChem*, 2012, **5**, 2354-2360.

30. M. Saleh, V. Chandra, K. C. Kemp and K. S. Kim, *Nanotechnology*, 2013, **24**, 8.

31. K. C. Kemp, V. Chandra, M. Saleh and K. S. Kim, *Nanotechnology*, 2013, **24**, 8.

32. Z. S. Zhang, J. Zhou, W. Xing, Q. Z. Xue, Z. F. Yan, S. P. Zhuo and S. Z. Qiao, *Phys. Chem. Chem. Phys.*, 2013, **15**, 2523-2529.

33. Z. X. Yang, Y. D. Xia and R. Mokaya, *J. Am. Chem. Soc.*, 2007, **129**, 1673-1679.

34. N. Alam and R. Mokaya, *Energy Environ. Sci.*, 2010, **3**, 1773-1781.

35. M. Sevilla, R. Foulston and R. Mokaya, *Energy Environ. Sci.*, 2010, **3**, 223-227.

36. M. Sevilla, N. Alam and R. Mokaya, *J. Phys. Chem. C*, 2010, **114**, 11314-11319.

37. Y. D. Xia, G. S. Walker, D. M. Grant and R. Mokaya, *J. Am. Chem. Soc.*, 2009, **131**, 16493-16499.

38. A. Pacula and R. Mokaya, *J. Phys. Chem. C*, 2008, **112**, 2764-2769.

39. Z. X. Yang, Y. D. Xia, X. Z. Sun and R. Mokaya, *J. Phys. Chem. B*, 2006, **110**, 18424-18431.

40. N. Alam and R. Mokaya, *Microporous Mesoporous Mater.*, 2011, **142**, 716-724.

41. N. Alam and R. Mokaya, *Microporous Mesoporous Mater.*, 2011, **144**, 140-147.

42. Y. D. Xia, R. Mokaya, D. M. Grant and G. S. Walker, *Carbon*, 2011, **49**, 844-853.

43. M. Sevilla, A. B. Fuertes and R. Mokaya, *Int. J. Hydrogen Energy*, 2011, **36**, 15658-15663.

44. A. Almasoudi and R. Mokaya, *J. Mater. Chem.*, 2012, **22**, 146-152.

45. Y. D. Xia, Z. X. Yang and R. Mokaya, *Chem. Vap. Deposition*, 2010, **16**, 322-328.

46. E. Masika and R. Mokaya, *Energy Environ. Sci.*, 2014, **7**, 427-434.

47. Y. D. Xia, R. Mokaya, G. S. Walker and Y. Q. Zhu, *Adv. Energy Mater.*, 2011, **1**, 678-683.

48. E. Masika and R. Mokaya, *RSC Adv.*, 2013, **3**, 17677-17681.

49. C. Robertson and R. Mokaya, *Microporous Mesoporous Mater.*, 2013, **179**, 151-156.

50. A. Almasoudi and R. Mokaya, *J. Mater. Chem. A*, 2014, **2**, 10960-10968.

51. A. Almasoudi and R. Mokaya, *Microporous Mesoporous Mater.*, 2014, **195**, 258-265.

52. B. Adeniran, E. Masika and R. Mokaya, *J. Mater. Chem. A*, 2014, **2**, 14696-14710.

53. D. H. Everett and J. C. Powl, *J. Chem. Soc., Faraday Trans. 1: Phys. Chem. Condensed Phases*, 1976, **72**, 619-636.

54. M. Sevilla and R. Mokaya, *Energy Environ. Sci.*, 2014, **7**, 1250-1280.

55. G. P. Hao, W. C. Li, D. Qian and A. H. Lu, *Adv. Mater.*, 2010, **22**, 853–857.

56. T. C. Drage, A. Arenillas, K. M. Smith, C. Pevida, S. Piippo and C. E. Snape, *Fuel*, 2007, **86**, 22-31.

57. W. Xing, C. Liu, Z. Y. Zhou, L. Zhang, J. Zhou, S. P. Zhuo, Z. F. Yan, H. Gao, G. Q. Wang and S. Z. Qiao, *Energy Environ. Sci.*, 2012, **5**, 7323-7327.

58. G. P. Hao, W. C. Li, D. Qian, G. H. Wang, W. P. Zhang, T. Zhang, A. Q. Wang, F. Schüth, H. J. Bongard and A. H. Lu, *J. Am. Chem. Soc.*, 2011, **133**, 11378-11388.

59. J. C. Wang, A. Heerwig, M. R. Lohe, M. Oschatz, L. Borchardt and S. Kaskel, *J. Mater. Chem.*, 2012, **22**, 13911-13913.

60. Y. F. Zhao, L. Zhao, K. X. Yao, Y. Yang, Q. Zhang and Y. Han, *J. Mater. Chem.*, 2012, **22**, 19726-19731.

61. A. Wahby, J. M. Ramos-Fernández, M. Martínez-Escandell, A. Sepúlveda-Escribano, J. Silvestre-Albero and F. Rodríguez-Reinoso, *ChemSusChem*, 2010, **3**, 974-981.

62. D. Lee, C. Y. Zhang, C. Wei, B. L. Ashfeld and H. F. Gao, *J. Mater. Chem. A*, 2013, **1**, 14862-14867.

63. G. Srinivas, V. Krungleviciute, Z. X. Guo and T. Yildirim, *Energy Environ. Sci.*, 2014, **7**, 335-342.

64. Z. Z. Yang, L. N. He, J. Gao, A. H. Liu and B. Yu, *Energy Environ. Sci.*, 2012, **5**, 6602-6639.

65. C. A. Grande, R. Ribeiro and A. E. Rodrigues, *ChemSusChem*, 2010, **3**, 892-898.

66. L. Estevez, R. Dua, N. Bhandari, A. Ramanujapuram, P. Wang and E. P. Giannelis, *Energy. Environ. Sci.*, 2013, **6**, 1785-1790.

67. Z. Q. Zhang, K. Wang, J. D. Atkinson, X. L. Yan, X. Li, M. J. Rood and Z. F. Yan, *J. Hazard. Mater.*, 2012, **229**, 183-191.

68. J. Romanos, M. Beckner, T. Rash, L. Firlej, B. Kuchta, P. Yu, G. Suppes, C. Wexler and P. Pfeifer, *Nanotechnology*, 2012, **23**, 7.

69. M. Sevilla, A. B. Fuertes and R. Mokaya, *Energy Environ. Sci.*, 2011, **4**, 1400-1410.

70. B. Adeniran and R. Mokaya, *J. Mater. Chem. A*, 2015, **3**, 5148-5161.

71. B. Ashourirad, A. K. Sekizkardes, S. Altarawneh and H. M. El-Kaderi, *Chem. Mater.*, 2015, **27**, 1349-1358.

72. B. Adeniran and R. Mokaya, *Nano Energy*, 2015, **16**, 173-185.

73. Suhas, P. J. M. Carrott and M. Carrott, *Bioresour. Technol.*, 2007, **98**, 2301-2312.

74. B. N. Kuznetsov and M. L. Shchipko, *Bioresour. Technol.*, 1995, **52**, 13-19.

75. E. S. Kikkinides, R. T. Yang and S. H. Cho, *Ind. Eng. Chem. Res.*, 1993, **32**, 2714-2720.

76. K. T. Chue, J. N. Kim, Y. J. Yoo, S. H. Cho and R. T. Yang, *Ind. Eng. Chem. Res.*, 1995, **34**, 591-598.

77. D. Ko, R. Siriwardane and L. T. Biegler, *Ind. Eng. Chem. Res.*, 2005, **44**, 8084-8094.

78. L. Wang, Y. Yang, W. L. Shen, X. M. Kong, P. Li, J. G. Yu and A. E. Rodrigues, *Ind. Eng. Chem. Res.*, 2013, **52**, 7947-7955.

79. J. M. Simmons, H. Wu, W. Zhou and T. Yildirim, *Energy Environ. Sci.*, 2011, **4**, 2177-2185.

80. Y. Belmabkhout, G. Pirngruber, E. Jolimaitre and A. Methivier, *Adsorption*, 2007, **13**, 341-349.

81. M. Sevilla, R. Mokaya and A. B. Fuertes, *Energy Environ. Sci.*, 2011, **4**, 2930-2936.

82. J. P. Marco-Lozar, M. Kunowsky, F. Suárez-García, J. D. Carruthers and A. Linares-Solano, *Energy Environ. Sci.*, 2012, **5**, 9833-9842.

83. H. Furukawa, N. Ko, Y. B. Go, N. Aratani, S. B. Choi, E. Choi, A. O. Yazaydin, R. Q. Snurr, M. O'Keeffe, J. Kim and O. M. Yaghi, *Science*, 2010, **329**, 424-428.

84. S. R. Caskey, A. G. Wong-Foy and A. J. Matzger, *J. Am. Chem. Soc.*, 2008, **130**, 10870.

85. Y. Peng, V. Krungleviciute, I. Eryazici, J. T. Hupp, O. K. Farha and T. Yildirim, *J. Am. Chem. Soc.*, 2013, **135**, 11887-11894.

86. P. D. C. Dietzel, R. E. Johnsen, H. Fjellvag, S. Bordiga, E. Groppo, S. Chavan and R. Blom, *Chem. Commun.*, 2008, 5125-5127.

Chapter 6. Biomass to Porous Carbon in One Step: Directly Activated Biomass for High Performance CO_2 Storage

6.1 Aim of this Chapter

A main motivation of this chapter is:

- To demonstrate a general route for the direct conversion of biomass to activated forms of carbon. The chapter explores the direct activation of Eucalyptus sawdust biomass and seeks to establish whether such a direct, simpler and cheaper process offers advantages with respect to carbon yield, textural properties and application as energy materials for gas (CO_2) storage. The characteristics of directly activated biomass-derived carbons and their CO_2 uptake properties are compared to those generated *via* a conventional two-step (hydrothermal carbonisation HTC + activation) process.

6.2 Abstract

This chapter explores the direct conversion of biomass to activated carbons in one step. The work reported herein demonstrates the successful conversion of biomass, namely; sawdust, to activated carbons *via* a direct activation process that negates the need for hydrothermal carbonisation or pyrolysis. This is a departure from established practice that requires that biomass source (Eucalyptus sawdust) to be first enriched to carbonaceous matter *via* hydrothermal carbonisation or pyrolysis prior to activation. The direct activation, with KOH as activating agent, generated activated carbon at yields that are comparable or higher than those of conventional activation routes. The directly activated carbons, whilst offering the advantage of simplicity, lower cost and a greener more sustainable synthesis route, have properties that are similar or superior to analogous carbons prepared *via* conventional methods. In particular the textural properties, surface functionality and level of graphitic ordering were found to be similar to that of conventionally generated activated carbons. Depending on the activation conditions, the porosity of the directly activated carbons may be tailored towards pore channels of size 5 Å – 7 Å, which favour post-combustion CO_2 uptake and thus the carbons capture up to 1.3 mmol g^{-1} and 4.6 mmol g^{-1} of CO_2 at 0.15 bar and 1 bar, respectively and 25 ^oC with high selectivity. On the other hand, at higher levels of activation, the directly activated carbons can be tailored towards possessing a greater proportion of larger micropores (10 Å – 20 Å pores) and small mesopores (20 Å – 30 Å pores) so as to optimize CO_2 uptake at moderate to high pressure, for example up to 22 mmol g^{-1} (at 20 bar and at 25 ^oC) and 31 mmol g^{-1} (at 20 bar and at 0 ^oC).

6.3 Introduction

The discovery of new materials is a central requirement in many anticipated advances in the energy and sustainability arena.[1-3] For new materials to be interesting they need to fit into one of three categories; (i) exhibit new or improved desirable properties, (ii) be easier or cheaper to prepare, and (iii) be sustainable. Improved or new properties may be achieved by careful material design based on deep understanding of underlying phenomena, while lower cost and ease of preparation may be possible by the use of new starting (raw) materials or simple reduction of the number of steps required. In this regard, nanostructured carbons prepared *via* simple processes and which use readily available and low cost precursors are now considered as key materials for the generation and storage of sustainable energy and for environmental remediation.[4, 5] This is typified by the broad class of nanostructured carbons that are currently under intense study for use as, amongst other applications, gas (hydrogen, CO_2, methane, etc.) storage materials [4, 6, 7] and as electrode materials for supercapacitors.[4, 8] For the next generation of nanostructured carbons, the drive is towards materials that are simple to prepare *via* cost effective routes, and which may involve use of renewable resources as precursors wherein there is the possibility of valorisation of the starting (raw) materials. Amongst nanostructured carbons, activated carbons are attracting a great deal of interest due to their tuneable pore size, porosity and good chemical stability.[4-8] A particular attraction of activated carbons is that their 'green' credentials may be enhanced if they are prepared from sustainable biomass resources that would normally be considered as waste.

Recently, Mokaya and co-workers have reported on new synthesis routes to activated carbons generated from sustainable precursors or renewable biomass.[9-15] The carbons have improved gas (CO_2 and hydrogen) storage

capacity [9-14] and are excellent electrode materials for supercapacitors.[15] In general, activated carbons are traditionally synthesized *via* physical or chemical activation.[4-8] The former involves gasification of a carbon precursor with oxidizing gases such as steam or air at high temperature (800 ^{o}C – 1100 ^{o}C), while for the later, the carbon precursor is thermally treated under inert conditions in the presence of an activating agent (KOH, NaOH or $ZnCl_2$, etc.).

For conversion of biomass to activated carbons, the conventional process is to first convert the biomass into carbon-rich carbonaceous matter, which is then activated.[4-15] The two main processes for the conversion of biomass to activateable carbonaceous matter are; (i) hydrothermal carbonisation (HTC) [16-20] and (ii) pyrolysis.[21-24] Hydrothermal carbonization proceeds *via* thermochemical decomposition of biomass into so-called hydrochar in the presence of superheated water,[16-20] while pyrolysis occurs *via* processes that increase the carbon content of biomass precursors during heating in the absence of oxygen.[21-24] In the search for sustainable and cheaper biomass-derived activated carbons it is desirable to simplify the synthesis process and in particular to negate the need for hydrothermal carbonisation or pyrolysis prior to activation. In other words, it is desirable to directly activate biomass to activated carbons that have similar or improved yield and/or properties compared to those that are prepared *via* the conventional, and longer, two-step route incorporating HTC or pyrolysis prior to activation. There are hardly any reports of such direct activation of biomass and no comprehensive data exists on how the resulting carbons compare to conventionally activated carbons.

6.4 Experimental Section

This section presents a detailed description of the materials and chemicals, experimental procedures, and approach used in **Chapter 6**.

6.4.1 Materials and Chemicals

The list of chemicals/materials used in this chapter, their sources and purity are presented in **Table 6.1**.

Table 6.1: List of chemical reagents/materials used in experiment.

Chemical/Material	Source	Purity/Concentration
Biomass sawdust	eucalyptus wood sawdust	-
Potassium Hydroxide (KOH)	Fisher Scientific	-
N_2 Compressed gas (cylinder)	BOC Ltd	100%
Hydrochloric acid (HCl)	Fisher Scientific	37%

6.4.2 Material Synthesis

6.4.2.1 Direct Activation

The required amount of KOH was added to sawdust. The resulting KOH/sawdust mixture was placed in a ceramic boat and inserted into a tubular furnace and heated (at a ramp rate of 5 ^{o}C min^{-1}) to between 600 ^{o}C and 800 ^{o}C and held at the target temperature (600 ^{o}C, 700 ^{o}C or 800 ^{o}C) for 1 h (**Figure 4.5** and **Table 6.2**). The resulting carbonaceous matter was recovered and washed with 2M HCl at room temperature until all inorganic impurities were removed as confirmed by thermogravimetric analysis. The directly prepared activated carbons were then filtered, washed with deionised water and dried in an oven at 120 ^{o}C for 6 h. The directly activated carbons were designated as *SDXTD* (from sawdust) where *X* is the KOH/sawdust ratio (2 or 4) and *T* is the activation temperature (600 ^{o}C, 700 ^{o}C or 800 ^{o}C). See **Table 6.3** for abbreviations.

6.4.2.2 Conventional Activation

The sawdust was first converted to hydrochar *via* hydrothermal carbonisation as follows; an aqueous dispersion of biomass (sawdust) at a concentration of 320 gL^{-1} (6.4 g of sawdust in 20 ml of water) was placed in a stainless steel autoclave and heated up to 250 ^{o}C and the temperature was held for 2 h. The resulting solid (the hydrochar) was recovered by filtration and washed thoroughly with distilled water and then dried at 120 ^{o}C for 4 h. The hydrochar was then activated as described above. The hydrochar-derived activated carbons were designated as *SDXT* (from sawdust) where *X* is the KOH/hydrochar ratio (2 or 4) and *T* the activation temperature (600 ^{o}C, 700 ^{o}C or 800 ^{o}C). See **Table 6.3** for abbreviations.

Table 6.2: Summary of ACs synthesis: parameters and conditions.

Carbon Precursor	Eucalyptus wood sawdust Eucalyptus wood sawdust hydrochar
Activating Agent	KOH (powder)
KOH ratio	KOH/sawdust 2:1 or 4:1 KOH/hydrochar 2:1 or 4:1
Activation Temperature	600 ^{o}C or 700 ^{o}C or 800 ^{o}C
Ramp Rate	5 ^{o}C/min
Process Hold Time	1 hour
Environment/Gas	Nitrogen flow

6.5 Abbreviations

Table 6.3 summarized the samples abbreviations of directly activated carbons and conventionally activated carbons *via* hydrothermal carbonisation HTC.

Table 6.3: Abbreviations list for directly activated carbons and conventionally activated carbons.

Direct Activation Sawdust-Derived Activated Carbons	**Conventional Activation Hydrochar-Derived Activated Carbons**
Directly activated carbons prepared from sawdust at various KOH/sawdust ratio and at various temperatures. ***SDXTD*** Where; *X* is the KOH/sawdust ratio (2:1 or 4:1). *T* is the activation temperature (600, 700 or 800 ^{o}C).	Conventionally activated carbons prepared from hydrochar at various KOH/hydrochar ratio and at various temperatures. ***SDXT*** Where; *X* is the KOH/hydrochar ratio (2:1 or 4:1). *T* is the activation temperature (600, 700 or 800 ^{o}C).
SD2600D	SD2600
SD2700D	SD2700
SD2800D	SD2800
SD4800D	SD4800

6.6 Results and Discussion

6.6.1 Thermal Stability Analysis

The activated carbons prepared directly were fully carbonaceous which confirmed by performing thermogravimetric analysis (TGA) following the procedure mentioned in **Chapter 2**.

The TGA curves of the directly synthesised (SD2800D and SD4800D) and analogous conventionally prepared (SD2800 and SD4800) activated carbons are very similar and both show virtually no residual mass at 700 ^{o}C (**Figure 6.1 A** and **Figure 6.1 B**). Additionally both the directly and conventionally synthesised activated carbons have a similar level of thermal stability which suggests similar levels of graphitisation. Furthermore, in both cases the carbons prepared at higher activation temperature show greater resistance to combustion as expected. It appears therefore that direct activation does not have any effect on the nature of the carbon. This was confirmed by both powder XRD patterns (**Figure 6.2**) and elemental analysis data (**Table 6.4**).

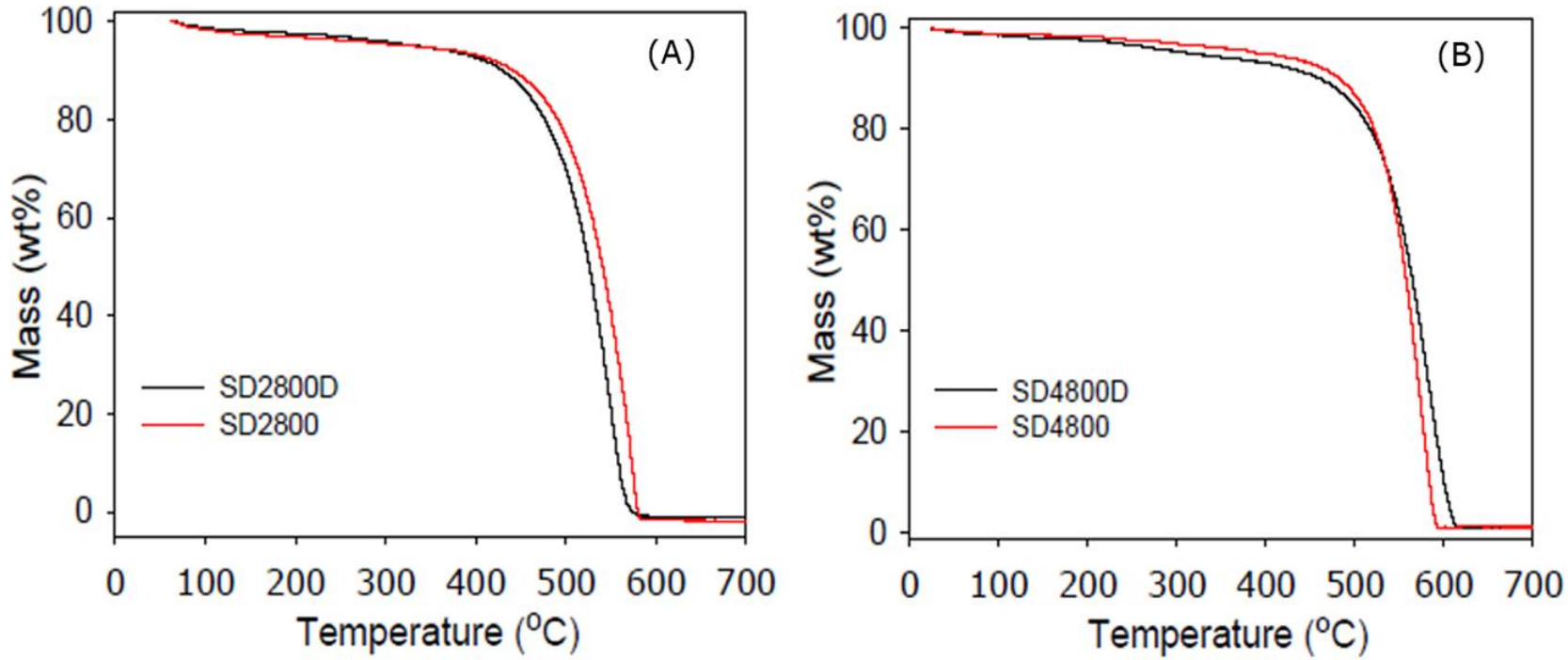


Figure 6.1: Thermogravimetric analysis (TGA) curves of directly synthesised (SD2800D and SD4800D) and analogous conventionally prepared (SD2800 and SD4800) activated carbons at **(A)** KOH/carbon ratio of *2* or **(B)** KOH/carbon ratio of *4*.

6.6.2 Structural Ordering Analysis PXRD

Powder X-ray diffraction (XRD) used to confirm the nature and purity of activated carbons prepared directly (SD2600D, SD2700D, SD2800D and SD4800D), and activated carbons conventionally prepared (SD2600, SD2700, SD2800 and SD4800). The XRD patterns (**Figure 6.2 A**, **B**) suggest a similar level of graphitic ordering for the conventional samples and directly synthesised samples.

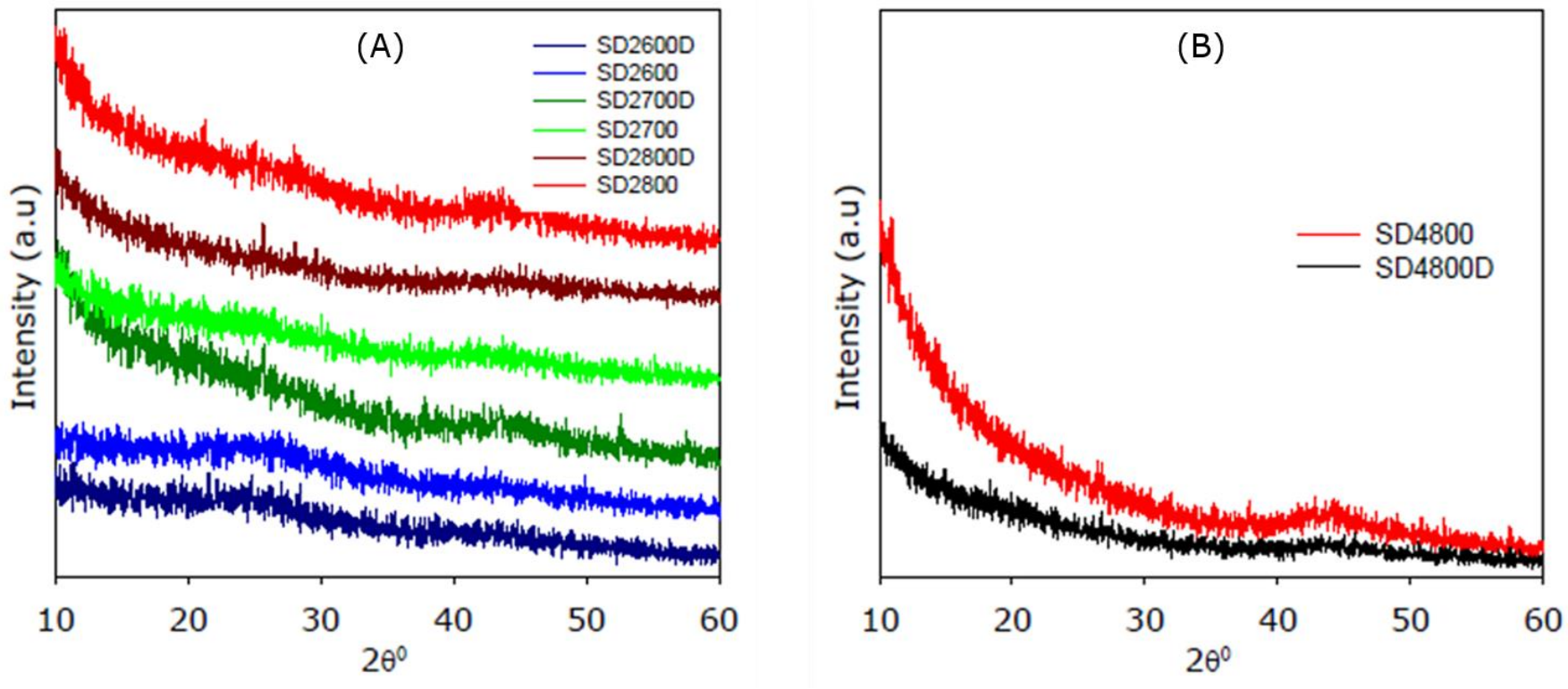


Figure 6.2: Powder XRD patterns of directly activated carbons (sawdust-derived, *SDXTD*) or conventionally activated carbons (hydrochar-derived, *SDXT*) prepared at **(A)** KOH/carbon ratio of *2* or **(B)** KOH/carbon ratio of *4*.

6.6.3 Elemental Composition Analysis

The elemental analysis data in **Table 6.4** shows that the C, H and O contents are very similar and that for all sample sets, the C content in the activated carbons increases for samples prepared at higher activation temperature.

Table 6.4: Elemental composition of sawdust SD, SD-derived hydrochar and activated carbons (directly and conventionally).

Sample	Chemical composition				
	C [%] [a]	H [%] [a]	O+X [%] [b]	(O/C)[c]	(H/C)[c]
Sawdust	46.4	5.8	47.8	0.773	1.500
SD hydrochar	57.4	5.6	37.0	0.483	1.171
SD2600D	71.4	0.7	27.9	0.293	0.118
SD2600	72.3	0.7	27.0	0.280	0.116
SD2700D	75.6	0.3	24.1	0.239	0.048
SD2700	72.4	0.3	28.3	0.293	0.049
SD2800D	85.6	0.4	14.0	0.123	0.056
SD2800	85.2	0.1	14.8	0.130	0.014
SD4800D	85.8	0.3	13.9	0.122	0.042
SD4800	89.7	0.1	10.3	0.086	0.013

[a] Determined from CHN microanalysis.
[b] Obtained by difference as follows: Oxygen content + X (where X any other elements (%) =[100–(C+H+N)].
[c] Atomic ratio.

6.6.4 The Inorganic Metal Content K, Na, Ca, Fe, Mn, Ba and Mg Analysis

The metal content of the carbons determined *via* ICP-OES analysis using a Perkin Elmer Optima 2000 DV ICPOES with an S10 autosampler following the procedure discussed in **Chapter 2**.

The carbons analysed for K, Na, Ca, Fe, Mn, Ba and Mg, and found only trace amounts of Ca (*ca.* 0.2 wt%), and hardly detected amounts of K, Mg and Na, all of which were typically less than 0.1 wt%. The amounts were similar to those of analogous directly and conventionally activated carbons. It appears therefore that direct activation does not have any effect on the nature of the carbons (**Table 6.5**). This was confirmed by both powder XRD patterns (**Figure 6.2**) and elemental analysis data (**Table 6.4**).

Table 6.5: Showing detected amounts of Ca, K, Mg and Na in analogous directly activated carbons and conventionally activated carbons.

Metal	Metal content/amount (wt %)
Ca	0.2
K	less than 0.1
Mg	less than 0.1
Na	less than 0.1

6.6.5 Yield of Activated Carbons

The overall yield of activated carbons obtained to ascertain whether the direct activation route offered any disadvantages or otherwise (

Table 6.6). For conventional activation *via* HTC, the carbon yield from sawdust to hydrochar was ca. 43%, which is similar to what has previously been reported. [19, 25-27] The yield of activated carbons from the hydrochar (at KOH/carbon ratio of 2) varied between 32% (at 800 ^{o}C) and 47% (at 600 ^{o}C), which is in agreement with previous studies. [9, 14, 28-31] Thus the yield of activated carbon with respect to the sawdust was between 14% (at 800 ^{o}C) and 20% (at 600 ^{o}C). On the other hand the carbon yield *via* the direct activation route (at KOH/carbon ratio of 2) was between 22% (at 800 ^{o}C) and 30% (at 600 ^{o}C). Thus the activated carbon yields (with respect to sawdust biomass) are higher for direct activation than for the conventional route that includes HTC.

Table 6.6: Showing the yield of activated carbons obtained by direct activation route and conventional activation *via* HTC.

Sample	Yield [a]
Hydrochar	43%
SD2600D	22%
SD2600	20% (47% [b])
SD2800D	30%
SD2800	14% (32% [b])

[a] The yields values are based on biomass.
[b] The yields values are based on the hydrochar.

6.6.6 Raman Analysis

Raman analysis performed to further ascertain the similarity between the directly activated carbons and conventionally activated carbons. The Raman spectra obtained following the procedure discussed in **Chapter 2**. The Raman spectra are shown in **Figure 6.3**. And the values of I_D/I_G ratio summarized in **Table 6.7**.

The carbons exhibit bands at 1340 cm^{-1} - 1350 cm^{-1} and 1586 cm^{-1} - 1590 cm^{-1} that are the D peak (disordered carbon) and the G-peak (graphitic domains), respectively.[32] The spectra show no discernible differences between the two sets of samples at all activation conditions. The ratio of peak intensity (i.e., area) of the D-peak to G-peak (I_D/I_G), based on the two-band fitting model is very similar for the two sets of samples (**Table 6.7**). The I_D/I_G ratio is 0.78 and 0.79 for SD2600 and SD2600D, respectively, increases to 0.81 and 0.83 for SD2700 and SD2700D, respectively, is similar (0.84) for samples prepared at 800 ^oC and KOH/carbon ratio of 2 (SD2800 and SD2800D) and highest at 0.86 and 0.87 for SD4800 and SD4800D, respectively. The similar I_D/I_G ratio confirms that direct activation does not alter the nature of or level of graphitisation in activated carbons, which is consistent with the XRD patterns (**Figure 6.2**). I_D/I_G ratio of 0.78 - 0.87 is consistent with the amorphous (i.e., non-graphitic) nature of the carbons.[32] The ratio increases for carbons prepared at higher temperature, suggesting that greater activation disrupt any graphitic domains that are present.

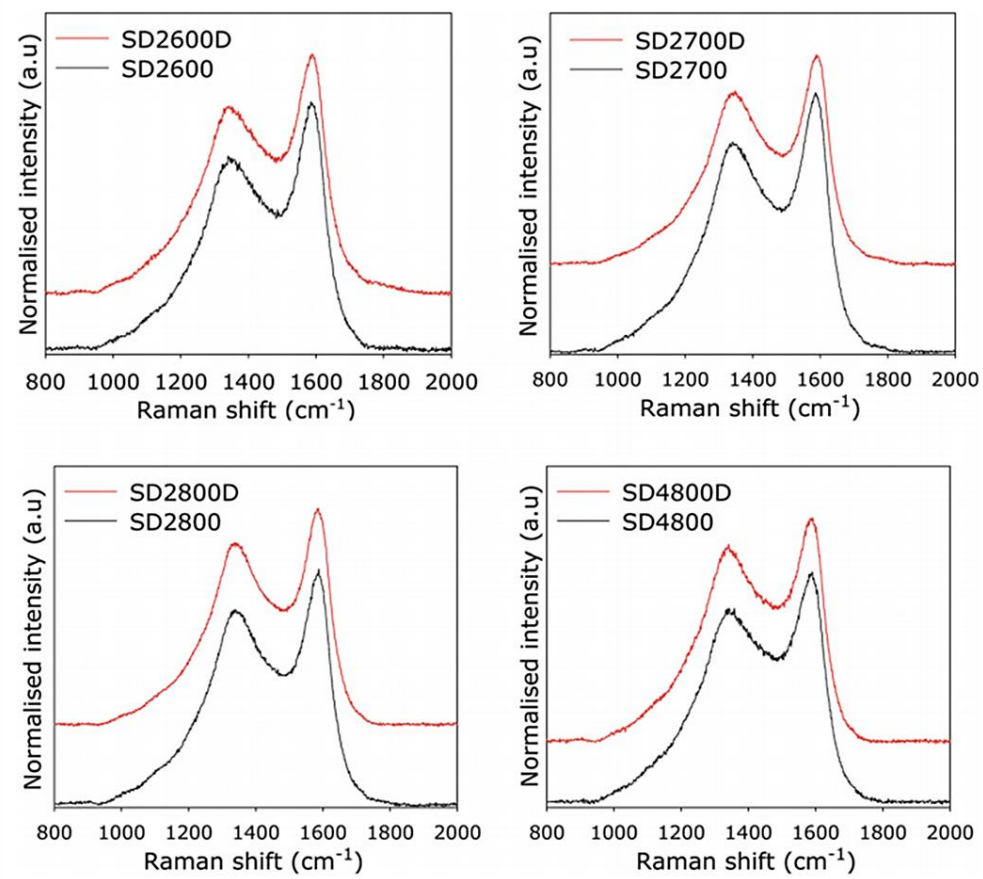


Figure 6.3: Raman spectra of directly activated carbons *(*sawdust-derived, SDXTD*)* and conventionally activated carbons *(*hydrochar-derived*,* SDXT*)*.

Table 6.7: The ratio of peak intensity of the D-peak to G-peak (I_D/I_G) of directly activated carbons or conventionally activated carbons derived from sawdust biomass.

Sample	I_D/I_G ratio
SD2600D	0.79
SD2600	0.78
SD2700D	0.83
SD2700	0.81
SD2800D	0.84
SD2800	0.84
SD4800D	0.87
SD4800	0.86

6.6.7 IR Spectroscopy Analysis

IR spectroscopy used to probe the nature and similarity of functional groups on the conventionally and directly prepared activated carbons. The IR spectra of both sets of carbons (**Figure 6.4**) show the C–OH stretching band at ca. 3430 cm^{-1}, and the C–OH bending band at ca. 1630 cm^{-1}. [9, 19, 29] The IR spectra also exhibit peaks attributable to C–O vibrations at ca. 1385 cm^{-1} (sharp peak), and a C=O peak at 1710 cm^{-1}. [9, 19, 29]

For both sets of samples, the intensity of the peaks decreases at higher activation temperatures and at higher KOH/carbon ratios, i.e., at higher levels of activation. This decrease in peak intensity, which signifies a decrease in O-functional groups, is consistent with the trend in elemental composition (i.e., reduction in O content) as shown in **Table 6.4**. Thus the IR spectra of samples SD2600D and SD2600, which are prepared at 600 ^{o}C and a KOH/carbon ratio of 2 have an O content of 27–28 wt% (**Table 6.4**), exhibit the most prominent peaks (**Figure 6.4 A**). The intensity of the O-functional groups decreases for samples SD2800D and SD2800 (**Figure 6.4 B**), which are prepared at 800 ^{o}C and a KOH/carbon ratio of 2 and have a lower O content of 14–15 wt% (**Table 6.4**). This decreasing trend of the intensity of IR peaks continues for the most activated samples SD4800D and SD4800 (**Figure 6.4 C**), which have the lowest O content of 10–14 wt%. It is, however, noteworthy that there is no difference in the IR spectra of the directly prepared carbons when compared to the conventional samples. This confirms that direct activation does not alter the surface functionality of activated carbons.

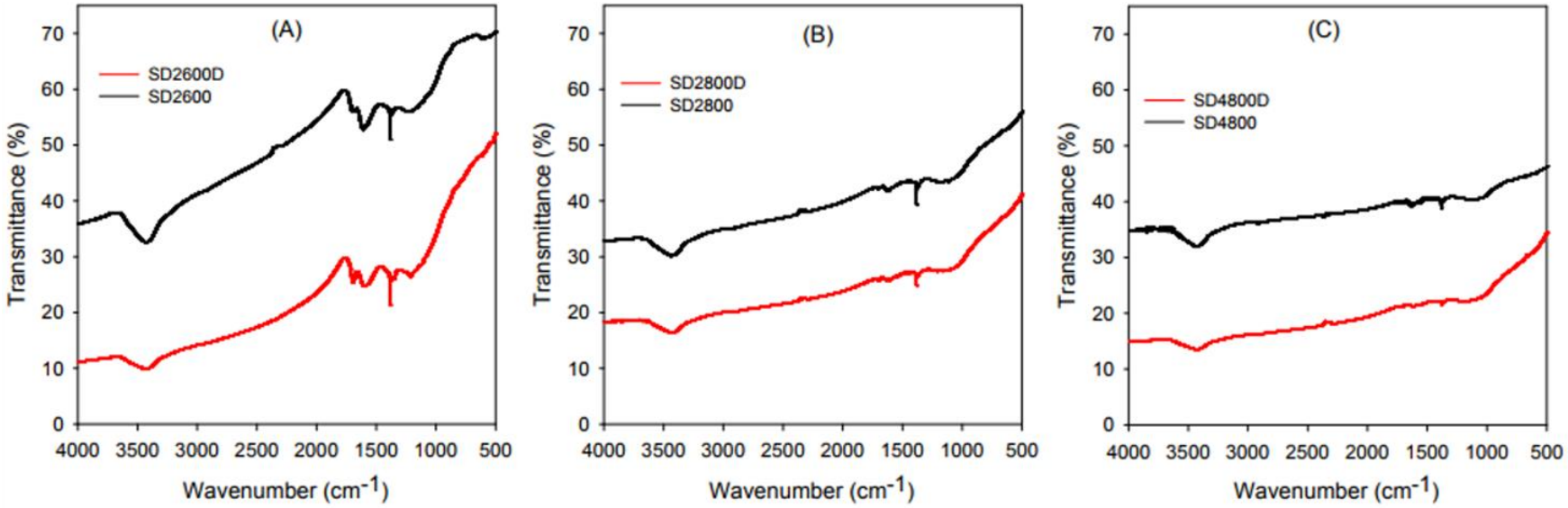


Figure 6.4: IR spectra of directly activated carbons (sawdust-derived, *SD2TD*) and conventionally activated carbons (hydrochar-derived, *SD2T*) prepared at **(A)** 600 °C KOH/carbon ratio of *2*, **(B)** 800 °C KOH/carbon ratio of *2* and **(C)** 800 °C KOH/carbon ratio of *4*.

6.6.8 Morphology Analysis

The direct activation process was explored further by observing the SEM micrographs images of directly activated carbons and comparing them to those prepared *via* the conventional route (**Figure 6.13**). For sawdust derived carbons, we first note that the morphology of the raw eucalyptus wood sawdust and its respective hydrochar (**Figure 6.5** and **Figure 6.6**, respectively) are similar to what has previously been reported.[33]

The morphology of both directly activated carbons (**Figure 6.7**, **Figure 6.9**, **Figure 6.11** and **Figure 6.13**), and conventionally activated carbons (**Figure 6.8**, **Figure 6.10**, **Figure 6.12** and **Figure 6.13**), is radically different from the fibrous nature of the sawdust (**Figure 6.5**). In both cases the morphology of the activated carbons is dominated by particles with smooth surfaces and large conchoidal cavities, which is consistent with what has previously been reported for hydrochar-derived activated carbons.[7, 9, 33] However, there is an important difference between the two sets of carbons wherein the directly activated carbons show much greater connectivity giving the impression of larger monolith-like particles. This greater connectivity in the directly activated carbons (**Figure 6.13**) may be a preserved characteristic from the sawdust particles as opposed to the conventionally prepared samples that are derived from hydrochar that has a significant proportion of stand-alone spherical particles.[9, 33]

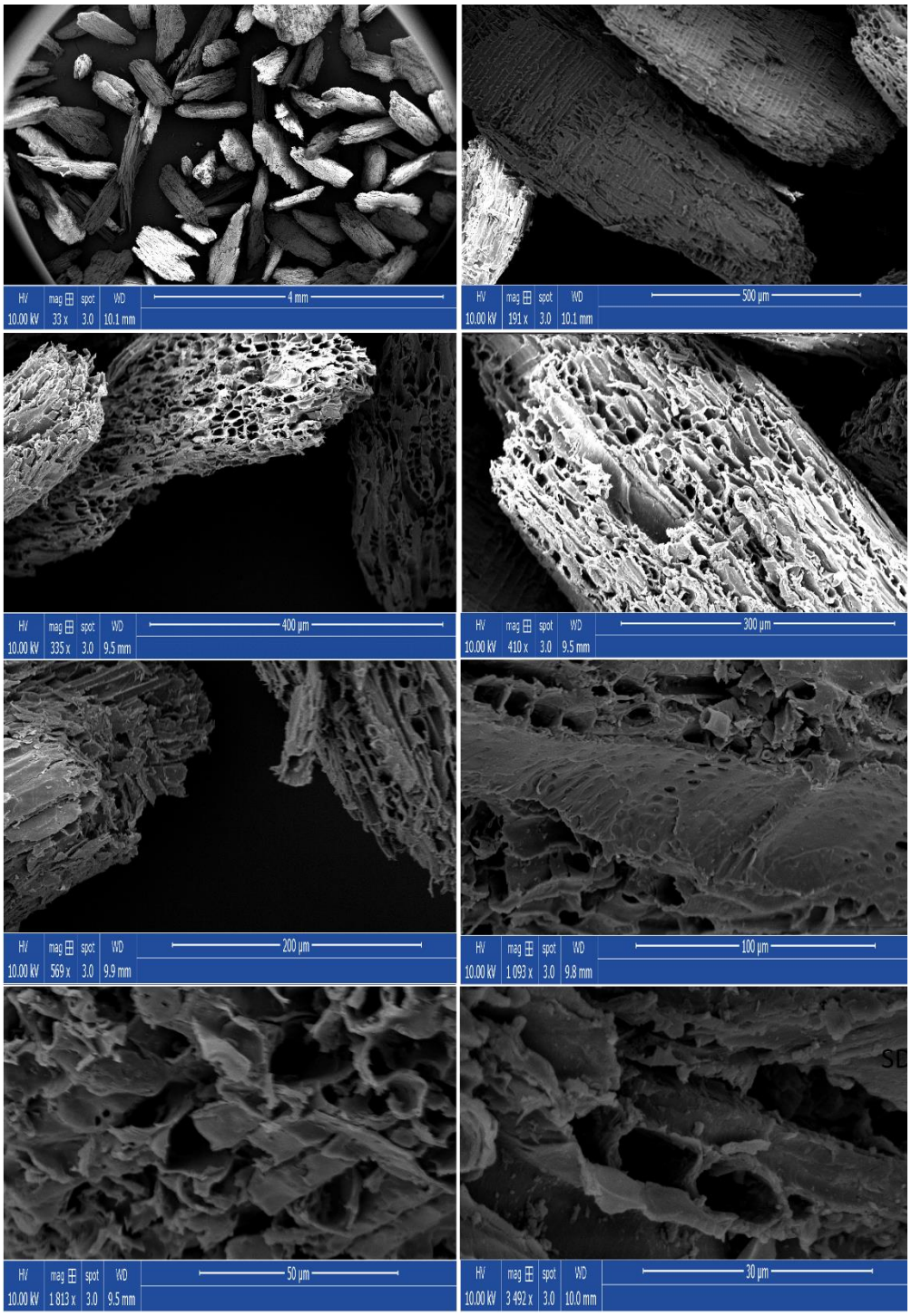


Figure 6.5: SEM micrographs images of raw eucalyptus wood sawdust SD (biomass).

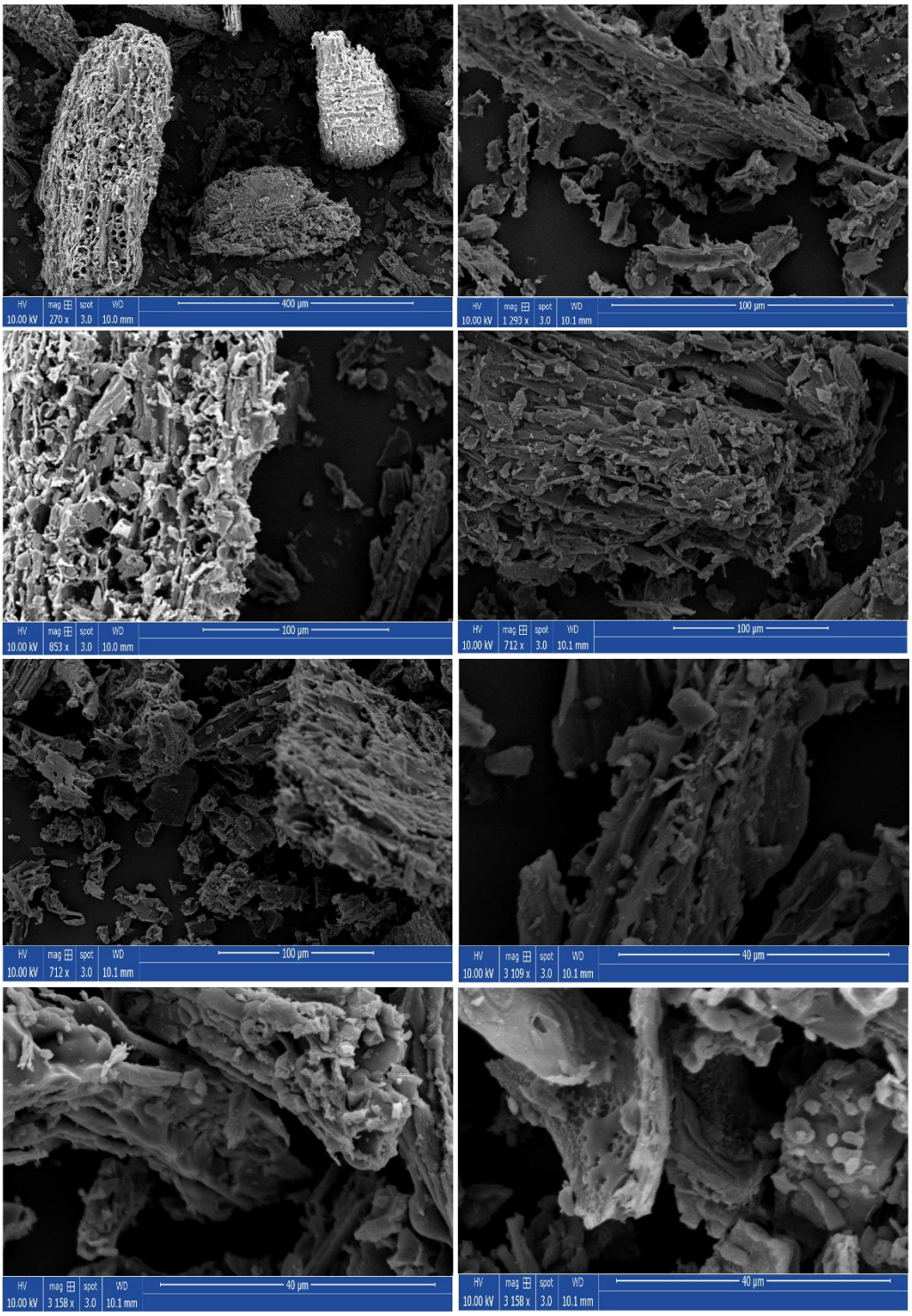


Figure 6.6: SEM micrographs images of hydrochar produced by hydrothermal process of eucalyptus wood sawdust (H).

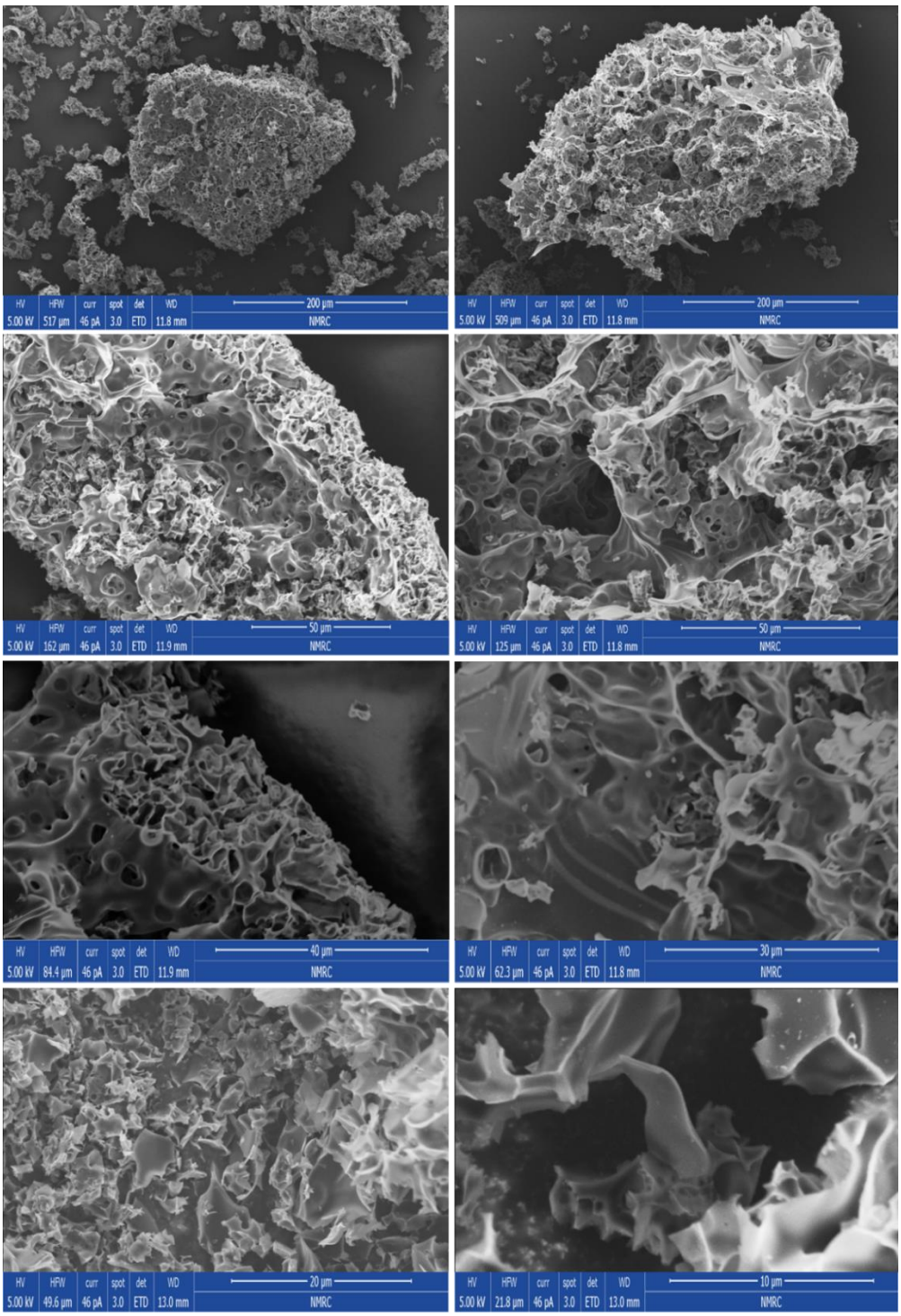


Figure 6.7: SEM micrographs images of **SD2600D**. See **Table 6.3** for samples abbreviations.

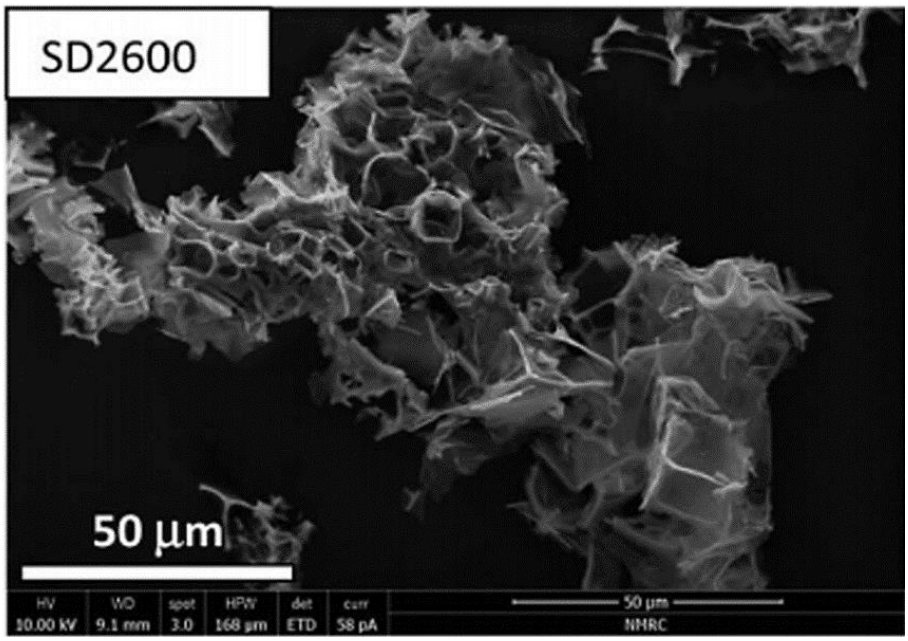


Figure 6.8: SEM micrographs images of **SD2600**. See **Table 6.3** for samples abbreviations.

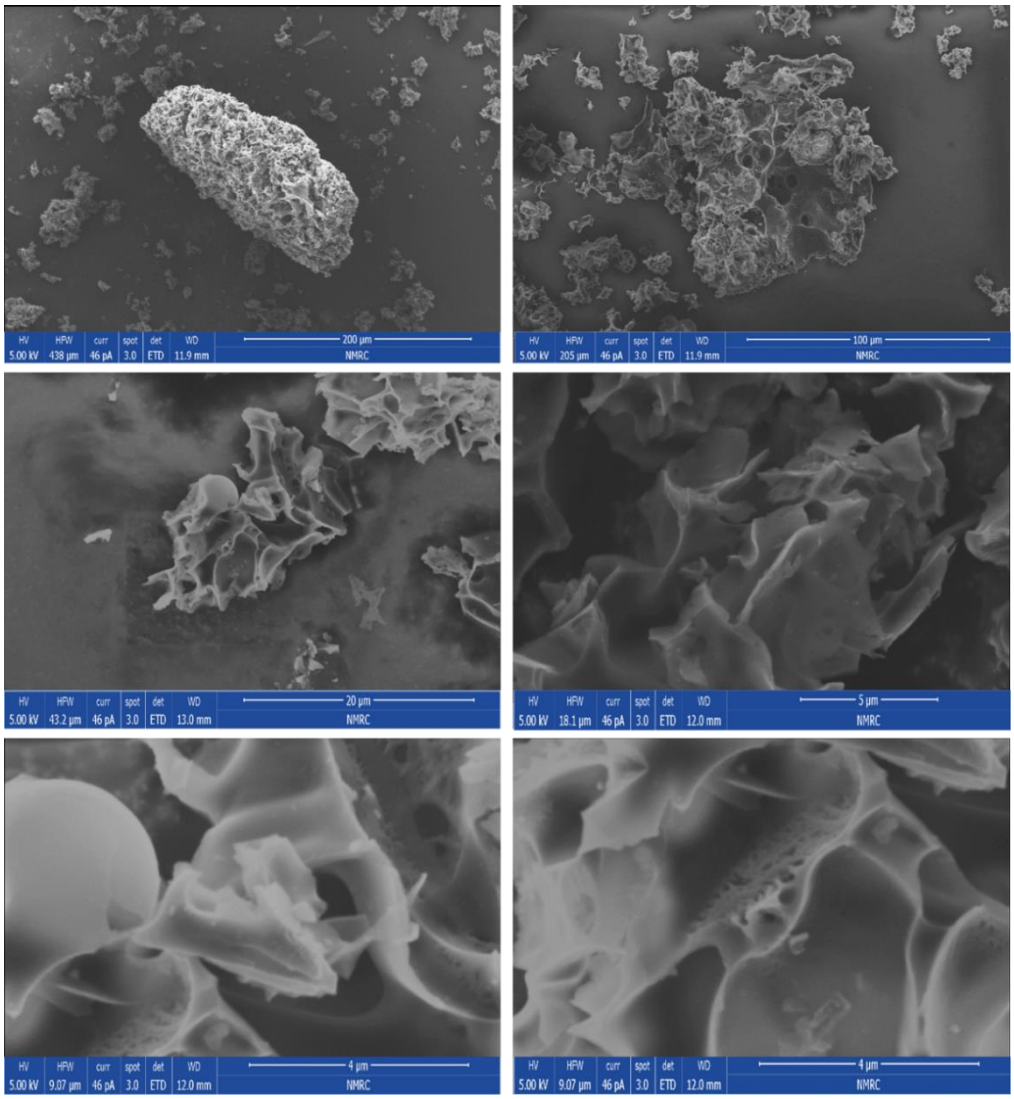


Figure 6.9: Representative SEM micrographs images of **SD2700D**. (See **Table 6.3** for samples abbreviations).

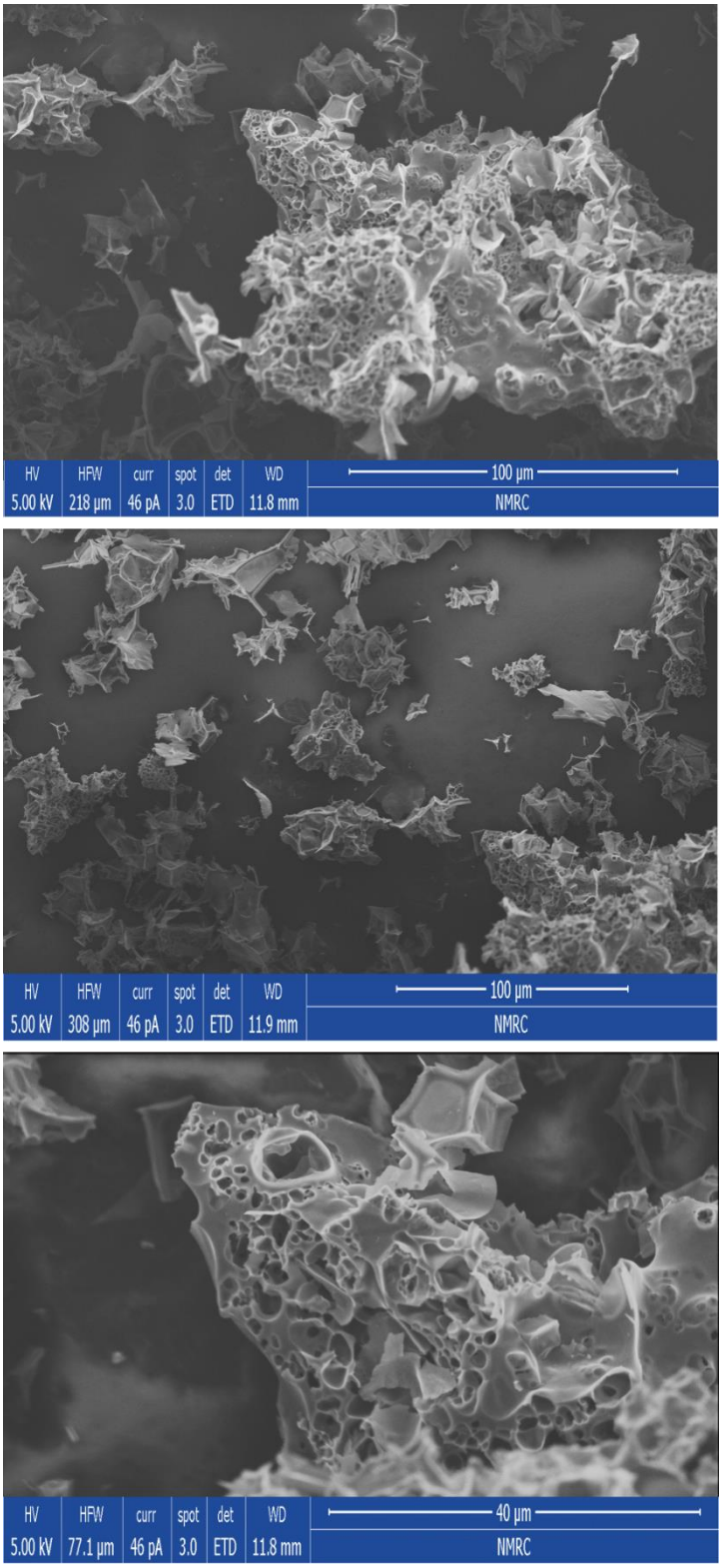


Figure 6.10: Representative SEM micrographs images of **SD2700**. See **Table 6.3** for samples abbreviations.

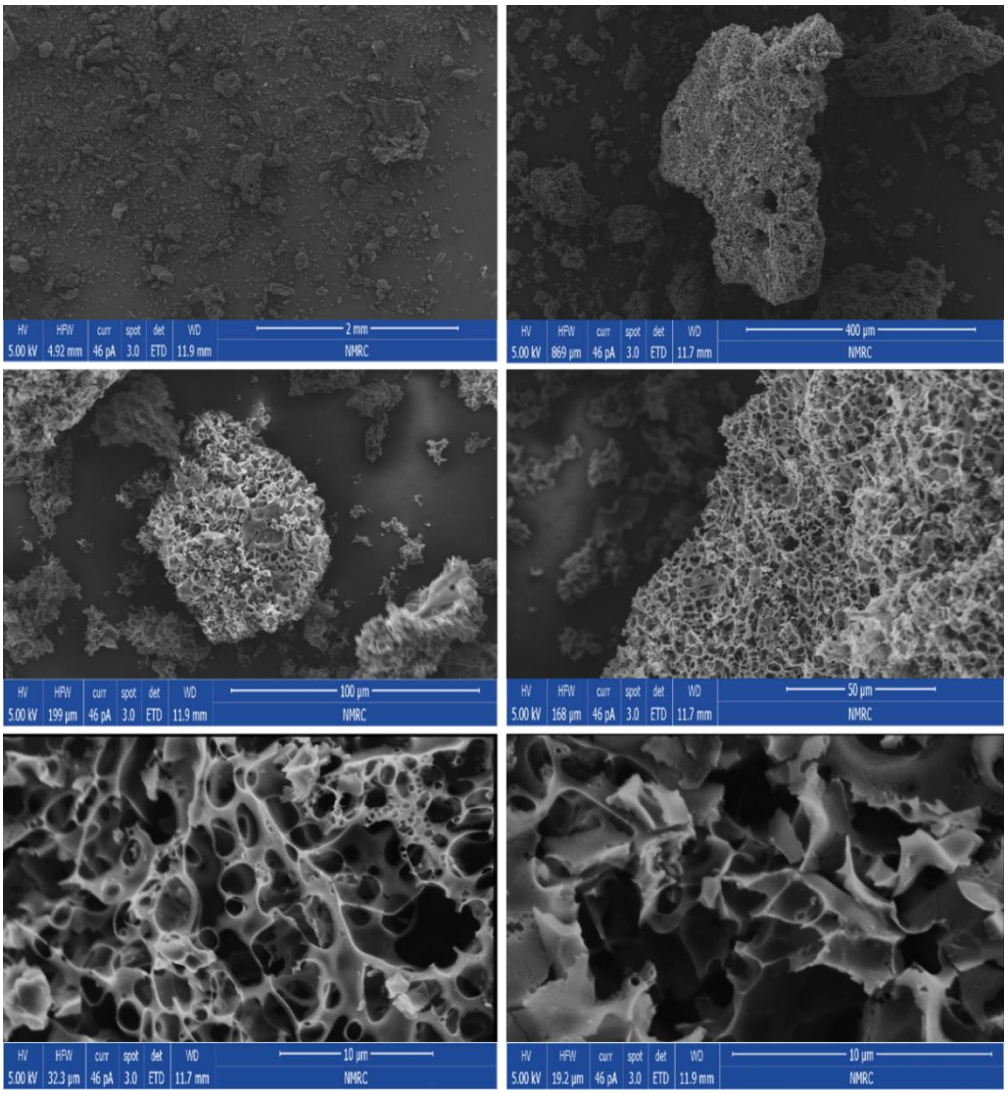


Figure 6.11: Representative SEM micrographs images of **SD2800D**. See **Table 6.3** samples abbreviations.

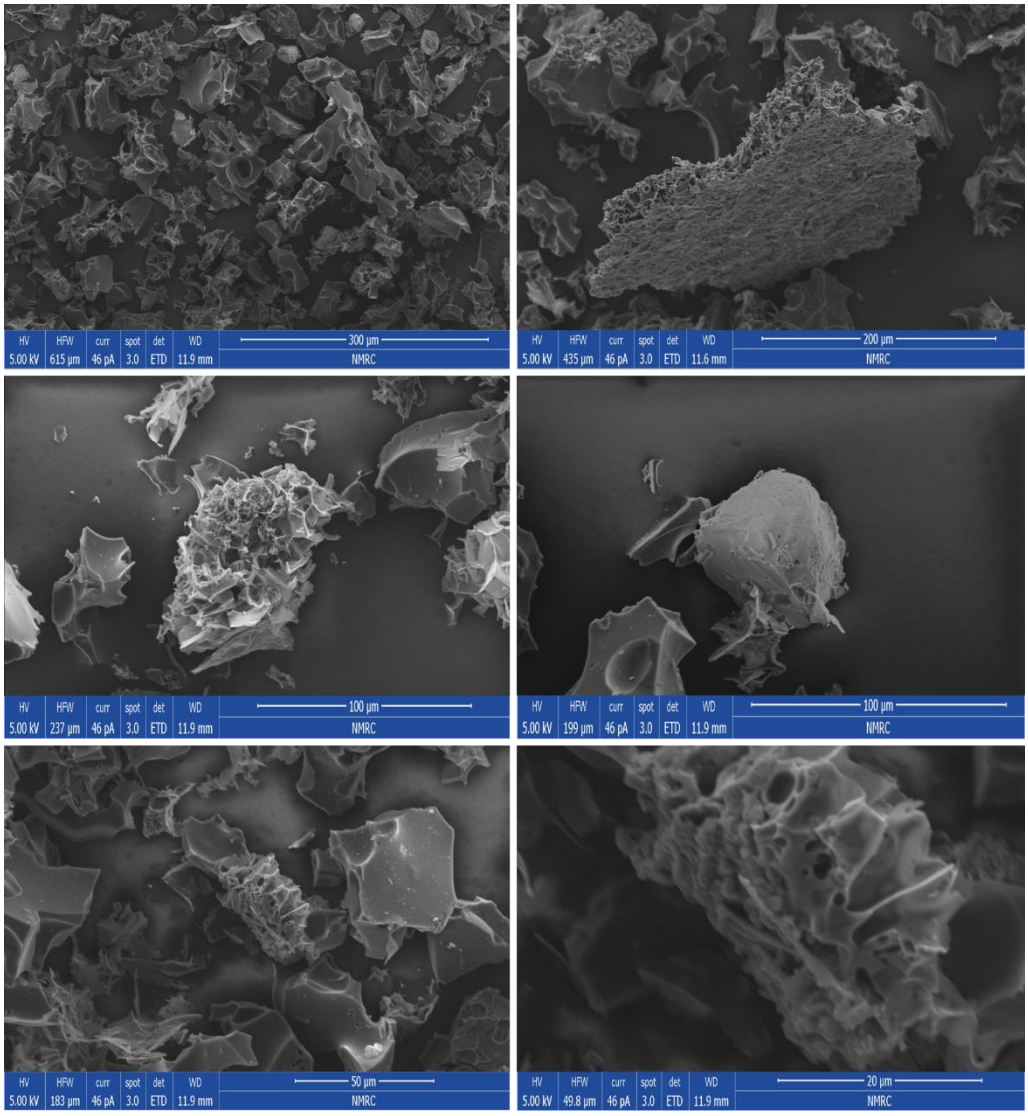


Figure 6.12: Representative SEM micrographs images of **SD4800**. See **Table 6.3** for samples abbreviations.

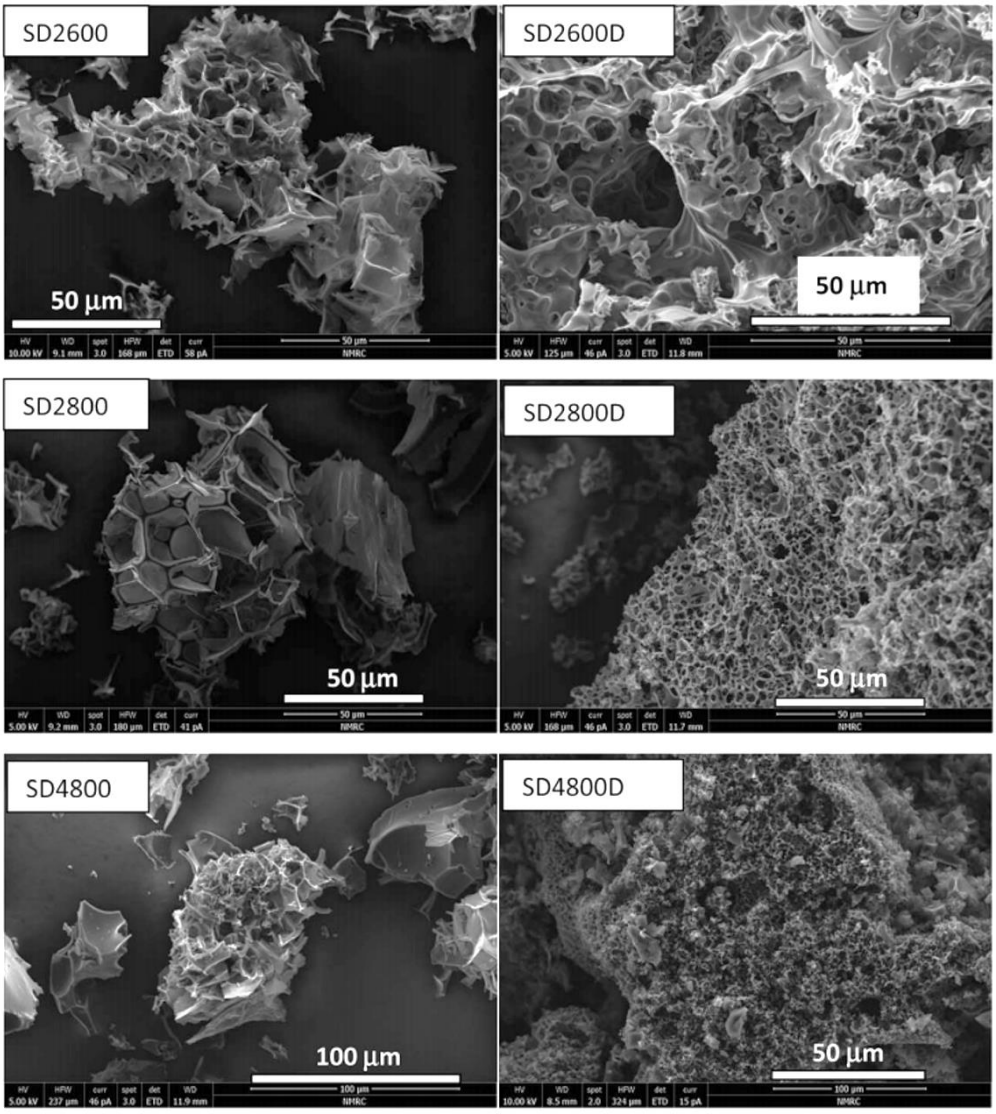


Figure 6.13: For comparison SEM micrographs images of activated carbons; directly activated carbons (sawdust-derived, SDXTD) and conventionally activated carbons (hydrochar-derived, SDXT). See **Table 6.3** for samples abbreviations.

6.6.9 Structural Ordering Analysis TEM

The pore channel ordering of both sets of activated carbons was observed by TEM analysis as shown in **Figure 6.14** and **Figure 6.15**, following the procedure mentioned in **Chapter 2**.

Both sets of samples have wormhole type pores that are typical for activated carbons.[34, 35] From the TEM micrographs images it is clear that there is no difference in the pore channel type meaning that direct activation does not alter the nature of the pores. The TEM micrographs images for both sets of activated carbons show no evidence of the presence of graphitic domains, which is consistent with the XRD patterns (**Figure 6.2**).

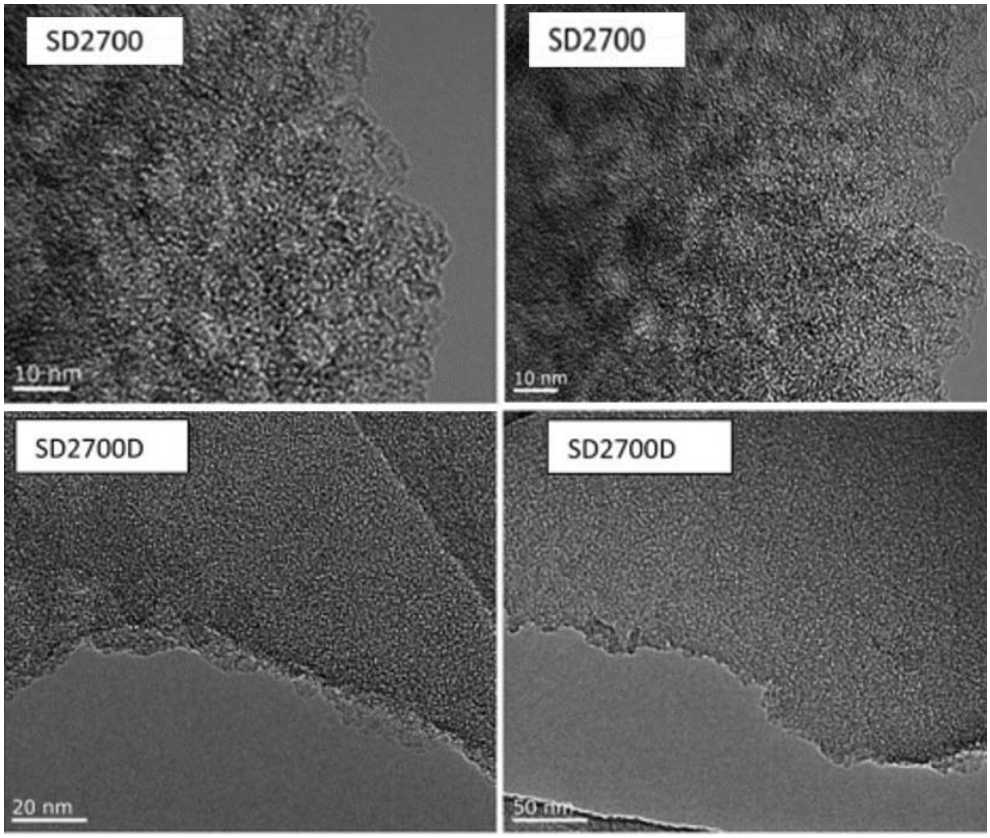


Figure 6.14: TEM micrographs images of directly activated carbons (sawdust-derived, SDXTD) and conventionally activated carbons (hydrochar-derived SDXT). See **Table 6.3** for samples abbreviations.

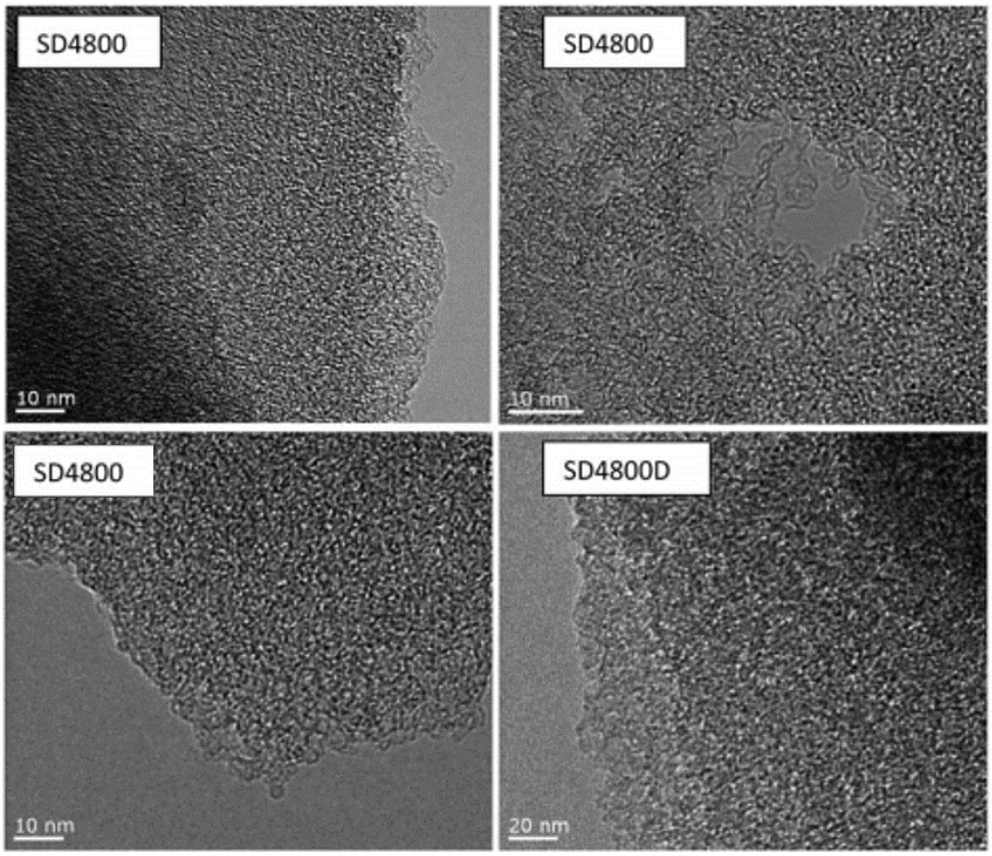


Figure 6.15: TEM micrographs images of directly activated carbons (sawdust-derived, SDXTD) and conventionally activated carbons (hydrochar-derived, SDXT). See **Table 6.3** for samples abbreviations.

6.6.10 Textural Proprieties and Porosity Analysis

The nitrogen sorption isotherms of sawdust-derived directly activated and conventionally synthesised carbons, prepared at KOH/carbon ratio of 2, are shown in **Figure 6.16** and the corresponding pore size distribution (PSD) curves are given in **Figure 6.17**. At any given activation temperature (600, 700 or 800 ^{o}C), the isotherms of the two sets of samples are generally similar implying that comparable levels of porosity are generated *via* either direct or conventional synthesis. Only at 800 ^{o}C does the conventional sample (SD2800) appear to adsorb more nitrogen at higher relative pressures (P/P_o >0.3) compared to the equivalent directly activated carbon (SD2800D). In all cases, however, both sets of carbons have similar adsorption at low relative pressure (P/P_o < 0.2). It is interesting to observe from the PSD curves in **Figure 6.17** that, at any given activation temperature, the two sets of samples have very similar micropore pore size distribution. Furthermore, the mesopore and macropore pore size distribution (20–4000 Å) of both sets of samples prepared under identical conditions is also similar as shown by wide pore size distribution plots (**Figure 6.19**). This confirms that the size of pores and the overall pore channel system generated *via* direct activation are virtually identical to those from conventional synthesis. Overall, therefore, direct activation causes no disadvantages with respect to the nature of the porosity in the carbons.

The textural parameters of the two sets of carbon (directly and conventionally synthesised) are summarised in **Table 6.8**. In general, the surface area and pore volume of the directly activated carbons are comparable to those of equivalent conventional samples. This is an important observation, which confirms that porosity is not compromised when activation is performed *via* the more environmentally friendly direct route.

Indeed, in some cases the surface area and the level of microporosity (i.e., micropore surface area and pore volume) are higher for the directly activated carbons.

The pore size data in **Table 6.8** confirm that there is virtually no change in the size of pores generated in directly activated carbons when compared to equivalent conventional samples. All samples possess small micropores along with some larger micropores wherein the proportion of the latter increases at higher activation temperature. Similar trends that confirm comparable porosity are observed for samples prepared at 800 ^{o}C and KOH/carbon ratio of 4 either *via* the direct (SD4800D) or conventional (SD4800) route (**Figure 6.18** and **Table 6.8**). It is worth noting that for both synthesis routes, activation of the carbonaceous matter using KOH first proceeds according to the following equation:

$$KOH + C \longrightarrow 2K + 3H_2 + 2K_2CO_3 \quad \textbf{Equation 6.1}$$

The generated K is intercalated within the carbon layers, while K_2CO_3 decomposes at high temperature yielding $K_2O + CO_2$. Porosity in the activated carbon is generated *via* C etching according to the equation given above, and also *via* the generated CO_2 escaping through the carbon substrate during the activation process. Furthermore, the carbon substrate reacts with the CO_2, yielding CO whilst generating microporosity. After activation, washing with water to remove any inorganic salts and residues generates or releases further porosity in the activated carbon.

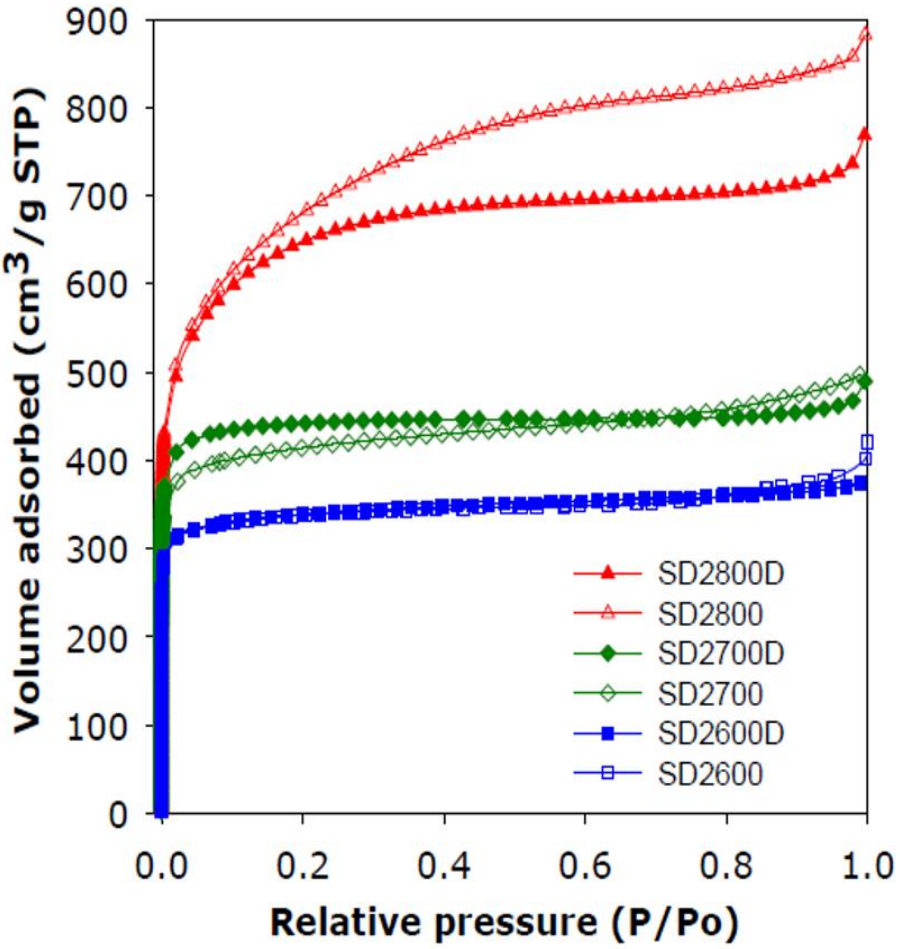


Figure 6.16: Nitrogen sorption isotherms of directly activated carbons (sawdust-derived, SD2TD) and conventionally activated carbons (hydrochar-derived, SD2T) prepared at KOH/carbon ratio of *2* and various temperatures (T); 600 °C, 700 °C and 800 °C.

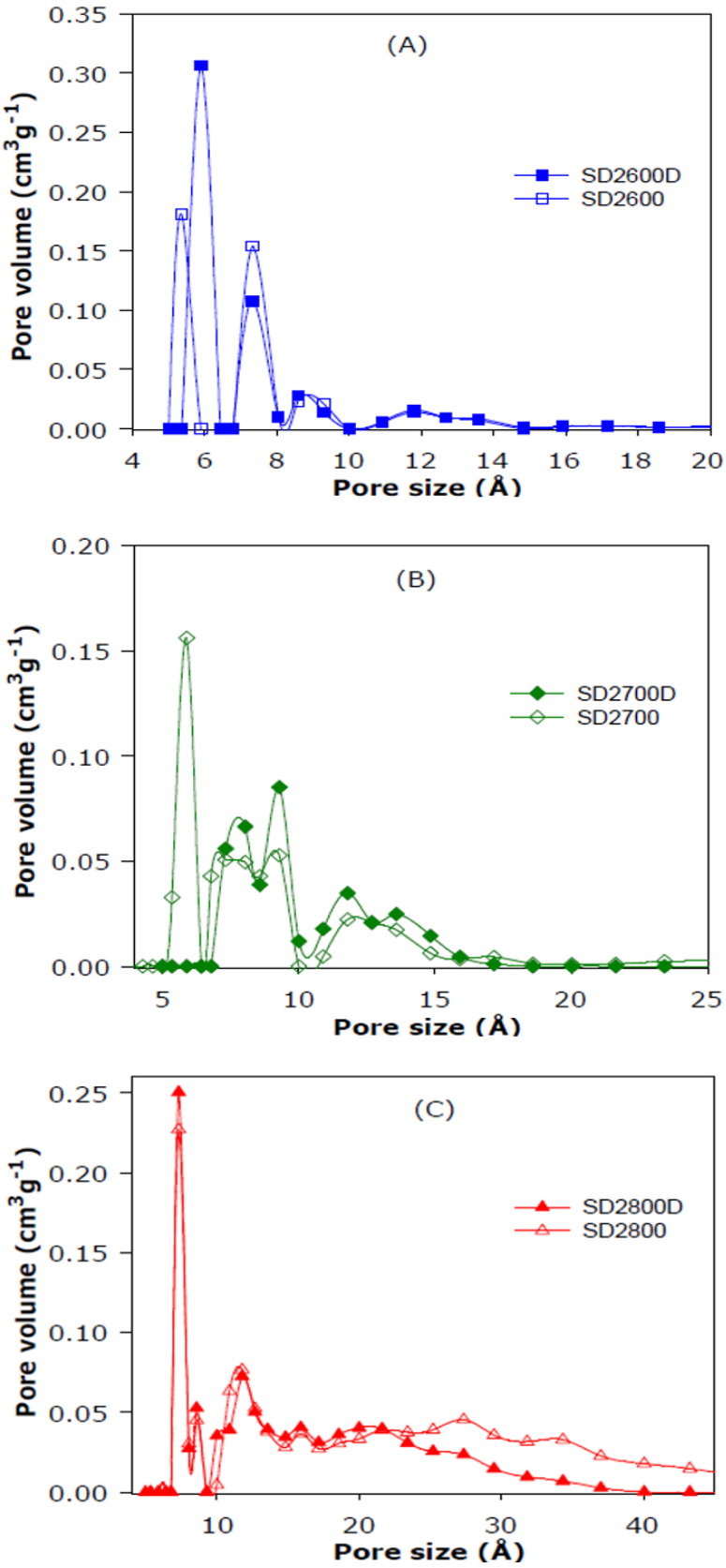


Figure 6.17: Pore size distribution (PSD) curves of directly activated carbons (sawdust-derived, SD2TD) and conventionally activated carbons (hydrochar-derived, SD2T) prepared at KOH/carbon ratio of *2* and various temperatures; **(A)** 600 °C, **(B)** 700 °C and **(C)** 800 °C.

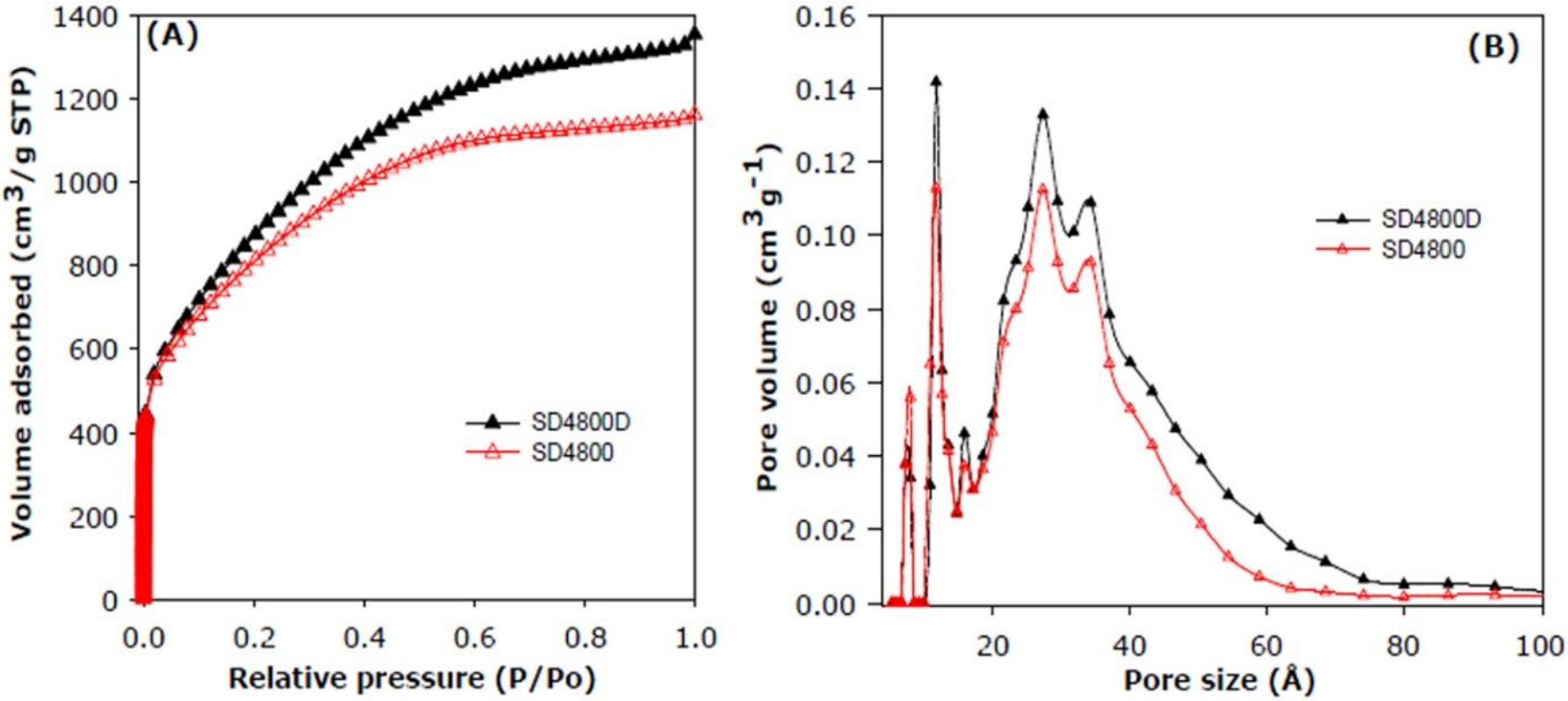


Figure 6.18: (A) Nitrogen sorption isotherms and **(B)** corresponding pore size distribution curves of directly activated carbons (sawdust-derived, SD4800D) or conventionally activated carbons (hydrochar-derived, SD4800) carbons prepared at 800 °C and KOH/carbon ratio of *4*.

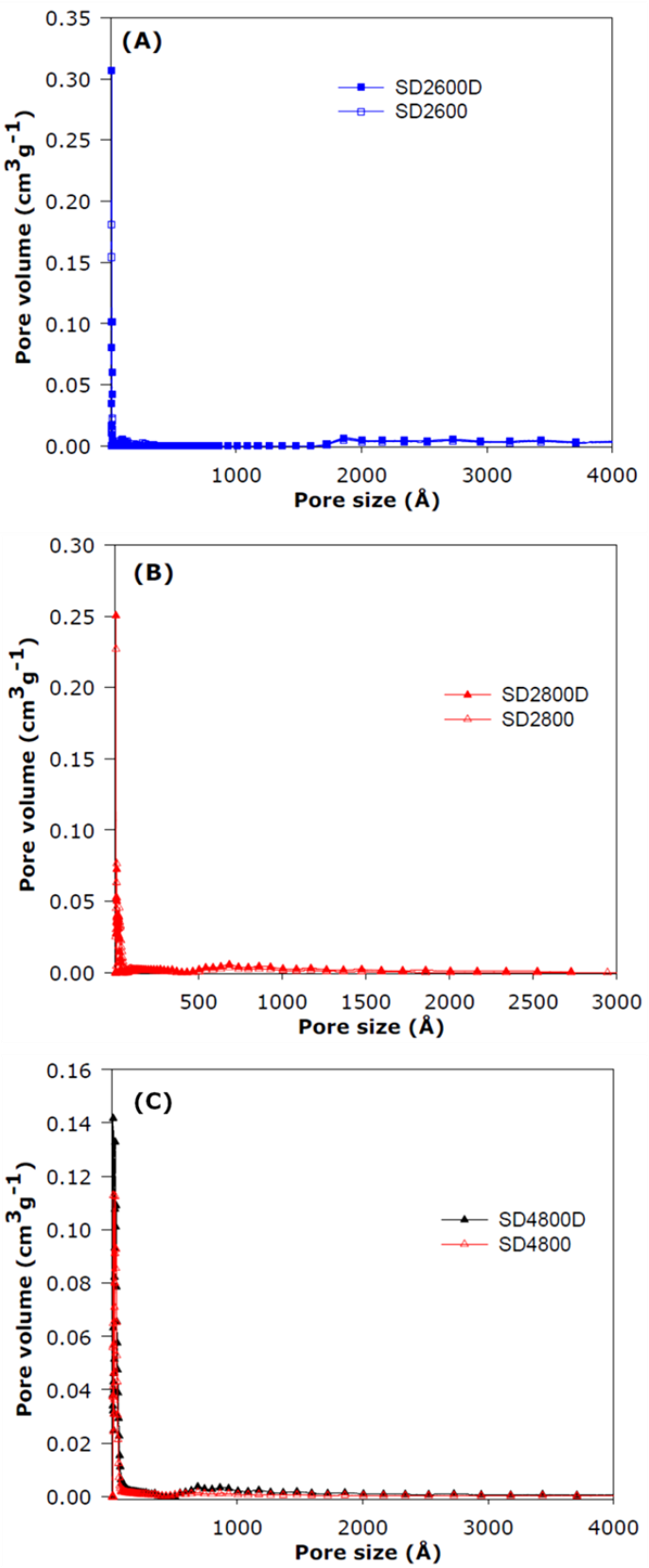


Figure 6.19: Wide pore size distribution of directly activated carbons (sawdust-derived, SD2TD) and conventionally activated carbons (hydrochar-derived, SD2T): **(A)** at 600 °C and at KOH/carbon ratio of *2* **(B)** at 800 °C and at KOH/carbon ratio of *2* and **(C)** at 800 °C and at KOH/carbon ratio of *4* and 800 °C.

Table 6.8: Textural properties of directly activated carbons derived from sawdust biomass or conventionally activated carbons derived from hydrochar of sawdust biomass.

Sample	Surface area [a] ($m^2\ g^{-1}$)	Pore volume [b] ($cm^3\ g^{-1}$)	Pore size [c] (Å)
SD2600D	1281 (1119)	0.57 (0.45)	6/7/9
SD2600	1202 (1133)	0.65 (0.49)	5/7/9
SD2700D	1575 (1535)	0.80 (0.70)	8/9/12
SD2700	1557 (1294)	0.75 (0.53)	6/8/12
SD2800D	2274 (1923)	1.20 (0.90)	7/12/20
SD2800	2377 (1512)	1.40 (0.70)	7/12/25
SD4800D	2980 (478)	2.10 (0.30)	8/12/30
SD4800	2783 (694)	1.80 (0.36)	8/12/30

[a] The values in the parentheses refer to micropore surface area.
[b] The values in the parentheses refer to micropore volume
[c] Pore size distribution maxima obtained from NLDFT analysis.

6.6.11 CO_2 Uptake Measurements

Activated carbons derived from biomass have recently attracted a great deal of attention as solid state storage materials for energy related gases such as CO_2 and H_2.[4, 9-12] However, in previous studies, the activated carbons have been prepared *via* routes that include either hydrothermal carbonisation or pyrolysis prior to the activation step.[4, 9-12] Given that the textural properties of the directly activated carbons are similar to those of samples prepared *via* the longer hydrothermal carbonisation route, we determined their CO_2 uptake and compared it to that of analogous conventionally activated samples. The capacity for CO_2 capture and storage was measured at room temperature (25 ^oC) and at 0 ^oC and a pressure range of 0 to 20 bar.

6.6.11.1 CO_2 Uptake Measurements at 25 ^oC

The CO_2 uptake isotherms at high pressure range of 0-20 bar and at low pressure range of 0-1 bar of directly activated carbons (*SDXTD*) and conventionally synthesised activated carbons (*SDXT*) are shown in **Figure 6.20** and **Figure 6.21**, and the storage capacity at various pressures (0.15 bar, 1 bar and 20 bar) is stated in **Table 6.9**.

For SD2 samples prepared at a KOH/carbon ratio of 2, the storage capacity at 1 bar (**Figure 6.20 B**) ranges from 3.6 mmol g^{-1} for samples prepared at 800 ^oC (SD2800 and SD2800D), to between 4.4 mmol g^{-1} and 4.6 mmol g^{-1} for samples prepared at 600 ^oC and 700 ^oC. It is also clear that the uptake of the directly activated samples very closely matches that of analogous conventionally activated carbons. Thus despite being prepared *via* a simpler, cheaper and more direct route, the directly activated carbons are able to achieve very high gravimetric CO_2 uptake that is amongst the highest ever

reported for porous carbons (**Table** 6.10).[9-12, 34-48] A similar trend is observed for SD4 samples (**Figure 6.21 B** and **Table 6.9**), which however show lower CO_2 uptake at 1 bar due to their more mesoporous nature (i.e., possess lower levels of microporosity).

Also in **Table 6.9** the CO_2 uptake at 0.15 bar so as to mimic post-combustion flue gas streams from power stations which typically consist of ca. 15% CO_2 with the remainder being mainly N_2 (70–75%) and water (5–7%).[49, 50] The CO_2 uptake at 0.15 bar ranges between 0.8 mmol g^{-1} and 1.3 mmol g^{-1} for SD2 samples and is ca. 0.6 mmol g^{-1} for SD4 samples. The uptake of 1.3 mmol g^{-1} at such low pressure is at the high end of what has previously been observed and correlates well with the microporosity of the samples.[9-12, 34-48] On the other hand, at 20 bar (**Figure 6.21 A**), the CO_2 uptake correlates with the total surface area, which means that for sawdust derived carbons, the directly activated samples generally have greater storage capacity (**Table 6.9**) that reaches a high of ca. 22 mmol g^{-1} for SD4 carbons.

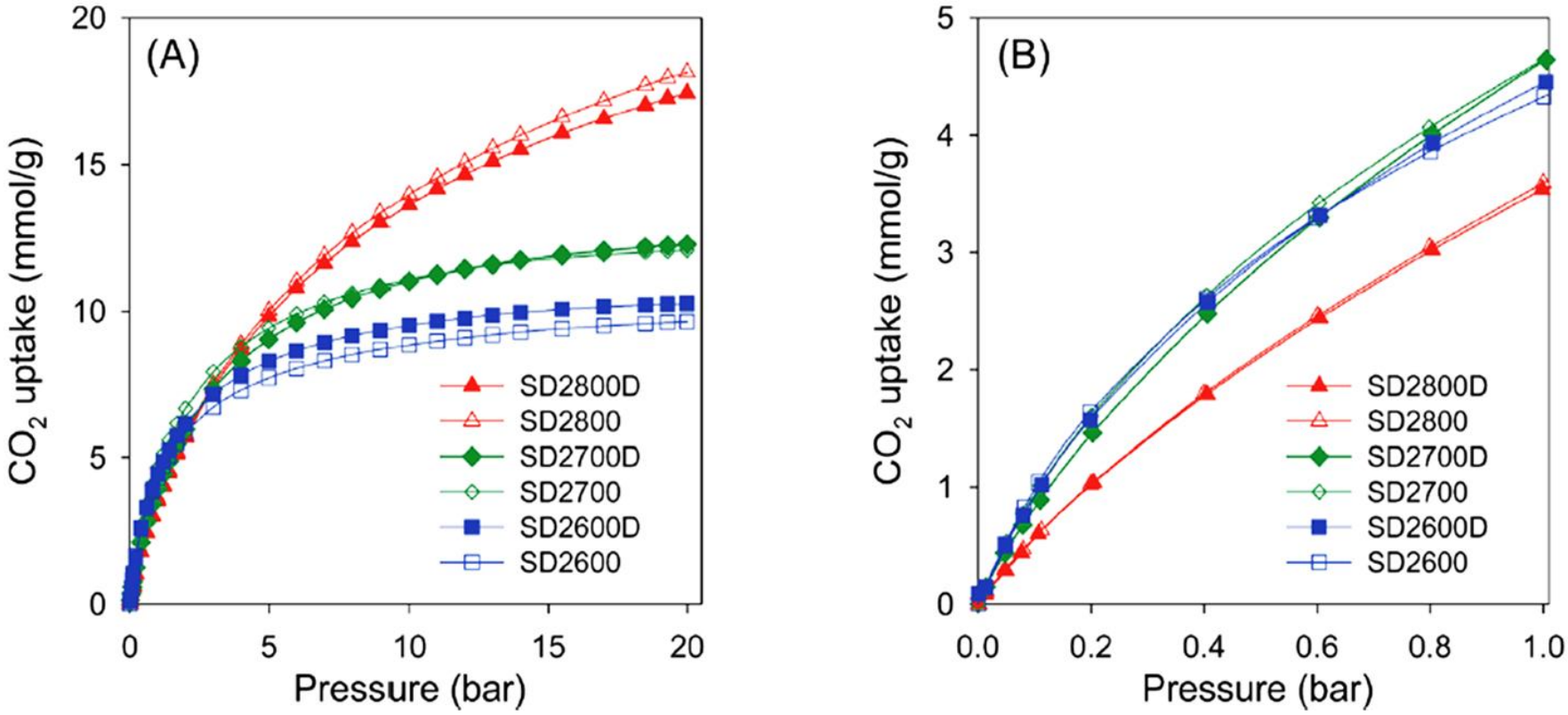


Figure 6.20: CO_2 uptake isotherms ***at 25 °C*** and **(A) 0–20 bar** and **(B) 0–1 bar** for directly activated carbons (sawdust-derived, *SD2TD*) and conventionally activated carbons. (hydrochar-derived, *SD2T*)

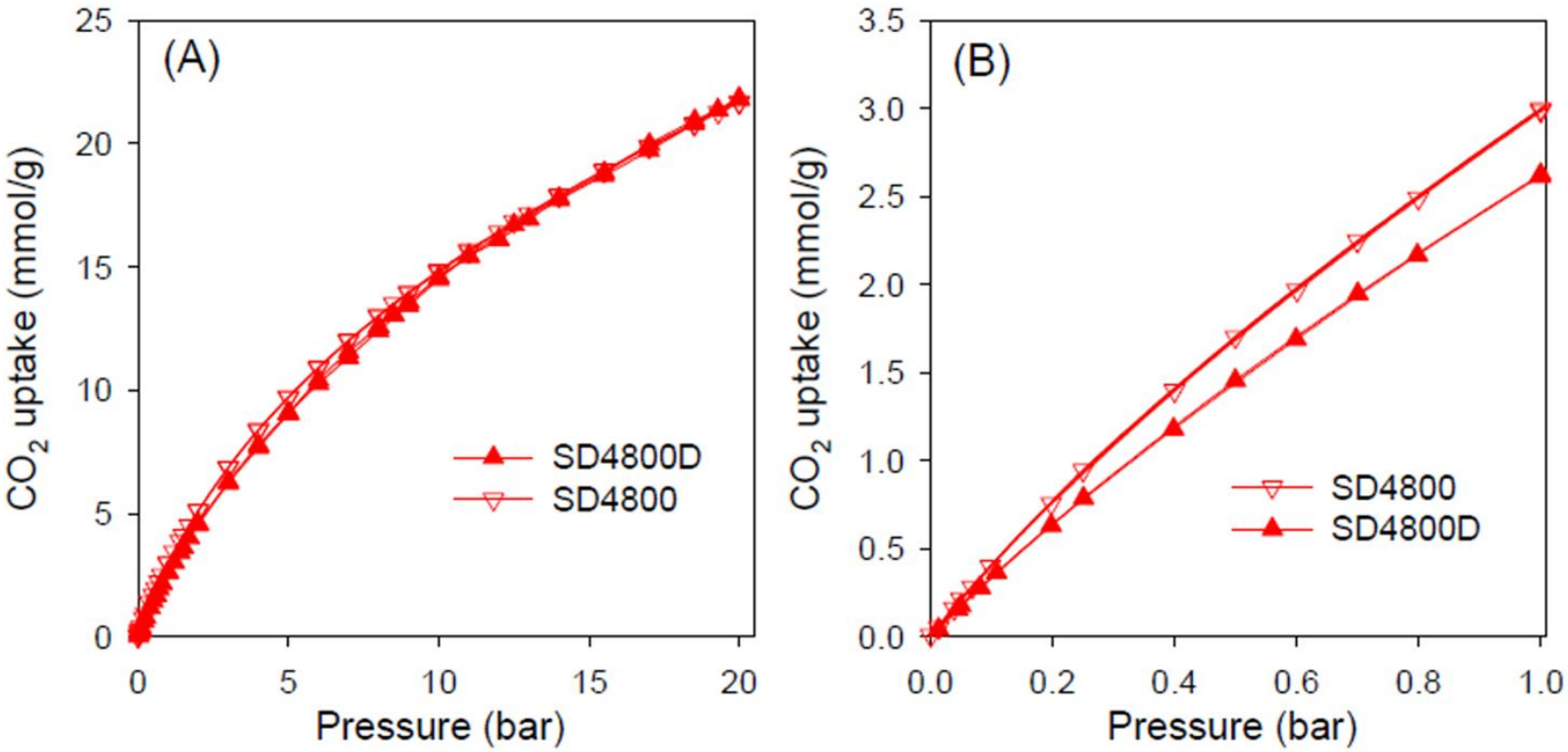


Figure 6.21: CO_2 uptake isotherms ***at 25 °C*** **(A) 0-20 bar** and **(B) 0–1 bar** for directly activated (sawdust-derived, SD4800D) or conventionally activated carbons (hydrochar-derived, SD4800) prepared at 800 °C and KOH/carbon ratio of *4*.

Table 6.9: CO_2 uptake ***at 25 °C*** of directly activated carbons or conventionally activated carbons derived from sawdust biomass.

Sample	CO_2 Uptake [a] (mmol g^{-1})		
	0.15 bar	1 bar	20 bar
SD2600D	1.3	4.5	10.3
SD2600	1.3	4.4	9.7
SD2700D	1.3	4.6	12.3
SD2700	1.3	4.6	12.1
SD2800D	0.8	3.6	17.5
SD2800	0.8	3.6	18.1
SD4800D	0.5	2.7	21.8
SD4800	0.6	3.0	21.7

[a] CO_2 uptake *at 25 °C* and various pressures (i.e., 0.15 bar, 1 bar and 20 bar).

Table 6.10**:** CO_2 uptake of various porous carbons ***at 25 °C*** and 0.15 bar or 1 bar (Table adapted from reference [41])

Sample	CO_2 uptake (mmol g^{-1})		Ref.
	1 bar	0.15 bar	
Sawdust-derived activated carbon	4.8	1.2	51
KOH-activated templated carbons	3.4	~1.0	52
Hierarchical porous carbon (HPC)	3.0	~0.9	53
Petroleum pitch-derived activated carbon	4.55	~1.0	46
Activated carbon spheres	4.55	~1.1	37
Phenolic resin activated carbon spheres	4.5	~1.2	38
Poly(benzoxazine-co-resol)-derived carbon	3.3	1.0	54
Fungi-derived activated carbon	3.5	~1.0	55
Chitosan-derived activated carbon	3.86	~1.1	42
Polypyrrole derived activated carbon	3.9	~1.0	56
Soya bean derived N-doped activated carbon	4.24	1.2	57
N-doped ZTCs	4.4	~1.0	43
Activated templated N-doped carbon	4.5	1.4	58
Polyaniline derived activated carbon	4.3	1.38	36
N-doped activated carbon monoliths	5.14	1.25	40
Activated N-doped carbon	3.2	1.5	59
Activated hierarchical N-doped carbon	4.8	1.4	45
Activated N-doped carbon from algae	4.5	~1.1	60

6.6.11.2 CO_2 Uptake Measurements at 0 °C

The CO_2 uptake of the carbons *at 0 °C* and a pressure of up to 20 bar also determined. The CO_2 uptake isotherms are shown in **Figure 6.22** and **Figure 6.23**, and the storage capacities at various pressures (0.15, 1 and 20 bar) are summarised in **Table 6.11**.

The storage capacity at 1 bar (**Figure 6.22 B**) ranges from 5.8 mmol g^{-1} to 7.3 mmol g^{-1}, with samples prepared at 700 °C showing the highest capacity. The uptake of the directly activated samples is very similar to that of analogous conventionally activated carbons. The level of uptake at 1 bar of up to 7.3 mmol g^{-1} places the directly synthesised samples at the high end of what has been reported for carbons (**Table 6.12**) despite their being prepared *via* a simpler, cheaper and more direct route.[9-12, 34-48]

At 20 bar (**Figure 6.22 A**), the CO_2 uptake correlates with the total surface area, and thus the directly activated samples generally have greater storage capacity (**Table 6.11**) with the highest uptake of 30.7 mmol g^{-1} exhibited by sample SD4800D (**Figure 6.23 A**). The CO_2 uptake of the directly prepared samples is much higher than that of previously reported carbons **Table 6.12**.

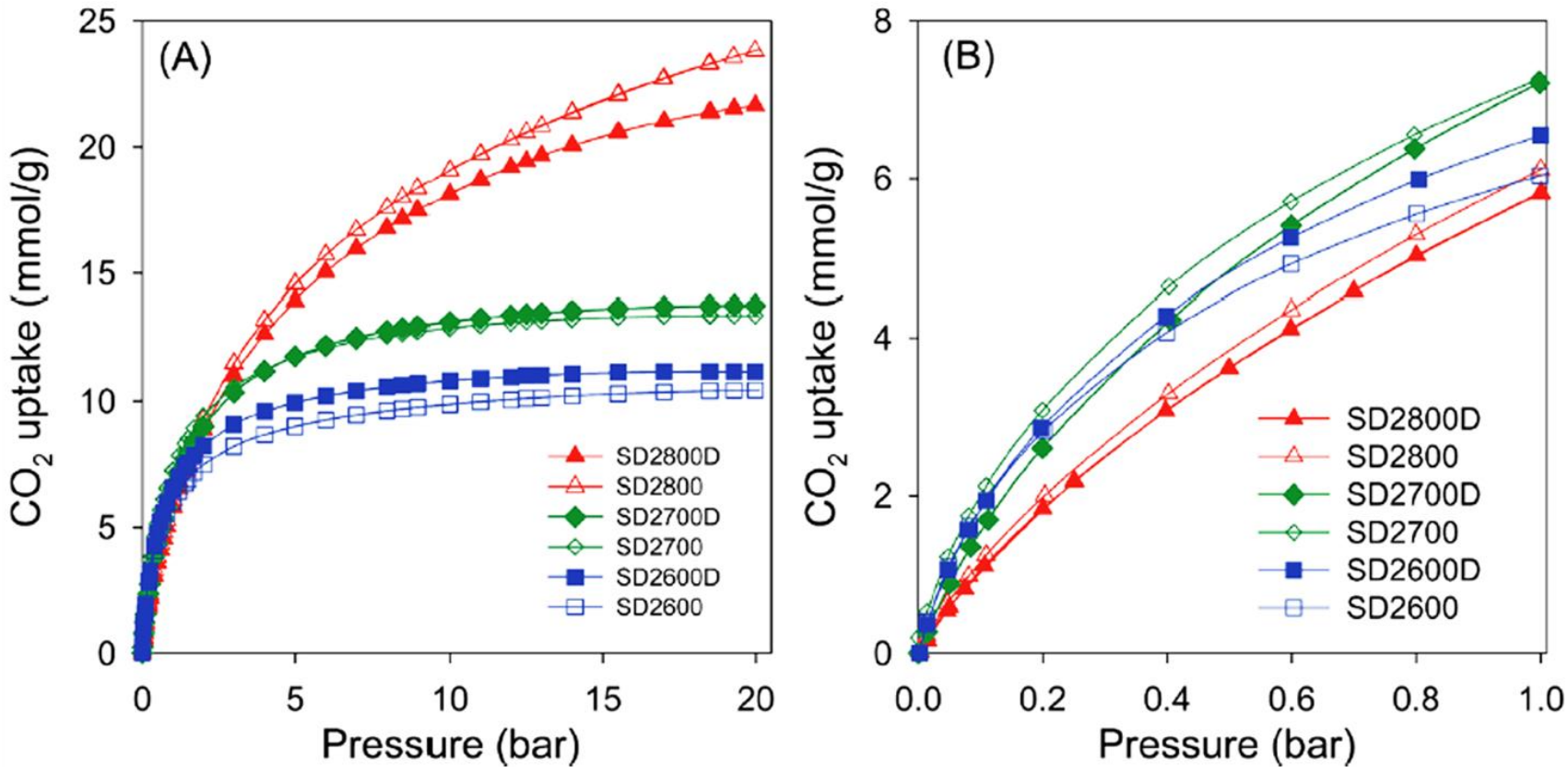


Figure 6.22: CO_2 uptake isotherms ***at 0 °C*** and **(A) 0–20 bar** and **(B) 0–1 bar** for directly activated carbons (sawdust-derived, SD2TD) and conventionally activated carbons (hydrochar-derived, SD2T).

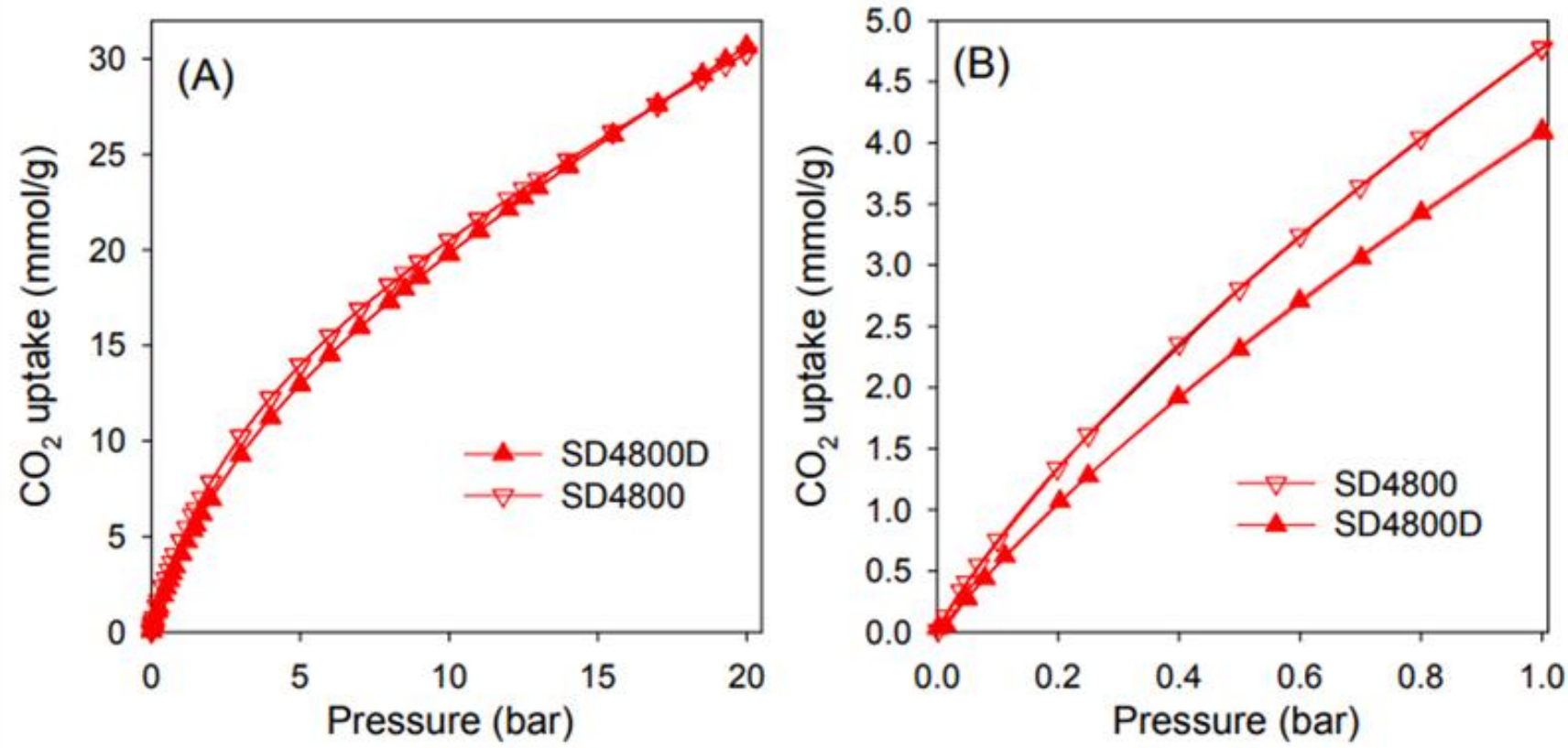


Figure 6.23: CO_2 uptake isotherms ***at 0 °C*** and **(A) 0-20 bar** and **(B) 0–1 bar** for directly activated carbons (sawdust-derived, SD4800D) or conventionally activated carbons (hydrochar-derived, SD4800) prepared at 800 °C and KOH/carbon ratio of *4*.

Table 6.11: CO_2 uptake ***at 0 °C*** of directly activated carbons or conventionally activated carbons derived from sawdust biomass.

Sample	CO_2 Uptake [a] (mmol g^{-1})		
	0.15 bar	1 bar	20 bar
SD2600D	2.4	6.1	10.4
SD2600	2.5	6.6	11.2
SD2700D	2.6	7.3	13.4
SD2700	2.2	6.8	13.8
SD2800D	1.7	6.1	23.8
SD2800	1.5	5.8	21.7
SD4800D	1.1	4.8	30.3
SD4800	0.9	4.1	30.7

[a] CO_2 uptake *at 0 °C* and various pressure (i.e., 0.15 bar,1 bar and 20 bar).

Table 6.12: CO_2 uptake ***at 0 °C*** and 1 bar of various carbons compared to study carbons.

Sample	CO_2 uptake (mmol g^{-1}) [a]	Reference
SD2600D	6.1	This work
SD2600	6.6	This work
SD2700D	7.3	This work
SD2700	6.8	This work
SD2800	6.1	This work
SD2800D	5.8	This work
SD4800	4.8	This work
SD4800D	4.1	This work
N-Doped microporous carbon	2.7	[61]
Microporous carbon	2.3	[62]
Microporous organic polymer	3.5	[63]
Covalent organic framework	4.0	[64]
Hollow octahedral carbon cage	4.0	[65]
Hierarchically porous carbon	4.6	[66]
N-Doped carbon monolith	4.2	[67]
Porous carbon sheets	4.3	[68]
NPCNS carbon	4.4	[69]

[a] CO_2 uptake *at 0 °C* and 1 bar.

6.6.12 Selectivity

The selectivity of one of the better performing directly synthesised samples (SD2700D) for CO_2 uptake assessed by comparing the relative amounts of CO_2 and N_2 stored at 25 ^oC and 1 bar as shown in **Figure 6.24**.

At 1 bar, sample SD2700 has a CO_2 storage capacity of 4.6 mmol g^{-1}, which is far greater than the N_2 uptake of 0.22 mmol g^{-1} (**Figure 6.24**), which translates to an equilibrium CO_2/N_2 adsorption ratio of 21. The CO_2/N_2 adsorption ratio of 21 for sample SD2700D is higher than values of between 5 and 11 that are typically observed for carbon materials, [26, 43, 51, 56] and comparable to that of heavily doped N-rich carbons,[70] or highly microporous organic salt-derived carbons.[41] We also estimated the selectivity for CO_2 adsorption from simulated post-combustion flue gas streams in which the proportion of CO_2 is ca. 15% with the remainder being mainly nitrogen by considering the relative uptake of CO_2 at 0.15 bar and N_2 uptake at 0.85 bar. This is based on the fact that flue gas streams from fossil fuel power stations contain only ca. 15% CO_2, with the rest being mainly N_2, and thus comparison of the CO_2 uptake of the carbons at 0.15 bar with their N_2 uptake at 0.85 bar gives a realistic estimation of selectivity for CO_2.

Selectivity analysis was performed using the ideal adsorbed solution theory (IAST) model, which is often used to estimate the relative uptake (or selectivity) of adsorbents for any two gases in a binary gas mixture.[71] The selectivity for CO_2 from the IAST model was derived from the following equation:

$$S = n(CO_2)\, p(N_2)/n(N_2)\, p(CO_2) \qquad \textbf{Equation 6.2}$$

Where

S	the selectivity for CO_2.
$n(CO_2)$	the uptake of CO_2 in mmol g^{-1} at 0.15 bar.
$n(N_2)$	the uptake of N_2 in mmol g^{-1} at 0.85 bar.
$p(N_2)$	0.85 bar.
$p(CO_2)$	0.15 bar.

This comparison yielded high to very high selectivity factors (**Table 6.13**) of between 23 and 47, with the selectivity decreasing at higher levels of activation and therefore larger pore size. The selectivity of the directly synthesised samples was similar to that of analogous conventional samples. Overall, therefore, the present directly activated carbons are at the top end of carbon materials with respect to selectivity for CO_2 uptake under post-combustion conditions. The direct synthesis does not compromise the selectivity for CO_2 uptake. The data presented above demonstrate a clear advantage for our more direct and simple synthesis routes, which is generally desirable in materials synthesis.[72-75]

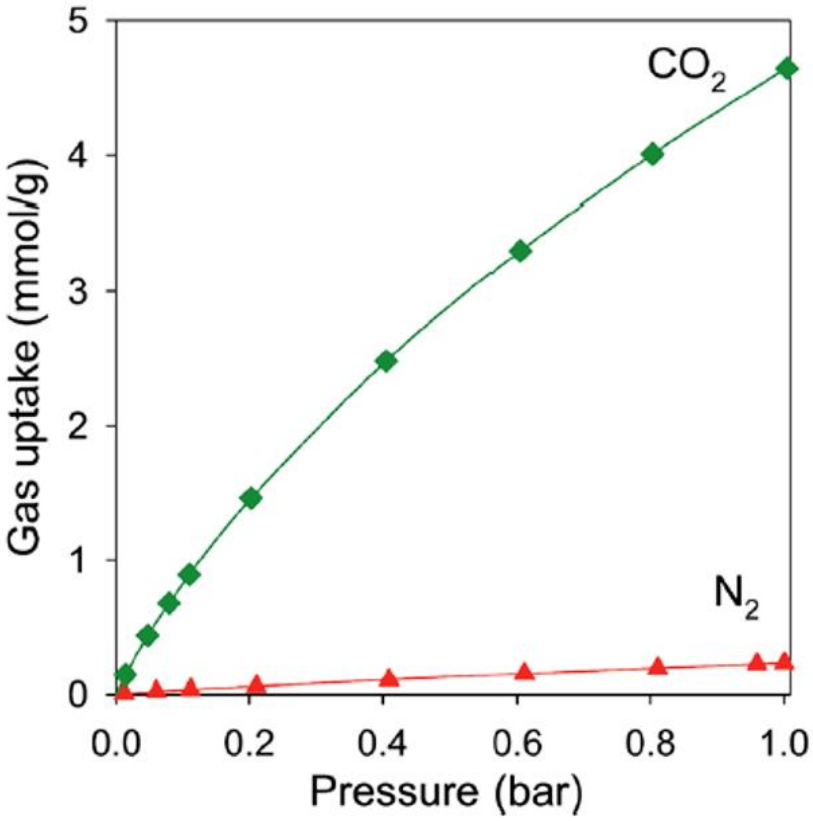


Figure 6.24: Comparison of CO_2 and N_2 uptake ***at room temperature*** for sample **SD2700D**. The CO_2/N_2 adsorption ratio is 21 at 1 bar.

Table 6.13: Selectivity (S) for CO_2 of directly activated carbons or conventionally activated carbons derived from sawdust biomass calculated using the IAST model.

Sample	IAST selectivity (S)
SD2600D	46
SD2600	47
SD2700D	42
SD2700	41
SD2800D	30
SD2800	29
SD4800D	23
SD4800	25

Selectivity (S) was calculated according to the equation;

$S = n(CO_2)\ p(N_2)/n(N_2)\ p(CO_2)$

Where; S is selectivity for CO_2,

$n(CO_2)$ is uptake of CO_2 in mmol g^{-1} at 0.15 bar.

$n(N_2)$ is uptake of N_2 in mmol g^{-1} at 0.85 bar.

$p(N_2)$ is 0.85.

$p(CO_2)$ is 0.15.

6.7 Conclusions

Activated carbons were successfully produced from eucalyptus sawdust wood biomass *via* direct activation that negates the need for hydrothermal carbonisation or pyrolysis. The direct carbonisation, with KOH as activating agent, generated activated carbon yields that are comparable or higher than those of conventional activation routes. A range of characterisation techniques confirmed that the directly activated carbons, whilst offering the advantage of simplicity, lower cost and a greener route, have properties that are similar to those prepared *via* conventional methods. In particular the textural properties and level of graphitic ordering was found to be similar to that of conventionally generated activated carbons. The nature of the direct activation, however, generated carbons with a monolith-like particle morphology. Depending of the activation conditions, the porosity of the directly activated carbons can be tailored to arise primarily from pore channels of size 5 – 7 Å pores, which favour post-combustion CO_2 uptake and thus the carbons capture up to 1.3 mmol g^{-1} and 4.6 mmol g^{-1} at 0.15 bar and 1 bar, respectively, and 25 ^{o}C. At higher levels of activation, directly activated carbons with greater proportion of larger micropores (10 Å – 20 Å pores) and small mesopores (20 Å – 30 Å pores) can be generated that have optimized CO_2 uptake at moderate to high pressure, for example up to 22 mmol g^{-1} at 20 bar and 25 ^{o}C or 31 mmol g^{-1} at 20 bar and 0 ^{o}C.

6.8 References

1. J. A. Turner, *Science*, 1999, **285**, 687-689.

2. L. Schlapbach and A. Züttel, *Nature*, 2001, **414**, 353-358.

3. C. Liu, F. Li, L. P. Ma and H. M. Cheng, *Adv. Mater.*, 2010, **22**, E28-E62.

4. M. Sevilla and R. Mokaya, *Energy Environ. Sci.*, 2014, **7**, 1250-1280.

5. F. Çeçen and Ö. Aktas, *Activated Carbon for Water and Wastewater Treatment*, Wiley-VCH, Weinheim, 2011.

6. Y. D. Xia, Z. X. Yang and Y. Q. Zhu, *J. Mater. Chem. A*, 2013, **1**, 9365-9381.

7. J. C. Wang and S. Kaskel, *J. Mater. Chem.*, 2012, **22**, 23710-23725.

8. L. Wei and G. Yushin, *Nano Energy*, 2012, **1**, 552-565.

9. M. Sevilla, A. B. Fuertes and R. Mokaya, *Energy Environ. Sci.*, 2011, **4**, 1400-1410.

10. H. M. Coromina, D. A. Walsh and R. Mokaya, *J. Mater. Chem.*, 2016, **4**, 280-289.

11. W. Sangchoom and R. Mokaya, *ACS Sustainable Chem. Eng.*, 2015, **3**, 1658-1667.

12. N. Balahmar, A. C. Mitchell and R. Mokaya, *Adv. Energy Mater.*, 2015, **5**.

13. C. Robertson and R. Mokaya, *Microporous Mesoporous Mater.*, 2013, **179**, 151-156.

14. M. Sevilla, W. Sangchoom, N. Balahmar, A. B. Fuertes and R. Mokaya, *ACS Sustainable. Chem. Eng.*, 2016, **4**, 4710-4716.

15. L. Wei, M. Sevilla, A. B. Fuertes, R. Mokaya and G. Yushin, *Adv. Energy Mater.*, 2011, **1**, 356-361.

16. B. Hu, K. Wang, L. H. Wu, S. H. Yu, M. Antonietti and M. M. Titirici, *Adv. Mater.*, 2010, **22**, 813-828.

17. M. M. Titirici and M. Antonietti, *Chem. Soc. Rev.*, 2010, **39**, 103-116.

18. M. M. Titirici, R. J. White, C. Falco and M. Sevilla, *Energy Environ. Sci.*, 2012, **5**, 6796-6822.

19. M. Sevilla and A. B. Fuertes, *Carbon*, 2009, **47**, 2281-2289.

20. J. A. Libra, K. S. Ro, C. Kammann, A. Funke, Y. N. N. D. Berge, M. M. Titirici, C. Fünher, J. K. O. Bens and and K. H. Emmerich, *Biofuels*, 2011, **2**, 71-106.

21. F. Shafizadeh, *J. Anal. Appl. Pyrolysis*, 1982, **3**, 283-305.

22. A. Demirbas and G. Arin, *Energy Sources*, 2002, **24**, 471-482.

23. M. X. Fang, D. K. Shen, Y. X. Li, C. J. Yu, Z. Y. Luo and K. F. Cen, *J. Anal. Appl. Pyrolysis*, 2006, **77**, 22-27.

24. A. V. Bridgwater, D. Meier and D. Radlein, *Org. Geochem.*, 1999, **30**, 1479-1493.

25. E. Sermyagina, J. Saari, J. Kaikko and E. Vakkilainen, *J. Anal. Appl. Pyrolysis*, 2015, **113**, 551-556.

26. J. G. Lynam, M. T. Reza, W. Yan, V. R. Vásquez and C. J. Coronella, *Biomass Convers. Biorefin*, 2015, **5**, 173-181.

27. Z. G. Liu, A. Quek, S. K. Hoekman and R. Balasubramanian, *Fuel*, 2013, **103**, 943-949.

28. M. Sevilla, R. Mokaya and A. B. Fuertes, *Energy Environ. Sci.*, 2011, **4**, 2930-2936.

29. B. Adeniran and R. Mokaya, *Nano Energy*, 2015, **16**, 173-185.

30. M. Sevilla, A. B. Fuertes and R. Mokaya, *Int. J. Hydrogen Energy*, 2011, **36**, 15658-15663.

31. E. Haffner-Staton, N. Balahmar and R. Mokaya, *J. Mater. Chem. A*, 2016, **4**, 13324-13335.

32. A. C. Ferrari and J. Robertson, *Phys. Rev. B: Condens. Matter Mater. Phys.*, 2000, **61**, 14095-14107.

33. M. Sevilla, J. A. Maciá-Agulló and A. B. Fuertes, *Biomass Bioenergy*, 2011, **35**, 3152-3159.

34. B. Adeniran and R. Mokaya, *J. Mater. Chem. A*, 2015, **3**, 5148-5161.

35. A. Almasoudi and R. Mokaya, *J. Mater. Chem. A*, 2014, **2**, 10960-10968.

36. Z. S. Zhang, J. Zhou, W. Xing, Q. Z. Xue, Z. F. Yan, S. P. Zhuo and S. Z. Qiao, *Phys. Chem. Chem. Phys.*, 2013, **15**, 2523-2529.

37. N. P. Wickramaratne and M. Jaroniec, *ACS Appl. Mater. Interfaces*, 2013, **5**, 1849-1855.

38. N. P. Wickramaratne and M. Jaroniec, *J. Mater. Chem. A*, 2013, **1**, 112-116.

39. B. Adeniran and R. Mokaya, *Chem. Mater.*, 2016, **28**, 994-1001.

40. M. Nandi, K. Okada, A. Dutta, A. Bhaumik, J. Maruyama, D. Derks and H. Uyama, *Chem. Commun.*, 2012, **48**, 10283-10285.

41. B. Adeniran, E. Masika and R. Mokaya, *J. Mater. Chem. A*, 2014, **2**, 14696-14710.

42. X. Q. Fan, L. X. Zhang, G. B. Zhang, Z. Shu and J. L. Shi, *Carbon*, 2013, **61**, 423-430.

43. Y. D. Xia, R. Mokaya, G. S. Walker and Y. Q. Zhu, *Adv. Energy Mater.*, 2011, **1**, 678-683.

44. A. Almasoudi and R. Mokaya, *J. Mater. Chem.*, 2012, **22**, 146-152.

45. D. Lee, C. Y. Zhang, C. Wei, B. L. Ashfeld and H. F. Gao, *J. Mater. Chem. A*, 2013, **1**, 14862-14867.

46. J. Silvestre-Albero, A. Wahby, A. Sepúlveda-Escribano, M. Martínez-Escandell, K. Kaneko and F. Rodríguez- Reinoso, *Chem. Commun.*, 2011, **47**, 6840-6842.

47. A. Wahby, J. M. Ramos-Fernández, M. Martínez-Escandell, A. Sepúlveda-Escribano, J. Silvestre-Albero and F. Rodríguez-Reinoso, *ChemSusChem*, 2010, **3**, 974-981.

48. G. Srinivas, J. Burress and T. Yildirim, *Energy Environ. Sci.*, 2012, **5**, 6453-6459.

49. J. D. Figueroa, T. Fout, S. Plasynski, H. McIlvried and R. D. Srivastava, *Int. J. Greenhouse Gas Control*, 2008, **2**, 9-20.

50. Z. Q. Zhang, K. Wang, J. D. Atkinson, X. L. Yan, X. Li, M. J. Rood and Z. F. Yan, *J. Hazard. Mater.*, 2012, **229**, 183-191.

51. M. Sevilla and A. B. Fuertes, *Energy Environ. Sci.*, 2011, **4**, 1765-1771.

52. M. Sevilla and A. B. Fuertes, *J. Colloid Interface Sci.*, 2012, **366**, 147-154.

53. G. Srinivas, V. Krungleviciute, Z. X. Guo and T. Yildirim, *Energy Environ. Sci.*, 2014, **7**, 335-342.

54. G. P. Hao, W. C. Li, D. Qian, G. H. Wang, W. P. Zhang, T. Zhang, A. Q. Wang, F. Schuth, H. J. Bongard and A. H. Lu, *J. Am. Chem. Soc.*, 2011, **133**, 11378-11388.

55. J. C. Wang, A. Heerwig, M. R. Lohe, M. Oschatz, L. Borchardt and S. Kaskel, *J. Mater. Chem.*, 2012, **22**, 13911-13913.

56. M. Sevilla, P. Valle-Vigon and A. B. Fuertes, *Adv. Funct. Mater.*, 2011, **21**, 2781-2787.

57. W. Xing, C. Liu, Z. Y. Zhou, L. Zhang, J. Zhou, S. P. Zhuo, Z. F. Yan, H. Gao, G. Q. Wang and S. Z. Qiao, *Energy Environ. Sci.*, 2012, **5**, 7323-7327.

58. Y. F. Zhao, L. Zhao, K. X. Yao, Y. Yang, Q. Zhang and Y. Han, *J. Mater. Chem.*, 2012, **22**, 19726-19731.

59. M. Saleh, J. N. Tiwari, K. C. Kemp, M. Yousuf and K. S. Kim, *Environ. Sci. Technol.*, 2013, **47**, 5467-5473.

60. M. Sevilla, C. Falco, M. M. Titirici and A. B. Fuertes, *RSC Advances*, 2012, **2**, 12792-12797.

61. J. C. Wang, I. Senkovska, M. Oschatz, M. R. Lohe, L. Borchardt, A. Heerwig, Q. Liu and S. Kaskel, *ACS Appl. Mater. Interfaces*, 2013, **5**, 3160-3167.

62. D. L. Sivadas, R. Narasimman, R. Rajeev, K. Prabhakaran and K. N. Ninan, *J. Mater. Chem. A*, 2015, **3**, 16213-16221.

63. R. Du, N. Zhang, H. Xu, N. N. Mao, W. J. Duan, J. Y. Wang, Q. C. Zhao, Z. F. Liu and J. Zhang, *Adv. Mater.*, 2014, **26**, 8053.

64. N. Huang, X. Chen, R. Krishna and D. L. Jiang, *Angew. Chem. Int. Ed.*, 2015, **54**, 2986-2990.

65. A. Aijaz, J. K. Sun, P. Pachfule, T. Uchida and Q. Xu, *Chem. Commun.*, 2015, **51**, 13945-13948.

66. S. J. Yang, M. Antonietti and N. Fechler, *J. Am. Chem. Soc.*, 2015, **137**, 8269-8273.

67. N. López-Salas , M. C. Gutiérrez , C. O. Ania, J. L. G. Fierro, M. L. Ferrer and F. del Monte, *J. Mater. Chem. A*, 2014, **2**, 17387-17399.

68. G. P. Hao, Z. Y. Jin, Q. Sun, X. Q. Zhang, J. T. Zhang and A. H. Lu, *Energy Environ. Sci.*, 2013, **6**, 3740-3747.

69. J. Gong, H. J. Lin, M. Antonietti and J. Y. Yuan, *J. Mater. Chem. A*, 2016, **4**, 7313-7321.

70. C. Chen, J. Kim and W. S. Ahn, *Fuel*, 2012, **95**, 360-364.

71. A. L. Myers and J. M. Prausnitz, *AIChE J.*, 1965, **11**, 121-127.

72. Y. D. Xia, R. Mokaya, D. M. Grant and G. S. Walker, *Carbon*, 2011, **49**, 844-853.

73. R. Mokaya, *Chem. Commun.*, 2001, 633-634.

74. R. Mokaya and W. Jones, *Chem. Commun.*, 1996, 983-984.

75. R. Mokaya, W. Jones, S. Moreno and G. Poncelet, *Catal. Lett.*, 1997, **49**, 87-94.

Chapter 7. Pre-mixed Precursors for Mediating the Porosity of Activated Carbons for Gas Storage (CO_2 and H_2) Applications

7.1 The Aim of this Chapter

A main motivation of this chapter is:

- To prepare high and ultrahigh surface area activated carbons by using a variety of carbon precursors (namely; polypyrrole (PPY) and/or eucalyptus wood sawdust) *via* two ways; (i) direct activation of mixtures of polypyrrole and sawdust, and (ii) conversion of sawdust to hydrochar followed by activation of sawdust/polypyrrole mixtures.

- To vary activation conditions (i.e., amount of activating agent KOH, ratio of polypyrrole to sawdust or sawdust hydrochar and activating temperature), as a means of targeting porosity and elemental compositions (i.e., N content) that is suitable for CO_2 or hydrogen uptake.

7.2 Abstract

High to very high surface area activated carbons were successfully prepared from premixed precursors containing polypyrrole and sawdust or sawdust derived hydrochar. The premixed precursors offer carbon materials with ultrahigh surface area (up to 3815 m^2 g^{-1}) and pore volume (up to ~2.6 cm^3 g^{-1}) comprising of mainly two pore systems; one pore size system in the micropore range (6 - 12 Å) and the other in the mesopore range (22 – 35 Å). The mix of mesoporosity and microporosity is such that some samples are predominantly mesoporous. Carbons prepared from polypyrrole and sawdust have greater porosity (higher surface area and pore volume) than those generated from polypyrrole and sawdust hydrochar, and higher amounts of polypyrrole favour greater mesoporosity. On the other hand, the highest proportion of microporosity is generated for samples with greatest amount of sawdust hydrochar in the precursor mix. The best performing carbons for CO_2 uptake at moderate pressure (20 – 40 bar) and room temperature are those that have a near total absence of micropores; microporosity appears to limit high pressure CO_2 uptake. The gravimetric (mmol g^{-1}) CO_2 uptake capacities obtained for the carbons are among the highest ever reported for porous carbons. The carbons also exhibit excellent excess hydrogen uptake of up to 3.6 wt% and 6.3 wt% (at -196 ºC and 1 or 20 bar, respectively), which translates to total uptake of 7.5 wt% (at -196 ºC and 20 bar). The best performing carbons achieve up to 9.4 wt% total hydrogen storage at 40 bar, which is much higher than that of many currently available benchmark materials.

7.3 Introduction

One of the possible solutions to control the increase in level of CO_2 emissions to the atmosphere is material based CO_2 capture and storage.[1-5] Such materials need to be efficient for the capture and storage of CO_2.[1, 5, 6] Recently, a wide range of materials have extensively studied, including, porous carbons,[7-10] metal organic frameworks (MOFs),[11, 12] and zeolites.[13-15] Carbon-based materials, in particular, are attractive and increasingly receiving attention as solid state materials for CO_2 and H_2 storage. More specifically, activated carbons are one of the most studied carbon-based porous materials that have been investigated and widely used [16-22] in many applications dependent on their porosity such as water treatment, [23-28] as catalysts, [29] gas separation,[30] and energy related gas storage.[17-19, 21, 22] This is because activated carbons offer several attractive features such as high surface area with well-developed porosity (micropores and mesopores), controllable pore structure (structural flexibility), low cost, availability, stability (chemical and mechanical), ease of preparation and handling.[1, 21, 31-35] The unique structural features of activated carbons are dependent the type and nature of carbon precursor used, activation method and activation conditions.

Activated carbons may be obtained from a wide range of carbonaceous matter such as coal, wood, sawdust, fruit, nutshells, bones, carbon rich polymers etc. *via* activation processes, which generate pore channels and constrained spaces (i.e., porosity) thereby transforming enhancing porosity.[16-19, 21, 22, 36] One of the most commonly used activating agents is KOH due to its ability to generate activated carbons from precursors such as hydrothermally carbonized carbonaceous matter,[17, 21, 22] carbon rich polymers such as polythiophene,[20] and polypyrrole,[21, 37-40] zeolite-templated carbon ZTCs [41] and graphene.[42]

Recently, biomass-derived activated carbons have received a great deal of attention due to their being environment-friendly, cheap, readily available, and renewable.[43-48] However, recently, due to the heterogeneity and low carbon yield of biomass precursors, there have been moves to use so-called hydrochar which is enriched carbonaceous matter that is produced *via* the relatively simple process of hydrothermal carbonisation involving heating an aqueous solution of biomass at relatively low temperature (typically up to 250 ^{o}C) at autogenous pressure.[49] Mokaya *et. al.* have successfully obtained activated carbons with a range of surface areas (1048 to 3537 m^2 g^1), and pore volume (0.51 to 1.85 cm^3 g^1) *via* a simple and green method of hydrothermal carbonization followed by KOH-chemical activation using renewable, available and low cost biomass precursors such as Jujun grass and Camellia japonica.[46] On the other hand, Fuertes *et. al.*[50] successfully produced N-doped carbons using polypyrrole as a carbon precursor. More recently, Mokaya *et. al.*[38] successfully produced ultra-high surface area (2800– 4000 m^2 g^{-1}) mesoporous carbons with extremely high mesopore volume with hardly any micropores present using either polypyrrole or eucalyptus wood sawdust as carbon precursors.

This chapter explores the preparation of activated carbons from polypyrrole and/or eucalyptus wood sawdust *via* two ways, namely (i) direct activation of mixtures of polypyrrole and sawdust, and (ii) conversion of sawdust to hydrochar followed by activation of sawdust/polypyrrole mixtures. The activation conditions (i.e., amount of activating agent KOH, ratio of polypyrrole to sawdust or sawdust hydrochar and activating temperature) were varied as a means of targeting porosity and elemental compositions (i.e., N content) in an attempt to generate materials that are suitable for CO_2 or hydrogen uptake.

7.4 Experimental Section

This section presents a detailed description of the materials and chemicals, experimental procedures, and approach used in **Chapter 7**.

7.4.1 Materials and Chemicals

The list of chemicals and materials used in this chapter, and their sources and purity are presented in **Table 7.1**.

Table 7.1: List of chemical reagents/materials used in the experiment.

Chemical/Material	Source	Purity/Concentration
Biomass sawdust	Eucalyptus wood sawdust	-
Eucalyptus wood sawdust-derived hydrochar	Eucalyptus wood sawdust	-
Pyrrole	Sigma-Aldrich	reagent grade 98%
Iron Chloride ($FeCl_3$)	Sigma-Aldrich	reagent grade 97%
Potassium Hydroxide (KOH)	Fisher Scientific	-
N_2 Compressed gas (Cylinder)	BOC Ltd	100%
Hydrochloric acid (HCl)	Fisher Scientific	37%

7.4.2 Materials Synthesis

7.4.2.1 Carbon Precursors

7.4.2.1.1 Eucalyptus Wood Sawdust

Eucalyptus wood sawdust was firstly washed with distilled water to remove impurities then filtered under vacuum. After being dried in an oven at 120 ^{o}C overnight the sawdust was sieved to obtain a homogenous product designated as *SD*. The elemental composition (wt%) of the eucalyptus wood sawdust is given in **Table 7.3**.

7.4.2.1.2 Sawdust-Derived Hydrochar

Eucalyptus wood sawdust was converted to hydrochar *via* hydrothermal carbonization as previously reported.[45, 47, 51-53] An aqueous dispersion of eucalyptus wood sawdust at a concentration of 320 gL^{-1} (6.4 g of eucalyptus wood sawdust in 20 ml of water) was placed in a stainless steel autoclave and heated, at a ramp rate of 5 ^{o}C min^{-1}, to 250 ^{o}C for 2 h. The resulting carbon-rich brown solid product (hydrochar) was recovered by filtration under vacuum, washed thoroughly with distilled water and then dried in an oven at 120 ^{o}C. The elemental composition (wt%) of the resulting hydrochar is presented in **Table 7.3**.

7.4.2.1.3 Polypyrrole

Polypyrrole (designated as PPY) may be readily prepared, [21, 37, 38, 40, 50, 54] which means it is a good precursor for activated carbons.[21, 37, 38] PPY was prepared as follows;[21, 37, 38, 40] 3 g of pyrrole was added to 200 mL of 0.5 M $FeCl_3$ solution and the mixture was magnetically stirred continuously for 2 h at room temperature until the color changed gradually from yellow to thick black (**Figure 7.1** and **Figure 7.2**). The generated polypyrrole was recovered by filtration under vacuum, thoroughly washed with distilled water several times to remove any impurities and non-reacted/excess $FeCl_3$ and other by-products. Finally, the resulting black solid product was dried in an oven at 120 ^{o}C. The elemental composition (wt%) of the polypyrrole is presented in **Table 7.3**.

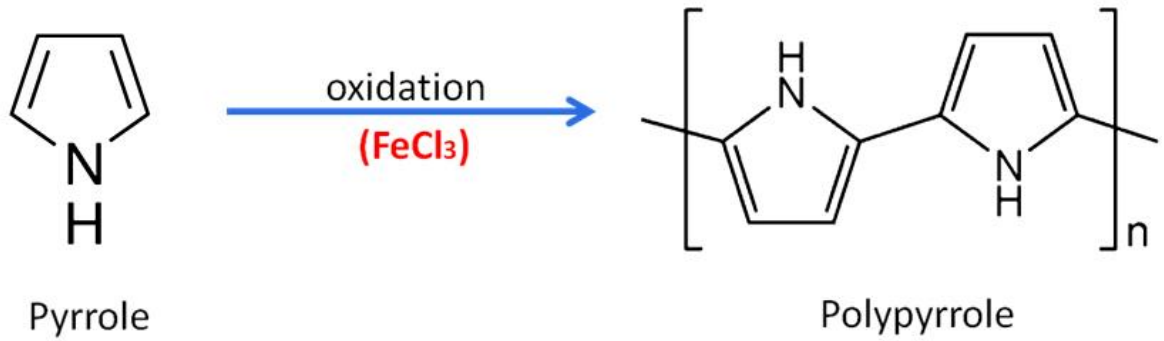


Figure 7.1: Reaction for the formation of Polypyrrole.

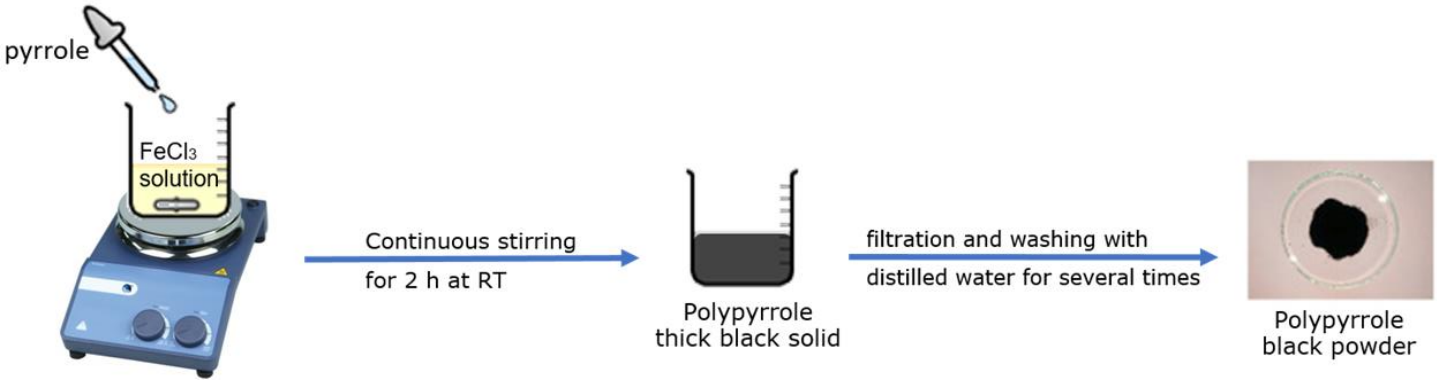


Figure 7.2: Polypyrrole synthesis steps.

7.4.2.2 Production of Activated Carbons

7.4.2.2.1 Polypyrrole/Sawdust Derived Activated Carbons

A mixture of PPY:SD:KOH, where SD is the sawdust, at weight ratio of 1:1:3, 1:1:4 or 1:1:5 was activated at 800 ºC or 900 ºC, while a PPY:SD:KOH mixture at weight ratio of 1:2:4, 1:3:4, 2:1:4 or 3:1:4 was activated at 800 ºC. The mixtures were placed in a crucible and activated for 1 h at target temperatures (800 or 900 ºC) under nitrogen flow for 1 h following a heating ramp rate of 3 ºC/min (**Figure 4.5**). After cooling, the activated carbons were thoroughly washed with 10 wt% HCl to remove any inorganic salts, followed by washing with distilled water until neutral pH was achieved for the filtrate. The activated carbons were dried overnight in an oven 120 ºC (See **Table 7.2** for sample abbreviations).

7.4.2.2.2 Polypyrrole/Hydrochar Derived Activated Carbons

A mixture of PPY:H:KOH, where H is the hydrochar, at weight ratio of 1:1:3, 1:1:4 or 1:1:5 was activated at 800 ºC and 900 ºC, while for weight ratio of 1:2:4, 1:3:4, 2:1:4, 3:1:4, the activation was performed at 800 ºC. The mixtures were placed in a crucible and activated for 1 h at target temperatures (800 ºC or 900 ºC) under nitrogen flow following a temperature ramp rate of 3 ºC/min (**Figure 4.5**). After cooling, the activated carbons were thoroughly washed with 10 wt% HCl to remove any inorganic salts, and then with distilled water until neutral pH. Finally, the carbons were dried overnight in an oven at 120 ºC (See **Table 7.2** for samples abbreviations).

7.5 Abbreviations

7.5.1 Polypyrrole/Sawdust Derived Carbons

Polypyrrole/sawdust derived carbons were designated as PPYSD*xyzt where; x*= PPY ratio (1, 2, or 3), *y*= sawdust ratio (1, 2, or 3), *z*= KOH ratio (3, 4, or 5), *t*= temperature of activation (800 °C or 900 °C). See **Table 7.2** for samples abbreviations.

7.5.2 Polypyrrole/Hydrochar Derived Carbons

Polypyrrole/hydrochar derived carbons were designated as PPYH*xyzt where*; *x*= PPY ratio (1, 2, or 3), *y*= hydrochar ratio (1, 2, or 3), *z*= KOH ratio (3, 4, or 5), *t*= temperature of activation (800 °C or 900 °C). See **Table 7.2** for samples abbreviations.

Table 7.2: Summary of activated carbons abbreviations.

Polypyrrole/sawdust derived carbons (PPYSD*xyzt*)	Polypyrrole/hydrochar derived carbons (PPYH*xyzt*)
PPYSD114800	PPYH114800
PPYSD115800	PPYH115800
PPYSD214800	PPYH214800
PPYSD314800	PPYH314800
PPYSD124800	PPYH124800
PPYSD134800	PPYH134800
PPYSD113900	PPYH113900
PPYSD114900	PPYH114900
PPYSD115900	PPYH115900

7.6 Results and Discussion

7.6.1 Carbon Precursors

7.6.1.1 Structural Ordering

Typical X-ray diffraction patterns of starting materials (carbon precursors) namely; polypyrrole (PPY), eucalyptus wood sawdust (SD) and its respective hydrochar (H) are shown in **Figure 7.3**.

For polypyrrole, the XRD pattern shows a broad peak in the region of 2θ= 22°-26°, revealing that the polypyrrole is amorphous in nature which agrees well with the structure reported in literature [55-58] as well as with data discussed in SEM analysis (**Figure 7.4**).

For eucalyptus wood sawdust, three peaks were detected at 2θ of 16° (101 diffraction), 22° (002 diffraction), both of which correspond to the arrangement of cellulose crystallites,[59-62] and a broad peak at 42° (004 diffraction) related to hemicelluloses and lignin are both are largely amorphous in nature.

The hydrochar exhibited similar XRD patterns to that of the sawdust which suggests no change in crystallinity of cellulosic components. At 2θ= 42°, there is a broad peak similar to that in raw SD arising from the amorphous nature of the carbon in the hydrochar.[63, 64] The XRD analysis results, are consistent with SEM analysis (**Figure 7.6**) where the original morphology of the particles is mainly preserved after the HTC treatment at 250 °C. However, a study by Kang *et. al.*,[62] suggested that HTC of biomass at 245 °C for 20 h generated hydrochar with no crystalline cellulosic sharp peaks. It is however, noteworthy that in the present study, HTC was performed for a much shorter duration of 2 h (compared to 20 h for Kang's study), which may act to preserve the cellulosic order within the hydrochar.[62]

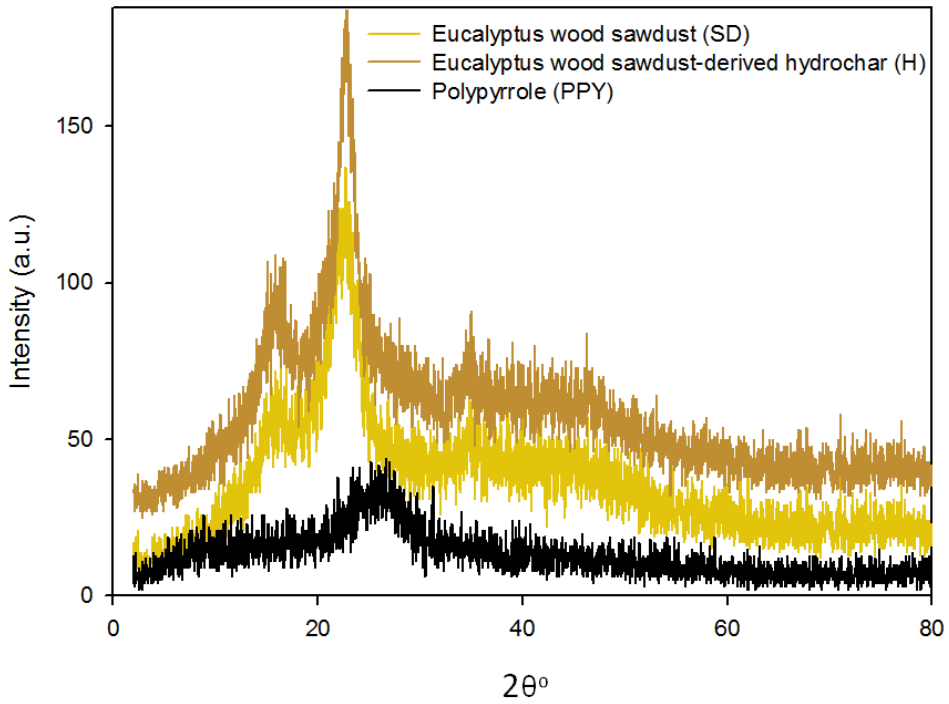


Figure 7.3: Powder XRD patterns of starting materials; polypyrrole (PPY), sawdust (SD) and its respective hydrochar (H).

7.6.1.2 Morphology and Surface Analysis

The changes in surface structure and morphology of the carbon precursors; polypyrrole, the eucalyptus wood sawdust and its respective hydrochar, were investigated using scanning electron microscopy (SEM), and the micrographs images are shown in **Figure 7.4**, **Figure 7.5** and **Figure 7.6**, respectively.

The morphology of polypyrrole (**Figure 7.4**) consists of larger particles loosely aggregated with globular structure and spherical shapes, which is similar to what has previously been observed.[37, 39, 50, 55, 57, 65] However, on activation to sample PPY14800 (**Figure 7.10**), the original morphology is altered completely to irregular shaped particles with large voids that are typical for activated carbons.[37, 39, 47]

Both the eucalyptus wood sawdust and its respective hydrochar (**Figure 7.5** and **Figure 7.6**, respectively) show well-defined cellular surface fibre-like particles with honeycomb holes/voids, typical of lignocellulosic biomass materials and char particles formed from lignocellulosic biomass.[43, 47, 51, 66-69]

The morphology of hydrochar (**Figure 7.6**) clearly shows the effect of hydrothermal treatment; the hydrochar particles appear uneven and with rougher surface topology, which may be ascribed to decomposition of hemicellulose as well as the depolymerisation of cellulose and partial degradation of lignin.[70-74]

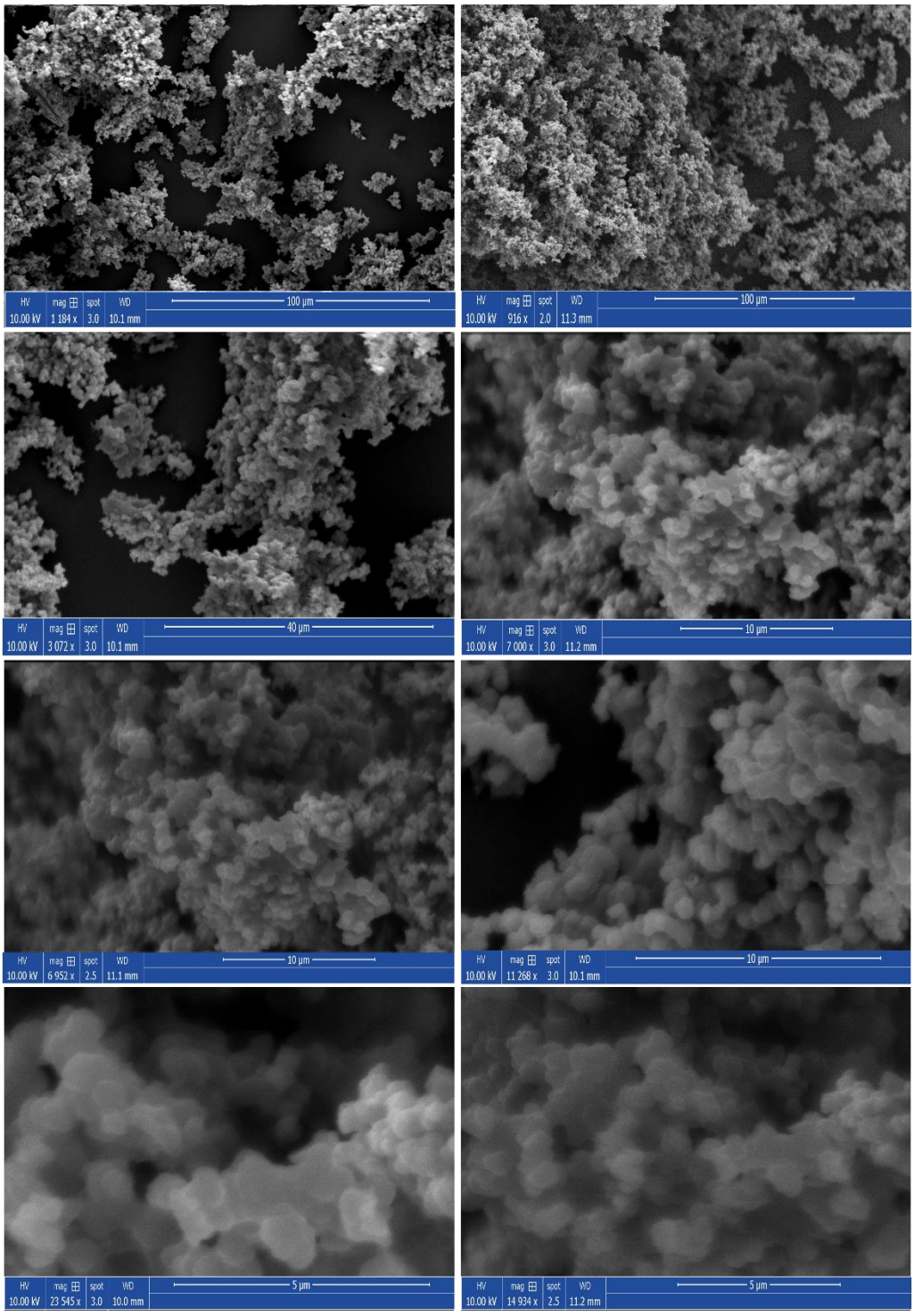


Figure 7.4: SEM micrographs images of Polypyrrole (PPY).

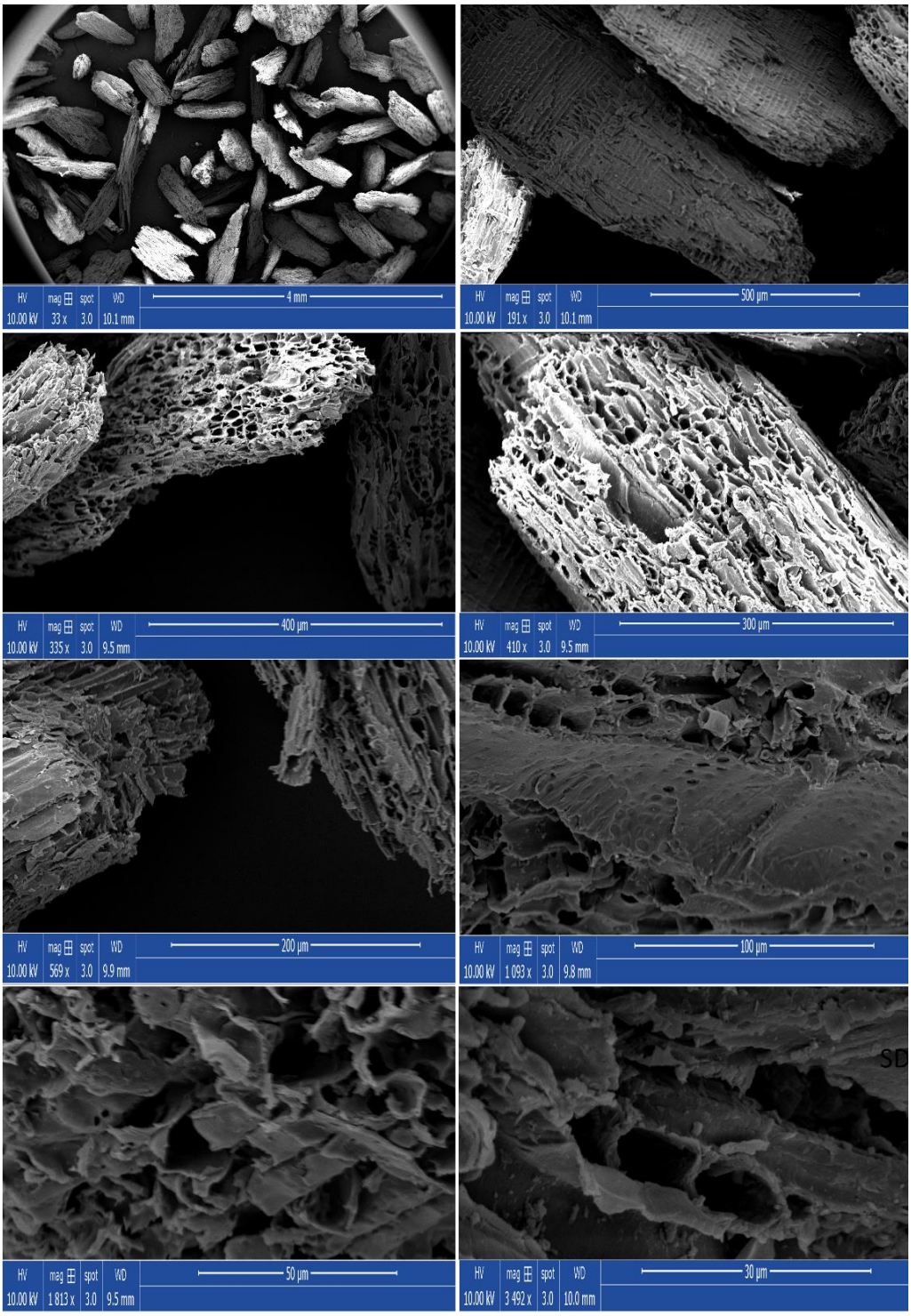


Figure 7.5: SEM micrographs images of eucalyptus wood sawdust (SD).

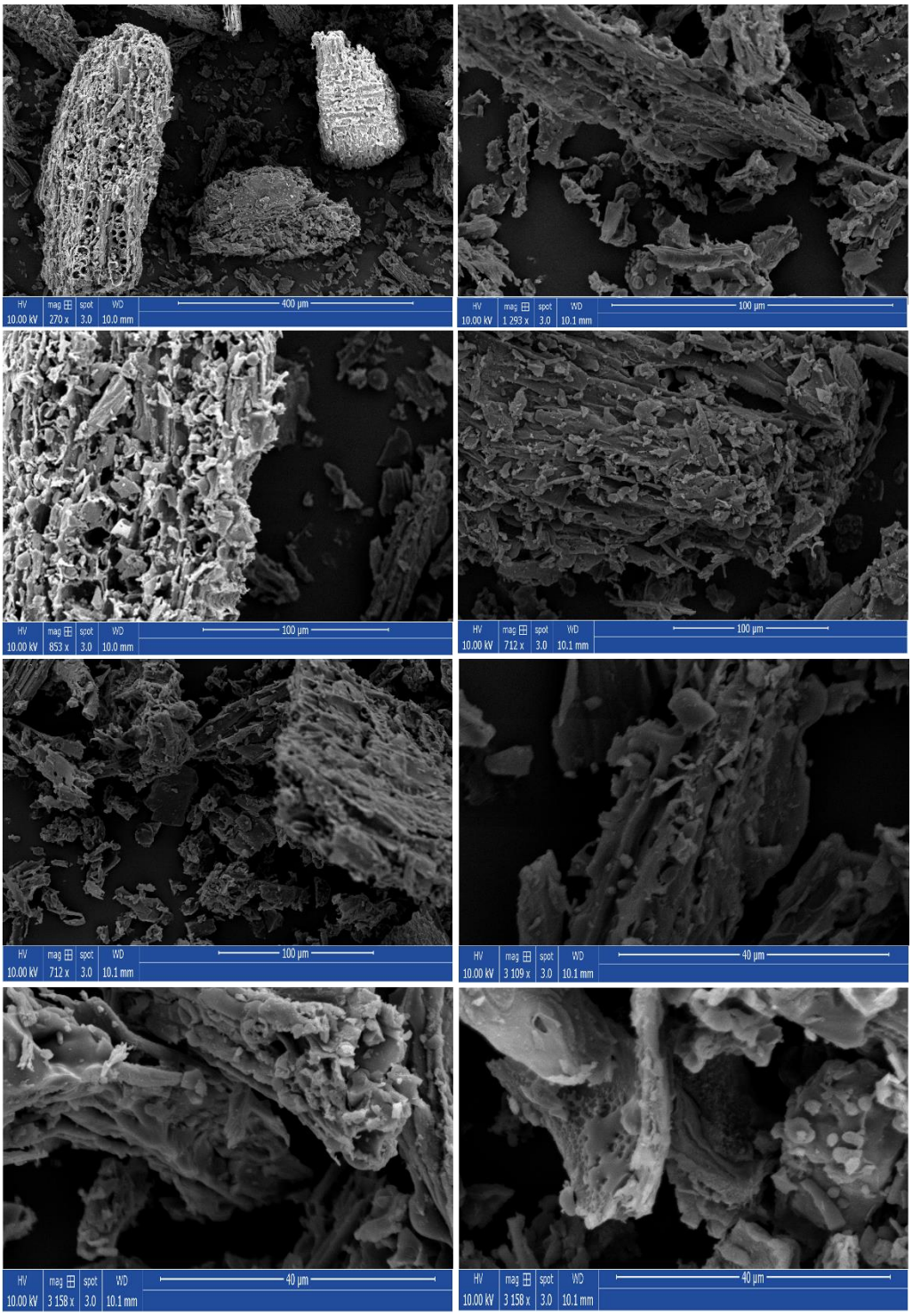


Figure 7.6: SEM micrographs images of hydrochar derived from eucalyptus wood sawdust (H).

7.6.1.3 Elemental Composition

The chemical composition of the carbon precursors is presented in **Table 7.3**. As expected, for the sawdust to hydrochar transformation, the carbon yield increased from 46.4 wt% to 57.7 wt% a trend similar to that observed by Mokaya *et. al.*[51] On the other hand, the hydrogen and oxygen content decreased from 6.0 wt% to 5.4 wt% and from 47.5 wt% to 36.9 wt%, respectively. This trend is consistent and generally comparable with that of other biomass-derived chars previously reported [53] as shown in **Table 7.4**. The elemental composition of the polypyrrole, is comparable to what has been reported previously; [37, 38] carbon content of 44.5%, nitrogen at 3.0% and oxygen content of 12.6%.

Table 7.3: Chemical composition of starting materials.

Sample	Elemental Composition [%]			
	C	H	N	O + X [a]
Eucalyptus Wood Sawdust (SD)	46.4	6.0	0.10	47.5
Hydrochar (H)	57.7	5.4	0.0	36.9
Polypyrrole (PPY)	44.5	3.0	12.6	39.9

[a] Oxygen content + X (where *X* represent the presence of other elements) is estimated as O + X (wt%) = [100-(C+H+N)].

Table 7.4: Elemental composition of hydrochar from other biomass precursors.

Sample	Carbonisation Conditions		Elemental Composition [wt%]				Reference
	Environment	Temperature (°C)	C	H	N	O + X [a]	
Sawdust hydrochar	Water	250	57.7	5.4	0	36.9	This work
CNL1 carbon	Air	-	77.7	3.1	0	19.2	67
Air-carbonized sawdust-derived carbon ACSD	N_2 then Air	400	72.4	3.2	0	24.2	47
Rice husk char	N_2	400	71.5	-	-	25.5	75
Cherry stone char	Ar	400	77.6	4.6	0.8	16.9	76
Beech pellet char	Ar	800	82.7	2.0	0.4	14.9	77
Tire char	O_2 Free	450	72.5	4.7	4.8	15.3	78
Lignite char	N_2	475	65.0	2.4	0.9	18.2	79
Lignin hydrochar	Water	390	66.6	5.1	0	28.3	80
Saw-dust hydrochar	Water	250	69.3	6.8	0	23.9	21

[a] Oxygen content + X (where *X* represent the presence of other elements) is estimated as O + X (wt%) = [100-(C+H+N)].

7.6.2 Activated Carbons

7.6.2.1 Purity and Thermal Stability

Thermogravimetric analysis was performed under flowing air conditions following the procedure discussed in **Chapter 2**. **Figure 7.7 A** shows TGA curves of PPY/SD derived activated carbons while **Figure 7.7 B** shows TGA curves for PPY/H derived activated carbons.

For all TGA curves there is an initial mass loss of ca. 20 wt% below 300 ^{o}C, which is attributable to loss of water or volatiles. This is followed by further mass loss event, due to carbon burn off, between ca. 500 ^{o}C and 600 ^{o}C for PPY/SD samples, and between ca. 400 ^{o}C and 600 ^{o}C for PPY/H samples. According to the TGA curves, the activated carbons derived from a combination of PPY and sawdust show better thermal stability (as indicated by carbon burn off maxima) than PPY/hydrochar-derived samples. The carbon burn off temperature ranges from 500 °C to 600 °C for PPY/SD samples. In contrast, activated carbons derived from PPY/hydrochar show carbon burn off between 400 °C and 600 °C. Activated carbons prepared at higher activation temperature (900 ^{o}C) are more thermally stable and show greater resistance to combustion (**Figure 7.7 A** and **Figure 7.7 B**), which may be related to the level of graphitisation due to exposure to higher temperature. However, the overall level of graphitisation in the samples was generally low as indicated by powder XRD analysis.[38]

Generally, for activated carbons derived from PPY/hydrochar, increase in the hydrochar content (i.e., PPYH124800 vs PPYH134800) results in decrease in thermal stability. All the activated carbons had very low residual matter after thermal treatment in air, which confirms their carbonaceous nature. If a significant amount of non-carbonized wood (e.g., lignocellulosic matter) had

been present, the mass loss due to burn-off would not have occurred in a single event, as the main components of wood (lignin, cellulose, and hemicellulose) decompose at different temperatures.[67, 81]

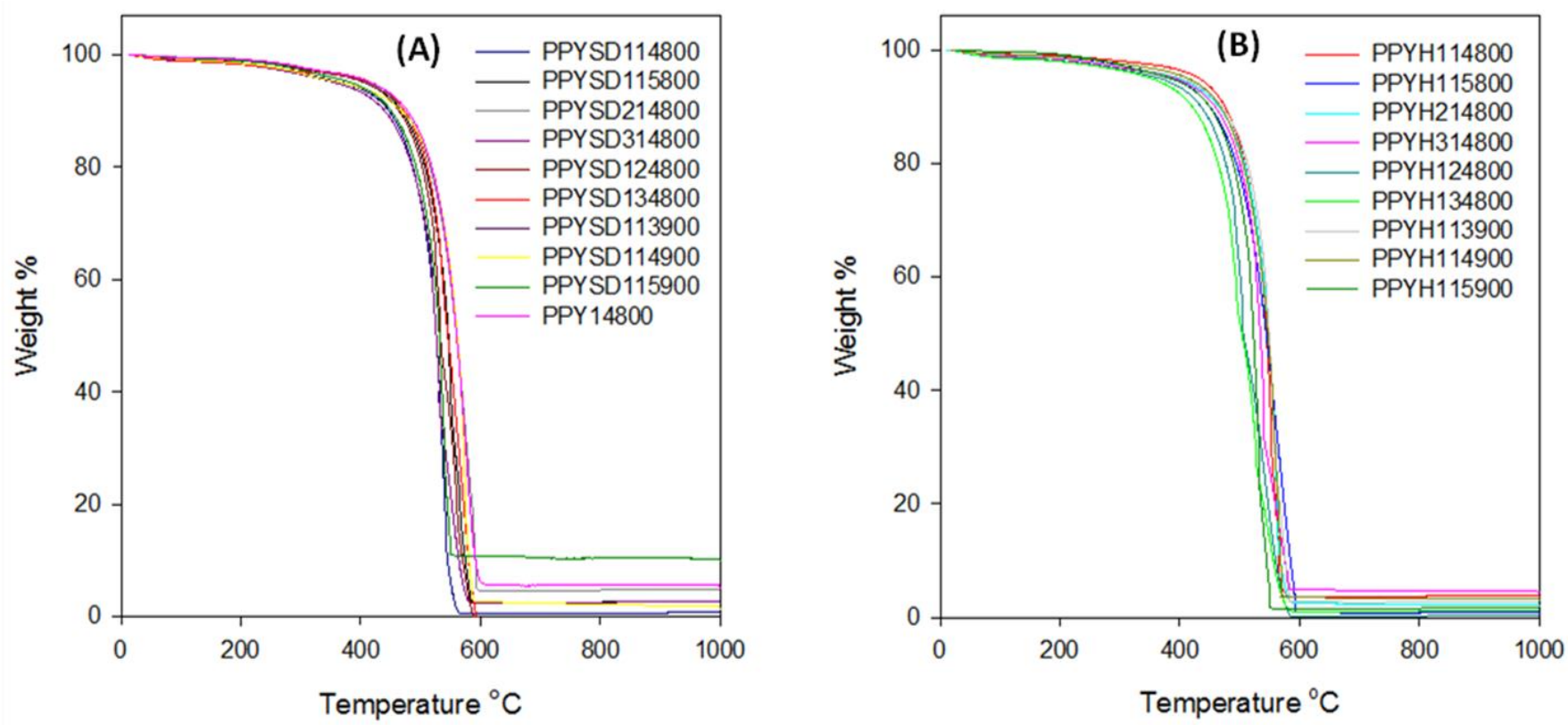


Figure 7.7: Thermal gravimetric analysis curves for **(A)** PPY/SD derived carbons, and **(B)** PPY/H derived carbons.

7.6.2.2 Structural Ordering

Powder XRD patterns for both sets of activated carbons are shown in **Figure 7.8** for PPY/SD and **Figure 7.9** for PPY/H.

For both sets, there are no clear differences in the nature of the carbons prepared at different activation level (i.e. KOH ratio, activation temperature) and different ratio of precursors with respect to their apparent levels of graphitisation. The peaks that indicate graphitization in a carbon are expected at 2θ = 22° for the (002) diffraction and at 2θ = 43° for the (101) diffraction.[47] Both sets have a very board peak at ca. 2θ=44°. The peak expected at 2θ= 22° is not clearly observed due to being masked by the gradient of the baseline. As the level of activation increases (i.e. temperature of activation and KOH ratio) from 800°C and ratio of 4 (in PPYSD114800 and PPYSD115800) to 900°C and ratio of 5 (in PPYSD114900 and PPYSD115900), the graphitic peaks normally present at 2θ= 22-26° and 44° are diminished [38] Overall, the graphitic peaks are very broad, which indicates that both sets of activated carbons mainly contain amorphous carbon but with some small amounts of disordered turbostratic domains. The XRD patterns of the PPY/SD carbons are very similar to those of PPY/H analogues. The powder XRD pattern of PPYSD113900, PPYSD114900 and PPYSD115900 (**Figure 7.8**) have small sharp peaks suggesting the presence of minor inorganic impurities, which are likely related to potassium compounds that survived from HCl-washing step.

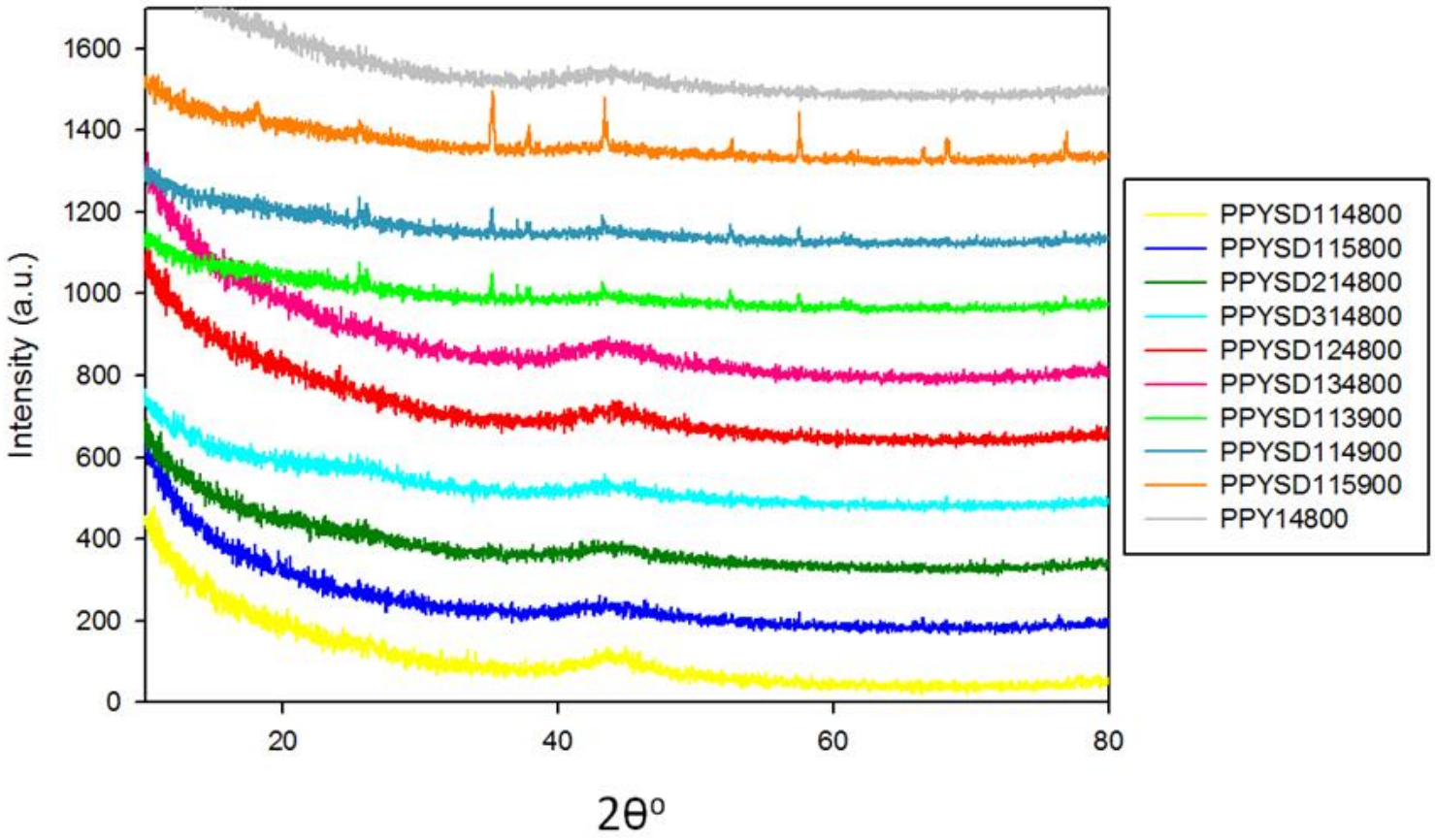


Figure 7.8: Powder XRD patterns of PPY/SD activated carbons.

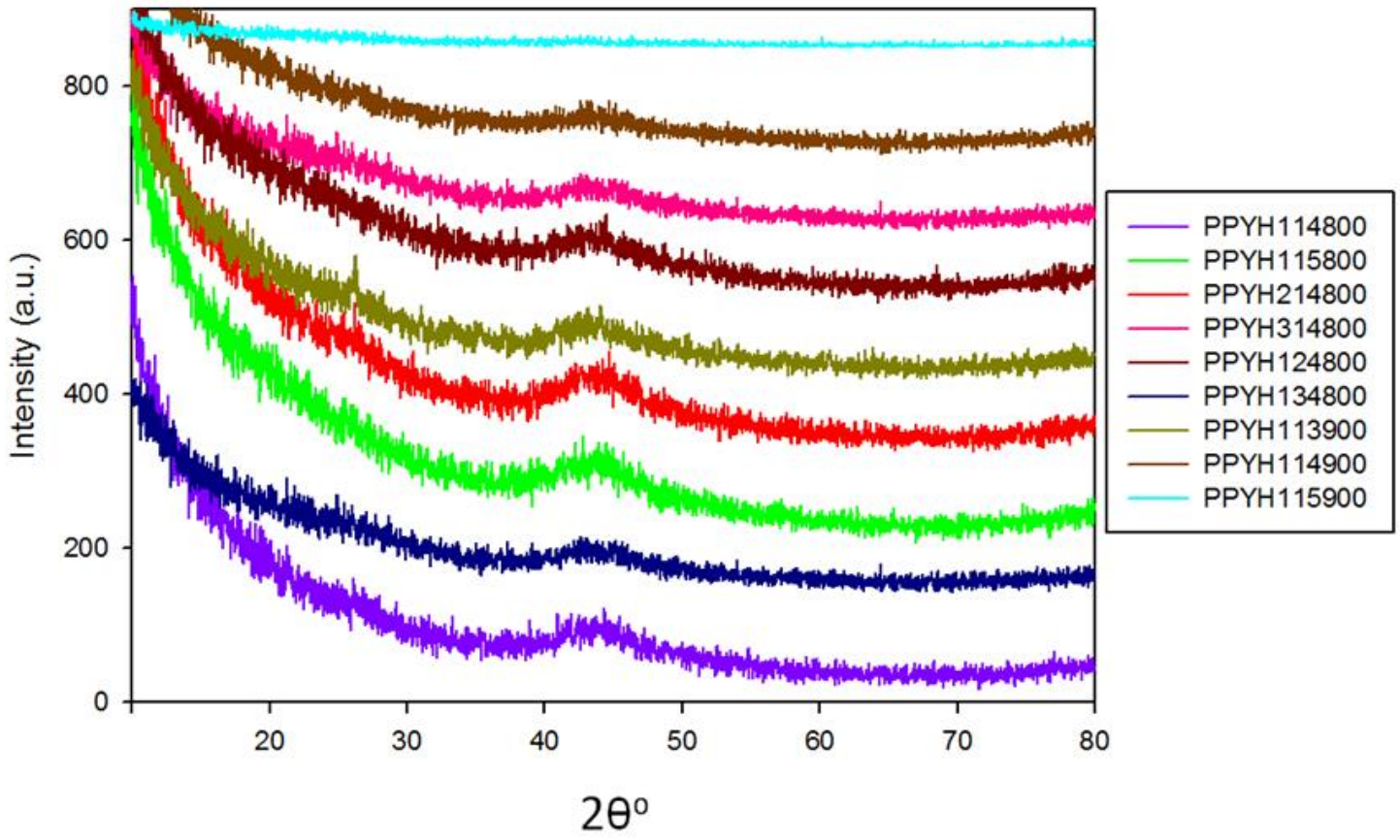


Figure 7.9: Powder XRD patterns of PPY/H activated carbons.

7.6.2.3 Elemental Composition

The elemental composition of the two sets of activated carbons PPY/SD and PPY/H is presented in **Table 7.5**.

The C content of the activated carbons increases for samples prepared at higher level of activation, accompanied with decrease in the N, H and O content. When polypyrrole is subjected to KOH activation (sample PPY14800), the carbon content (wt%) increases from 44.5 to 87.0. In contrast, the N-content (wt%) and H-content (wt%) decreases to 0.92 and by 0.24, respectively. In general, as expected, there is an increases in the carbon content at higher levels of activation (i.e. activation temperature= 900 °C and KOH ratio of 5) accompanied by a decrease in the N, H and O content which is in agreement with the fact that the N-content of activated carbons prepared from N-containing precursors such as polypyrrole generally reduces at high levels of activation.[37, 38, 52] It is noteworthy that for any given activation temperature, a higher PPY content in the activation mixture results in greater amount of N in the activated carbons; PPYSD214800 vs PPYSD314800, and PPYH214800 vs PPYH314800.

Table 7.5: Elemental analysis of PPYSD and PPYH activated carbons.

	Sample	Activation Conditions		Elemental Composition [a] [%]			
		T °C	KOH ratio	C	H	N	O + X [b]
Activated Carbons	PPY14800	800	4	87.01	0.24	0.92	11.83
	PPYSD114800	800	4	87.55	0.12	0.92	11.41
	PPYSD115800	800	5	87.45	0.16	1.02	11.37
	PPYSD214800	800	4	84.53	0.00	1.24	14.23
	PPYSD314800	800	4	82.00	0.10	2.60	15.30
	PPYSD124800	800	4	87.79	0.00	0.81	11.40
	PPYSD134800	800	4	88.96	0.00	0.63	10.41
	PPYSD113900	900	3	76.12	0.13	0.63	23.12
	PPYSD114900	900	4	77.40	0.88	0.90	20.82
	PPYSD115900	900	5	72.69	0.30	0.57	26.44
	PPYH114800	800	4	88.84	0.02	0.63	10.51
	PPYH115800	800	5	83.79	0.30	1.10	14.61
	PPYH214800	800	4	86.95	0.00	1.57	11.48
	PPYH314800	800	4	82.89	0.01	2.20	14.90
	PPYH134800	800	4	82.81	0.20	1.45	15.14
	PPYH124800	800	4	82.96	0.00	1.20	15.84
	PPYH113900	900	3	87.24	0.03	0.92	11.81
	PPYH114900	900	4	88.76	0.02	0.42	10.80
	PPYH115900	900	5	88.89	0.02	0.63	10.46

[a] Obtain from CHN analysis.
[b] Estimated by: O + X (where X presence of other elements) %= [100-(C+H+N)].

7.6.2.4 Morphology and Surface Analysis

SEM micrographs images of all the carbons PPY/SD and PPY/H are shown in **Figure 7.10** to **Figure 7.28**.

In general, the morphology of the activated carbons is completely different from the nature of the starting materials meaning that the morphology of the precursors is not retained in the activated. The morphology of all the activated carbons is similar to that typically observed for activated carbons.[37, 47, 50, 51, 82] SEM micrographs images show that the carbons have particles with sharp corners/edges and large conchoidal cavities depending on level of activation.

PPY/SD activated carbons (**Figure 7.11**, **Figure 7.13**, **Figure 7.15**, **Figure 7.17**,**Figure 7.19**, **Figure 7.21**, **Figure 7.23**, **Figure 7.25**, and **Figure 7.27**), exhibit morphology characterized by irregular shaped particles and smooth surfaces and show much greater connectivity and larger monolith-like particles which may be a preserved characteristic from the sawdust particles.[46, 83]

On the other hand, for PPY/H activated carbons (**Figure 7.12**, **Figure 7.14**, **Figure 7.16**, **Figure 7.18**, **Figure 7.20**, **Figure 7.22**, **Figure 7.24**, **Figure 7.26**, and **Figure 7.28**) the morphology exhibited irregular shaped particles with less smooth uneven and rougher surfaces morphology with large conchoidal cavities, which is consistent with what has previously been observed for hydrochar-derived activated carbons.[69, 83]

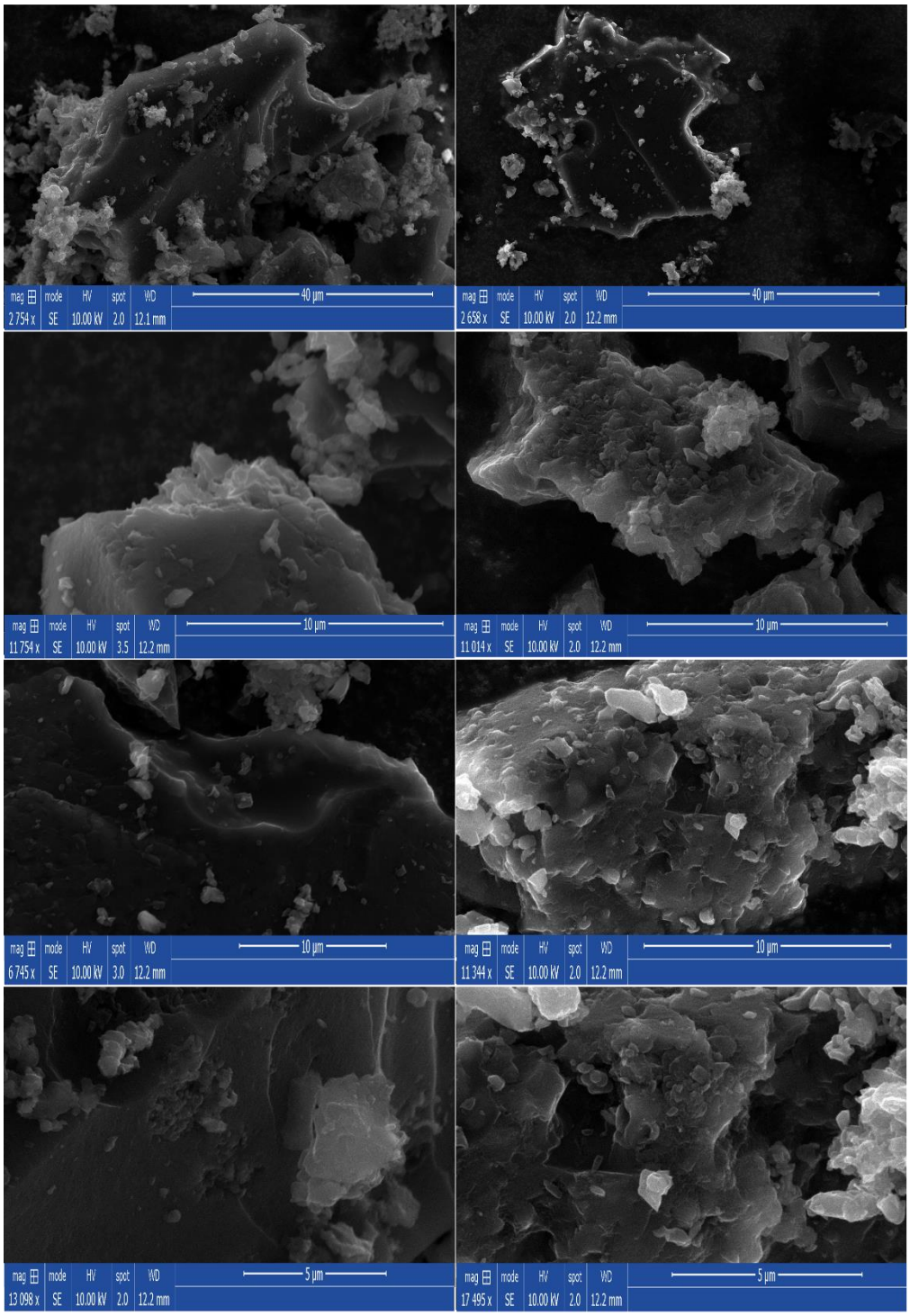


Figure 7.10: SEM micrographs images of PPY14800.

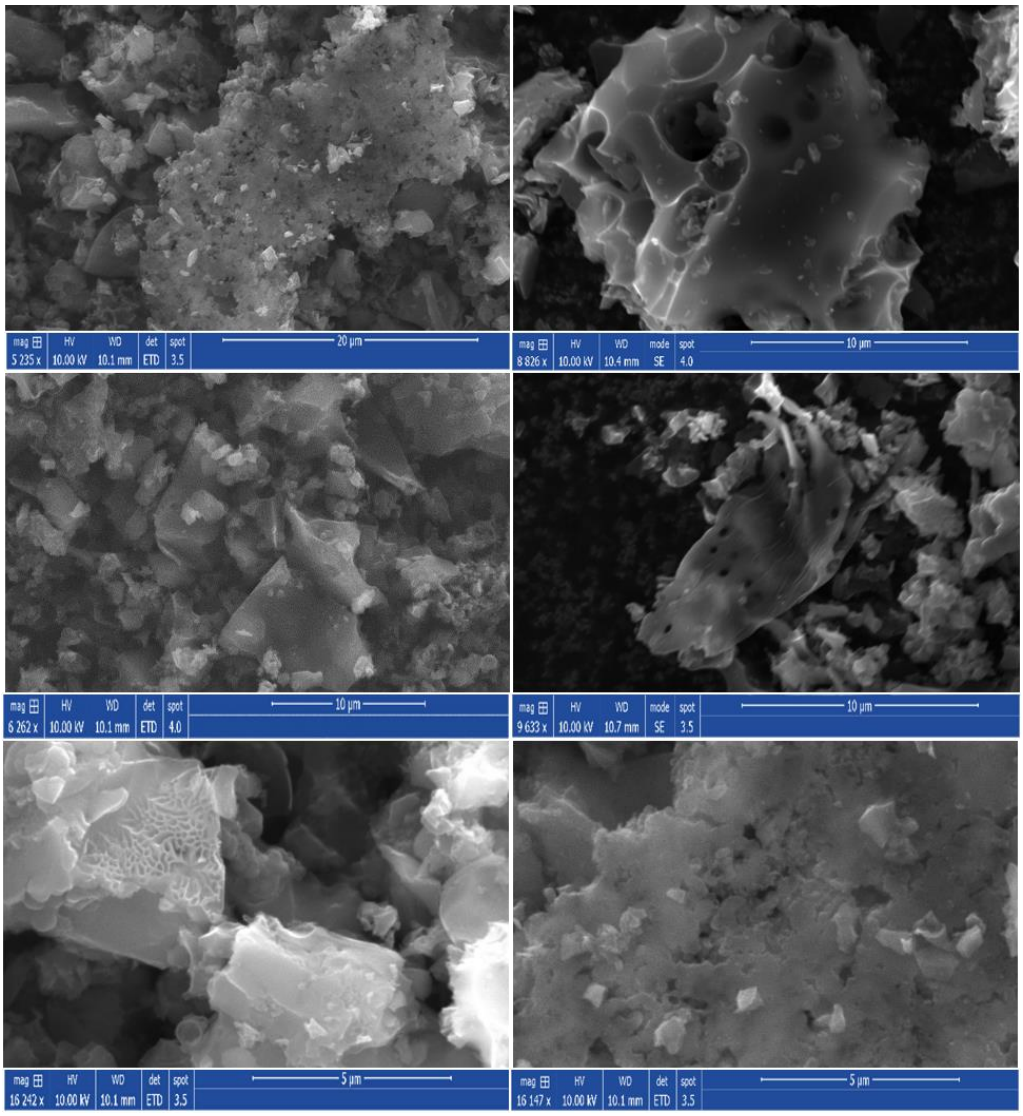


Figure 7.11: SEM micrographs images of PPYSD114800.

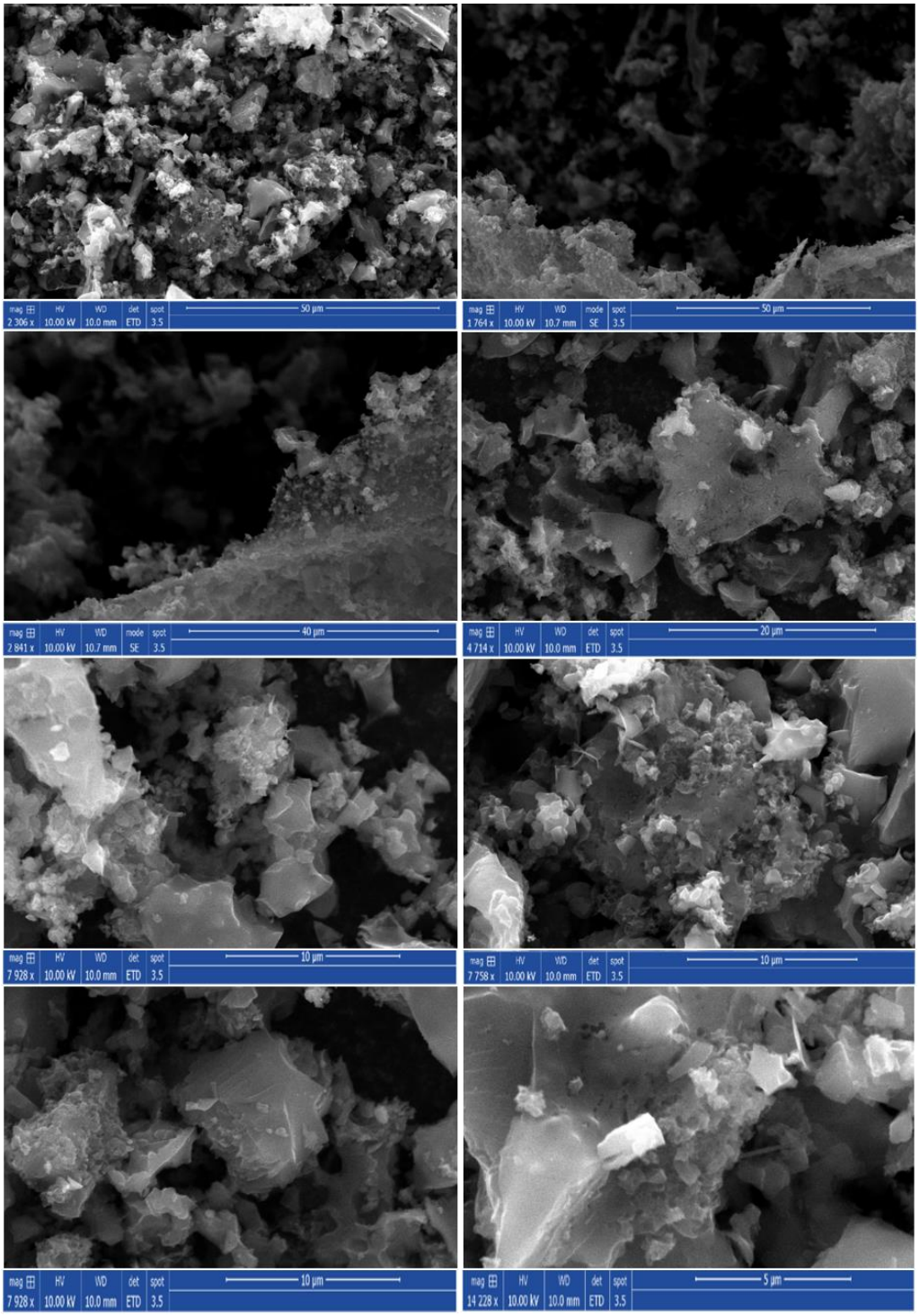


Figure 7.12: SEM micrographs images of PPYH114800.

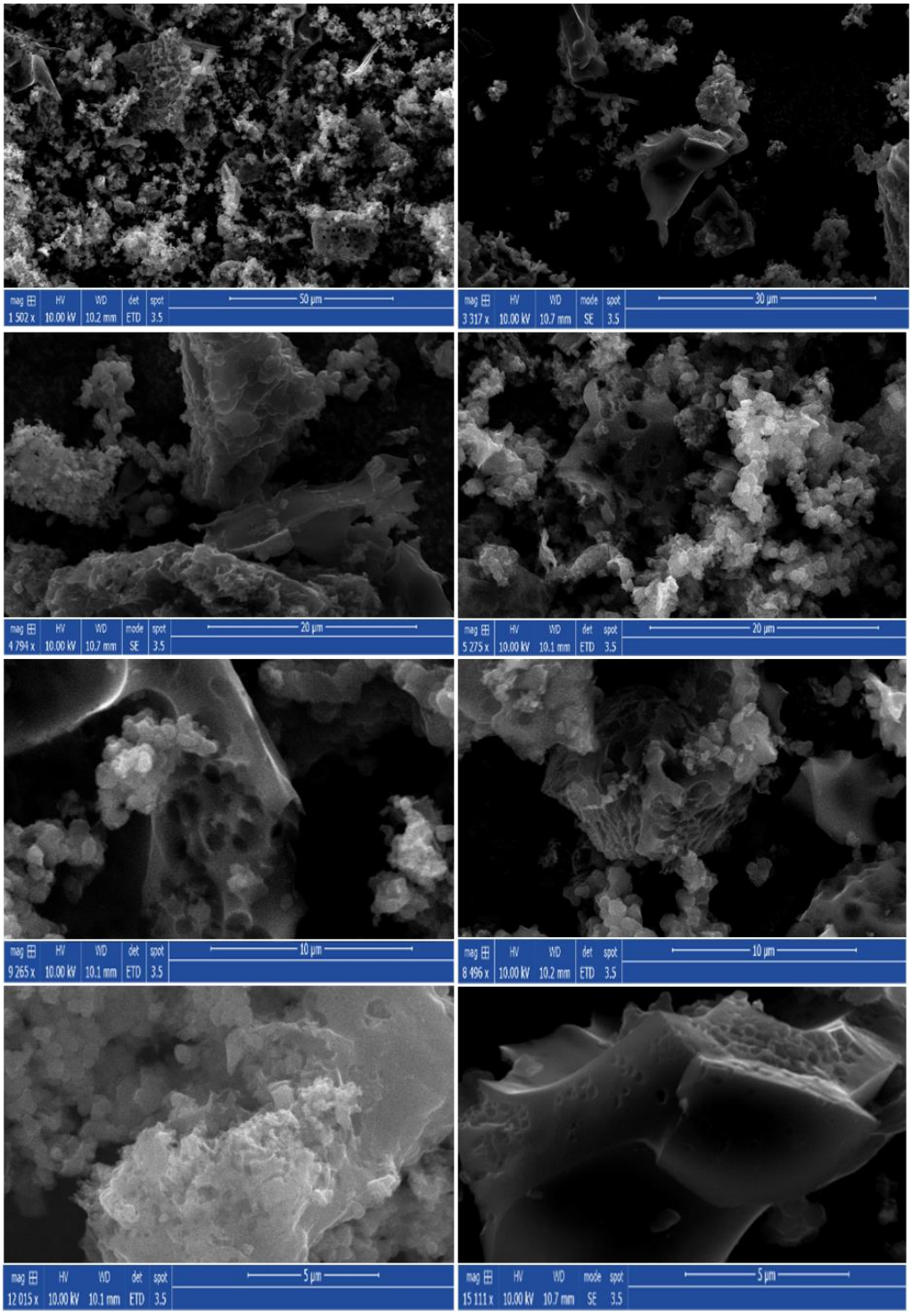


Figure 7.13: SEM micrographs images of PPYSD214800.

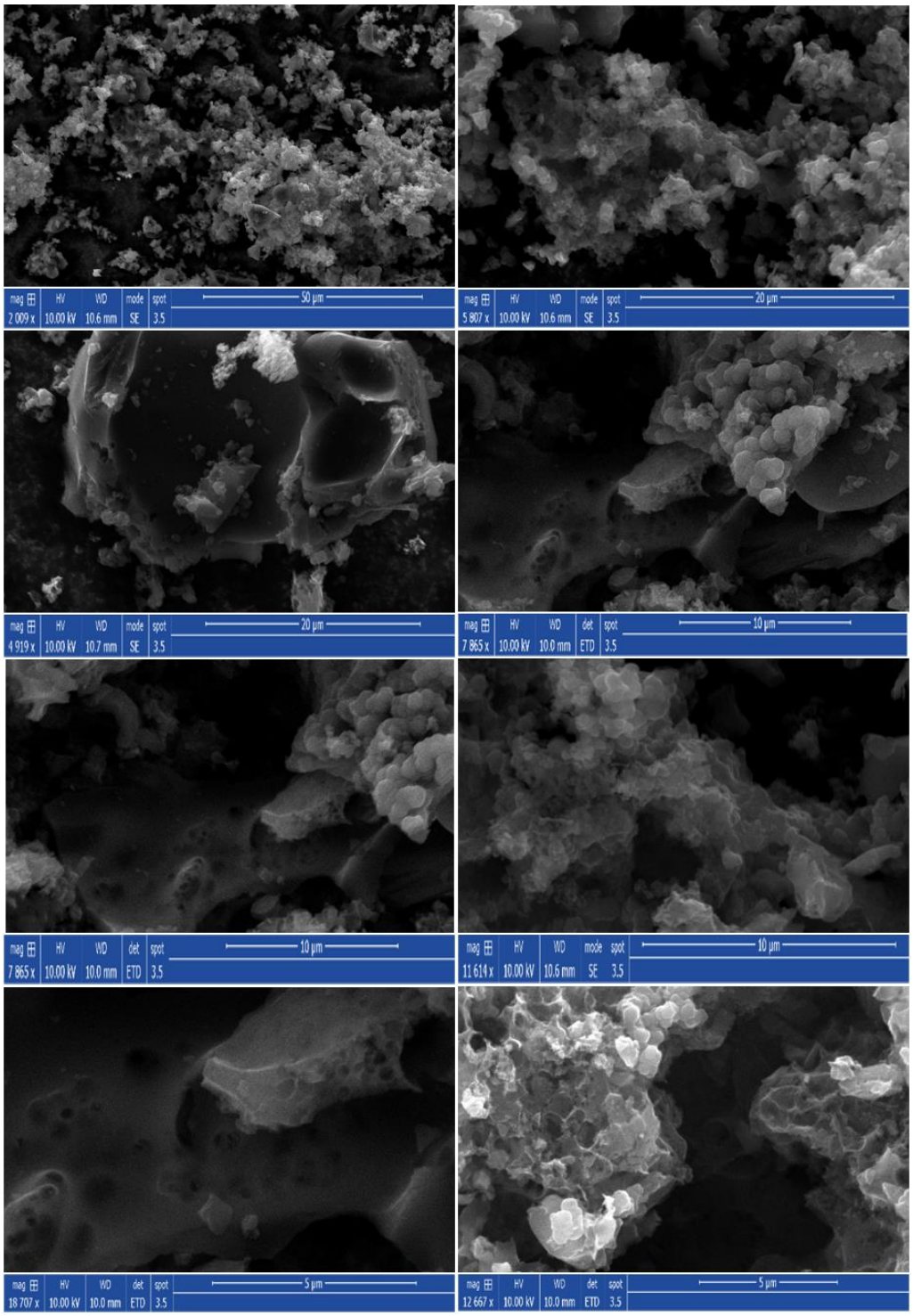


Figure 7.14: SEM micrographs images of PPYH214800.

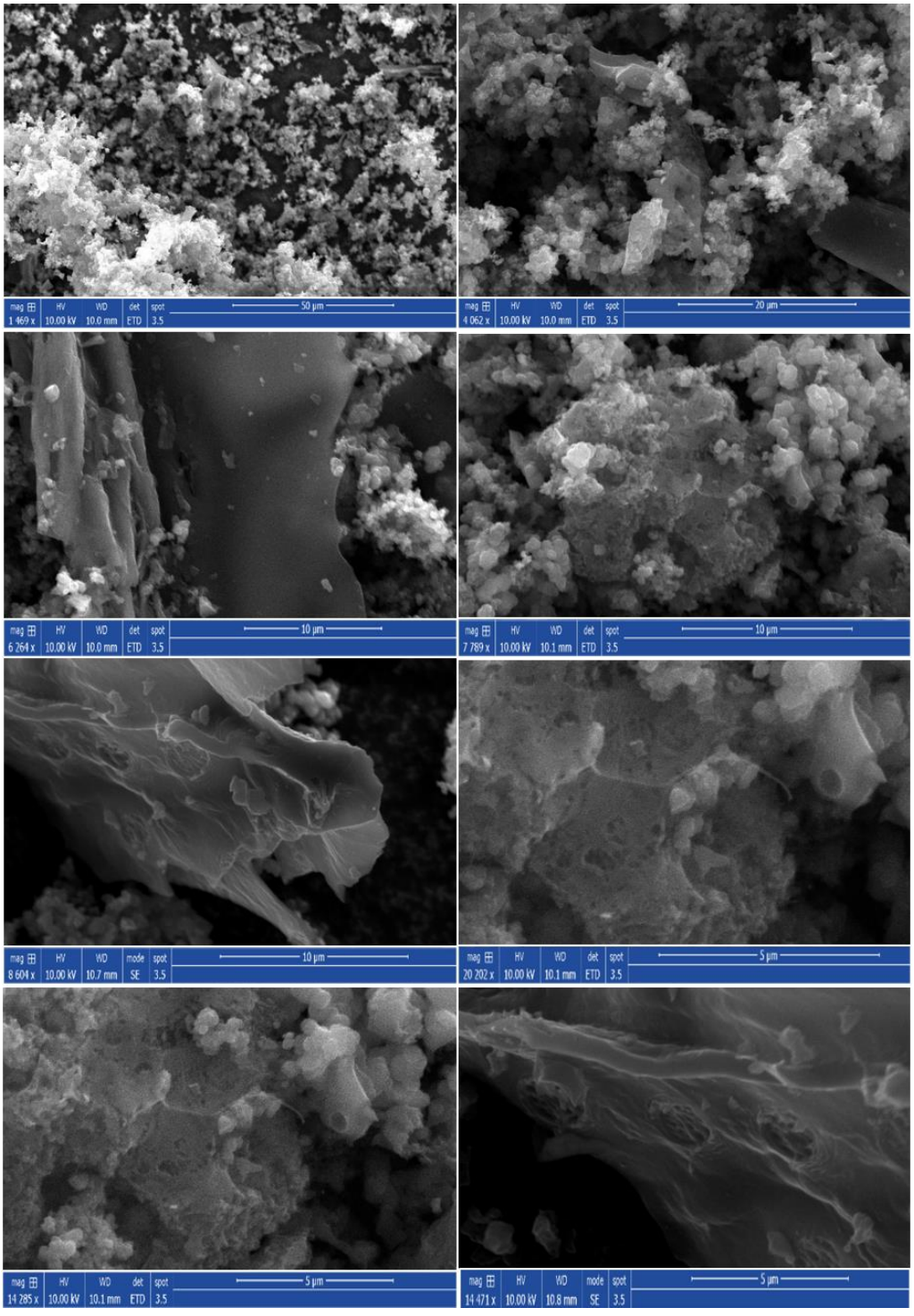


Figure 7.15: SEM micrographs images of PPYSD314800.

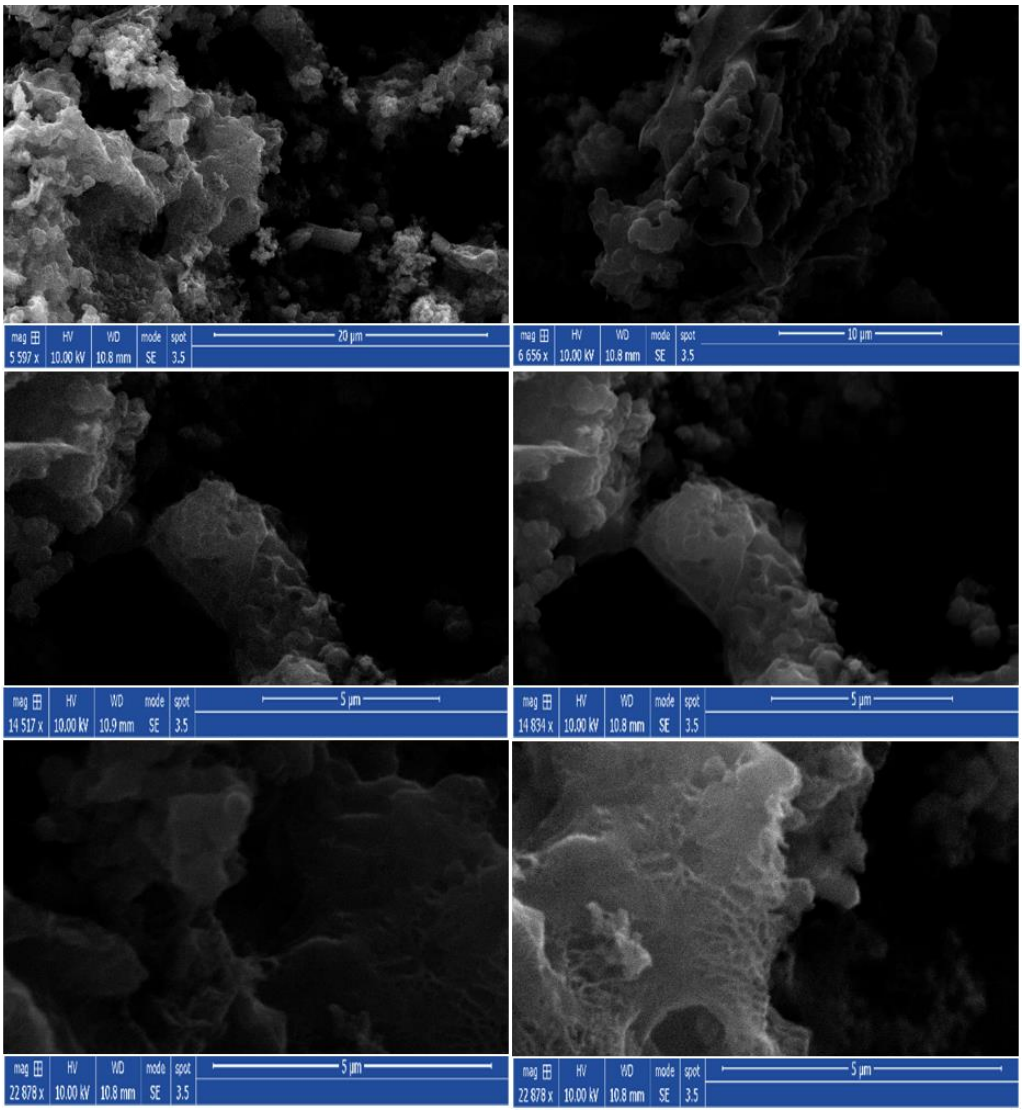


Figure 7.16: SEM micrographs images of PPYH314800

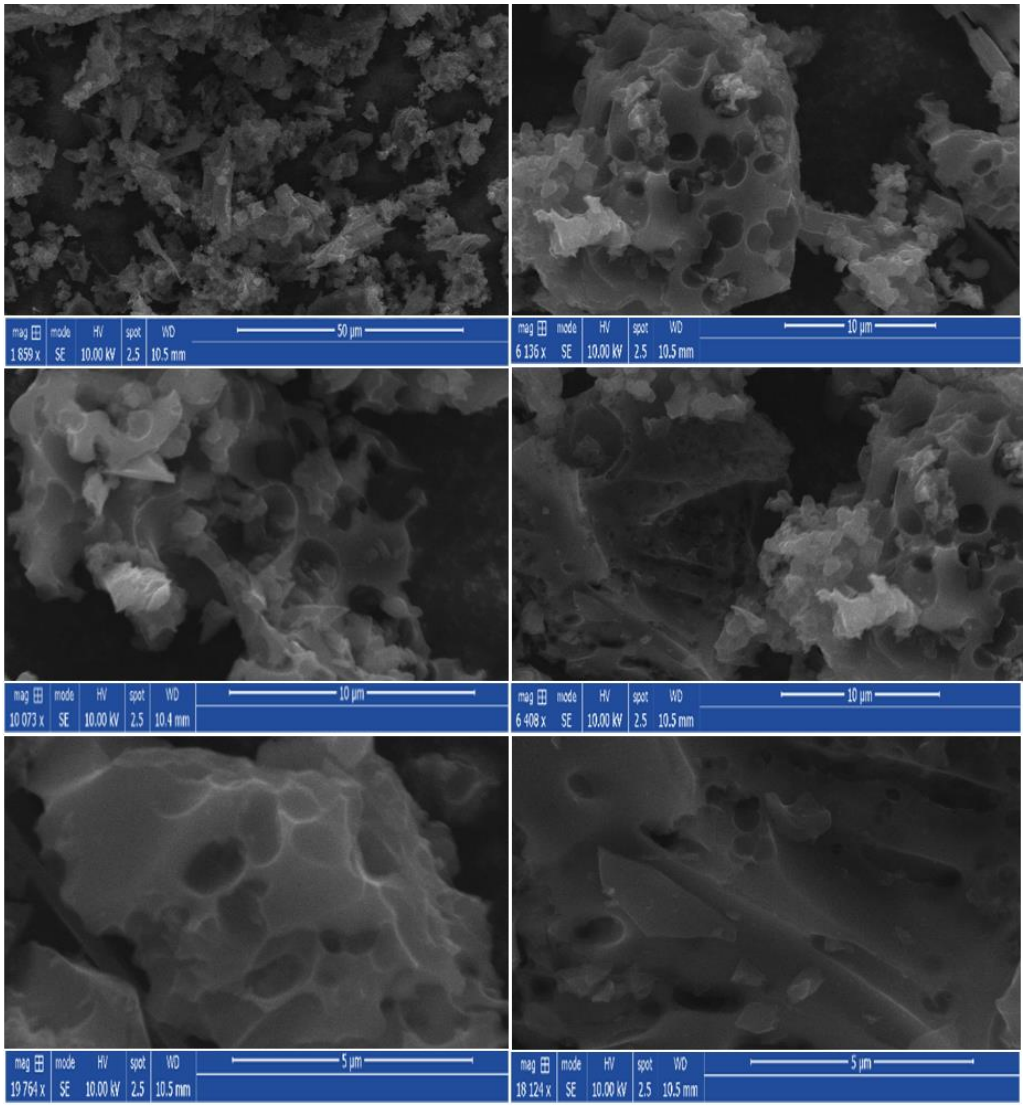


Figure 7.17: SEM micrographs images of PPYSD124800.

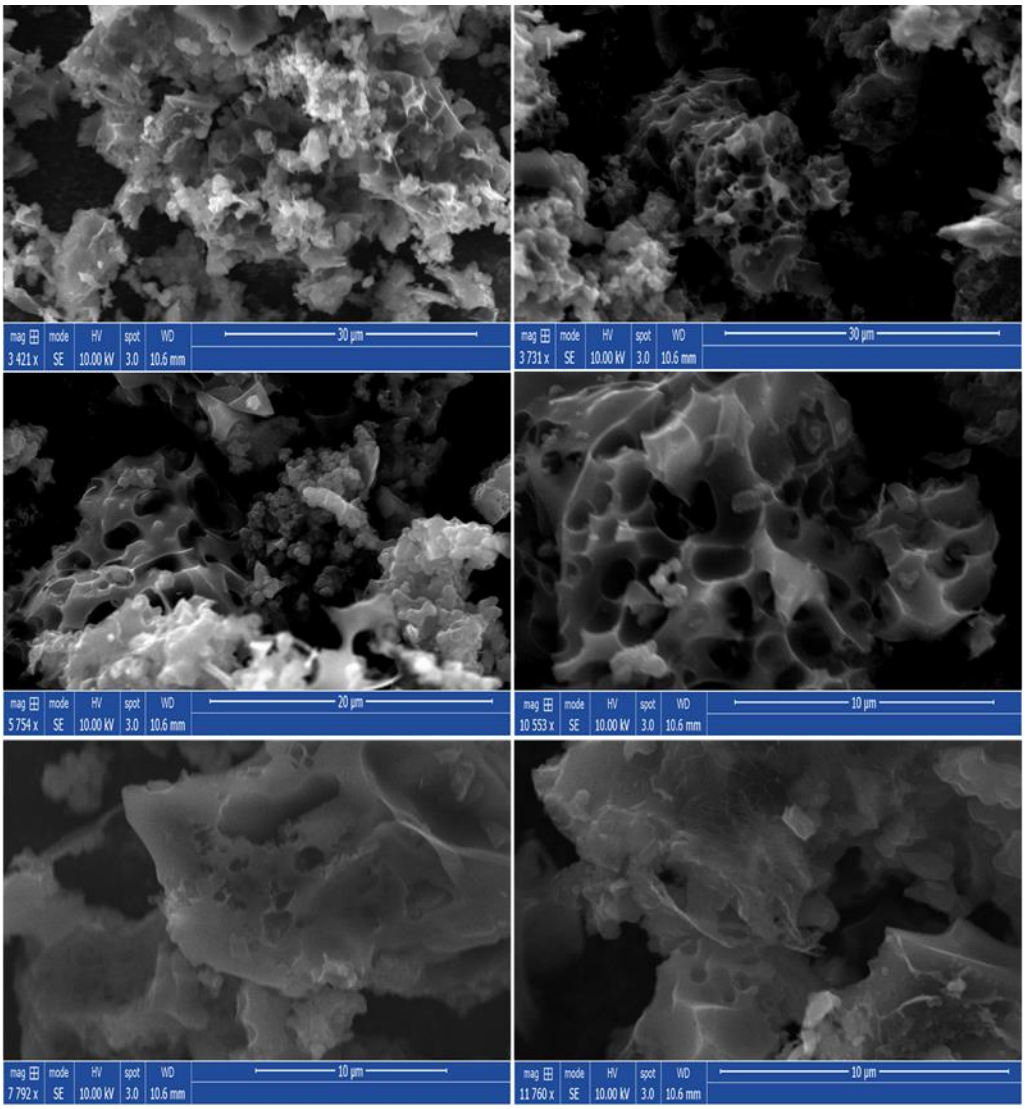


Figure 7.18: SEM micrographs images of PPYH124800.

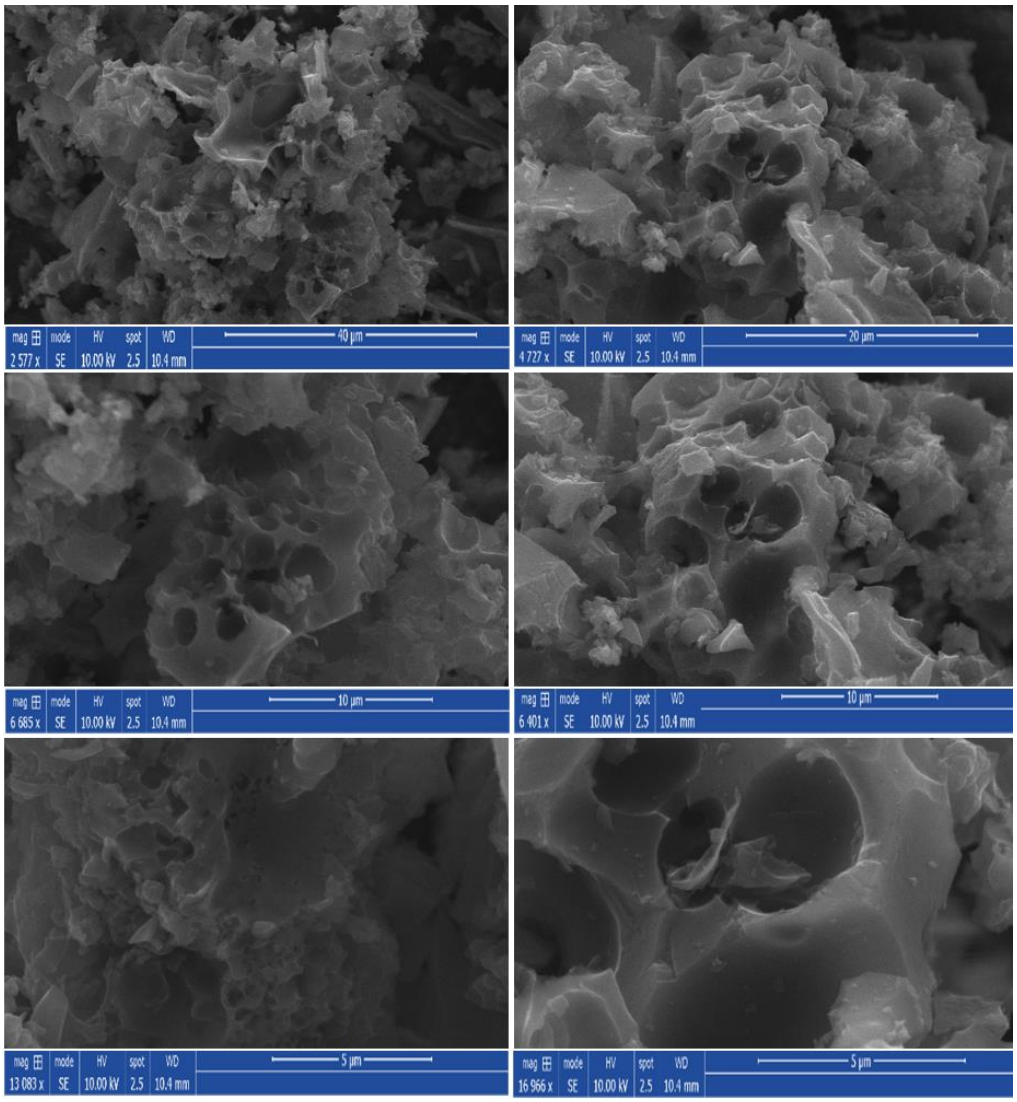


Figure 7.19: SEM micrographs images of PPYSD134800.

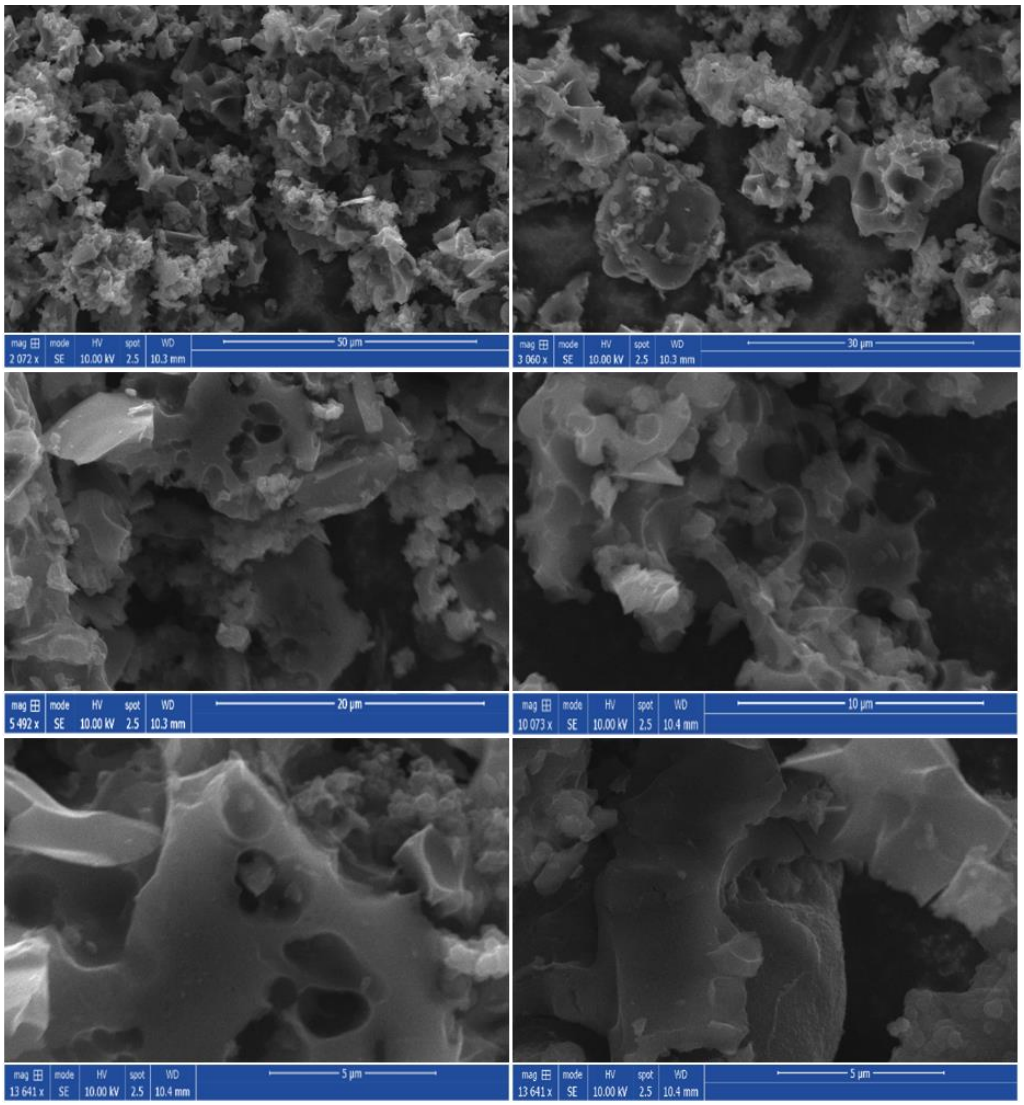


Figure 7.20: SEM micrographs images of PPYH134800.

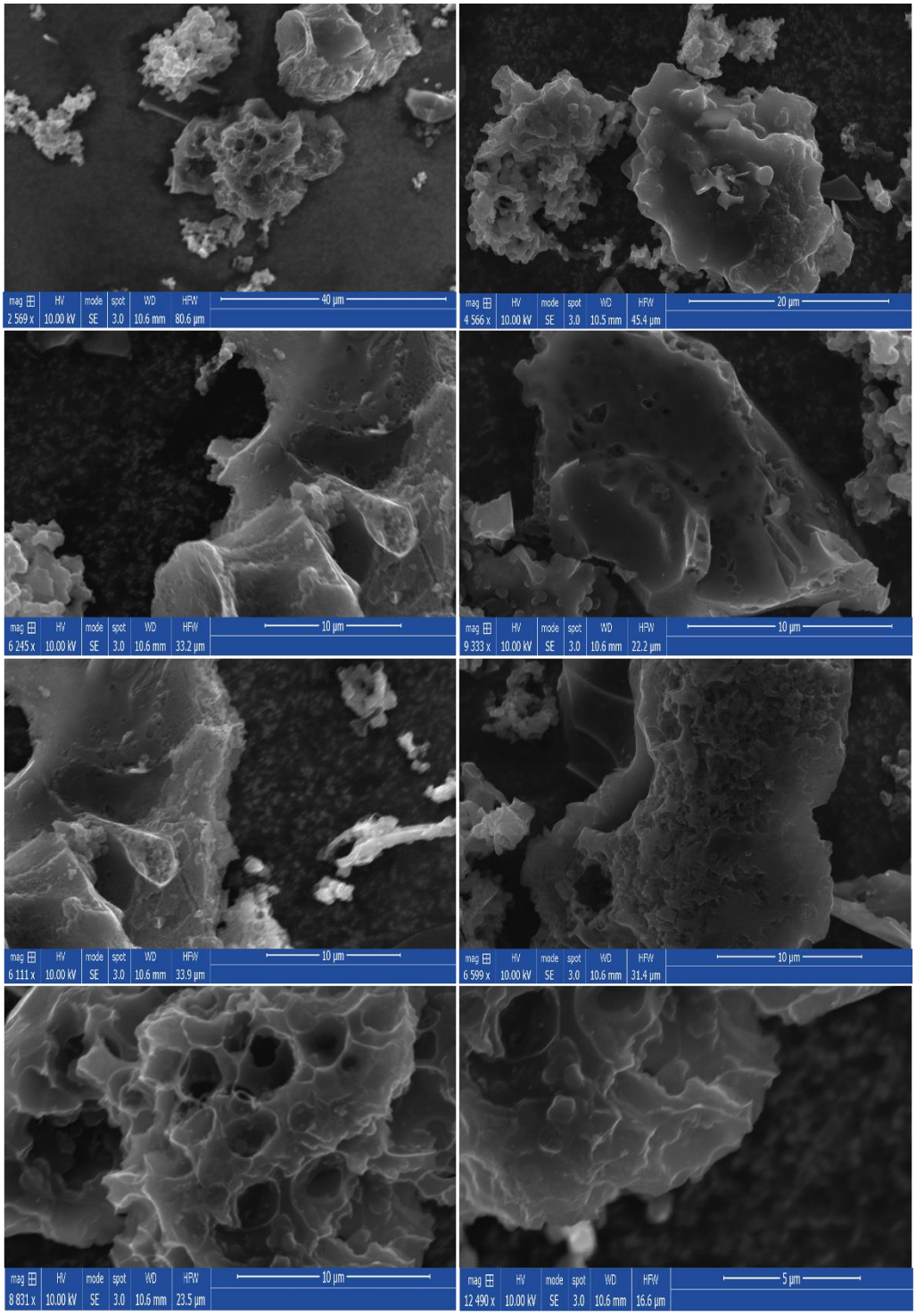


Figure 7.21: SEM micrographs images of PPYSD113900

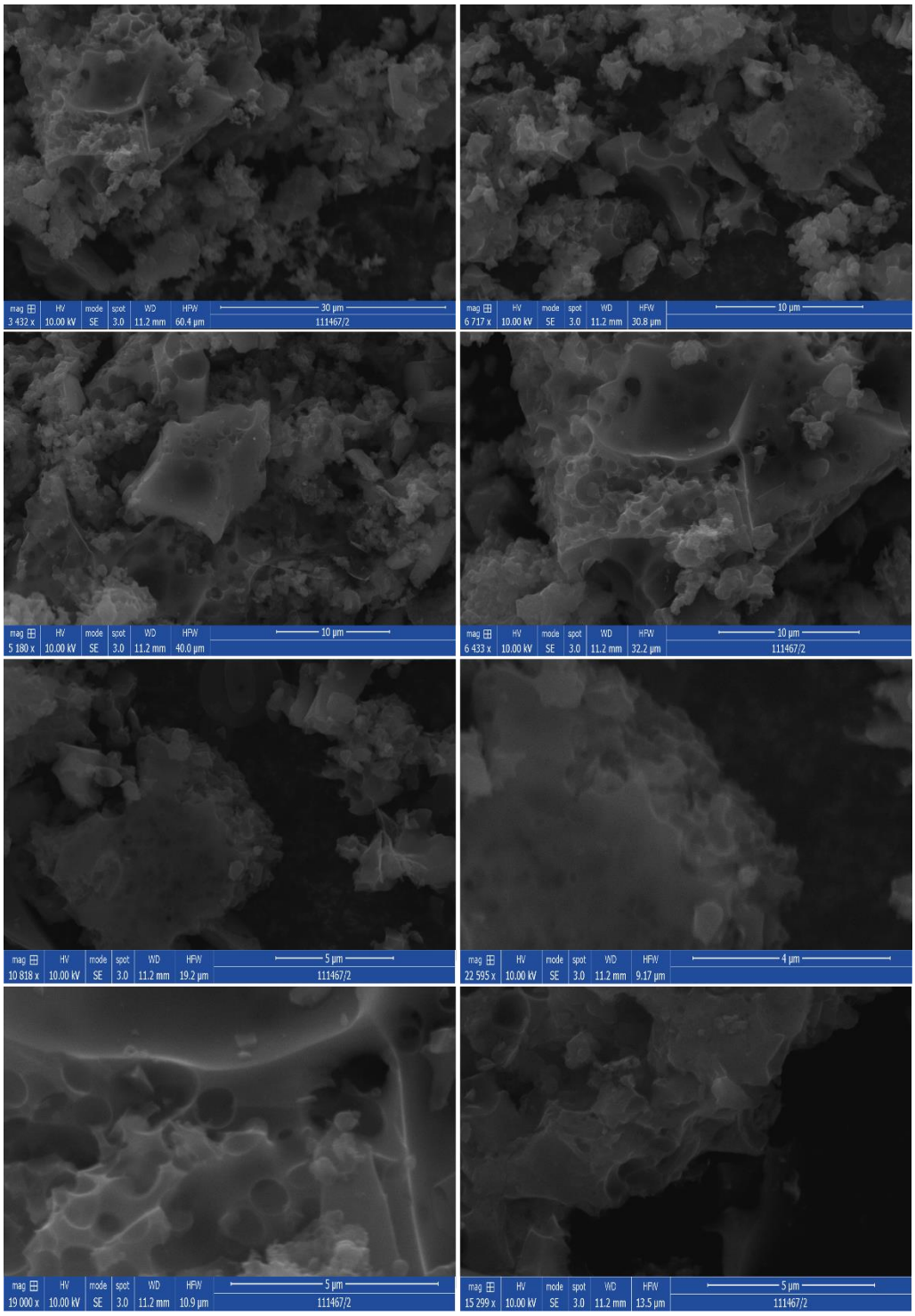


Figure 7.22: SEM micrographs images of PPYH113900.

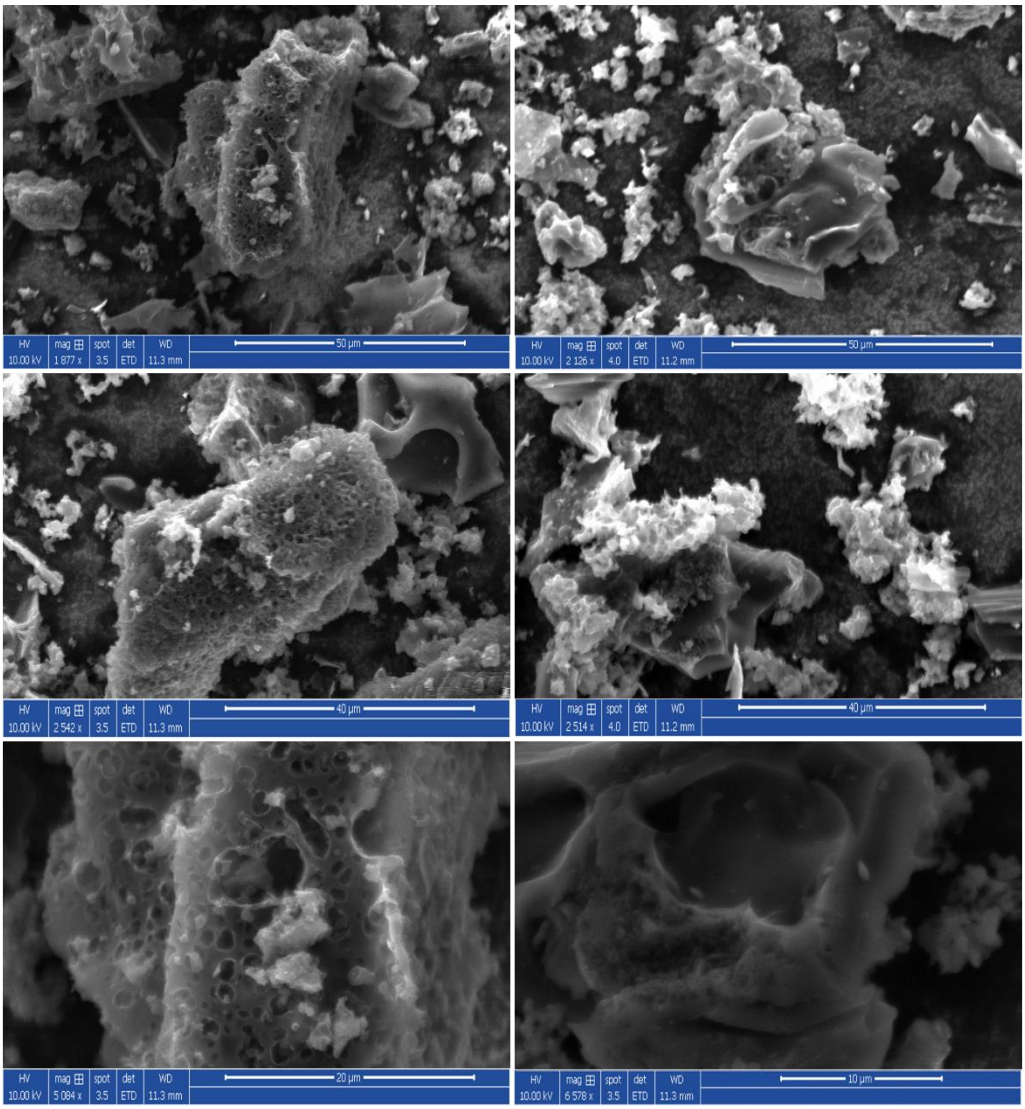


Figure 7.23: SEM micrographs images of PPYSD114900

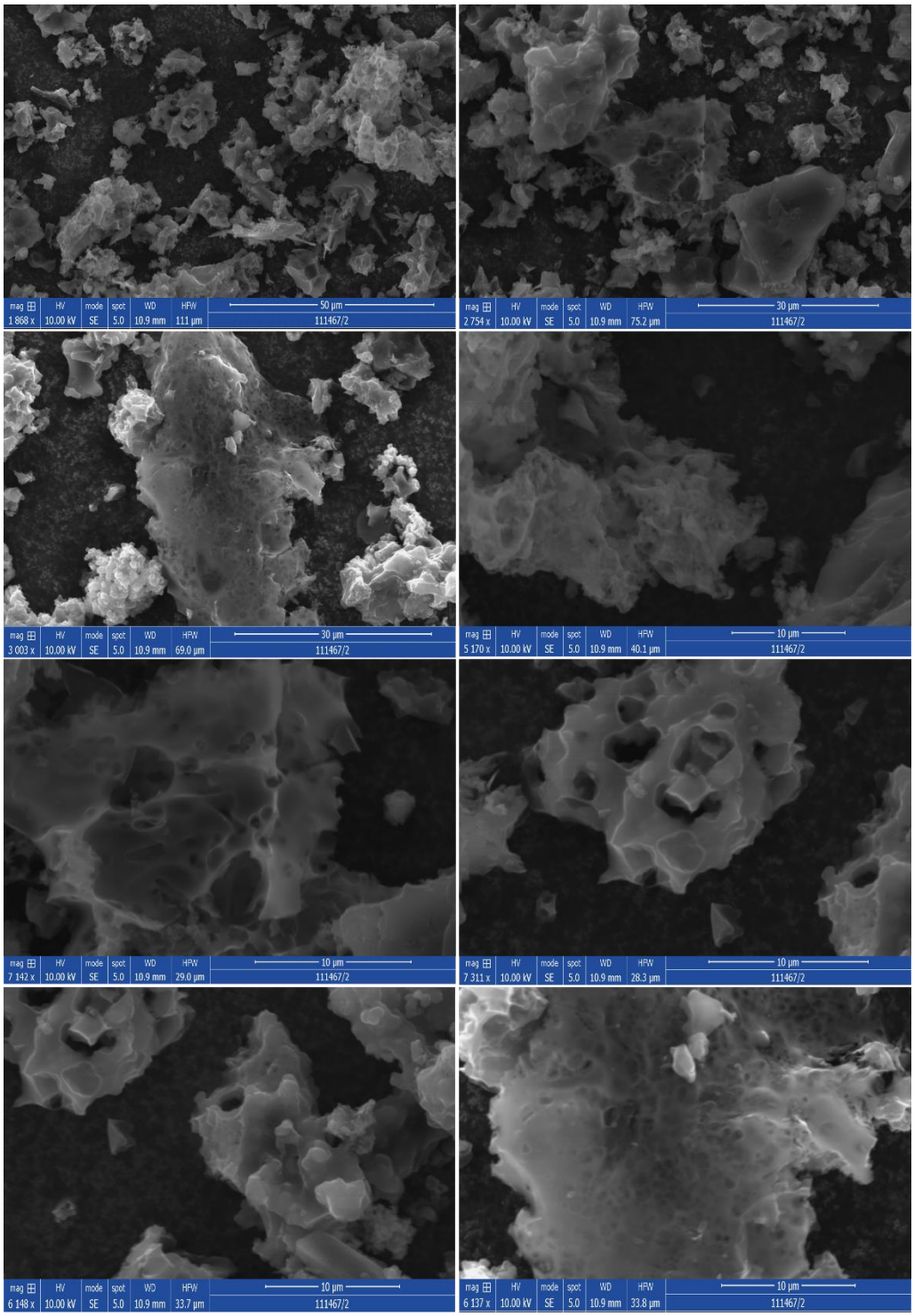


Figure 7.24: SEM micrographs images of PPYH114900

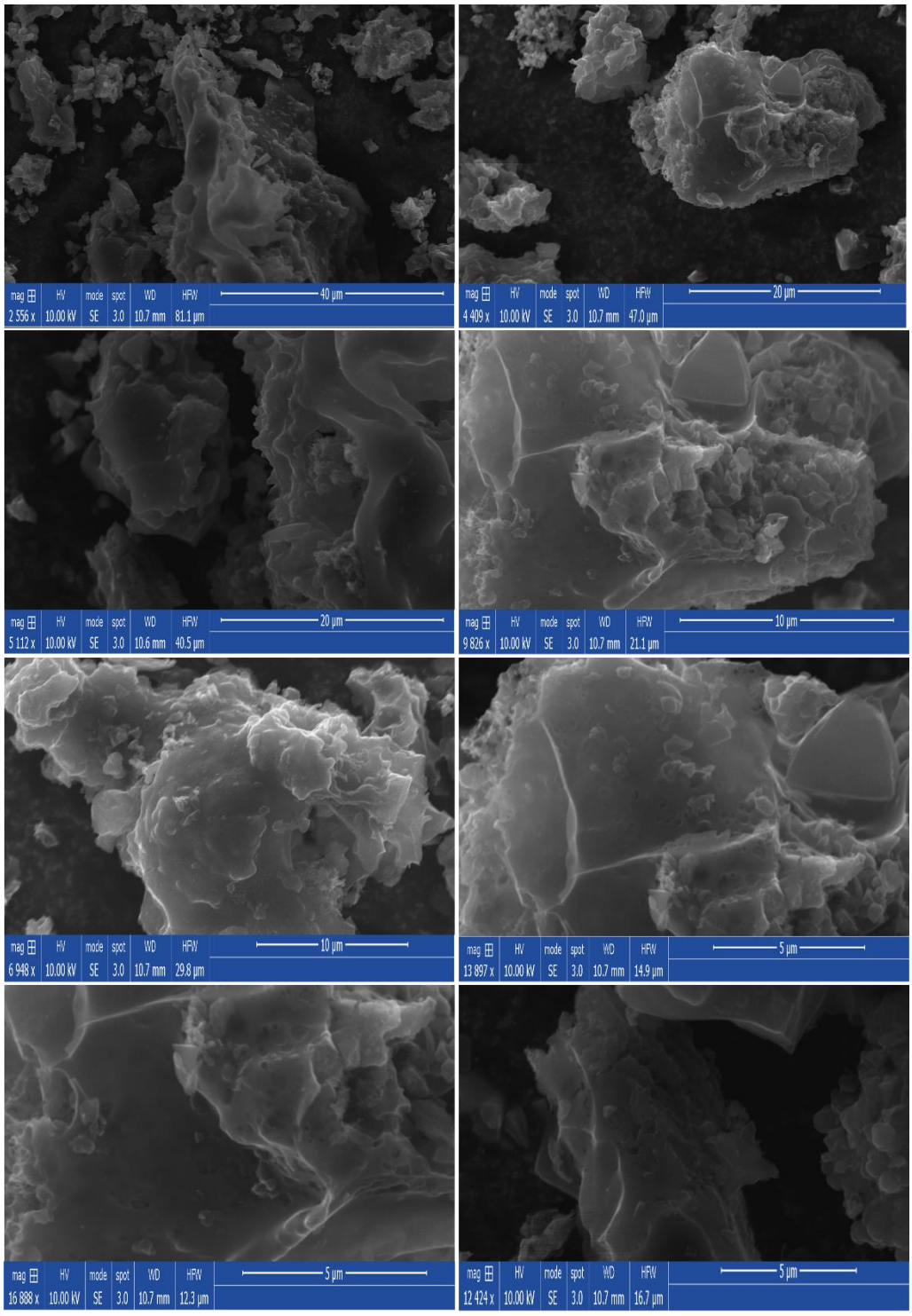


Figure 7.25: SEM micrographs images of PPYSD115800.

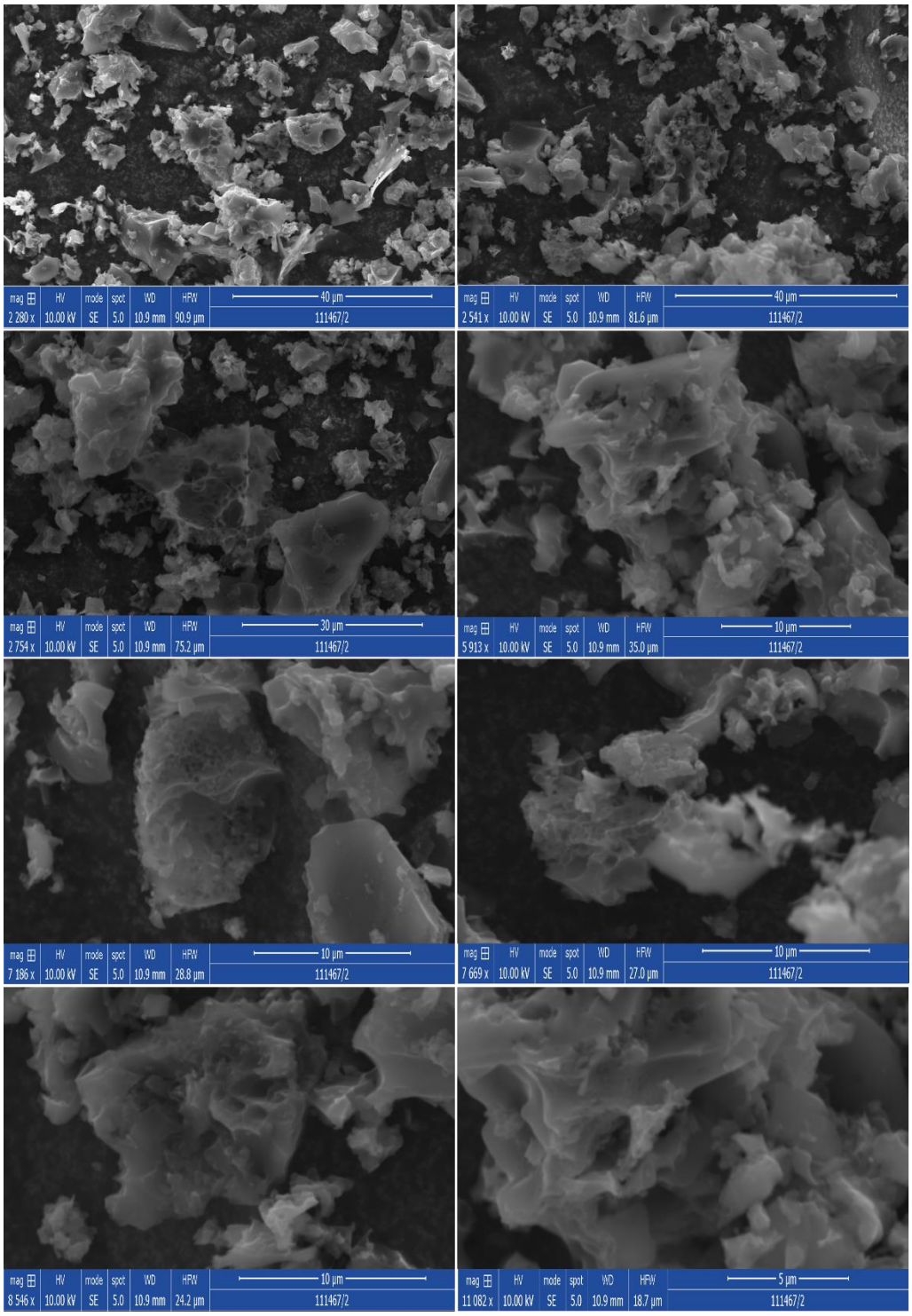


Figure 7.26: SEM micrographs images of PPYH115800.

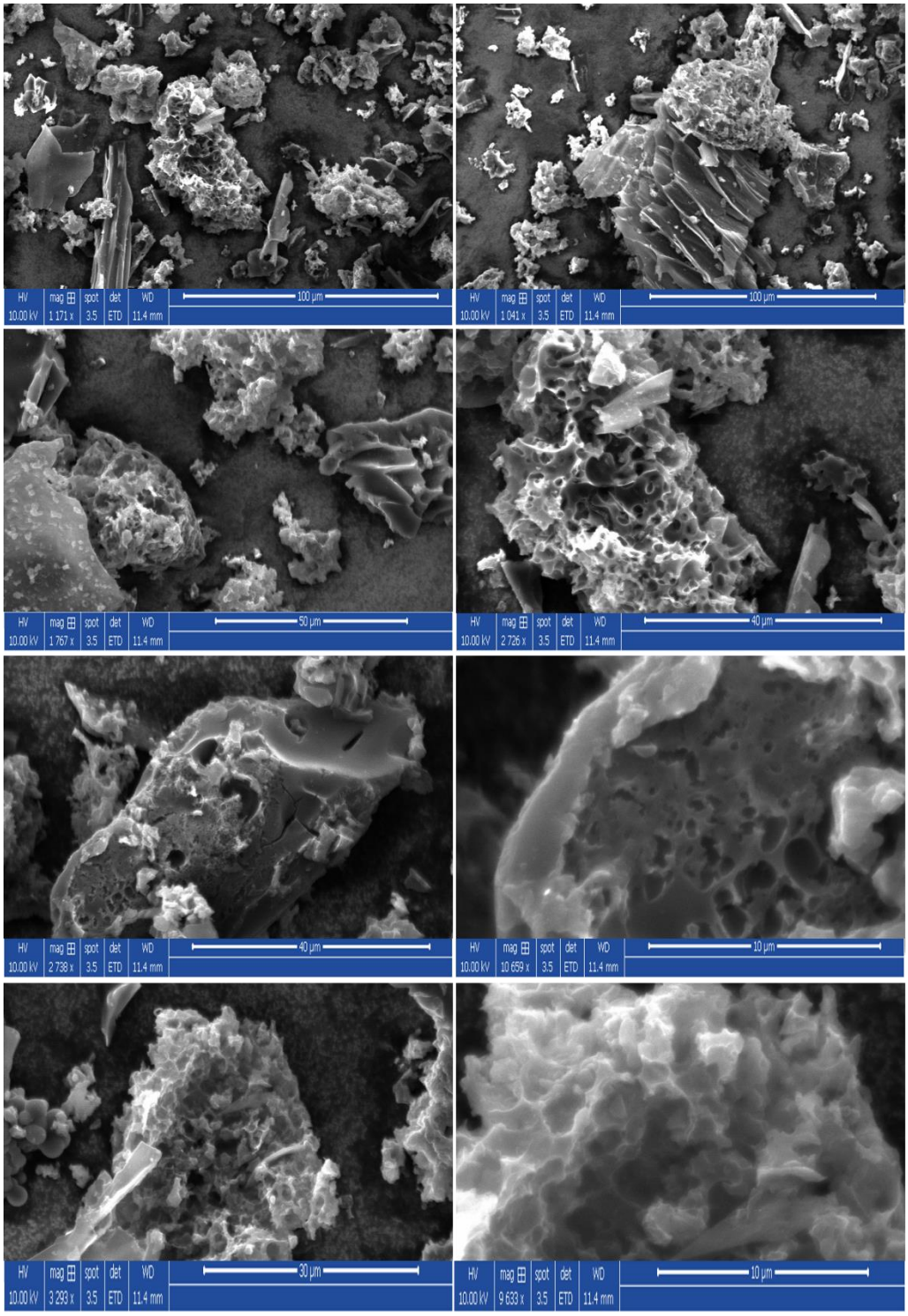


Figure 7.27: SEM micrographs images of PPSD115900.

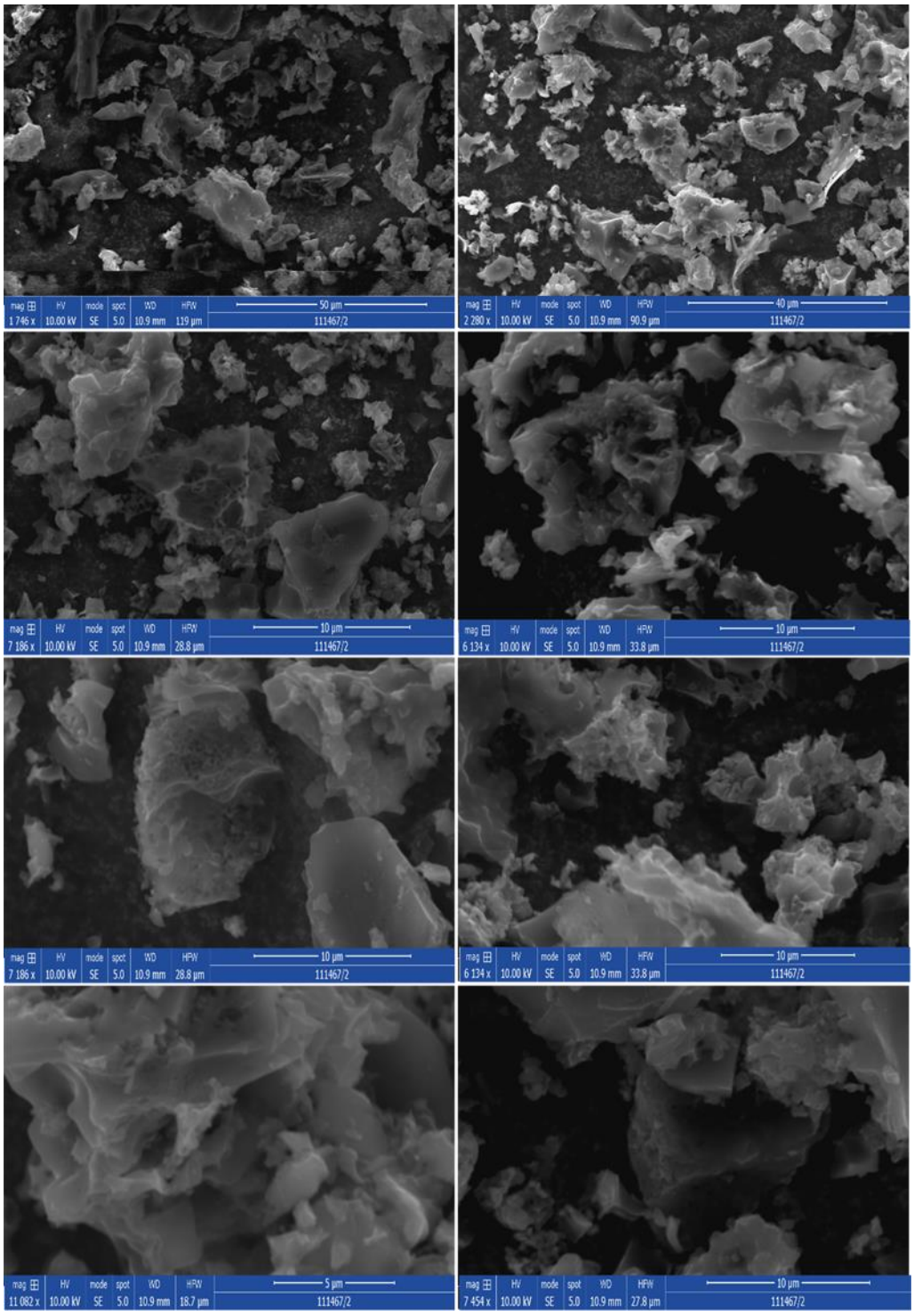


Figure 7.28: SEM micrographs images of PPYH115900.

7.6.2.5 Pore Channel Ordering

The pore channel ordering of both sets of carbons is shown in **Figure 7.29** to **Figure 7.47**.

PPY14800 (**Figure 7.29**) and both sets of carbons; PPY/SD activated carbons (**Figure 7.30, Figure 7.32, Figure 7.34, Figure 7.36, Figure 7.38, Figure 7.40, Figure 7.42, Figure 7.44, and Figure 7.46)** and PPY/SD activated carbons **(Figure 7.31, Figure 7.33, Figure 7.35, Figure 7.37, Figure 7.39, Figure 7.41, Figure 7.43, Figure 7.45**, and **Figure 7.47**) exhibit pore channel ordering that is typical of activated carbons, [46, 53, 67] of a highly disordered microstructure.[84-87] All the carbons exhibit wormhole type pores [37, 50] which is consistent with generation of porosity. The TEM micrographs images for both sets of activated carbons show no significant evidence of the presence of graphitic domains, which is consistent with the XRD patterns (**Figure 7.8** and **Figure 7.9**).

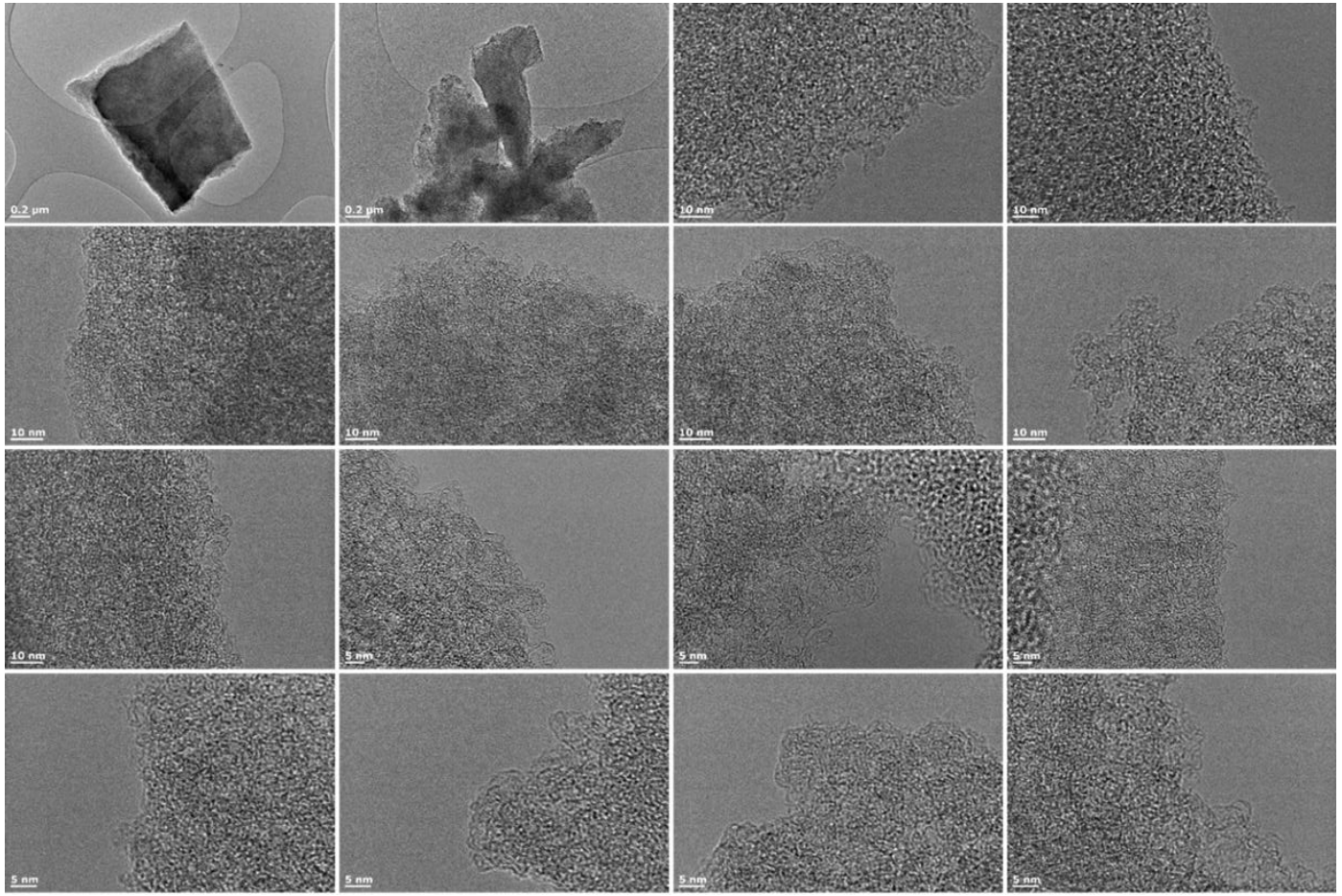


Figure 7.29: TEM micrographs images of PPY14800.

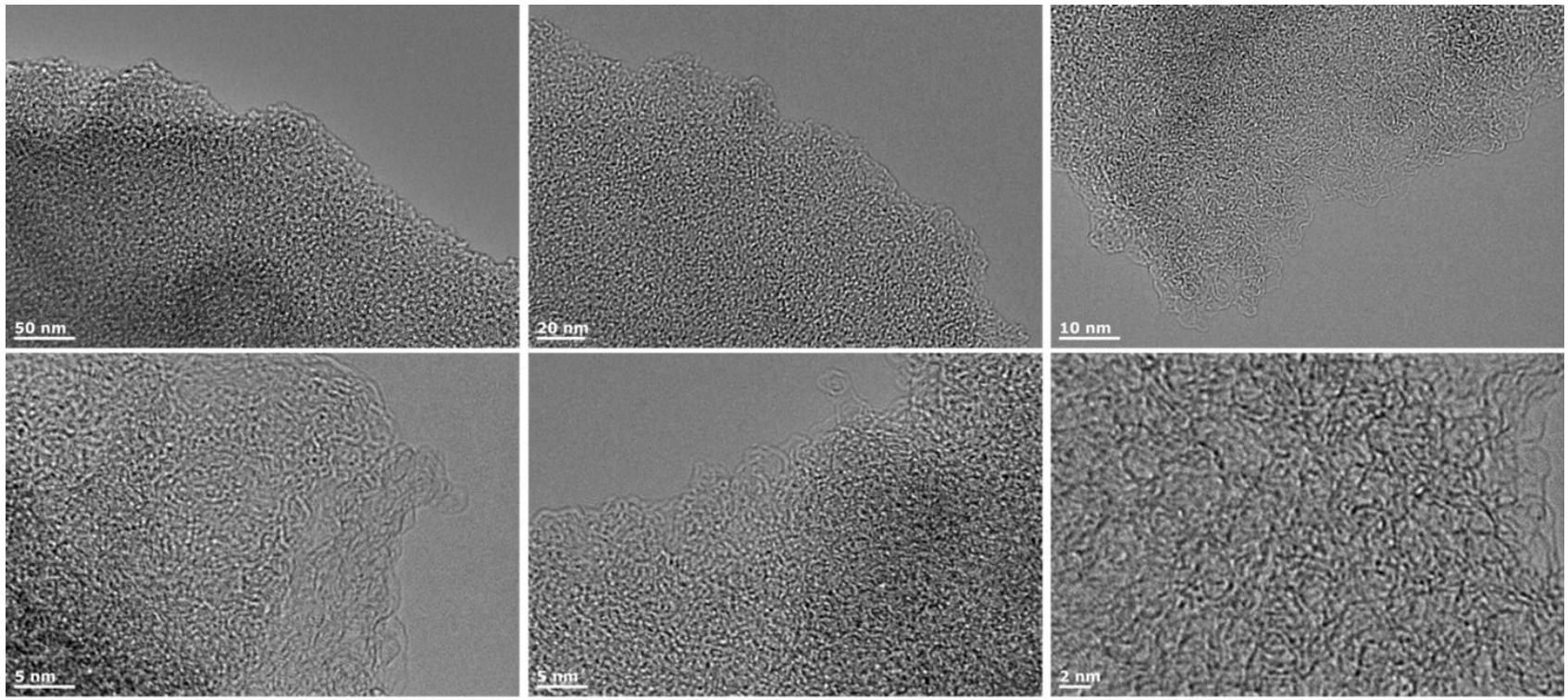


Figure 7.30: TEM micrographs images of PPYSD114800.

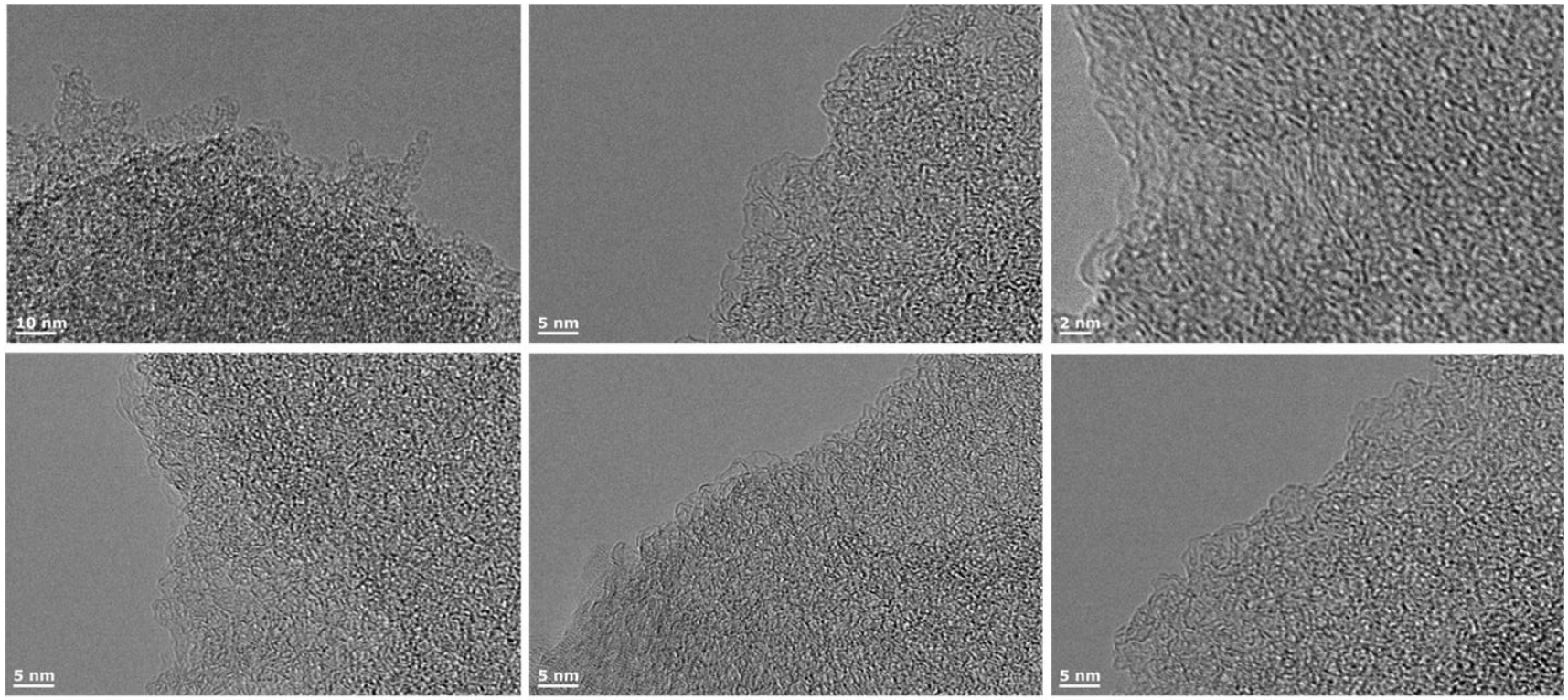


Figure 7.31: TEM micrographs images of PPYH114800.

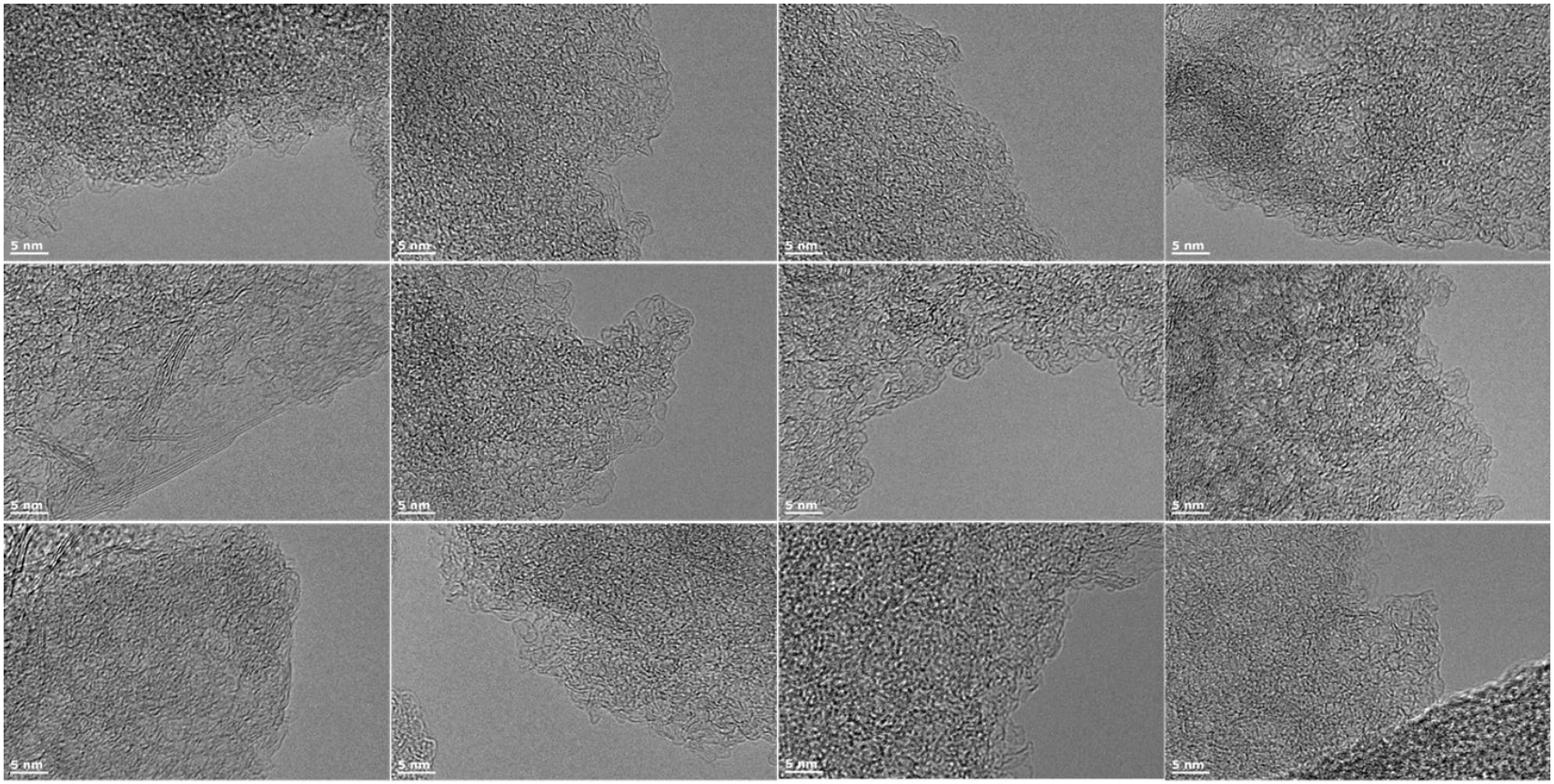


Figure 7.32: TEM micrographs images of PPYSD115800.

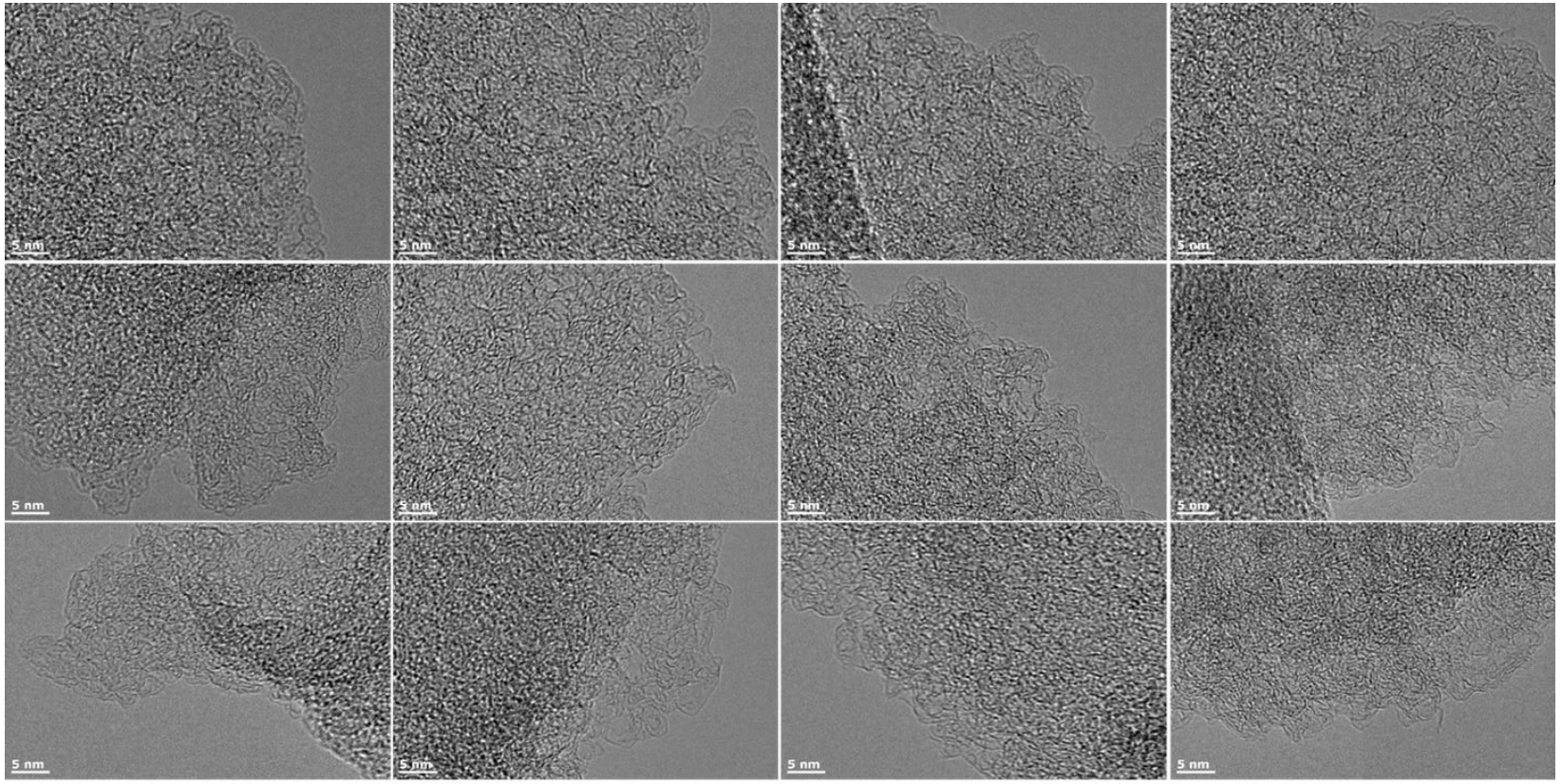


Figure 7.33: TEM micrographs images of PPYH115800.

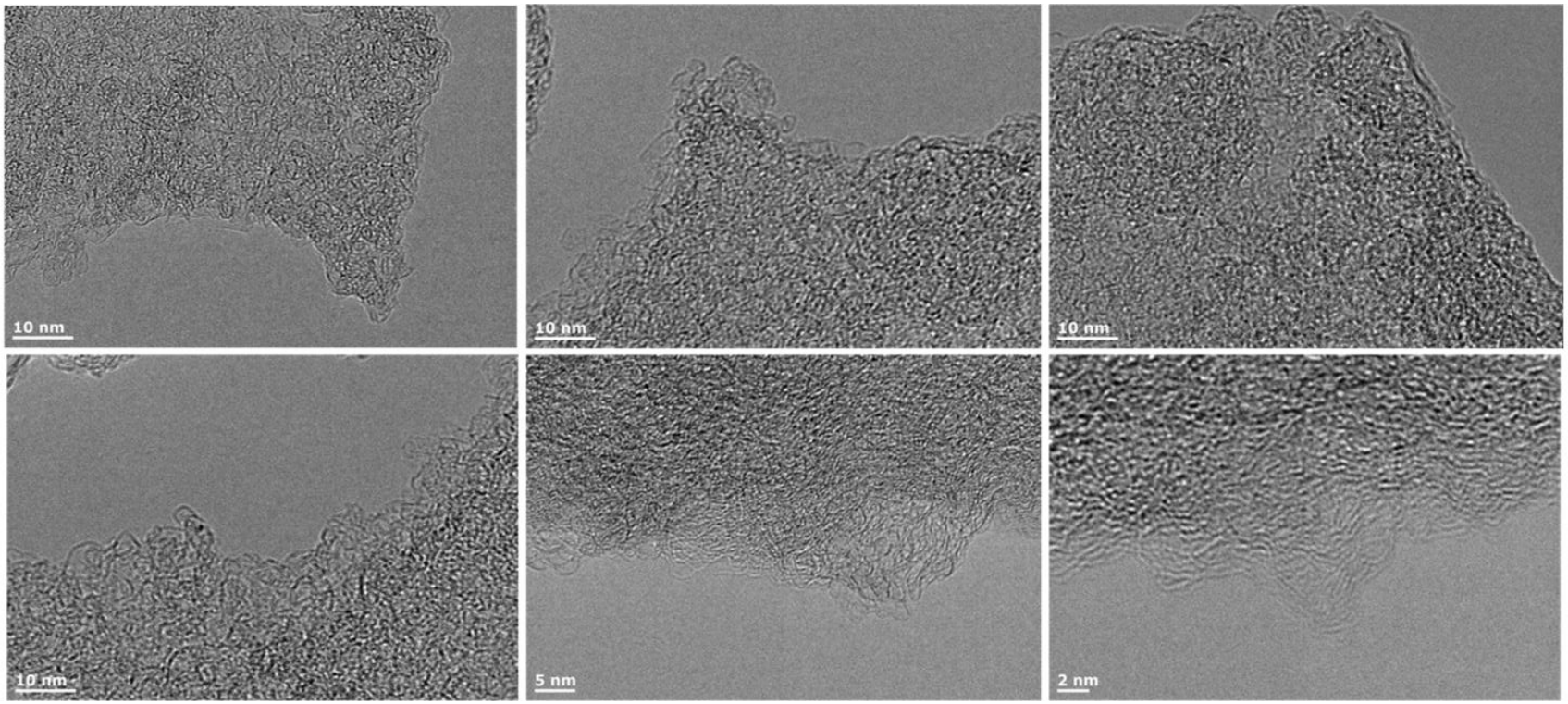


Figure 7.34: TEM micrographs images of PPYSD214800.

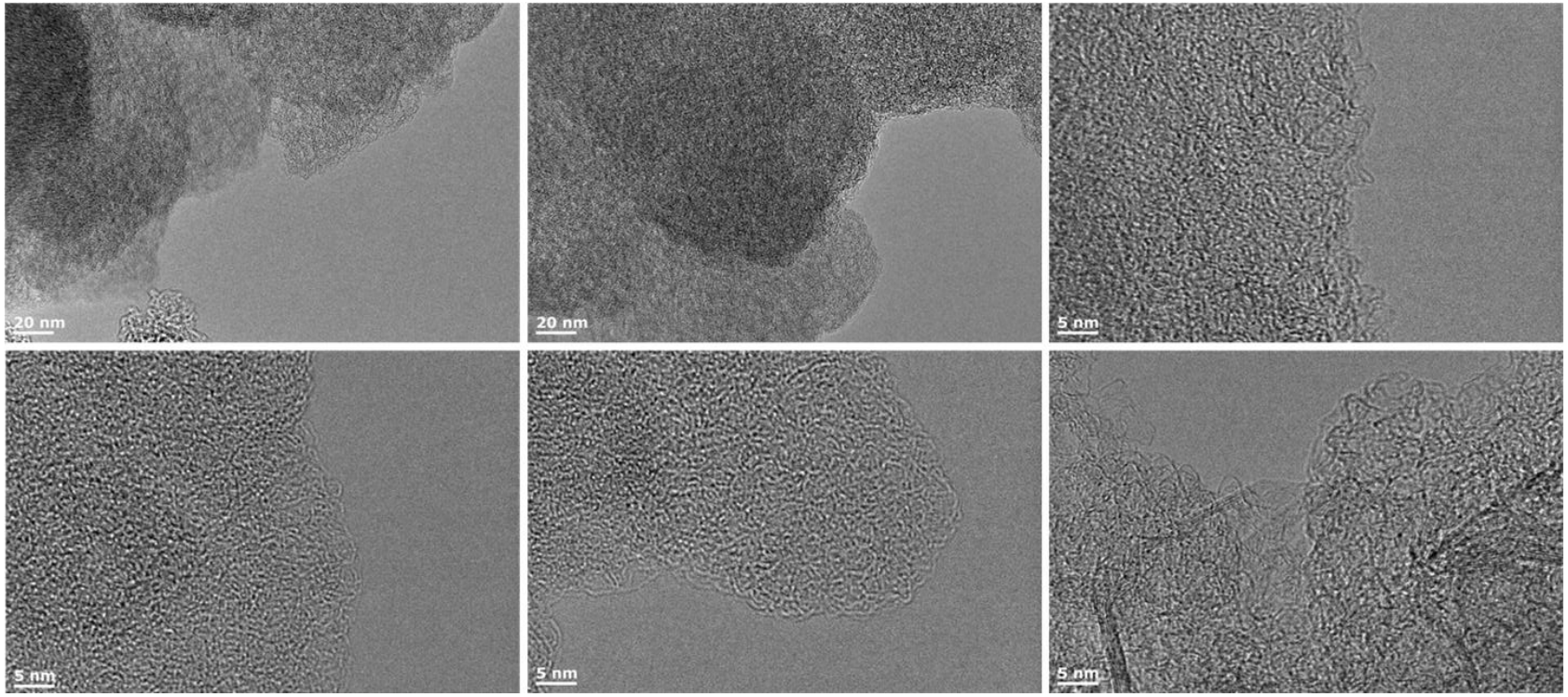


Figure 7.35: TEM micrographs images of PPYH214800.

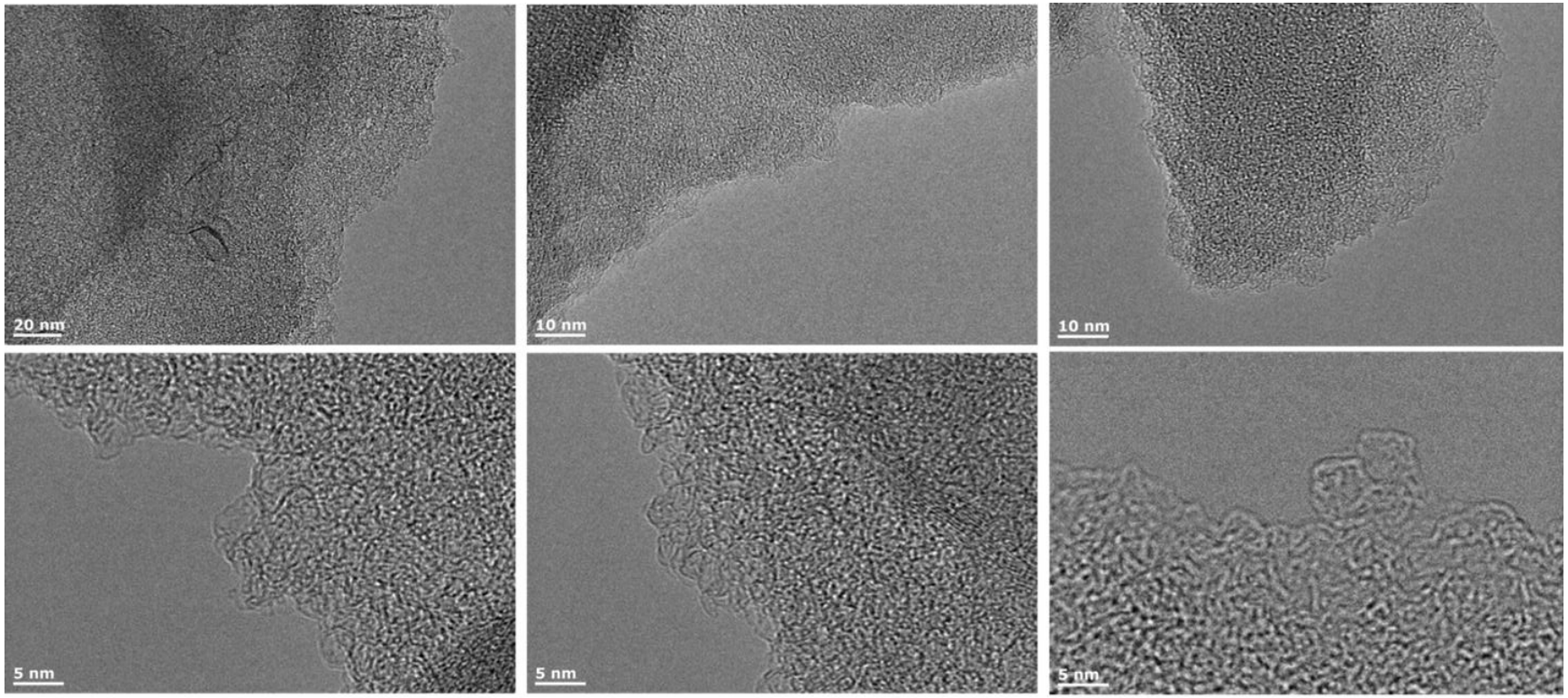


Figure 7.36: TEM micrographs images of PPYSD314800.

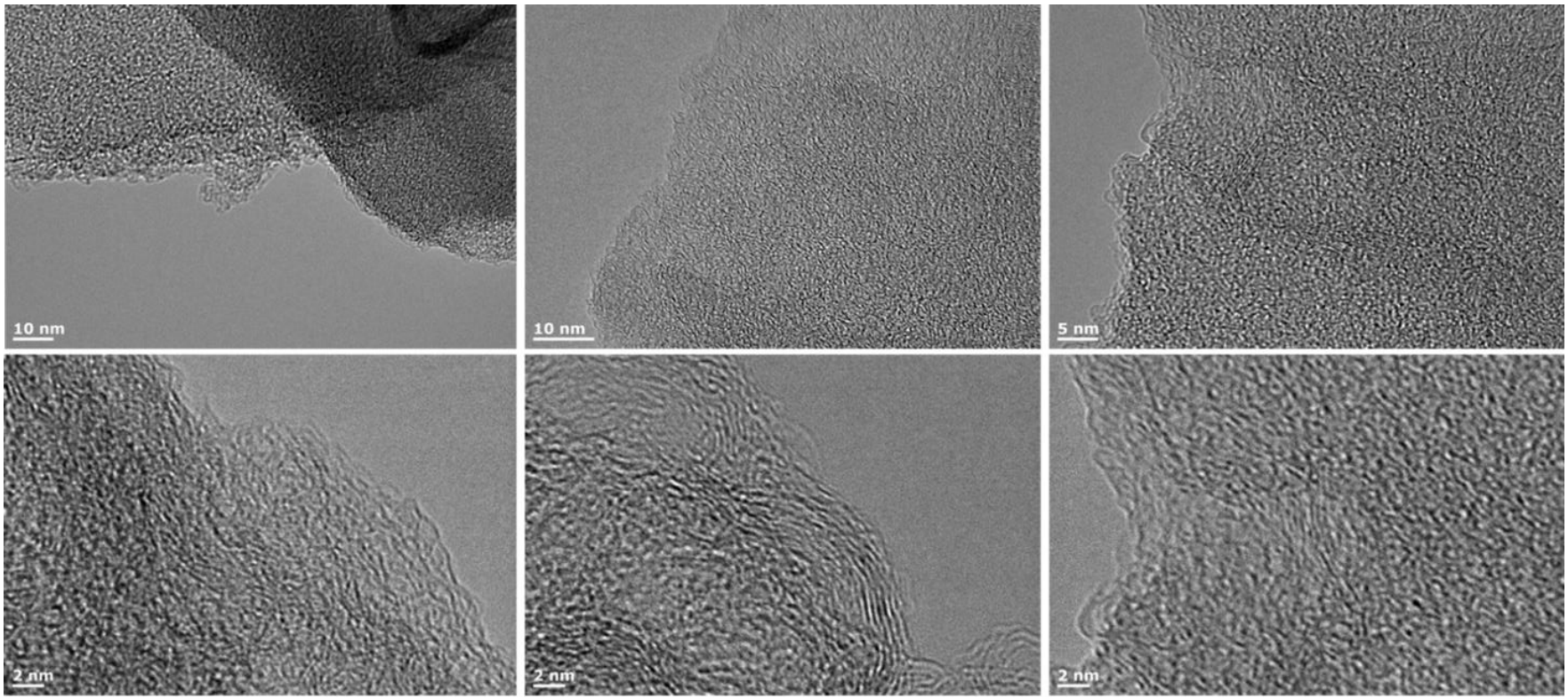


Figure 7.37: TEM micrographs images of PPYH314800.

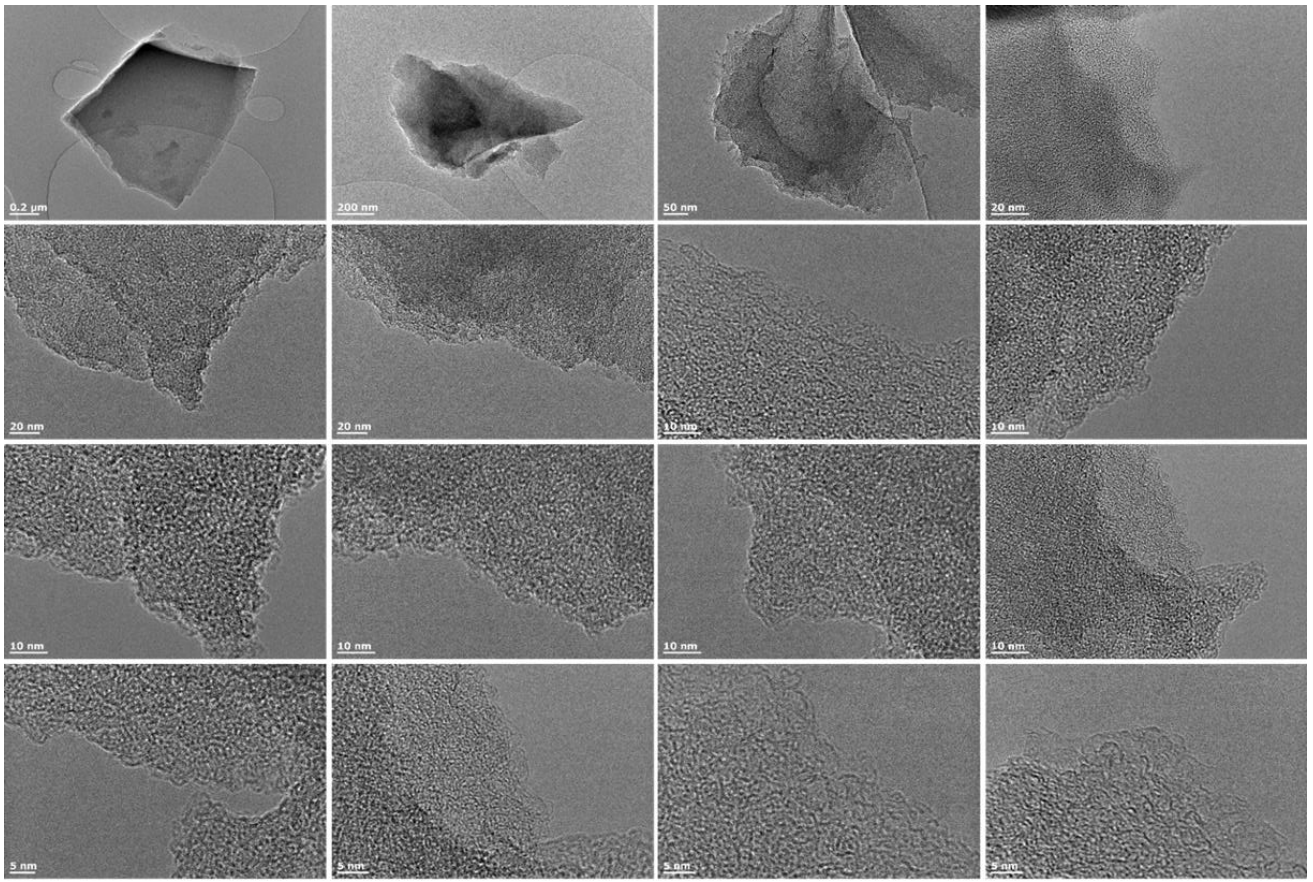


Figure 7.38: TEM micrographs images of PPYSD124800.

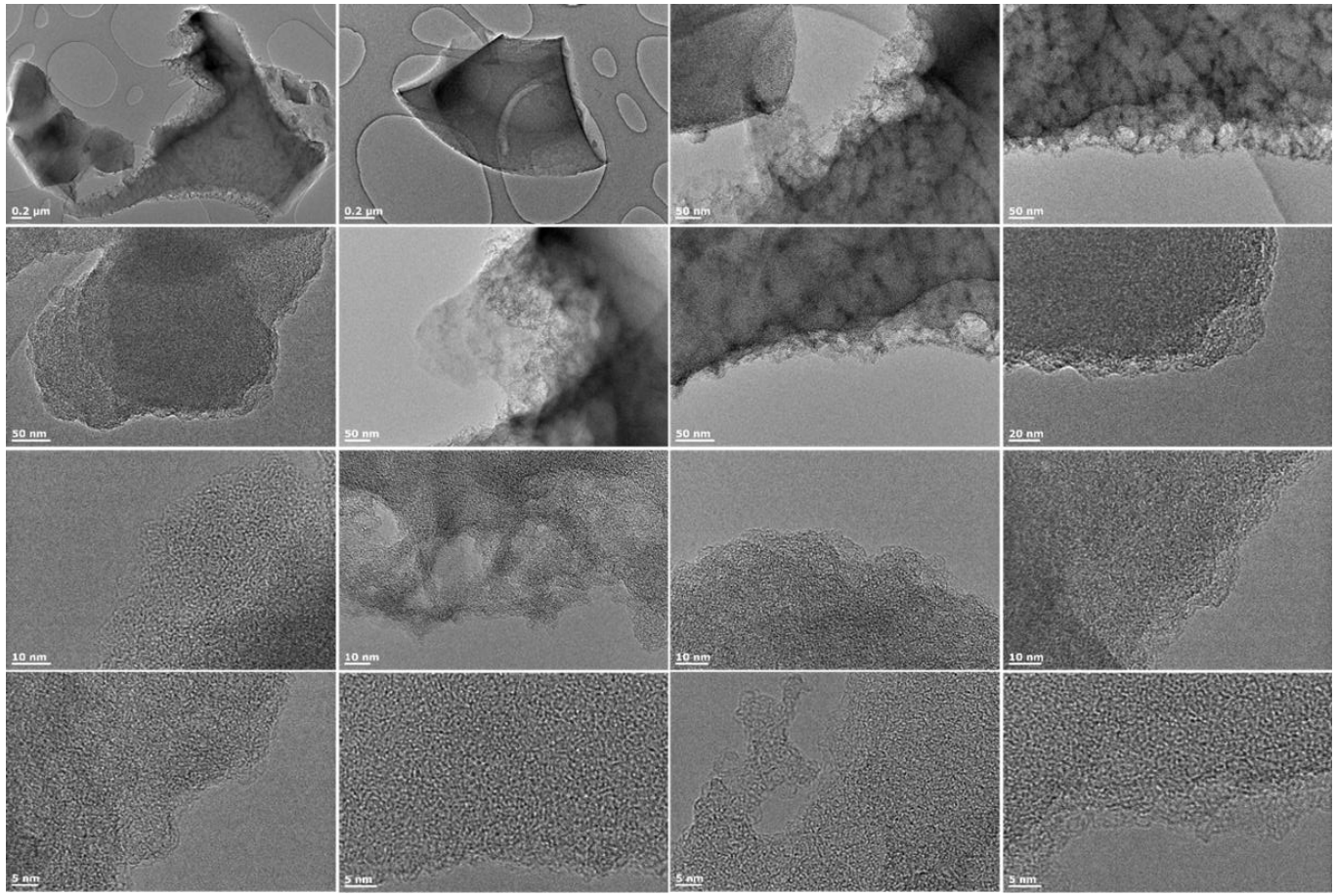


Figure 7.39: TEM micrographs images of PPYH124800.

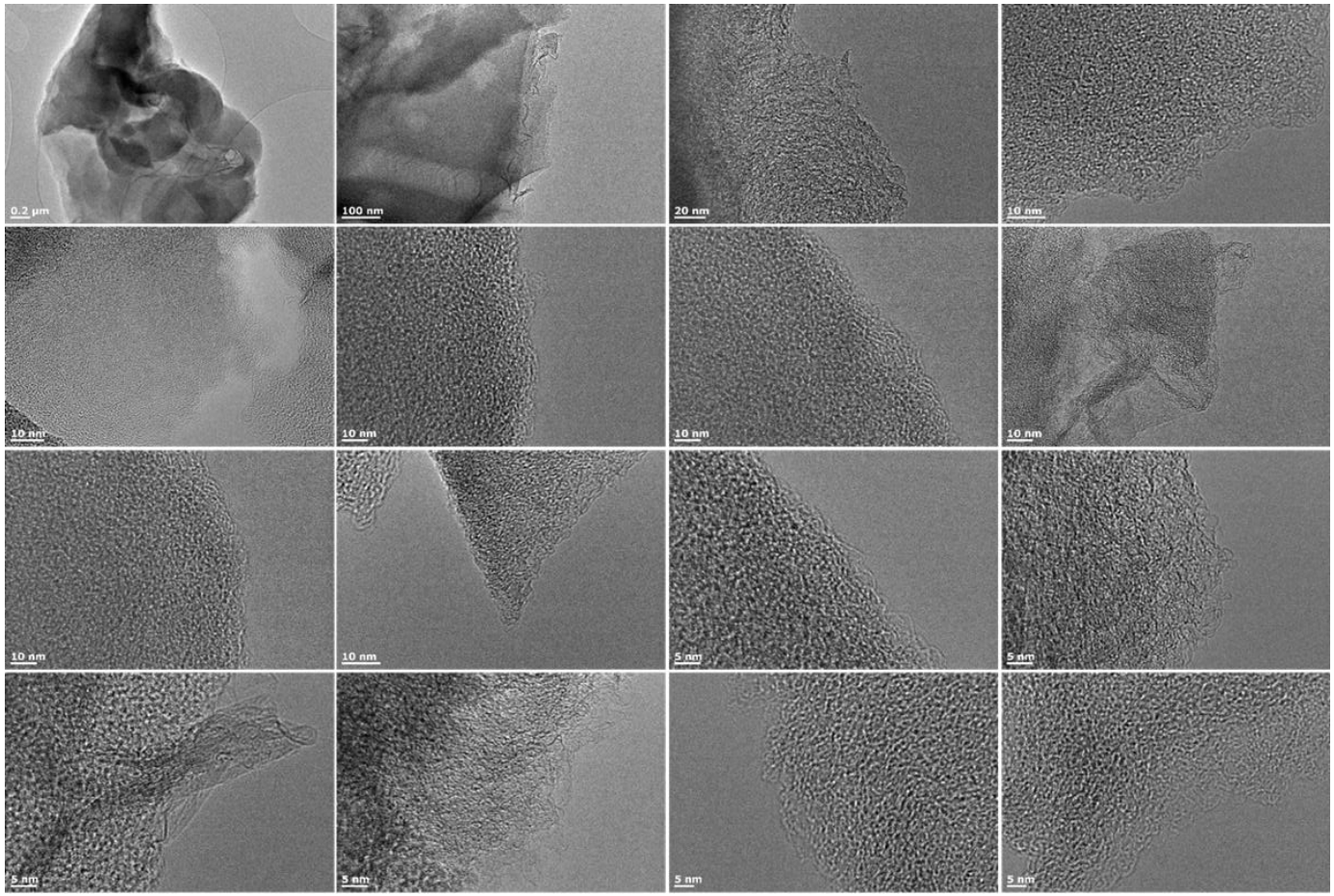


Figure 7.40: TEM micrographs images of PPYSD134800.

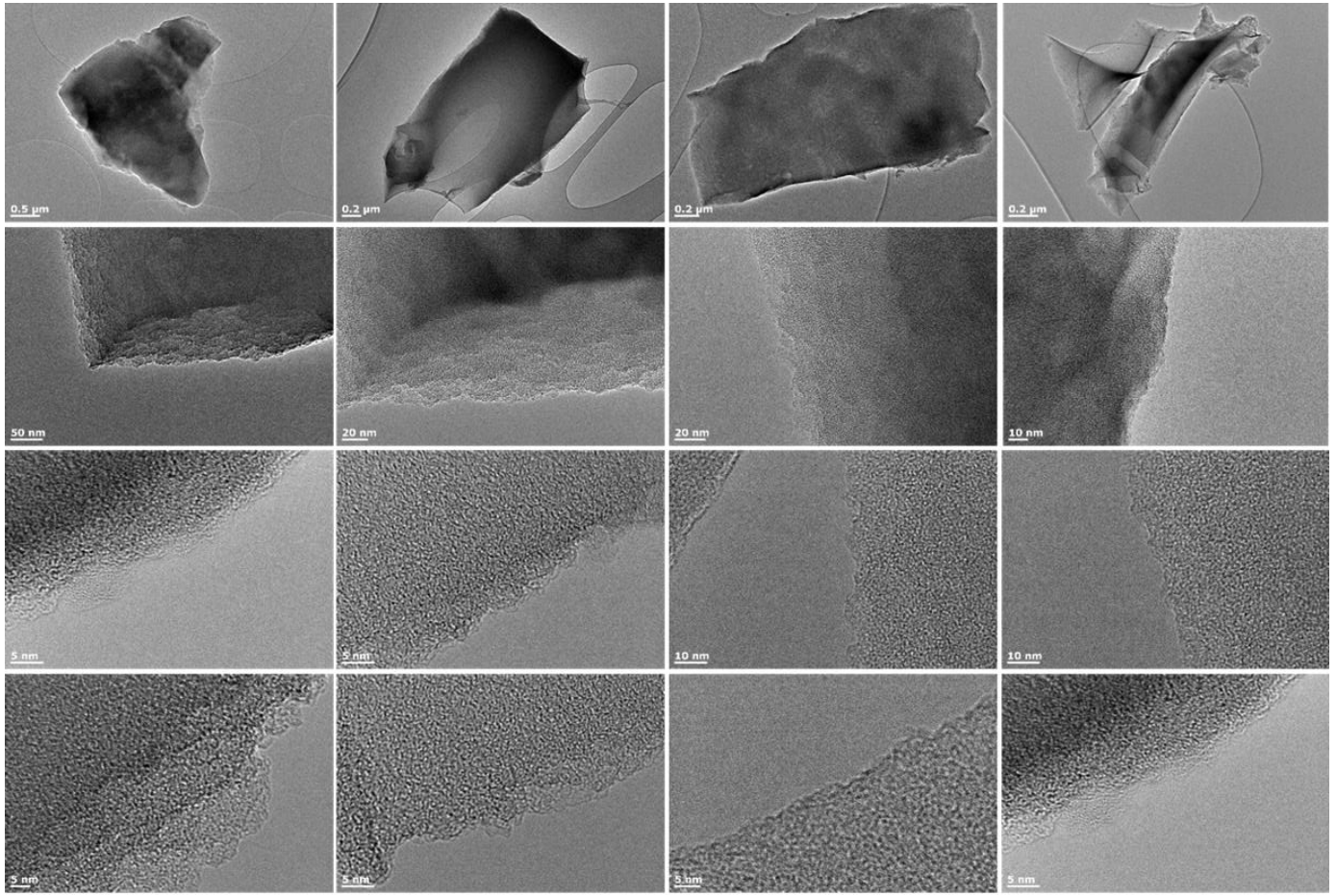


Figure 7.41: TEM micrographs images of PPYH134800.

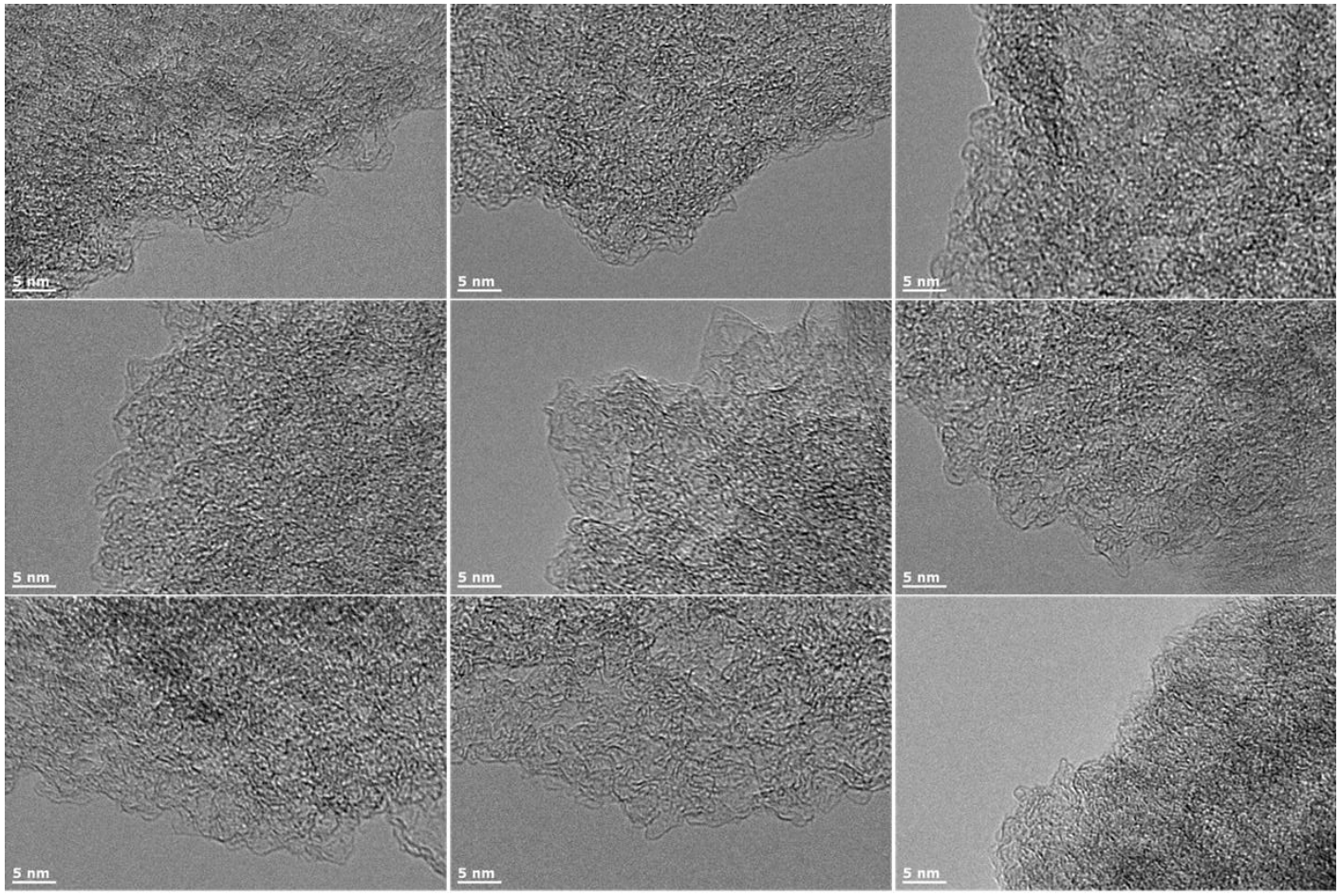


Figure 7.42: TEM micrographs images of PPYSD113900.

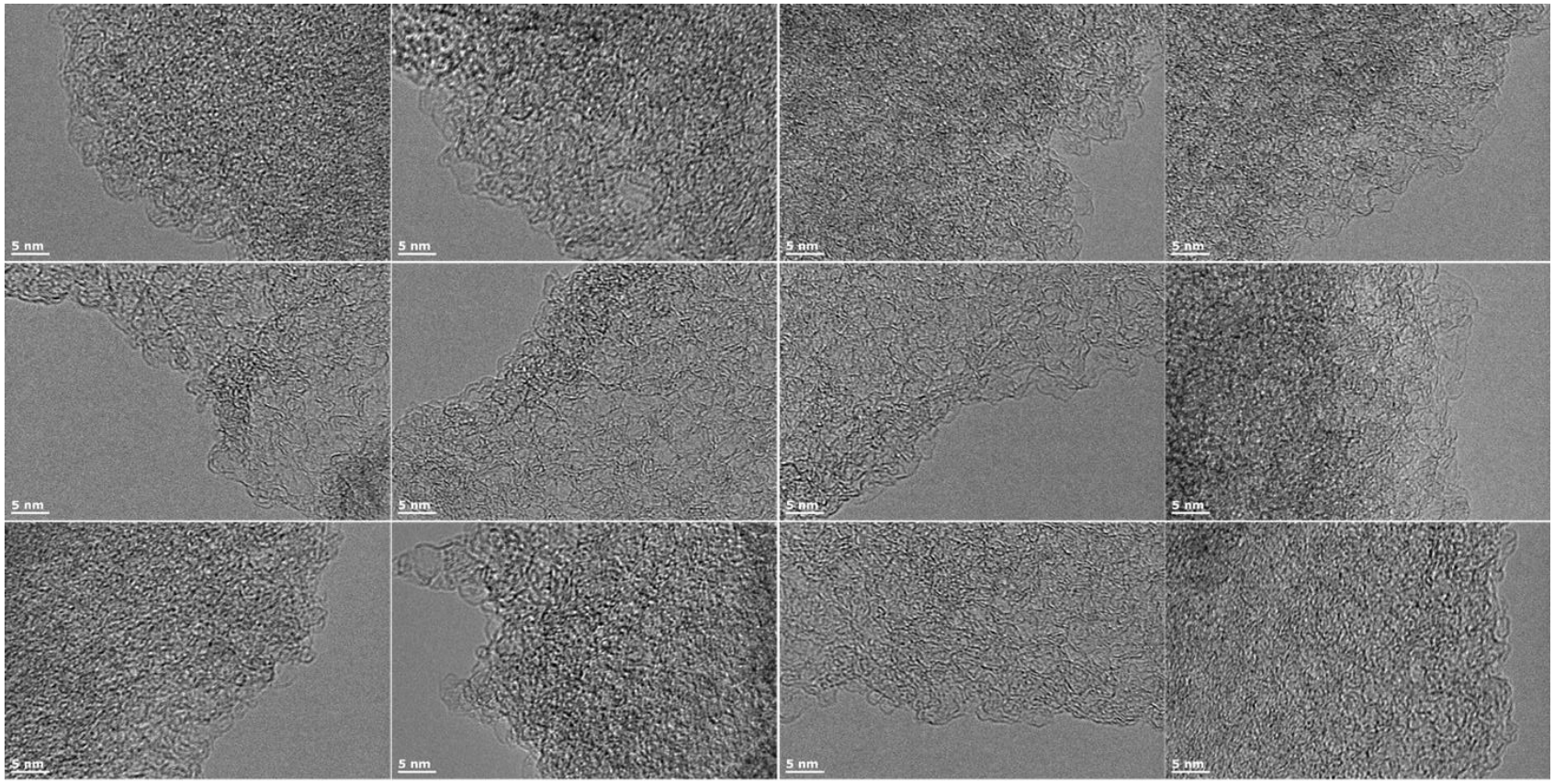


Figure 7.43: TEM micrographs images of PPYH113900.

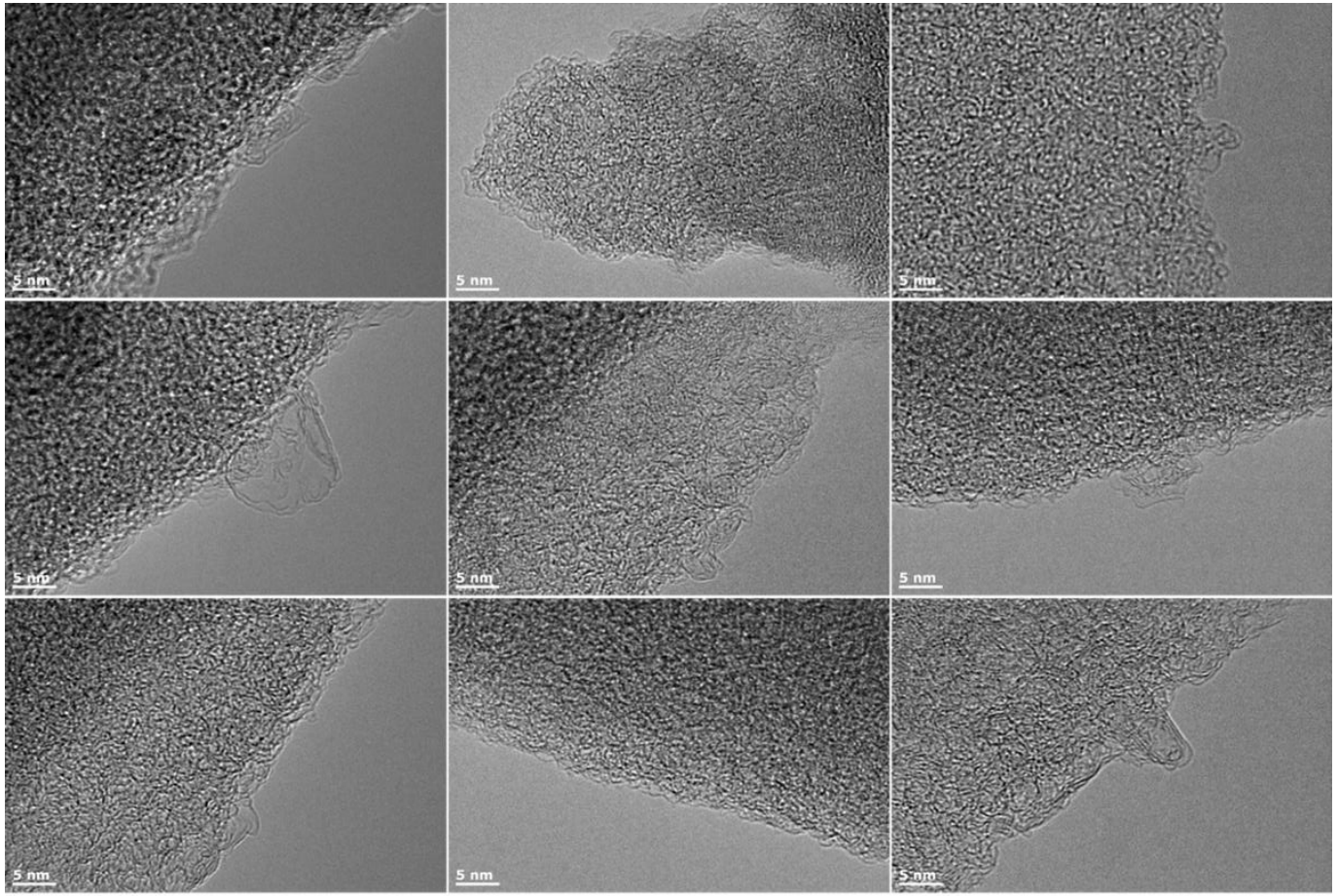


Figure 7.44: TEM micrographs images of PPYSD114900.

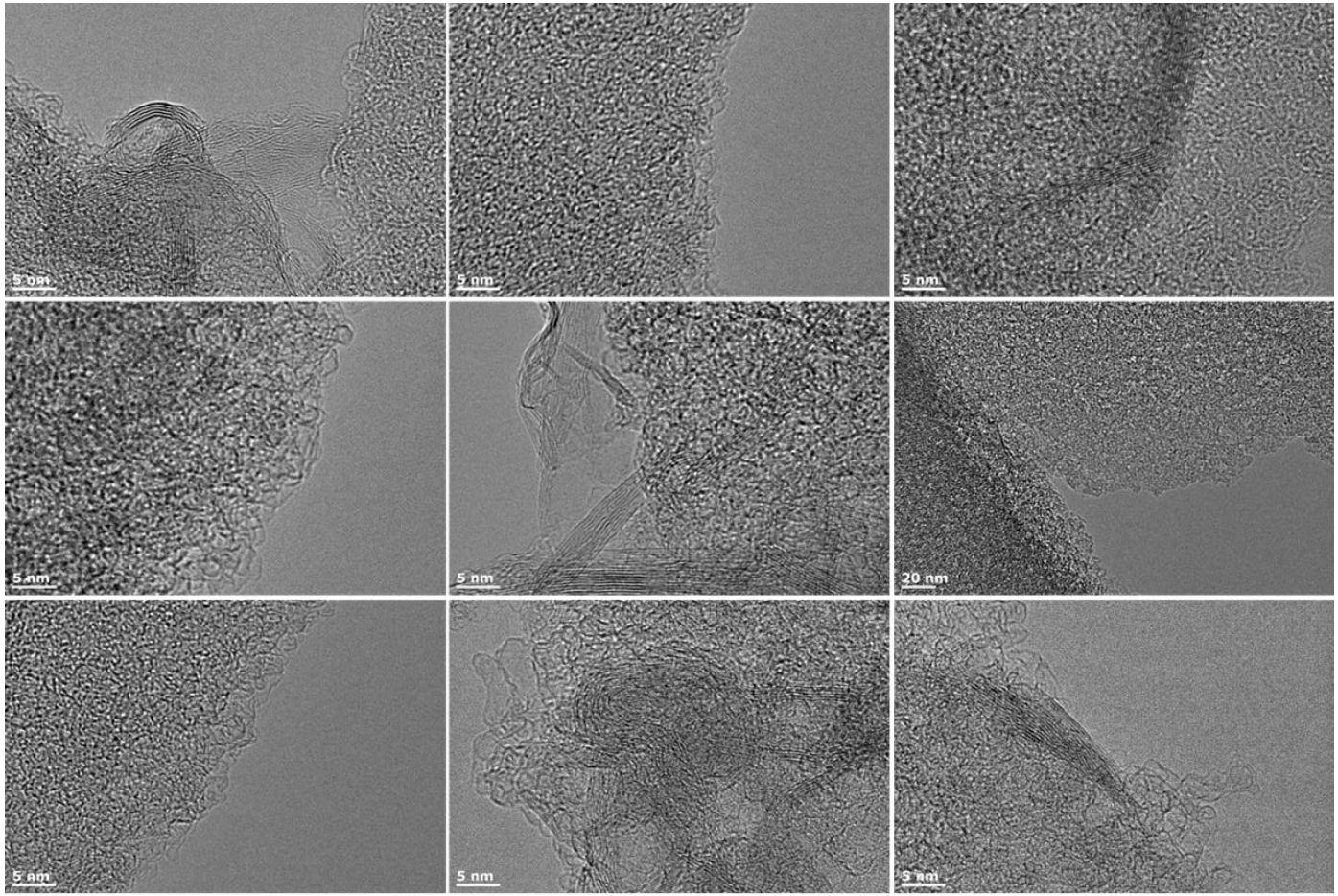


Figure 7.45: TEM micrographs images of PPYH114900.

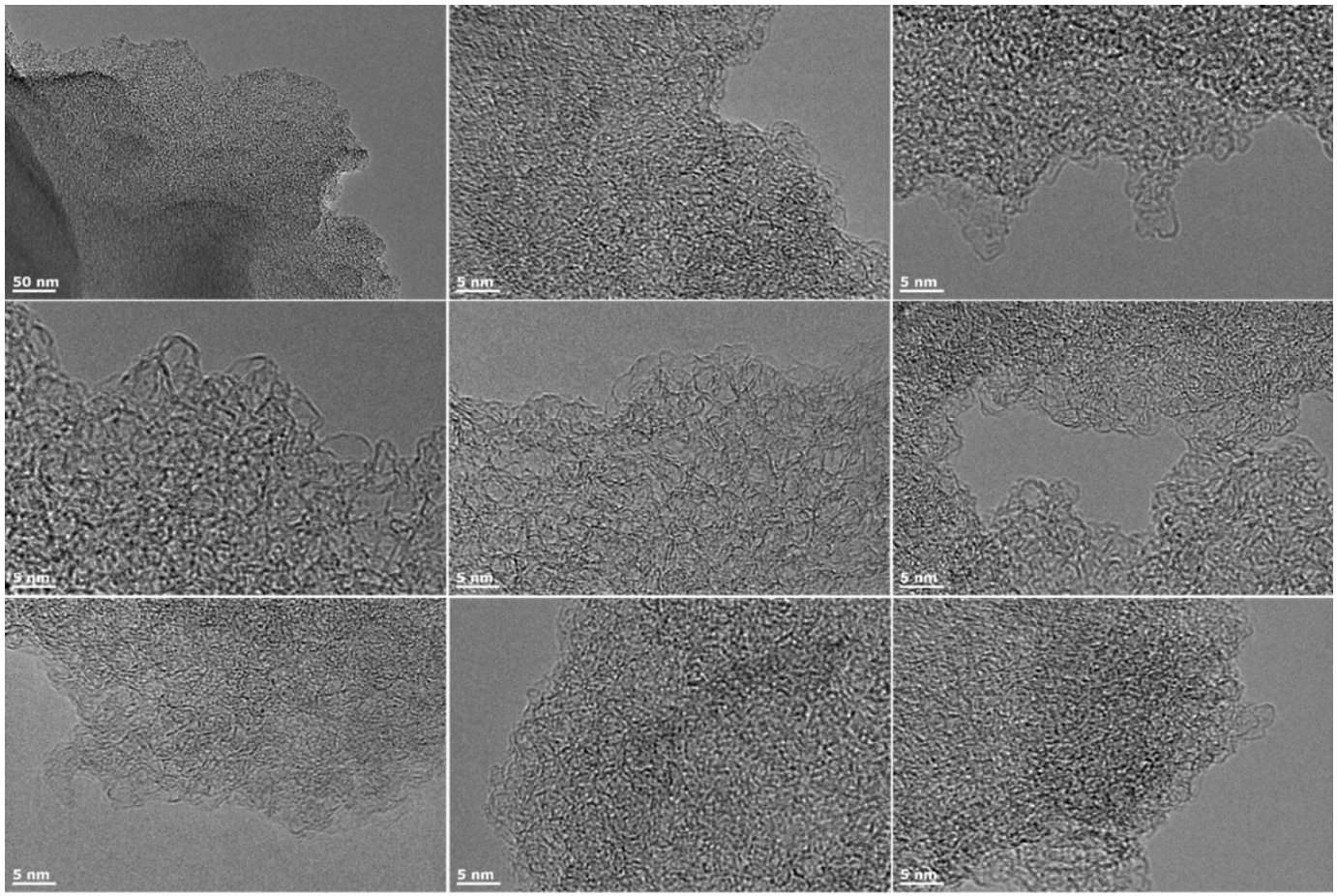


Figure 7.46: TEM micrographs images of PPYSD115900.

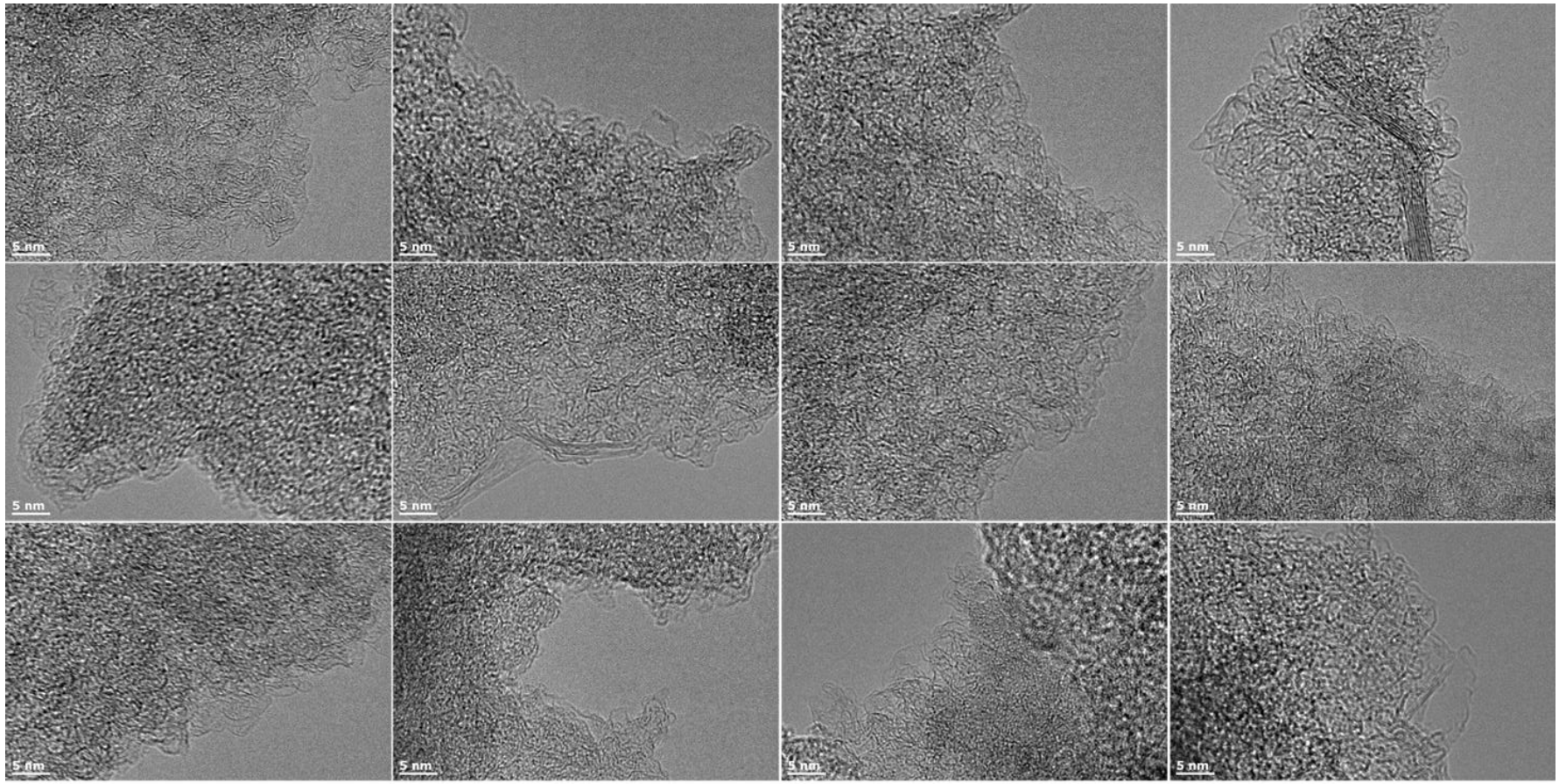


Figure 7.47: TEM micrographs images of PPYH115900.

7.6.2.6 Textural Properties and Porosity

The nitrogen sorption isotherms and corresponding pore size distribution (PSD) curves for PPY/SD and PPY/H are shown in **Figure 7.48 A, B** and **Figure 7.49 A, B,** respectively. The corresponding textural properties for both sets of activated carbons PPY/SD and PPY/H are summarized in **Table 7.6**. Polypyrrole has been previously used by many groups as a carbon precursor to fabricate porous carbons by means of nanocasting techniques.[88-90] while lignocellulosic biomass can also generate activated carbons with large surface areas.[28, 47, 91-97]

7.6.2.6.1 Polypyrrole/Sawdust Derived Activated Carbons

The nitrogen sorption isotherms of all PPY/SD carbons are shown in **Figure 7.48** A, and the corresponding pore size distribution (PSD) curves and the wide pore size distribution (PSD) curves are shown in **Figure 7.48 B** and **Figure 7.50**, respectively.

It is noteworthy that the PPY-only derived sample (PPY14800) exhibits an isotherm that is typical of a mesoporous material (**Figure 7.48 A**), which is consistent with previous reports. Given that all the other mixed precursor samples (PPY/SD and PPY/H) were prepared under similar or harsher conditions, the expectation was that they would all exhibit mesoporous characteristics similar to those of PPY14800. It is therefore interesting to note that not all the isotherms in **Figure 7.48 A** are indicative of mesoporosity. In particular, samples made from 1:3 or 3:1 mixtures of PPY/SD (i.e., samples PPYSD134800 and PPYSD314800) tend towards being microporous with relatively sharp adsorption knee. This clearly indicates that the nature of the precursor mix can significantly affect the micropore/

mesopore mix in the activated carbons. Samples prepared from 1:1, 1:2 and 2:1 PPY/SD mixtures (PPYSD114800, PPYSD124800, and PPYSD214800) show only moderate mesoporosity but which is higher than that for samples derived from 1:3 and 3:1 PPY/SD mixtures. It therefore appears that, for activation at 800 ^{o}C and KOH/precursor ratio of 4, the addition of sawdust to the precursor mix (i.e., ratios 1:1, 1:2. 2:1, 1:3 and 3:1) reduces the level of mesoporosity achieved but not in any systematic manner.

For samples activated at 900 ^{o}C (all at PPY/SD ratio of 1:1), the nature of the isotherm is determined the KOH/precursor ratio; mesoporosity increases as the KOH/precursor ratio rises from 3 to 4 and then decreases at a ratio of 5. Indeed sample PPYSD114900 appears to exhibit the highest mesoporosity that even surpasses that of the PPY-only sample. A comparison between sample PPYSD115800 and PPYSD115900 shows that the former has higher mesoporosity perhaps due to over-activation of the later arising from both a high KOH/precursor ratio of 5 and high activation temperature of 900 ^{o}C.

The pore size distribution of the PPY/SD carbons is shown in **Figure 7.48B**, and the pore size maxima values obtained from the curves are given in **Table 7.6**. The PPY-only derived sample (PPY14800) exhibits what may be described as a bimodal pore size distribution that is dominated by large micropores and small mesopores. The PPY14800 has small micropores centred at 6 to 7 Å, large micropores of size 12 Å, and small mesopores centered at 28 and 35 Å. Similar to the PPY14800 sample, all the PPY/SD carbons also exhibit the micropores centered at 6 to 9 Å, and 12 Å. However, the size of mesopores varies depending on the PPY:SD ratio, amount of activating agent used and activation temperatures. The mesopores size distribution of samples prepared at 900 ^{o}C is comparable to that of PPY14800, i.e., small mesopores centered at 28 Å and 35 Å. Samples made

from 1:3 or 3:1 mixtures of PPY and SD (i.e., samples PPYSD134800 and PPYSD314800) have a relatively small proportion of the smallest mesopores centred at 22 Å, which is consistent with the observation that these samples tend towards being microporous. Indeed, only a small proportion of these two samples, and also samples PPYSD214800 and PPYSD124800, are larger than 20 Å. This confirms that the nature of the precursor mix significantly affected the size of pores generated in the activated carbons. Therefore, for activation at 800 ^{o}C and KOH/precursor ratio of 4, the addition of sawdust to the precursor mix (i.e., ratios 1:1, 1:2. 2:1, 1:3 and 3:1) reduces the size of pores generated towards being predominantly in the micropore range.

The textural parameters of the PPY/SD activated carbons are summarised in **Table 7.6**. All the carbons possess high or ultra-high surface area, which ranges between 2450 and 3600 m^2g^{-1}, and pore volume in the range 1.3 – 2.60 cm^3g^{-1}. The PPY-only derived sample (PPY14800) has surface area of 2965 m^2g^{-1} and pore volume of 2.34 cm^3g^{-1}. The highest surface area for a PPY/SD sample is for PPYSD114900 (3563 m^2g^{-1}) followed closely by PPYSD115800 (3458 m^2g^{-1}) and PPYSD124800 (3477 m^2g^{-1}), while sample PPYSD114900 also has the highest pore volume of 2.54 cm^3g^{-1}. For PPYSD carbons activated at 800 ^{o}C and KOH/precursor ratio of 4, the addition of sawdust to the precursor mix (i.e., ratios 1:1, 1:2. 2:1, 1:3 and 3:1) does not appear to have a significant effect of the total surface area except for sample PPYSD124800. However, in all cases the addition of sawdust to the precursor mix acts to reduce to achievable pore volume, with the greatest reductions being for samples prepared from 3:1 or 1:3 PPY:SD ratios (samples PPYSD314800 and PPYSD134800, respectively). Increase in the KOH/precursor ratio to 5, for activation at 800 ^{o}C, increases both the surface area and pore volume (PPYSD114800 vs PPYSD115800). For samples activated at 900 ^{o}C (all at PPY/SD ratio of 1:1), the surface area and pore

volume increase as the KOH/precursor ratio rises from 3 to 4 and then decreases at a ratio of 5. Thus sample PPYSD114900 has both the highest surface area and pore volume for the PPYSD set of carbons, while sample PPYSD115900 has a much lower surface area. The surface and pore volume of PPYSD115800 are much higher than for PPYSD115900, which may be ascribed to over-activation of the later occasioned by both a high KOH/precursor ratio of 5 and activation temperature (900 ^{o}C). The PPY/SD carbons have moderate to very low levels of microporosity. The highest microporosity (ca. 50% of both pore volume and surface area) is exhibited by sample PPYSD134800. Samples prepared at PPY:SD ratio of 3:1 and 1:2 also exhibit considerable microporosity. The proportion of volume arising from mesopores (referred to as mesoporosity) for some of the PPY/SD carbons is above 90% and up to 98% (**Table 7.7**). Many of the PPY/SD carbons, especially those prepared at KOH/precursor ratio of 5 and/or 900 ^{o}C are highly mesoporous in character.

7.6.2.6.2 Polypyrrole/Hydrochar Derived Activated Carbons

The nitrogen sorption isotherms of all PPY/H carbons are shown in **Figure 7.49 A**, and the corresponding pore size distribution (PSD) curves and the wide pore size distribution (PSD) curves are shown in **Figure 7.49 B** and **Figure 7.51**, respectively.

The nitrogen sorption isotherms suggest that overall, the porosity of the PPY/SD carbons is generally lower than that of their PPY/SD analogues. The isotherms in show great variability between the samples. However, there are also some apparent trends. For carbons activated at 800 ^{o}C and KOH/ precursor ratio of 4, the amount of nitrogen adsorbed appears to be related

to the amount of PPY present in the precursor mix, i.e., decreases in the order PPYH314800 > PPYH214800 > PPYH124800 > PPYH134800. It appears therefore that the addition of sawdust to the precursor mix reduces the extent of porosity/mesoporosity generated to the extent that sample PPYH134800 has an isotherm that suggests significant microporosity while the isotherm of PPY314800 tends towards mesoporosity. This trend confirms that the nature of the precursor significantly affects the micropore/mesopore mix in the activated carbons. Despite not appearing to follow this trend, sample PPYH114800 exhibits an isotherms that suggests the presence of considerable microporosity. [50, 51, 80, 98-106] For samples prepared at 1:1 ratio of PPY:H, the amount of porosity generated is related to the activation conditions and thus increases in the order PPYH114800 < PPYH113900 < PPYH115900 < PPYH115800 ~ PPYH114900. For samples activated at 900 ^{o}C (all at PPY/H ratio of 1:1), the nature of the isotherm is determined the KOH/precursor ratio; mesoporosity increases as the KOH/precursor ratio rises from 3 to 4 and then decreases at a ratio of 5. Indeed sample PPYH114900 exhibits the highest mesoporosity for the PPY/H set of carbons. A comparison between sample PPYH115800 and PPYH115900 shows that the former has higher mesoporosity, which may be ascribed to slight over-activation of the later arising from both a high KOH/precursor ratio of 5 and activation temperature of 900 ^{o}C.

The pore size distribution of the PPY/H carbons is shown in **Figure 7.49 B**, and the pore size maxima values obtained from the curves are given in **Table 7.6**. Most of the PPY/H carbons exhibit a bimodal pore size distribution with small micropores centred at 6 to 9 Å, large micropores of size 11 - 12 Å, and small mesopores centered at 22 - 28 and, for samples PPYH114900 and PPYH115900, at 36 Å. The pore size of samples prepared from a precursor mix ratio of 1:2. 2:1, 1:3 or 3:1 is dominated by micropores with

hardly any pores larger than 20 Å; the presence of mesopores can be related to the amount of PPY in the precursor mix. However, the size of mesopores varies depending on the PPY:SD ratio, amount of activating agent used and activation temperatures. The mesopores size distribution of samples prepared at 900 ^{o}C is comparable to that of PPY14800, i.e., small mesopores centered at 28 and 35 Å. Samples. This confirms that the nature of the precursor mix significantly affected the size of pores generated in the activated carbons. Therefore, for activation at 800 ^{o}C and KOH/precursor ratio of 4, the addition of sawdust hydrochar to the precursor mix (i.e., ratios 1:1, 1:2. 2:1, 1:3 and 3:1) reduces the size of pores generated towards being predominantly in the micropore range. Samples prepared at 900 ^{o}C and or KOH/precursor mix ratio of 5 have the highest proportion of mesopores.

The textural parameters of the PPY/H carbons are summarised in **Table 7.6**. All the carbons possess moderate, high or ultra-high surface area, which ranges between 1800 and 36815 m^2g^{-1}, and pore volume in the range 0.8 – 2.3 cm^3g^{-1}. The highest surface area for a PPY/H sample is for PPYH114800 (33815 m^2g^{-1}) followed by PPYH214800 (3583 m^2g^{-1}) and PPYH14900 (3592 m^2g^{-1}), which also has the highest pore volume of 2.25 cm^3g^{-1}. For PPYH carbons activated at 800 ^{o}C and KOH/precursor ratio of 4, the addition of sawdust hydrochar to the precursor mix at non equal amounts (i.e., ratios 1:2. 2:1, 1:3 and 3:1) has a significant effect of the total surface area except for sample PPYH214800. However, in general, the addition of sawdust hydrochar to the precursor mix reduces the pore volume, with the greatest reductions being for samples prepared from 1:2 or 1:3 PPY:H ratios (samples PPYH124800 and PPYH134800, respectively). Increase in the KOH/precursor ratio to 5, for activation at 800 ^{o}C, decreases both the surface area and pore volume (PPYH114800 vs PPYH115800). For samples activated

at 900 °C (all at PPY/H ratio of 1:1), the surface area and pore volume increase as the KOH/precursor ratio rises from 3 to 4 and then decreases at a ratio of 5. Thus sample PPYH114900 has both the highest surface area and pore volume for the PPY/H set of carbons, while sample PPYH115900 has a lower surface area. The PPY/H carbons exhibit a wide variability with regard to levels of microporosity. The highest microporosity (ca. 71% of both pore volume and surface area) is exhibited by sample PPYH134800. Samples prepared at PPY:H ratio of 3:1 and 1:2 also exhibit considerable microporosity. The proportion of mesoporosity for some of the PPY/H carbons is above 90% (Table 1.8); carbons prepared at KOH/precursor ratio of 5 and/or 900 °C are highly mesoporous in character. Overall, however, the PPY/H carbons exhibit lower levels of mesoporosity (and consequently higher microporosity) compared to the PPY/SD set of samples.

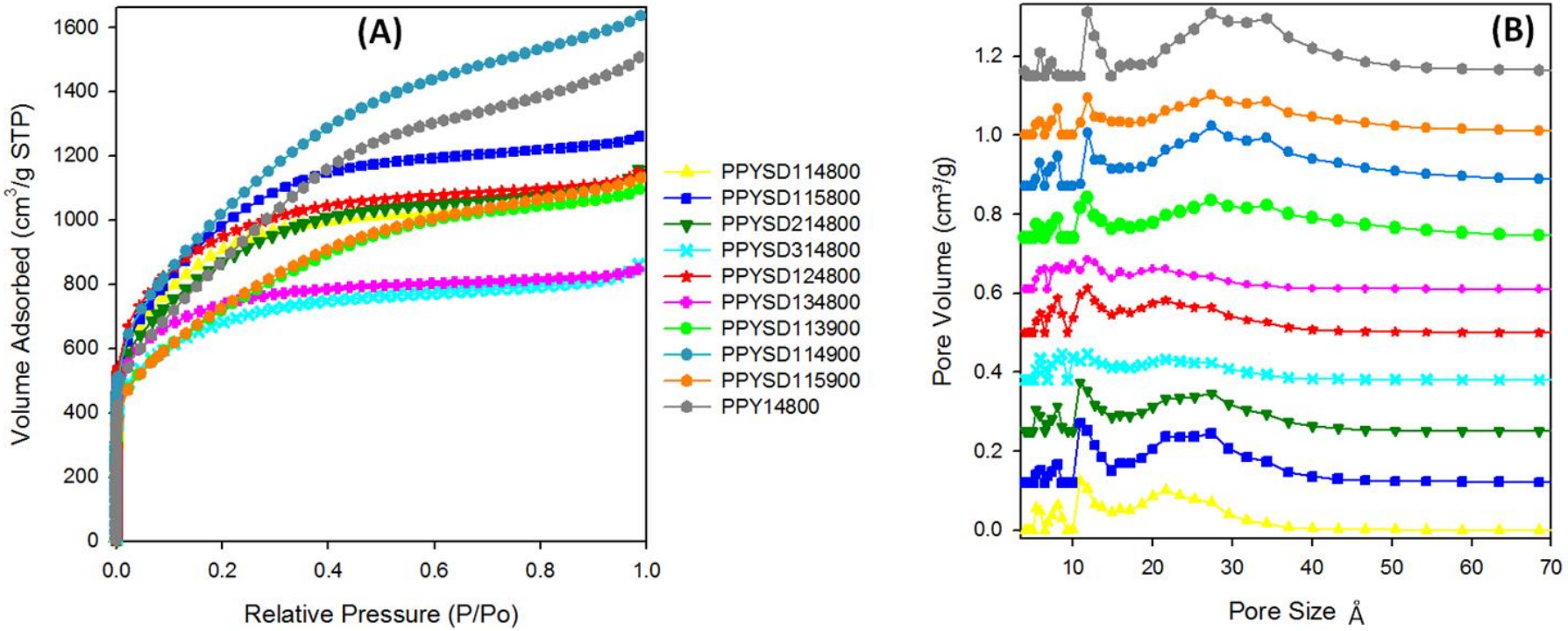


Figure 7.48: (A) Nitrogen sorption isotherms of **PPY/SD** carbons, and **(B)** Corresponding pore size distribution curves.

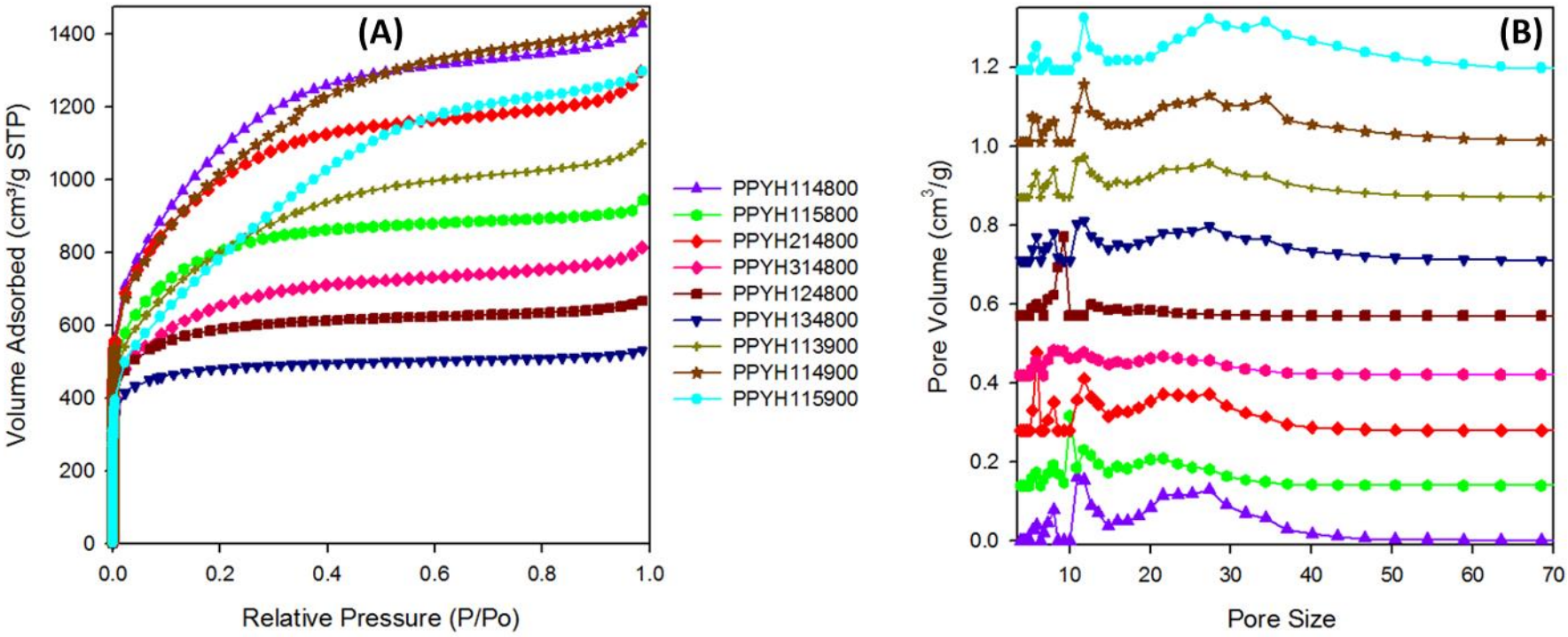


Figure 7.49: (A) Nitrogen sorption isotherms of **PPY/H** activated carbons, and **(B)** Corresponding pore size distribution curves.

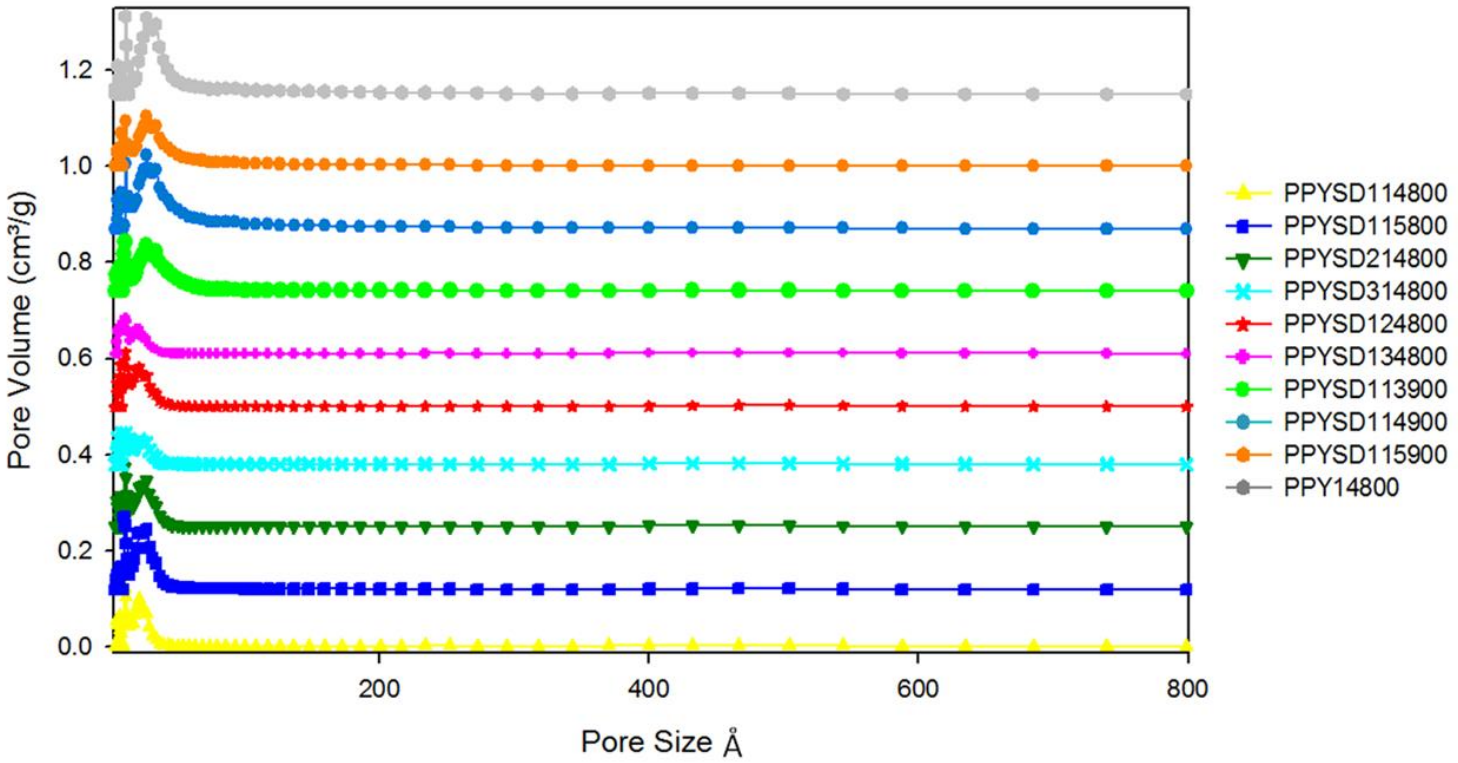


Figure 7.50: Wide pore size distribution of PPY/SD activated carbons.

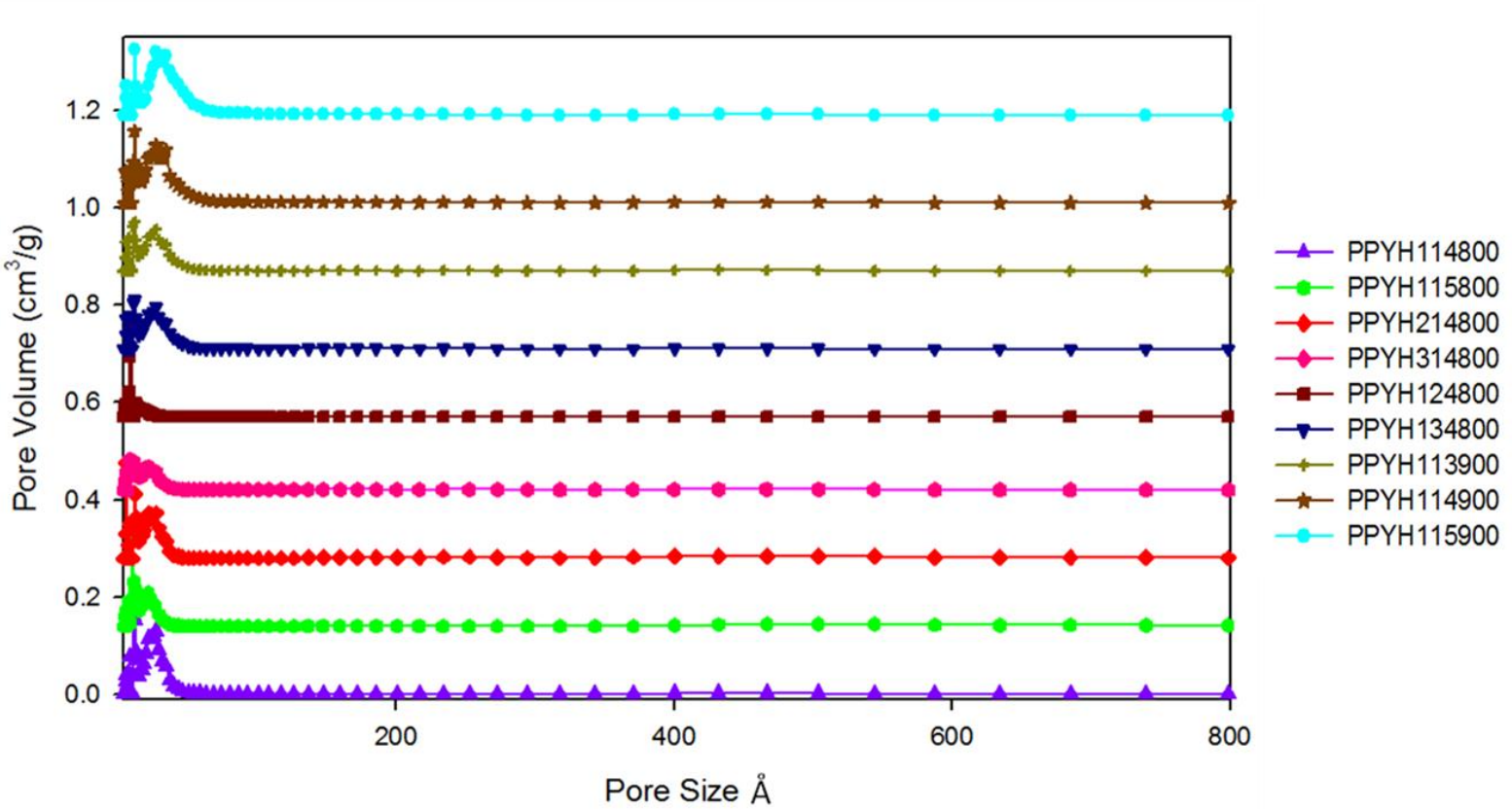


Figure 7.51: Wide pore size distribution of PPY/H activated carbons.

Table 7.6: Textural properties of PPY/SD and PPY/H carbons.

Sample	Activation Temperature (°C)	Surface Area [a] ($m^2\ g^{-1}$)	Pore Volume [b] ($cm^3\ g^{-1}$)	Pore Size [c] (Å)				
				Micro (less than 20)			Meso (20-500)	
PPY14800	800	2965	2.34 (0.29)	6	7	12	28	35
PPYSD114800	800	3279 (1015)	1.70 (0.39)	6	8	11	22	-
PPYSD115800	800	3458 (125)	1.95 (0.05)	6	8	11	28	-
PPYSD214800	800	3085 (452)	1.76 (0.18)	6	8	11	26	-
PPYSD314800	800	2485 (996)	1.29 (0.39)	6	8	12	22	-
PPYSD124800	800	3477 (1356)	1.78 (0.62)	6	8	12	22	-
PPYSD134800	800	2739 (1562)	1.31 (0.62)	6	8	12	22	-
PPYSD113900	900	2517 (47)	1.70 (0.03)	6	8	12	28	35
PPYSD114900	900	3563	2.54 (0.13)	6	8	12	28	35
PPYSD115900	900	2545 (624)	1.75 (0.03)	6	8	12	28	35
PPYH114800	800	3815 (377)	2.18 (0.16)	6	8	12	28	-
PPYH115800	800	2976 (1338)	1.46 (0.52)	6	8	12	22	-
PPYH214800	800	3583 (887)	1.97 (0.35)	6	8	12	28	-
PPYH314800	800	2396 (1133)	1.24 (0.45)	6	8	12	-	-
PPYH124800	800	2227 (1569)	1.04 (0.62)	6	9	-	-	-
PPYH134800	800	1828 (1468)	0.83 (0.59)	6	9	12	28	-
PPYH113900	900	2841 (490)	1.70 (0.21)	6	8	12	28	-
PPYH114900	900	3592 (355)	2.25 (0.15)	5	8	12	28	36
PPYH115900	900	2690	2.01 (0.18)	6	8	12	28	36

[a] Activated carbons are designated as PPYSD*xyzt* for PPY/SD or PPYH*xyzt* for PPY/H carbons.
[b] The values in the parenthesis refer to micropore surface area.
[c] The values in the parenthesis refer to micropore volume.
[d] Pore size distribution maxima obtained from NLDFT analysis.

Table 7.7: Microporosity and mesoporosity of PPY/SD and PPY/H carbons.

Sample [a]	T-plot Micropore Volume ($cm^3\ g^{-1}$)	Total Pore Volume ($cm^3\ g^{-1}$)	Microporosity [a, b] (%)	Mesoporosity [c, d] (%)
PPY14800	0.29	2.34	13	87
PPYSD114800	0.39	1.70	23	77
PPYSD115800	0.05	1.95	2	98
PPYSD214800	0.18	1.76	10	90
PPYSD314800	0.39	1.30	30	70
PPYSD124800	0.53	1.78	30	70
PPYSD134800	0.62	1.31	47	53
PPYSD113900	0.03	1.70	2	98
PPYSD114900	0.13	2.54	5	95
PPYSD115900	0.03	1.75	2	98
PPYH114800	0.16	2.18	7	93
PPYH115800	0.52	1.46	35	65
PPYH214800	0.35	1.97	18	82
PPYH314800	0.45	1.24	37	63
PPYH124800	0.62	1.04	60	40
PPYH134800	0.59	0.83	71	29
PPYH113900	0.21	1.70	12	88
PPYH114900	0.15	2.25	7	93
PPYH115900	0.18	2.01	8	92

[a] Proportion of pore volume arising from micropores.
[b] Calculated as (Micropore volume/Total pore volume) X100%.
[c] Proportion of pore volume arising from mesopores.
[d] Calculated as Mesoporosity (%) = 100 – Microporosity (%).

7.6.2.7 CO_2 Uptake Measurements

Recently, activated carbons derived from polypyrrole or biomass have received a great deal of attention as solid state storage materials for energy related gases such as CO_2 and H_2.[17, 38, 45, 47, 51-53, 67, 69, 80] The CO_2 uptake capacity of the carbons was measured at room temperature (25 °C) and pressure range of 0-40 bars using a XEMIS gravimetric analyser following the procedure discussed in **Chapter 2**. The focus was the CO_2 uptake at low to moderate pressure under conditions that attempt to mimic pre or post combustion CCS. The high pressure (up to 40 bar) gravimetric CO_2 uptake isotherms of all the carbons are shown in and **Figure 7.52** for PPY/SD and **Figure 7.53** for PPY/H samples. Low pressure (up to 1 bar) gravimetric CO_2 uptake isotherms are shown in **Table 7.8** and **Figure 7.54 A** for PPY/SD and **Figure 7.54 B** for PPY/H samples.

For all samples the CO_2 uptake was found to be fully reversible and no hysteresis was observed. Furthermore, none of the carbons appear to attain saturation in the 0–40 bar pressure range except for sample PPYH134800. **Table 7.8** and summarizes the amount of CO_2 adsorbed at various pressures.

7.6.2.7.1 Polypyrrole/Sawdust Activated Carbons

At 1 bar (**Figure 7.54** and **Table 7.9**), the CO_2 uptake for PPY/SD carbons is in the range 2.1 – 3.41 mmol g^{-1}, which is moderate capacity compared to benchmark carbon materials. [7-13, 15, 21, 40, 43, 45, 51, 52, 67, 80, 98-102, 104, 105, 107-109] The storage capacity at 1 bar is very clearly related to the level of microporosity in the PPY/SD samples as discussed above. The PPY/SD

sample with the highest microporosity (i.e., PPYSD134800) has the best performance for CO_2 uptake at 1 bar (3.41 mmol g^{-1}). The next most microporous samples, PPYSD314800 and PPYSD124800 are the next best performers with uptake of 3.25 mmol g^{-1} and 3.1 mmol g^{-1}, respectively.

On the other hand, the most mesoporous samples, PPYSD113900, PPYSD114900 and PPYSD115900, have the lowest uptake of between 2.1 mmol g^{-1} and 2.3 mmol g^{-1}. The uptake at 0.15 bar follows a generally similar trend to that observed at 1 bar. The trends observed are consistent with the well-established fact that it is not the total surface area or pore volume, but the pore size that determines the CO_2 uptake at low pressure.[7, 10-15, 21, 40, 43, 45, 51, 52, 67, 80, 98-102, 104, 105, 107-111]

On the other hand, the CO_2 uptake of the PPY/SD samples increases continuously at higher pressures to reach very high levels of storage at 40 bar. At 20 bar the PPY/SD samples have excess storage capacity of between 16.8 and 21.5 mmol g^{-1}. The uptake of close to 22 mmol g^{-1} is much higher than that previously reported for most carbon materials. [7-15, 21, 40, 43, 45, 51, 52, 67, 80, 98-102, 104, 105, 107-109] It is also noteworthy that some of the PPY/SD samples surpass the uptake of the PPY-only carbon (PPY14800). At 30 bar the CO_2 storage capacity rises to between 19.0 and 26.2 mmol g^{-1}, which is comparable to that of benchmark carbons such as polyaniline cross-linked polymer networks (SU-AC-400) that store 28.3 mmol g^{-1} under similar conditions (i.e., 25 ^{o}C and 30 bar).[112] At 40 bar, which is the highest pressure used in this study, the PPY/SD carbons have very high CO_2 storage capacity of up to 31 mmol g^{-1}. It is clear that the more microporous samples (e.g., PPYSD314800 and PPYSD134800) have relatively lower CO_2 uptake at high pressures ($\leq$ 10 bar), which is the reverse of their performance at low pressure ($\geq$ 1 bar). It appears, therefore, that the gravimetric CO_2 uptake at high pressure (10 – 40 bar) follows the trend in mesoporosity and total

pore volume such that the best performing PPY/SD samples at high pressure have both the highest pore volume and highest levels of mesoporosity.

7.6.2.7.2 Polypyrrole/Hydrochar Activated Carbons

For the PPY/H set of samples, at 1 bar (**Figure 7.54** and **Table 7.9**), the CO_2 uptake is in the range 2.1 – 4.02 mmol g^{-1}. Three of the PPY/H samples, namely, PPYH134800, PPYH124800 and PPYH134800, achieve uptake higher than 3.5 mmol g^{-1}, which is comparable to some of the best benchmark carbon materials.[7-12, 40, 43, 45, 46, 52, 67, 80, 98-102, 104, 105, 107, 109] The storage capacity at 1 bar is closely matched related with the level of microporosity in the PPY/H samples. Indeed, the PPY/H sample with the highest microporosity (i.e., 70% for PPYH134800) has the best performance for CO_2 uptake at 1 bar (4.02 mmol g^{-1}). The next most microporous sample (PPYH124800) are the next best uptake of 3.78 mmol g^{-1}. On the other hand, the most mesoporous samples, PPYH113900, PPYH114900 and PPYH115900, have the lowest uptake of between 2.1 and 2.7 mmol g^{-1}. The uptake at 0.15 bar follows a generally similar trend to that observed at 1 bar and confirm the well-established fact that it is not the total surface area or pore volume, but the pore size that determines the CO_2 uptake at low pressure.[7-15, 21, 40, 43, 45, 51, 52, 67, 80, 98-102, 104, 105, 107-109] It is also noteworthy that, at pressure of up to 1 bar, the best PPY/H samples outperform the top PPY/SD carbons due to the fact that the former are relatively more microporous as discussed above.

As expected, the CO_2 uptake of the PPY/H samples increases at higher pressures. At 20 bar the PPY/SD samples have excess storage capacity of between 13 and 21 mmol g^{-1}. The most microporous sample (PPYH134800) has uptake of only 13.4 mmol g^{-1} compared to ~ 20 mmol g^{-1} for the more

mesoporous materials (PPYH115800 and PPYH115900). At 30 bar the CO_2 storage capacity rises to between 14 and 25 mmol g^{-1}, with the more mesoporous materials storing almost double the capacity of the more microporous PPYH134800 sample. At 40 bar, the PPY/H carbons have excess CO_2 storage capacity of up to 28 mmol g^{-1}, which is somewhat lower than that achieved by the best PPY/SD carbons. The relatively lower performance of the PPY/H carbons may be attributed to the fact that they achieve lower levels of total pore volume, and in particular mesopore volume. It is noteworthy that sample PPYH134800, which is the most microporous, appears to attain CO_2 uptake saturation at 40 bar. Considering that this is the best performing sample at low pressure ($\leq$ 1 bar), this observation further emphasizes the important role played by the micro/mesopore mix and pore size in determining uptake under various pressure conditions.

Pore size is known to be the main factor in determining physisorption-based CO_2 uptake onto solid state materials under conditions that low pressure conditions that mimic post-combustion flue gas streams.[1, 43, 98, 101, 113, 114] It has been shown that pores of size 6–7 Å are the most efficient in CO_2 capture and storage under low pressure conditions (0.1 – 1 bar).[1, 43, 98, 101, 113, 114] Presser *et al.*[115] and Hu *et. al.*[116] have shown that CO_2 uptake on microporous carbons at low pressure (1 bar) is related to the presence of pores of size <1 nm. It should be pointed out that the trends in CO_2 uptake observed in this chapter may not be attributed to N-doping as the carbons have low amounts of N. Furthermore, it has previously been shown that N-doping does not play a significant role in CO_2 uptake.

In the case of the present PPY/SD and PPY/H carbons, it is evident that the porosity is the main factor in determining the CO_2 uptake. The findings show that the use of a mix of precursors, namely, polypyrrole, sawdust or sawdust hydrochar, is a very effective way of varying the porosity of the carbons

whist retaining similar or relatively similar activation conditions. It is noteworthy that the addition of raw sawdust rather than sawdust hydrochar to polypyrrole offers carbons with significantly different porosity and consequently CO_2 uptake properties.

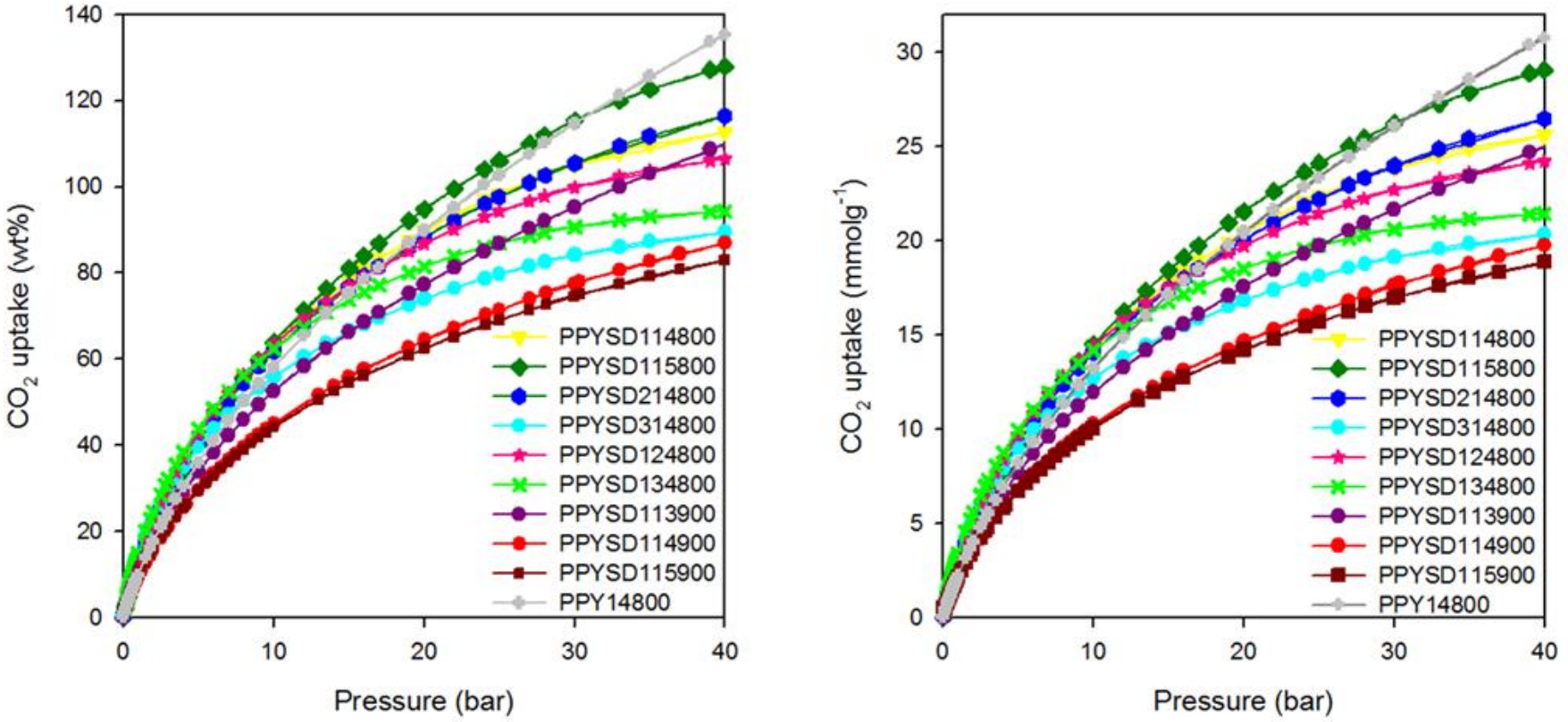


Figure 7.52: CO_2 uptake isotherms ***at 25 °C*** and pressure range of **0-40 bar** for PPY/SD activated carbons.

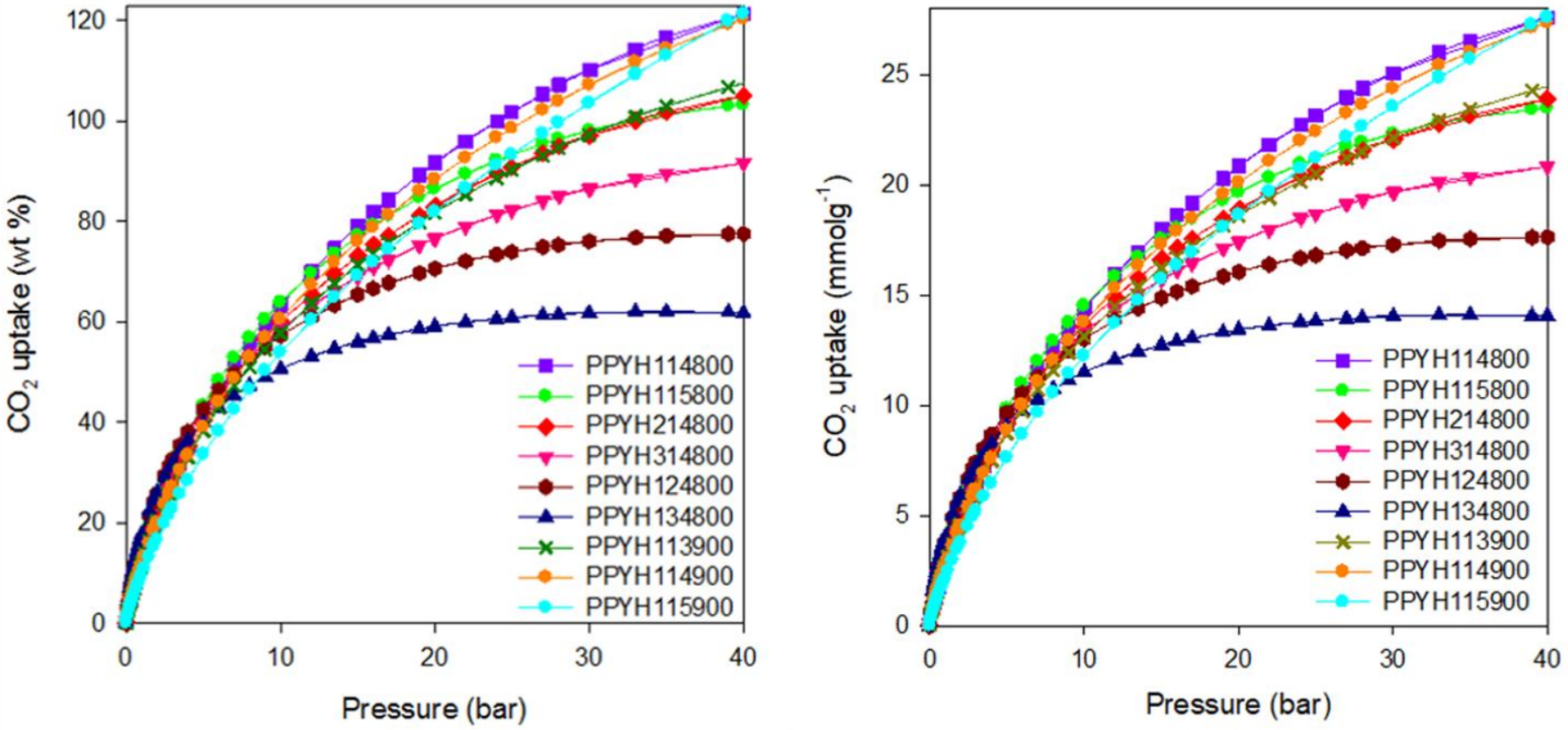


Figure 7.53: CO_2 uptake isotherms ***at 25 °C*** and pressure range of **0- 40 bar** for PPY/H activated carbons.

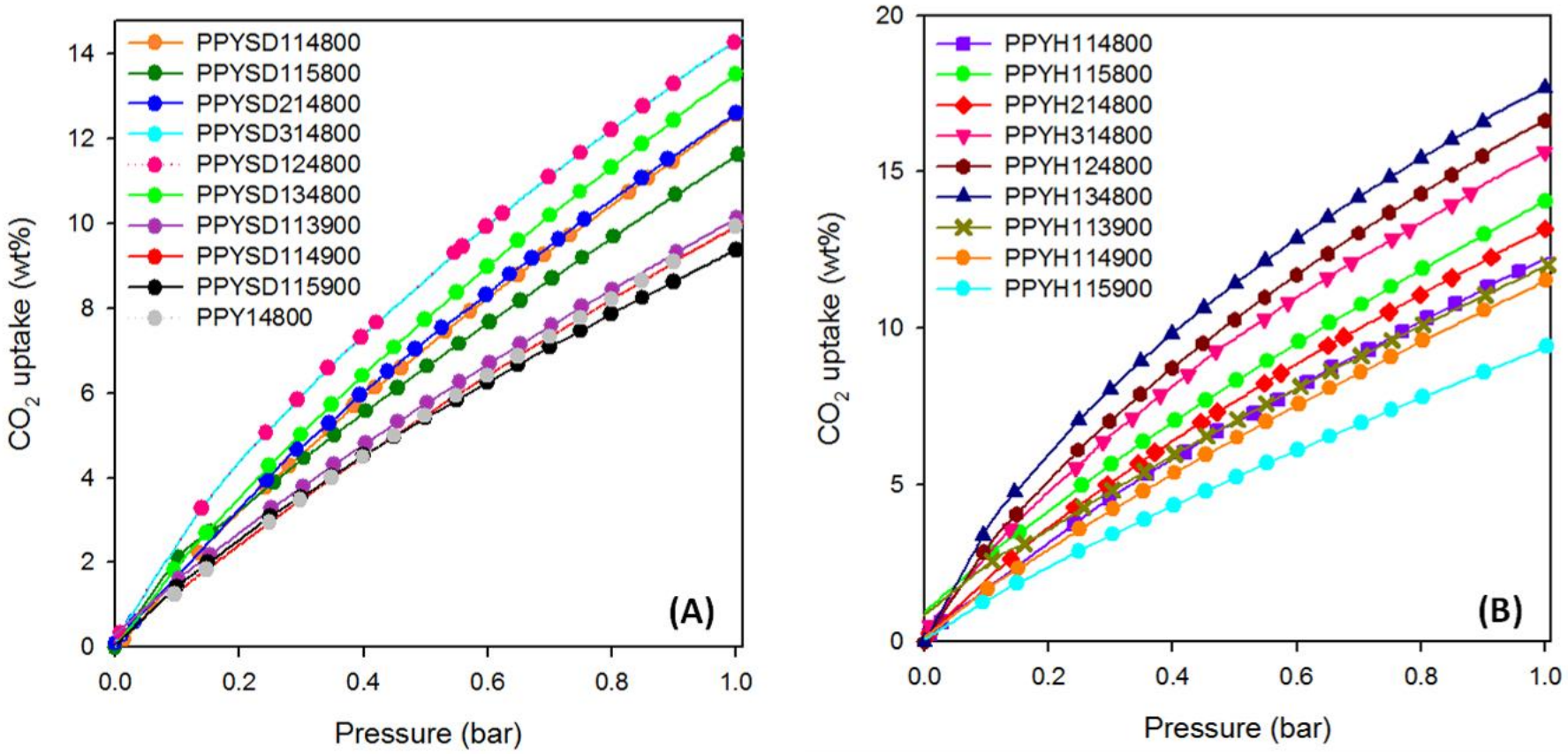


Figure 7.54: CO_2 uptake isotherms ***at 25 °C*** and pressure range **0-1 bar** for **(A)** PPY/SD carbons, and **(B)** PPY/H carbons.

Table 7.8: Gravimetric CO_2 uptake (in wt%) *at 25 °C* and various pressures for PPY/SD activated carbons, and PPY/H activated carbons.

Sample	CO_2 uptake (wt%)					
	0.15 bar	1 bar	10 bar	20 bar	30 bar	40 bar
PPY14800	2.0	9.9	58.3	89.8	114.6	135.3
PPYSD114800	0.2	12.6	63.4	89.7	105.1	112.6
PPYSD115800	2.7	11.6	63.9	94.7	115.3	127.8
PPYSD214800	3.2	12.6	61.9	88.2	105.4	116.5
PPYSD314800	3.3	14.3	55.9	74.0	84.1	89.4
PPYSD124800	2.7	13.5	63.4	86.8	99.8	106.5
PPYSD134800	3.3	15.0	62.4	81.5	90.6	94.3
PPYSD113900	2.2	10.1	52.6	77.3	95.3	109.9
PPYSD114900	2.0	9.4	44.9	64.2	77.5	87.0
PPYSD115900	2.3	9.6	44.2	62.4	74.6	83.0
PPYH114800	2.2	14.3	63.2	91.6	110.3	121.4
PPYH115800	3.5	14.1	63.8	86.4	98.1	103.3
PPYH214800	3.5	13.2	59.9	83.0	97.1	105.1
PPYH314800	4.6	15.6	58.5	76.6	86.5	91.6
PPYH124800	4.1	16.6	57.2	70.6	76.0	77.6
PPYH134800	4.8	17.7	50.6	59.1	61.8	61.8
PPYH113900	2.9	12.0	57.8	81.8	97.3	107.6
PPYH114900	2.3	11.5	60.6	88.4	107.2	120.3
PPYH115900	1.9	9.4	53.9	81.9	103.5	121.4

Table 7.9: Gravimetric CO_2 uptake (in $mmolg^{-1}$) *at 25 °C* and various pressures for PPY/SD activated carbons, and PPY/H activated carbons.

Sample	CO_2 uptake [a] ($mmol\ g^{-1}$)					
	0.15 bar	1 bar	10 bar	20 bar	30 bar	40 bar
PPY14800	0.5	2.3	13.2	20.4	26.1	30.8
PPYSD114800	0.04	2.9	14.4	20.4	23.9	25.6
PPYSD115800	0.6	2.6	14.5	21.5	26.2	29.1
PPYSD214800	0.7	2.9	14.1	20	24	26.5
PPYSD314800	0.7	3.3	13	16.8	19.1	20.3
PPYSD124800	0.6	3.1	14.4	20	22.7	24.2
PPYSD134800	0.8	3.41	14.2	19	20.6	21.4
PPYSD113900	0.5	2.3	12	18	21.7	25.0
PPYSD114900	0.5	2.1	10.2	15	17.6	19.8
PPYSD115900	0.5	2.2	10.1	14.2	17	18.9
PPYH114800	0.5	3.3	14.1	20.8	25.1	27.6
PPYH115800	0.8	3.2	14.5	19.6	22.3	23.5
PPYH214800	0.8	3	13.6	18.9	22.1	23.9
PPYH314800	1	3.6	13.3	17.4	19.7	20.8
PPYH124800	1	3.8	13	16.1	17.3	17.6
PPYH134800	1.1	4.02	11.5	13.4	14	14.05
PPYH113900	0.7	2.7	13.4	18.6	22.1	24.5
PPYH114900	0.5	2.6	13.8	20.1	24.1	27.4
PPYH115900	0.4	2.1	12.2	18.6	23.5	27.6

7.6.2.8 Hydrogen Capacity

To date, the best performing carbon-based hydrogen storage materials are zeolite-templated carbons,[69, 117-120] carbide-derived carbons (CDCs)[121] and activated carbons.[17, 21, 80, 122, 123] The highest reported values of hydrogen uptake, at -196 ^{o}C and 20 bar, are between 7 and 8 wt%.[21, 118, 122, 123] Hydrogen storage capacities of the PPY/SD and PPY/H carbons was determined at -196 ^{o}C and in the pressure range 0 – 100 bar using a gravimetric method on a Hiden XEMIS sorption analyser following the procedure discussed in **Chapter 2**. The assessment conditions (at -196 °C and 0 – 100 bar) were chosen due to the fact that cryo-storage has recently received strong consideration as being viable for low-pressure vehicular hydrogen storage.[124-127]

The hydrogen uptake isotherms of the present PPY/SD and PPY/H carbons are presented in **Figure 7.55** and **Figure 7.56**, respectively, and **Table 7.10** summarises the hydrogen storage capacities for both sets of carbons (PPY/SD and PPY/H). The hydrogen uptake isotherms are completely reversible with no hysteresis in the pressure range 0 –100 bar. For porous materials, it is known that the cryogenic hydrogen storage capacity requires high surface area and that narrow micropores (~0.7 nm) are the most efficient hydrogen storage spaces.[37, 117, 119, 128-135] Therefore, in order to improve the hydrogen adsorption capacity, activated carbons with ultrahigh surface area and appropriately sized pores are required. Thus, in this study, only PPY/SD and PPY/H samples with high surface area ≥ 3000 m^2 g^{-1} have been investigated for hydrogen storage.

The hydrogen storage capacity at 1 bar ranges between 2.7 wt% and 3.6 wt% for PPY/SD samples, while for the PPY/H samples it is somewhat lower at 2.3 to 2.8 wt%. An uptake of 3.6 wt% at 1 bar for sample PPYSD124800 is very high

and one of the highest ever reported for carbons.[18, 21, 69, 80, 98, 101, 122, 123, 130, 136-143] The uptake at between 20 bar and 40 bar is an often used measure of a carbons efficiency for hydrogen storage under low to moderate pressure. As shown in **Table 7.10**, at 20 bar, the excess hydrogen uptake of the selected carbons varies between 5.3 and 6.3 wt% for PPY/SD carbons, and 5.0 to 5.6 wt% for the PPY/H set. For PPY/SD carbons activated at 800 ^{o}C and KOH/precursor ratio of 4, the excess hydrogen uptake at 20 bar appears to be determined by several factors; (i) the total surface area with uptake of 6.3 wt% for the highest surface area sample (PPYSD124800), followed (according to the trend in decreasing surface area) by PPYSD114800 with 5.4 wt% and PPYSD214800 with 5.3 wt%; (ii) the trend in micropore surface area, which decreases in the same manner as the hydrogen uptake, and (iii) the PPY:SD ratio in the precursor mix with greater amounts of sawdust appearing to favour higher hydrogen uptake. This may simply be due to the fact that greater amounts of sawdust in the precursor mix lead to higher levels of microporosity, but may also be related to the amount of N in the final activated carbons. Furthermore, by considering the isosteric heat of hydrogen adsorption and excess hydrogen uptake on N-free or N-doped carbons, it is shown that N-doping can be beneficial at lower coverage (low hydrogen uptake) but is detrimental at higher coverage (higher hydrogen uptake). The findings are consistent with previous theoretical predictions on the effect of N-doping of carbon on hydrogen uptake. The findings, therefore, add new insights that are useful for the development of carbon materials with enhanced hydrogen storage capacity.[117]

A comparison between sample PPYSD114900 and PPYSD114800 shows that a rise in the activation temperature from 800 ^{o}C to 900 ^{o}C (at PPY:SD ratio of 1:1) improves the excess hydrogen uptake at 20 bar due presumably to higher total surface area of the sample activated at 900 ^{o}C. In the same manner, a comparison between sample PPYSD115800 and PPYSD114800 shows that a rise

in the KOH/precursor mix ratio from 4 to 5 (at PPY:SD ratio of 1:1) also improves the excess hydrogen uptake at 20 bar due to the higher total surface area of PPYSD115800. These trends emphasise the importance of total surface area rather than just micropore area, in determining the excess hydrogen uptake of the carbons at 20 bar. The importance of total surface area is underlined by considering the trends in hydrogen uptake at 20 bar for the PPY/H set of carbons wherein the uptake follows the trend in total surface area, i.e., sample PPYH114800, which has the highest surface area (3815 m^2 g^{-1}) exhibits the largest uptake (5.6 wt%), while PPYH214800 and PPYH114900 with comparable surface area (3583 m^2 g^{-1} and 3592 m^2 g^{-1}, respectively) have similar uptake of 5.0 wt%.

As shown in **Figure 7.55** and **Figure 7.56**, the carbons achieve their maximum excess uptake at ca. 4 bar. The excess uptake at 40 bar is summarised in **Table 7.10** and generally follows the trends discussed above for uptake at 20 bar. The highest excess uptake at 40 bar is 6.6 wt for sample PPYSD124800, while the lowest is 5.2 wt% for PPYH214800. The total hydrogen uptake of the carbons, which is a key measure of the efficiency of hydrogen storage, has also been determined as described in **Chapter 2** and reported in **Table 7.10**.

For PPY/SD carbons, the total hydrogen uptake at 20 bar is in the range 6.3 to 7.5 wt%. For PPY/H carbons, the total hydrogen uptake at 20 bar is in the range 6.0 to 76.6 wt%. Uptake of 7.5 wt% for sample PPYSD124800 is very impressive and compares favourably with the best carbons reported so far. For context, we note that amongst the best reported hydrogen uptake values under such conditions (-196 ^oC and 20 bar) are; 7.03 wt%,[37] and 7.3 wt%,[21] for polypyrrole-only derived activated and compactivated carbons, respectively, 7.08 wt% for a carbon that was both physically and chemically activated,[123] 7.1 wt%, for a sawdust-derived compactivated carbon,[21] and 7.3 wt% for a zeolite templated

carbon.[144] It is therefore clear that the use of mixed precursors offers carbons with hydrogen uptake that outperforms all previously reported materials generated singly from polypyrrole or sawdust. At 40 bar, for PPY/SD carbons, the total hydrogen uptake is in the range 7.8 to 9.4 wt%, while for PPY/H samples it is 7.7 wt% to 8.7 wt%. A total hydrogen uptake of up to 9.4 wt% at 40 bar is all round very impressive and outperforms that of materials prepared singly from polypyrrole or sawdust.

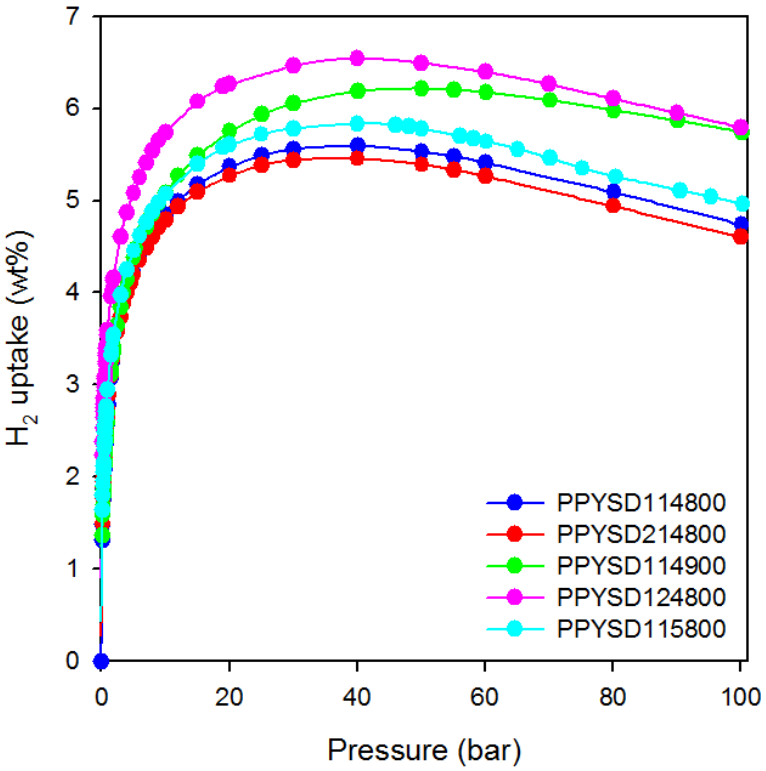


Figure 7.55: Excess H_2 uptake isotherms at -197 °C and pressure range of 0-100 bar for PPY/sawdust-derived activated carbons.

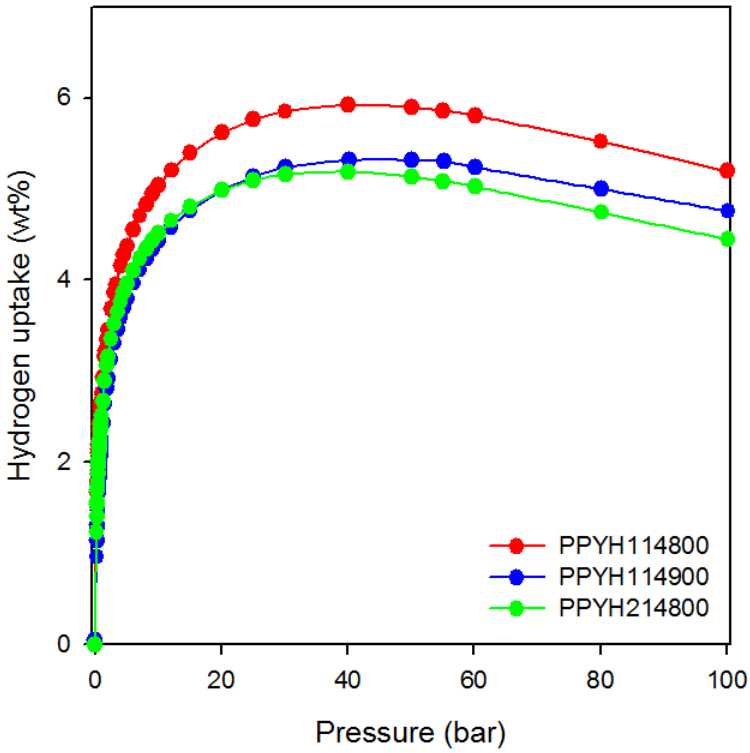


Figure 7.56: Excess H_2 uptake isotherms at -197 °C and pressure range of 0-100 bar for PPY/hydrochar-derived activated carbons.

Table 7.10: Excess and Total H_2 uptake at -196 °C and various pressures for selected ultrahigh surface area activated carbos.

Sample [a]	Surface Area [b] ($m^2\ g^{-1}$)	H_2 Uptake [c] (wt%)		
		1 bar	20 bar [d]	40 bar [d]
PPYSD214800	3085 (452)	2.7	5.3 (6.3)	5.5 (7.8)
PPYSD114800	3279 (1015)	2.7	5.4 (6.4)	5.6 (7.8)
PPYSD124800	3477 (1356)	3.6	6.3 (7.5)	6.6 (8.9)
PPYSD114900	3563	2.7	5.8 (6.8)	6.2 (9.4)
PPYSD115800	3458 (125)	2.9	5.6 (6.6)	5.8 (8.3)
PPYH214800	3583 (887)	2.5	5.0 (6.0)	5.2 (7.7)
PPYH114800	3815 (377)	2.8	5.6 (6.6)	5.9 (8.7)
PPYH114900	3592 (355)	2.3	5.0 (6.0)	5.3 (8.2)

[a] Activated carbons with highest surface area.
[b] The values in the parenthesis refer to micropore surface area.
[c] Excess H_2 uptake (in wt%) at -196 °C.
[d] The values in the parenthesis refer to Total H_2 uptake.

7.7 Conclusions

Homogeneous activated carbons were successfully prepared from premixed precursors containing polypyrrole and sawdust or sawdust derived hydrochar. The sawdust was either added to the polypyrrole directly or following conversion (*via* hydrothermal carbonisation) to hydrochar. The properties of the carbons prepared from premixed precursors were compared to those of carbons generated singly from each of the precursors under similar activation conditions. The premixed precursors offer carbon materials with ultrahigh surface area (up to 3815 $m^2 g^{-1}$) and pore volume (up to ~2.6 $cm^3 g^{-1}$) comprising of mainly two pore systems; one pore size system in the micropore range (6 - 12 Å) and the other in the mesopore range (22 – 35 Å). The mix of mesoporosity and microporosity is such that some samples are predominantly mesoporous depending on the composition of the premixed precursor and activation conditions. Firstly, in general, carbons prepared from polypyrrole and sawdust have greater porosity with higher surface area and pore volume than those generated from polypyrrole and sawdust hydrochar. Secondly, in general, higher amounts of polypyrrole favour greater mesoporosity. Thirdly, the highest proportion of microporosity is generated for samples with greatest amount of sawdust hydrochar in the precursor mix. The choice of precursor mix is therefore key to tailoring the porosity of the carbons. The N-content of the carbons was found to be dependent on the amount of polypyrrole in the precursor mix. However, the N-content was generally low to very low and did not appear to have any direct influence of the gas uptake properties of the carbons.

The mesoporosity of the carbons is found to be ideal for CO_2 uptake under conditions that closely mimic pre combustion carbon capture and storage, i.e., 25 ^oC and pressure of 20 to 40 bar. The best performing carbons are found to be those that have a near total absence of micropores; microporosity appears to

limit high pressure CO_2 uptake. The gravimetric (mmol g^{-1}) CO_2 uptake capacities obtained for the carbons are among the highest ever reported for porous carbons. The carbons also exhibit excellent excess hydrogen uptake of up to 3.6 wt% and 6.3 wt% (at -196 ºC and 1 or 20 bar, respectively), which translates to total uptake of 7.5 wt% (at -196 ºC and 20 bar). The best performing carbons achieve up to 9.4 wt% total hydrogen storage at 40 bar, which is much higher than that of many currently available benchmark materials.

7.8 References

1. S. Choi, J. H. Drese and C. W. Jones, *ChemSusChem*, 2009, **2**, 796-854.

2. H. J. Schellnhuber, *Proc. Natl. Acad. Sci. U.S.A.*, 2011, **108**, 20277-20278.

3. K. Z. House, A. C. Baclig, M. Ranjan, E. A. van Nierop, J. Wilcox and H. J. Herzog, *Proc. Natl. Acad. Sci. U.S.A.*, 2011, **108**, 20428-20433.

4. K. S. Lackner, S. Brennan, J. M. Matter, A. H. A. Park, A. Wright and B. van der Zwaan, *Proc. Natl. Acad. Sci. U.S.A.*, 2012, **109**, 13156-13162.

5. M. E. Boot-Handford, J. C. Abanades, E. J. Anthony, M. J. Blunt, S. Brandani, N. Mac Dowell, J. R. Fernandez, M. C. Ferrari, R. Gross, J. P. Hallett, R. S. Haszeldine, P. Heptonstall, A. Lyngfelt, Z. Makuch, E. Mangano, R. T. J. Porter, M. Pourkashanian, G. T. Rochelle, N. Shah, J. G. Yao and P. S. Fennell, *Energy Environ. Sci.*, 2014, **7**, 130-189.

6. T. C. Drage, C. E. Snape, L. A. Stevens, J. Wood, J. W. Wang, A. I. Cooper, R. Dawson, X. Guo, C. Satterley and R. Irons, *J. Mater. Chem.*, 2012, **22**, 2815-2823.

7. G. P. Hao, W. C. Li, D. Qian and A. H. Lu, *Adv. Mater.*, 2010, **22**, 853–857.

8. J. Silvestre-Albero, A. Wahby, A. Sepúlveda-Escribano, M. Martínez-Escandell, K. Kaneko and F. Rodríguez- Reinoso, *Chem. Commun.*, 2011, **47**, 6840-6842.

9. J. P. Marco-Lozar, M. Kunowsky, F. Suárez-García, J. D. Carruthers and A. Linares-Solano, *Energy Environ. Sci.*, 2012, **5**, 9833-9842.

10. M. Sevilla and A. B. Fuertes, *J. Colloid Interface Sci.*, 2012, **366**, 147-154.

11. K. Sumida, D. L. Rogow, J. A. Mason, T. M. McDonald, E. D. Bloch, Z. R. Herm, T. H. Bae and J. R. Long, *Chem. Rev.*, 2012, **112**, 724-781.

12. Z. J. Zhang, Z. Z. Yao, S. C. Xiang and B. L. Chen, *Energy Environ. Sci.*, 2014, **7**, 2868-2899.

13. R. V. Siriwardane, M. S. Shen and E. P. Fisher, *Energy Fuels*, 2005, **19**, 1153-1159.

14. J. Merel, M. Clausse and F. Meunier, *Ind. Eng. Chem. Res.*, 2008, **47**, 209-215.

15. M. R. Hudson, W. L. Queen, J. A. Mason, D. W. Fickel, R. F. Lobo and C. M. Brown, *J. Am. Chem. Soc.*, 2012, **134**, 1970-1973.

16. F.S. Baker, C.E. Miller, A.J. Repik and E. D. Tolles, *Kirk-Othmer Encyclopedia of Chemical Technology, 5th Edition*, 2003, 741–761.

17. M. Sevilla and R. Mokaya, *Energy Environ Sci.*, 2014, **7**, 1250-1280.

18. J. C. Wang and S. Kaskel, *J. Mater. Chem.*, 2012, **22**, 23710-23725.

19. L. L. Zhang and X. S. Zhao, *Chem. Soc. Rev.*, 2009, **38**, 2520-2531.

20. M. Sevilla, A. B. Fuertes and R. Mokaya, *Int. J. Hydrogen Energy*, 2011, **36**, 15658-15663.

21. B. Adeniran and R. Mokaya, *Nano Energy*, 2015, **16**, 173-185.

22. L. Wei and G. Yushin, *Nano Energy*, 2012, **1**, 552-565.

23. J. Rivera-Utrilla, M. Sánchez- Polo, V. Gomez-Serrano, P. M. Alvarez, M. C. M. Alvim-Ferraz and J. M. Dias, *J. Hazard. Mater.*, 2011, **187**, 1-23.

24. D. Mohan and C. U. Pittman, *J. Hazard. Mater.*, 2006, **137**, 762-811.

25. D. Mohan and C. U. Pittman, *J. Hazard. Mater.*, 2007, **142**, 1-53.

26. T. Otowa, Y. Nojima and T. Miyazaki, *Carbon*, 1997, **35**, 1315-1319.

27. F. a. Çeçen and Ö. Aktas, *Activated Carbon for Water and Wastewater Treatment: Integration of Adsorption and Biological Treatment*, 2012, 1-388.

28. V. K. Gupta, I. Ali, T. A. Saleh, A. Nayak and S. Agarwal, *RSC Adv.*, 2012, **2**, 6380-6388.

29. J. L. Song, S. A. Feng, J. H. Zhao, J. F. Zheng and Z. P. Zhu, *Mater. Res. Bull.*, 2010, **45**, 1234-1239.

30. J. Guo, W. S. Xu, Y. L. Chen and A. C. Lua, *J. Colloid Interface Sci.*, 2005, **281**, 285-290.

31. R. V. Siriwardane, M. S. Shen, E. P. Fisher and J. A. Poston, *Energy Fuels*, 2001, **15**, 279-284.

32. K. T. Chue, J. N. Kim, Y. J. Yoo, S. H. Cho and R. T. Yang, *Ind. Eng. Chem. Res.*, 1995, **34**, 591-598.

33. R. E. Morris and P. S. Wheatley, *Angew. Chem. Int. Ed.*, 2008, **47**, 4966-4981.

34. M. Radosz, X. D. Hu, K. Krutkramelis and Y. Q. Shen, *Ind. Eng. Chem. Res.*, 2008, **47**, 3783-3794.

35. E. Bottani and J. Tascón, *Adsorption by Carbons, 1st Edition*, Elsevier, New York, 2008.

36. Y. D. Xia, Z. X. Yang and Y. Q. Zhu, *J. Mater. Chem. A*, 2013, **1**, 9365-9381.

37. M. Sevilla, R. Mokaya and A. B. Fuertes, *Energy Environ. Sci.*, 2011, **4**, 2930-2936.

38. M. Cox and R. Mokaya, *Sustainable Energy & Fuels*, 2017, **1**, 1414-1424.

39. L. Wei, M. Sevilla, A. B. Fuertes, R. Mokaya and G. Yushin, *Adv. Funct. Mater.*, 2012, **22**, 827-834.

40. B. Adeniran and R. Mokaya, *Chem. Mater.*, 2016, **28**, 994-1001.

41. M. Sevilla, N. Alam and R. Mokaya, *J. Phys. Chem. C*, 2010, **114**, 11314-11319.

42. Y. W. Zhu, S. Murali, M. D. Stoller, K. J. Ganesh, W. W. Cai, P. J. Ferreira, A. Pirkle, R. M. Wallace, K. A. Cychosz, M. Thommes, D. Su, E. A. Stach and R. S. Ruoff, *Science*, 2011, **332**, 1537-1541.

43. M. Sevilla and A. B. Fuertes, *Energy Environ. Sci.*, 2011, **4**, 1765-1771.

44. M. Nandi, K. Okada, A. Dutta, A. Bhaumik, J. Maruyama, D. Derks and H. Uyama, *Chem. Commun.*, 2012, **48**, 10283-10285.

45. N. Balahmar, A. C. Mitchell and R. Mokaya, *Adv. Energy Mater.*, 2015, **5**.

46. H. M. Coromina, D. A. Walsh and R. Mokaya, *J. Mater. Chem. A*, 2016, **4**, 280-289.

47. E. A. Hirst, A. Taylor and R. Mokaya, *J. Mater. Chem. A*, 2018, **6**, 12393-12403.

48. K. Y. Foo and B. H. Hameed, *Bioresour. Technol.*, 2012, **111**, 425-432.

49. M. Sevilla, C. Falco, M. M. Titirici and A. B. Fuertes, *Rsc Advances*, 2012, **2**, 12792-12797.

50. M. Sevilla, P. Valle-Vigon and A. B. Fuertes, *Adv. Funct. Mater.*, 2011, **21**, 2781-2787.

51. H. M. Coromina, D. A. Walsh and R. Mokaya, *J. Mater. Chem.*, 2016, **4**, 280-289.

52. M. Sevilla, W. Sangchoom, N. Balahmar, A. B. Fuertes and R. Mokaya, *ACS Sustainable. Chem. Eng.*, 2016, **4**, 4710-4716.

53. N. Balahmar, A. S. Al-Jumialy and R. Mokaya, *J. Mater. Chem. A*, 2017, **5**, 12330-12339.

54. M. Nishizawa, H. Nozaki, H. Kaji, T. Kitazume, N. Kobayashi, T. Ishibashi and T. Abe, *Biomaterials*, 2007, **28**, 1480-1485.

55. M. Chougule, S. Pawar, P. Godse, R. Mulik, Shashwati Sen and V. Patil, *SNL*, 2011, **1**.

56. R. Partch, S. G. Gangolli, E. Matijevic, W. Cai and S. Arajs, *J. Colloid Interface Sci.*, 1991, **144**, 27-35.

57. S. Ahmad, B. Gangaraj, H. Eisazadeh and E. Sadeghi, *J. Vinyl Addit. Technol.*, 2016, **22**, 362-367.

58. P. Gahiout and V. Choudhary, *Synth. Met.*, 2016, **222**, 170-179.

59. M. Poletto, A. J. Zattera, M. M. C. Forte and R. M. C. Santana, *Bioresour. Technol.*, 2012, **109**, 148-153.

60. S. Naik, V. V. Goud, P. K. Rout, K. Jacobson and A. K. Dalai, *Renew. Energy*, 2010, **35**, 1624-1631.

61. S. Kumar, V. A. Loganathan, R. B. Gupta and M. O. Barnett, *J. Environ. Manage.*, 2011, **92**, 2504-2512.

62. S. M. Kang, X. H. Li, J. Fan and J. Chang, *Ind. Eng. Chem. Res.*, 2012, **51**, 9023-9031.

63. X. P. Wu, W. Y. Zhu, X. L. Zhang, T. H. Chen and R. L. Frost, *Appl. Clay Sci.*, 2011, **52**, 400-406.

64. Z. L. Xie, R. J. White, J. Weber, A. Taubert and M. M. Titirici, *J. Mater. Chem.*, 2011, **21**, 7434-7442.

65. L. X. Wang, X. G. Li and Y. L. Yang, *React. Funct. Polym.*, 2001, **47**, 125-139.

66. F. C. Wu and R. L. Tseng, *J. Colloid Interface Sci.*, 2006, **294**, 21-30.

67. E. Haffner-Staton, N. Balahmar and R. Mokaya, *J. Mater. Chem. A*, 2016, **4**, 13324-13335.

68. F. C. Wu, R. L. Tseng and R. S. Juang, *Sep. Purif. Technol.*, 2005, **47**, 10-19.

69. M. Sevilla, A. B. Fuertes and R. Mokaya, *Energy Environ. Sci.*, 2011, **4**, 1400-1410.

70. M. Sevilla and A. B. Fuertes, *Chem. Eur. J.*, 2009, **15**, 4195-4203.

71. H. S. Kambo and A. Dutta, *Energy Conv. Manag.*, 2015, **105**, 746-755.

72. J. X. Cai, B. Li, C. Y. Chen, J. Wang, M. Zhao and K. Zhang, *Bioresour. Technol.*, 2016, **220**, 305-311.

73. S. Nizamuddin, N. S. J. Kumar, J. N. Sahu, P. Ganesan, N. M. Mubarak and S. A. Mazari, *Can. J. Chem. Eng.*, 2015, **93**, 1916-1921.

74. Q. Xu, Q. F. Qian, A. Quek, N. Ai, G. N. Zeng and J. W. Wang, *ACS Sustain. Chem. Eng.*, 2013, **1**, 1092-1101.

75. L. Muniandy, F. Adam, A. R. Mohamed and E. P. Ng, *Microporous Mesoporous Mater.*, 2014, **197**, 316-323.

76. R. Pietrzak, P. Nowicki, J. Kazmierczak, I. Kuszynska, J. Goscianska and J. Przepiorski, *Chem. Eng. Res. Des.*, 2014, **92**, 1187-1191.

77. K. Zeng, D. P. Minh, D. Gauthier, E. Weiss-Hortala, A. Nzihou and G. Flamant, *Bioresource Technol.*, 2015, **182**, 114-119.

78. V. Makrigianni, A. Giannakas, C. Daikopoulos, Y. Deligiannakis and I. Konstantinou, *App. Catal. B*, 2015, **174**, 244-252.

79. G. Chattopadhyaya, D. G. Macdonald, N. N. Bakhshi, J. S. Soltan and A. K. Dalai, *Fuel Proces. Technol.*, 2006, **87**, 997-1006.

80. W. Sangchoom and R. Mokaya, *ACS Sustainable Chem. Eng.*, 2015, **3**, 1658-1667.

81. M. X. Fang, D. K. Shen, Y. X. Li, C. J. Yu, Z. Y. Luo and K. F. Cen, *J. Anal. Appl. Pyrolysis*, 2006, **77**, 22-27.

82. M. L. Martínez , M. M. Torres, C. A. Guzmán and D. M. Maestri, *Ind. Crops. Prod.*, 2006, **23**, 23-28.

83. M. Sevilla, J. A. Maciá-Agulló and A. B. Fuertes, *Biomass Bioenergy*, 2011, **35**, 3152-3159.

84. A. Kajdos, A. Kvit, F. Jones, J. Jagiello and G. Yushin, *J. Ame. Chem. Soc.*, 2010, **132**, 3252-3253.

85. M. Rose, Y. Korenblit, E. Kockrick, L. Borchardt, M. Oschatz, S. Kaskel and G. Yushin, *Small*, 2011, **7**, 1108-1117.

86. Y. Korenblit, M. Rose, E. Kockrick, L. Borchardt, A. Kvit, S. Kaskel and G. Yushin, *ACS Nano*, 2010, **4**, 1337-1344.

87. Z. G. Cambaz, G. N. Yushin, Y. Gogotsi, K. L. Vyshnyakova and L. N. Pereselentseva, *J. Am. Ceram. Soc.*, 2006, **89**, 509-514.

88. A. B. Fuertes and T. A. Centeno, *J. Mater. Chem.*, 2005, **15**, 1079-1083.

89. C. M. Yang, C. Weidenthaler, B. Spliethoff, M. Mayanna and F. Schuth, *Chem. Mater.*, 2005, **17**, 355-358.

90. M. Lezanska, P. Pietrzyk and Z. Sojka, *J. Phys. Chem. C*, 2010, **114**, 1208-1216.

91. T. Y. Zhang, W. P. Walawender, L. T. Fan, M. Fan, D. Daugaard and R. C. Brown, *Chem. Eng. J.*, 2004, **105**, 53-59.

92. E. Demirbas, N. Dizge, M. T. Sulak and M. Kobya, *Chem. Eng. J.*, 2009, **148**, 480-487.

93. M. J. Martin, A. Artola, M. D. Balaguer and M. Rigola, *Chem. Eng. J.*, 2003, **94**, 231-239.

94. I. A. W. Tan, B. H. Hameed and A. L. Ahmad, *Chem. Eng. J.*, 2007, **127**, 111-119.

95. J. X. Han, Z. J. Du, W. Zou, H. Q. Li and C. Zhang, *Chem. Eng. J.*, 2015, **262**, 571-578.

96. N. K. Hamadi, X. D. Chen, M. M. Farid and M. G. Q. Lu, *Chem. Eng. J.*, 2001, **84**, 95-105.

97. J. Acharya, J. N. Sahu, C. R. Mohanty and B. C. Meikap, *Chem. Eng. J.*, 2009, **149**, 249-262.

98. B. Adeniran and R. Mokaya, *J. Mater. Chem. A*, 2015, **3**, 5148-5161.

99. N. P. Wickramaratne and M. Jaroniec, *ACS Appl. Mater. Interfaces*, 2013, **5**, 1849-1855.

100. N. P. Wickramaratne and M. Jaroniec, *J. Mater. Chem. A*, 2013, **1**, 112-116.

101. B. Adeniran, E. Masika and R. Mokaya, *J. Mater. Chem. A*, 2014, **2**, 14696-14710.

102. X. Q. Fan, L. X. Zhang, G. B. Zhang, Z. Shu and J. L. Shi, *Carbon*, 2013, **61**, 423-430.

103. M. Saleh, J. N. Tiwari, K. C. Kemp, M. Yousuf and K. S. Kim, *Environ. Sci. Technol.*, 2013, **47**, 5467-5473.

104. H. R. Wei, S. B. Deng, B. Y. Hu, Z. H. Chen, B. Wang, J. Huang and G. Yu, *ChemSusChem*, 2012, **5**, 2354-2360.

105. Z. S. Zhang, J. Zhou, W. Xing, Q. Z. Xue, Z. F. Yan, S. P. Zhuo and S. Z. Qiao, *Phys. Chem. Chem. Phys.*, 2013, **15**, 2523-2529.

106. M. C. Baquero, L. Giraldo, J. C. Moreno, F. Suárez - García , A. Martínez -Alonso and J. M. D. Tascȯn *, J. Anal. Appl. Pyrolysis*, 2003, **70**, 779-784.

107. G. Srinivas, J. Burress and T. Yildirim, *Energy Environ. Sci.*, 2012, **5**, 6453-6459.

108. A. Almasoudi and R. Mokaya, *J. Mater. Chem. A*, 2014, **2**, 10960-10968.

109. C. Robertson and R. Mokaya, *Microporous Mesoporous Mater.*, 2013, **179**, 151-156.

110. J. Silvestre-Albero, A. Wahby, A. Sepulveda-Escribano, M. Martinez-Escandell, K. Kaneko and F. Rodriguez-Reinoso, *Chem. Commun.*, 2011, **47**, 6840-6842.

111. J. P. Marco-Lozar, M. Kunowsky, F. Suarez-Garcia, J. D. Carruthers and A. Linares-Solano, *Energy Environ. Sci.*, 2012, **5**, 9833-9842.

112. J. J. He, J. W. F. To, P. C. Psarras, H. P. Yan, T. Atkinson, R. T. Holmes, D. Nordlund, Z. N. Bao and J. Wilcox, *Adv. Energy Mater.*, 2016, **6**, 11.

113. Q. A. Wang, J. Z. Luo, Z. Y. Zhong and A. Borgna, *Energy Environ. Sci.*, 2011, **4**, 42-55.

114. Y. D. Xia, R. Mokaya, G. S. Walker and Y. Q. Zhu, *Adv. Energy Mater.*, 2011, **1**, 678-683.

115. V. Presser, J. McDonough, S. H. Yeon and Y. Gogotsi, *Energy Environ. Sci.*, 2011, **4**, 3059-3066.

116. X. Hu, M. Radosz, K. A. Cychosz and M. Thommes, *Environ. Sci.Technol.*, 2011, **45**, 7068-7074.

117. Y. D. Xia, G. S. Walker, D. M. Grant and R. Mokaya, *J. Am. Chem. Soc.*, 2009, **131**, 16493-16499.

118. Y. D. Xia, R. Mokaya, D. M. Grant and G. S. Walker, *Carbon*, 2011, **49**, 844-853.

119. N. Alam and R. Mokaya, *Energy Environ. Sci.*, 2010, **3**, 1773-1781.

120. Y. Xia and R. Mokaya, *J. Phys. Chem. C*, 2007, **111**, 10035-10039.

121. G. Yushin, R. Dash, J. Jagiello, J. E. Fischer and Y. Gogotsi, *Adv. Funct. Mater.*, 2006, **16**, 2288-2293.

122. B. Panella, M. Hirscher and S. Roth, *Carbon*, 2005, **43**, 2209-2214.

123. H. L. Wang, Q. M. Gao and J. Hu, *J. Am. Chem. Soc.*, 2009, **131**, 7016-7022.

124. T. S. Blankenship and R. Mokaya, *Energy Environ. Sci.*, 2017, **10**, 2552-2562.

125. D. A. Gómez-Gualdrón, Y. J. Colón, X. Zhang, T. C. Wang, Y. S. Chen, J. T. Hupp, T. Yildirim, O. K. Farha, J. Zhang and R. Q. Snurr, *Energy Environ. Sci.*, 2016, **9**, 3279-3289.

126. U. Eberle, B. Müller and R. von Helmolt, *Energy Environ. Sci.*, 2012, **5**, 8780-8798.

127. U. Eberle and R. von Helmolt, *Energy Environ. Sci.*, 2010, **3**, 689-699.

128. N. Texier-Mandoki, J. Dentzer, T. Piquero, S. Saadallah, P. David and C. Vix-Guterl, *Carbon*, 2004, **42**, 2744-2747.

129. S. K. Bhatia and A. L. Myers, *Langmuir*, 2006, **22**, 1688-1700.

130. Z. X. Yang, Y. D. Xia and R. Mokaya, *J. Am. Chem. Soc.*, 2007, **129**, 1673-1679.

131. I. Cabria, M. J. López and J. A. Alonso, *Carbon*, 2007, **45**, 2649-2658.

132. A. Pacula and R. Mokaya, *J. Phys. Chem. C*, 2008, **112**, 2764-2769.

133. Y. Gogotsi, C. Portet, S. Osswald, J. M. Simmons, T. Yidirim, G. Laudisio and J. E. Fischer, *Int. J. Hydrogen Energy*, 2009, **34**, 6314-6319.

134. X. B. Zhao, B. Xiao, A. J. Fletcher and K. M. Thomas, *J. Phys. Chem. B*, 2005, **109**, 8880-8888.

135. D. Hulicova-Jurcakova, M. Seredych, G. Q. Lu and T. J. Bandosz, *Adv. Funct. Mater.*, 2009, **19**, 438-447.

136. M. Sevilla and R. Mokaya, *Energy Environ. Sci.*, 2014, **7**, 1250-1280.

137. J. Juan-Juan, J. P. Marco-Lozar, F. Suárez-García, D. Cazorla-Amorós and A. Linares-Solano, *Carbon*, 2010, **48**, 2906-2909.

138. T. S. Blankenship, N. Balahmar and R. Mokaya, *Nat. Commun.*, 2017, **8**, 12.

139. G. Sethia and A. Sayari, *Carbon*, 2016, **99**, 289-294.

140. M. Jordá-Beneyto, F. Suárez-García, D. Lozano-Castelló, D. Cazorla-Amorós and A. Linares-Solano, *Carbon*, 2007, **45**, 293-303.

141. M. Jordá-Beneyto, D. Lozano-Castelló , F. Suárez-García , D. Cazorla-Amorós and A. Linares-Solano, *Microporous Mesoporous Mater.*, 2008, **112**, 235-242.

142. A. Almasoudi and R. Mokaya, *Microporous Mesoporous Mater.*, 2014, **195**, 258-265.

143. J. Burress, M. Kraus, M. Beckner, R. Cepel, G. Suppes, C. Wexler and P. Pfeifer, *Nanotechnology*, 2009, **20**, 10.

144. E. Masika and R. Mokaya, *Energy Environ. Sci.*, 2014, **7**, 427-434.

Chapter 8. Conclusion and Further Work

8.1 Conclusion

In summary, in this thesis, the development of nanostructured carbonaceous materials (activated carbons or zeolite templated carbons), with high and ultrahigh surface area, tuneable porosity, and promising CO_2 and H_2 storage capacities, have been successfully obtained and investigated.

Synthesis Routes

Porous nanostructured carbon materials have been synthesised using three synthesis routes;

1. Zeolite templated carbons (ZTCs), *via* a nanocasting technique using zeolite 13X and zeolite Y as hard templates. The effects of zeolite compaction before use as hard templates was investigated through the compression of powder forms of zeolites at 370 MPa (equivalent to 5 tonnes) or 740 MPa (equivalent to 10 tonnes) prior to their use as templates.

2. Activated carbons using KOH as activating agent with a variety of carbon precursors, including Eucalyptus wood sawdust biomass, polythiophene and polypyrrole. The activated carbons prepared *via* two different routes;

The properties of generated carbon materials (activated carbons or zeolite templated carbons) was effected by many factors, which were examined by many characterization techniques as shown in **Figure 8.1**.

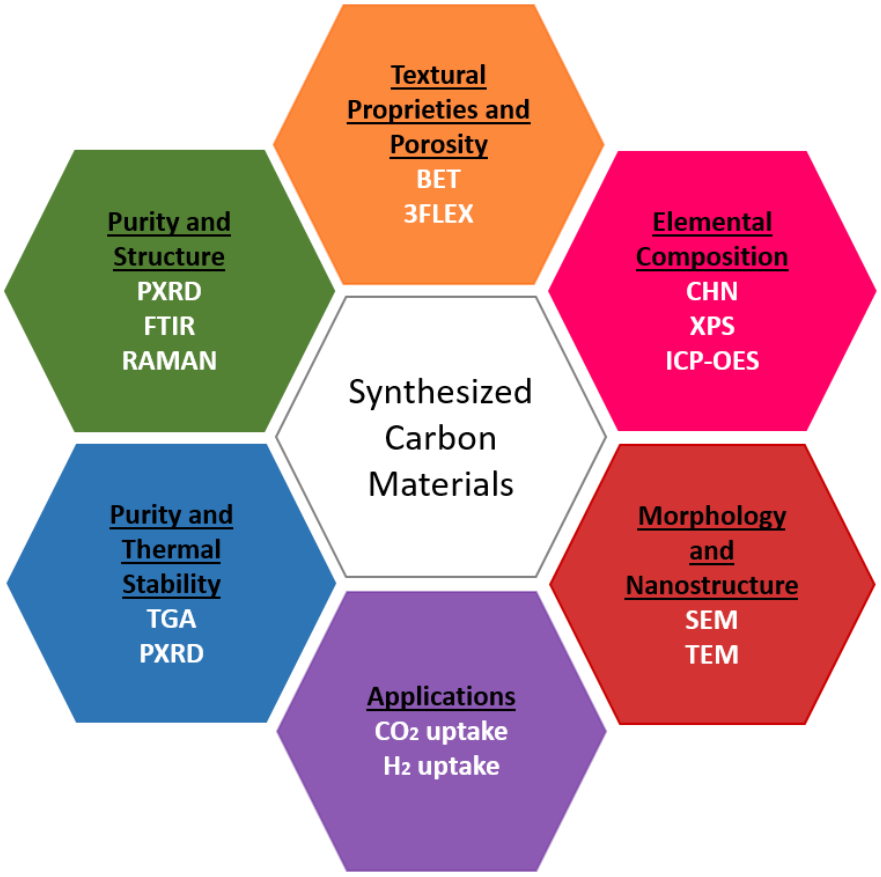


Figure 8.1: Schematic of investigation steps of synthesised carbon materials

Chapter 3, explores the use of zeolite Y and zeolite 13X compacted at 370 MPa or 740 MPa as hard templates for the preparation of pelletized zeolite templated carbons (ZTCs). The templating process involved liquid impregnation of zeolite 13X with furfuryl alcohol followed by chemical vapour deposition (CVD) of ethylene at variable CVD temperatures. The use of compacted zeolite pellets results in pelletized ZTCs that simultaneously

exhibit higher porosity and higher packing density, which translates to highly enhanced volumetric gas (H_2 uptake and CO_2 capture).

In Chapter 4, activated carbons derived from a sulphur-rich polymer (polythiophene. PTh) as a carbon precursor have been successfully synthesized by one-step chemical activation using KOH as activating agent. The activation process was performed for 1 h under nitrogen atmosphere, KOH/PTh weight ratio of 2:1 and various reaction temperatures in the 600-800 ^oC range. Conventional activated carbons obtained at 800 ^oC (sample PT2800) have high surface area of up to 2035 m^2g^{-1}, pore volume of up to 1.3 cm^3g^{-1} with micropores of size 0.7 nm - 1.1 nm, and achieve excess hydrogen uptake of 4.2 wt% at -196 ^oC and 20 bar. Sample PT2800 also exhibits attractive excess CO_2 uptake; 21 mmol g^{-1} (at 25 ^oC and 40 bar), 19 mmol g^{-1} (at 25 ^oC and 20 bar), and 25 mmol g^{-1} (at 0 ^oC and at 20 bar). On the other hand, compactivated carbons, prepared *via* a route that includes compaction of the polythiophene at load of *10 tonnes* equivalent to compression pressure of 740 MPa prior to activation, exhibited higher porosity. The compactivated carbon prepared at 800 ^oC (sample PT2800P) has surface area and pore volume of 2250 m^2g^{-1} and 1.6 cm^3g^{-1}, respectively but with no change in the micropores size range of 0.7 nm - 1.1 nm. The higher porosity resulted in an increase in gas uptake; excess hydrogen storage capacity at -196 ^oC and 20 bar of 4.8 wt%, with CO_2 storage capacity of 21 mmol g^{-1} (at 25 ^oC and at 20 bar) and 29 mmol g^{-1} at 0 ^oC. Their ease of preparation and high uptake makes the polythiophene-derived carbons attractive for hydrogen and CO_2 storage.

In Chapter 5, novel mechanochemical activation generates biomass-derived carbons with unprecedented CO_2 storage capacity due to higher porosity than analogous conventionally activated carbons. The

mechanochemical activation, or so-called compactivation, process involves compression, at 740 MPa, of mixtures of activating agent (KOH) and biomass hydrochar into pellets/disks prior to thermal activation. Despite the increase in surface area and pore volume of between 25% and 75% compared to conventionally activated carbons, virtually all of the porosity of the biomass (sawdust and lignin) derived mechanochemically activated carbons is from small micropores (5.8–6.5 Å), which results in a dramatic increase in CO_2 storage capacity at 25 °C and low pressure (≤1 bar). The ambient temperature CO_2 uptake for a carbon derived from sawdust at 600 °C and a KOH/carbon ratio of 2, rises from 1.3 to 2.0 mmol g^{-1} at 0.15 bar, and from 4.3 to 5.8 mmol g −1 at 1 bar, which is the highest ever reported for carbonaceous materials. The mechanochemically activated carbons have a superior CO_2 working capacity for pressure swing adsorption and vacuum swing adsorption processes and, due to a high packing density, they exhibit excellent volumetric CO_2 uptake that is higher than for any material reported to date.

In Chapter 6, activated carbons were successfully produced from eucalyptus sawdust wood biomass using KOH as activating agent at different ratio (2 or 4) and different activation temperature (600 ^oC, 700 ^oC, or 800 ^oC) *via* direct activation offering the advantages of simplicity, lower cost and a greener more sustainable synthesis route, and have properties that are similar or superior to analogous carbons prepared *via* conventional methods which negates the need for hydrothermal carbonisation or pyrolysis. In particular the textural properties and level of graphitic ordering was found to be similar to that of conventionally generated activated carbons. The nature of the direct activation, however, generated carbons with a monolith-like particle morphology. Depending of the activation conditions, the porosity of the directly activated carbons can be tailored to primarily arises from pore

channels of size 5 Å – 7 Å pores, which favour post-combustion CO_2 uptake and thus the carbons capture up to 1.3 mmol g^{-1} and 4.6 mmol g^{-1} at 0.15 bar and 1 bar, respectively, and 25 ^oC. At higher levels of activation, directly activated carbons with greater proportion of larger micropores (10 Å – 20 Å pores) and small mesopores (20 Å – 30 Å pores) can be generated that have optimized CO_2 uptake at moderate to high pressure, for example up to 22 mmol g^{-1} at 20 bar and 25 ^oC or 31 mmol g^{-1} at 20 bar and 0 ^oC.

Chapter 7, reports the preparation of high to very high surface area activated carbons (up to 3815 m^2 g^{-1}) and pore volume (up to ~2.6 cm^3 g^{-1}) comprising of mainly two pore systems; one pore size system in the micropore range (6 - 12 Å) and the other in the mesopore range (22 – 35 Å), from premixed precursors containing polypyrrole and sawdust or sawdust derived hydrochar. The carbons were prepared *via* two ways, namely (i) direct activation of mixtures of polypyrrole and sawdust, or (ii) conversion of sawdust to hydrochar followed by activation of polypyrrole/hydrochar mixtures. The activation conditions (i.e., amount of activating agent KOH, ratio of polypyrrole to sawdust or sawdust hydrochar and activating temperature) were varied as a means of targeting porosity and elemental compositions (i.e., N content) in an attempt to generate materials that are suitable for CO_2 or hydrogen uptake. The mix of mesoporosity and microporosity is such that some samples are predominantly mesoporous. Carbons prepared from polypyrrole and sawdust have greater porosity (higher surface area and pore volume) than those generated from polypyrrole and sawdust hydrochar, and higher amounts of polypyrrole favour greater mesoporosity. On the other hand, the highest proportion of microporosity is generated for samples with greatest amount of sawdust hydrochar in the precursor mix. The best performing carbons for CO_2 uptake at moderate pressure (20 – 40 bar) and room temperature are those that have a near total absence of micropores; microporosity appears to

limit high pressure CO_2 uptake. The gravimetric (mmol g^{-1}) CO_2 uptake capacities obtained for the carbons are among the highest ever reported for porous carbons. The carbons also exhibit excellent excess hydrogen uptake of up to 3.6 wt% and 6.3 wt% (at -196 ºC and 1 or 20 bar, respectively), which translates to total uptake of 7.5 wt% (at -196 ºC and 20 bar). The best performing carbons achieve up to 9.4 wt% total hydrogen storage at 40 bar, which is much higher than that of many currently available benchmark materials.

Table 8.1: Summarized the best performing samples with their proprieties.

Chapter Number	Sample	Packing Density (g cm^{-3})	Surface Area (m^2 g^{-1})	Pore Volume (cm^3 g^{-1})	Pore Size (Å)	CO_2 Uptake (mmol g^{-1})		H_2 Uptake (mmol g^{-1})	
						1 bar	20 bar	wt%	gl^{-1}
Chapter 3 Zeolite Templated Carbons using Z13X and ZY as hard templates (compaction route)	CZ13XP	0.82	2038 (1601)	1.22 (0.75)	7.5/12/24	2.8 (101)	13.1 (473)	-	-
	CZYP	0.88	1897(1413)	1.29 (0.66)	8/11.5/24	2.5 (97)	13.7 (531)	-	-
	CZ13XFAET	0.69	2702 (2341)	1.30 (0.95)	7.5/12	2.5 (48)	18.6 (360)	5.5 (4.7)	24 (21)
	CZ13XFAETP	0.44	3021(2448)	1.56 (1.00)	7.5/12	2.6 (79)	22.0 (668)	6.6 (5.5)	46 (38)
Chapter 4 Direct Activated and Compactivated carbons using polythiophene as a carbon precursor and KOH as activation agent	PT2800	-	2035 (1414)	1.30 (0.65)	6.4/8/11.79	3.4	18.8	4.2	-
	PT2800P	-	2250 (1964)	1.44 (0.90)	7.3/8.6/11.8	3.2	21.1	4.8	-
Chapter 5 Compactivated carbons using sawdust SD and lignin L as carbon precursor and KOH as activation agent	SD2650P	-	1313 (1258)	0.72 (0.60)	6.5/8.5	5.3	11.6	-	-
	L2600P	-	2224 (2089)	1.02 (0.91)	6/7/9/12	4.5	12.8	-	-
Chapter 6 Activated carbons using sawdust and its respective hydrochar as carbon precursors and KOH as activation agent	SD2800D	-	2274 (1923)	1.20 (0.90)	7/12/20	3.6	17.5	-	-
	SD2800	-	2377 (1512)	1.40 (0.70)	7/12/25	3.6	18.1	-	-
	SD4800D	-	2980 (478)	2.10 (0.30)	8/12/30	2.7	21.8	-	-
	SD4800	-	2783 (694)	1.80 (0.36)	8/12/30	3.0	21.7	-	-
Chapter 7 Activated carbons using sawdust and its respective hydrochar and polypyrrole as carbon precursors and KOH as activation agent	PPYSD114800	-	3279 (1015)	1.70 (0.39)	6/8/12/22	2.9	20.8	5.4 (6.4)	-
	PPYSD115800	-	3458 (125)	1.95 (0.05)	6/8/12/28	2.6	21.5	5.6 (6.6)	-
	PPYH114800	-	3815 (377)	2.18 (0.16)	6/8/12/28	3.3	20.8	5.6 (6.6)	-
	PPYH114900	-	3592 (355)	2.25 (0.15)	5/8/12/28/36	2.6	20.1	5.0 (6.0)	-

8.2 Further Work

There are several areas that are worthy of additional investigation in this thesis such as; the effect of varying the experiment parameters on the produced carbons, applying additional techniques and exploring other possible applications.

The experiment parameters that might be explored include; KOH was used as activating agent, but there is scope to investigate other possible activators that may be milder and more amenable to generating targeted pores. The environmental impacts of the activation agent can be minimized by choice of a less corrosive substitute. It may also be interesting to study the effect of non-carbon impurities before HCl washing on CO_2 and H_2 adsorption, and also to study the effect of heating ramp rate of activation process.

Additional techniques that could be used to investigate the produced carbons include SEM combined with EDX to study the non-carbon residues. Copley Tapped Density Tester could be used to study the Tapped Density. Bulk density measurements by using a Micromeritics AutoPore IV. X-ray fluorescence analytical technique (XRF) could be used to determine the elemental composition of the carbons materials.

Several possible applications of activated carbons and zeolite templated carbons can be highlighted for future research such as; pelletized ZTCs which possess very high surface area and excellent mechanical stability, which can be used for storage of other gases such as methane, acetylene and natural gas, and separation of CO_2 and methane. Using high surface area; nanostructured activated carbons ACs, as electrode materials for supercapacitors, due to their properties such as; large surface area, good electrical conductivity and low manufacturing costs due to their synthesise

from readily available, cheap and renewable waste materials. Furthermore, the influence of porous structure on the electrochemical capacitive performance could be investigated. The carbons can be studied as air filters to remove undesired compounds or as odour reduction from the breathable air.